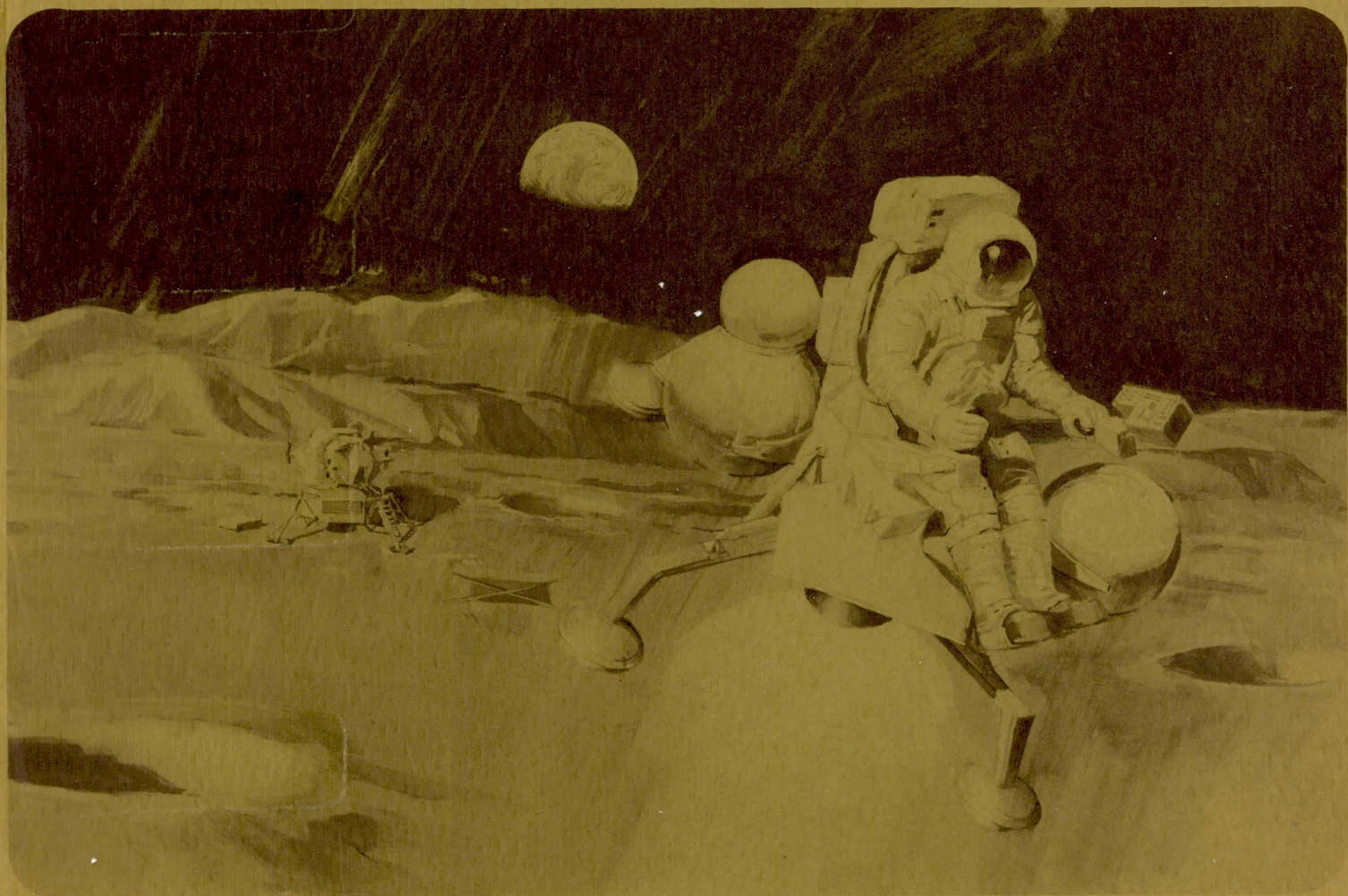


CASE FILE  
COPY

N69-38204  
NASA-CR-101919

SD 69-419-3



Study of **ONE-MAN LUNAR FLYING VECHICLE**  
**FINAL REPORT**

Volume III  
Subsystem Studies



Space Division  
North American Rockwell

NASA CR 101919

SD 69-419-3

STUDY OF ONE-MAN LUNAR FLYING VEHICLE  
FINAL REPORT

VOLUME III  
SUBSYSTEM STUDIES

Contract NAS9-9045

31 August 1969



## FOREWORD

This volume presents the results of the subsystem studies for the one man lunar flying vehicle. This work was performed under the One-Man Lunar Flying Vehicle Contract (NAS9-9045), conducted by the North American Rockwell Space Division for the National Aeronautics and Space Administration Manned Spacecraft Center, Houston, Texas. Each of the three sections contained in this volume (Propulsion, Control, and Thermal) have separate introductions. Other volumes of this final report are:

- Volume 1. Summary
- Volume 2. Mission Analysis
- Volume 4. Configuration Design
- Volume 5. Preliminary Design and Specifications
- Volume 6. Resources and Training Plans

TECHNICAL REPORT INDEX/ABSTRACT

ACCESSION NUMBER				DOCUMENT SECURITY CLASSIFICATION UNCLASSIFIED			
TITLE OF DOCUMENT STUDY OF ONE-MAN LUNAR FLYING VEHICLE - FINAL REPORT: VOLUME 1 - SUMMARY; VOLUME 2 - MISSION ANALYSIS; VOLUME 3 - SUBSYSTEM STUDIES; VOLUME 4 - CONFIGURATION DESIGN; VOLUME 5 - PRELIMINARY DESIGN AND SPECIFICATIONS; VOLUME 6 - TRAINING AND RESOURCES PLANS						LIBRARY USE ONLY	
AUTHOR(S)							
CODE QN085282	ORIGINATING AGENCY AND OTHER SOURCES NORTH AMERICAN ROCKWELL, SPACE DIVISION				DOCUMENT NUMBER SD69-419-1,-2,-3,-4,-5,-6		
PUBLICATION DATE 31AUG69				CONTRACT NUMBER NAS9-9045			
DESCRIPTIVE TERMS *ONE-MAN LUNAR FLYING VEHICLE, *CONTROL SYSTEMS, *PROPULSION SYSTEMS, *TRAJECTORIES, *DESIGN, *TRAINING, *RESOURCES, *MISSION ANALYSIS							

ABSTRACT

THE PRIMARY OBJECTIVES OF THIS STUDY WERE TO OPTIMIZE THE DESIGN AND TO DEVELOP SYSTEM SPECIFICATIONS OF THE LUNAR FLYING VEHICLE. THE SCOPE ENCOMPASSED PARAMETRIC INVESTIGATIONS, CONCEPT GENERATION, AND EVALUATION EFFORT FOR THE DEFINITION OF A RECOMMENDED CONCEPT; PRODUCTION OF A PRELIMINARY DESIGN AND DEVELOPMENT OF SYSTEMS SPECIFICATIONS OF THE RECOMMENDED CONCEPT; AND DEFINITION OF RESOURCES AND CREW TRAINING PLANS. IN ADDITION TO GENERATION OF THE LFV DESIGN, THE SCOPE OF THE STUDY INCLUDED LUNAR MODULE INTEGRATION, FLIGHT SUIT INTERFACE STUDIES, AND DEFINITION OF GROUND SUPPORT EQUIPMENT FOR EARTH AND LUNAR OPERATIONS.

AS A RESULT OF PARAMETRIC STUDIES CONDUCTED DURING THE FIRST PHASE OF THIS EFFORT, A CONCEPT WAS SELECTED WHICH HAS THE FOLLOWING CHARACTERISTICS: /1/ STABILITY-AUGMENTED CONTROL, /2/ FOUR GIMBALED ENGINES WHICH ARE CLUSTERED BENEATH THE VEHICLE, /3/ A SEATED PILOT POSITION, AND /4/ AN INTEGRAL X-FRAME LANDING GEAR WITH 6 HYDRAULIC ATTENUATORS. THIS VEHICLE IS CAPABLE OF CARRYING A 370-LB PAYLOAD IN ADDITION TO THE PILOT. THE DRY WEIGHT OF THE VEHICLE IS 304 LB. WHEN LOADED WITH 300 POUNDS OF LM DESCENT STAGE PROPELLANTS, THE VEHICLE CAN OPERATE WITH A 4.6 NAUTICAL MILE RADIUS WITH NO PAYLOAD.

## CONTENTS

Section	Page
I	<b>PROPULSION SUBSYSTEM STUDIES . . . . . 1</b> SUMMARY . . . . . 1 <b>PARAMETRIC SYSTEM STUDIES . . . . . 3</b> Scope of Study . . . . . 3 Basic Engine Considerations . . . . . 3 Propulsion Subsystem Arrangement . . . . . 14 Engine Optimization Study . . . . . 24 Thrust Vector Control . . . . . 96 <b>PROPULSION SYSTEM DEFINITION . . . . . 129</b> Rocket Engines . . . . . 129 Engine Development Requirements . . . . . 133 Lunar Module Constraints . . . . . 152 Basic Design Tradeoffs . . . . . 154 Design Requirements . . . . . 156 <b>APPENDIXES</b> A. ROCKET ENGINE SUBCONTRACTOR PARAMETRIC DESIGN DATA . . . . . 181 B. PROPULSION SUBSYSTEM OPTIMIZATION PROGRAM . . . . . 305
II	<b>CONTROL SYSTEMS STUDIES . . . . . 317</b> SUMMARY . . . . . 317 <b>SYSTEMS ANALYSIS . . . . . 325</b> Handling Qualities Analysis . . . . . 327 Thrust Vector Control Configuration Analysis . . . . . 401 Control System Failure Mode Analysis . . . . . 405 <b>SYSTEMS MECHANIZATION . . . . . 427</b> Introduction . . . . . 427 Gimbal Command Histogram . . . . . 427 Subsystem Studies . . . . . 429 <b>APPENDIXES</b> C—PART 1. KINESTHETIC EQUATIONS OF MOTION . . . . . 461 C—PART 2. HARDWIRE EQUATIONS OF MOTION WITH PIVOT BELOW CENTER OF GRAVITY . . . . . 481 C—PART 3. HARDWIRE EQUATIONS OF MOTION WITH PIVOT ABOVE CENTER OF GRAVITY . . . . . 499 D. HARDOVER ACTUATOR FAILURE ANALYSIS . . . . . 507



Section	Page
III THERMAL STUDIES . . . . .	535
INTRODUCTION AND SUMMARY . . . . .	535
ENVIRONMENTAL CONSIDERATIONS . . . . .	537
Thermal Environment on the Moon . . . . .	537
Vehicle Temperature Limits . . . . .	541
COMPONENT TEMPERATURE ANALYSIS AND THERMAL PROTECTION . . . . .	545
Thermal Analysis of Propellant Tanks . . . . .	545
Engine and Feedline Thermal Protection . . . . .	565
Structural and Attenuator Thermal Protection . . . . .	565
Clustered Engines Heat Transfer . . . . .	574
Base Heating Studies . . . . .	578
Plume Heating . . . . .	582
Design Implications . . . . .	585
APPENDIXES	
E. STEADY-STATE TEMPERATURES OF SINGLE OBJECTS ON THE MOON . . . . .	587
F. $A_p/A_s$ FOR LATERAL SURFACE OF A RIGHT CONE . . . . .	589
REFERENCES . . . . .	595

## ILLUSTRATIONS

Figure		Page
1-1	TRW Variable-Thrust Engine . . . . .	6
1-2	Bell Thrust Chamber Concept . . . . .	7
1-3	Marquardt Thrust Chamber Concept . . . . .	8
1-4	Aerojet Thrust Chamber Concept . . . . .	9
1-5	Rocketdyne Thrust Chamber Concept . . . . .	10
1-6	Two-Piece Interregenerative Heat Flow Schematic . . . . .	11
1-7	Throttling Options . . . . .	12
1-8	Engine Performance . . . . .	15
1-9	Propulsion Subsystem Schematic Showing Propellant Feed Alternatives . . . . .	20
1-10	LFV Slosh Model . . . . .	22
1-11	LFV Tank Geometry . . . . .	23
1-12	LFV Propellant Tank Sloshing and Feedout Control Scheme . . . . .	25
1-13	Nominal LFV Thrust Versus Time Schedule . . . . .	27
1-14	Comparison of Propulsion Subsystems Weights . . . . .	29
1-15	Single-Engine Subsystem Weight Comparison, $\epsilon = 40$ . . . . .	30
1-16	Three-Engine Subsystem Weight Comparison, $\epsilon = 40$ . . . . .	31
1-17	Four-Engine Subsystem Weight Comparison, $\epsilon = 40$ . . . . .	32
1-18	Variation of Total Loaded Subsystem Weight as a Function of Chamber Pressure for Various Nozzle-Area Ratios (14 sheets) . . . . .	34
1-19	Variation of LFV Range as a Function of Nozzle-Area Ratio for Various Chamber Pressures (23 sheets) . . . . .	49
1-20	Propulsion Subsystem Resupply Weight for Five Nominal Flights . . . . .	73
1-21	Resupply Weight for Five Nominal Flights as a Function of Chamber Pressure and Nozzle-Area Ratio (14 sheets) . . . . .	74
1-22	Typical Cavitating Venturi Flow Valve . . . . .	89
1-23	Throttle Method Performance Comparison . . . . .	90
1-24	Variable Area Injectors . . . . .	91
1-25	Throttling Method Comparison for Nominal Trajectory . . . . .	93
1-26	Yaw RCS Arrangement and Configuration . . . . .	98
1-27	RCS and Main Engine Propellant Consumption . . . . .	100
1-28	Thrust Versus Maneuvering Time (Yaw Rate) With Various Firing Times From 0.5 to 3 Seconds, Maximum Payload . . . . .	103



Figure		Page
1-29	Thrust Versus Maneuvering Time (Yaw Rate) With Various Firing Times From 0.5 to 2 Seconds, Burnout Weight, No Payload . . . . .	105
1-30	Yaw RCS Thruster Characteristics . . . . .	106
1-31	Yaw RCS System Weight Versus Maneuvering Time, Four-Thruster System . . . . .	108
1-32	Yaw RCS System Weight Versus Maneuvering Time, Eight-Thruster System . . . . .	109
1-33	Yaw RCS System Weight, Eight-Thruster Configuration, Nitrogen Propellant . . . . .	113
1-34	Yaw RCS System Weight, Eight-Thruster Configuration, Helium Cold Gas Propellant System . . . . .	113
1-35	Yaw RCS System Weight Comparison . . . . .	115
1-36	RCS Pitch and Roll Control Duty Cycle . . . . .	115
1-37	Combined Pitch, Yaw, and Roll RCS Characteristics . . . . .	118
1-38	Thrust Vector Control Concepts . . . . .	120
1-39	Jet Vane Thrust Vector Control . . . . .	125
1-40	Thrust Ratio Requirements for Differential Throttling . . . . .	125
1-41	150-Pound Thrust Throttleable Engine Manually Operated Valve . . . . .	131
1-42	150-Pound Thrust Throttleable Rocket Engine Assembly . . . . .	135
1-43	100-Pound Thrust Model 18414 Engine Development Plan (Man-Rated) . . . . .	137
1-44	Six-Task, 17-Month Program to Bring the LFV Rocket Engine Assembly Through Man-Rated Lunar Environment Qualification . . . . .	140
1-45	Lunar Flying Vehicle Propulsion Subsystem System Diagram . . . . .	157
1-46	Lunar Flying Vehicle Propulsion Subsystem Schematic . . . . .	161
1-47	Regulator-Failure Logic Diagram . . . . .	169
1-48	LFV Propellant Quantity Indicator Conceptual Design . . . . .	175
2-1	Pitch and Roll Controls Mechanization Concepts . . . . .	328
2-2	Degradation of Cooper Ratings Due to Pilot Load Requirements . . . . .	334
2-3	LFV Kinesthetic Dynamics Model . . . . .	336
2-4	Lunar Flying Vehicle Response . . . . .	342
2-5	Kinesthetic Attitude and Path Control Block Diagram . . . . .	343
2-6	Kinesthetic Control of Lunar Flying Vehicle . . . . .	345
2-7	Path Reversal Problem . . . . .	348
2-8	Three Solutions to the Path Reversal Problem . . . . .	348
2-9	Hardwire Path Control System Block Diagram . . . . .	349
2-10	LFV Hardwire Control, Attitude Closure . . . . .	350
2-11	LFV Hardwire Control, Path Closure . . . . .	350



Figure		Page
2-12	Overhead Pivot and Nozzle Beneath Configurations . . . . .	352
2-13	Stability Cases . . . . .	352
2-14	Two-C.G. LFV Configurations . . . . .	354
2-15	Improvements to Basic Hardwire System . . . . .	358
2-16	Basic Hardwire Control System . . . . .	358
2-17	Hardwire Control System Compensation Network . . . . .	358
2-18	Revised Hardwire Control System Compensation Network . . . . .	358
2-19	Mechanical Hardwire Compensation Networks . . . . .	359
2-20	Simplified LFV Attitude Control System . . . . .	360
2-21	Simplified LFV Attitude Control System With Lead Compensation . . . . .	361
2-22	Two-Loop LFV With Shaping Network . . . . .	362
2-23	Generic Two-Loop Root Locus, Simple Lead Network . . . . .	363
2-24	Two-Loop Root Locus, $T_{LX} = 0.33$ . . . . .	363
2-25	Stability-Augmented LFV Block Diagram . . . . .	366
2-26	Attitude-Loop Root Locus for LFV Stability Augmentation System . . . . .	366
2-27	Path Root Locus for LFV Stability Augmentation System . . . . .	367
2-28	Visual Simulator Functional Flow Diagram . . . . .	369
2-29	HOTRAN Simulation Facility . . . . .	370
2-30	Simulator Display Panel . . . . .	371
2-31	Visual Simulation Approach . . . . .	372
2-32	Comparison of Simulator Recordings for Three Control Modes . . . . .	376
2-33	Status of Control Configurations Based on Long-Range Course . . . . .	378
2-34	Landing Course . . . . .	379
2-35	Comparison of Simulator Recordings for Two Control Modes . . . . .	379
2-36	Status of Control Configurations Based on Landing Course . . . . .	381
2-37	Comparison of Prediction Tasks for Various Control Methods . . . . .	384
2-38	Bottom View of the Tethered Flight Vehicle . . . . .	390
2-39	Tethered Flight Vehicle . . . . .	392
2-40	Tethered Flight Vehicle Constraints . . . . .	393
2-41	Tethered Flight Vehicle Center-of-Gravity Ranges . . . . .	395
2-42	Tethered Flight Vehicle Moment-of-Inertia Ranges . . . . .	396
2-43	Tethered Flight Vehicle Kinesthetic Results . . . . .	400
2-44	Failure Mode Analysis for Three Configurations . . . . .	406
2-45	Gimbal Actuation Power-Flow Diagram . . . . .	407



Figure		Page
2-46	Engine and Actuator Configurations . . . . .	410
2-47	Actuator Hardover Failure of Translating TVC . . . . .	418
2-48	Altitude Loss From Actuator Hardover Failure of Translating TVC . . . . .	419
2-49	Actuator Hardover of Four Two-in-a-Can Actuators . . . . .	421
2-50	Actuator Failure Sensors . . . . .	425
2-51	Histogram of LFV Gimbal Requirements From LAD Flight Simulator . . . . .	428
2-52	Cable Mechanization of Throttle . . . . .	432
2-53	Electrical Mechanization of Throttle . . . . .	432
2-54	Hydraulic Mechanization of Throttle, Gang Shutoff on Throttle . . . . .	433
2-55	Apollo Rotation Hand Controller . . . . .	437
2-56	Minuteman II (P106A) Actuator . . . . .	440
2-57	Electrical Power and Signal Flow Diagram . . . . .	444
2-58	Control Unit Flow Diagram . . . . .	446
2-59	LFV Power and Signal Flow . . . . .	447
2-61	LFV Control Unit Flow Diagram, Engine Actuation System Commands . . . . .	451
2-62	LFV Control Unit Flow Diagram, Display Functions . . . . .	453
2-63	Electrical Power Flow Diagram, One Battery . . . . .	456
2-64	ECA Wiring Diagram . . . . .	456
2-65	Rate Gyro Wiring Diagram . . . . .	457
2-66	Actuator Wiring Diagram . . . . .	457
2-67	Display Panel Wiring Diagram . . . . .	458
2-68	Rotational Hand Controller Wiring Diagram . . . . .	458
2-69	Preliminary Display Panel Layout . . . . .	459
3-1	Average Lunar Surface Temperature . . . . .	538
3-2	Lunar Ravine Temperatures . . . . .	540
3-3	Propellant Tank Thermal Model . . . . .	546
3-4	Lunar Day Propellant and Tank Temperatures . . . . .	549
3-5	Normal Dawn Mission Timeline Considerations . . . . .	550
3-6	Lunar Morning Propellant and Tank Temperatures . . . . .	550
3-7	Timeline Thermal Considerations . . . . .	552
3-8	Maximum Propellant and Tank Temperatures at Subsolar Point . . . . .	552
3-9	Propellant Tank Power Requirements for Various Parameters (Sheet 1 of 3) . . . . .	555
3-10	Propellant Tank Power Requirements for Various Parameters (Sheet 2 of 3) . . . . .	555
3-11	Propellant Tank Power Requirements for Various Parameters (Sheet 3 of 3) . . . . .	556

Figure		Page
3-12	Propellant Tank Energy Requirements for Various Parameters (Sheet 1 of 3) . . . . .	556
3-13	Propellant Tank Energy Requirements for Various Parameters (Sheet 2 of 3) . . . . .	557
3-14	Propellant Tank Energy Requirements for Various Parameters (Sheet 3 of 3) . . . . .	557
3-15	Propellant Tank Power, Night Standby Period . . . . .	558
3-16	Propellant Tank Energy Requirements, Night Standby Period . . . . .	561
3-17	Propellant Tank Energy Requirements, Night Storage Period . . . . .	562
3-18	Propellant Tank Energy Requirements, Day Standby Periods . . . . .	563
3-19	LFV Earthshine Operations, Thermal Considerations . . . . .	564
3-20	Typical Propellant Tank TPS Weights . . . . .	564
3-21	Estimated Engine Cooldown, Lunar Night . . . . .	566
3-22	Landing Attenuators, Schematic Diagram . . . . .	566
3-23	Projected Area to Surface Area Ratios for Landing Attenuators . . . . .	569
3-24	Solar Incidence on Landing Attenuators . . . . .	569
3-25	Timeline Considerations for Nominal Dawn Mission . . . . .	570
3-26	Lunar Morning Landing Attenuator Temperature . . . . .	572
3-27	Engine to Actuator Relationships . . . . .	572
3-28	Radiative Heating to Landing Attenuators . . . . .	573
3-29	SM RCS Engine Submerged Installation, Schematic Drawing . . . . .	575
3-30	Flow Model and Physical Data . . . . .	579
3-31	Base Heating Geometry . . . . .	580
3-32	Base Heating Schematic Drawings . . . . .	581
3-33	Base Heating Results . . . . .	583
3-34	Structural Ablator Protection . . . . .	584

## TABLES

Table		Page
1-1	Propulsion Study Matrix . . . . .	4
1-2	Thrust Chamber Characteristics . . . . .	13
1-3	Initial Throttle-Method Screening . . . . .	14
1-4	Throttling-Experience Comparison . . . . .	16
1-5	Tank-Configuration Evaluation . . . . .	17
1-6	LFV Parameters Near End-Burn . . . . .	24
1-7	Required Engine Thrust . . . . .	26
1-8	Engine-Size Effects on Structural Weight . . . . .	28
1-9	Range-Comparison Summary . . . . .	48
1-10	Propulsion-Subsystem Weight Comparison . . . . .	72
1-11	Throttle-Method Comparison, Four-Engine Configuration . . . . .	94
1-12	Attitude-Control Requirements . . . . .	96
1-13	Main-Engine Propellant-Consumption Rate . . . . .	101
1-14	Main-Engine Hovering Propellant During Three 180 Degree Yaw Maneuvers . . . . .	101
1-15	RCS Orientation Propellant for Three 180 Degree Yaw Maneuvers . . . . .	102
1-16	Total Impulse Per Thruster Per Firing . . . . .	104
1-17	Yaw RCS Thrust Size . . . . .	104
1-18	Limit-Cycle Propellant Weights for Thrust Levels Corresponding to Yaw-Orientation Maneuvering Times . . . . .	107
1-19	Yaw RCS System Weight Summary, Bipropellant Type (Using Main-Engine Tankage) . . . . .	110
1-20	Propellant Weight Requirements for Cold-Gas System . . . . .	111
1-21	Nitrogen RCS System Weight Summary . . . . .	112
1-22	Helium RCS System Weight Summary . . . . .	114
1-23	RCS System Weight Comparison . . . . .	116
1-24	RCS Control-Mode Weight Summary . . . . .	119
1-25	Secondary-Injection TVC Injectant Requirements . . . . .	121
1-26	Summary of Applicable TVC Experience . . . . .	123
1-27	LFV Engine-Design Criteria . . . . .	130
1-28	LFV Engine-Characteristics Summary . . . . .	138
1-29	Lunar Ejecta From LFV Engine Exhaust . . . . .	155
1-30	LFV Propulsion Subsystem and Related Components . . . . .	163
1-31	LFV Component Capabilities . . . . .	165



Table		Page
1-32	Line-Flow Pressure Drops for Oxidizer and Fuel . . . . .	170
1-33	Properties of T-1 Hose . . . . .	172
1-34	Gaging Concept Comparison . . . . .	174
2-1	Pilot Opinion Rating System for Universal Use . . . . .	331
2-2	Expanded Cooper Rating Scale . . . . .	332
2-3	Dominant Natural Frequencies and Damping Ratios of Various Acceptable Handling Qualities Aircraft During Land Phase (Reference 2-4) . . . . .	335
2-4	Summary of Visual Simulation . . . . .	373
2-5	Long-Range Course . . . . .	375
2-6	Long-Range Course Data . . . . .	377
2-7	Landing Data . . . . .	380
2-8	Visual Simulation Conclusions . . . . .	386
2-9	Onboard Display Requirements Based on Pilot Preference . . . . .	388
2-10	Tethered Flight Vehicle . . . . .	391
2-11	Tethered Flight Vehicle Mass Properties . . . . .	394
2-12	Tethered Flight Vehicle Results . . . . .	399
2-13	Candidate Engine Gimbal Configurations . . . . .	402
2-14	Electrical System Failure Mode Results . . . . .	408
2-15	Thrust Force and Moment Equations . . . . .	411
2-16	Steady-State Gimbal Angle Trim and Platform Tilt Requirements for Single Engine Thrust Failure . . . . .	414
2-17	Actuator Requirements for Engine Thrust Failure . . . . .	415
2-18	Actuator Hardover Analysis . . . . .	417
2-19	Results of Actuator Hardover Failure Analysis . . . . .	422
2-20	Results of Failure Mode Analysis . . . . .	423
2-21	LFV Simulation Runs Used for Histogram Compilation . . . . .	430
2-22	LFV Parameters Used on LAD Vicual Simulator . . . . .	430
2-23	Throttle Hand Controller . . . . .	431
2-24	Throttle Hand Controller Major Differences . . . . .	435
2-25	RHC Characteristics . . . . .	438
2-26	Actuator Characteristics . . . . .	441
2-27	Proposed Modification to MMIII Actuator . . . . .	443
2-28	Matrix of Linearized, Pitch/Roll Plane Equations of Motion for Hardware Geometry . . . . .	448
2-29	Control Unit Logic Nomenclature List . . . . .	449
3-1	Component Temperature Limits . . . . .	543
3-2	Surface Optical Properties . . . . .	559
3-3	Engine Heaters . . . . .	567
3-4	Comparison of Submerged and Free Radiation Thermal Characteristics (0/F = 1.6, N <sub>2</sub> O <sub>4</sub> /A-50, 100-Lb Thrust) . . . . .	577
3-5	Clustered Engine Thermal Results . . . . .	577

## I. PROPULSION SUBSYSTEM STUDIES

### SUMMARY

The propulsion subsystem studies were a major part of the lunar flying vehicle (LFV) program because this subsystem is a pacing item in the development program, even though a major keynote of the effort was to use state-of-the-art hardware. The overall approach to defining this system was carried out in two phases.

The objective of the Phase I study was to define the optimum propulsion-subsystem design criteria by conducting a parametric study of the major design alternatives throughout a wide range of significant operating variables. This required that major component data be obtained from various propulsion subcontractors. The key item was rocket-engine information supplied by the five competitive manufacturers. Considerable cooperation and exchanges of ideas were achieved in this area. In addition, the characteristics of various propellant tanks, pressurization and servicing alternatives, and components were required to (1) provide an initial basepoint design for parametric study and (2) collect data for the Phase II tradeoff study.

In Phase I, particular attention was paid to obtaining and optimizing engine characteristics, especially the throttling valve. Studies were also carried out in the areas of (1) selecting the number, thrust, and type of engines; (2) selecting number and arrangement of tanks; and (3) determining requirements of tank internals due to sloshing. An extensive analysis of all applicable methods of thrust vector control was carried out as a contribution to the overall vehicle studies on weight and reliability.

The objectives of the Phase II efforts were to conduct detailed design alternative tradeoffs, prepare a preliminary propulsion subsystem design, and to define its characteristics.

A major effort was completed to identify available hardware which could be applied to the LFV program. Once identified, the characteristics and minor changes required, where necessary, were detailed. Where hardware was not available, the simplest suitable alternatives were investigated. A complete engine-development-requirements program was outlined in the case that this alternative was necessary. In all cases,



details of availability, system characteristics, servicing, etc., were brought to the point so that a substantial base of information was available to start the next phase of LFV development.

The overall propulsion study coupled with vehicle control and other inputs resulted in the following system:

Number of engines	4 (pressure fed)
Engine reliability	0.999 (min)
Thrust	105 lb (max), 16 lb (min)
Mixture ratio	1.5
Area ratio	40
Type	Radiation or interregen
Throttle method	Variable $\Delta P$ Inlet valve
Chamber pressure	100 psia (rad) or 140 psia (interregen)
Tanks	Two 20-inch Gemini spheres
Tank internals	Screens and baffles
Pressurization	Helium bottles at 4000 psia (replaceable)
Propellant gaging	Fiber optics
Thrust vector control	Dual axis gimbal of each engine

Almost all feed system components were available from existing Apollo parts including the helium vessel assembly, pressure regulator assembly, and propellant manifold. Some new propellant servicing equipment, such as vent and fill hoses and vent relief would have to be provided.

## PARAMETRIC SYSTEM STUDIES

### SCOPE OF STUDY

Due to the maturity of today's propulsion technology and the extensive NASA space exploration program, a wide variety of propulsion subsystem and component concepts have been brought to the hardware stage. In many cases, directly applicable qualified components exist. In other cases, advanced development programs are yielding many promising concepts for consideration. The latter is particularly true of throttlable rocket engines, wherein several thrust chamber designs and throttling approaches must be evaluated. While many such alternatives are truly tradeoff study items (i. e., thrust-chamber cooling technique), they must be examined parametrically to define whether any unique and potentially desirable design points exist. Table 1-1 delineates the parametric study scope.

In order to provide a firm basis for the foregoing scope and assumptions, the discussion is now directed toward the component characteristics (engines, tanks, etc.) prior to the presentation of study results.

### BASIC ENGINE CONSIDERATIONS

The LFV rocket-engine cooling and throttling concepts yield the major variations in engine weight and performance. In addition, these two conceptual variables are specifically aligned with the existing technology at the respective rocket engine manufacturers. For example, Marquardt and Rocketdyne have extensive radiation- and interregeneratively-cooled thrust chamber technology, respectively. Likewise, Bell Aerosystems and TRW represent the most advanced capability in inlet-valve and variable-area injector-throttling technology, respectively, for these engine sizes. During the first phase of the LFV study, specific data were solicited from each of the five engine manufacturers. These, presented in part in Appendix A, were employed extensively throughout the study.

There are five basic techniques employed for rocket-engine cooling. These are regenerative, radiation, ablative, film, and transpiration. In addition, many qualified thrust chamber concepts use combinations of these techniques. However, the LFV requirements limit consideration to two specific modes.





Table 1-1. Propulsion Study Matrix

Parameter	Major Study Consideration	Considered in Initial Screening
Rocket engines		
Type	Radiation cooled Interregeneratively cooled (beryllium, bimetallic)	Ablative Regenerative
Manufacturer	Aerojet General Bell Aerosystems Marquardt Rocketdyne TRW Systems	Reaction Motors UTC
Number	1, 3, and 4	2
Chamber pressure	80 to 160 psia	-
Nozzle-area ratio	20:1 to 60:1	-
Throttling method	Inlet valve Inlet valve + variable-area injector Dual manifold	Helium injection Momentum exchange
Propellants		
Type	N <sub>2</sub> O <sub>4</sub> /A-50	-
Quantity	300 lb loaded weight at start of each sortie	Variable
Mixture ratio	1.6:1	
Propellant tanks		
Number	2	4
Material	6A14V titanium	
Factor of safety	1.5	
Expulsion	Screens	Bladders, bellows
Pressurant type	GHe	
Pressurant tanks		
Number	1	2
Material	6A14V titanium	
Factor of safety	1.5	
Duty cycle		
Trajectory	Nominal 5-mile	
Thrust/time history	Figure 1-12 For: 370-lb payload 185-lb payload 0-lb payload	
Operating temperature ranges		
Fuel tank	+25 to +120 F	
Oxidizer tank	+25 to +105 F	
Helium	+25 to +120 F	
Nominal maximum thrust/ vehicle weight	1.4	Variable
Resupply mode		
GHe	Replaceable pressurant subassembly	LEM transfer
N <sub>2</sub> O <sub>4</sub> /A-50	Refuel	LEM D residual

The required maximum subsystem thrust level varies between 300 pounds and 450 pounds, depending on thrust-to-weight ratio (T/W) and number of engines. For a T/W of 1.4, the individual engine thrust is 300 pounds, 150 pounds, and 100 pounds for 1, 3, and 4 engines, respectively. Such thrust levels are substantially below those at which regenerative and transpiration cooling are feasible or efficient. Ablatively cooled thrust chambers are well developed at this size range; however, they result in a substantial weight penalty (120 percent) over other concepts when designed for the required LFV engine life of multiple flights of approximately 420 seconds per flight. The remaining two techniques, radiation, and film cooling are employed in combination for both the radiation cooled and inter-regeneratively cooled thrust chamber concepts.

Radiation-cooled thrust chambers supplemented by head-end, fuel-film cooling have been highly developed for fixed-thrust and pulse-mode applications by Marquardt, Bell Aerosystems, and TRW. Such engines are employed on the Apollo CSM and LM, Lunar Orbiter, and various USAF programs. The major developmental history lies in the 20-lb to 100-lb thrust, 100-psia chamber-pressure regime with  $N_2O_4/A-50$  or MMH propellants. A brief comparison of thrust chamber concepts is shown in Table 1-2 and Figures 1-1 through 1-5.

The interregenerative thrust chamber cooling concept also uses the film and radiation cooling combination, but in a much different way. Figure 1-6 illustrates the cooling mechanism. A high-thermal-conductivity chamber-wall material (beryllium or copper) absorbs heat at the gas-wall interface and conducts it toward the injector. There, film cooling removes the heat from the wall. In this fashion, the chamber operates at a significantly lower temperature than the radiation cooled version (Table 1-2). The nozzle extension is radiation cooled to minimize weight. Both of the foregoing cooling concepts were evaluated throughout the parametric study using data from their respective manufacturers.

The LFV rocket engines' throttling method must provide the maximum vehicle range consistent with the desired subsystem reliability and the programmatic aspects of required development and cost. During the Phase I study, three throttling approaches were evaluated in depth. These were (1) inlet throttling with a variable-pressure-drop flow-control valve, (2) flow-control valve coupled mechanically with a variable-area injector, and (3) dual manifold. Two other techniques, namely, helium injection and momentum exchange, were considered but rejected due to lack of experience to or inapplicability for this low-thrust range. All concepts are shown schematically in Figure 1-7. Table 1-3 indicates the results of the initial concept screening.

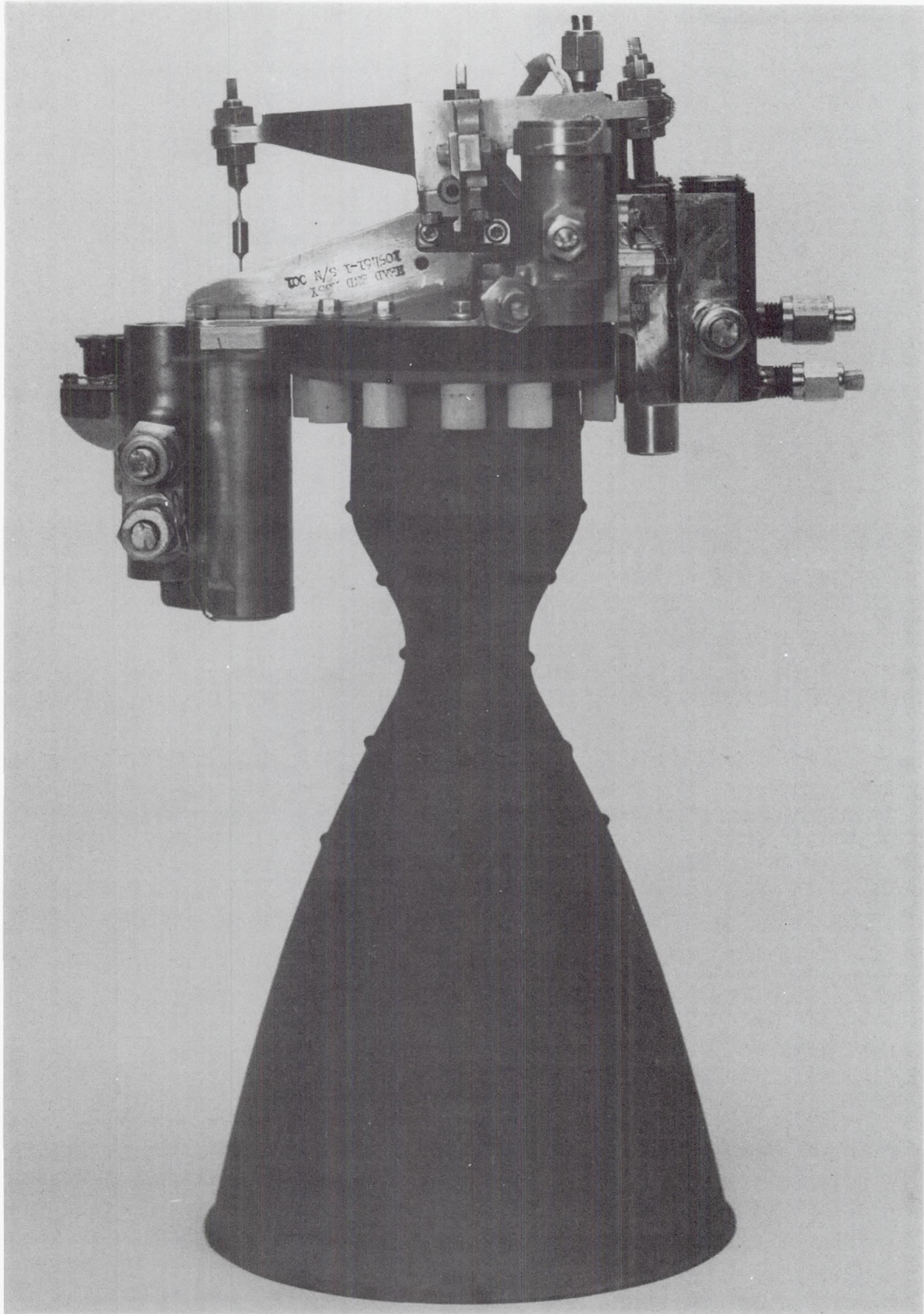


Figure 1-1. TRW Variable-Thrust Engine

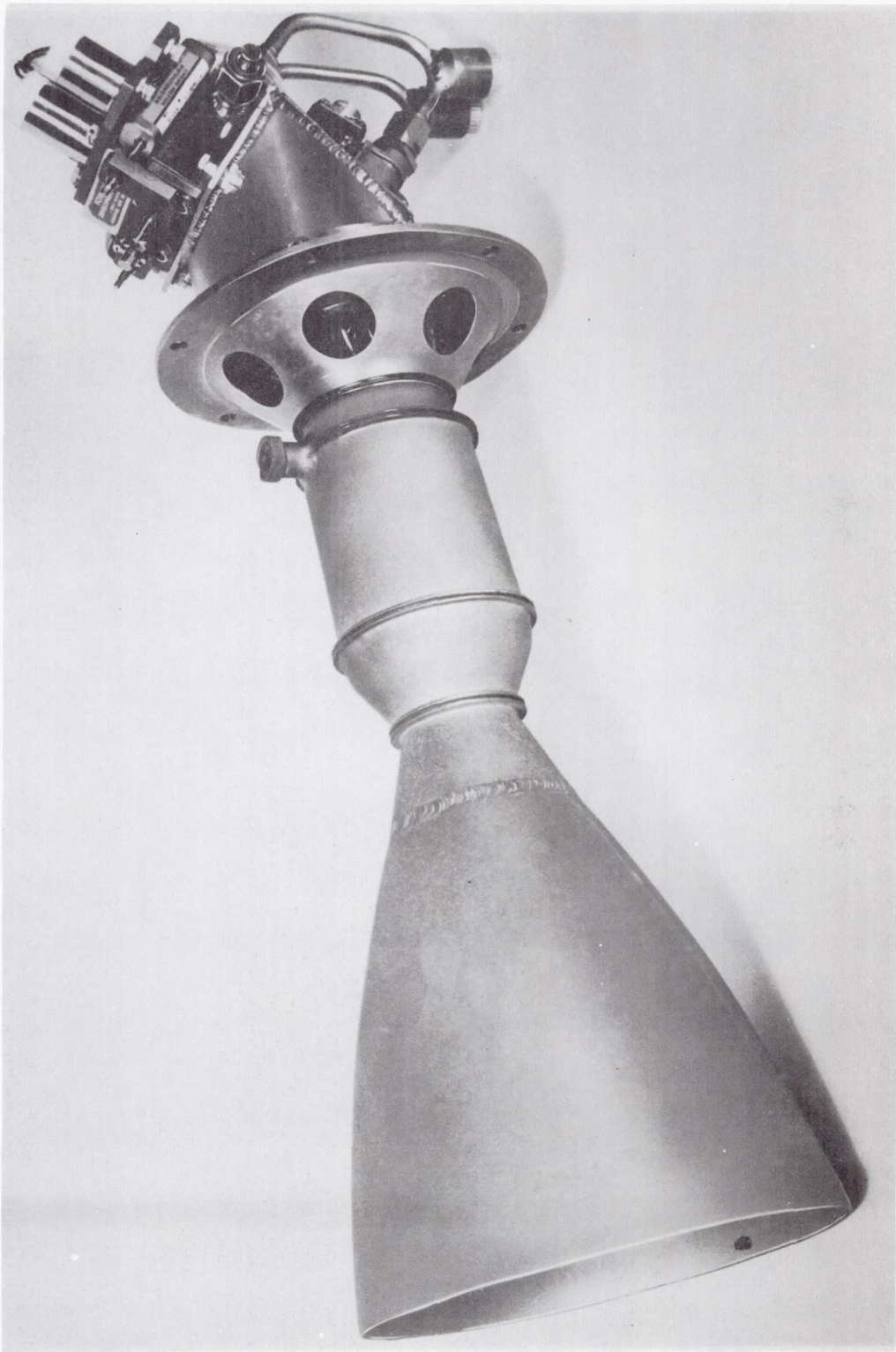
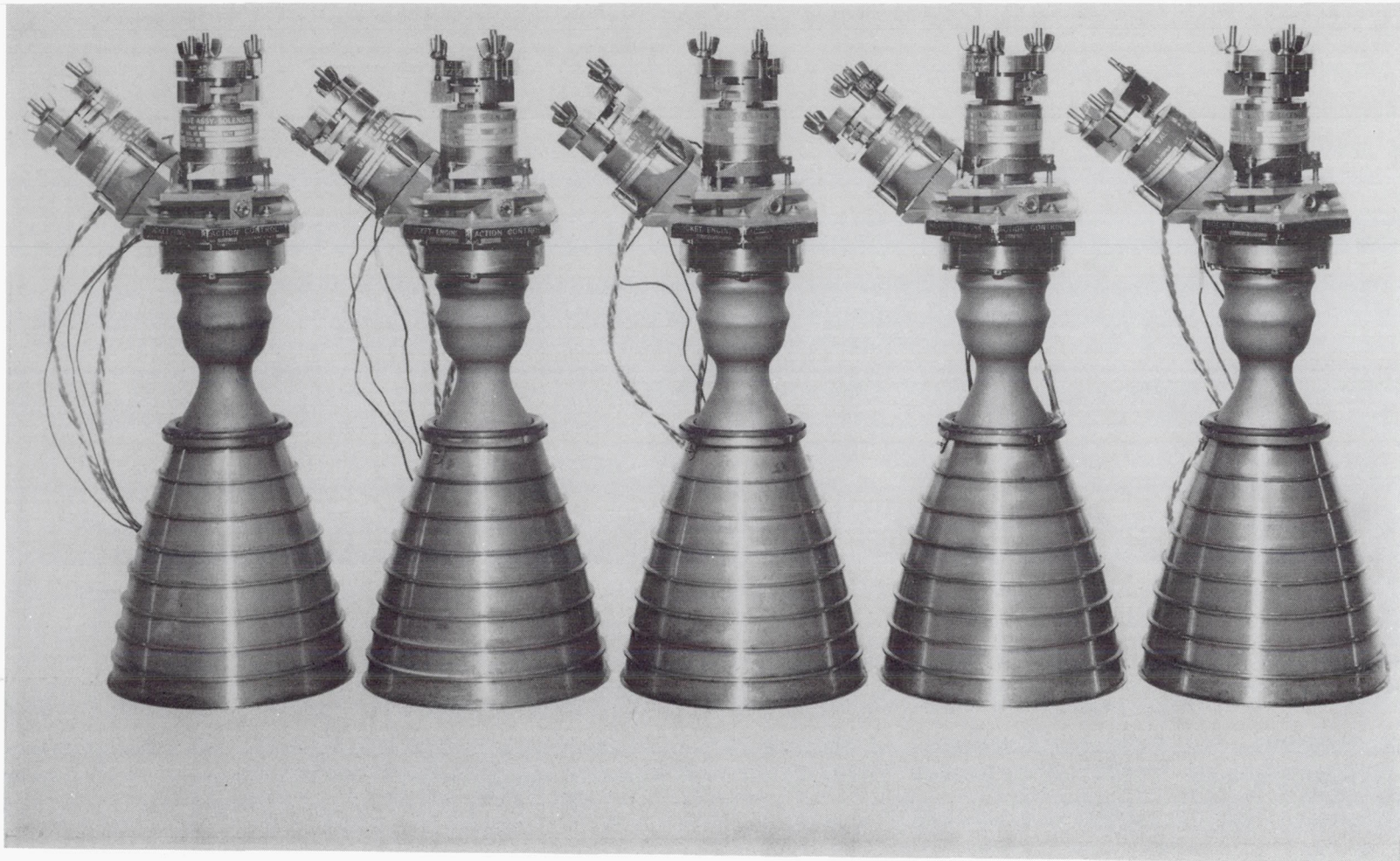


Figure 1-2. Bell Thrust Chamber Concept



**SMRCE QUALIFICATION ENGINES - Nos. 1, 2', 3, 4, AND 5 (LEFT TO RIGHT)  
ENGINE ASSEMBLY P/N 228687 S/N's 0002, 0049, 0013, 0017, AND 0005 (LEFT TO RIGHT)  
PHOTO TAKEN AFTER COMPLETION OF QUALIFICATION TEST PROGRAM (u) 5 JAN 66**

Figure 1-3. Marquardt Thrust Chamber Concept

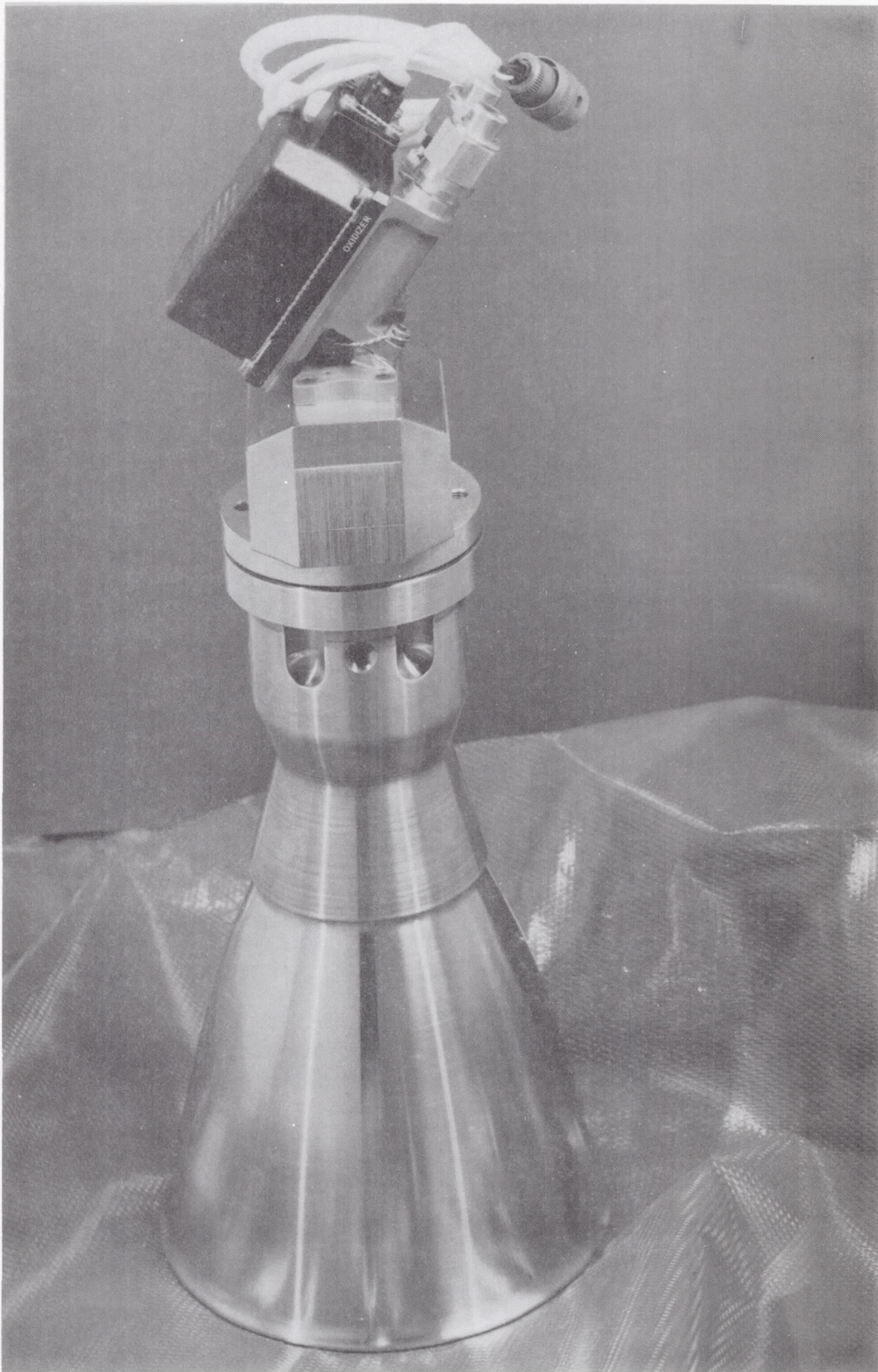


Figure 1-4. Aerojet Thrust Chamber Concept



Figure 1-5. Rocketdyne Thrust Chamber Concept

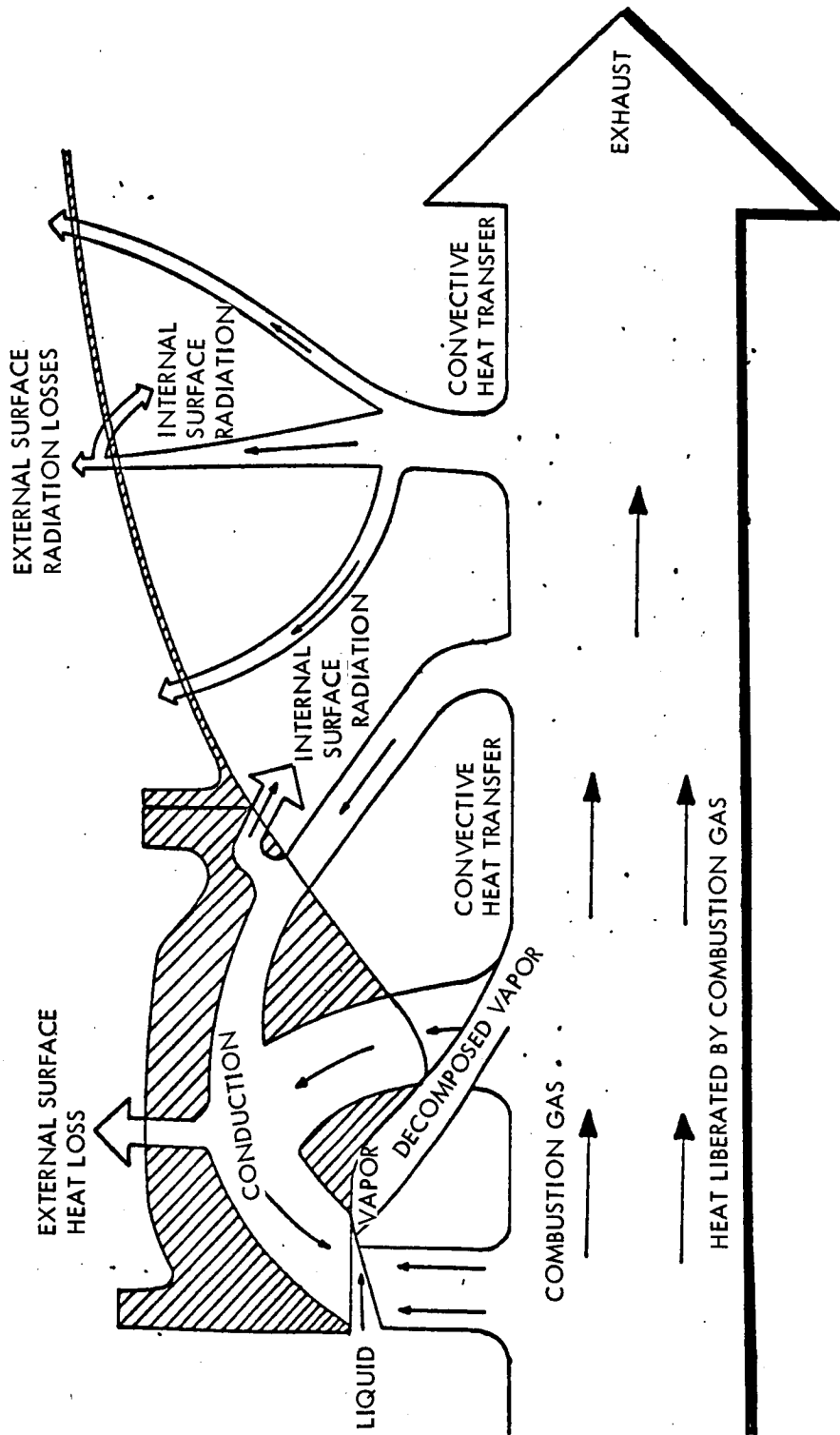


Figure 1-6. Two-Piece Interregenerative Heat Flow Schematic



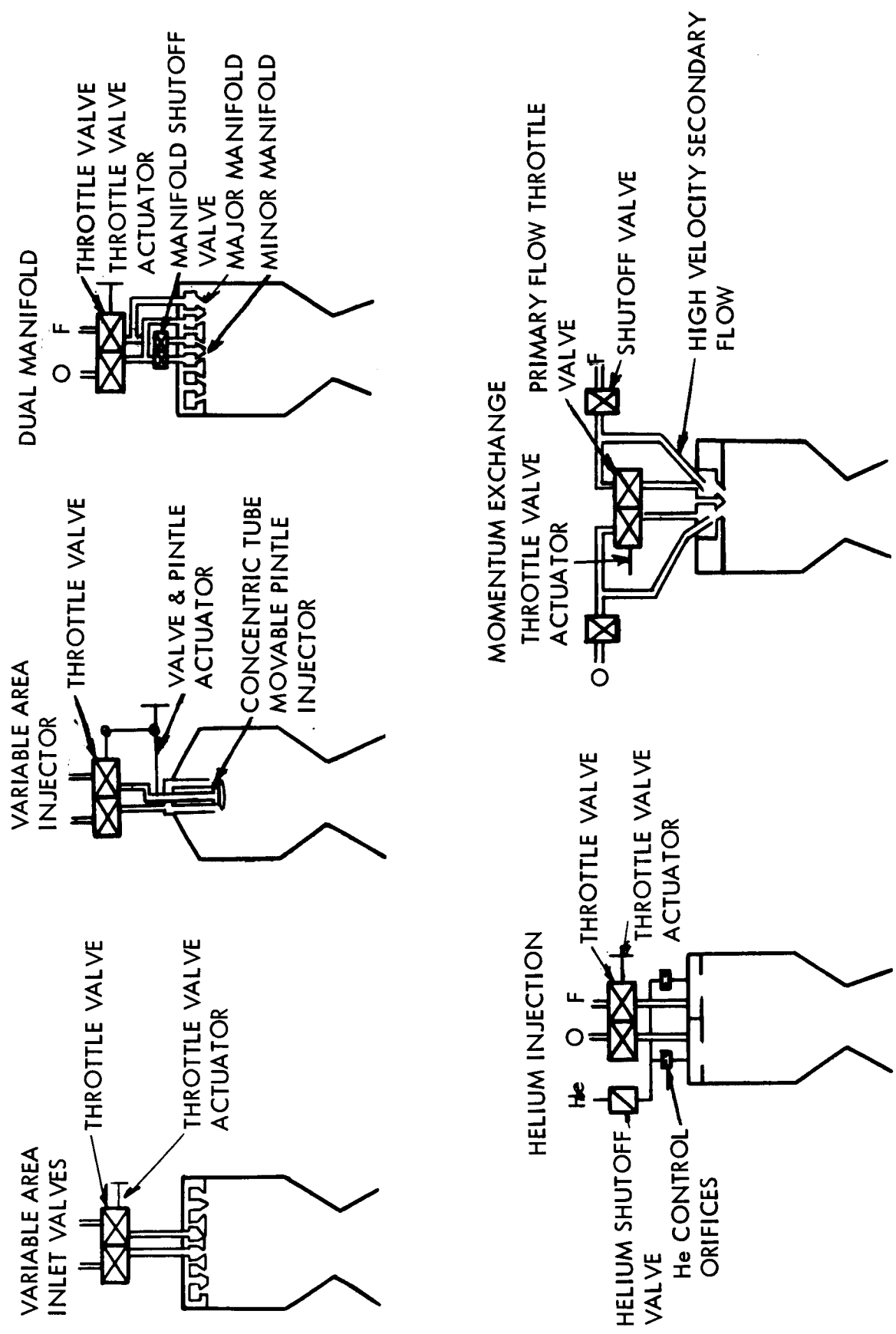


Figure 1-7. Throttling Options

Table 1-2. Thrust Chamber Characteristics

Consideration	Thrust Chamber (Company)				
	TRW (Figure 1-1)	Bell (Figure 1-2)	Marquardt (Figure 1-3)	Aerojet (Figure 1-4)	Rocketdyne (Figure 1-5)
Material	Columbium	Columbium	Molybdenum + L-605 extension	Inconel 600 liner + copper body	Beryllium C. C. + L-605 extension
Cooling	Radiation	Radiation	Radiation	Interregenerative + radiation	Interregenerative + radiation
Maximum temperature (° F)	2470	2600	2200	1550*	1770*
Weight per 100 lbf	9.0	8.5	6.5	7.7	
Development status for LFV	Compatibility with current injector not proven at desired mixture ratio	Considered to be in pre-PFRT status requires manual valve development.	Basic feasibility of thrust chamber throttability proven. Requires manual valve development.	Concept being developed under two NASA (100-lb and 20-lb Del MSFC) and USAF (75-lb) contracts. Proven design concept. Needs throttle application development.	Basic engine developed for PBPS application; numerous engines tested at various sizes.
Remarks	Experience with columbium thruster development, Ursa 100	Extensive development on various space program backups. Less sensitive to pressure spikes than molybdenum	Most extensive thrust chamber development proven in space performance. Brittle material when cold.	Rugged thrust chamber. Insensitive to local hot spots.	Rugged thrust chamber. Insensitive to local hot spots.
Qualified thrust chamber exists	No	No	No	No	No
Throttlable	Yes	Yes	Yes	No	Yes
Fixed-thrust					

\*With MMH instead of A-50

Table 1-3. Initial Throttle-Method Screening

Concept	System Features	Conclusion
1. Variable-pressure-drop valve	Simplicity and availability	Selected for detailed study
2. Variable-area injector	High performance and availability	Selected for detailed study
3. Dual manifold	High performance and moderate simplicity	Selected for detailed study
1. Momentum exchange	No development experience for low-thrust systems	Rejected
2. Helium injector	High weight, no development at low-thrust, complexity	Rejected

The throttling concepts selected for evaluation represent those submitted by the engine manufacturers as described in Table 1-4. The experimental performance of both the Bell 8414 and Mira 150R is shown in Figure 1-8 along with the analytical predictions of Aerojet, Rocketdyne, and Marquardt. All such data were corrected to the required operating conditions shown but were not adjusted to reflect NR SD confidence.

#### PROPULSION SUBSYSTEM ARRANGEMENT

Several potentially desirable approaches to the LFV propulsion subsystem arrangement were investigated. These studies were concerned with number and type of propellant tanks, feed-system concept, tank internals, and the general component requirements (i. e., regulators, connectors, etc.). The results of this effort established the baseline subsystem which was then used for the optimization study and subsequent design tradeoffs.

The major items studied were the number, arrangement, and feed method of propellant tanks. Table 1-5 illustrates the various alternatives considered. Criteria for evaluation were (1) weight, (2) servicing time,

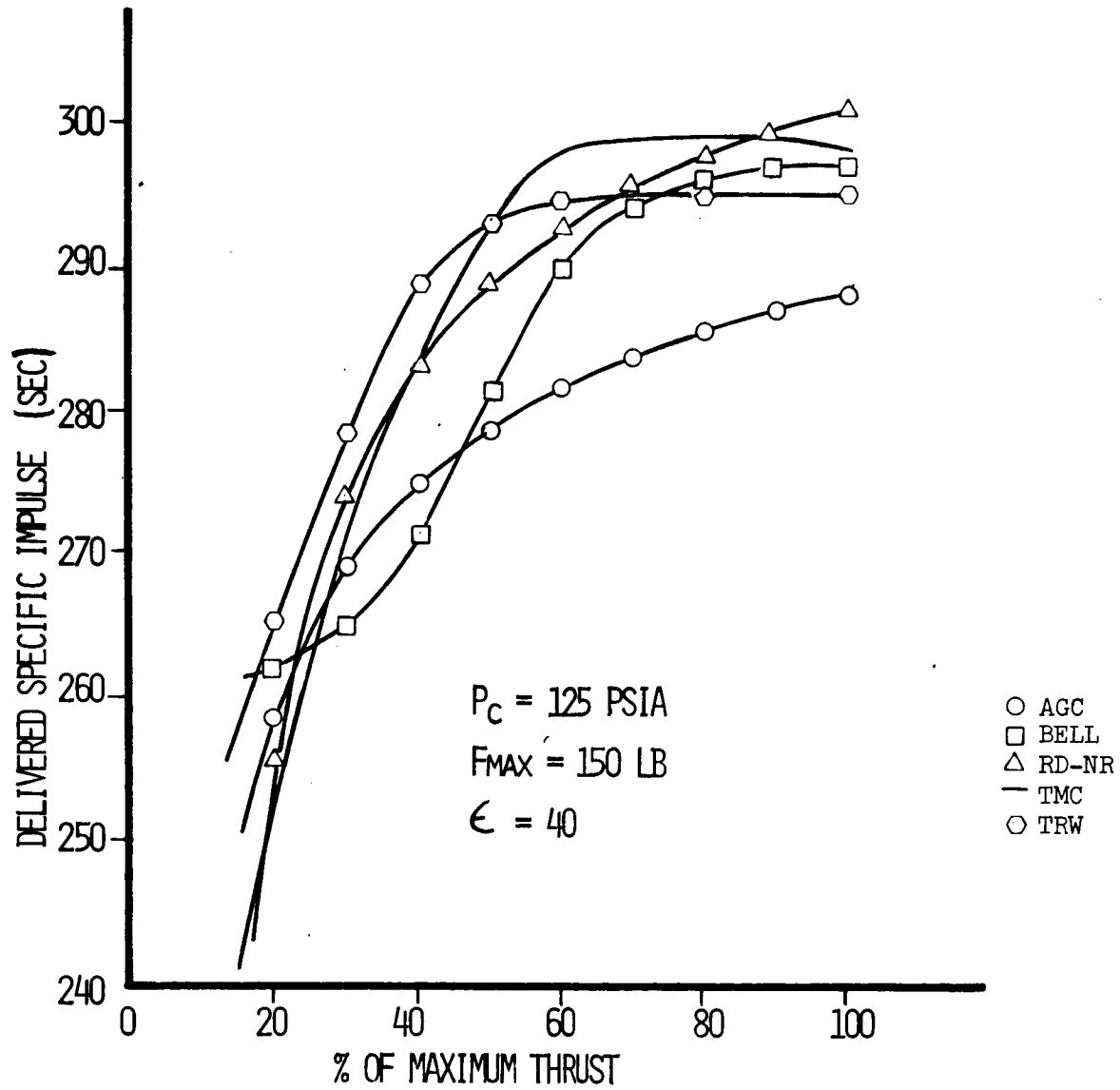


Figure 1-8. Engine Performance

**Table 1-4. Throttling-Experience Comparison**

Consideration	Manufacturer				
	TRW	Bell	Marquardt	Aerojet	Rocketdyne
Engine shut-off	Helium pilot-actuated poppet valves	Electrical torque-motor actuated bipropellant valve (Moog)	Manually operated ball valves	Seating of propellant control valves	Seating of propellant control valves
Flow control valves	Mechanically actuated, linked, cavitating-venturi-type, bipropellant valves	Mechanically actuated, linked, cavitating-venturi-type, bipropellant valves	Manually operated ball valves with contoured ball orifice area	Cavitating-venturi-type, bipropellant valve, mechanically linked and actuated	Three pintle bipropellant valves. Third pintle controls boundary-layer cooling flow
Injector	Concentric tube with movable contoured pintle	Fixed geometry, balanced triplet, six sets	Doublets	Hyperthin (platelet) showerhead	Fixed geometry
Actuation	Fuel-operated, electrically controlled servoactuator	Fuel-operated, electrically controlled servoactuator	Mechanical valve linkage, manually operated	Manual	Mechanical valve linkage, manually operated
Performance, $I_{sp}$ (sec)					
at 100 lbf	292 ( $P_c = 100$ )	294	295	286	300
at 20 lbf	203 ( $\epsilon = 40$ )	259	250	256	272
Required inlet pressure (psia)	200	224	212	247	297
Development status of LFV	Tested with ablative- and radiation-cooled thrust chambers. Required low mixture ratio (1.3 O/F) to avoid coating degradation and subsequent burn-through due to streaking in columbium chamber	Concept tested on four columbium thrust chambers. Basic feasibility proven. Required development of complete engine through qualification	Basic R4D TCA employed is man-rated and space-proven for a number of vehicles. TCA throttling feasibility proven. Valve must be developed and qualified	Hyperthin injector TCA's delivered to MSFC for evaluation testing. Complete valve development required	Throttling not part of basic PBPS engine development. Valve and injector configuration must be completely developed
Remarks	Proven on LEM-D engine (9859-lb thrust) over 10:1 regime. Also on MIRA 150 Surveyor backup program over 5:1 range (150-lb thrust). Complex system. Easily modified to vary injection parameters. High feed pressure required in MIRA 150.	Cavitating-venturi-type control valves well proven. Manual control and shutoff valve development required. Moderate feed pressure required.	Extensive valve development required. May have leakage problems. Operated over 30 to 1 throttle range with facility valves	Similar valves have been developed. Injector considered to have superior reliability	Basic TCA concept is considered to be desirable for throttling operation due to capability for distributing heat away from potential hot spots. Higher allowable $P_c$ results in smaller engines

(3) flexibility, (4) availability of hardware, (5) c.g. controllability, (6) cycle life, and (7) required development time. Two- and four-tank systems with various installations, series or parallel feed, and bladder, screen, or no tank internals were compared. Table 1-5 presents the results of this comparative evaluation which is described in the following discussion.

### Tank Internals

There are two basic requirements which require the use of propellant-tank internals for the LFV subsystem. These are to (1) provide an uninterrupted flow of propellant to the engines, and (2) prevent dynamic propellant slosh forces from affecting the LFV flight dynamics. For spacecraft (i. e., Apollo CSM, LM), Teflon bladders are employed to provide truly positive expulsion. Such bladders have been developed to a high confidence level for such operational and functional capabilities required by these applications. The number of expulsion cycles to which they are qualified is 10. The ultimate number of LFV sorties is 30, with additional expulsion cycles required for acceptance testing and checkout. In addition, the bladder-filling process must be performed in a precisely controlled fashion to avoid rupturing the

Table 1-5. Tank-Configuration Evaluation

Consideration	Arrangement							
	Parallel		Series		Single		Screen	
Feed type	Bladder	Screen	None	Screen	None	Screen	None	Screen
Internals								
Available hardware	Modify CM RCS cylinders			LM RCS cylinders, Gemini spheres (tooling)				
Stowability	Spheres or cylinders			Spheres only				
Mixture ratio	Flexible			Fixed				
ΔServicing time (minutes)	40	5	5	15	0	0	0	0
ΔWeight (pounds)	21	6.5	8.9	4.7	4.7	0.4	0.4	0
Internals	16	1	- .6	1	1	-0.6	-0.6	0
Lines, tanks	2	1	1	1.2	1.2	0	0	0
Outage, residuals	3	4.5	8.5	2.5	2.5	1	1	0
C. G. excursion (in. -lbF)	30	35	230	0	230	0	0	0
Mission cycle life	5	Fatigue limited						
ΔDevelopment time (months)	4	3	2	2	0	2	2	2
Evaluation: Acceptable Rank	NA	✓ 3	✓ 3	NA	✓ 2	NA	✓ 2	✓ 1

bladder. Such fill control would be quite difficult on the lunar surface when performed under the constraints of time, mobility, and available instrumentation. In addition, this positive-expulsion concept results in a significant weight penalty over the baseline approach. It was, therefore, eliminated from further consideration. Other such devices (i. e., bellows, metallic diaphragms, etc.) were also eliminated since they generally add about 40 additional pounds of weight to contain 300 pounds of propellant. The number of cycles available depends on the design chosen. Rolled bellows are a one-shot device; whereas, welded bellows can be used for more than 100 cycles.

The use of capillary barrier devices coupled with screened baffles for propellant location control and slosh suppression appears to provide the most attractive solution to the LFV tank internals problem, which is described in subsequent pages. The capillary barrier screen has been employed successfully on the Apollo CSM-SPS and a classified USAF program. Tests conducted at NR SD (Reference 1-1) and USAF-RPL (Reference 1-2) have proved conclusively that a suitable barrier configuration will not break down and admit pressurant to the engines feedline under expected LFV operational conditions. Additionally, the slosh frequency and amplitude may be excluded from the vehicle regime of interaction by the use of a screened, perforated baffle configuration. Again noting Table 1-5, the weight penalty for this approach is relatively low.

#### Tank Arrangement

For the four-tank arrangements, a comparison was made between parallel and series feed systems. The parallel feed arrangement requires that each line "leg" be precisely balanced for pressure drop. Otherwise, uneven outflow will result in an excessive propellant residual. To minimize this, either of two design approaches may be employed. These are:

1. Installing relatively high-delta-P orifices in each line leg that are precisely calibrated to provide the desired flow rates
2. Provide relatively high-cross-section tank-interconnect lines in addition to the feedlines to equalize tank static head and, thereby, equalize residuals

The first method requires a substantial increase in tank pressure, which in turn raises the pressurization subassembly weight. The latter concept requires tank interconnect lines which add weight and residual over a two-tank configuration.

The series-feed concept also requires tank interconnect lines which add hardware weight. It does, however, provide an acceptable vertical

vehicle c. g. excursion as propellant is depleted. Such a design concept was well developed for the Apollo CSM/SPS application. The Apollo CSM/CM-RCS tanks are nearest to the LFV four-tank requirement; however, they must be lengthened 0.75 in. to provide adequate propellant volume.

The tankage arrangement selection is therefore reduced to a choice between (1) a four tank, series feed concept, and (2) a two tank concept. Both of these utilize screens and screened baffles for propellant control. The two-tank configuration was then chosen for the following reasons:

1. Lightest weight -  $\Delta$  of -4.7 lb
2. Availability - 20-in. dia Gemini OMS tank
3. Minimum refueling time -  $\Delta$  of 15 mins due to transfer line  $\Delta P$  and level equalization requirement
4. Easier installation, although four-tank configuration stowed better in LM
5. Lightest LFV structure -  $\Delta$  of -21.6 lb
6. Simplest and least-expensive propulsion subsystem

The remaining propulsion subsystem subassemblies and components selected for the baseline concept are shown in the schematic (Figure 1-9). The concept is consistent with the well proven approaches of past manned subsystems. Propellant-tank pressurization is accomplished by gaseous helium stored at nominally 4000 psia in a titanium pressurant tank. Pressurant isolation prior to flight and during servicing is maintained by a manually operated isolation valve. Pressure regulation employs a series-parallel arrangement with appropriate downstream check valves and relief valves. Propellant-isolation valves are likewise manually operated. The propellant and pressurant disconnects for servicing are also noted.

### Slosh Analysis

An analysis was carried out to determine whether the LFV fuel tank feedport is likely to be uncovered because of slosh activity. The basic treatment is that given in Koell, Handbook of Astronautical Engineering. The excitation force is considered to be a 10-degree (hardover) step-engine command near endburn. This type of maneuver might be carried out in going from level flight into a vertical descent for landing (with 10 percent of the propellant remaining).



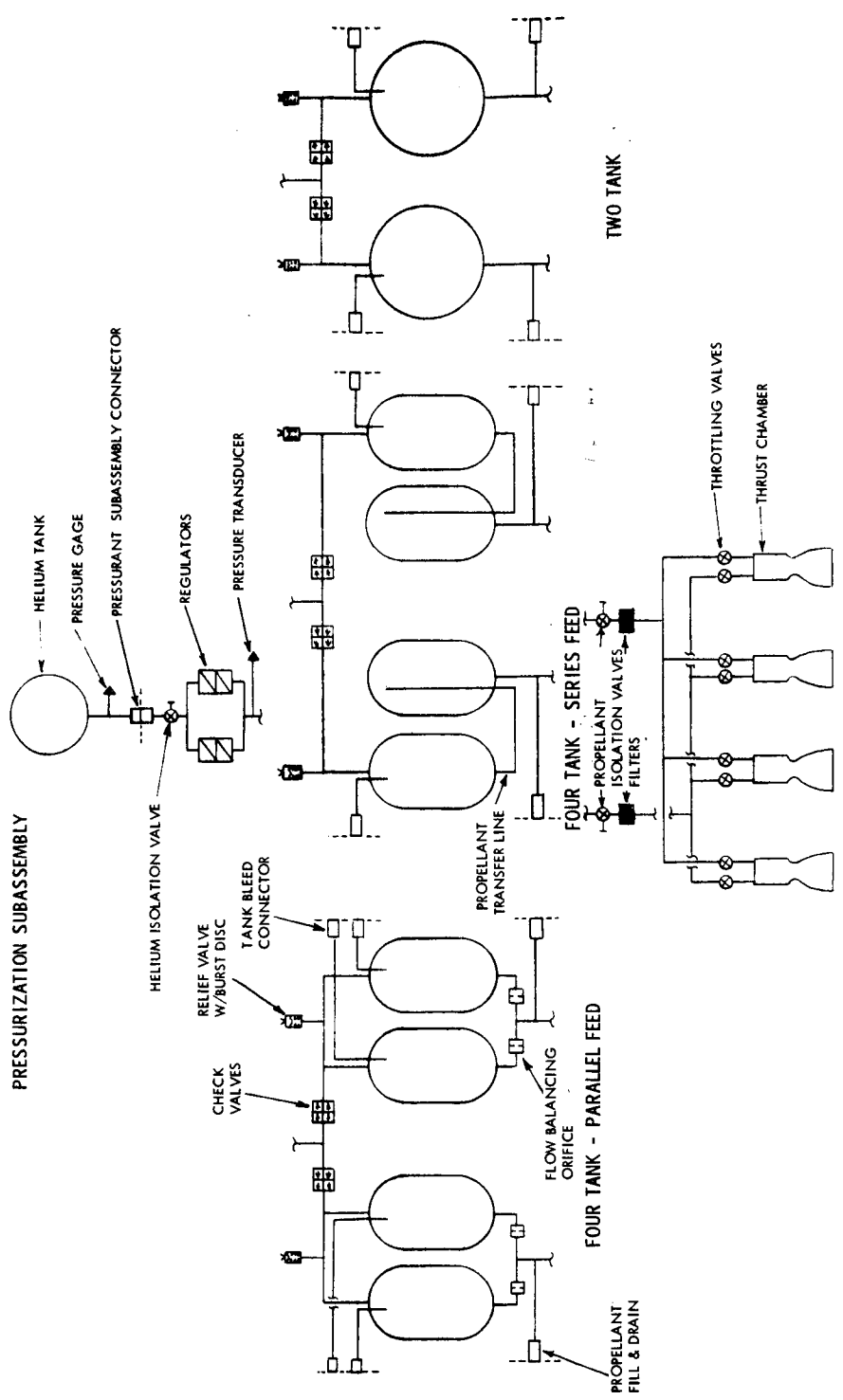


Figure 1-9. Propulsion Subsystem Schematic Showing Propellant Feed Alternatives

Following Koelle, the equations of motion of the system shown in Figure 1-10 are:

$$\phi_p = - \frac{[\ddot{Y} + (\ell_{sp} - L_p) \ddot{\theta}]}{L_p (S^2 + \omega_p^2)} \quad (1-1)$$

where S is the Laplace-transform variable. By polarity convention, a positive engine deflection yields positive pitching acceleration and a negative lateral acceleration, as in Equation 1-2.

$$\ddot{Y} = - \frac{T}{M_T} \delta$$

$$\ddot{\theta} = \frac{T \ell_{cg} \delta}{I_{yy}} \quad (1-2)$$

Substituting (1-2) in (1-1), and rearranging:

$$\frac{\phi_p}{\delta} = \frac{\frac{T}{L_p} \left\{ \frac{1}{M_T} + \frac{(L_p - \ell_{sp}) \ell_{cg}}{I_{yy}} \right\}}{S^2 + \omega_p^2} \quad (1-3)$$

Simple calculations show the fuel and oxidizer depths to be 0.28 ft. This in conjunction with Figure 1-11 shows that the sloshing amplitude required to uncover the feedport is:

$$\phi_{\text{critical}} = \arccos \left( \frac{r - h}{r} \right) = 48.2^\circ \quad (1-4)$$

Using given values from Table 1-6 in conjunction with graphs for the pendulum analogy slosh model in Koelle and a 10° step engine forcing function, we have:

$$\phi_p(S) = \frac{0.421}{S \left\{ \frac{S^2}{(3.6)^2} + 1 \right\}} \text{ radians} \quad (1-5)$$

The inverse transform of Equation 1-5 is:

$$\phi_p(t) = 0.421 \left\{ 1 - \cos 3.6t \right\} \quad (1-6)$$

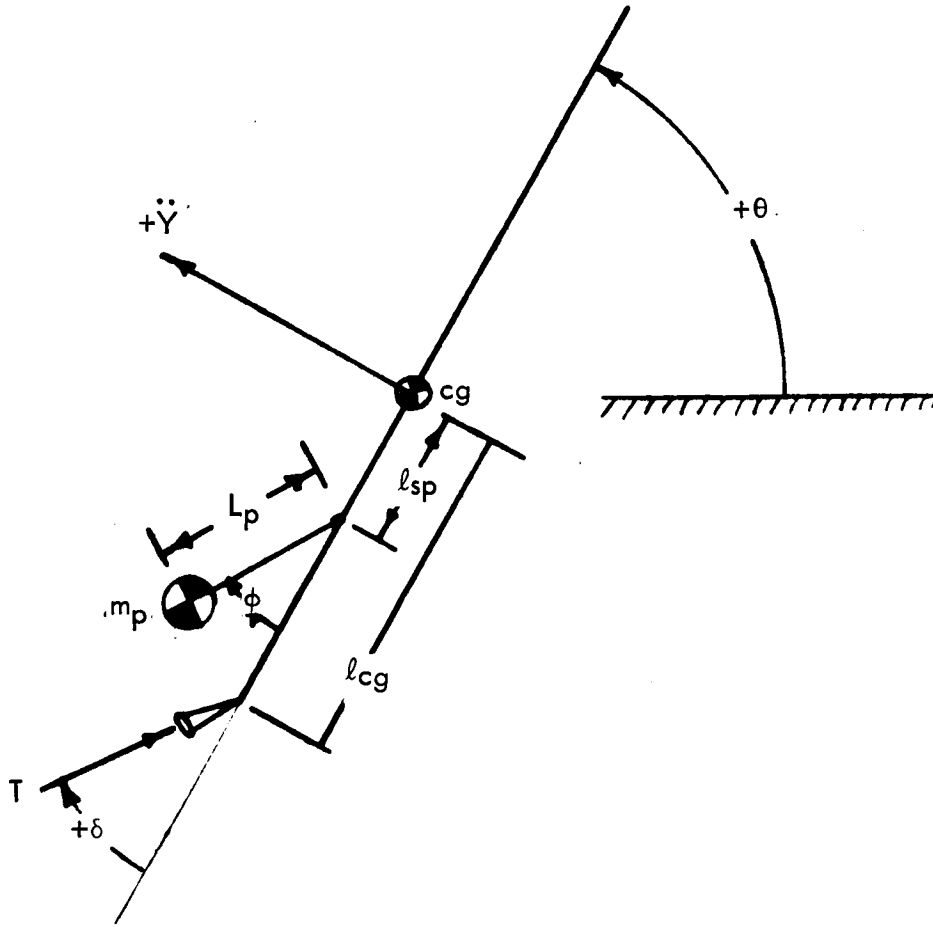


Figure 1-10. LFV Slosh Model

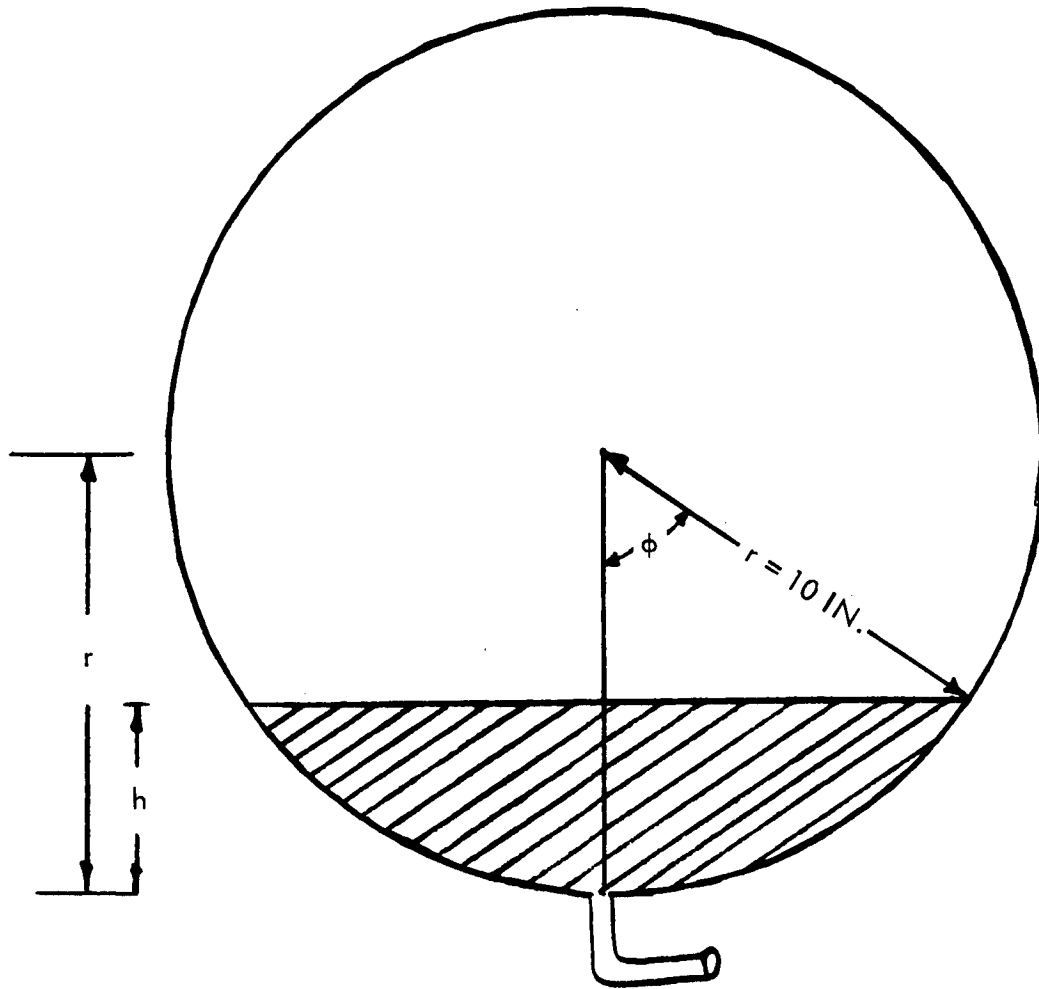


Figure 1-11. LFV Tank Geometry

Table 1-6. LFV Parameters Near End-Burn

Parameter	Value
Burnout weight (lb)	703.0
Moment of inertia (slug-ft <sup>2</sup> )	47.0
Oxidizer weight (lb)*	18.5
Fuel weight (lb)*	11.5
Oxidizer density (lb/ft <sup>3</sup> )	89.7
Fuel density (lb/ft <sup>3</sup> )	56.1
Tank diameter (in.)	20.0
Vehicle c. g. to propellant c. g. (in.)	16.4
*10% propellant remaining	

which shows a maximum amplitude of:

$$\phi_{P_{\max}}(t) = 0.841 \text{ radians} \quad (1-7)$$

which is close to the critical angle. Since this analysis shows that, to a first approximation, sloshing might, under very adverse conditions, uncover the propellant outflow port it was decided to incorporate screens and baffles into the tanks as shown in Figure 1-12.

#### ENGINE OPTIMIZATION STUDY

The parametric study encompassed the scope of variables delineated in Table 1-1. It was necessarily directed toward determining (1) optimum chamber pressure, (2) optimum nozzle-area ratio, and (3) the effects of engine type, throttling method, number of engines, and mission thrust-to-time profile on total loaded weight, burnout weight, resupply weight, and vehicle range. Due to the very wide range of variables required, an IBM 360-65 computer program (XH0099) was formulated specifically for the LFV study effort. The details of this program are delineated in Appendix B. However, a brief outline is given herein to provide discussion continuity.

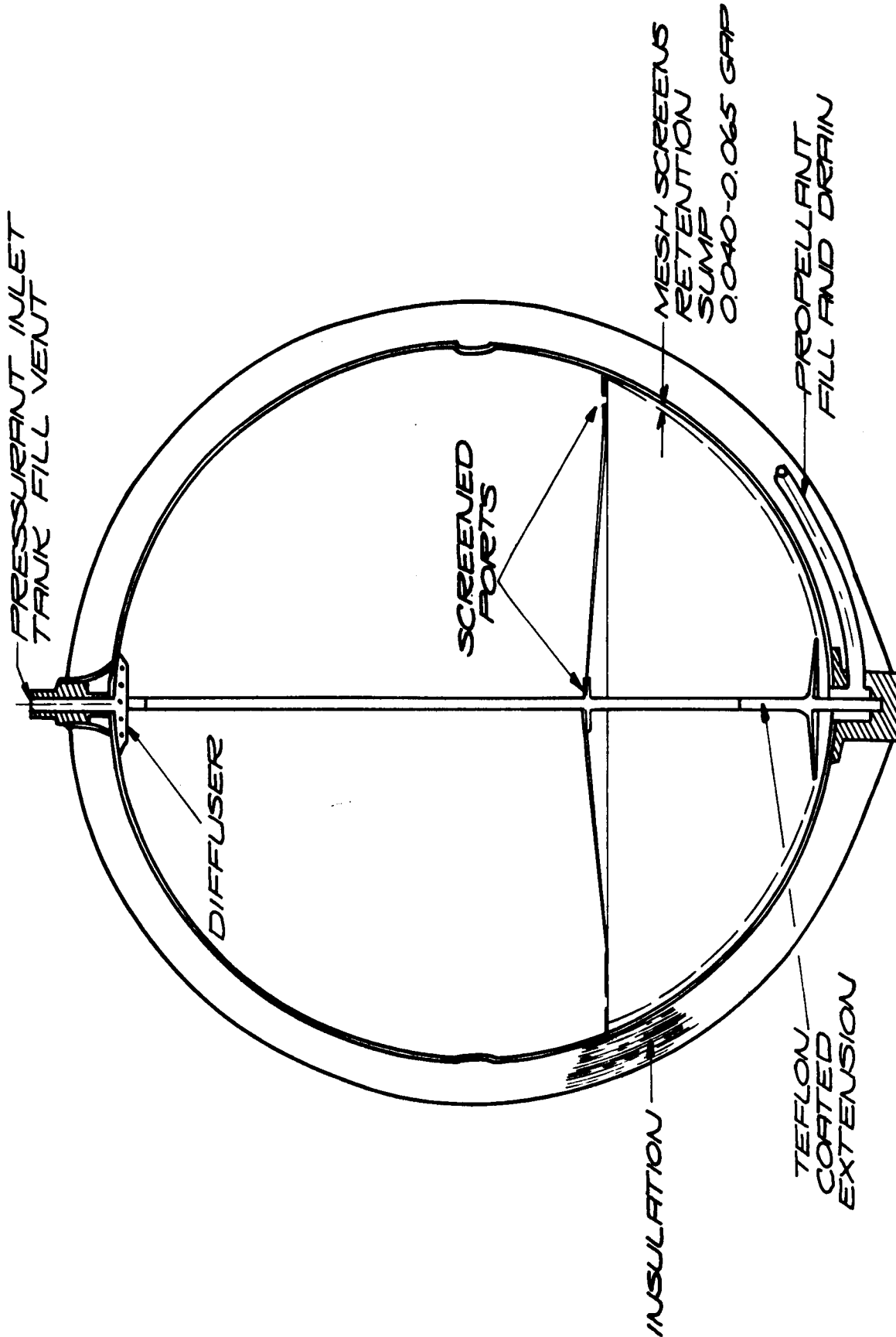


Figure 1-12. LFV Propellant Tank Sloshing and Feedout Control Scheme

As shown in Figure 1-13 there is a wide variation of thrust as a function of time for the nominal mission studied. Such variations must be considered along with variations in delivered specific impulse ( $I_{sp}$ ) defined in Figure 1-8 on a time-integrated basis. In this fashion, the correct propellant requirement for a given set of design conditions was determined.

Since the study also covers a wide range of chamber pressures and nozzle-area ratios, the  $I_{sp}$  was varied to reflect these variations for each engine type. Engine manufacturer data was used exclusively for this requirement. Such data reflected variations in combustion efficiency, nozzle efficiency (kinetic, friction, heat transfer, and divergence losses), and film cooling losses.

The required engine-design thrust level ( $F_D$ ), a function of maximum vehicle thrust-to-weight ratio ( $F/W$ ), is dependent on the number of engines. For a single-engine configuration,  $F_D$  was equivalent to maximum vehicle thrust; however, multiple-engine-configuration design criteria were different. One of the most outstanding reasons for multiple-engine installations is their potential capability to provide single-engine-out flight. Therefore, the three- and four-engine thrust requirement is:

$$F_D = \frac{\text{Maximum vehicle thrust}}{\text{Number of engines} - 1}$$

Trajectory and control-simulation studies have indicated the required  $F/W$  to be 1.4 (lunar). For a 1300-lb gross vehicle weight (earth), this results in the following engine-design thrust levels (Table 1-7). Again noting Figure 1-8, the impact of multiengine configurations on the integrated, average throttle setting is immediately apparent with respect to overall engine performance. A single engine operates, on the average, at 65 to 70 percent thrust. Three- and four-engine concepts operate at approximately 50 and 55 percent, respectively.

Table 1-7. Required Engine Thrust

No. Engines	Maximum Nominal Vehicle Thrust (lb)	Engine Out Vehicle Thrust (lb)	Engine Design Thrust (lb)
1	300	N. A.	300
3	300	300	150
4	300	300	100

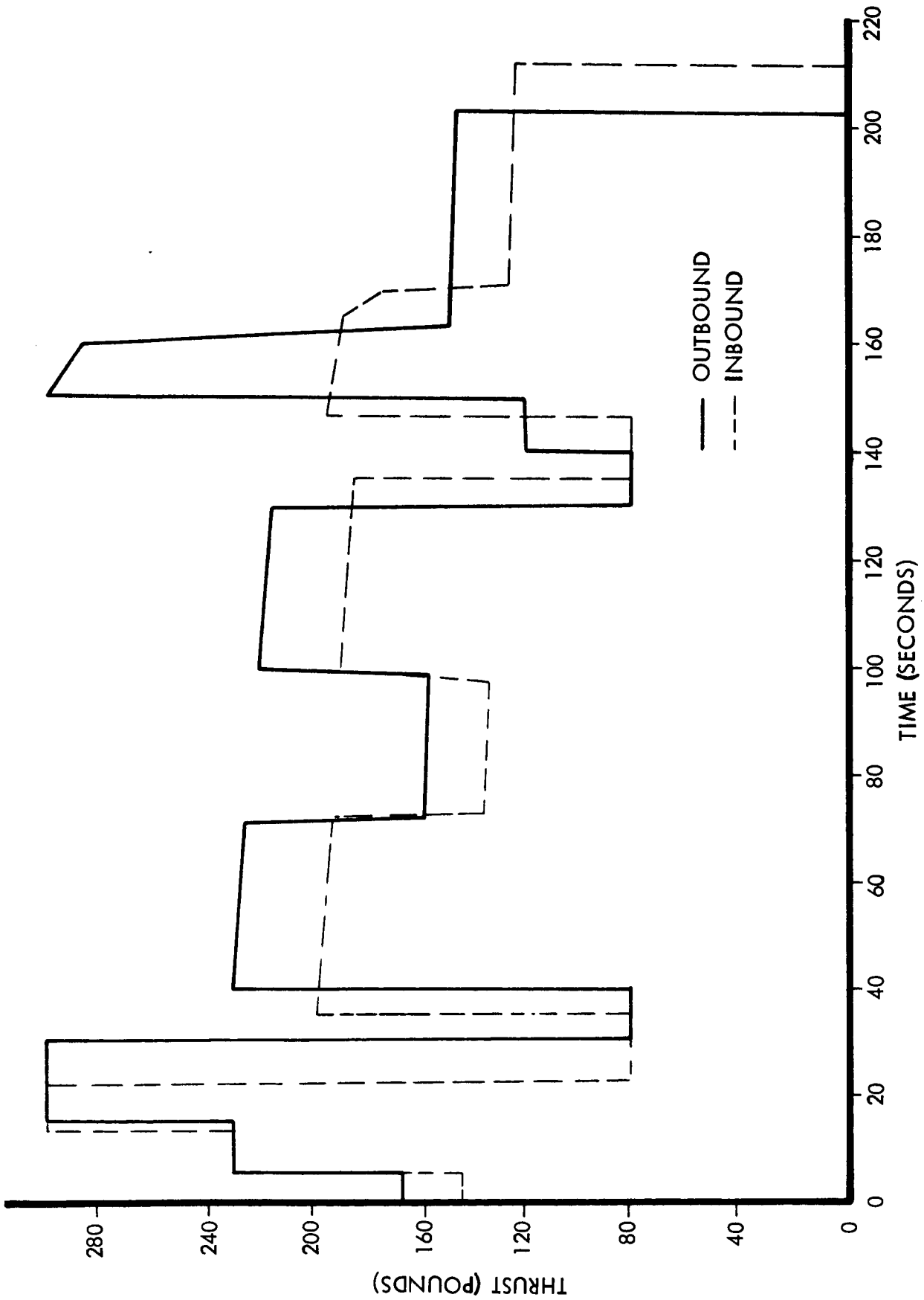


Figure 1-13. Nominal LFV Thrust Versus Time Schedule



Rocket-engine weight and geometry (length, diameter) data were also varied, depending on specific design concepts and operating conditions. These data are shown in Appendix A.

While engine weight has a direct and significant effect on propulsion subsystem weight, engine geometry affects LFV structural weight and size. These structural sensitivities, shown in Table 1-8, must be included to provide a valid comparison of the various criteria and alternatives.

Both propellant and pressurant tanks were assumed to be constructed of 6Al4V titanium alloys with a 1.5 factor of safety at 145,000 psi tensile strength. The minimum gage of 0.025-in. wall thickness resulted in all propellant tanks being minimum gage throughout the pressure and volume range studied. Required propellant-feed pressures were dependent upon chamber pressure and specific engine design concept. Subsystem component weights were derived empirically from the data of Reference 1-1 based on the schematic shown in Figure 1-9.

### Engine Study Results

The following discussion delineating the results of the subsystem optimization study is presented in a progressively more detailed manner along those lines of significant interest to LFV design criteria selection.

#### Number of Engines

Of general interest is the overall comparison of propulsion subsystem weights for 1-, 3-, and 4-engine configurations for the various engine design concepts. Figure 1-14 presents the summary results of Figures 1-15 through 1-17. It will be noted that in all cases the single-engine concept

Table 1-8. Engine-Size Effects on Structural Weight\*

Number of Engines	$\frac{\Delta \text{ Vehicle Weight (lb)}}{\Delta \text{ Engine Length (in.)}}$	$\frac{\Delta \text{ Vehicle Weight (lb)}}{\Delta \text{ Engine Diameter (in.)}}$
1	0.946	1.44
2	0.946	2.16
3	0.946	2.88

\*Baseline Configuration  $P_c = 100$  psia,  $\epsilon = 40:1$ .

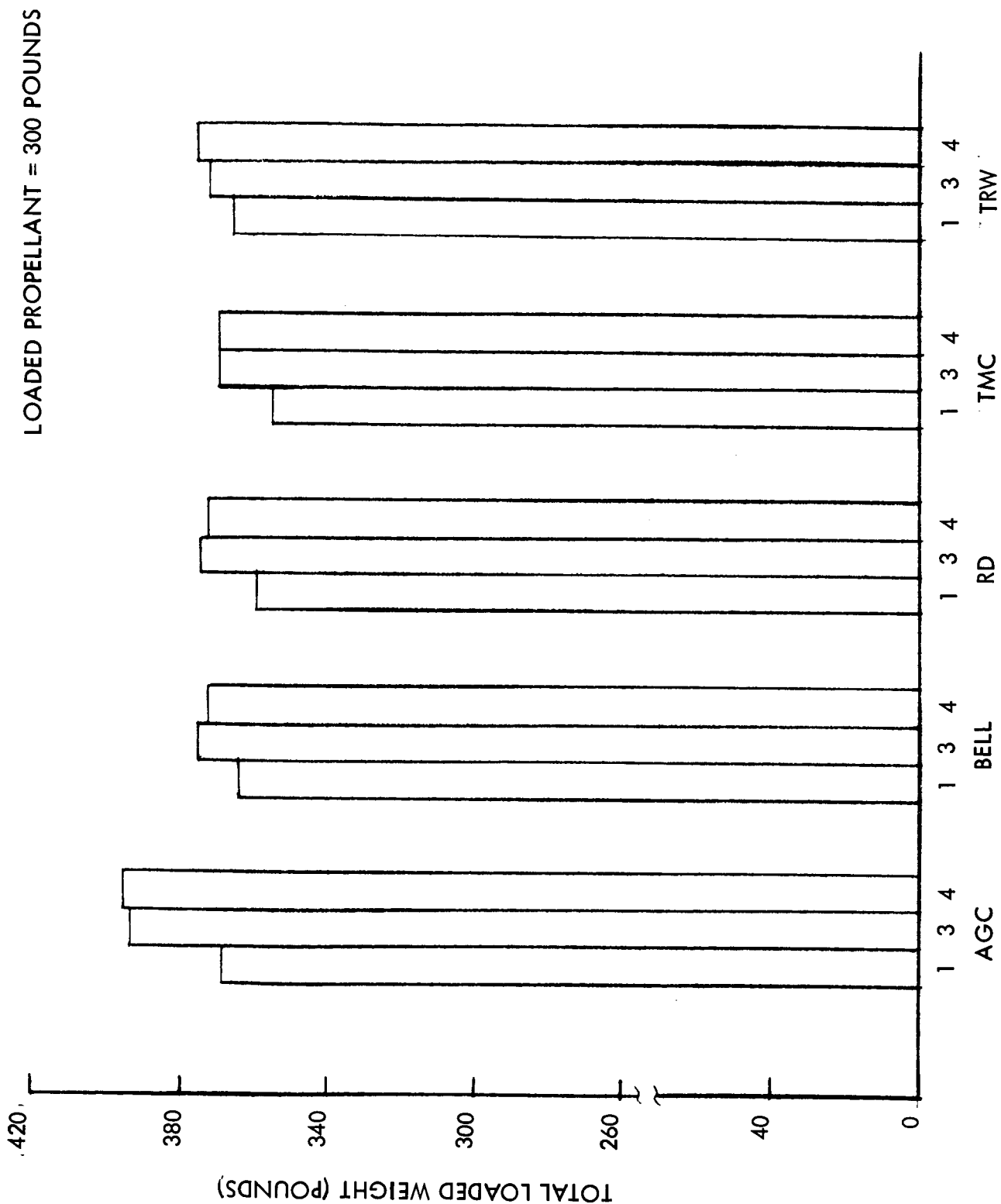


Figure I-14. Comparison of Propulsion Subsystems Weights

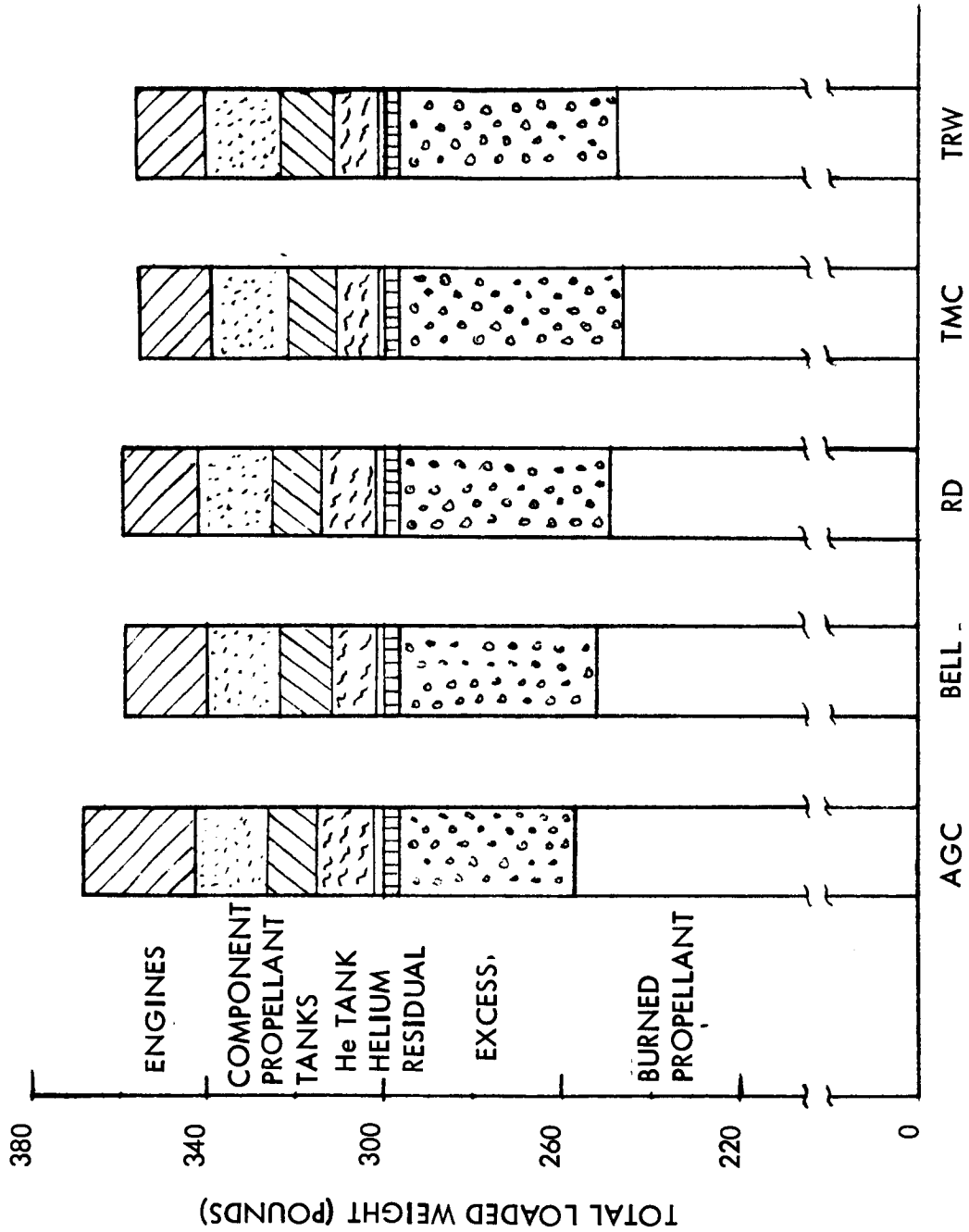


Figure 1-15. Single-Engine Subsystem Weight Comparison,  $\epsilon = 40$

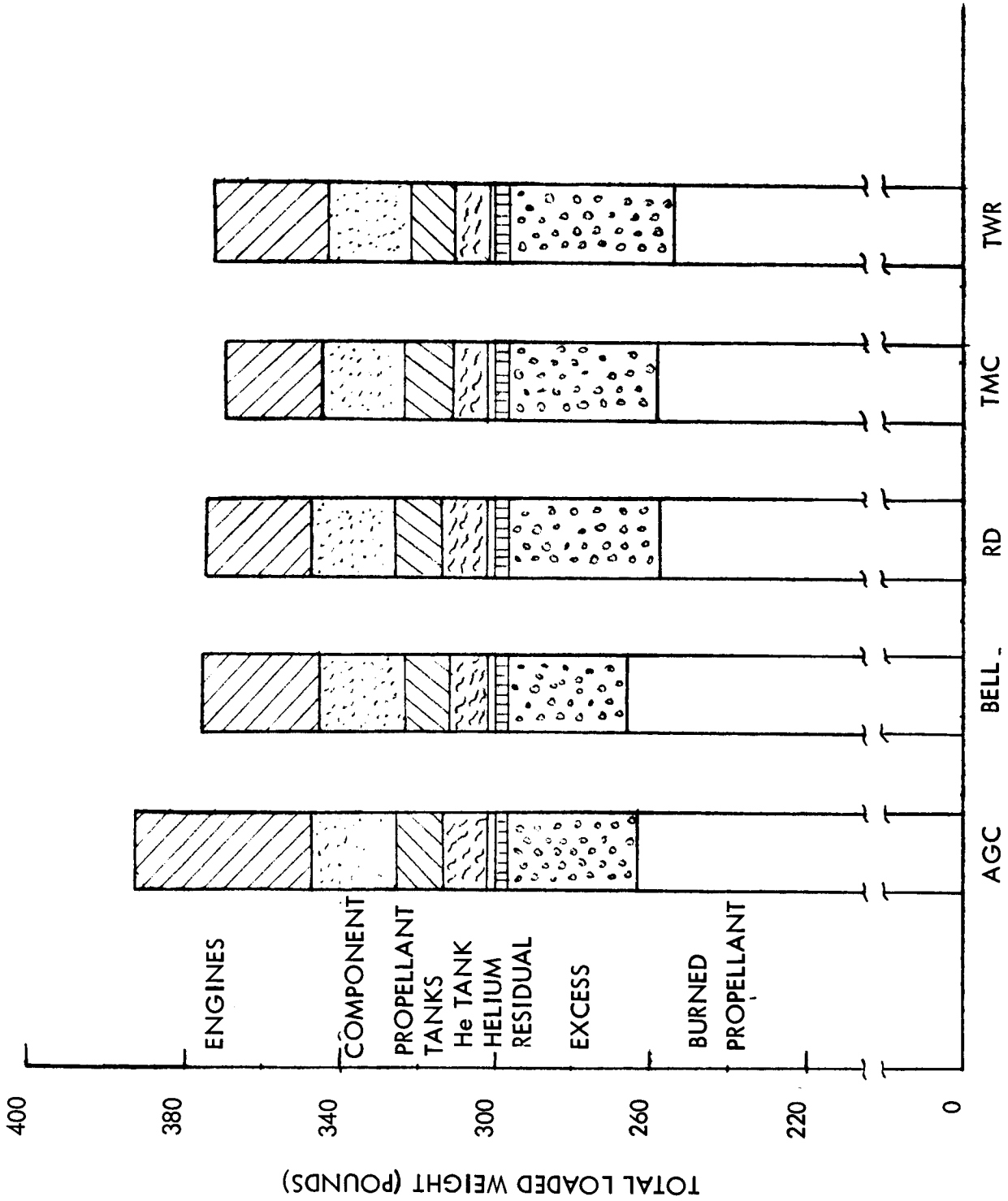


Figure 1-16. Three-Engine Subsystem Weight Comparison,  $\epsilon = 40$

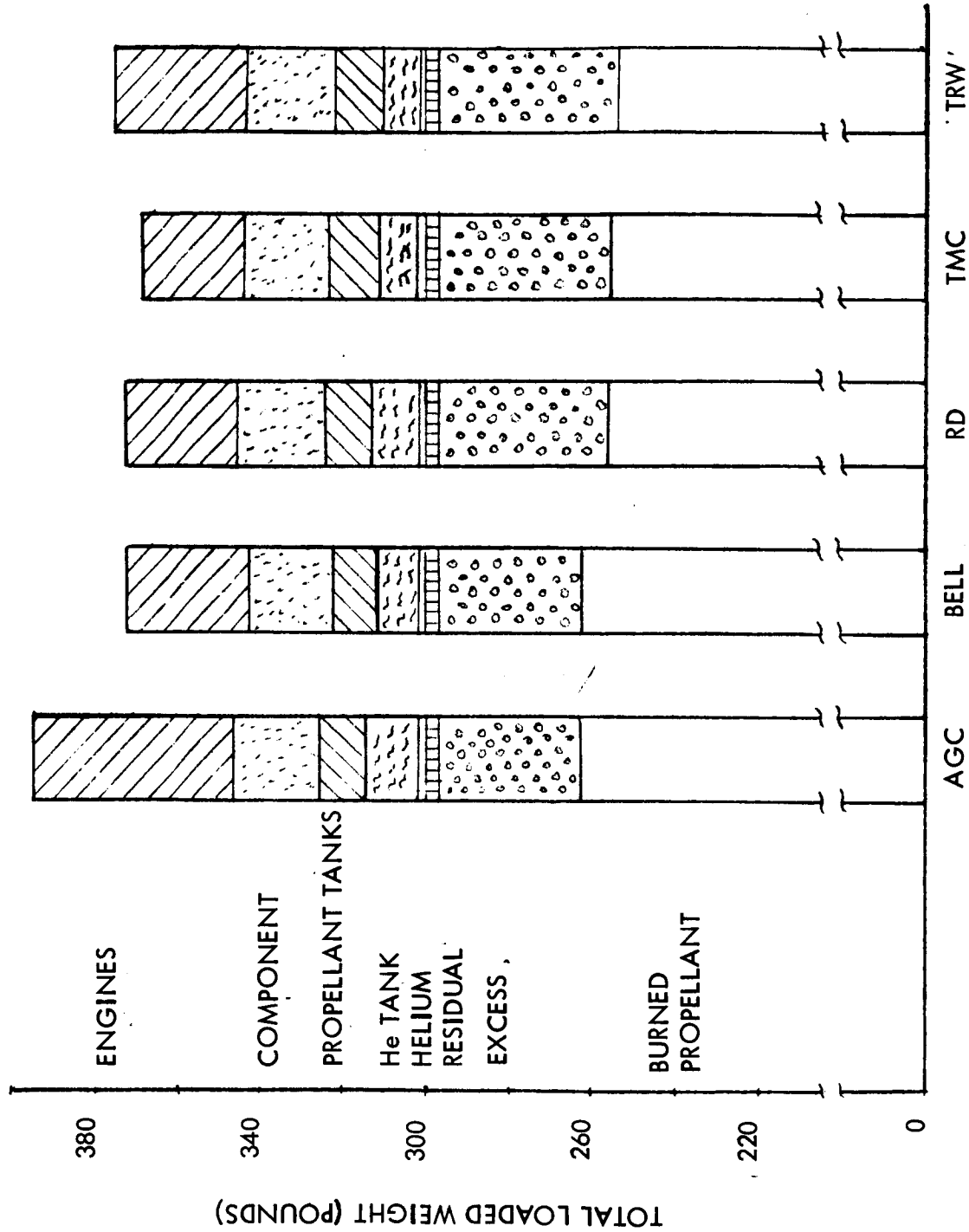


Figure 1-17. Four-Engine Subsystem Weight Comparison,  $\epsilon = 40$

yields minimum subsystem total weight. This expected result arises from the fact that the engine valve, thrust chamber, and associated hardware weight asymptotically approach a limiting value as individual engine thrust is reduced. (It is particularly significant with respect to the Aerojet and TRW concepts.) An even more pronounced difference would arise if loaded propellant weight were not held constant. In such a case, the effects of delivered specific impulse would be significant.

The high multiple-engine subsystem weight exhibited by the Aerojet Hypermet concept is particularly noted. For the three- and four-engine configurations, the dry weight is approximately 20 lb greater than the other manufacturer's concepts.

Figures 1-15, 1-16, and 1-17 also illustrate the propulsion subsystem weight breakdown. For the nominal mission profile, the burned propellant varies not more than 5.5 pounds for the most competitive four engine design concepts employed in single engine installations. The four-engine configuration yields a 9.1-pound variation for the same concepts. It is noted that, while the variable area injector provides higher performance at low throttle settings, its effect on overall loaded subsystems weight is minimal.

Comparison of one-, three-, and four-engine configuration dry-weight values indicate the single-engine subsystem is approximately 15 pounds lighter than the multiengine approaches.

#### Effect of Chamber Pressure

Figure 1-18 presents data illustrating the variation of total loaded subsystem weight as a function of chamber pressure for various nozzle area ratios. From the overall viewpoint, it is noted that the effect of chamber pressure is very minimal for the radiation-cooled concepts. However, minimum loaded subsystem weight is in the 100-psia regime. Weight differences resulting from the effect of area ratio on engine performance are masked by the constant propellant load. The beryllium thrust chamber subsystem weight optimizes at approximately 140 to 160 psia chamber pressure on this basis. No significant differences in optimum design points were noted between 1-, 3-, or 4-engine configurations.

In order to define the optimum nozzle-area ratio, it was necessary to evaluate its effect on vehicle range. This required that the nominal thrust-to-time mission duty cycle be extended over and above that shown in Figure 1-13 in the cruise portion (both outbound and inbound legs) to deplete the propellant. The vehicle gross weight and payload weight was held constant. Propellant quantity, subsystem dry weight, and vehicle structural weight varied in accordance with their computed values. Structural weight sensitivities were included to account for differences in engine geometry.

2421-02-02  
0013 0000

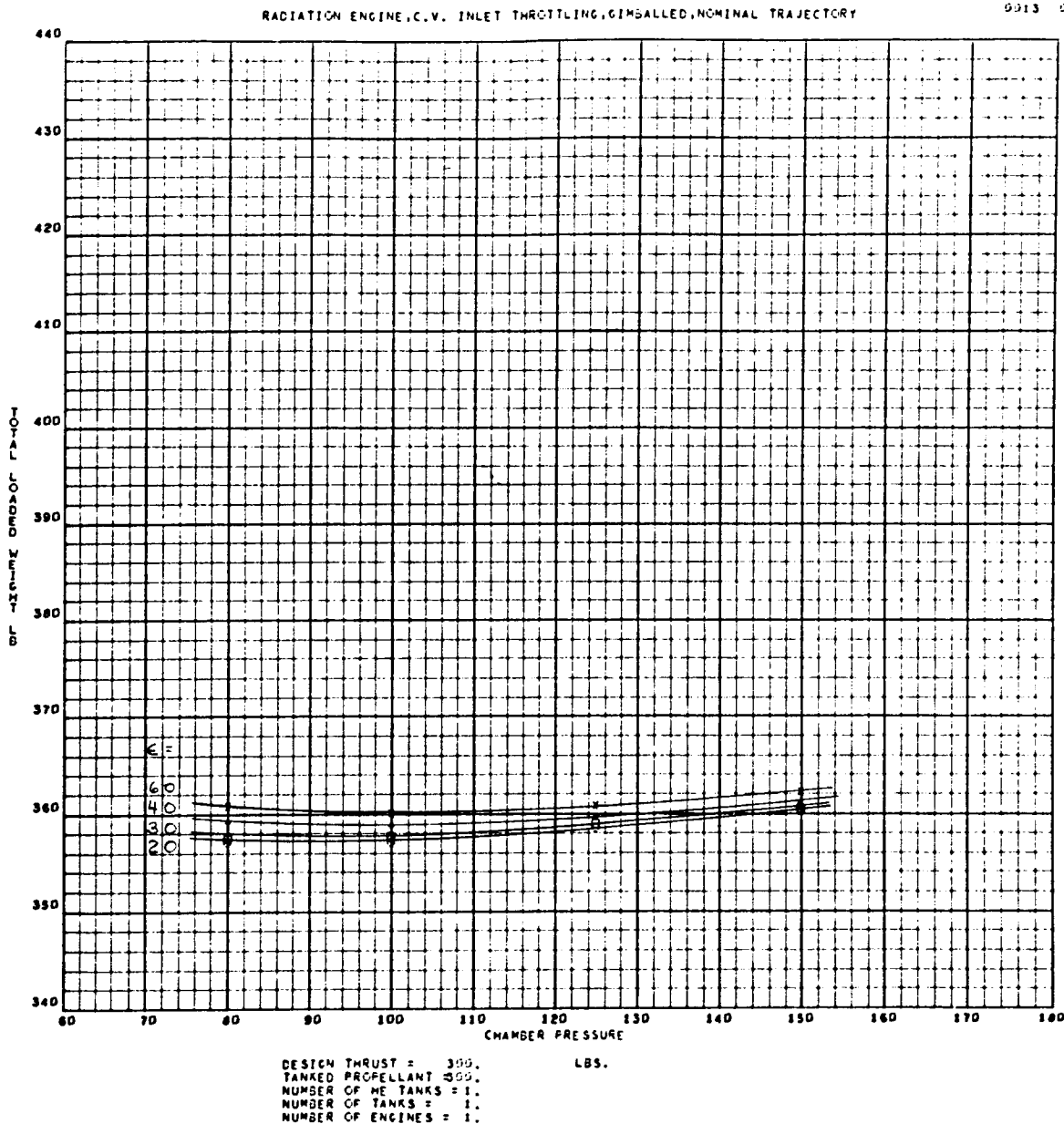
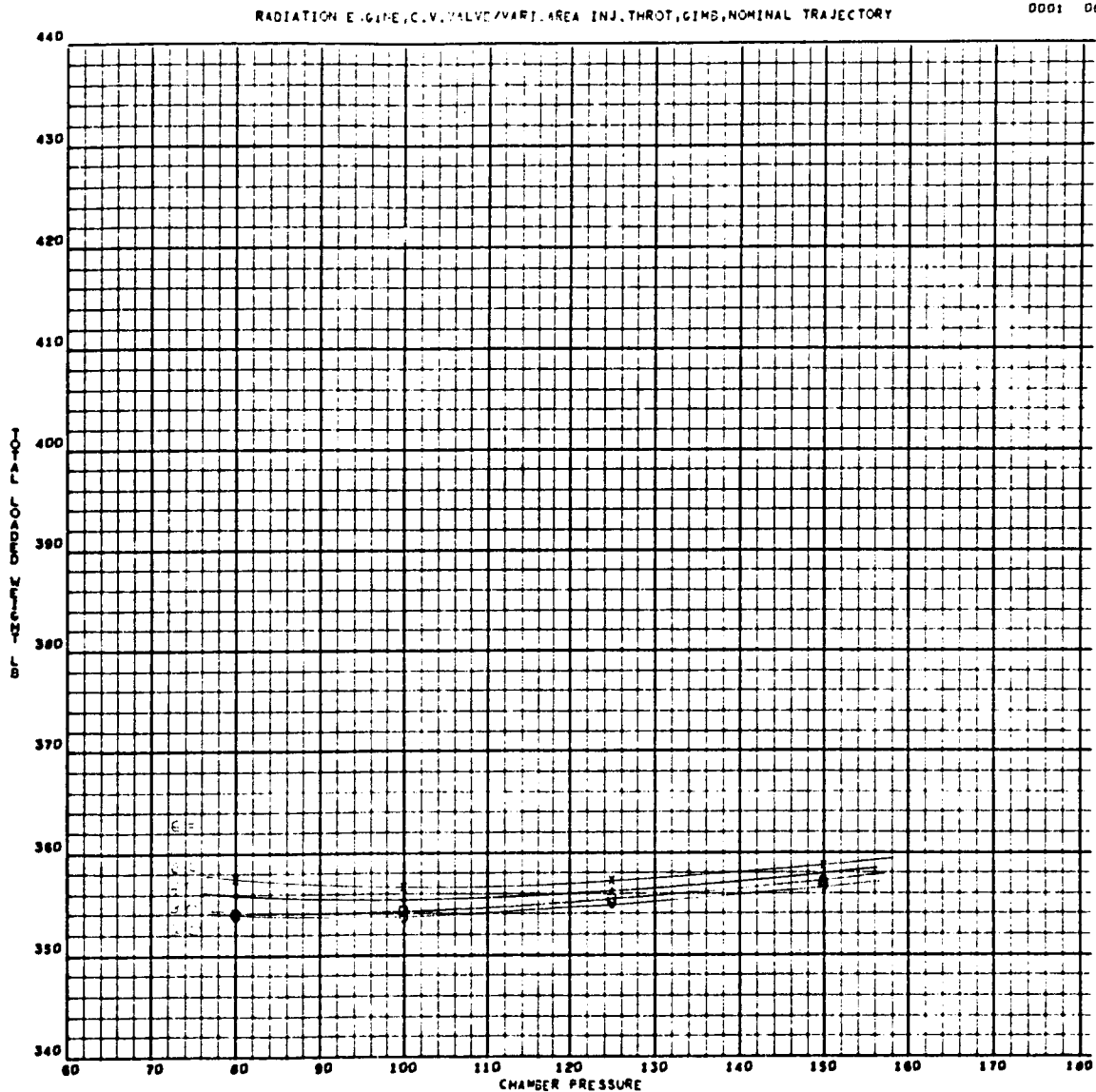


Figure 1-18. Variation of Total Loaded Subsystem Weight as a Function of Chamber Pressure for Various Nozzle-Area Ratios (Sheet 1 of 14)



DESIGN THRUST = 300.  
 TANKED PROPELLANT = 300.  
 NUMBER OF HE TANKS = 1.  
 NUMBER OF TANKS = 1.  
 NUMBER OF ENGINES = 1.

Figure 1-18. Variation of Total Loaded Subsystem Weight as a Function of Chamber Pressure for Various Nozzle-Area Ratios (Sheet 2 of 14)



2421-02-02  
0007 0000

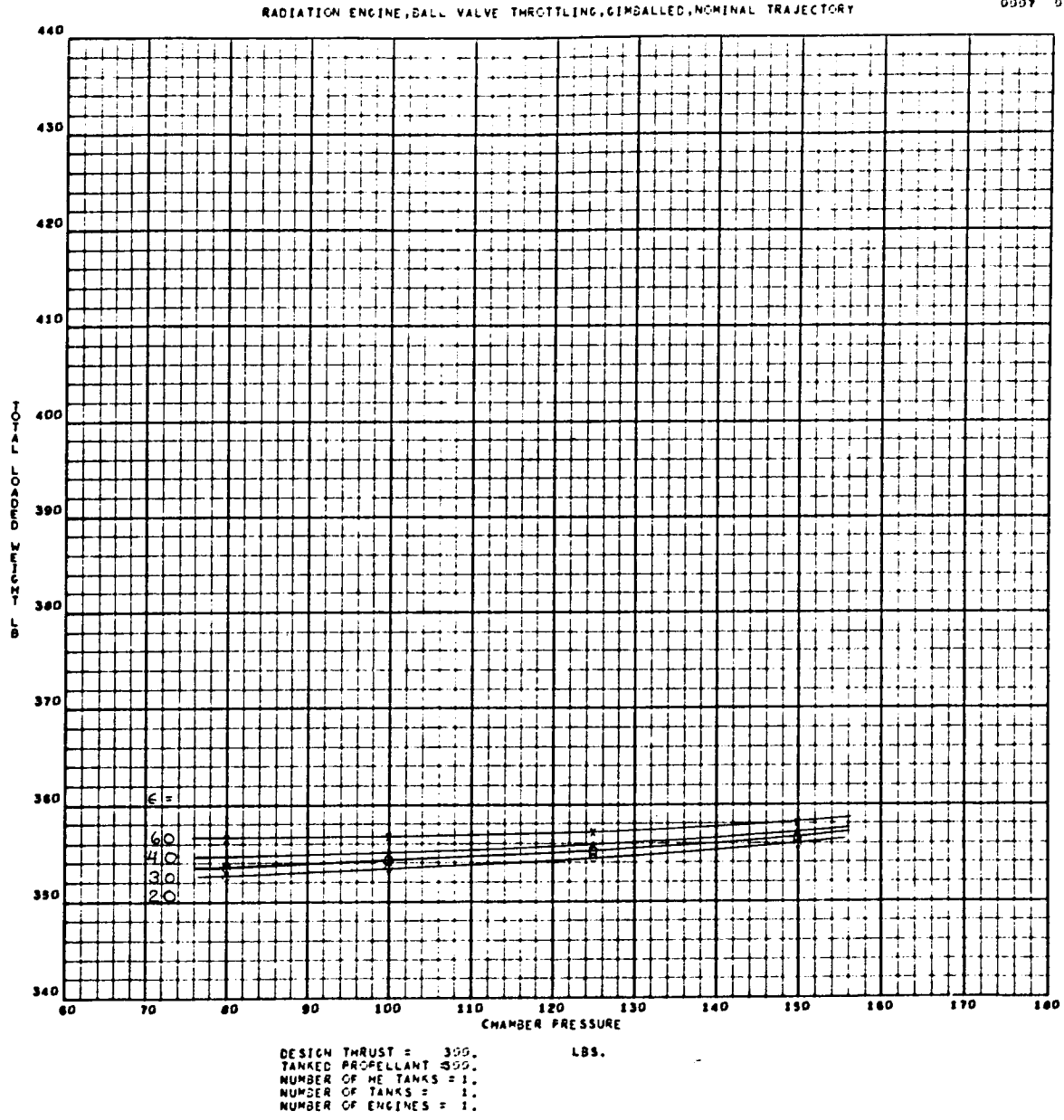


Figure 1-18. Variation of Total Loaded Subsystem Weight as a Function of Chamber Pressure for Various Nozzle-Area Ratios (Sheet 3 of 14)

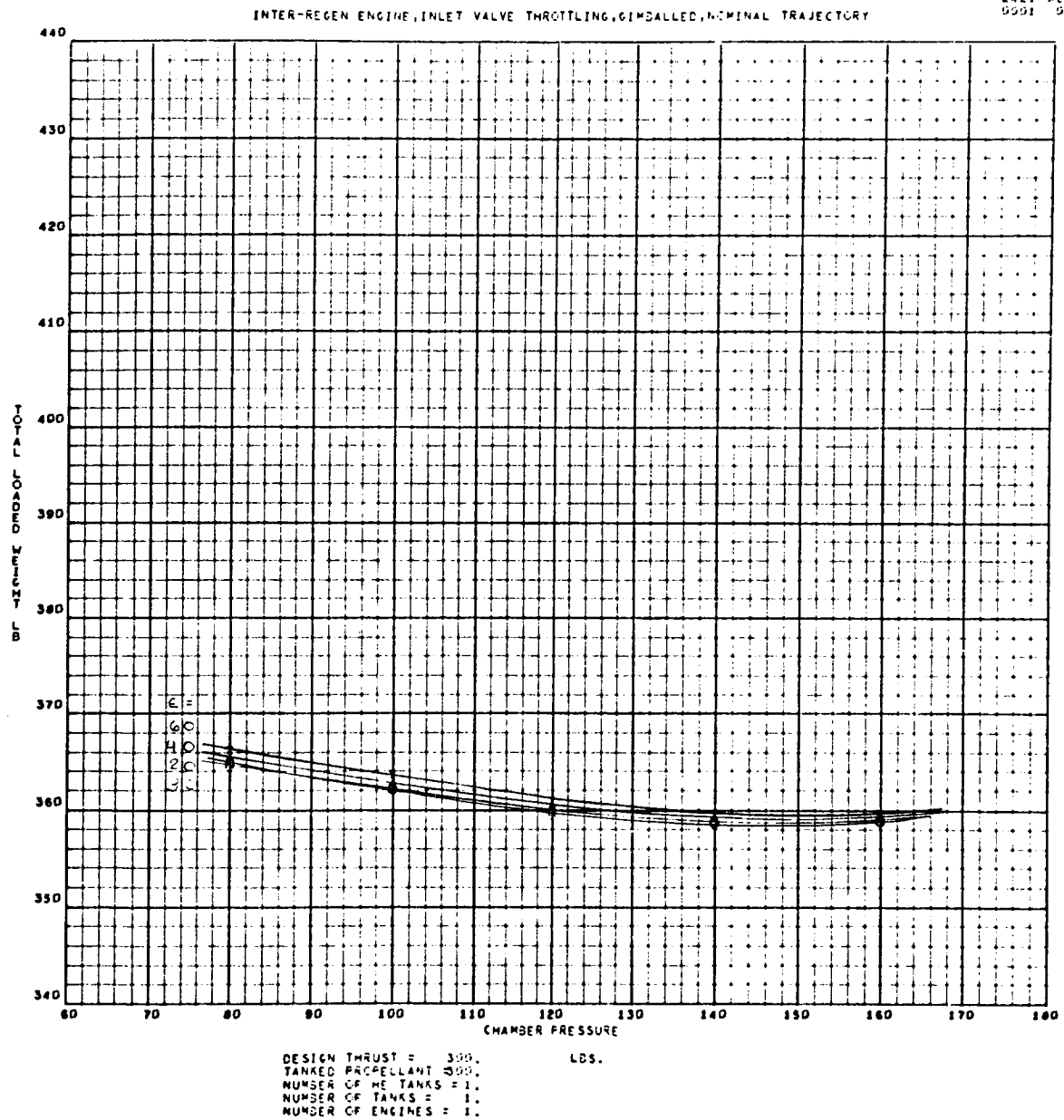


Figure 1-18. Variation of Total Loaded Subsystem Weight as a Function of Chamber Pressure for Various Nozzle-Area Ratios (Sheet 4 of 14)

2421-02-02  
0010 0000

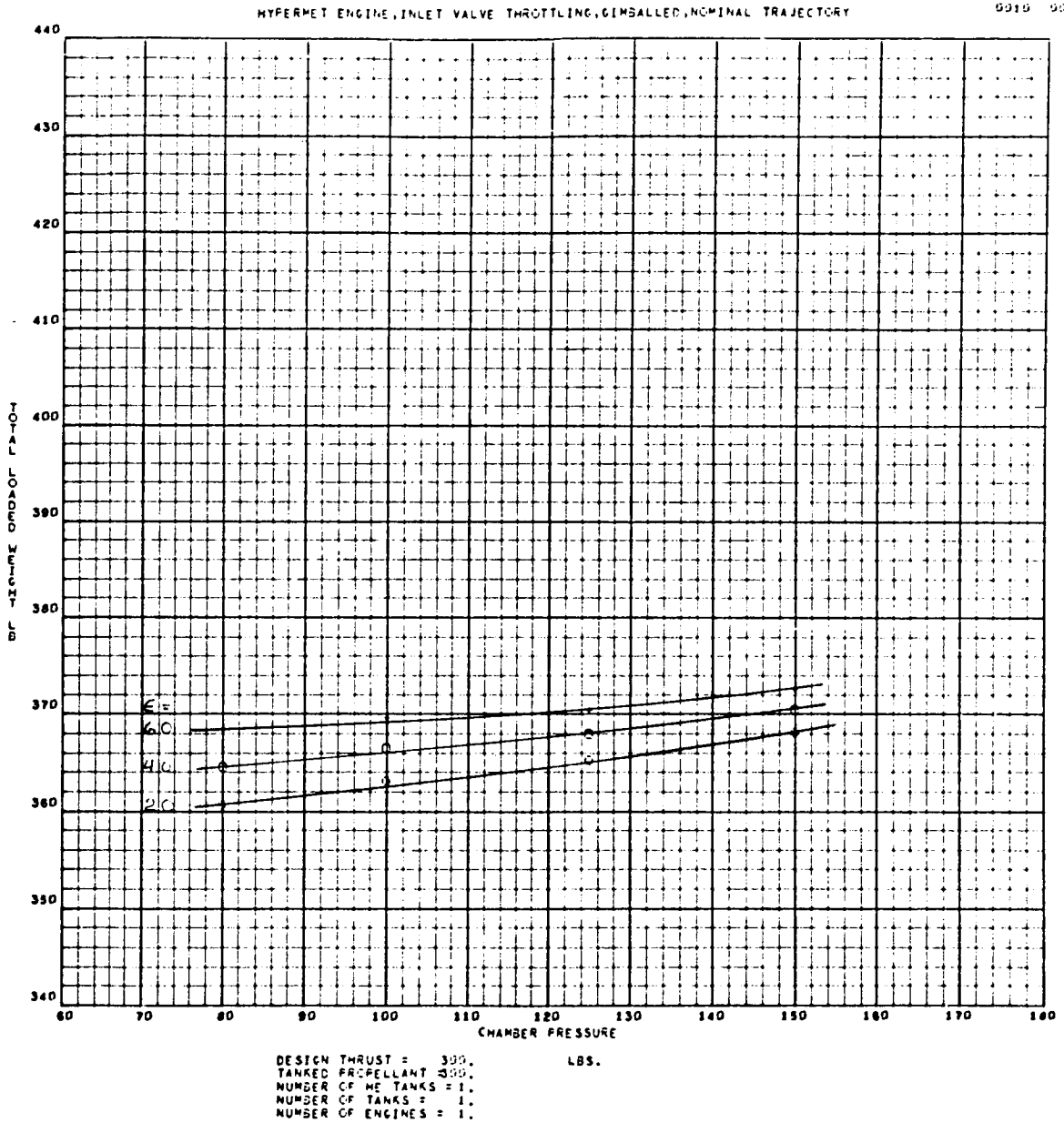


Figure 1-18. Variation of Total Loaded Subsystem Weight as a Function of Chamber Pressure for Various Nozzle-Area Ratios (Sheet 5 of 14)

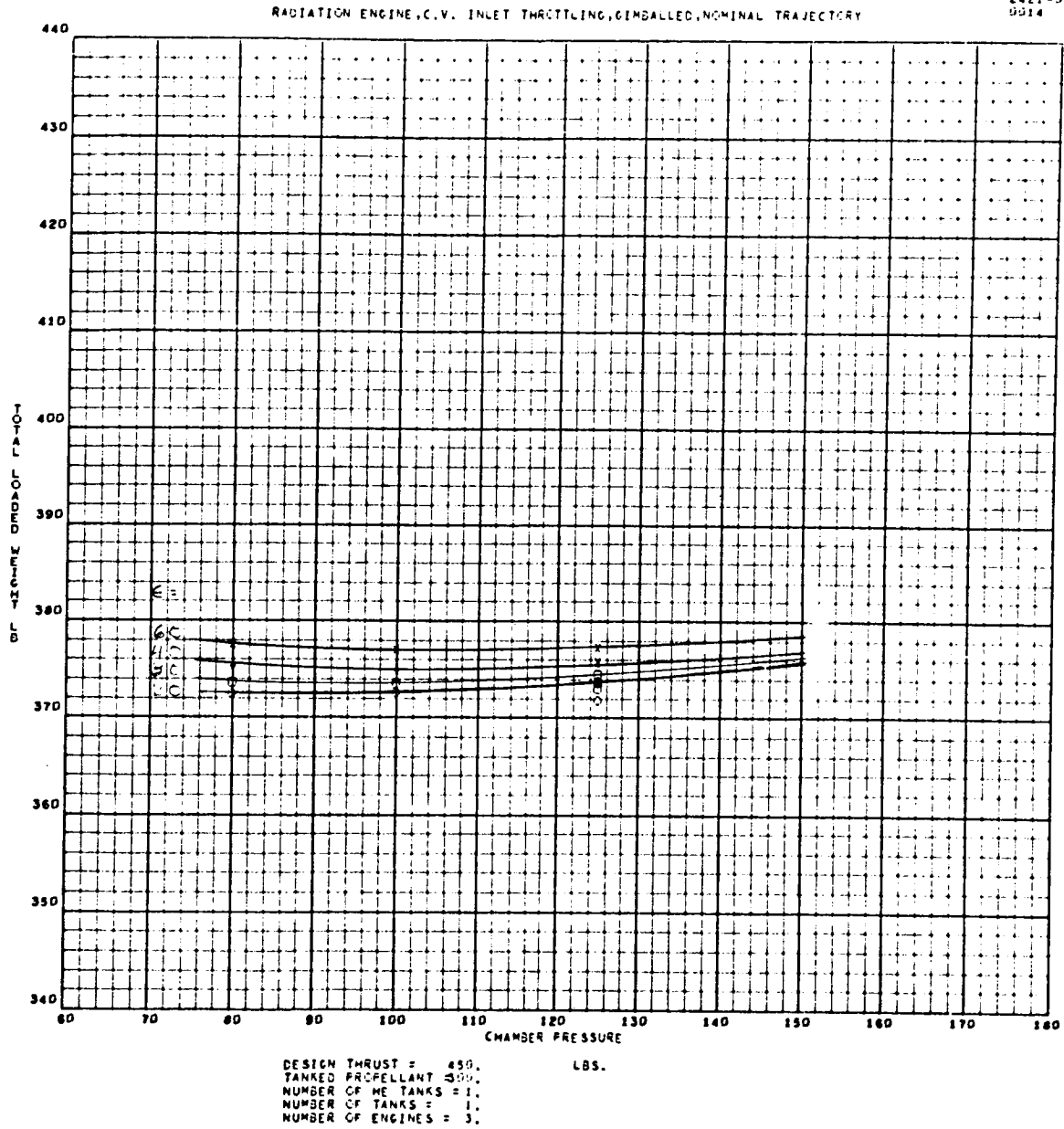


Figure 1-18. Variation of Total Loaded Subsystem Weight as a Function of Chamber Pressure for Various Nozzle-Area Ratios (Sheet 6 of 14)

RADIATION ENGINE, C.V. VALVE/VARI. AREA INJ. THROT, GIMS, NOMINAL TRAJECTORY

2421-02-05  
0002 0000

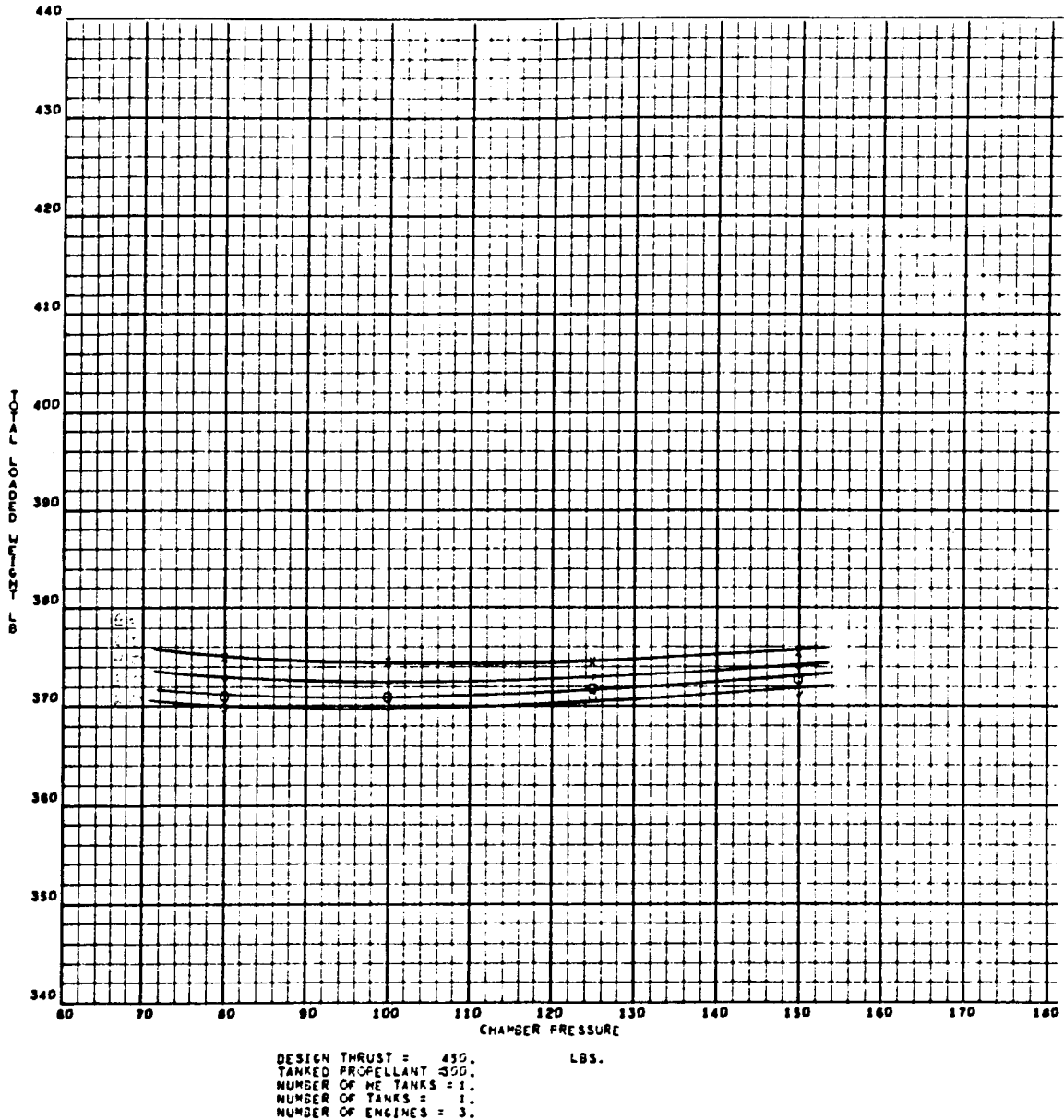


Figure 1-18. Variation of Total Loaded Subsystem Weight as a Function of Chamber Pressure for Various Nozzle-Area Ratios (Sheet 7 of 14)

2421-02-02  
0000 0000

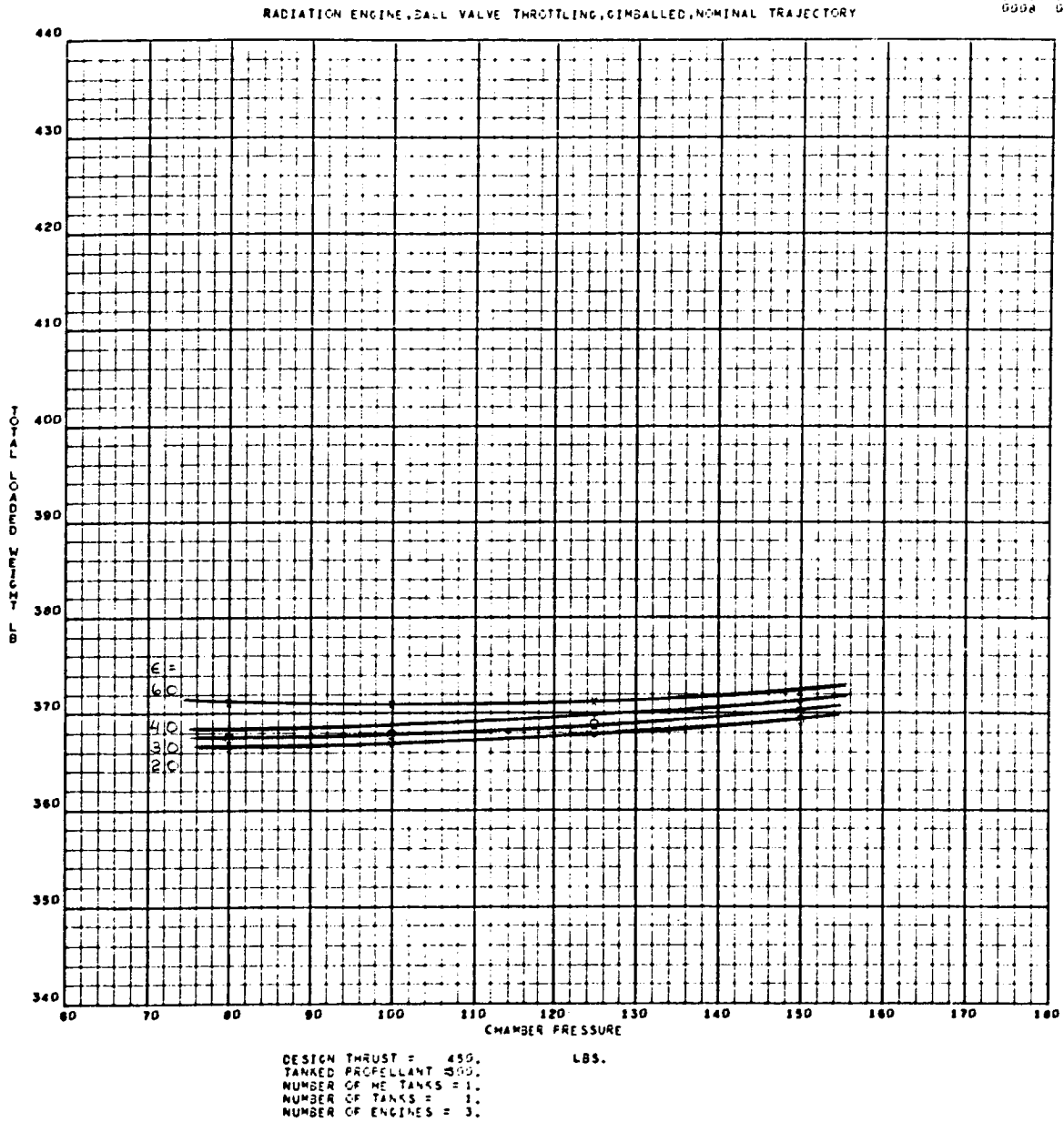


Figure 1-18. Variation of Total Loaded Subsystem Weight as a Function of Chamber Pressure for Various Nozzle-Area Ratios (Sheet 8 of 14)

2421-02-02  
0011 0000

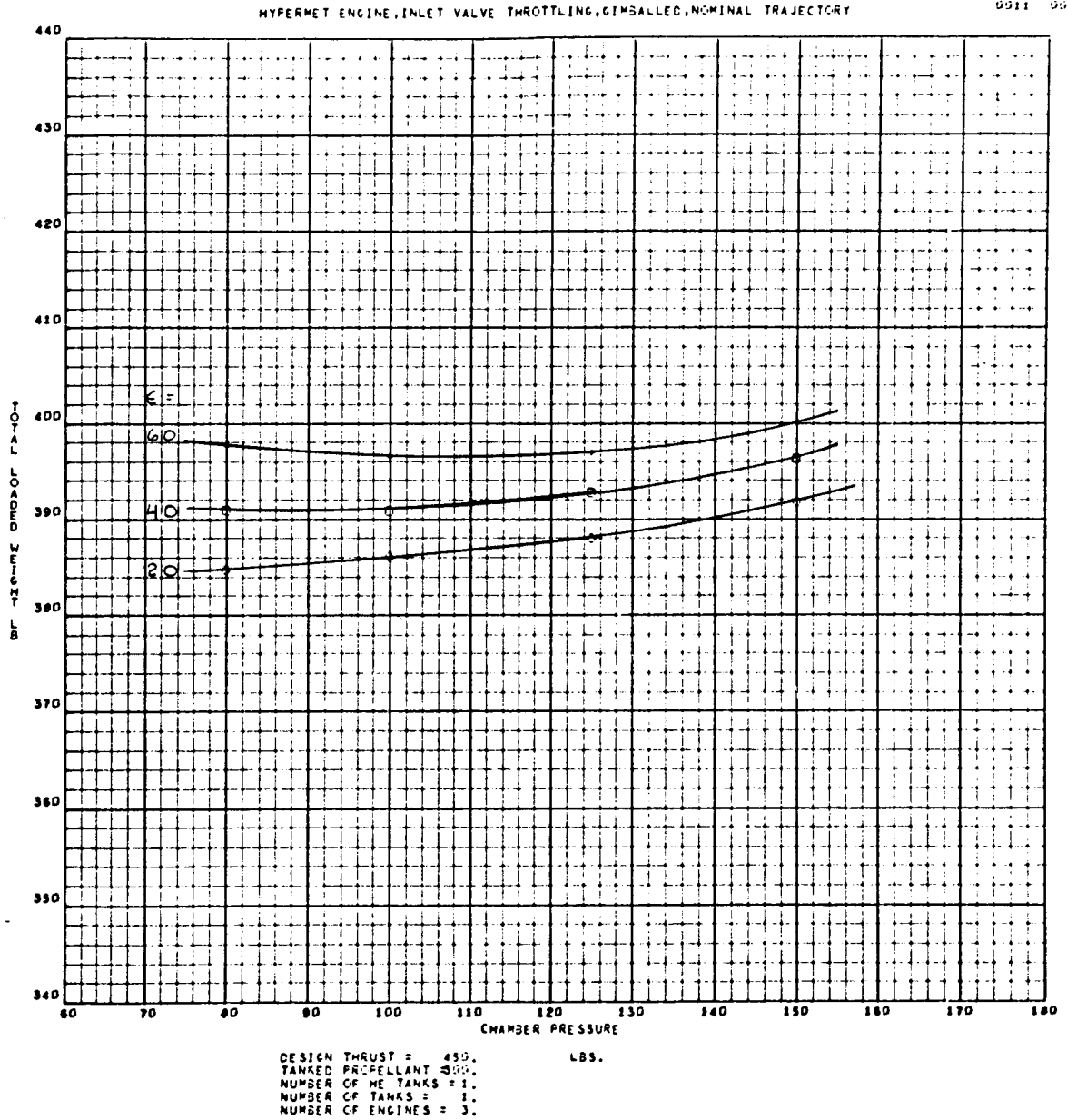


Figure 1-18. Variation of Total Loaded Subsystem Weight as a Function of Chamber Pressure for Various Nozzle-Area Ratios (Sheet 9 of 14)

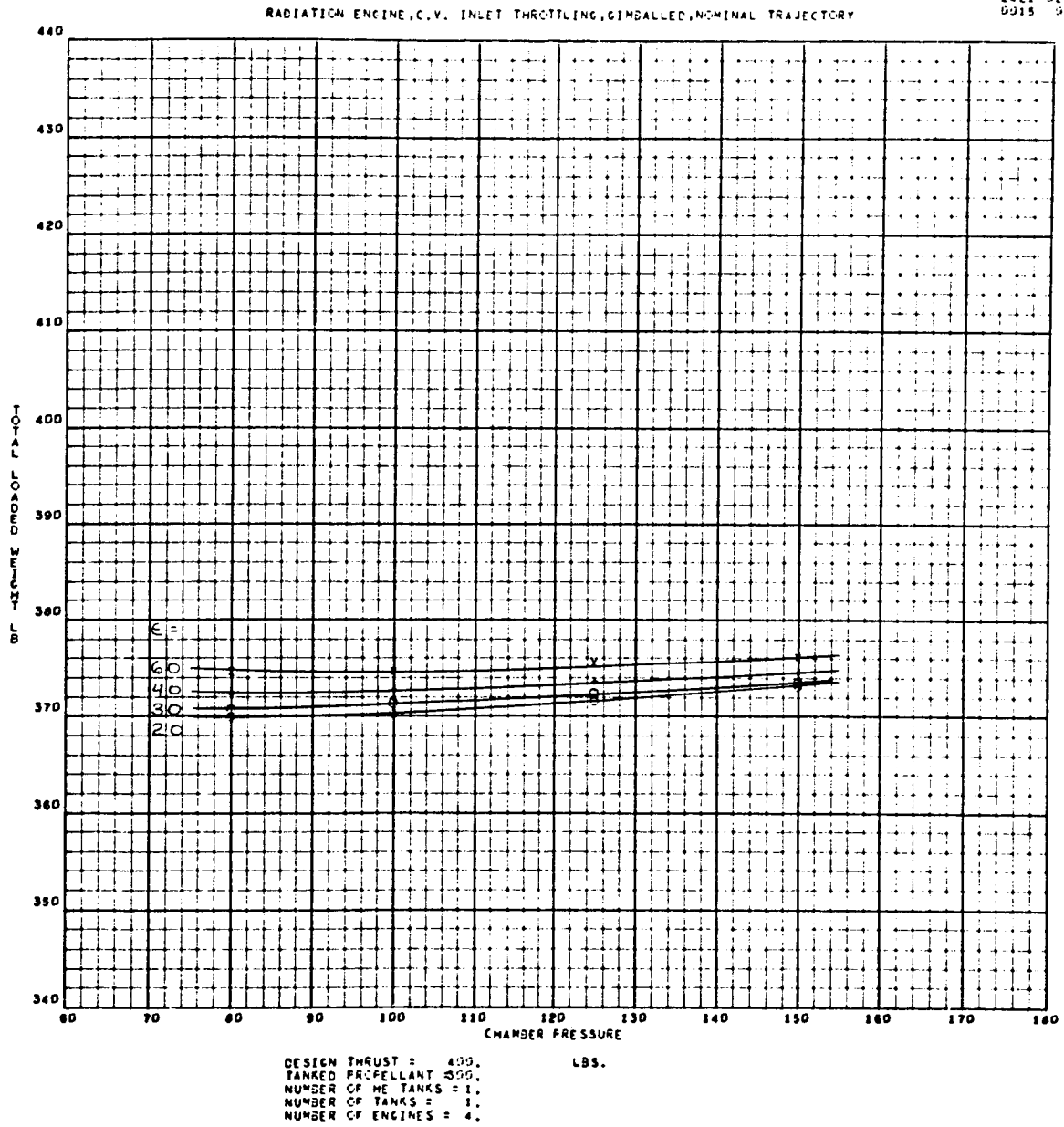


Figure 1-18. Variation of Total Loaded Subsystem Weight as a Function of Chamber Pressure for Various Nozzle-Area Ratios (Sheet 10 of 14)



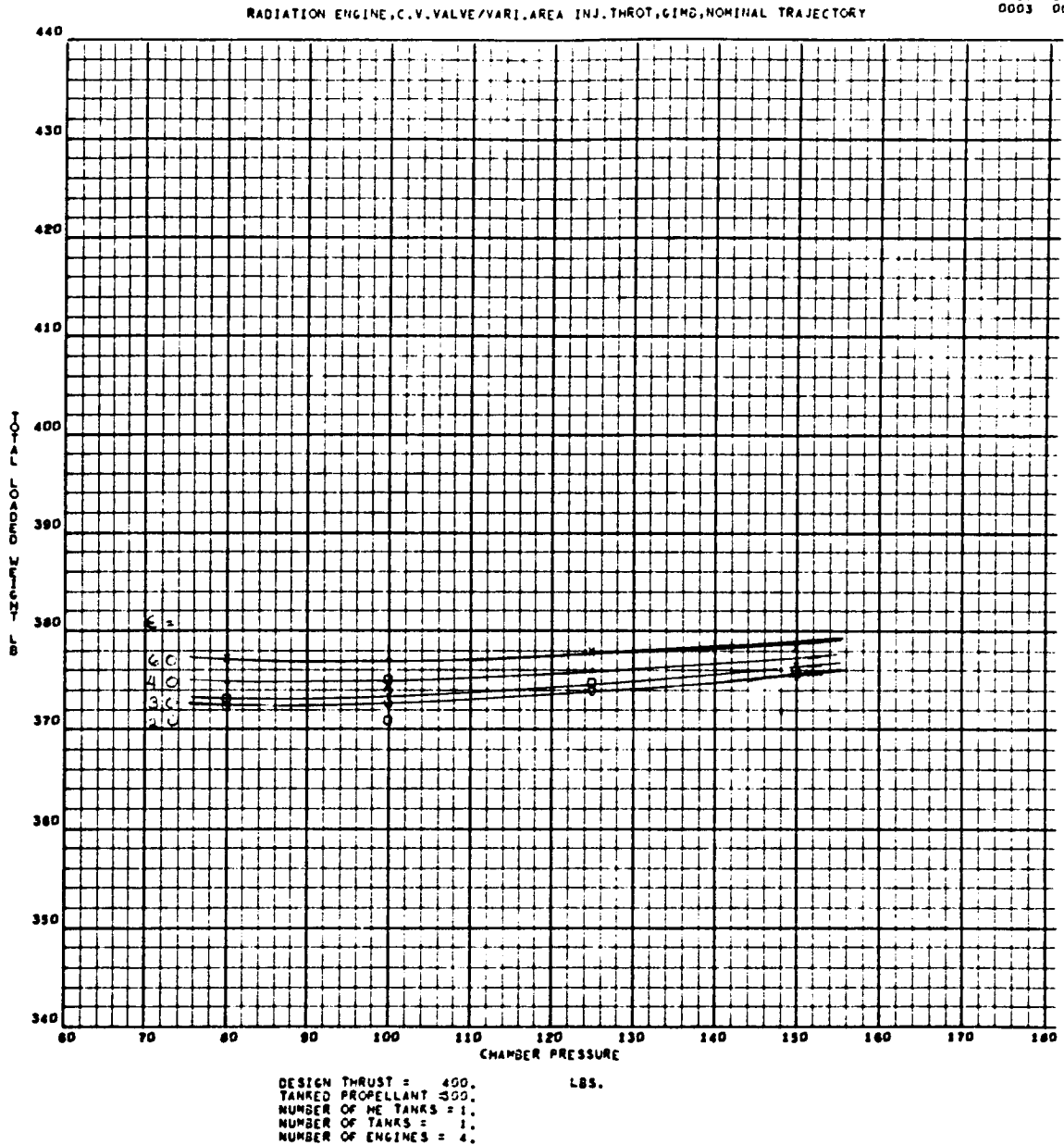


Figure 1-18. Variation of Total Loaded Subsystem Weight as a Function of Chamber Pressure for Various Nozzle-Area Ratios (Sheet 11 of 14)

2421-02-02  
0000 0000

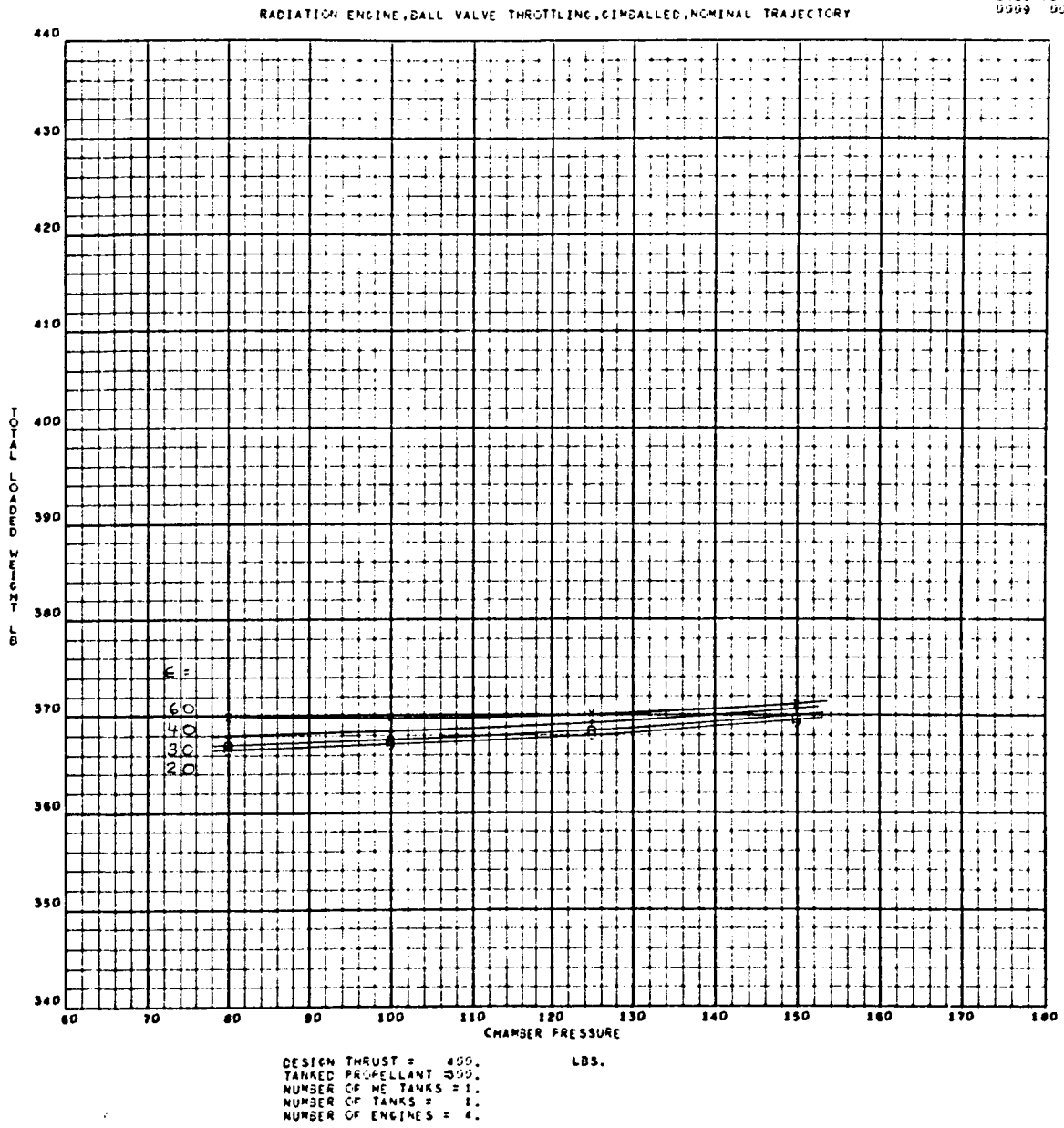


Figure 1-18. Variation of Total Loaded Subsystem Weight as a Function of Chamber Pressure for Various Nozzle-Area Ratios (Sheet 12 of 14)

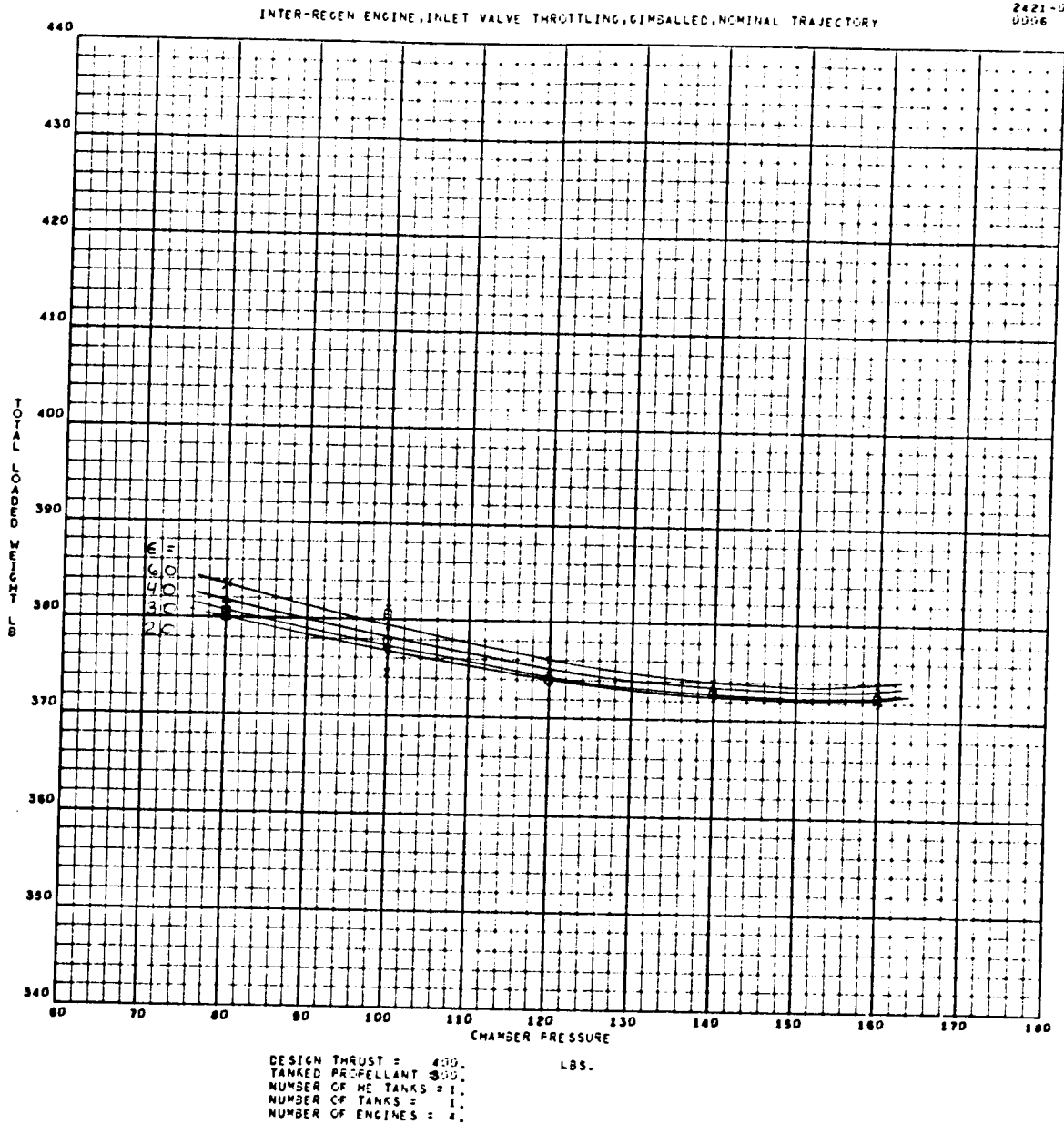


Figure 1-18. Variation of Total Loaded Subsystem Weight as a Function of Chamber Pressure for Various Nozzle-Area Ratios (Sheet 13 of 14)

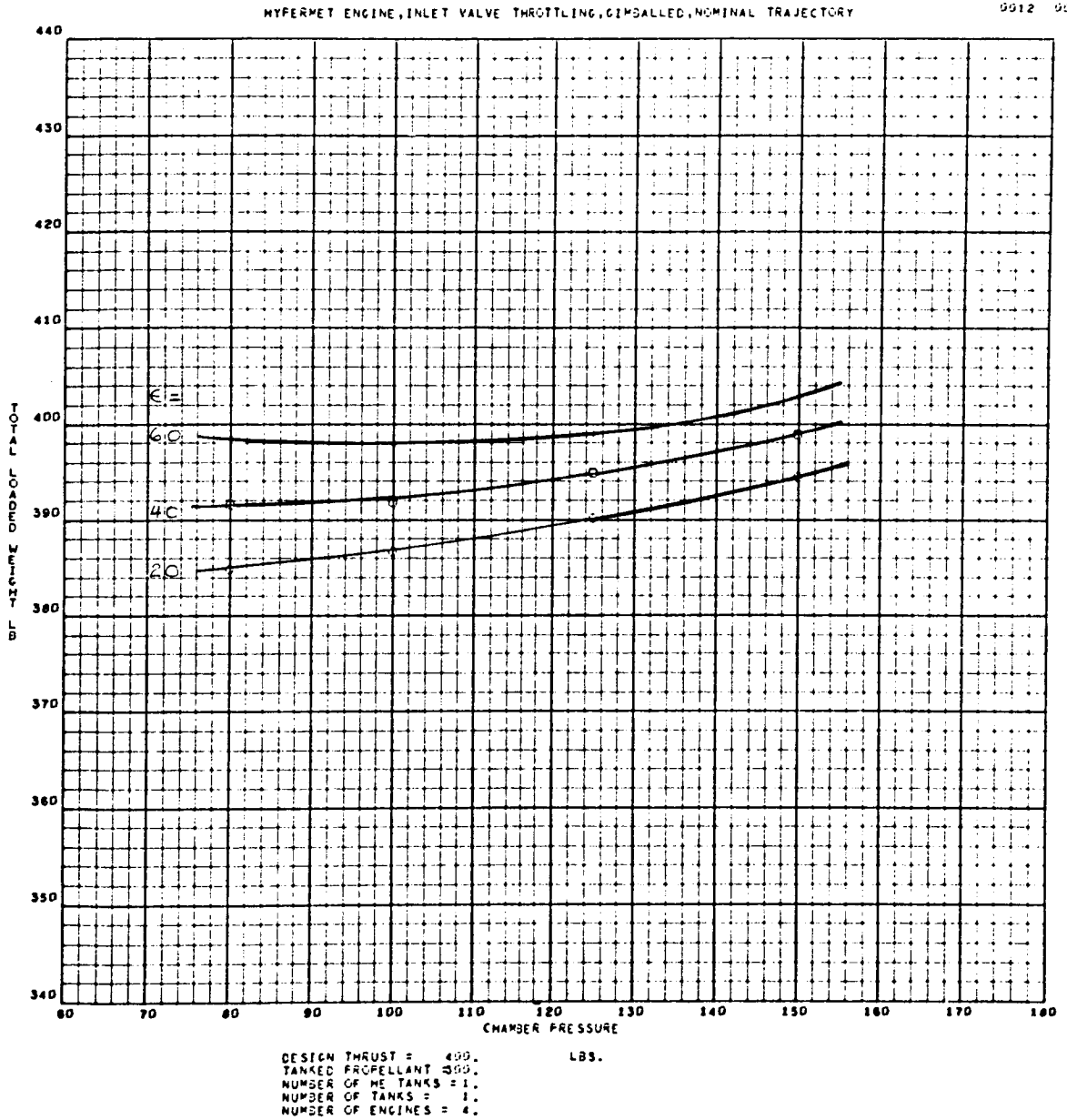


Figure 1-18. Variation of Total Loaded Subsystem Weight as a Function of Chamber Pressure for Various Nozzle-Area Ratios (Sheet 14 of 14)

Figure 1-19 presents data illustrating the variation of LFV range as a function of nozzle area ratio for various chamber pressures. Again the single engine system offers a performance advantage of approximately 0.4- to 0.6-nm range over a four-engine configuration. Table 1-9 provides a comparison of mission performance at selected design points.

Table 1-9. Range-Comparison Summary

Manufacturer	Range - 370-lb payload (nautical miles)	
	1 Engine	4 Engines
Bell*	5.86	5.25
Marquardt	6.14	5.60
Rocketdyne	6.02	5.55
TRW	6.03	5.38

\*Radiation cooled engines at  $P_c = 100$  psia, interregeneratively cooled engines at  $P_c = 140$  psia, optimum area ratio

Again noting Figure 1-19, it becomes apparent that increasing chamber pressure also increases range. With reference to the total loaded subsystem weight trends, it is concluded that the increase in engine performance and decrease in vehicle weight (engine-envelope effects) exceed the effects of increasing propulsion-subsystem burnout weight. There is, however, a specific reason for retaining the previously defined optimum chamber-pressure levels. The radiation-cooled engine has an overwhelming base of developed hardware technology at 100-psia chamber pressure. To depart from this regime would require extending the engine-development program. This component is already the pacing item in LFV development cycle.

The 140-psia chamber pressure weight and resupply optimum exhibited by the interregenerative engine concept is also considered a desirable LFV design point. Here again, existing hardware technology is felt to outweigh the small range increase attainable at higher pressures.

#### Area Ratio

Based on the foregoing considerations, the optimum nozzle area ratio is approximately 40:1 for the majority of configurations considered. The exception is the TMC single-engine configuration which displays an optimum at approximately 58:1.

2421-05-04  
0003 0500

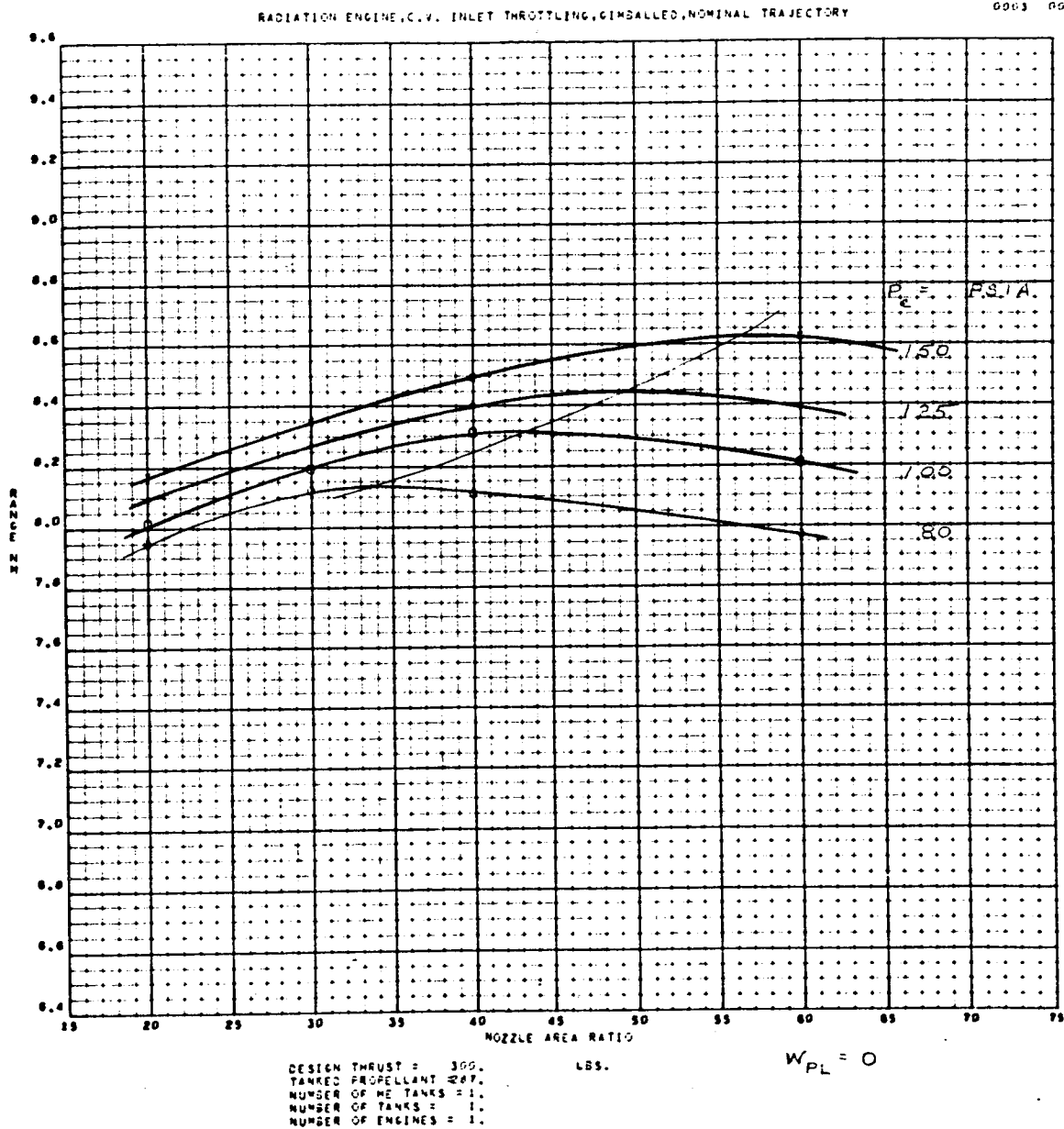


Figure 1-19. Variation of LFV Range as a Function of Nozzle-Area Ratio for Various Chamber Pressures (Sheet 1 of 23)

2421-03-03  
0001 0000

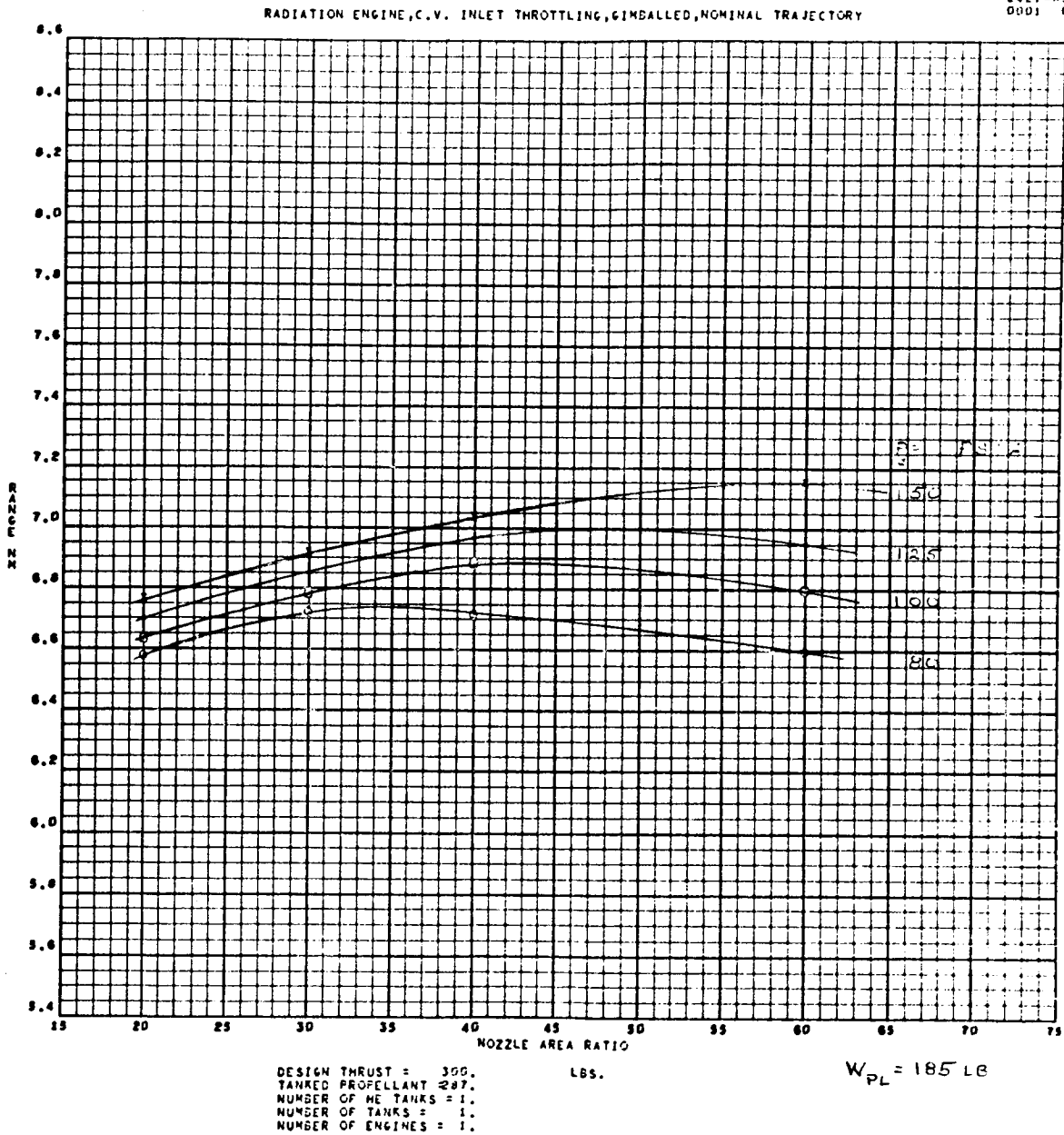


Figure 1-19. Variation of LFV Range as a Function of Nozzle-Area Ratio for Various Chamber Pressures (Sheet 2 of 23)

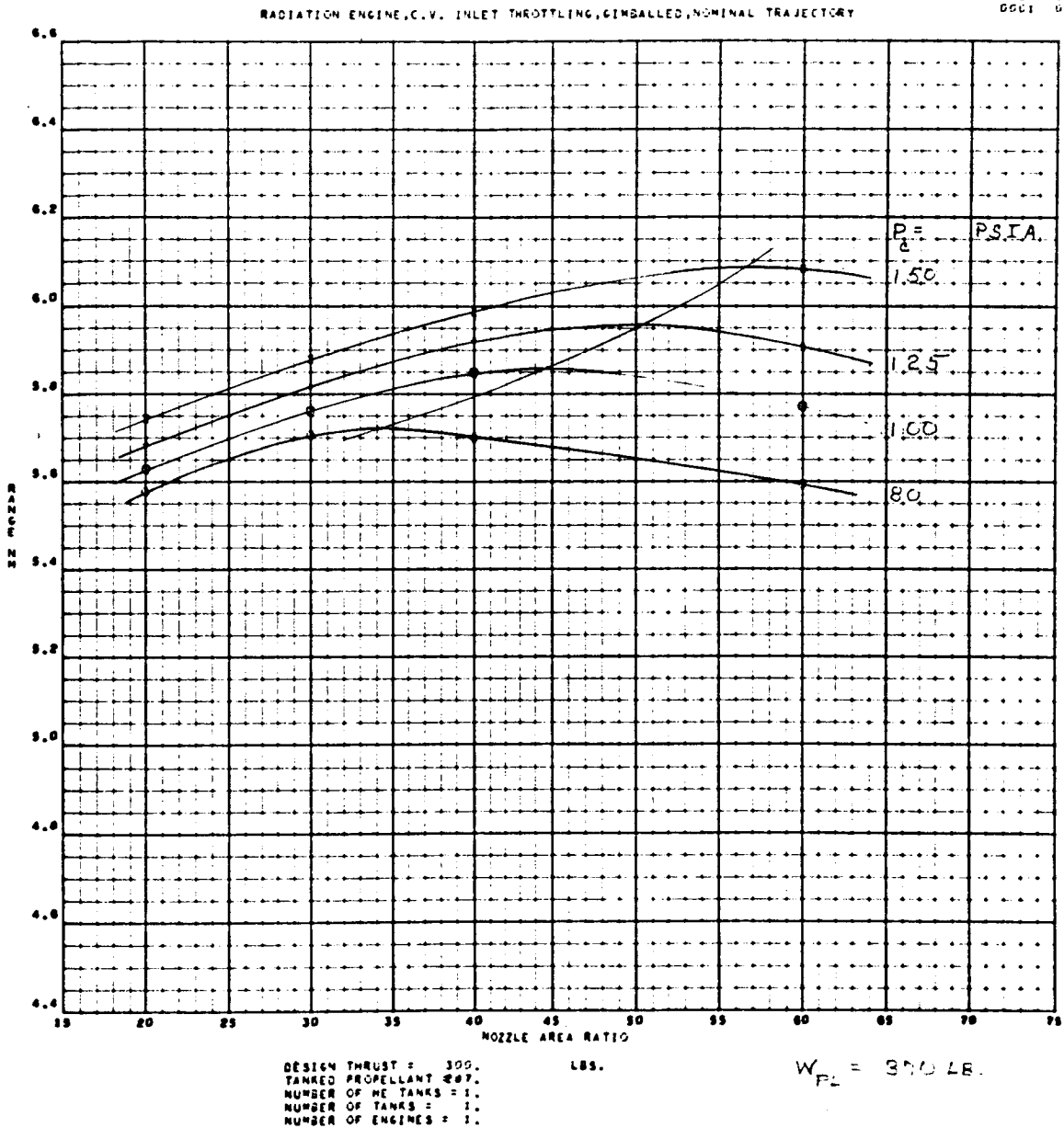


Figure 1-19. Variation of LFV Range as a Function of Nozzle-Area Ratio for Various Chamber Pressures (Sheet 3 of 23)



2421-05-04  
0006 0000

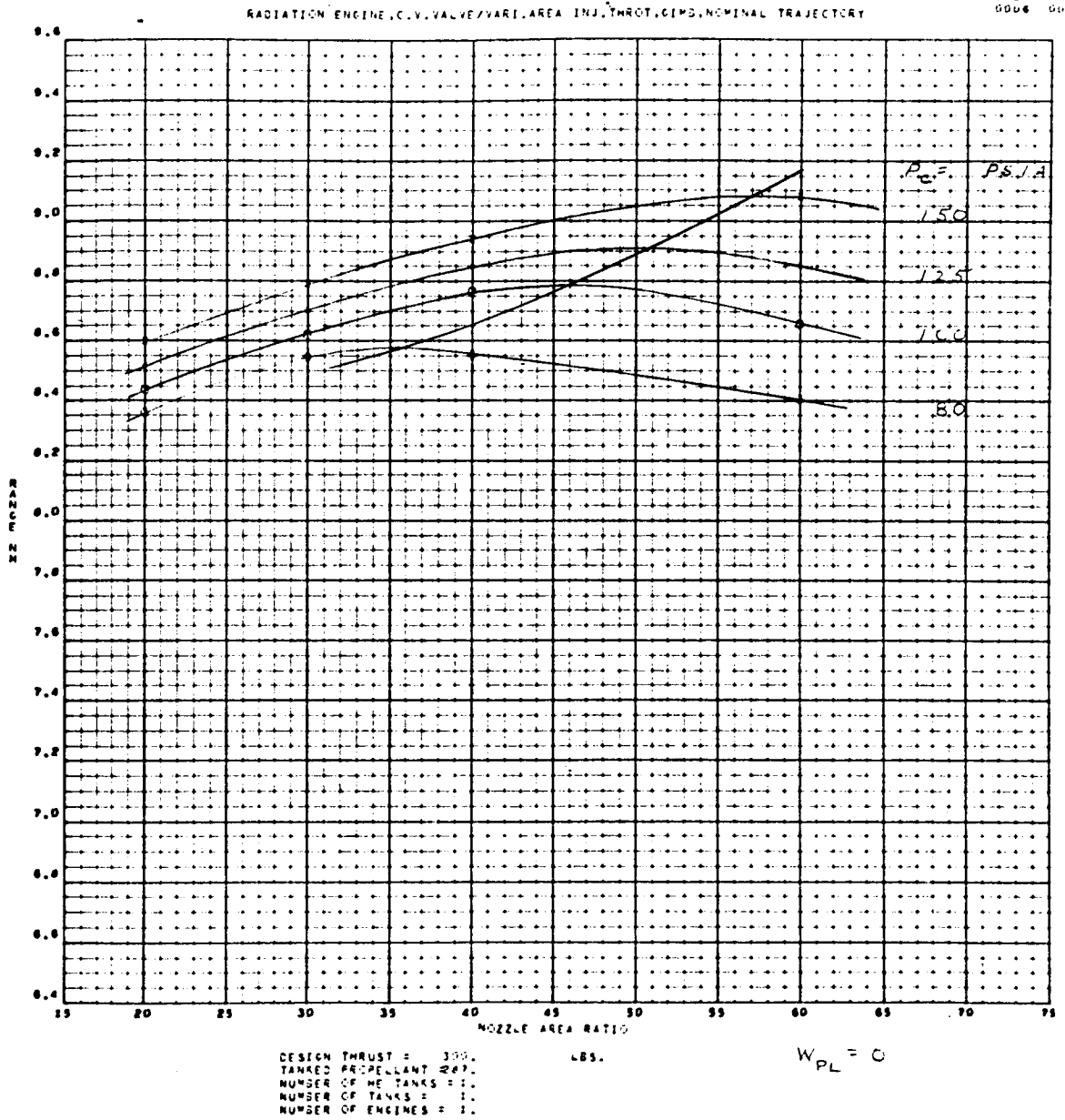


Figure 1-19. Variation of LFV Range as a Function of Nozzle-Area Ratio for Various Chamber Pressures (Sheet 4 of 23)

2421-03-05  
0004 0000

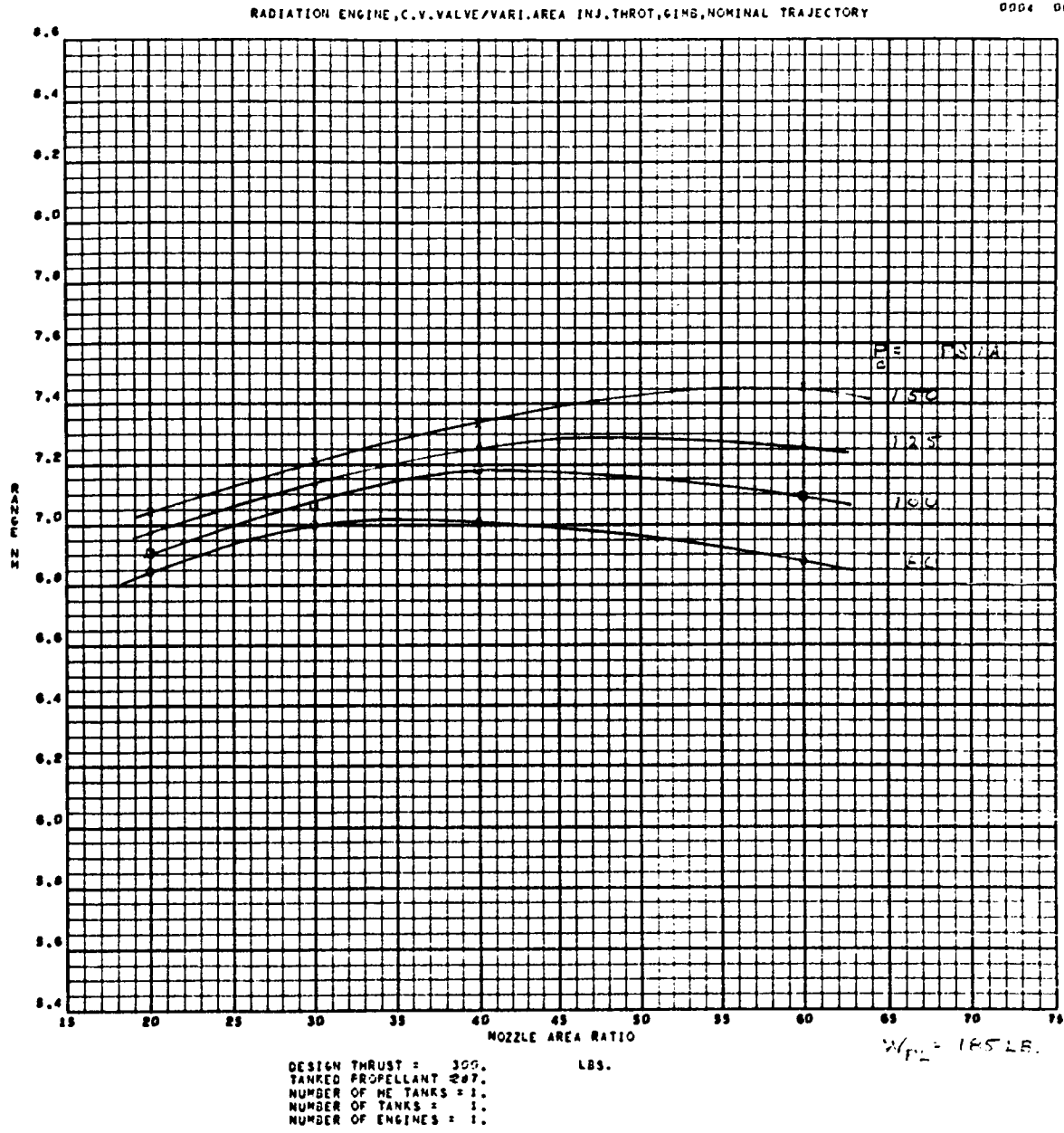


Figure 1-19. Variation of LFV Range as a Function of Nozzle-Area Ratio for Various Chamber Pressures (Sheet 5 of 23)

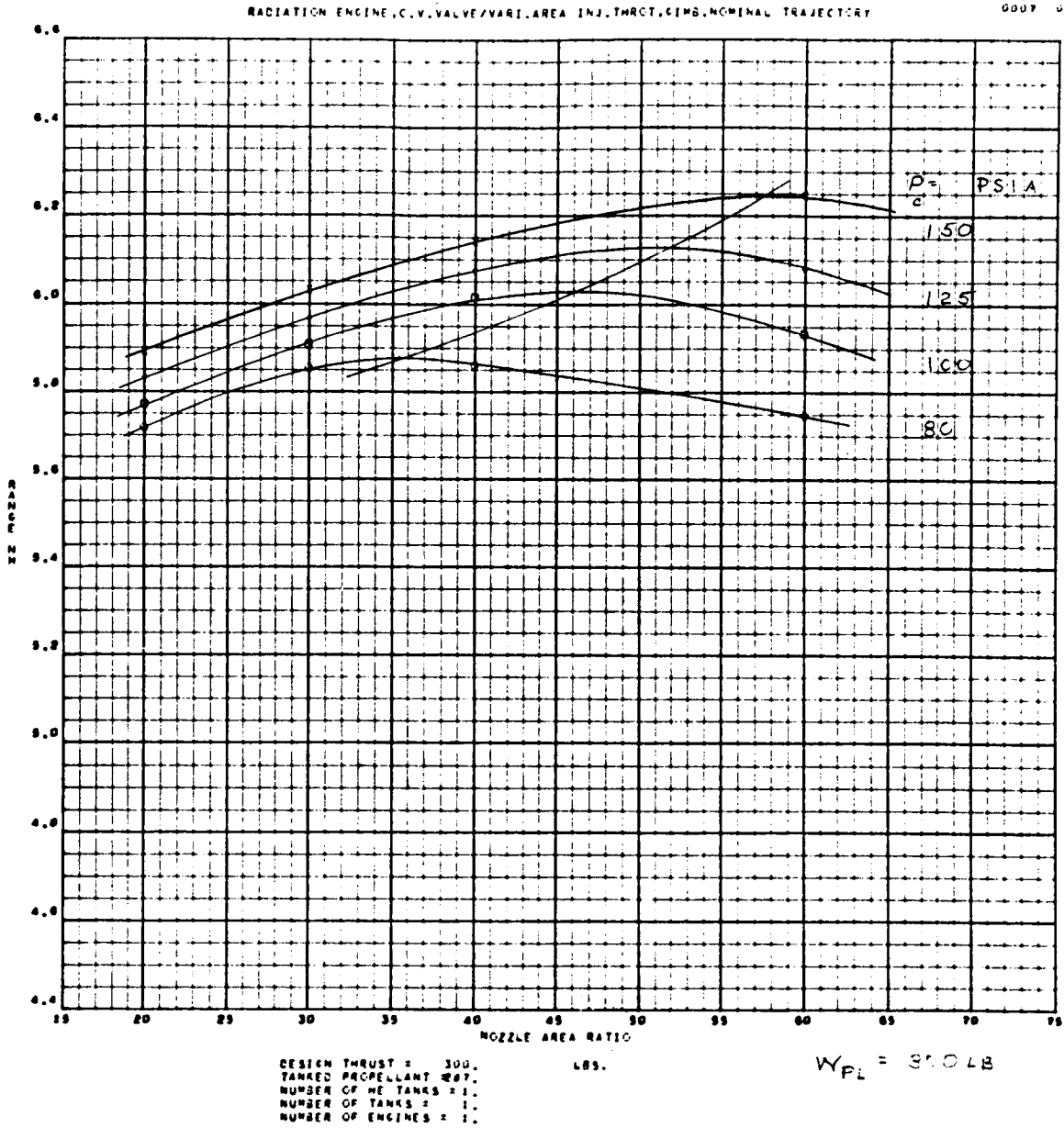
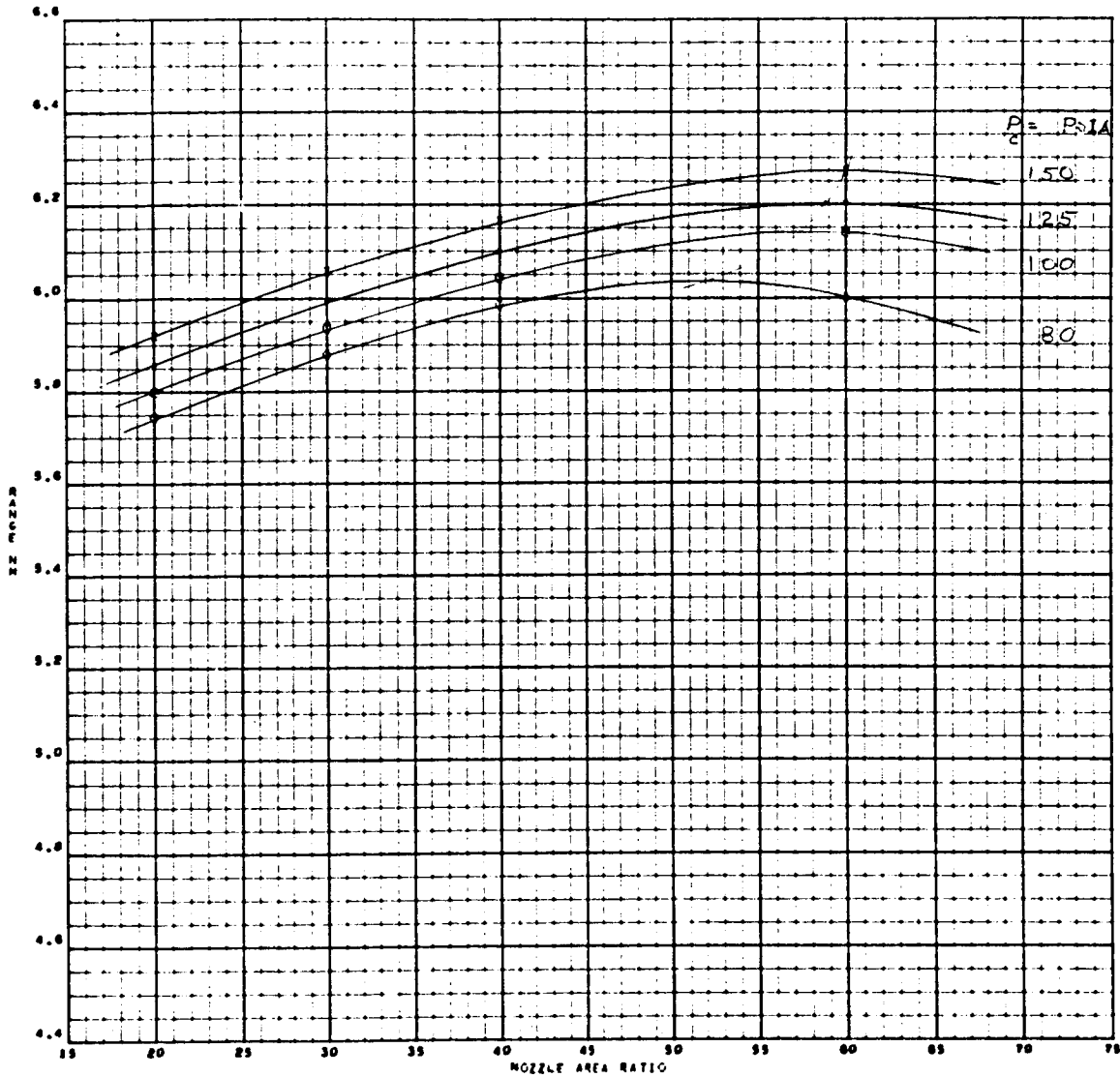


Figure 1-19. Variation of LFV Range as a Function of Nozzle-Area Ratio for Various Chamber Pressures (Sheet 6 of 23)

2421-95-03  
0004 0000

RADIATION ENGINE, BALL VALVE THROTTLING, GIMBALED, NOMINAL TRAJECTORY



DESIGN THRUST = 300.  
TANKED PROPELLANT #07.  
NUMBER OF HE TANKS = 1.  
NUMBER OF TANKS = 1.  
NUMBER OF ENGINES = 1.

LBS.

$W_{PL} = 370$  LB

Figure 1-19. Variation of LFV Range as a Function of Nozzle-Area Ratio for Various Chamber Pressures (Sheet 7 of 23)

2421-05-54  
9901 8900

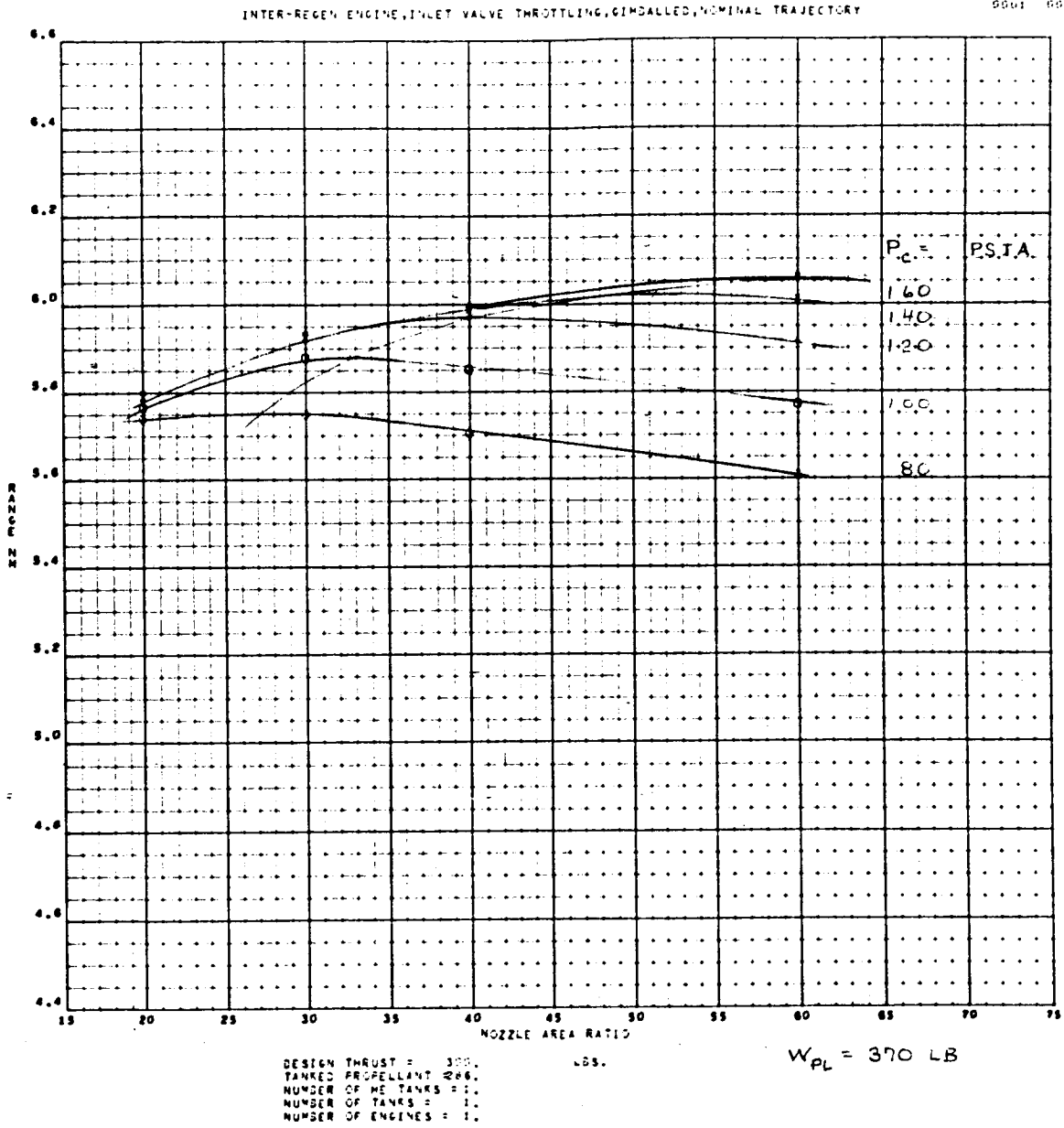


Figure 1-19. Variation of LFV Range as a Function of Nozzle-Area Ratio for Various Chamber Pressures (Sheet 8 of 23)

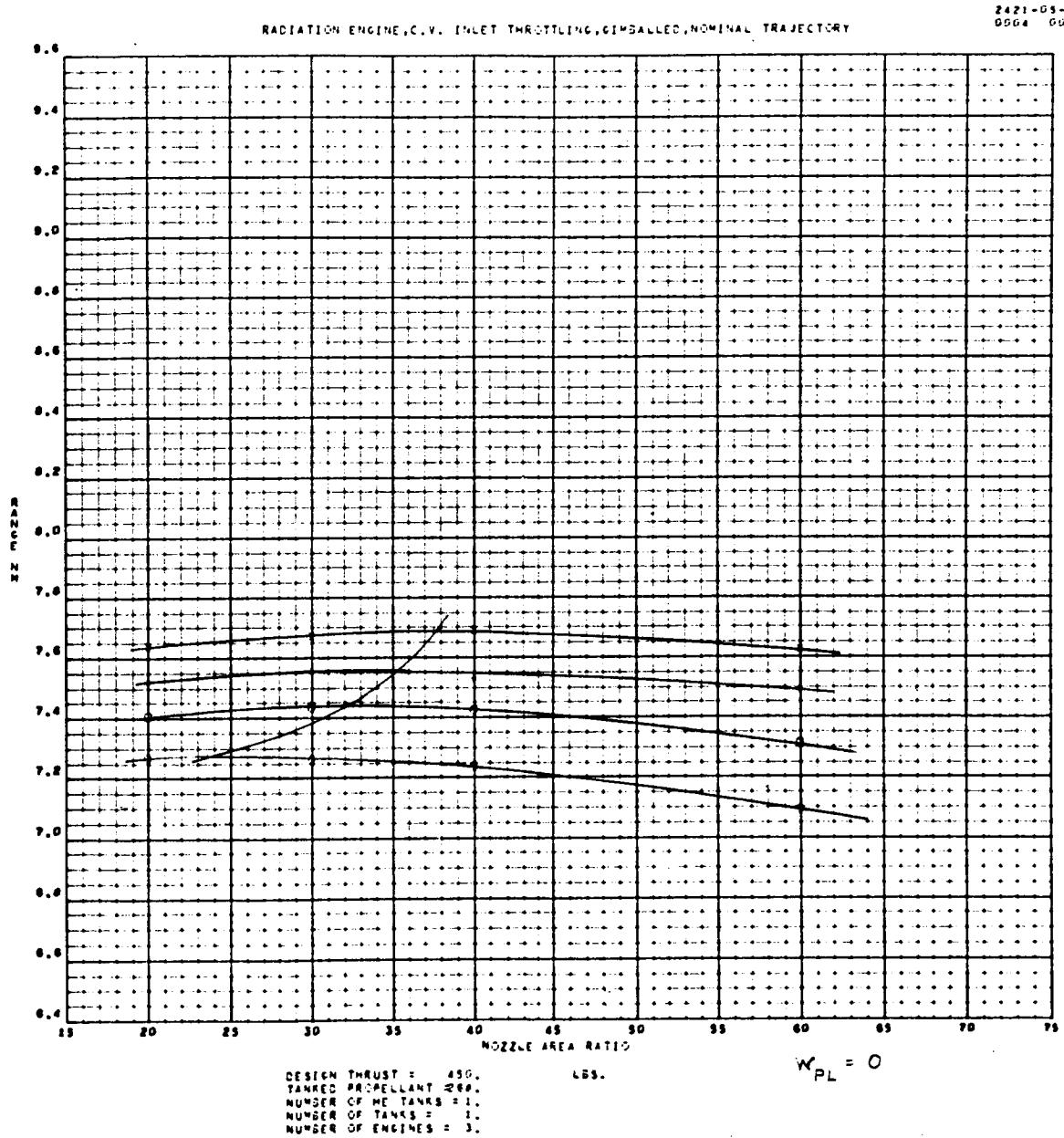


Figure 1-19. Variation of LFV Range as a Function of Nozzle-Area Ratio for Various Chamber Pressures (Sheet 9 of 23)

2421-05-05  
0002 0000

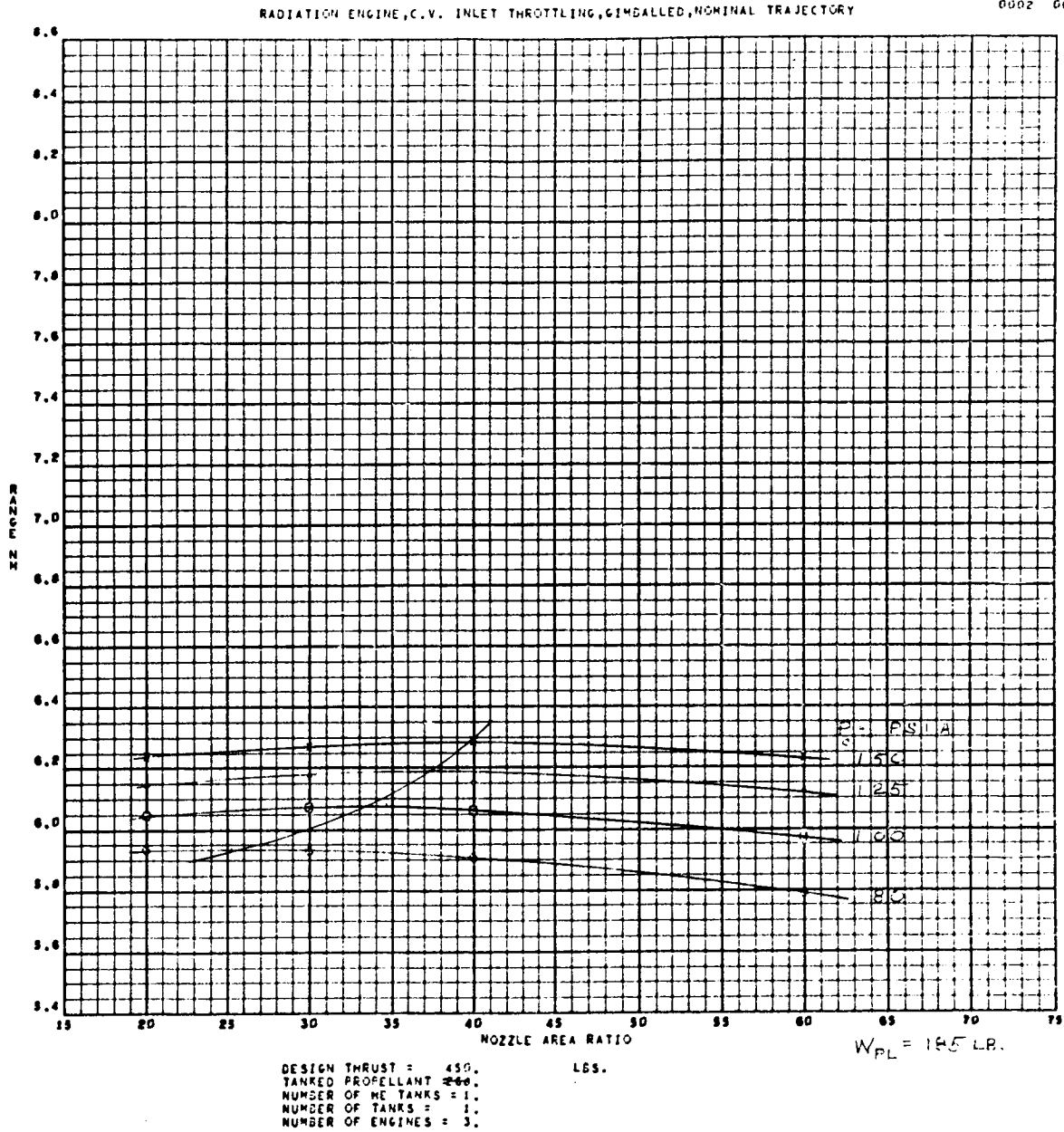


Figure 1-19. Variation of LFV Range as a Function of Nozzle-Area Ratio for Various Chamber Pressures (Sheet 10 of 23)

2421-03-03  
0002 0000

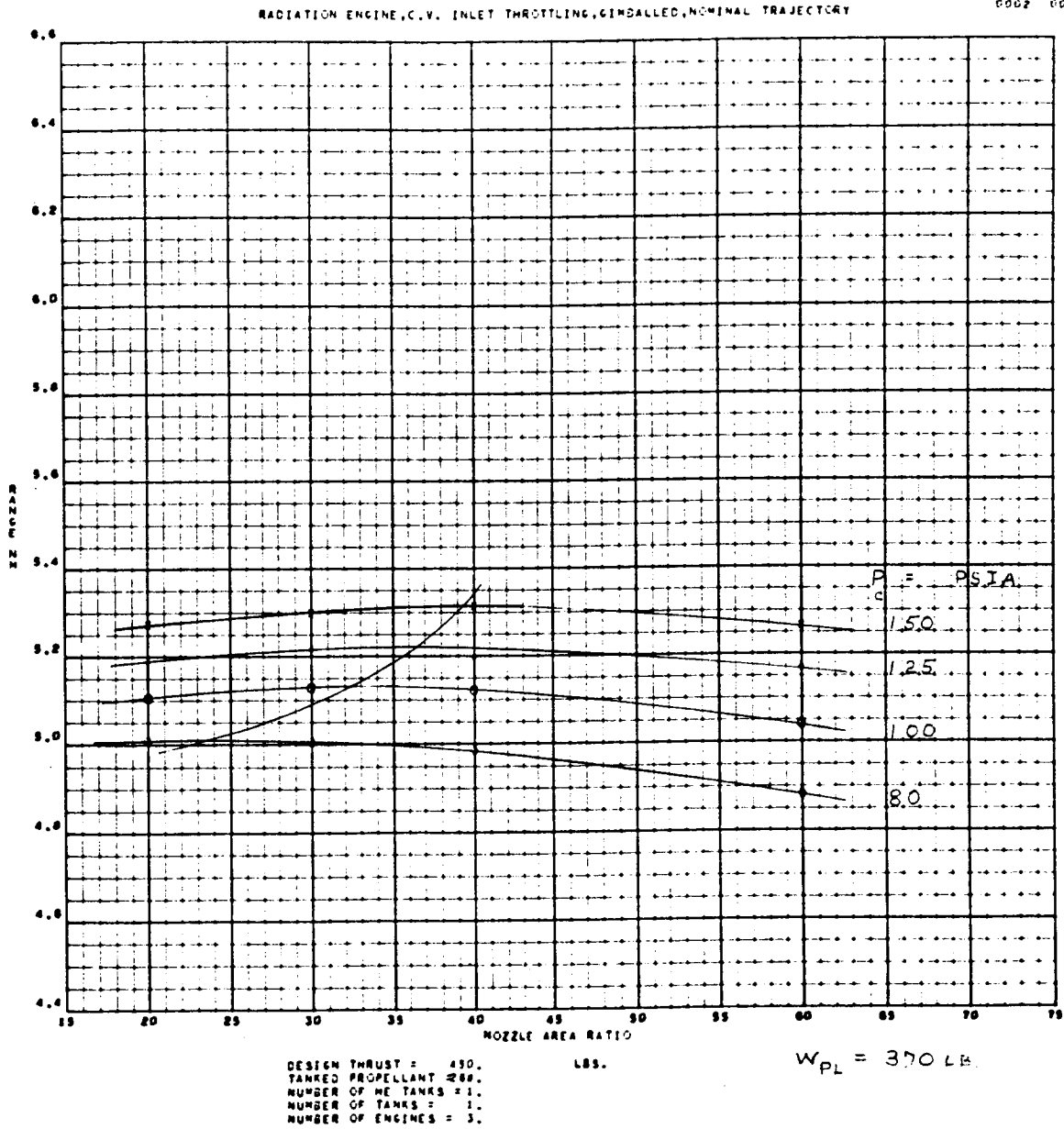


Figure 1-19. Variation of LFV Range as a Function of Nozzle-Area Ratio for Various Chamber Pressures (Sheet 11 of 23)



2421-95-04  
0007 0008

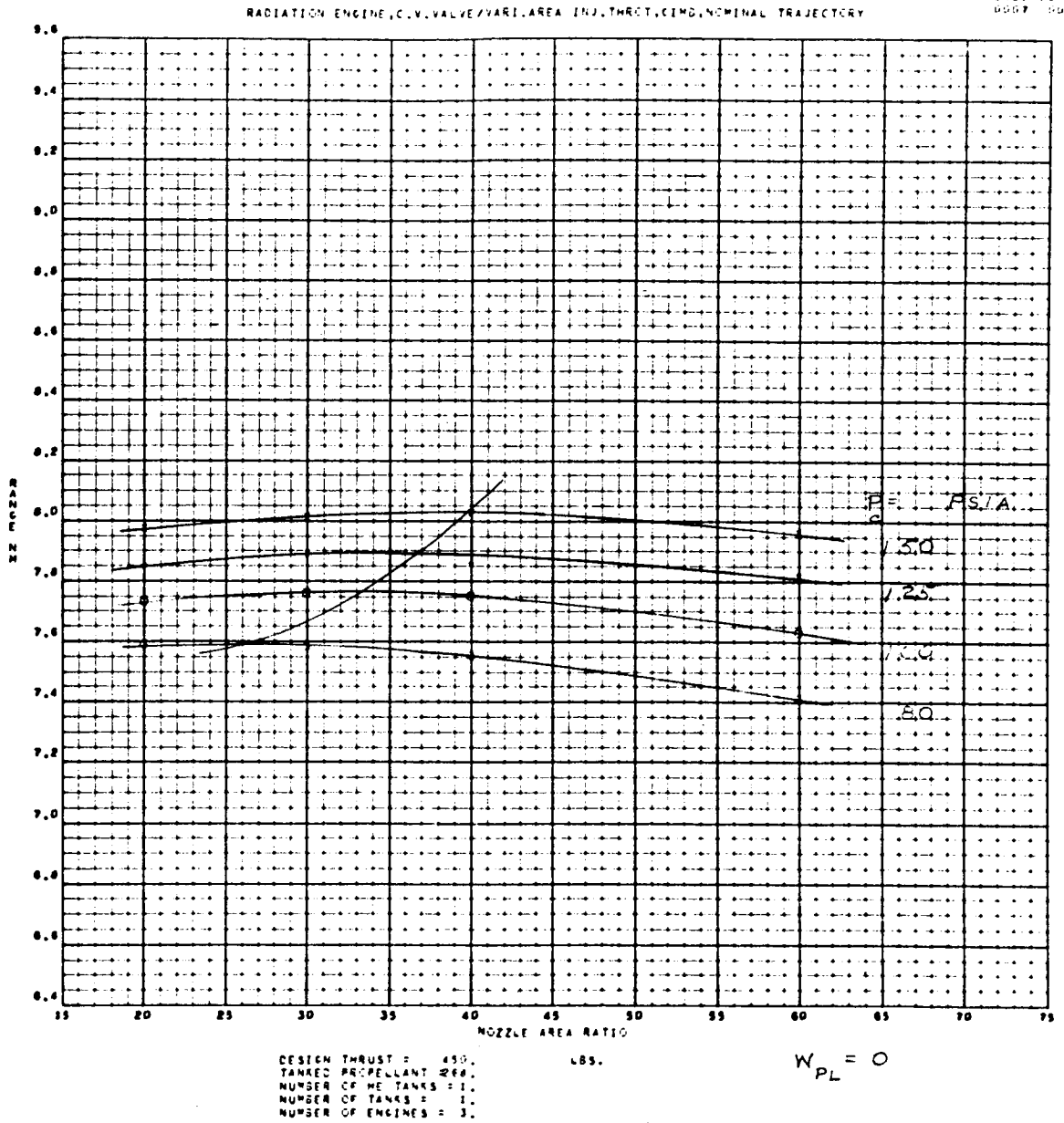


Figure 1-19. Variation of LFV Range as a Function of Nozzle-Area Ratio for Various Chamber Pressures (Sheet 12 of 23)

2421-05-03  
0005 0000

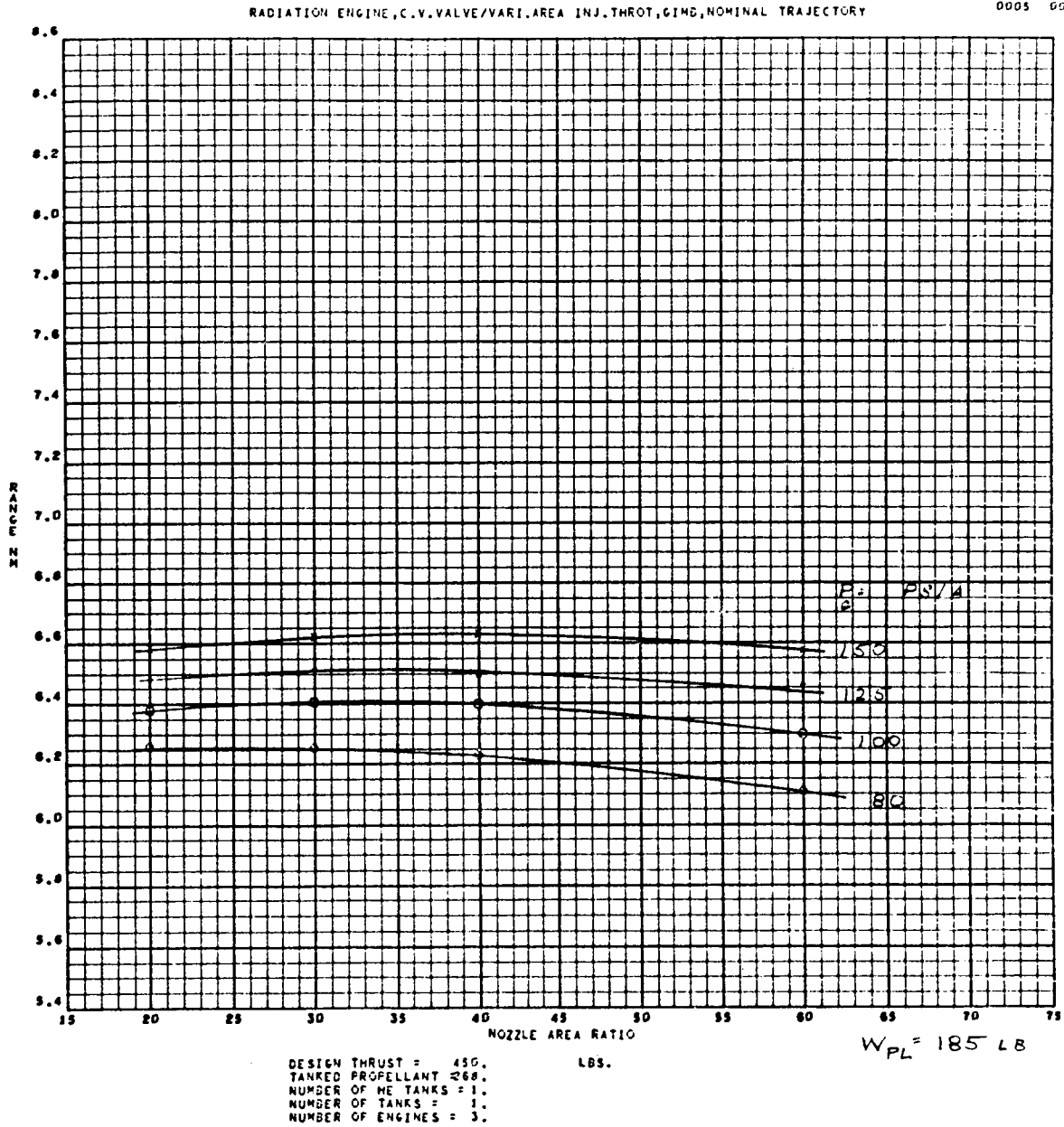


Figure 1-19. Variation of LFV Range as a Function of Nozzle-Area Ratio for Various Chamber Pressures (Sheet 13 of 23)

2421-01-01  
0000 0000

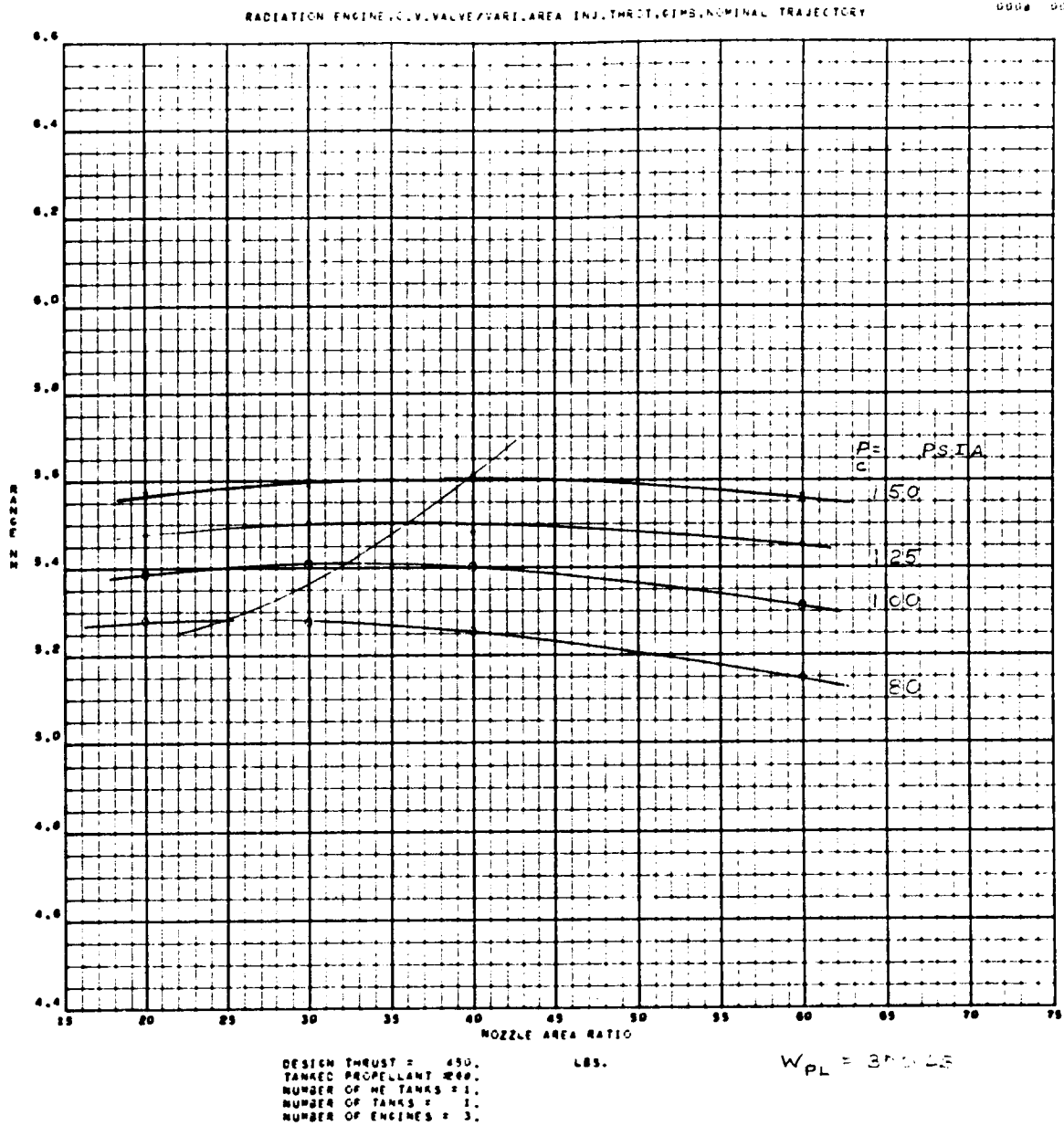


Figure 1-19. Variation of LFV Range as a Function of Nozzle-Area Ratio for Various Chamber Pressures (Sheet 14 of 23)

2421-03-03  
0005 0000

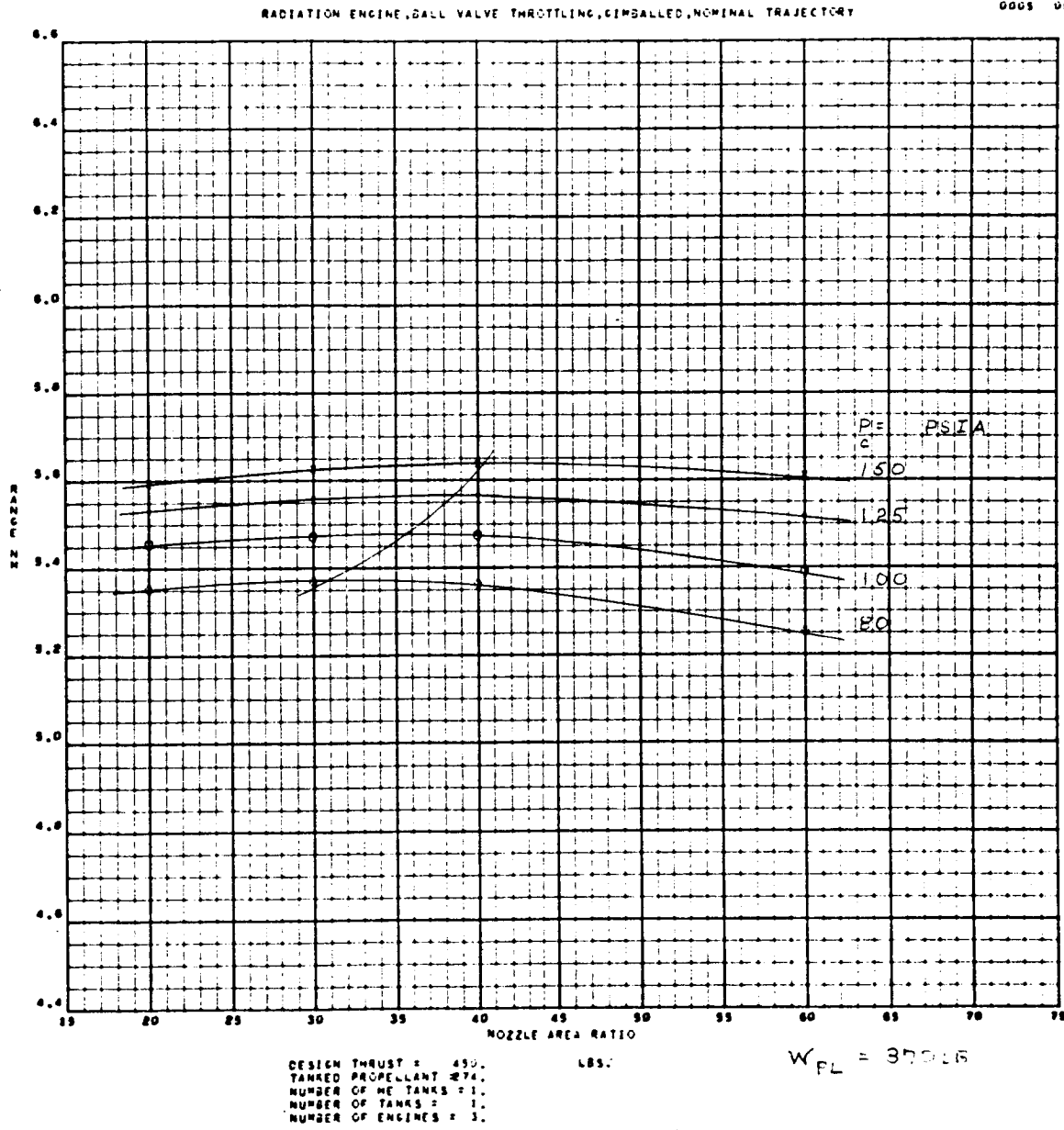


Figure 1-19. Variation of LFV Range as a Function of Nozzle-Area Ratio for Various Chamber Pressures (Sheet 15 of 23)



2421-05-04  
0000 0000

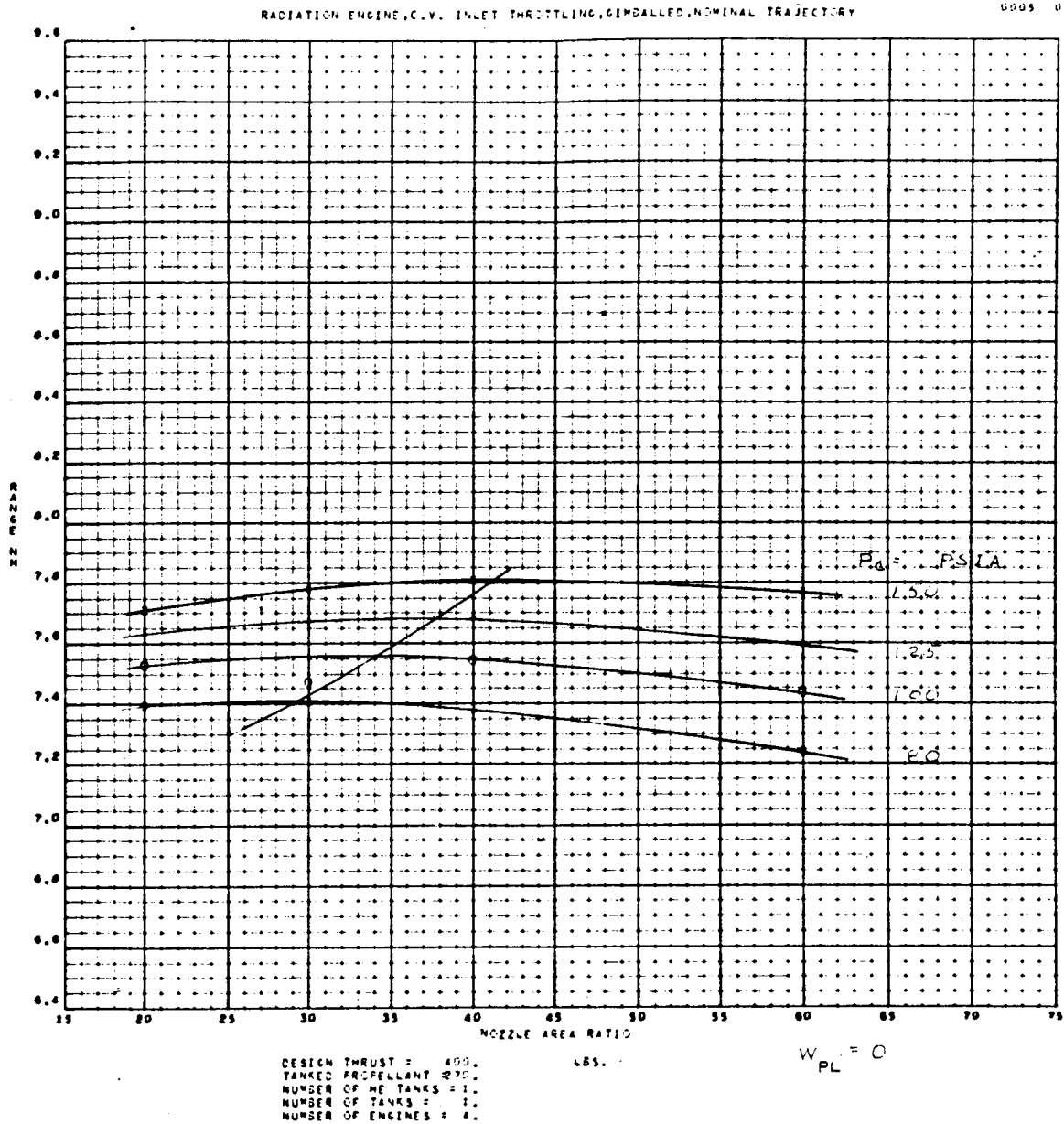


Figure 1-19. Variation of LFV Range as a Function of Nozzle-Area Ratio for Various Chamber Pressures (Sheet 16 of 23)

2421-05-03  
0003 0000

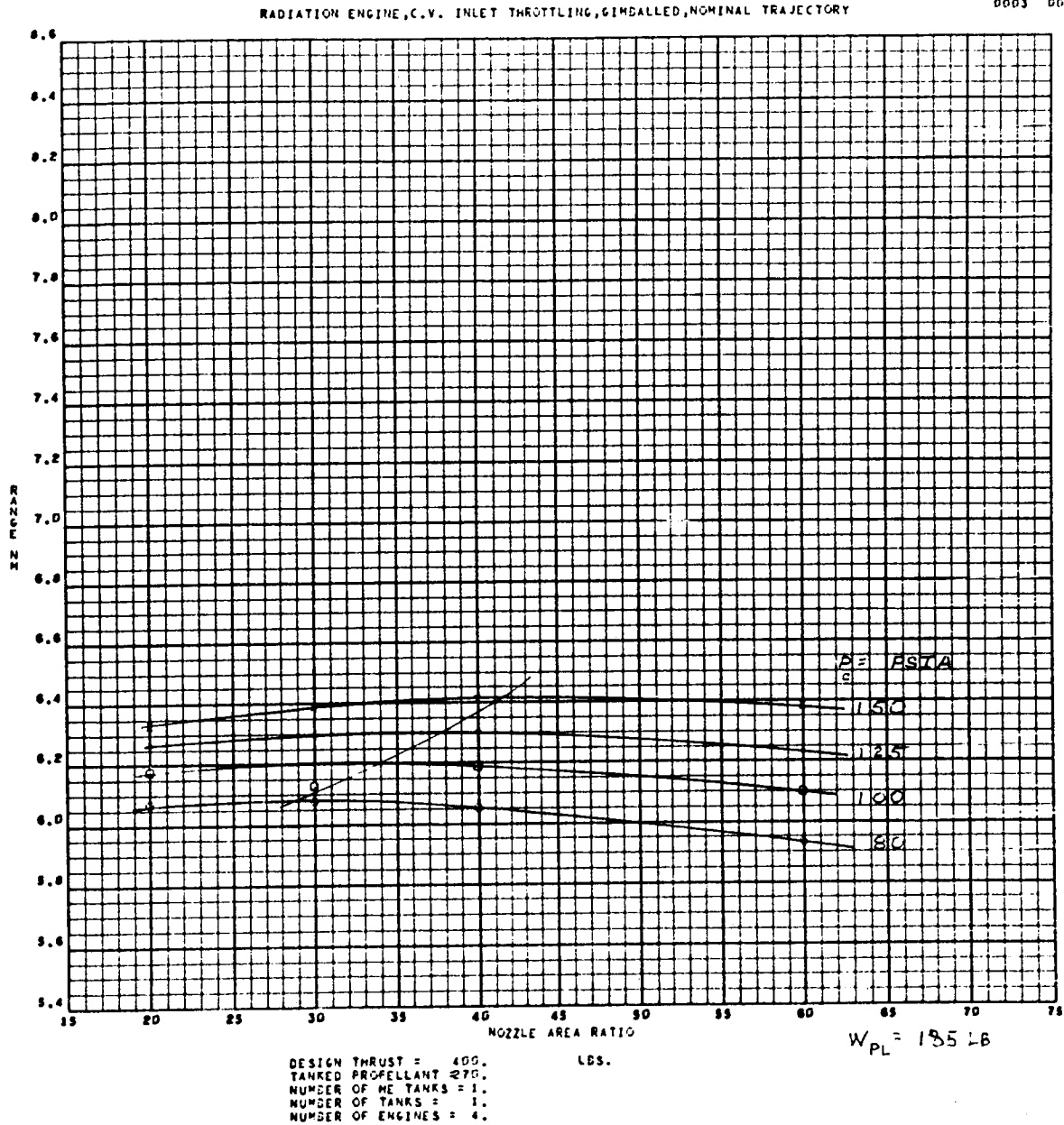


Figure 1-19. Variation of LFV Range as a Function of Nozzle-Area Ratio for Various Chamber Pressures (Sheet 17 of 23)



2421-05-03  
0003 0000

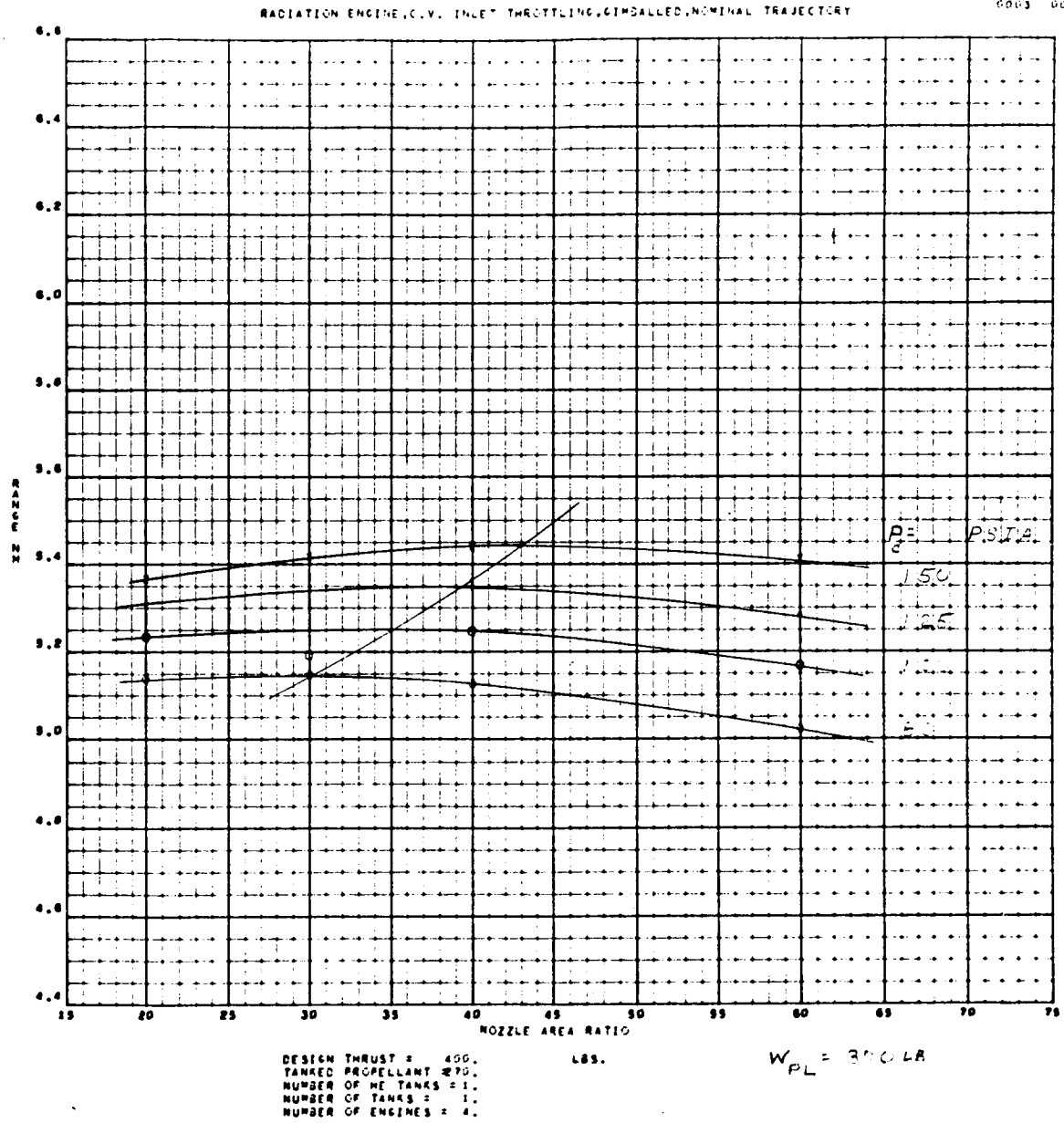


Figure 1-19. Variation of LFV Range as a Function of Nozzle-Area Ratio for Various Chamber Pressures (Sheet 18 of 23)

2421-05-04  
0000 0000

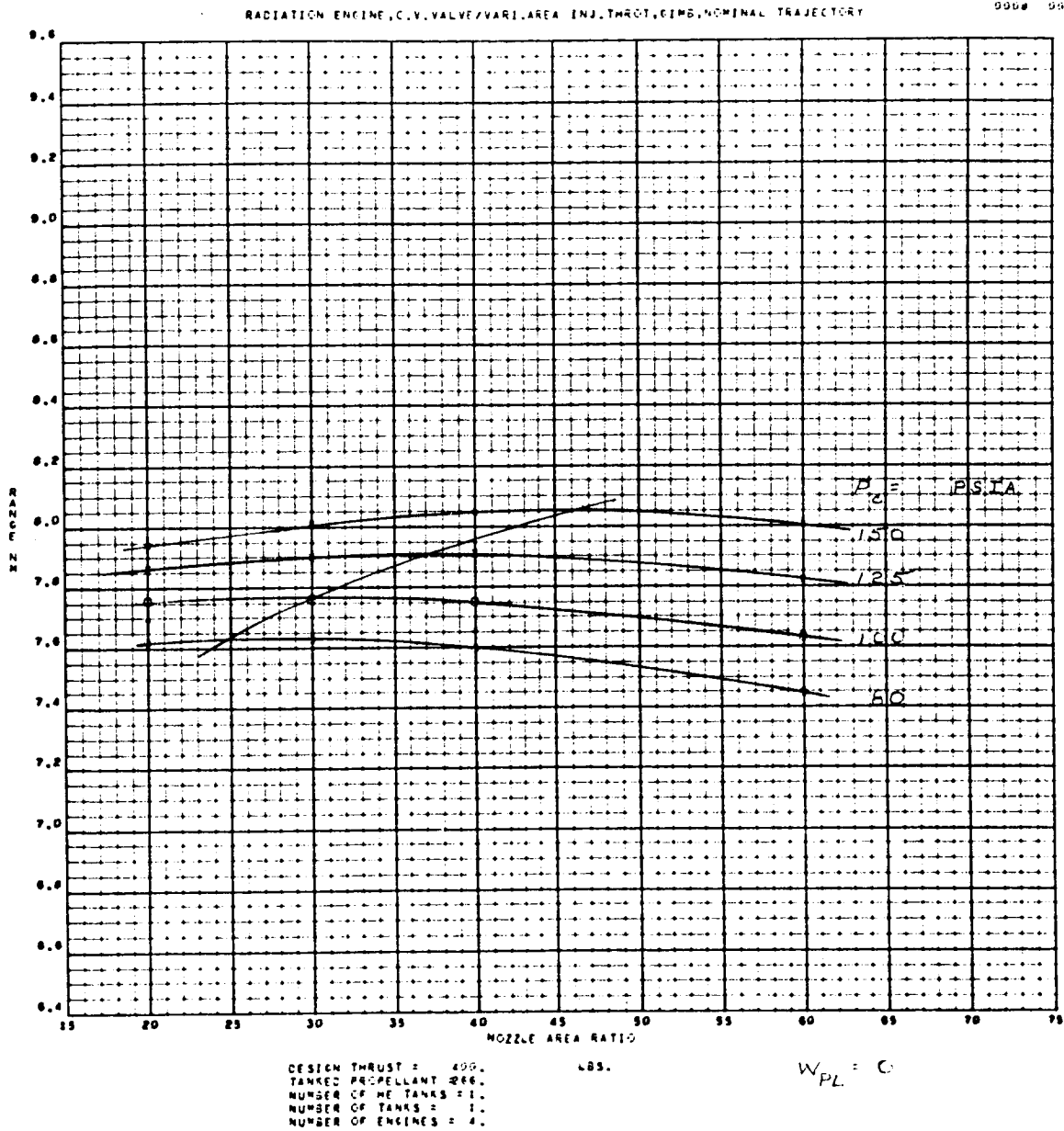


Figure 1-19. Variation of LFV Range as a Function of Nozzle-Area Ratio for Various Chamber Pressures (Sheet 19 of 23)





2421-05-05  
0006 0006

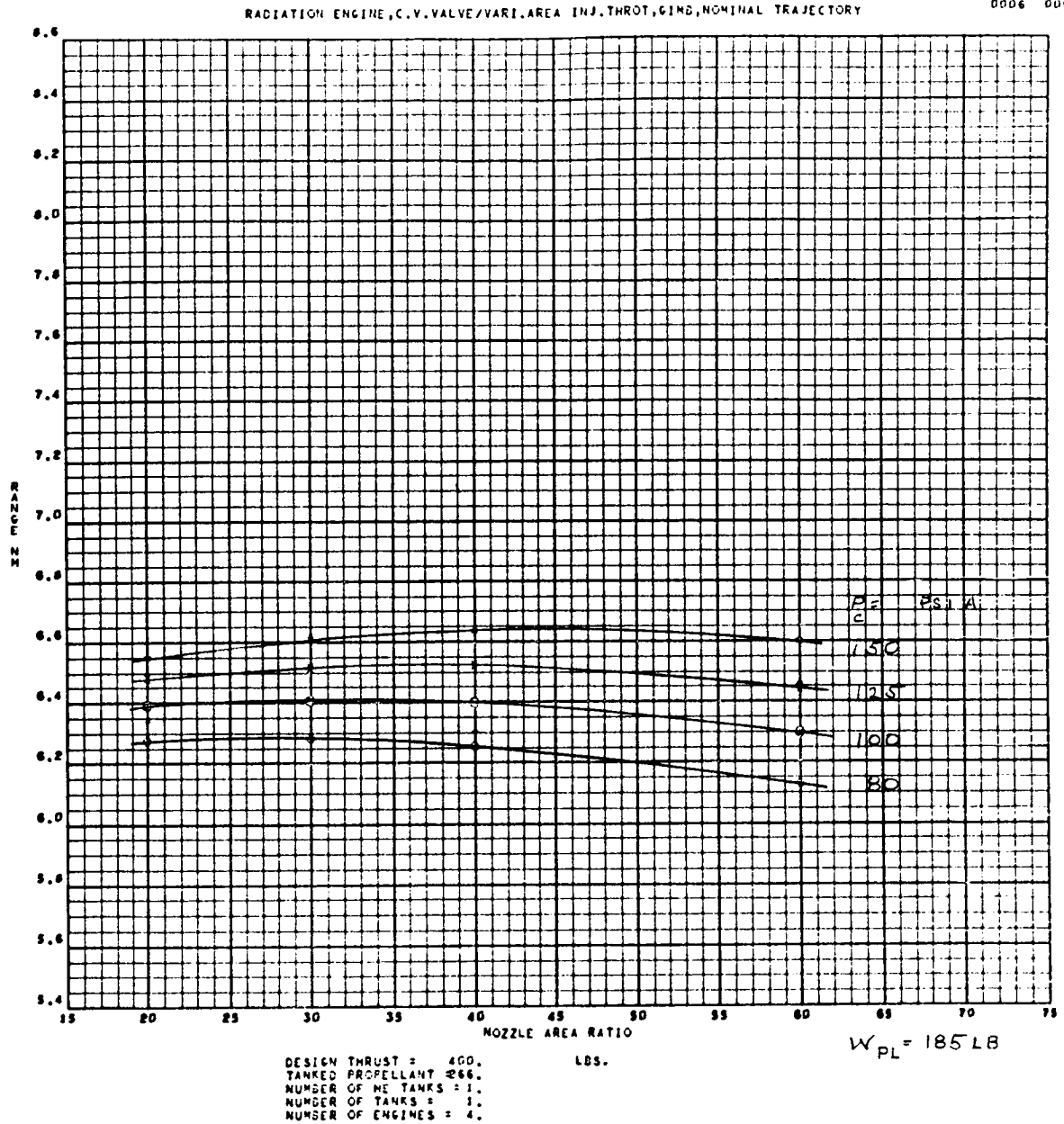


Figure 1-19. Variation of LFV Range as a Function of Nozzle-Area Ratio for Various Chamber Pressures (Sheet 20 of 23)

2421-05-03  
0000 0000

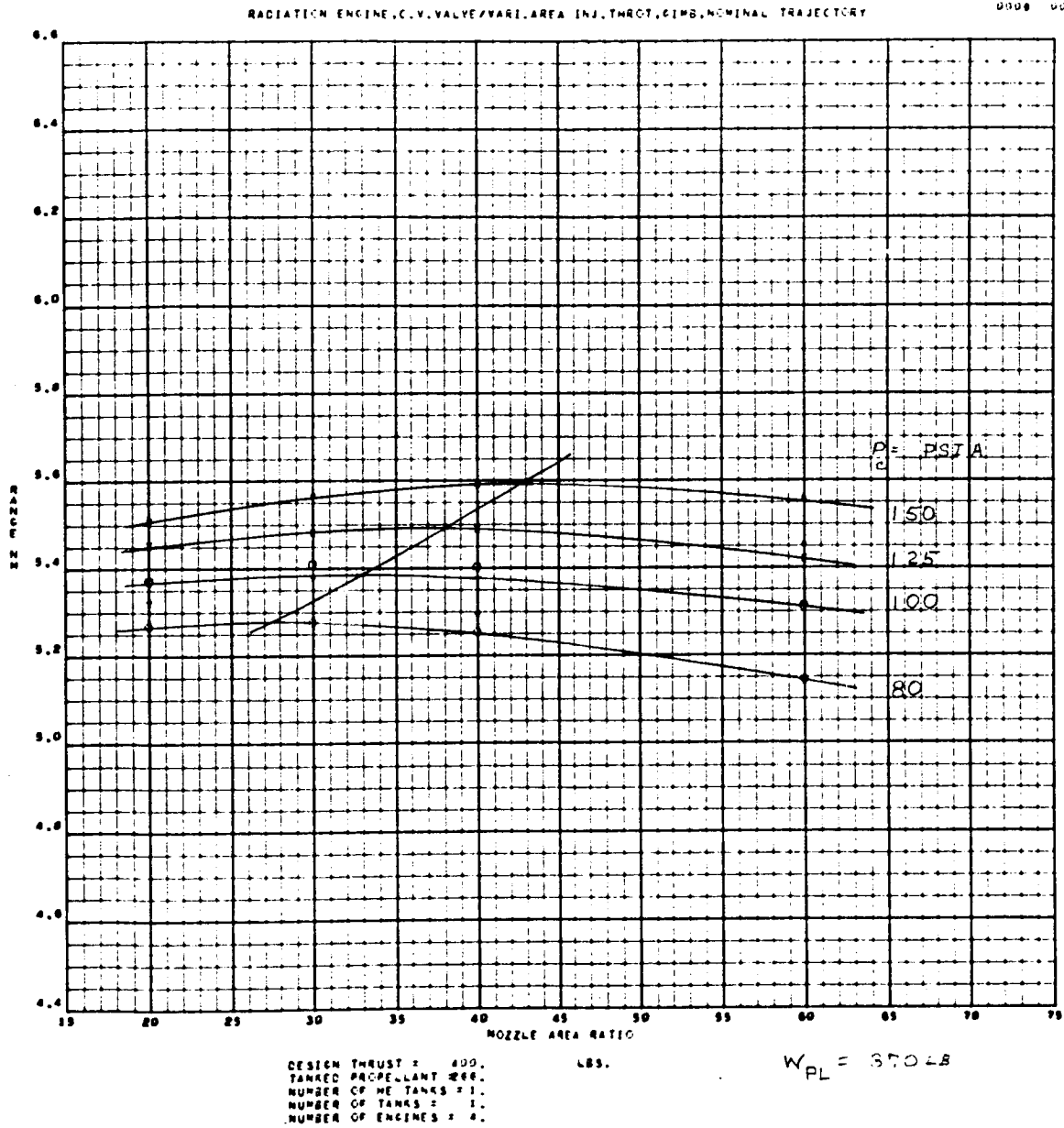


Figure 1-19. Variation of LFV Range as a Function of Nozzle-Area Ratio for Various Chamber Pressures (Sheet 21 of 23)



2421-05-11  
8802 8808

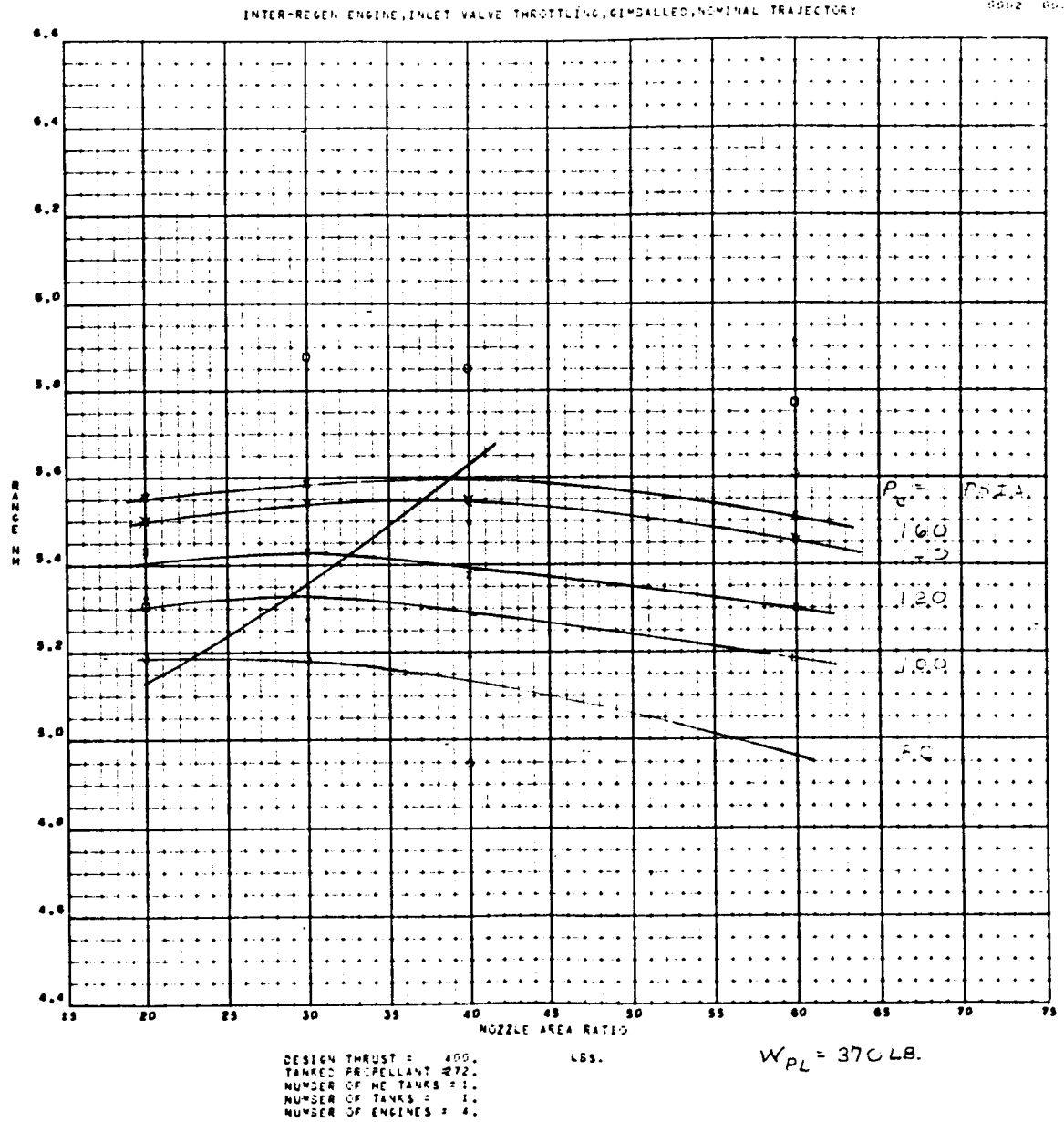


Figure 1-19. Variation of LFV Range as a Function of Nozzle-Area Ratio for Various Chamber Pressures (Sheet 22 of 23)

2421-03-03  
0000 0000

RADIATION ENGINE, BALL VALVE THROTTLING, GIMBALED, NOMINAL TRAJECTORY

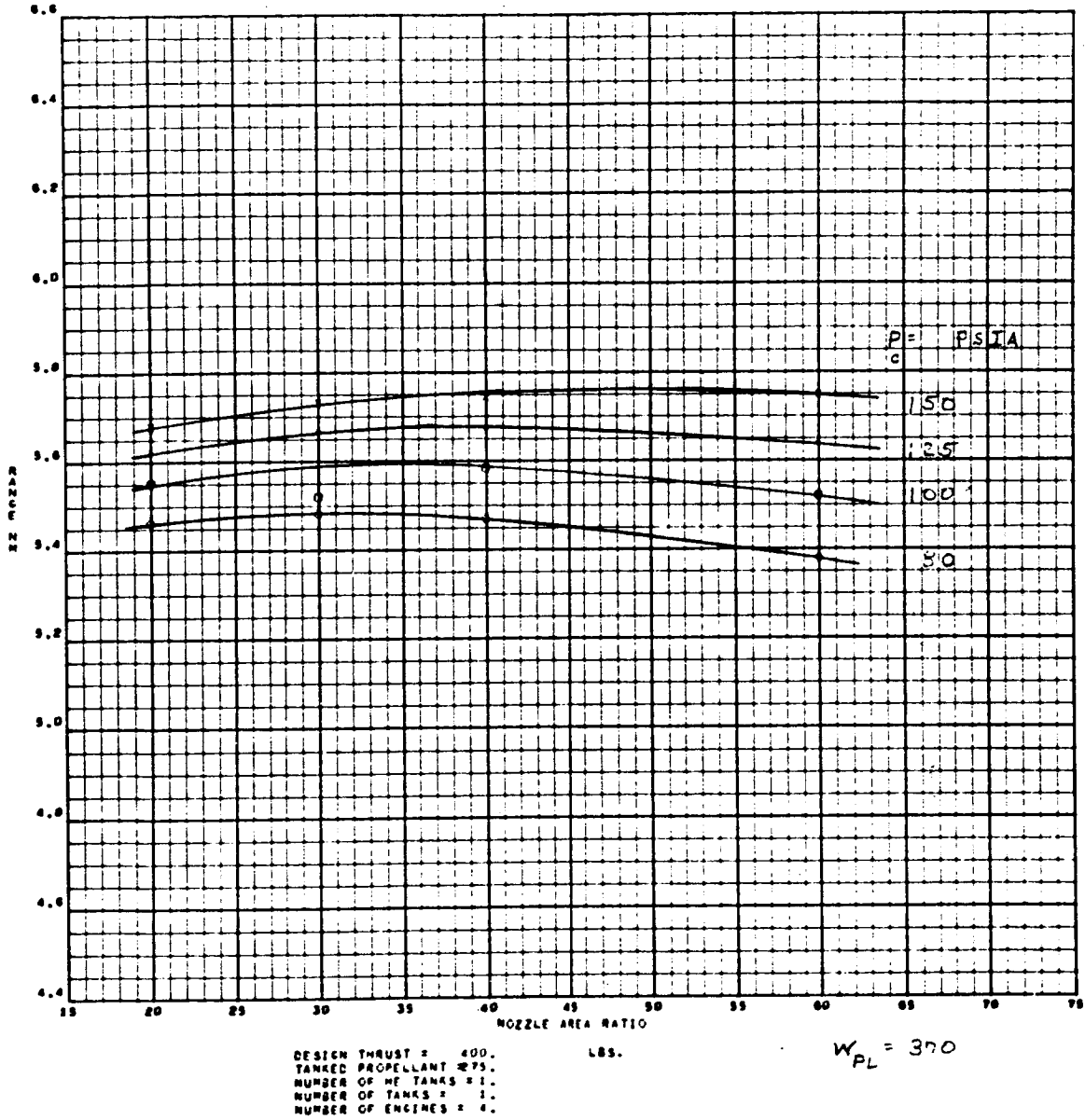


Figure 1-19. Variation of LFV Range as a Function of Nozzle-Area Ratio for Various Chamber Pressures (Sheet 23 of 23)



## Resupply Requirements

Another area which must be considered during the optimization process is the resupply requirements. The resupply weight required for a given number of nominal missions provides a point of comparison for each design alternative reflecting total mission system capability (Figure 1-20). The resupply requirements include the burned propellant plus the required number of pressurant subassemblies. Figure 1-21 presents resupply weight for five nominal flights as a function of chamber pressure and nozzle area ratio. This is shown for 1-, 3-, and 4-engine configurations. From the chamber-pressure viewpoint, the optimums occur in approximately the same regimes as when subsystem weight was evaluated. Namely 100 to 110 psia for radiation cooling and 140 to 160 psia for interregenerative cooling. The expected effect of nozzle-area ratio is to reduce resupply weight as specific impulse increases with increasing area ratio.

The summary data of Figure 1-20 provide a very clear indication of how both high average thrust (single-engine) and high  $I_{sp}$  at reduced thrust affect resupply weight. It is seen that the variable-area injector concept has up to a 60-lb resupply weight advantage (4-engine configuration). Table 1-10 provides an overall summary of subsystem weights.

Table 1-10. Propulsion-Subsystem Weight Comparison

Number of Engines	Weight (lb) Parameter	Manufacturer				
		AGC	Bell	RD/NR	TMC	TRW
1	Dry	66.5	57.7	57.8	54.0	54.4
	Burned propellant <sup>1</sup>	256.1	252.5	248.7	247.0	248.1
	Resupply <sup>2</sup>	1362.0	1329.0	1320.4	1298.0	1300.5
3	Dry	91.4	73.9	72.5	67.8	71.4
	Burned propellant	263.6	265.1	256.7	257.9	254.5
	Resupply	1403.5	1395.4	1364.5	1356.5	1336.8
4	Dry	93.6	71.6	71.9	67.3	74.2
	Burned propellant	262.4	262.3	256.1	254.9	253.2
	Resupply	1395.9	1380.0	1360.1	1340.4	1328.7
Notes: <sup>1</sup> Nominal duty cycle <sup>2</sup> Five nominal flights						

RESUPPLY WEIGHT INCLUDES (1) BURNED PROPELLANT  
(2) HELIUM, (3) HELIUM BOTTLE, AND (4) ISOLATION VALVE

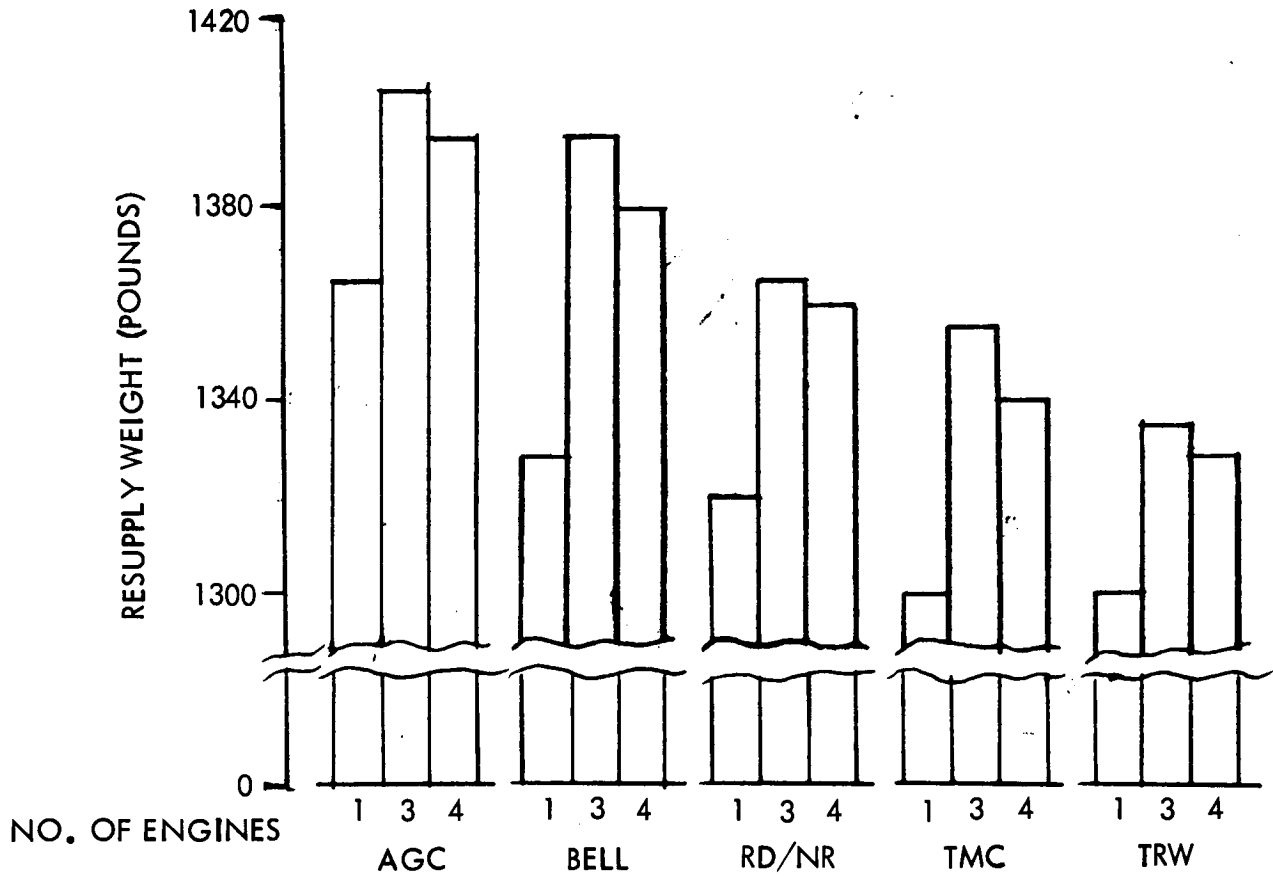


Figure 1-20. Propulsion Subsystem Resupply Weight for Five Nominal Flights

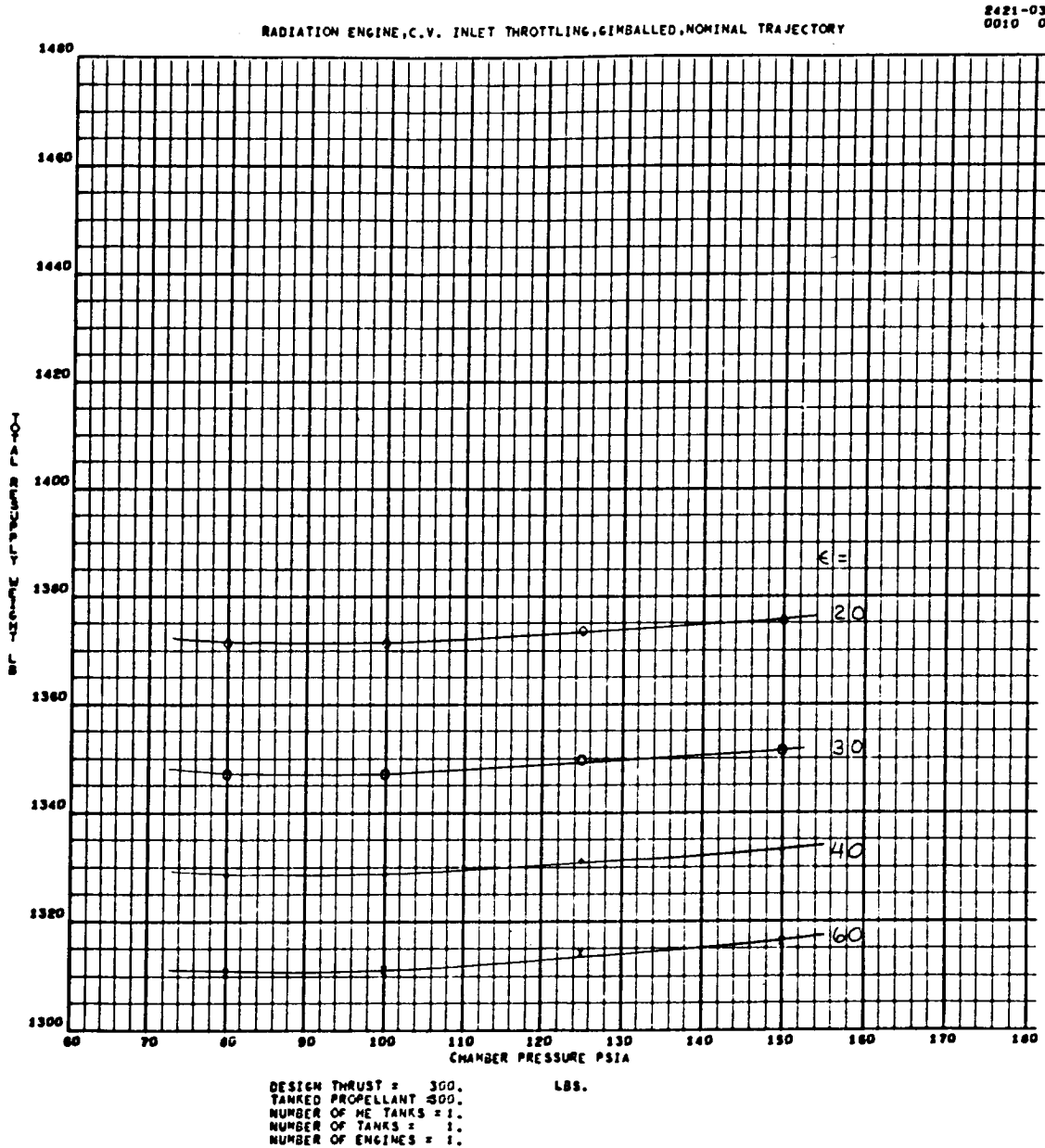


Figure 1-21. Resupply Weight for Five Nominal Flights as a Function of Chamber Pressure and Nozzle-Area Ratio (Sheet 1 of 14)

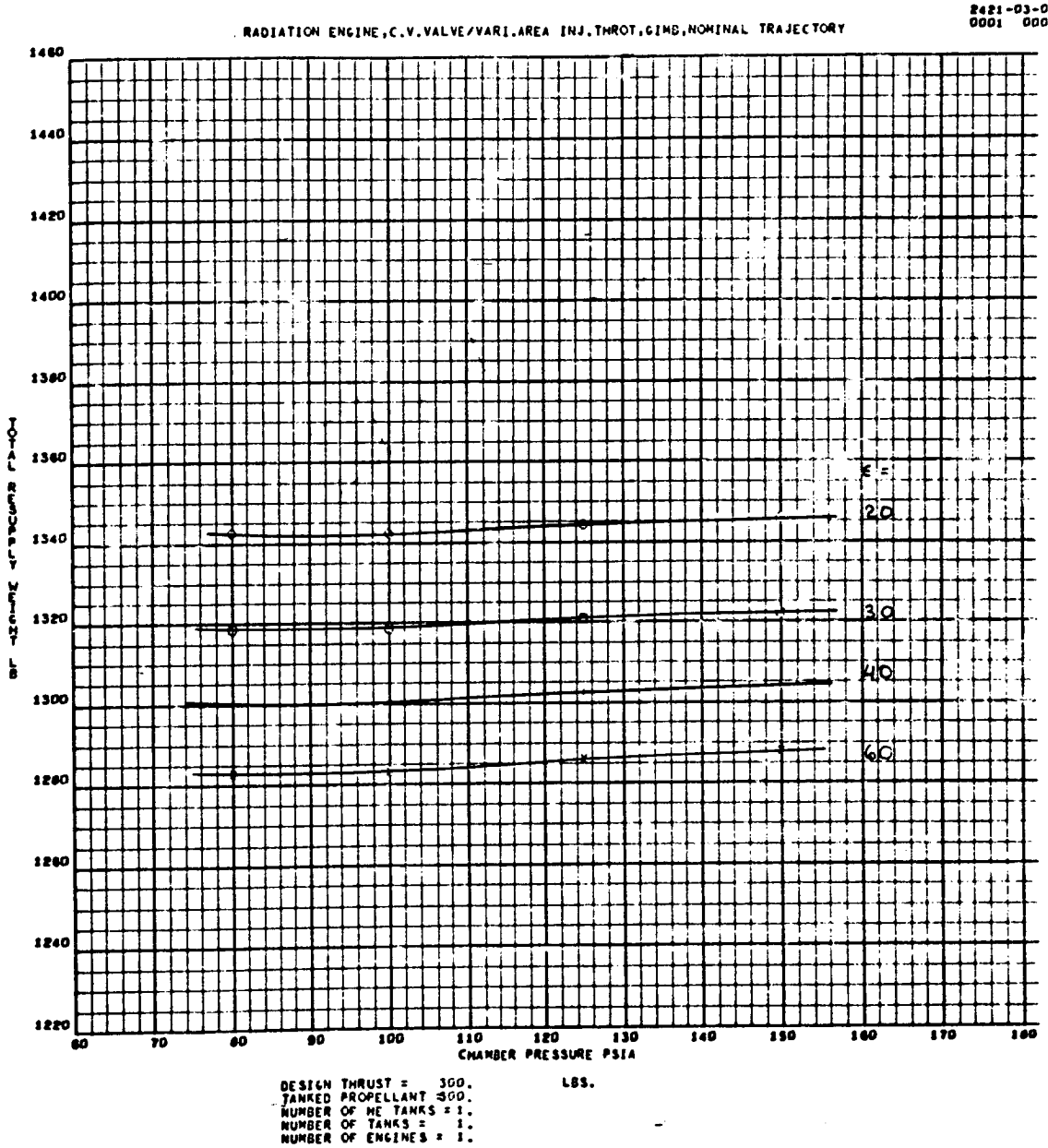


Figure 1-21. Resupply Weight for Five Nominal Flights as a Function of Chamber Pressure and Nozzle-Area Ratio (Sheet 2 of 14)



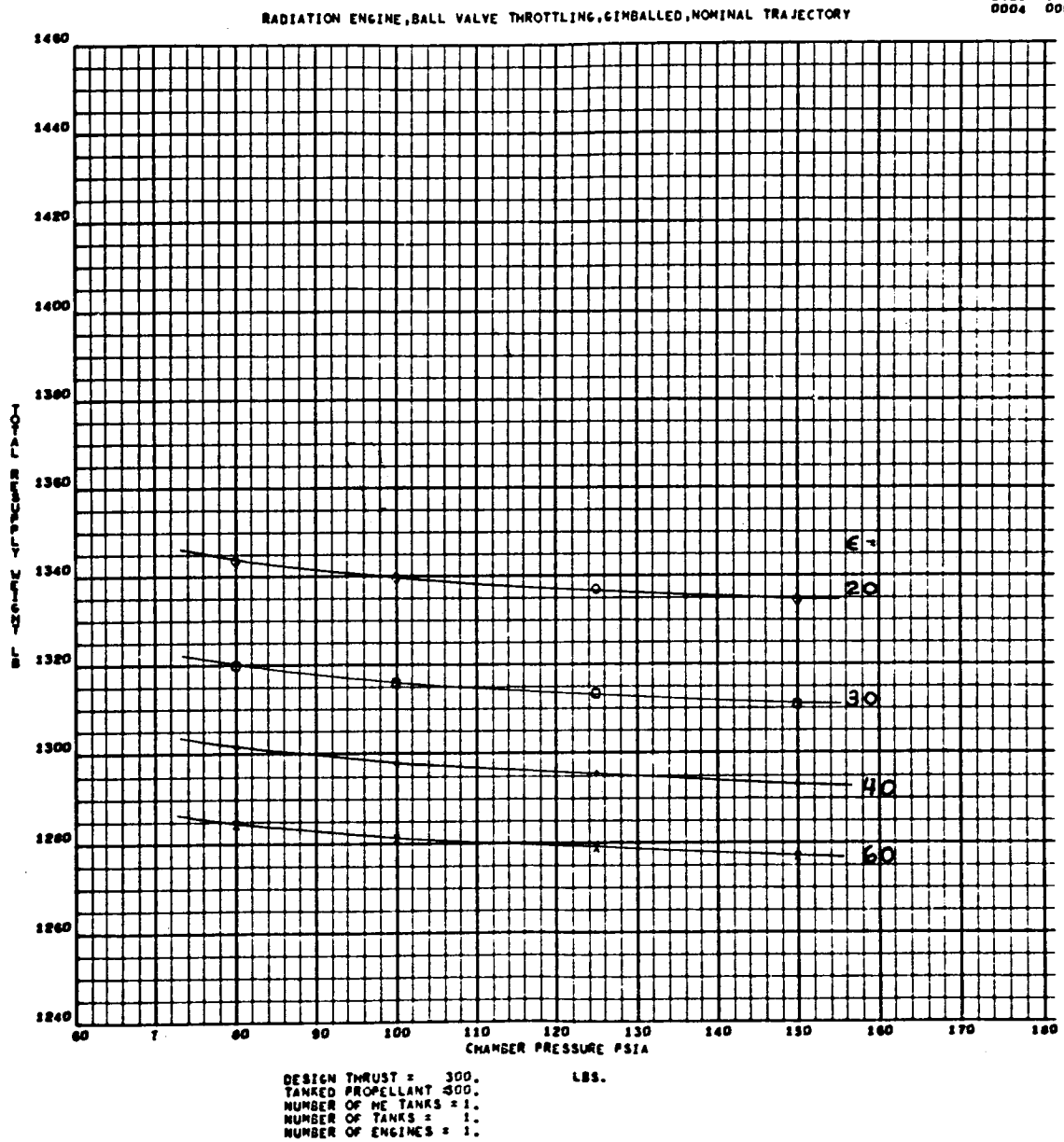


Figure 1-21. Resupply Weight for Five Nominal Flights as a Function of Chamber Pressure and Nozzle-Area Ratio (Sheet 3 of 14)

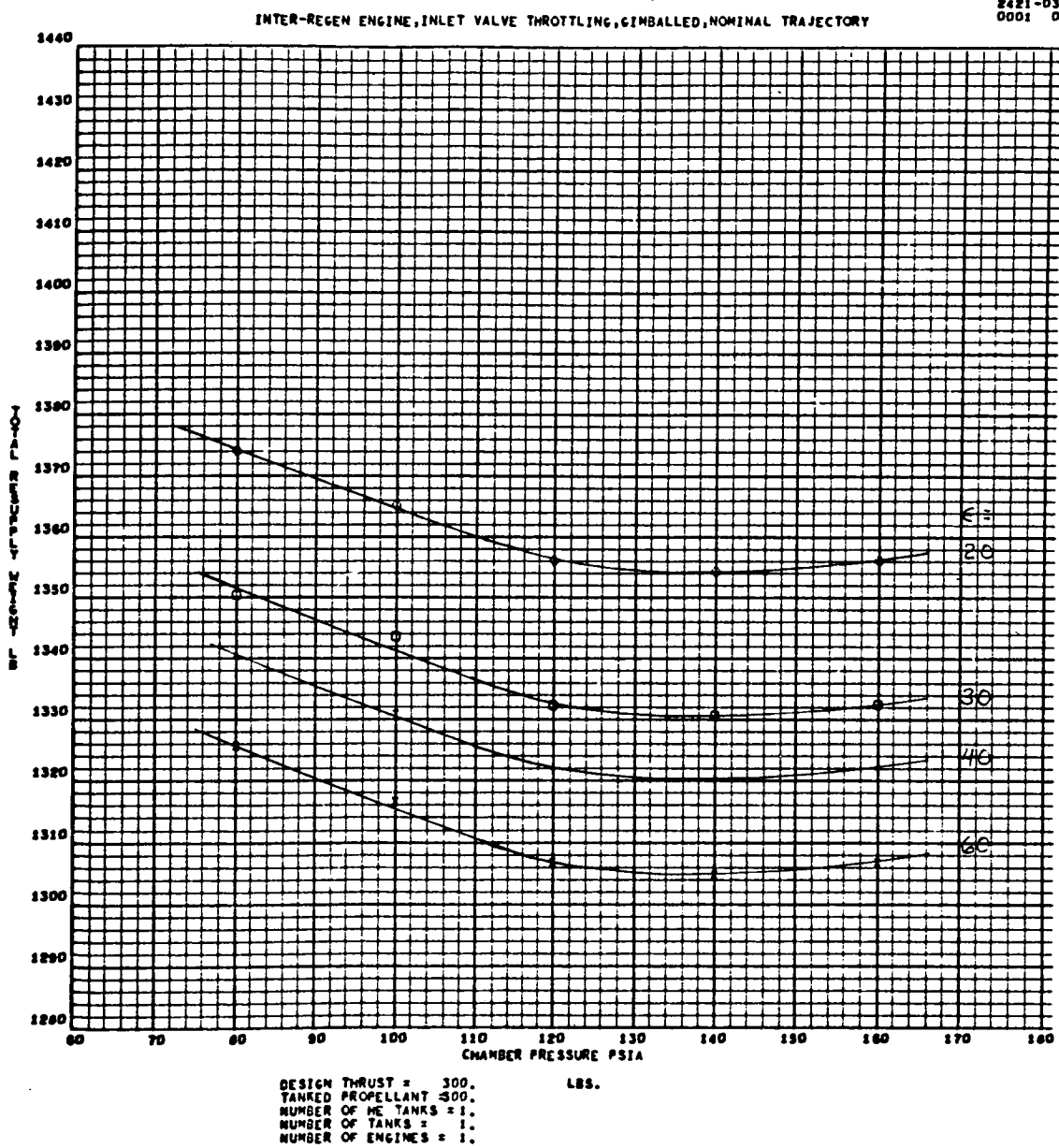
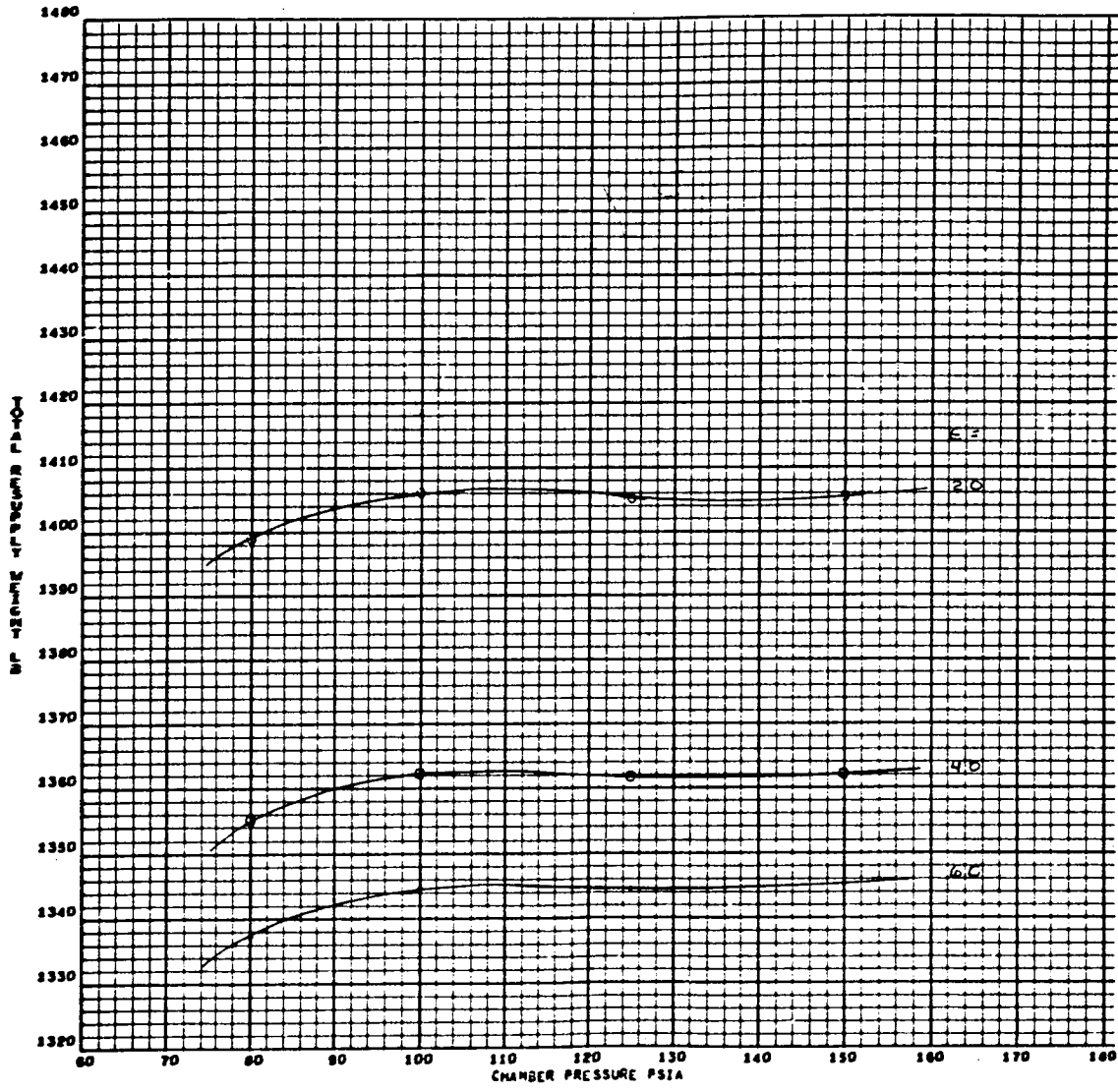


Figure 1-21. Resupply Weight for Five Nominal Flights as a Function of Chamber Pressure and Nozzle-Area Ratio (Sheet 4 of 14)



2421-03-02  
0007 0000

HYPERMET ENGINE, INLET VALVE THROTTLING, GIMBALLED, NOMINAL TRAJECTORY



DESIGN THRUST = 300. LBS.  
TANKED PROPELLANT 500.  
NUMBER OF HE TANKS = 1.  
NUMBER OF TANKS = 1.  
NUMBER OF ENGINES = 1.

Figure 1-21. Resupply Weight for Five Nominal Flights as a Function of Chamber Pressure and Nozzle-Area Ratio (Sheet 5 of 14)

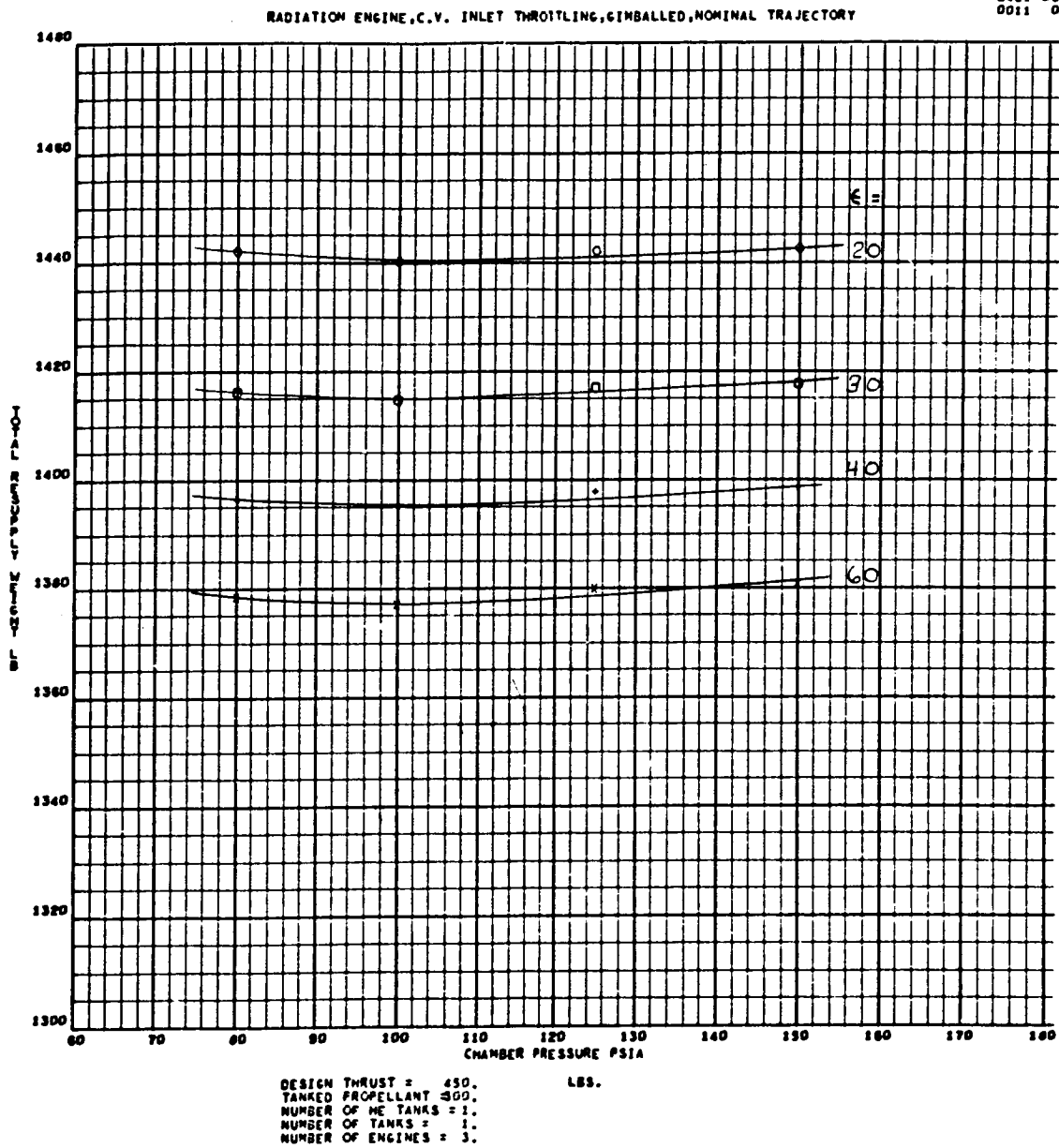


Figure 1-21. Resupply Weight for Five Nominal Flights as a Function of Chamber Pressure and Nozzle-Area Ratio (Sheet 6 of 14)

2421-03-03  
0002 0000

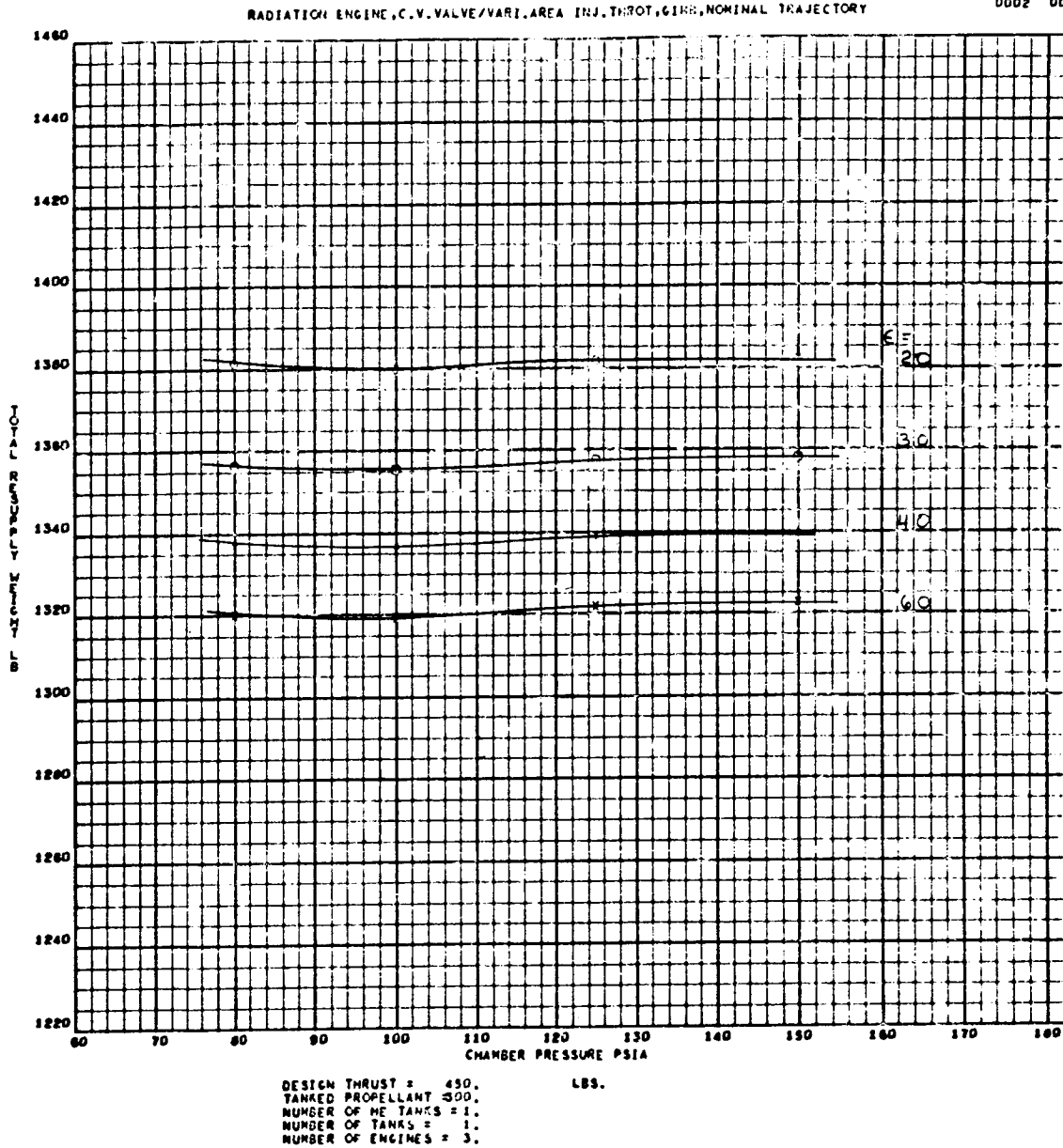


Figure 1-21. Resupply Weight for Five Nominal Flights as a Function of Chamber Pressure and Nozzle-Area Ratio (Sheet 7 of 14)

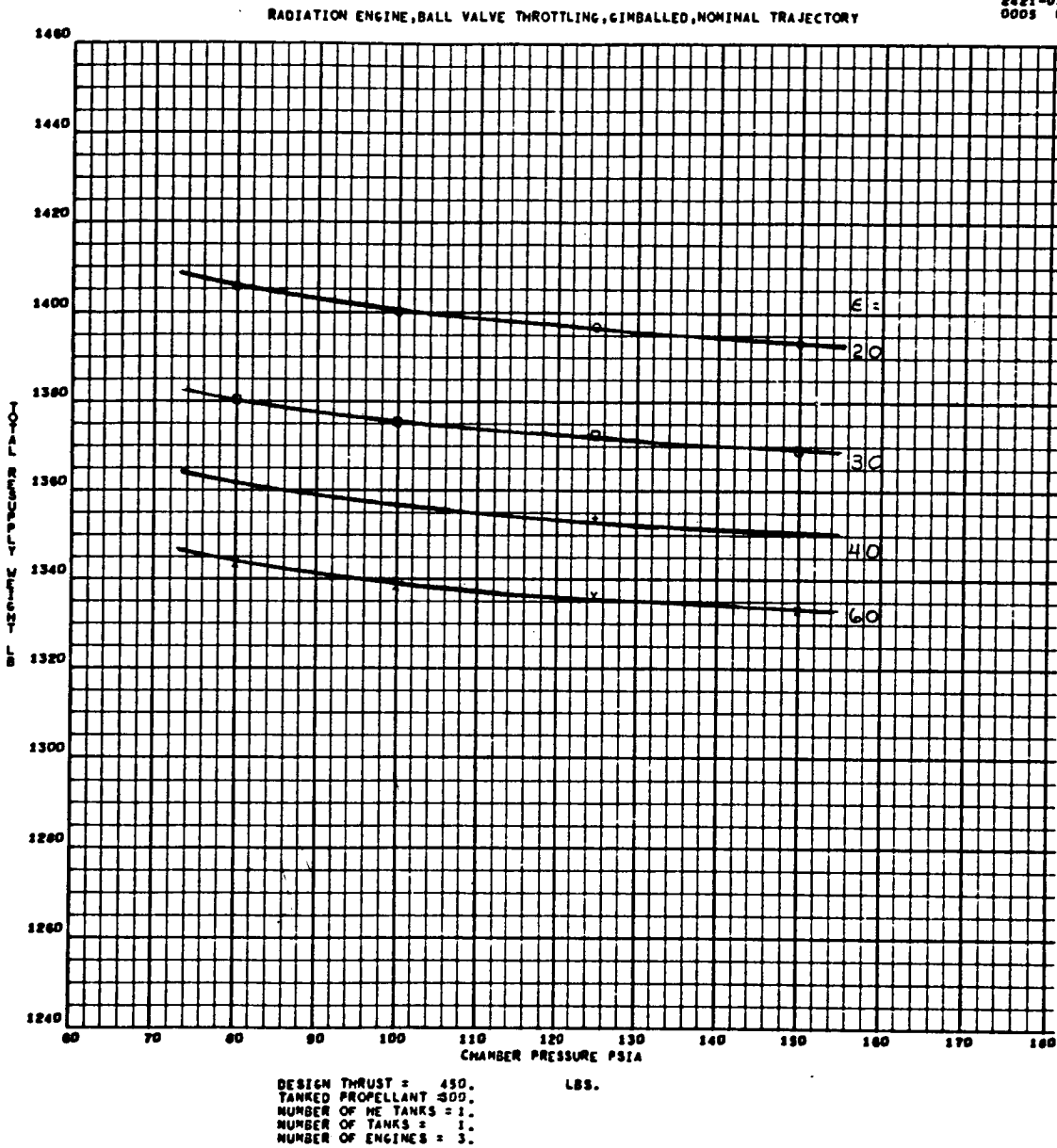


Figure 1-21. Resupply Weight for Five Nominal Flights as a Function of Chamber Pressure and Nozzle-Area Ratio (Sheet 8 of 14)

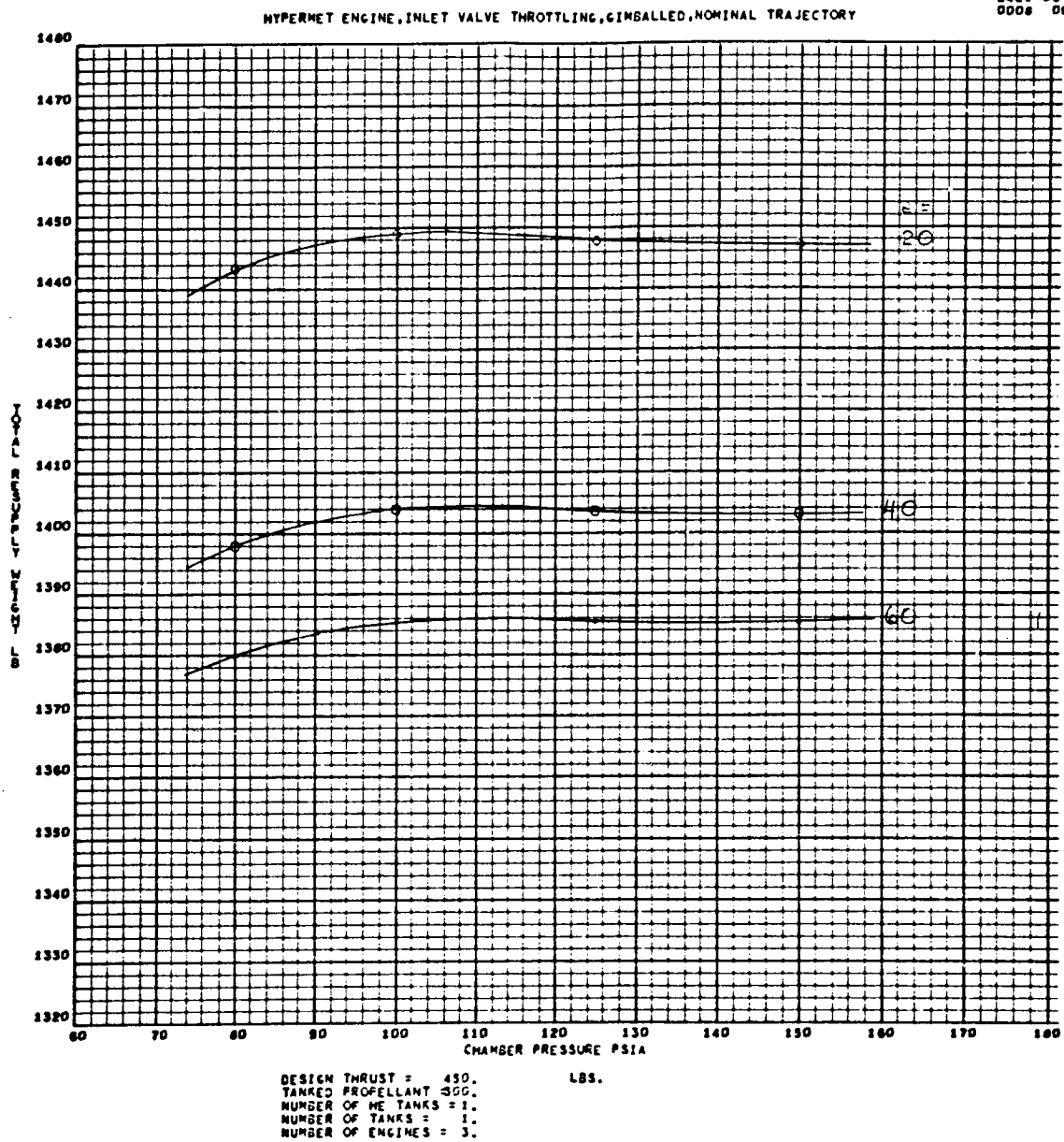


Figure 1-21. Resupply Weight for Five Nominal Flights as a Function of Chamber Pressure and Nozzle-Area Ratio (Sheet 9 of 14)

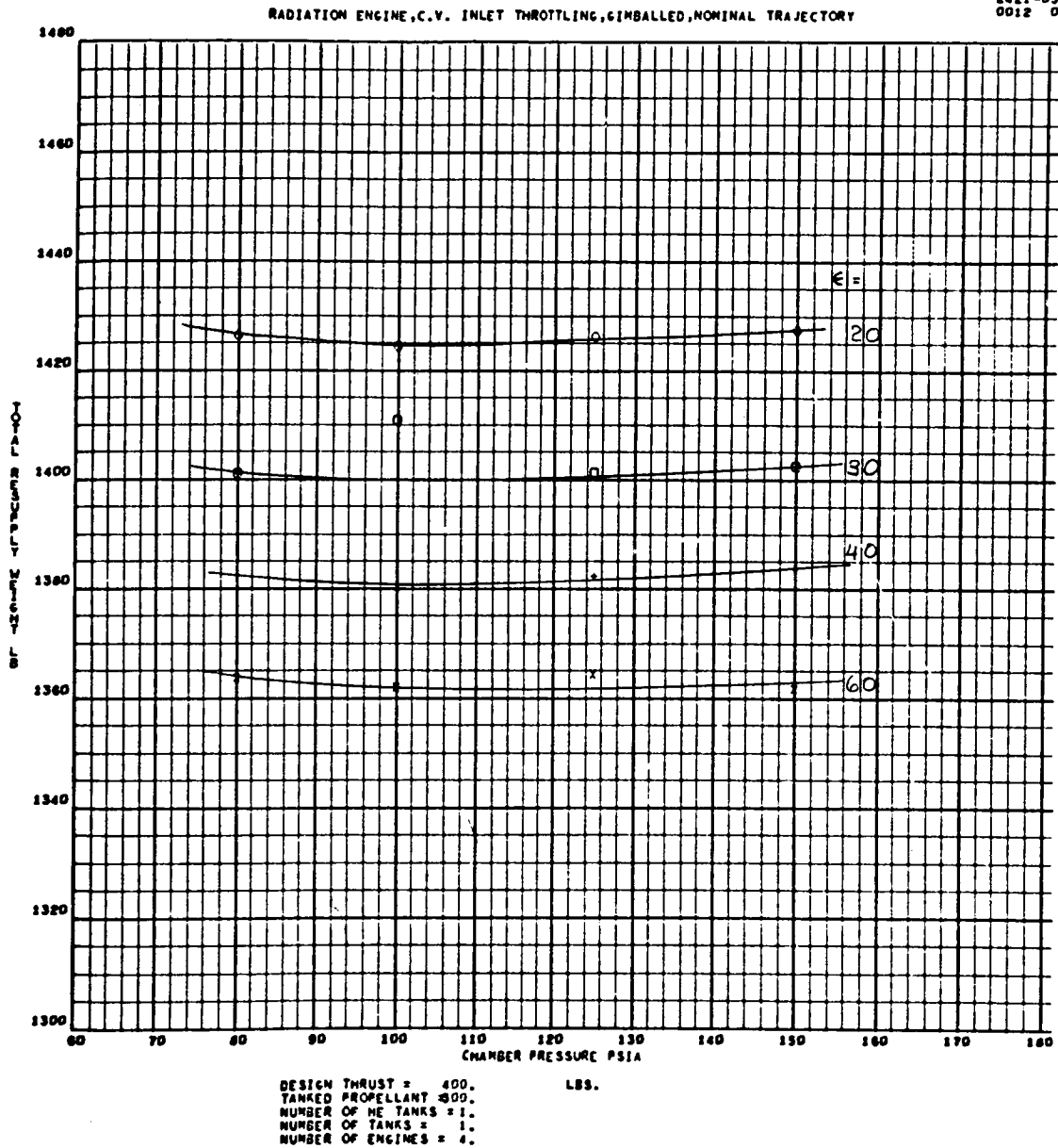


Figure 1-21. Resupply Weight for Five Nominal Flights as a Function of Chamber Pressure and Nozzle-Area Ratio (Sheet 10 of 14)



2421-03-03  
0003 0000

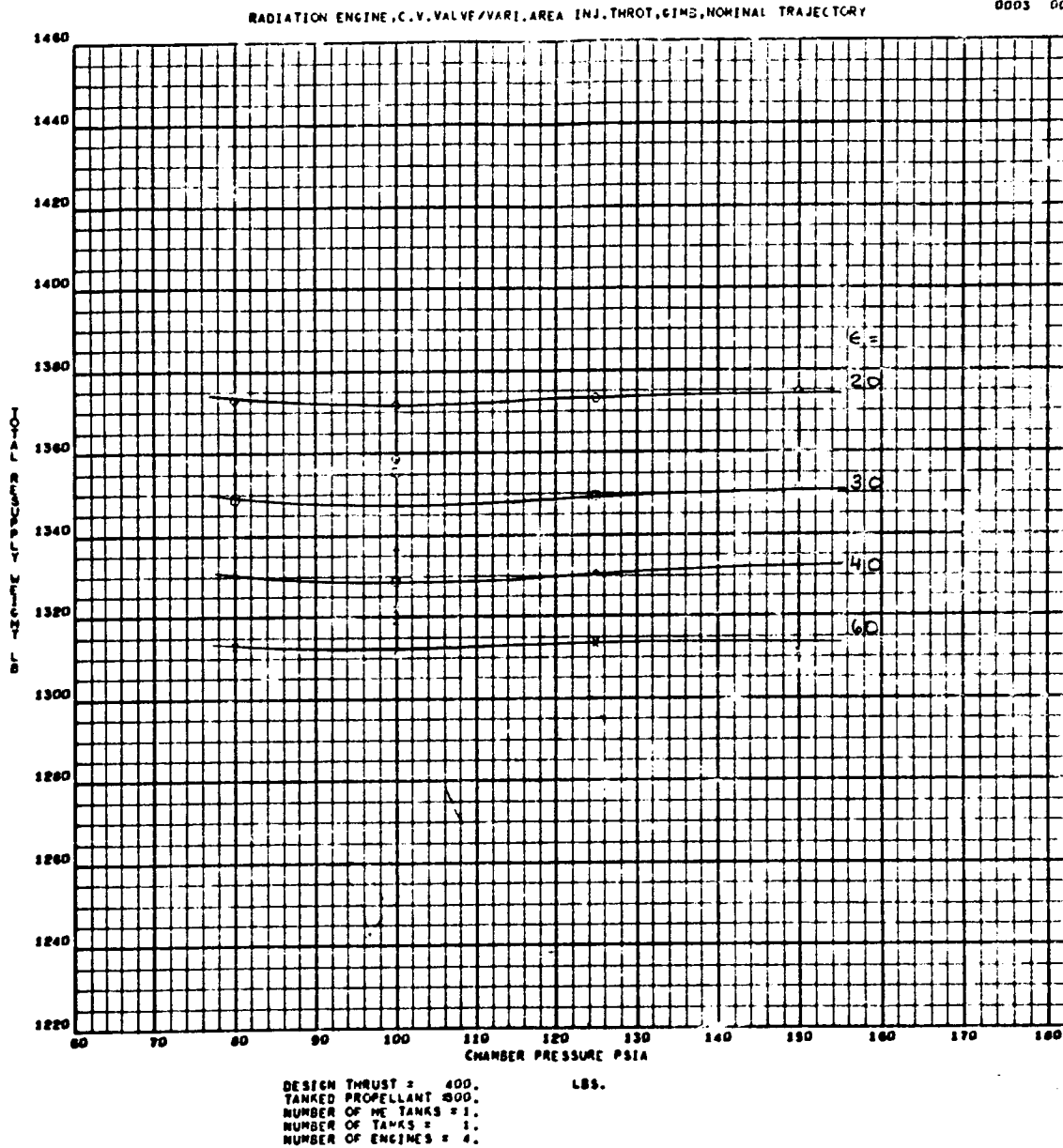


Figure 1-21. Resupply Weight for Five Nominal Flights as a Function of Chamber Pressure and Nozzle-Area Ratio (Sheet 11 of 14)

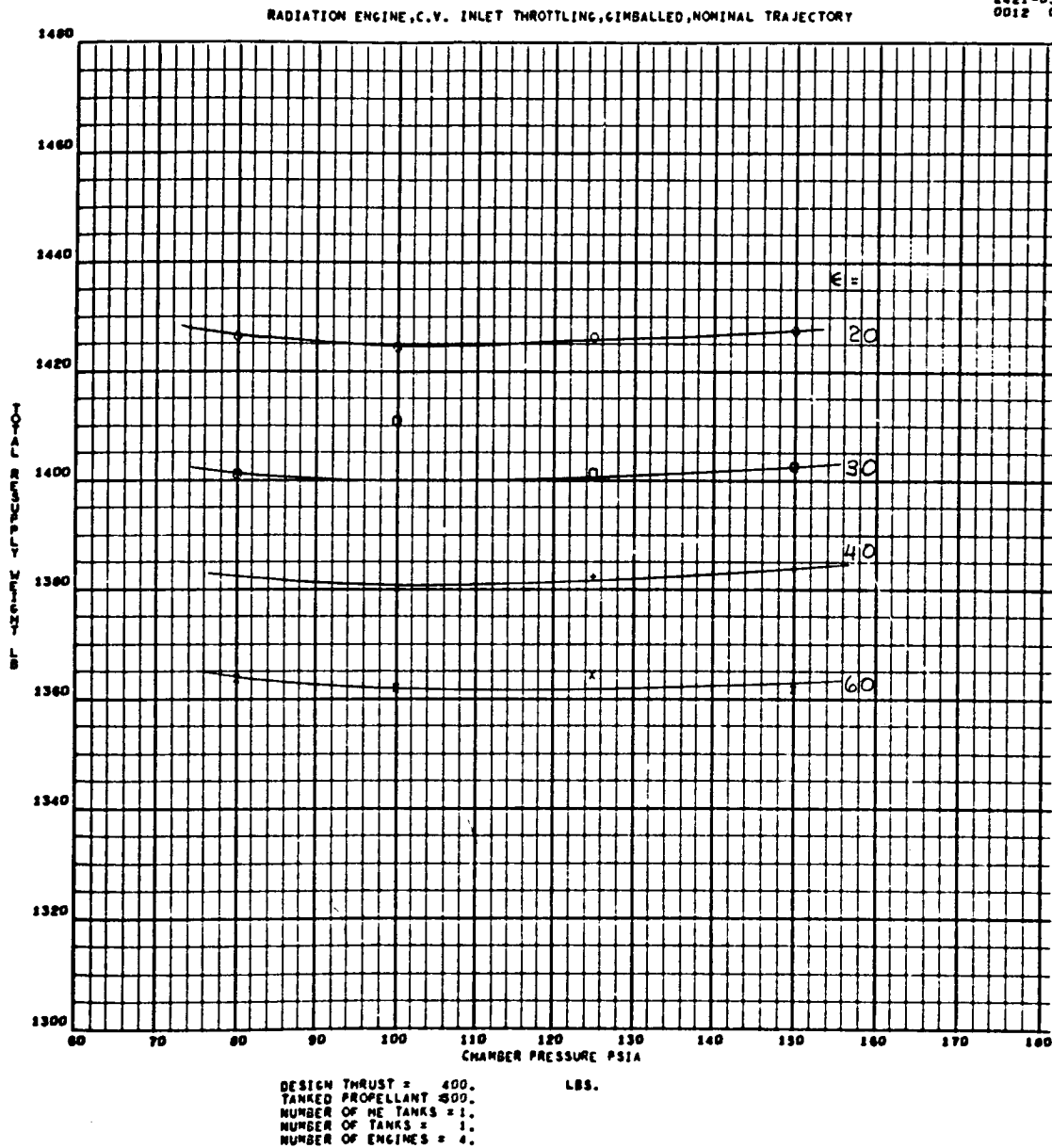


Figure 1-21. Resupply Weight for Five Nominal Flights as a Function of Chamber Pressure and Nozzle-Area Ratio (Sheet 10 of 14)

2421-03-03  
0003 0005

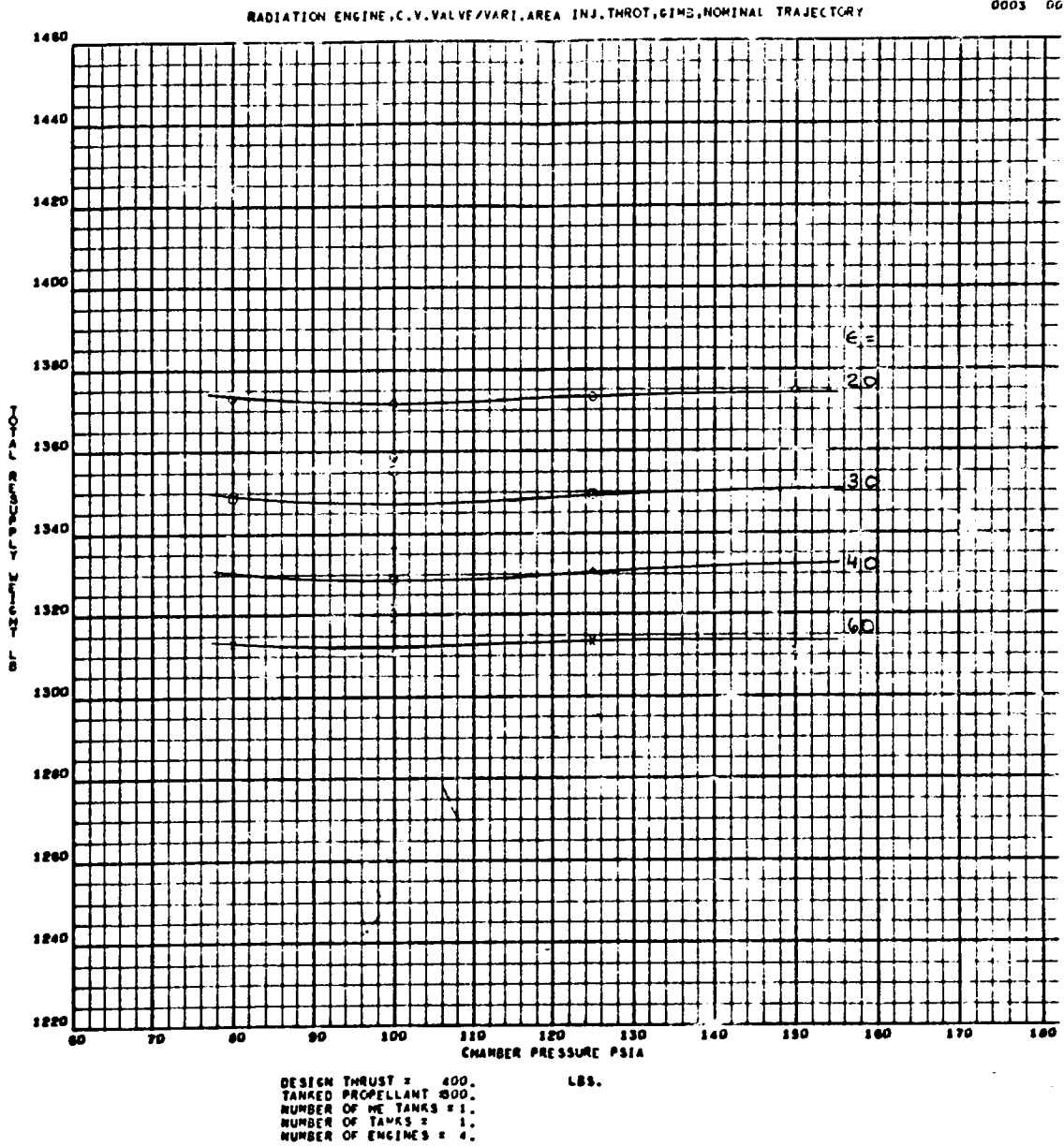


Figure 1-21. Resupply Weight for Five Nominal Flights as a Function of Chamber Pressure and Nozzle-Area Ratio (Sheet 11 of 14)

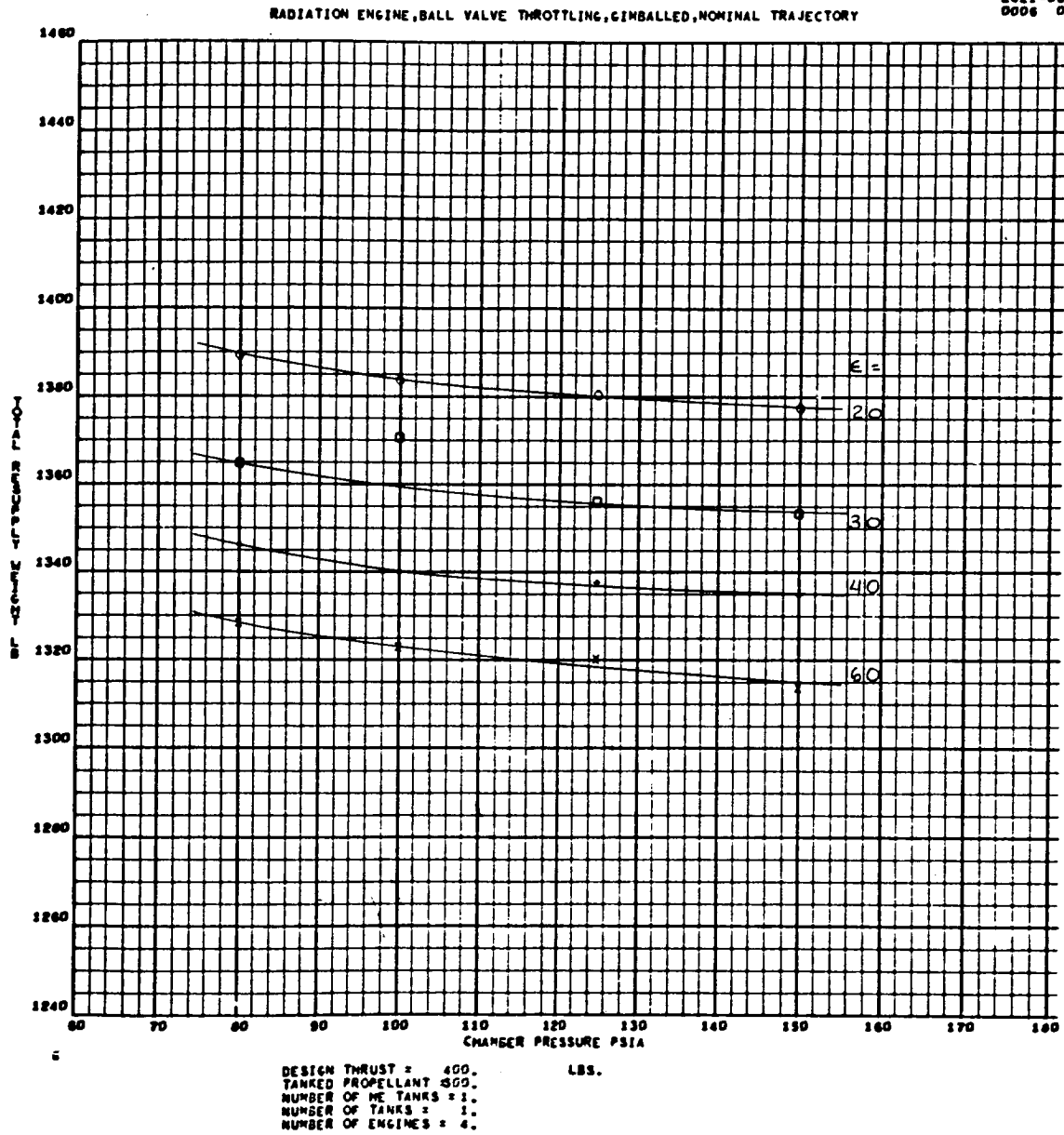


Figure 1-21. Resupply Weight for Five Nominal Flights as a Function of Chamber Pressure and Nozzle-Area Ratio (Sheet 12 of 14)



2421-03-02  
0003 0000

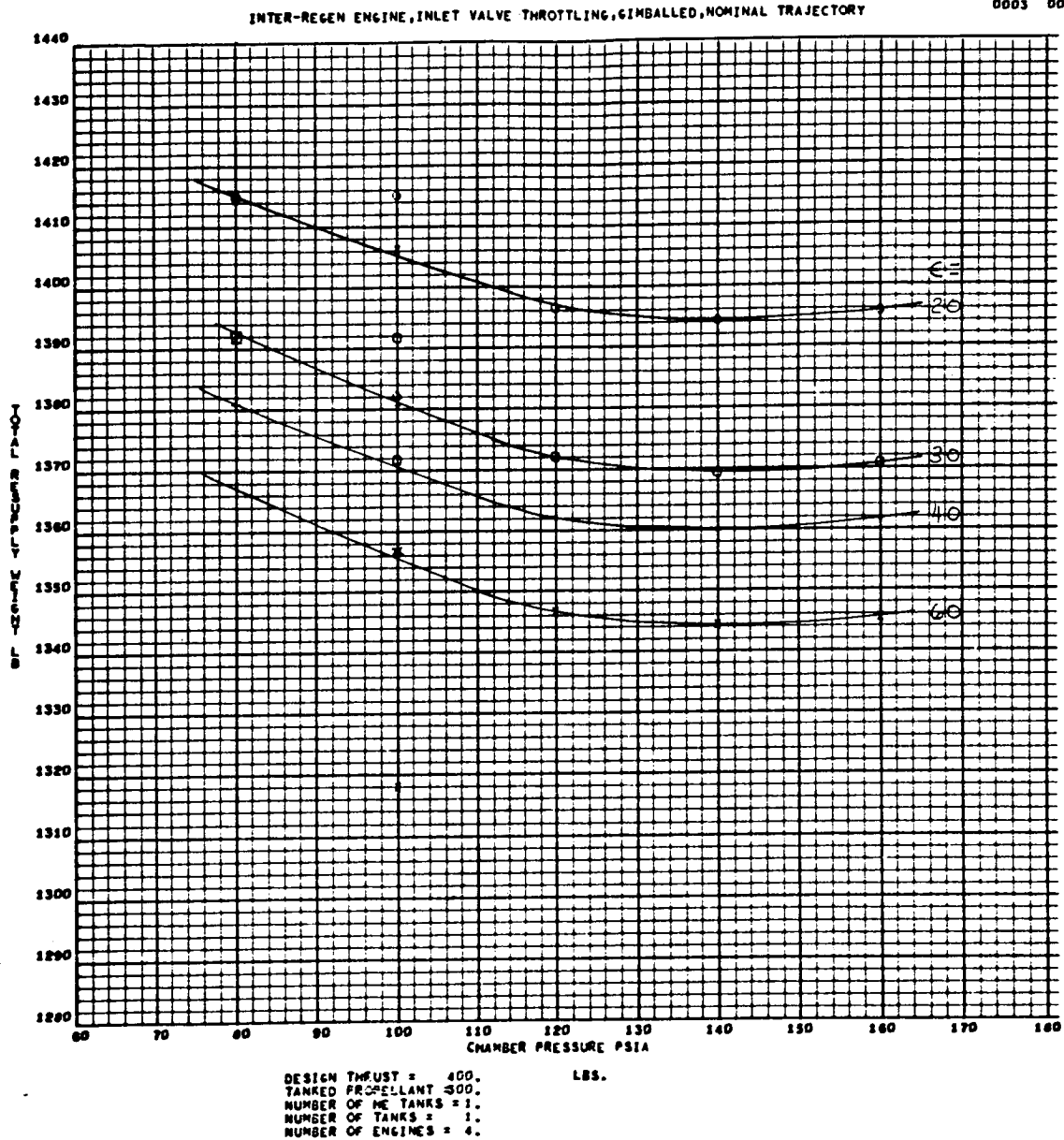


Figure 1-21. Resupply Weight for Five Nominal Flights as a Function of Chamber Pressure and Nozzle-Area Ratio (Sheet 13 of 14)

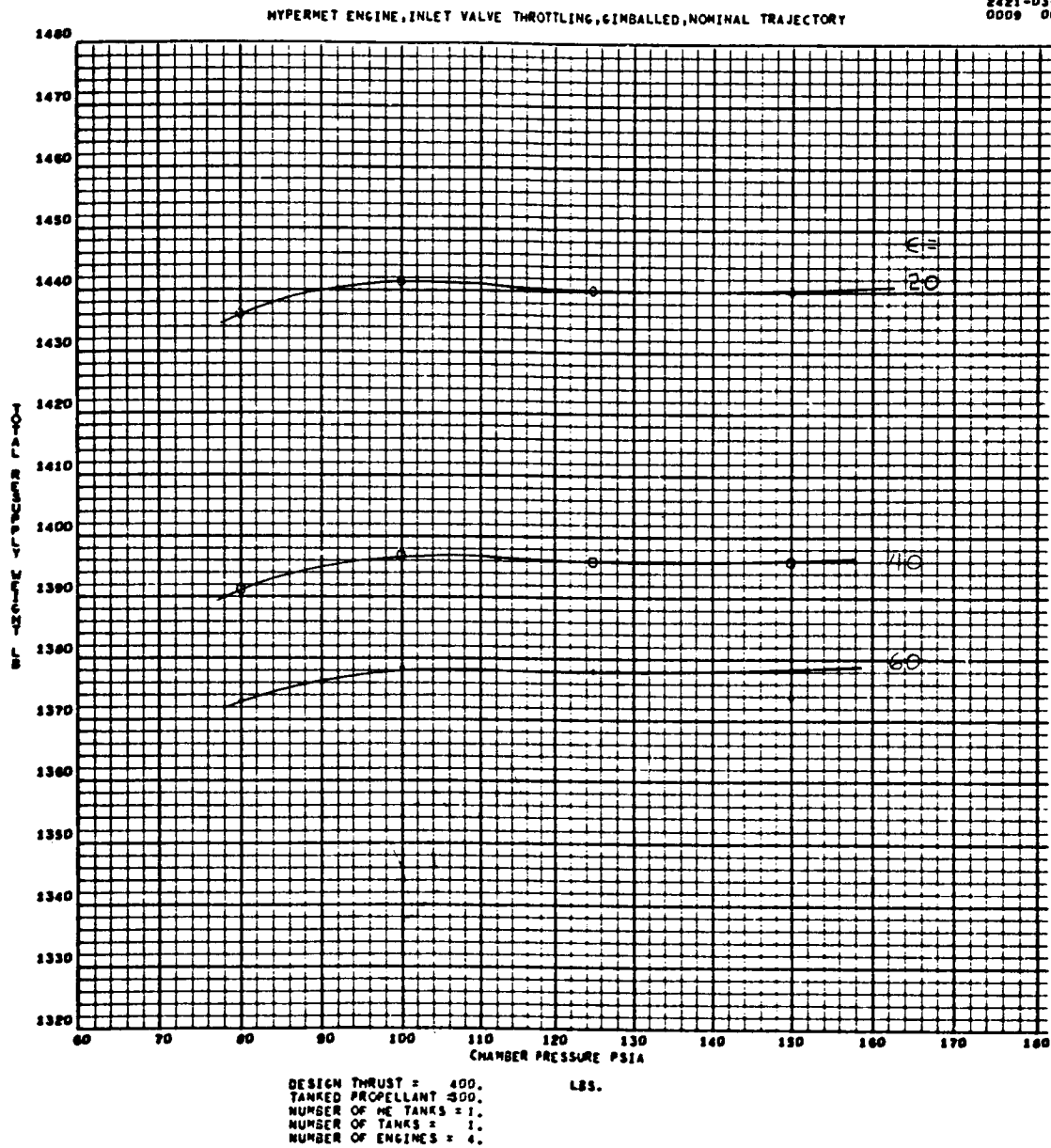


Figure 1-21. Resupply Weight for Five Nominal Flights as a Function of Chamber Pressure and Nozzle-Area Ratio (Sheet 14 of 14)

## Throttling-Method Selection

The three most applicable throttling methods are:

1. Inlet throttling with a variable pressure drop flow control valve (C. V.)
2. A variable-area flow-control valve coupled with a variable-area injector (CVVI).
3. Dual manifold

A selection of one of these concepts requires that a thorough evaluation must include mission performance, weight, actuation requirements, relative complexity, cost, and development status.

Throttling with a variable-area pressure-drop flow-control valve is a well proven technique. It was proven to be a reliable and effective method during the Surveyor program. The major prior application of this method was to engines not requiring deep throttling (>8:1) in which performance at low throttle settings is not of prime importance. It also represents the technique proposed by four out of five of the competitive engine manufacturers for the LFV. Figure 1-22 illustrates a typical cavitating venturi inlet flow control valve. The cavitating venturi valve provides precise flow and mixture-ratio control that is independent of downstream variables, such as, combustion efficiency, throat area, injector-pressure drop, and chamber-pressure fluctuations. It therefore eliminates feed system and engine coupling. Such valves have been developed for several applications and do not present a development problem. Potential suppliers are Fox, Moog, and Hydraulic Research. Bell Aerosystems used such a valve by the Fox Valve Development Company on their Model 8414 LFV engine advanced development program. The performance of this engine is shown in Figure 1-23.

Coupling the cavitating-venturi flow-control valve with the variable-area injector concept provides the highest performing throttling concept at low thrust levels. Its use has been flight proven at a higher thrust level on the LEM-D rocket engine. TRW Systems has also developed this technique for low-thrust engines. The MIRA 150 engine was developed as a backup for the Thiokol-RMD Surveyor vernier engine. Both such applications used ablative cooled thrust chambers. Figure 1-24 illustrates this concept in cross-section. Propellant injection is through a concentric tube, annular injector. To maintain an optimum momentum-vector balance between the two propellant streams, the mechanically coupled injector sleeve is moved axially in relation to the pintle and injector body. For a 5:1 throttle ratio,

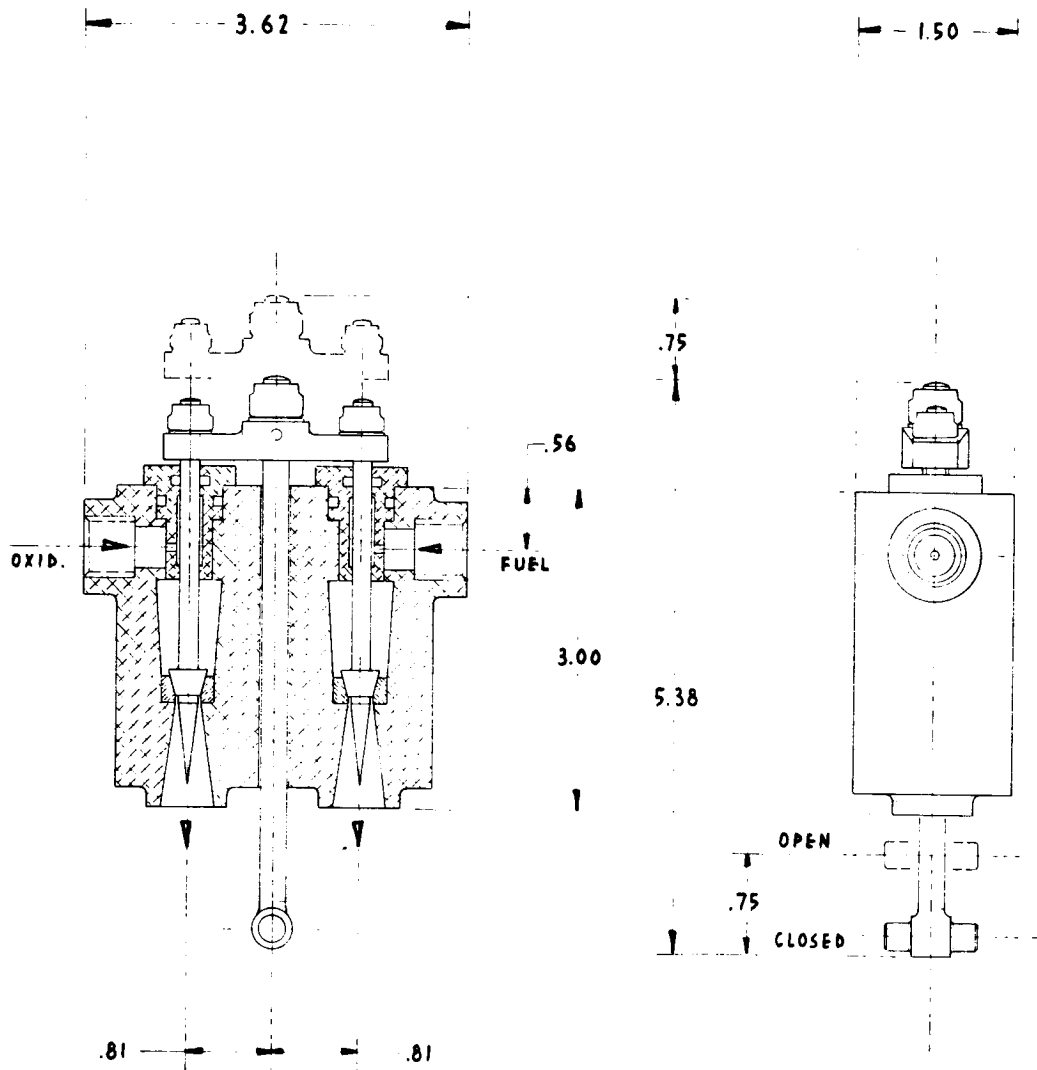


Figure 1-22. Typical Cavitating Venturi Flow Valve



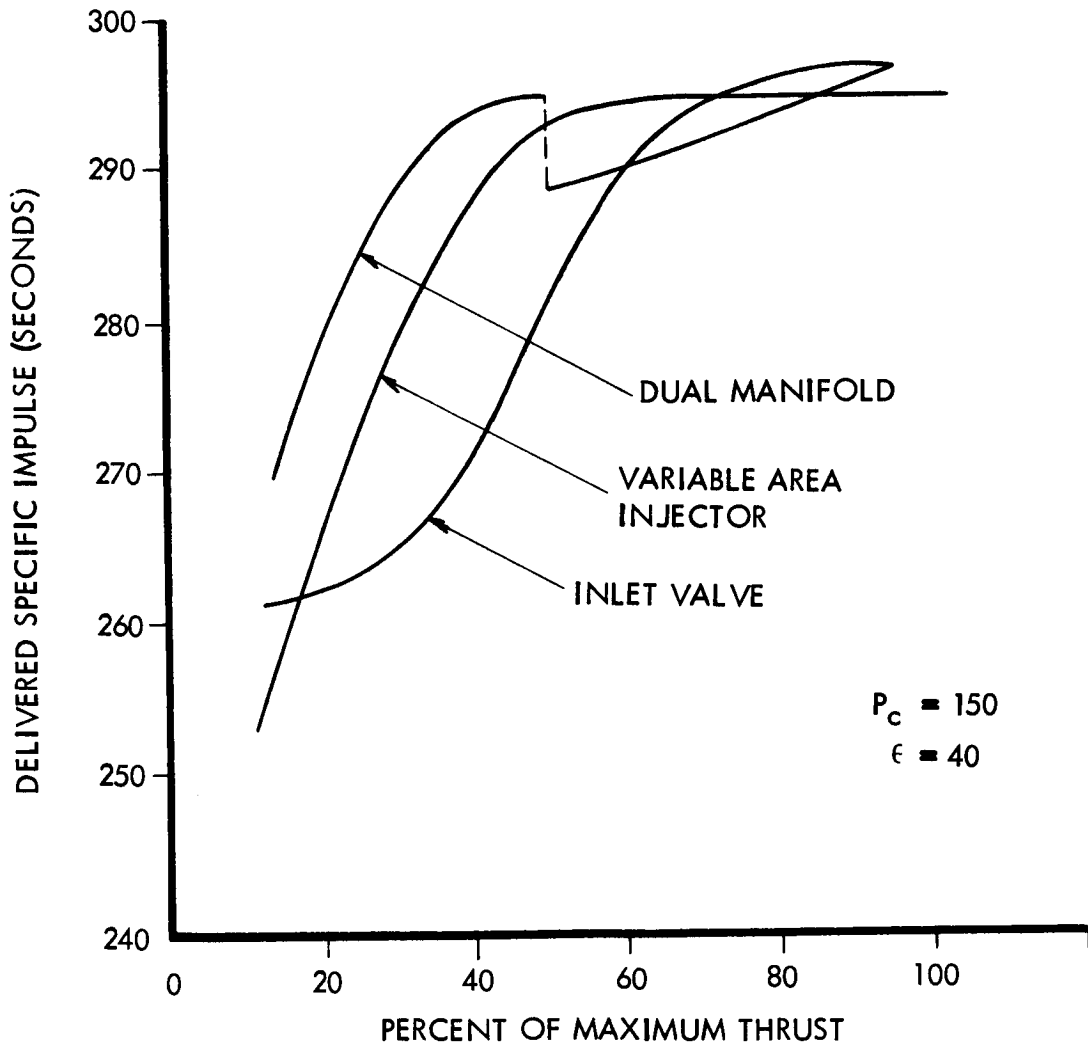


Figure 1-23. Throttle Method Performance Comparison

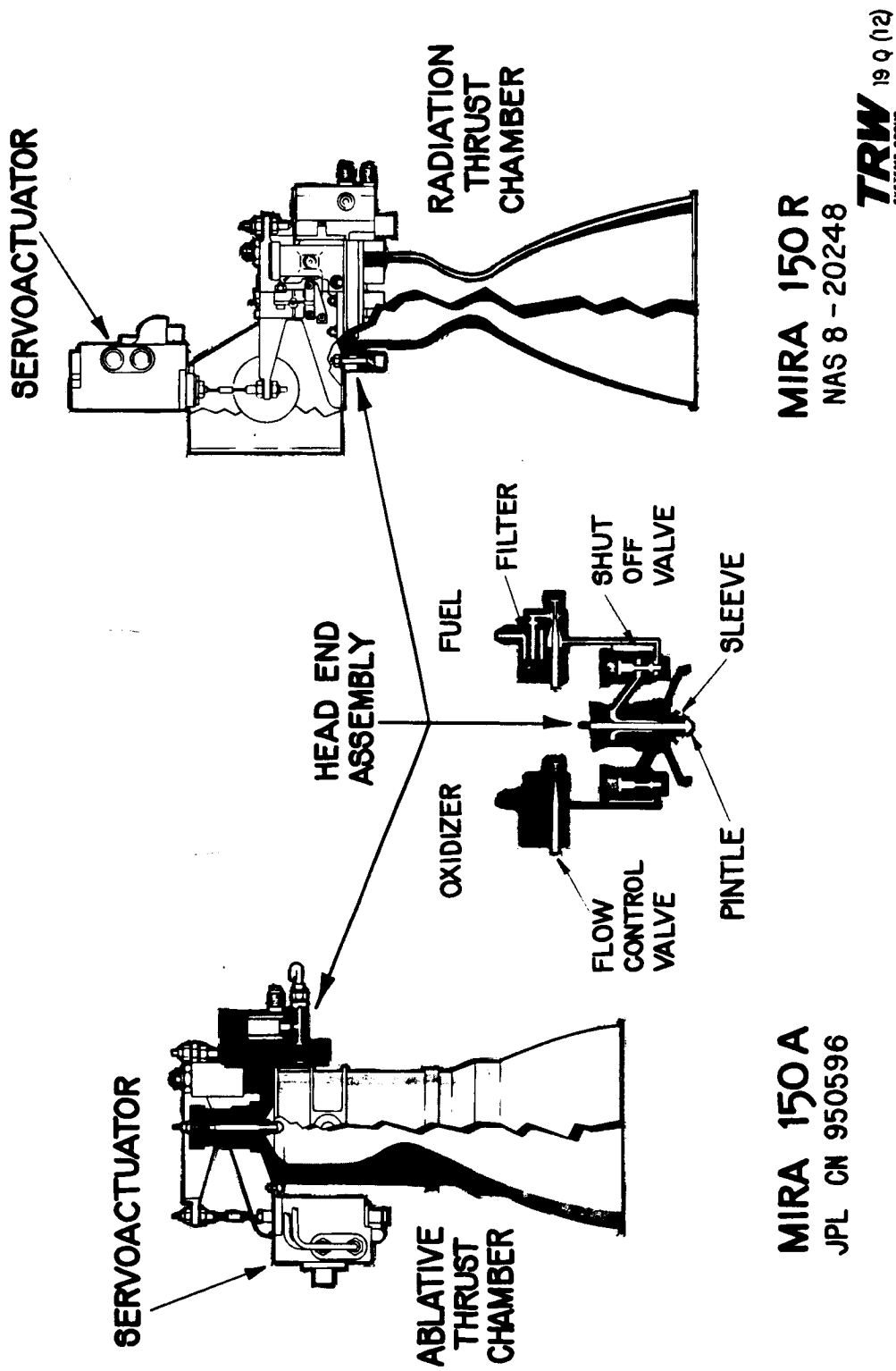


Figure 1-24. Variable Area Injectors

the sleeve moves 0.01 inch. An advanced development program conducted for the LFV application successfully mated this injector with a columbium, radiation-cooled thrust chamber.

The dual-manifold concept does not represent a significant development delta over inlet-valve throttling method. In effect, it provides two "design points" for the engine, one at 100 percent thrust and the other at 50 percent thrust. Two separate injector manifolds (note Figure 1-7) are simultaneously throttled by the cavitating venturi throttle valve for both fuel and oxidizer down to 50 percent thrust. As flow decreases, the injection momentum decreases with an attendant loss of combustion efficiency. At 50 percent thrust, the inner manifolds are isolated from the feed system. The outer manifold flow rates again rise to their design-point values, thereby raising combustion efficiencies. The net result is a substantial performance increase over the other throttling method shown in Figure 1-23 at low thrust.

Figure 1-25 provides a comparison of the relative range capabilities of each throttling concept as functions of payload weight for 1- and 4-engine configurations. At 370 pounds payload, the variable-area injector yields a 2-percent range increase over the inlet-valve throttling method (4 engines). At the no-payload condition, this delta is increased to 4.5 percent. Single-engine range is improved due to operation at a higher average thrust level. The comparable range deltas are 3 percent and 7.5 percent as payload decreases to zero. The dual-manifold concept range advantage is even less. Based on a four-engine vehicle mission performance alone, variable-area injection does not provide a significant capability increase. Table 1-11 also presents other important points of comparison.

Of particular significance is the greater complexity of the variable-area injector concept. Due to the movable injector sleeve and attendant mechanical coupling for actuation, it requires more moving parts (e. g. , seals and bearings). Also, the actuation force required may preclude manual operation. If mechanical actuation is required, the complexity delta will increase over that exhibited by the inlet-valve throttling method. The advanced development status of both concepts is considered to require an equal 18-month time-to-qualify. Costs for development and production again favor the least complex approach.

The cavitating-venturi inlet throttling is therefore recommended for LFV application due to its relative simplicity as compared to the more complex variable area injector which provides a negligible performance advantage.

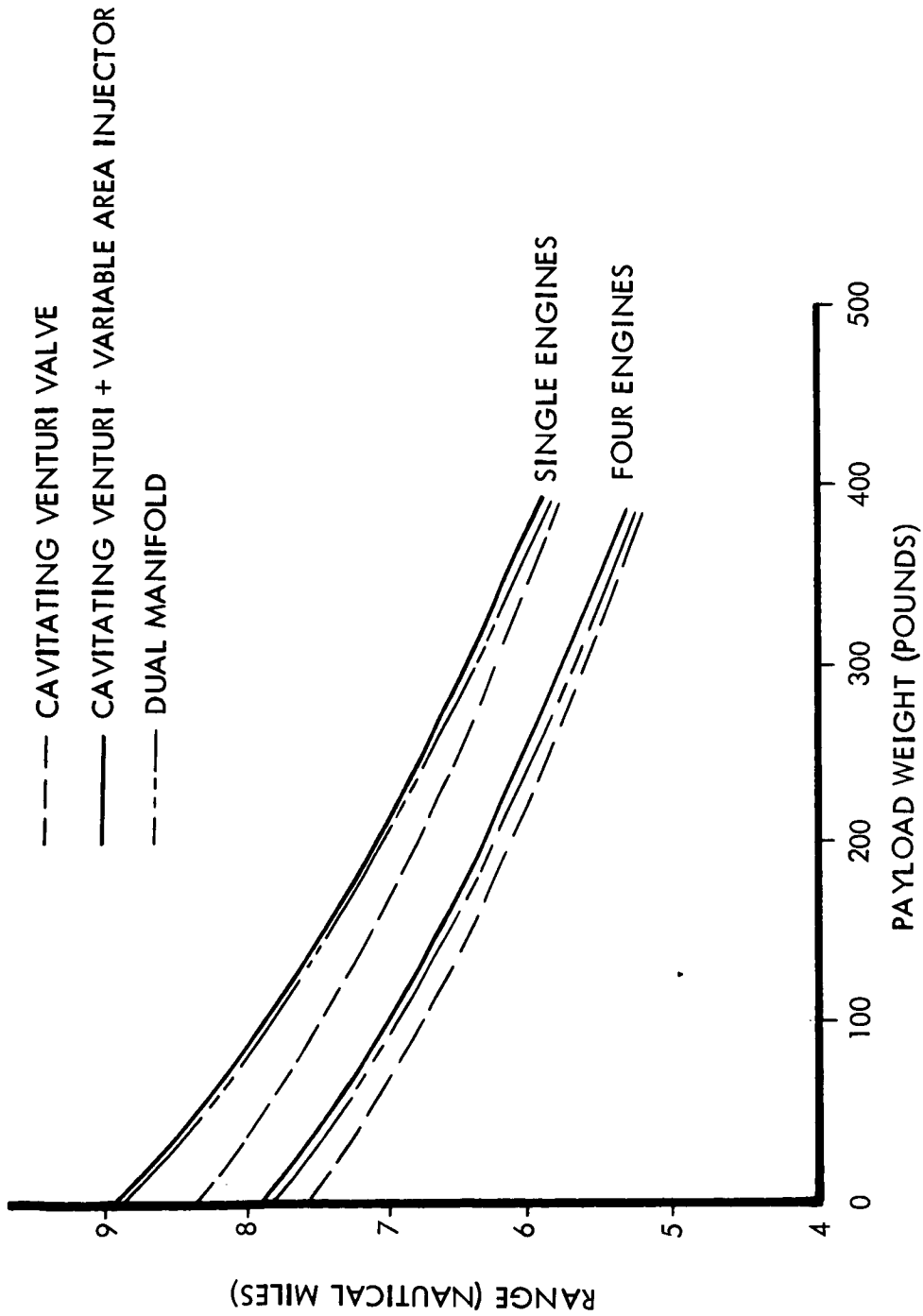


Figure 1-25. Throttling Method Comparison for Nominal Trajectory

Table 1-11. Throttle-Method Comparison, Four-Engine Configuration

Consideration	Throttle Method		
	Inlet Valve	Inlet Valve + Variable-Area Injector	Dual Manifold
Range - (nm) 370-lb payload 0-lb payload	5.25 7.55	5.38 7.9	5.30 7.8
Weight (lb) Burnout	72	74	99
Total loaded	373	375	399
Resupply*	1432	1404	---
No. moving parts (manual actuation)	1	3	3
No. seals	4	8	6
Bearings	2	5	4
Actuation force (in-lb/engine)	10 to 20	34 to 57	10 to 20
Development status	Pre-PFRT	Pre-PFRT	None
Conclusion: Inlet Valve Throttling Most Desirable			
* Nominal trajectory extended to propellant depletion - five flights.			

### Summary of Optimization Study Results

The results of the optimization study provide several significant conclusions which aid in establishing the desired LFV design criteria. These are as follows.

1. LFV propulsion subsystem loaded weight is relatively insensitive to  $P_C$ .
2. Optimum  $P_C = 100$  psia (radiation cooled),  $P_C = 140$  psia (interregenerative cooled).
3. Optimum nozzle area ratio is defined on the basis of range at 35-40:1.
4. Resupply-weight requirements are sensitive to engine-design criteria, but must be evaluated on an overall mission performance basis.
5. Throttling method has a minor effect on range; however, further evaluation for other mission duty cycles is required prior to a definite conclusion.
6. The single-engine configuration is the lightest and best performing; however, companion overall vehicle studies including the evaluation of reliability, development-program duration, and engine-out requirements have selected the four-engine configuration.
7. Two spherical propellant tanks employing capillary barriers and screened antislosh baffles are desired.
8. The bimetallic thrust chamber with the laminated injector is non-competitive on the basis of dry weight and performance.
9. The variable pressure drop valve used in conjunction with a cavitating venturi is recommended for its relative simplicity and good range capability when compared to more complex throttling systems.

## THRUST VECTOR CONTROL

A summary of attitude control requirements is shown in Table 1-12. The method for evaluating a suitable system for achieving this control will be to evaluate (1) bipropellant systems in detail for yaw as a weight datum basis; (2) cold gas for yaw; (3) bipropellant systems for pitch, roll and yaw integrated as a single system; and (4) other systems, such as, jet vanes, secondary injection, gimbaling, etc. The overall choice of systems will then be based on total vehicle considerations, such as vehicle weight, reliability, etc.

Table 1-12. Attitude-Control Requirements

TVC Mode	Control Mode		
	Kinesthetic	Non-Kinesthetic	
		Manual Flyby-Wire	Stability Augmented
Fixed Engine(s) 1, 2, 3, or 4	Yaw control required (or jet vane)	Pitch, roll, and yaw control required	Pitch, roll, and yaw control required
Gimballed 1 or 2 engines, pitch and roll	NA	Yaw control required	Yaw control required
3 or 4 engines, pitch, roll, and yaw	NA	None required	None required

### Yaw Requirements

The requirement for yaw orientation maneuvers consists of three 180-degree yaw orientations during hovering for the maximum-range type mission. The first maneuver is accomplished during hover after the initial takeoff, the second at the intermediate site (prior to landing or after takeoff), and the third at the return landing. The orientations are required to orient in azimuth to the desired direction of flight, and for possible use of vehicle shadow (sun to pilot's back) for cues during landing and takeoff. The yawing rate is a primary variable in the analysis and is dependent upon the time allowable (hovering) to accomplish the 180-degree yaw orientation. Typical

hovering durations are 7 seconds after each takeoff and 10 seconds prior to each landing. The hovering times (and resultant yaw rates) were varied in the analysis from 5 seconds to 20 seconds to determine the effects on RCS system weights. However, the selection of final values should be based on any maximum yaw rate limitation from human factors considerations, control system thresholds, etc. resulting from the visual and tethered flight simulation runs.

The requirement for yaw-limit cycle consisted of holding the vehicle within a yaw deadband angle of  $\pm 5$  degrees and using a bang-bang mode for cycling the vehicle at a low angular rate within this angular limit. To conserve propellant and provide a reasonably low rate, avoiding disorientation to the pilot, an angular velocity of 0.5 degrees per second was selected. This rate would allow the vehicle to cycle 10 times about the null of the deadband angle during the maximum flight time of 400 seconds. These rates with the short bang-bang firing times also provided adequate torque levels for handling any disturbance levels.

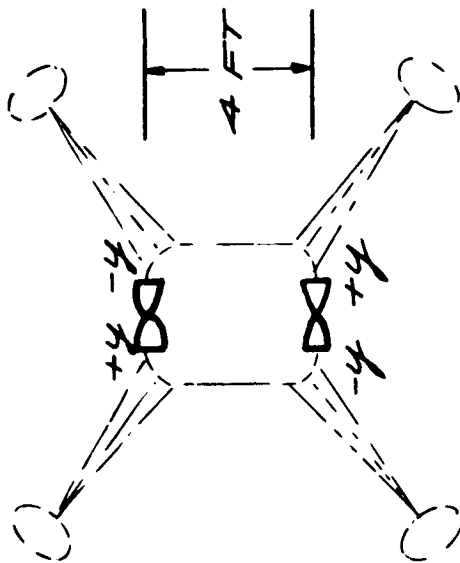
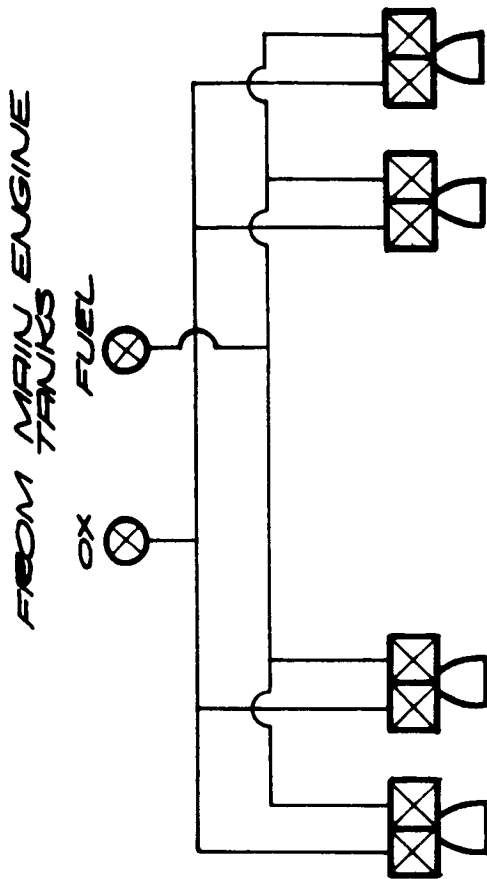
#### Bipropellant RCS Evaluation

Assumptions and criteria used in the analysis include the yaw RCS thruster arrangement and the vehicle weight conditions and yaw moments of inertia.

The RCS system weights were calculated for both a four-thruster system and an eight-thruster arrangement which provided a redundant thruster set in event of failure. For clarity, only the four-thruster arrangement is shown in Figure 1-26. The four thrusters are shown in a couple arrangement to provide  $\pm$  yaw moments, and are mounted around the pilot's platform base of the LFV with a distance between firing thrusters of four feet. The bipropellant-type system configuration is also shown in the figure. Oxidizer and fuel are provided from the main-engine propellant tankage through lines with isolation valves, then distributed to each of the four thrusters which have a set of bipropellant solenoid control valves as part of each thruster assembly. The eight thruster system would be similar with another four-thruster set with separate isolation valves. The additional four thrusters would be mounted similarly but on the other vehicle axis (90 degree).

The variation of vehicle weight conditions used in the analysis were the maximum gross weight (liftoff with maximum payload) and the minimum vehicle weight (burnout with no payload) as follows:





	VEHICLE WEIGHT	YAW MOMENT OF INERTIA
LIFTOFF CONDITION (MAX PAYLOAD)	1242 LB.	88 SLUG-FT <sup>2</sup>
BURNOUT CONDITION (NO PAYLOAD)	582 LB.	29 SLUG-FT <sup>2</sup>

Figure 1-26. Yaw RCS Arrangement and Configuration

Vehicle Weight (lb)	Yaw Moment of Inertia (slug/ft <sup>2</sup> )
Max 1,242	88
Min 582	29

The bipropellant RCS system weights were determined as the sum of the calculated propellant weight required for yaw-orientation and limit-cycle operations and estimated weights for thruster assemblies and system components (isolation valves, lines, and connectors). Main-engine propellant consumed during hovering was also calculated, since hovering time (yaw maneuvering time) was a primary variable.

The required yaw angular rates for performing a 180-degree yaw orientation maneuver is shown in the tabulation below for three values of allowable yaw maneuvering time (hovering time).

Yaw Maneuvering Time (sec)	Yaw Angular Rate (deg/sec)
5	36
10	18
20	9

The propellant consumption for each 180-degree yaw orientation maneuver is shown on Figure 1-27 versus yaw maneuvering time. Both yaw RCS propellant and main-engine hovering propellant are shown on the figure with separate curves, and for the extremes in vehicle weight condition.

The main-engine propellant consumption (Table 1-13) was based on the best engine throttled performance (TRW) for the hover condition at the vehicle-weight extremes, with maximum thrust (362 lb) based on four engines with an engine-out capability.

The total hovering propellant during the three yaw maneuvers is summarized in Table 1-14 based on the first hover occurring at maximum vehicle weight, the second at an intermediate weight, and the third occurring at minimum vehicle weight. In addition, a 50-percent contingency allowance was added to account for mission and weight uncertainty. The propellant weights are shown tabulated for three values of yaw maneuvering time (yaw rates).

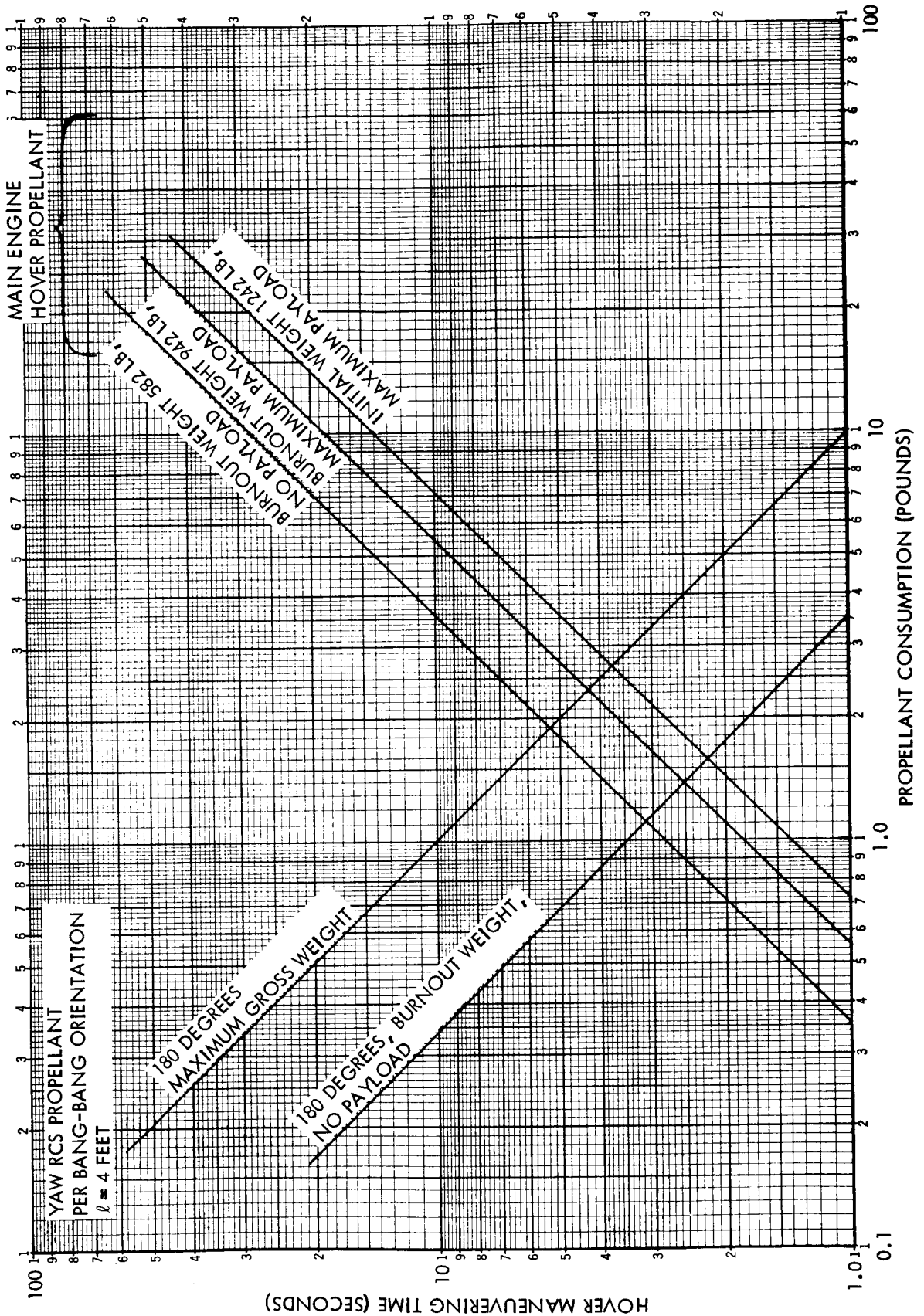


Figure 1-27. RCS and Main Engine Propellant Consumption

Table 1-13. Main-Engine Propellant-Consumption Rate

Parameter	Maximum Vehicle Weight	Minimum Vehicle Weight
Vehicle weight (lb)	1,242	582
Hover thrust (lb)	207	97
Hover thrust percent of maximum thrust	57	27
Specific impulse 292 at 100 percent $F_{max}$ (sec)	291	271
Propellant flow rate (lb/sec)	0.713	0.358

 Table 1-14. Main-Engine Hovering Propellant During  
 Three 180 Degree Yaw Maneuvers

Parameter	Case		
	1	2	3
Yaw maneuvering time (sec)	5	10	20
Yaw rate (reference) (deg/sec)	36	18	9
Propellant weight (lb)			
First hover	3.5	7.1	14.2
Second hover	2.5	5.0	10.0
Third hover	1.8	3.6	7.2
Subtotal	7.8 lb	15.7 lb	31.4 lb
50-percent contingency	3.9	7.8	15.7
Total	11.7 lb	23.5 lb	47.1 lb

The yaw orientation propellant shown on Figure 1-27 is that required for two firings per orientation (start - stop) using two thrusters in a couple arrangement for each firing. The propellant per thruster per firing was obtained for each yaw rate, using the yaw moment of inertia and the 4-foot distance between thrusters to obtain total impulse and, with a specific impulse value of 270 sec, obtaining the propellant weight per thruster per

firing. The total propellant per orientation is shown for both the maximum and minimum vehicle weight conditions.

The total yaw orientation propellant for the three, 180-degree yaw maneuvers are summed below based on the variable vehicle weight condition (similar to that for summing hovering propellant) and the addition of 50-percent contingency allowance to account for mission and weight uncertainty. The RCS-orientation propellant weights are shown tabulated (Table 1-15) for three values of yaw maneuvering time (yaw rates).

Table 1-15. RCS Orientation Propellant for Three 180 Degree Yaw Maneuvers

Parameter	Case		
	1	2	3
Yaw maneuvering time (sec)	5	10	20
Yaw rate (deg/sec)	36	18	2
Propellant Weight: (lb)			
First yaw	2.0	1.0	0.5
Second yaw	1.3	0.65	0.32
Third yaw	0.7	0.35	0.18
Subtotal	4.0 lb	2.0 lb	1.0 lb
50-percent contingency	2.0	1.0	0.5
Total	6.0 lb	3.0 lb	1.5 lb

The thruster sizing was based on the total impulse required per thruster per firing obtained in the orientation propellant analysis for the maximum vehicle weight condition, and for each of three values of maneuvering time and yaw rate (Table 1-16).

These total impulse per firing values consist of a thrust times a firing time and are shown on Figure 1-28 plotted as thrust versus maneuvering time (yaw rate) with various firing times from 0.5 to 3 seconds. In selecting the thrust level from this figure, the firing time,  $t_b$ , should be relatively as long as possible to avoid specific-impulse degradation whenever the vehicle is at the minimum-weight condition where firing times would be

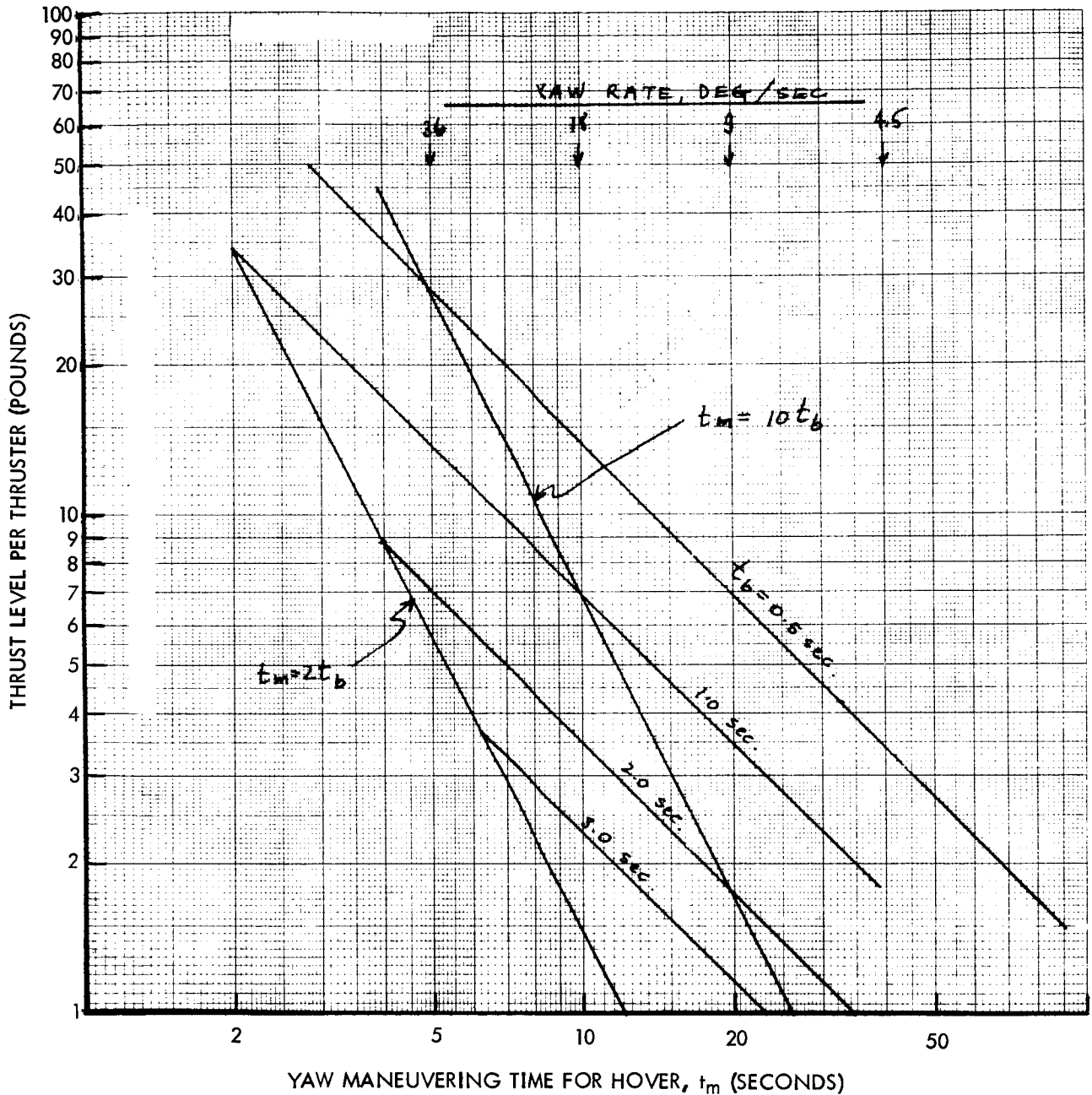


Figure 1-28. Thrust Versus Maneuvering Time (Yaw Rate) With Various Firing Times From 0.5 to 3 Seconds, Maximum Payload

Table 1-16. Total Impulse Per Thruster Per Firing

Parameter	Case		
	1	2	3
Yaw maneuvering time (sec)	5	10	20
Yaw rate (deg/sec)	36	18	9
Total impulse per thruster per firing (lb-sec)	13.8	6.9	3.45

shorter for the same yaw rates (see Figure 1-29). On the other hand, firing times should be as short as possible to minimize the time required to accelerate to the required yaw rate. A reasonable compromise resulted in selecting a firing time equal to 0.1 of the maneuvering time, as shown on Figure 1-28 as the line,  $t_m = 10 t_b$ , which was used in selecting the thruster size for each of the three values of yaw maneuvering rate (Table 1-17).

Table 1-17. Yaw RCS Thrust Size

Parameter	Case		
	1	2	3
Yaw maneuvering time (sec)	5	10	20
Yaw rate (deg/sec)	36	18	9
Thrust level (lb)	27.6	6.9	1.7

The yaw RCS-thruster characteristics are shown in Figure 1-30 and include thrust levels, firing times, and specific impulse versus the yaw maneuvering time (yaw rates). The firing times and specific impulse are shown for the maximum vehicle weight condition corresponding to the required thrust shown, as well as the resulting firing times and specific impulse in performing the orientations at the minimum vehicle weight with the same size thruster. Also shown are resulting values for performing the limit cycle operation with the same size thrusters, at moment of inertia and weight conditions averaged between minimum and maximum vehicle weight.

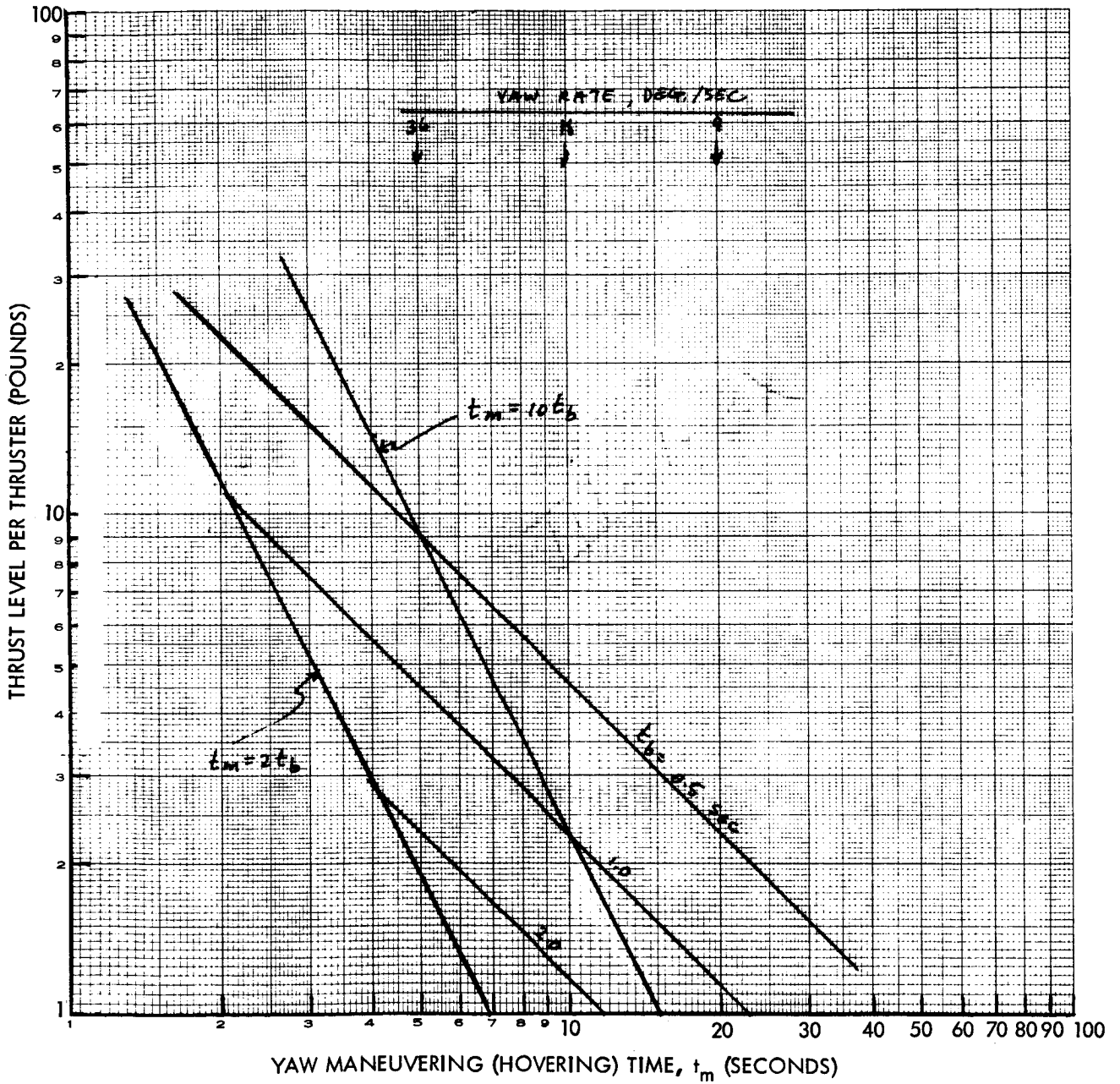


Figure 1-29. Thrust Versus Maneuvering Time (Yaw Rate) With Various Firing Times From 0.5 to 2 Seconds, Burnout Weight, No Payload



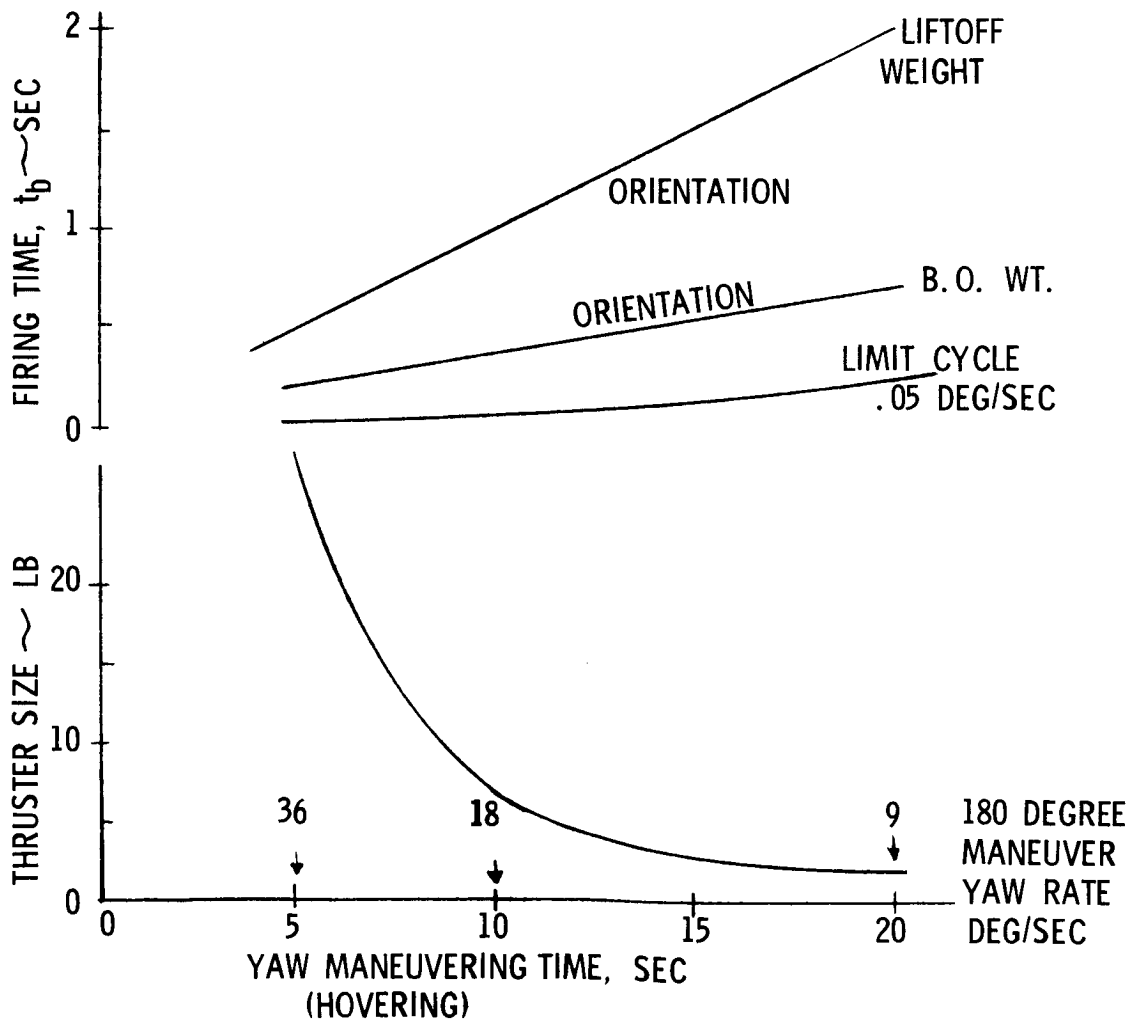
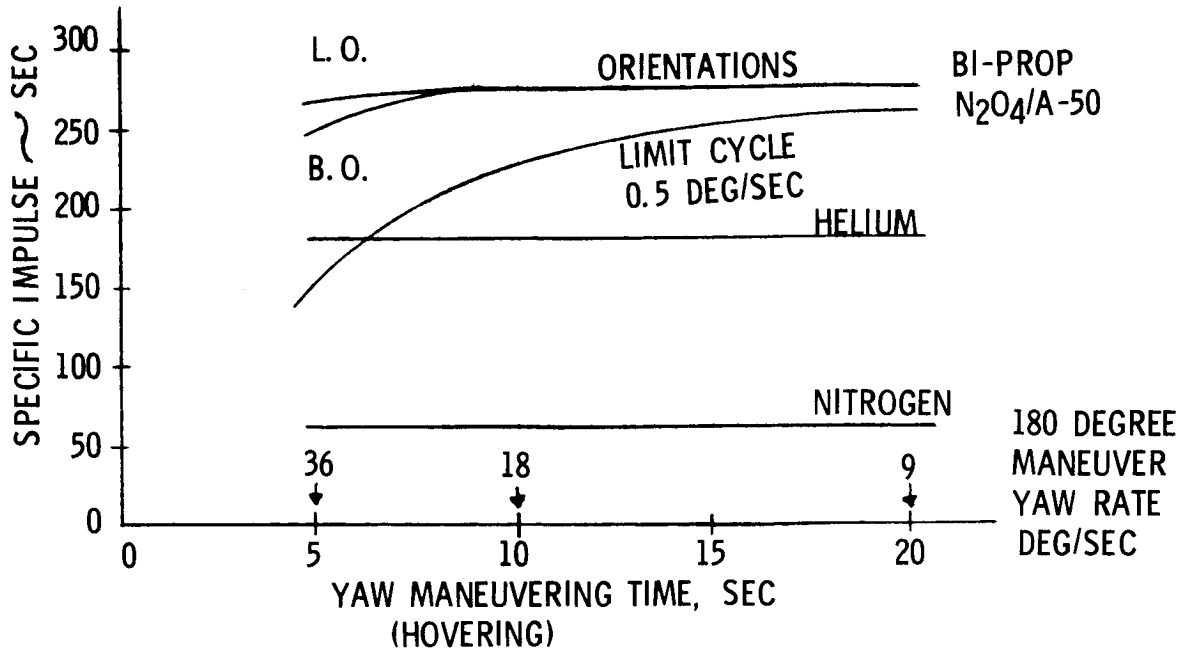


Figure 1-30. Yaw RCS Thruster Characteristics

The impulse bit per thruster per firing of 0.384 lb-sec was determined from the limit cycle requirements of 0.5 deg/sec for angular velocity,  $\pm 5$  degrees deadband angle, a 2-ft radius arm, 400-sec mission duration, and 88-slug-ft<sup>2</sup> yaw moment of inertia for max weight condition. Between minimum and maximum weight conditions, the average number of firings per thruster are 80 for the mission duration. This yielded a total impulse required of 31 lb-sec. For propellant-weight determination, specific impulse was varied according to Figure 1-30 for the firing pulse times corresponding to the design thrust levels shown. The limit-cycle propellant weights are shown for these thrust levels corresponding to yaw-orientation maneuvering times (yaw orientation rates) (Table 1-18).

Table 1-18. Limit-Cycle Propellant Weights for Thrust Levels Corresponding to Yaw-Orientation Maneuvering Times

Parameter	Case		
	1	2	3
Yaw maneuvering time (sec)	5	10	20
Yaw orientation rate (deg/sec)	36	18	9
Thrust level (lb)	27.6	6.9	1.7
Limit cycle pulse firing time (sec)	0.014	0.056	0.223
Specific impulse (sec)	155	228	261
Limit cycle propellant weight (total impulse 31 lb-sec) (lb)	0.20	0.136	0.119
100-percent contingency (lb)	0.20	0.136	0.119
Total limit-cycle propellant (lb)	0.40	0.27	0.24

The bipropellant yaw RCS system weight summary is shown in Table 1-19. These weights consist of RCS propellant (with orientation and limit-cycle) as calculated, estimates of thruster-assembly weight (thruster and bipropellant solenoid valves based on scaling data) and estimates for isolation valves, lines, connections, etc., for the four-thruster system configuration. Propellants are obtained from the main-engine tankage, so that no tank or pressurization system weights are necessary. These RCS system weights are also shown in the curves of Figure 1-31 for the four-thruster configuration and Figure 1-32 for the eight-thruster configuration.

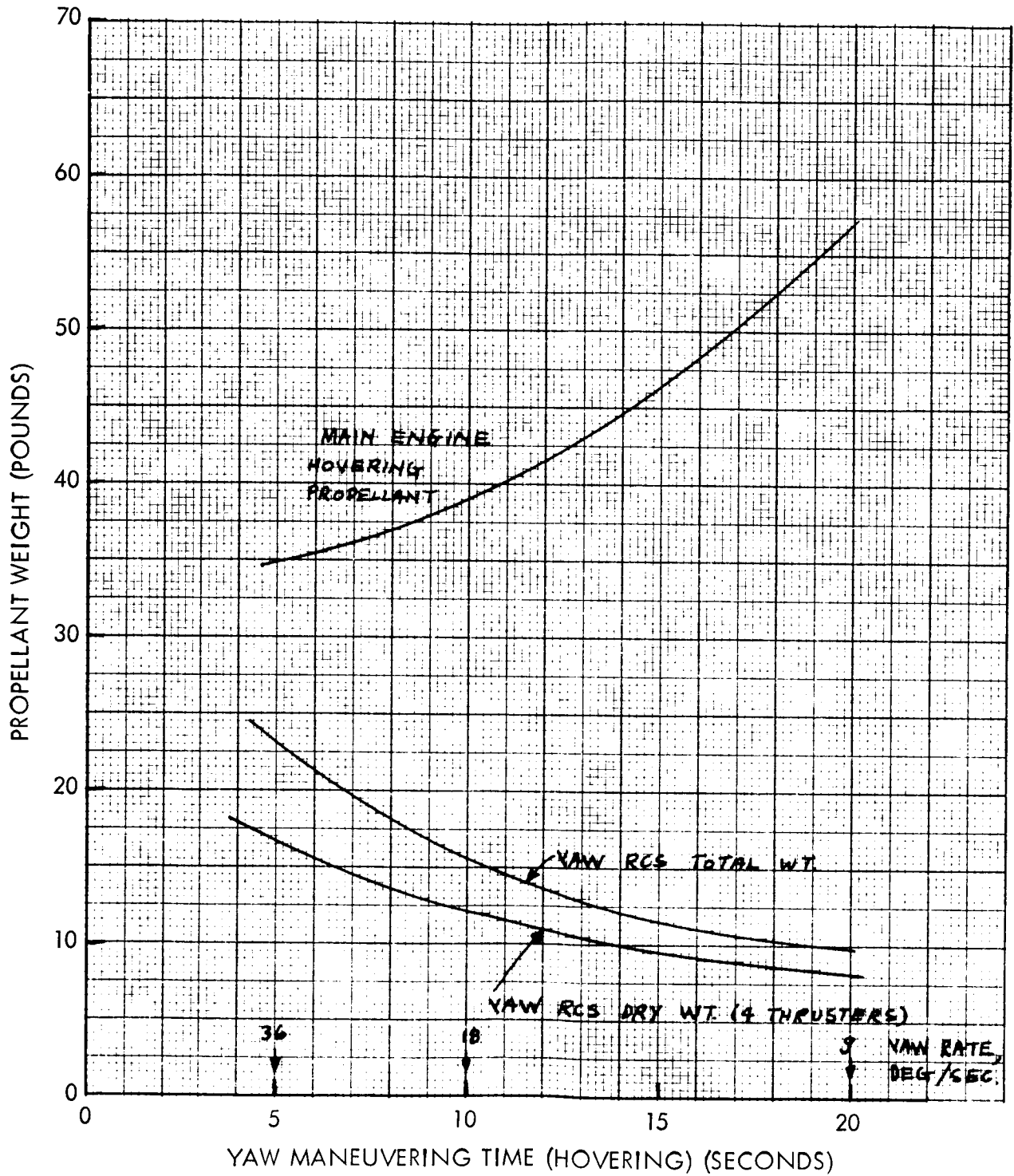


Figure 1-31. Yaw RCS System Weight Versus Maneuvering Time, Four-Thruster System

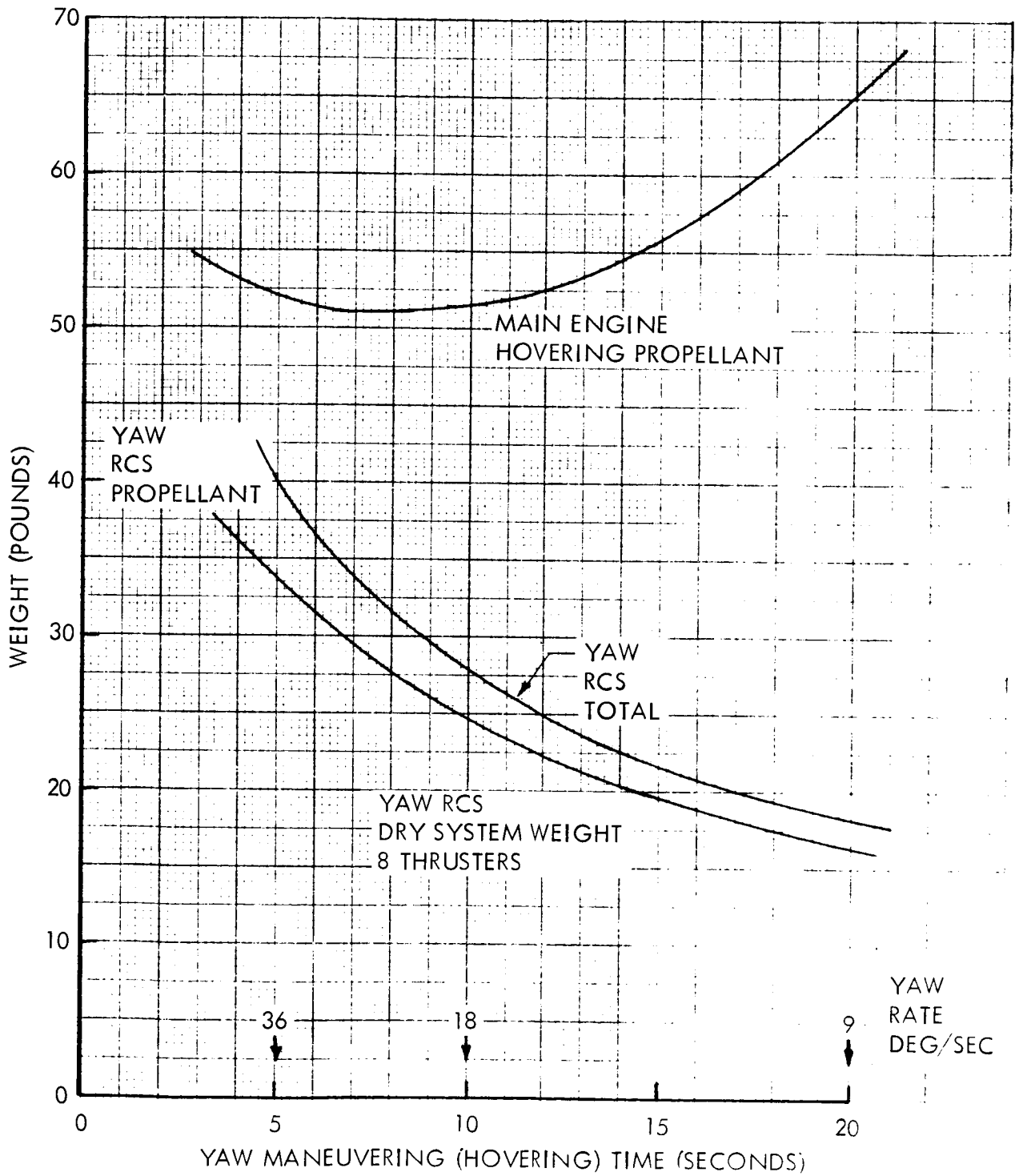


Figure 1-32. Yaw RCS System Weight Versus Maneuvering Time, Eight-Thruster System

Table 1-19. Yaw RCS System Weight Summary, Bipropellant Type  
 (Using Main-Engine Tankage)

Parameter	Case		
	1	2	3
1. Yaw maneuvering time (sec)	5	10	20
2. Yaw rate (deg/sec)	36	18	9
Propellant Weight: (lb)			
Orientations	6.0	3.0	1.5
Limit-Cycle	4.0	0.3	0.2
3. Total Propellant (lb)	6.4	3.3	1.7
Thruster size (lb)			
Assembly weight, each (lb)	(27.6)	(6.9)	(1.7)
	3.2	2.2	1.3
4. Total, 4 thruster* assemblies (lb)	12.8	8.8	5.2
5. Miscellaneous components, isolation valves, lines, and connections (lb)	<u>4.0</u>	<u>3.5</u>	<u>3.0</u>
Total system weight (sum of 3, 4, and 5)	23.2 lb	15.6 lb	9.9
*8 thruster configurations use twice the weight of items 4 and 5 (4-thruster configuration):			
Total system weight	40 lb	27.9 lb	18.1 lb

#### Cold-Gas RCS Systems

Weight comparisons were also made for cold-gas RCS systems to perform the yaw-control functions of orientations and limit-cycle operation. These systems included a helium propellant RCS and a gaseous nitrogen propellant RCS type. Separate tankage would be required to hold the propellant gas; and additional components for fill and vent, shutoff, and pressure regulation would be required. Thrust levels and the propellant distribution were similar to that for the bipropellant case; also in comparing a four-thruster configuration and an eight-thruster configuration.

Propellant weight requirements for the cold-gas systems were obtained from the bipropellant analysis, holding the total impulse (propellant weight times specific impulse) the same (Table 1-20).

Table 1-20. Propellant Weight Requirements for Cold-Gas System

Parameter	Case		
	1	2	3
Yaw maneuvering (sec)	5	10	20
Yaw rate (deg/sec)	36	18	9
Total impulse (lb-sec)	1725	890	460
Propellant weight (lb)			
Bipropellant system	6.4	3.3	1.7
N <sub>2</sub> O <sub>4</sub> /A-50			
I <sub>sp</sub> = 270 sec			
Helium, I <sub>sp</sub> = 180 sec	9.6	5.0	2.6
Nitrogen, I <sub>sp</sub> = 60 sec	29	15	8.0

The gas tank weights contribute the largest weight item to the cold gas systems, especially in the case of helium, due to its low density (2 lb/ft<sup>3</sup> compared to nitrogen of 14 lb/ft<sup>3</sup> at 3,000 psi and 70 F) and the resulting large volume required. Since helium is used as the main engine system pressurization gas, multiples of these tanks were used to obtain the helium tank weights. Each tank is an Apollo CM RCS tank that weighs 5.6 lb and contains 0.47 lb of usable helium gas. For the three cases considered, 20 tanks are required for the first case, 10 for the second, and 5 for the third, as shown in the helium RCS weight summary. For nitrogen, a factor of 1.3 lb of tank weight for each pound of propellant gas was used for tank weights.

For other components, estimates were made as in the case of bipropellant RCS. The eight-thruster configuration used twice the weight of the four-thruster configurations weights for thruster assemblies, distribution lines, isolation valves, etc. Thruster-assembly weights were estimated as

scaled-down weights from the bipropellant assemblies, since only one solenoid control valve was used, and these were only slight changes in thrust chambers.

The weight summary for the nitrogen RCS system (four thrusters) is shown in Table 1-21 and for the eight-thruster configuration in Figure 1-33 the helium RCS system weight summary is shown in Table 1-22 (four-thruster), and in Figure 1-34 for the eight-thruster configuration.

Table 1-21. Nitrogen RCS System Weight Summary

Parameter	Case		
	1	2	3
1. Yaw maneuvering time (sec)	5	10	20
2. Yaw rate (deg/sec)	36	18	9
3. Propellant weight (lb)	29	15	8
4. Tank weight (lb)	37	19.5	10
5. Feed system components pressure regulated, shutoff, fill and drain (lb)	8	5	3
Thrust size (lb)	27.6	6.9	1.7
Assembly weight, each (lb)	1.5	1.1	0.8
6. Thruster assembly weight (4)*(lb)	6	4.4	3.2
7. Miscellaneous components, isolation valve, lines, connections (lb)	3	2.5	2.0
Total system weight (sum of 3, 4, 5, 6, and 7)	83 lb	46.4 lb	26.2 lb
*8-thruster configurations use twice the weight of items 6 and 7 (4-thruster configuration):			
Total system weight	92 lb	53.3 lb	31.4 lb

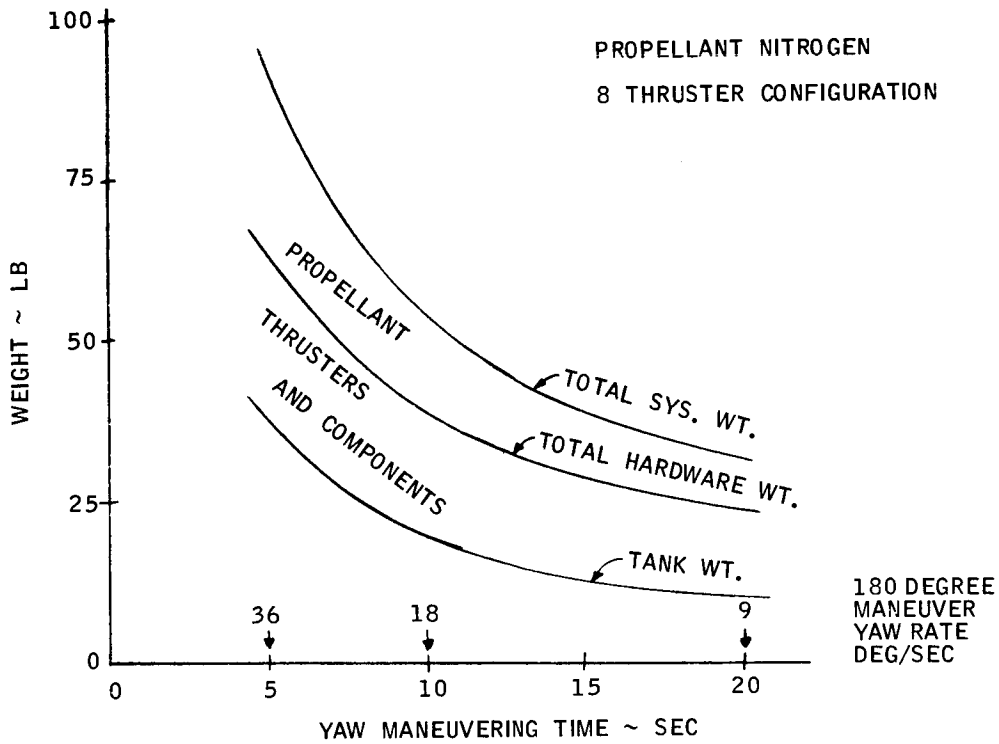


Figure 1-33. Yaw RCS System Weight, Eight-Thruster Configuration, Nitrogen Propellant

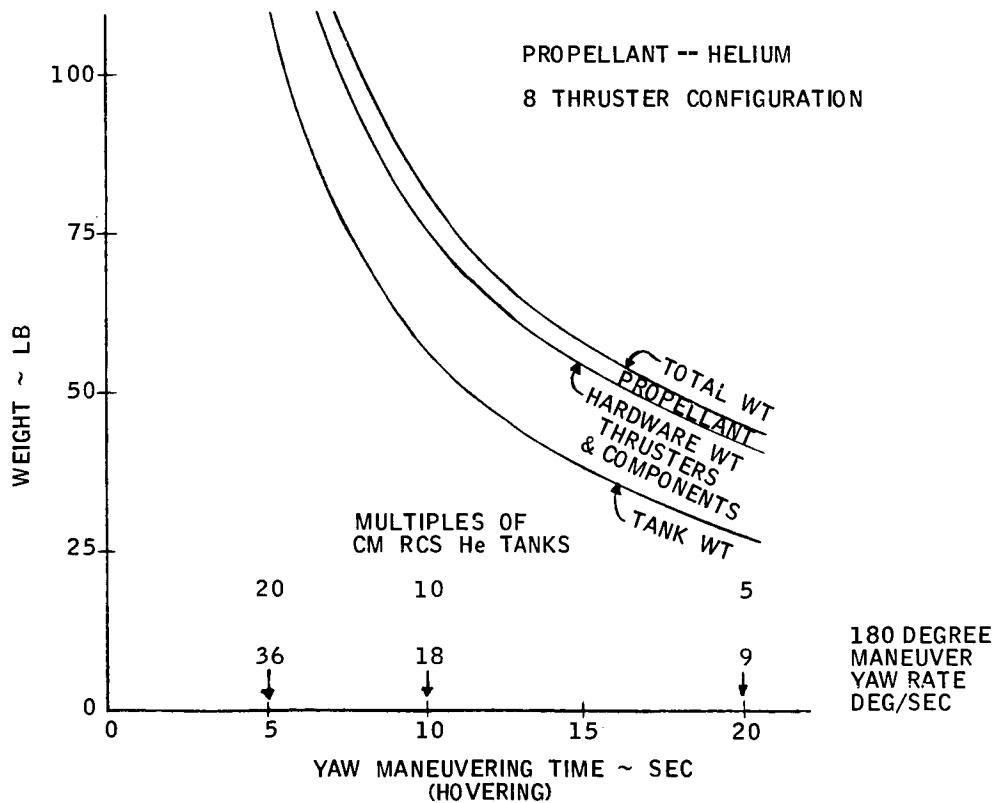


Figure 1-34. Yaw RCS System Weight, Eight-Thruster Configuration, Helium Cold Gas Propellant System



Table 1-22. Helium RCS System Weight Summary

Parameter	Case		
	1	2	3
1. Yaw maneuvering time (sec)	5	10	20
2. Yaw rate (deg/sec)	36	18	9
3. Propellant weight (lb)	9.6	5.0	2.6
4. Tank weight (lb)	112	56	27
5. Feed-system components, pressure regulator shutoff, fill, and drain valves (lb)	10	6	4
Thrust size (lb)	27.6	6.9	1.7
Assembly weight, each (lb)	1.5	1.1	0.8
6. Thruster assembly weight (4)* (lb)	6	4.4	3.2
7. Miscellaneous components, isolation valves, lines, connectors (lb)	3	2.5	2.0
Total system weight (sum of 3, 4, 5, 6 and 7)	140.6 lb	73.9 lb	38.8 lb
*8 thruster configurations use twice the weight of items 6 and 7 (4 thruster configurations):			
Total system weight	149.6 lb	80.8 lb	44.0 lb

### System Comparisons

The total loaded weights of the three RCS system types are shown in Figure 1-35 for both four-thruster and eight-thruster configurations. The bipropellant RCS using main engine propellant tankage is the lightest-weight system. Weight values for this system and the helium and nitrogen RCS system are given in Table 1-23 for an arbitrary value of yaw rate of 18 deg/sec (10-sec maneuvering time for a 180-deg yaw maneuver).

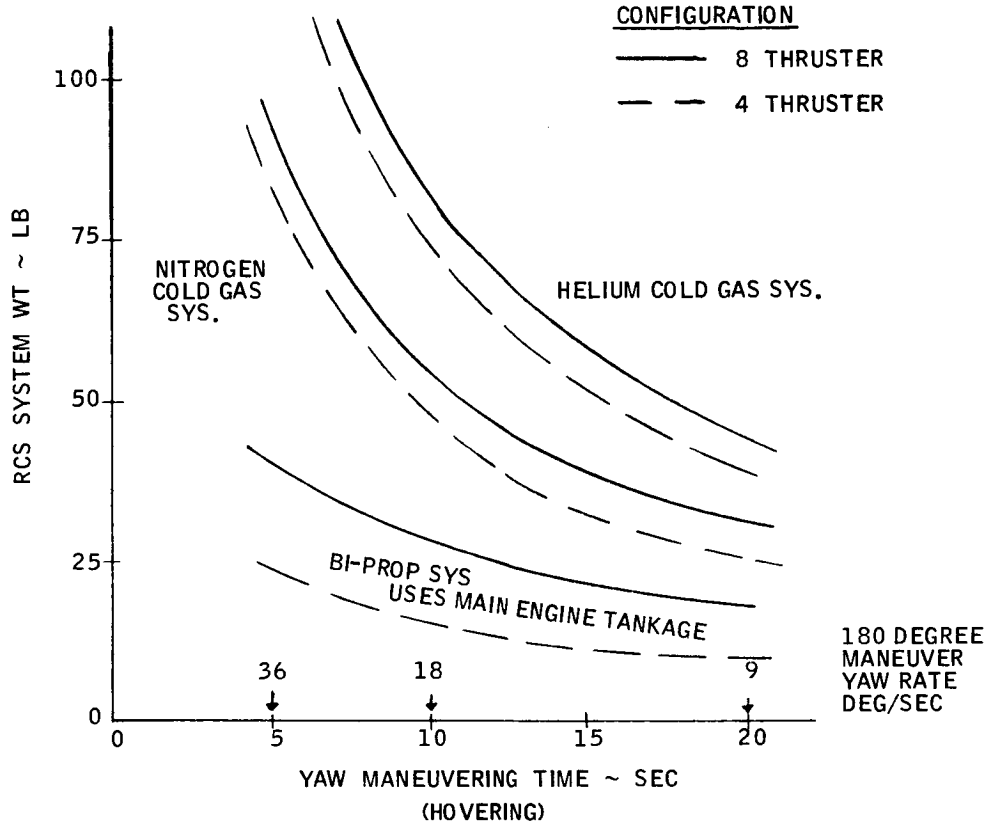


Figure 1-35. Yaw RCS System Weight Comparison

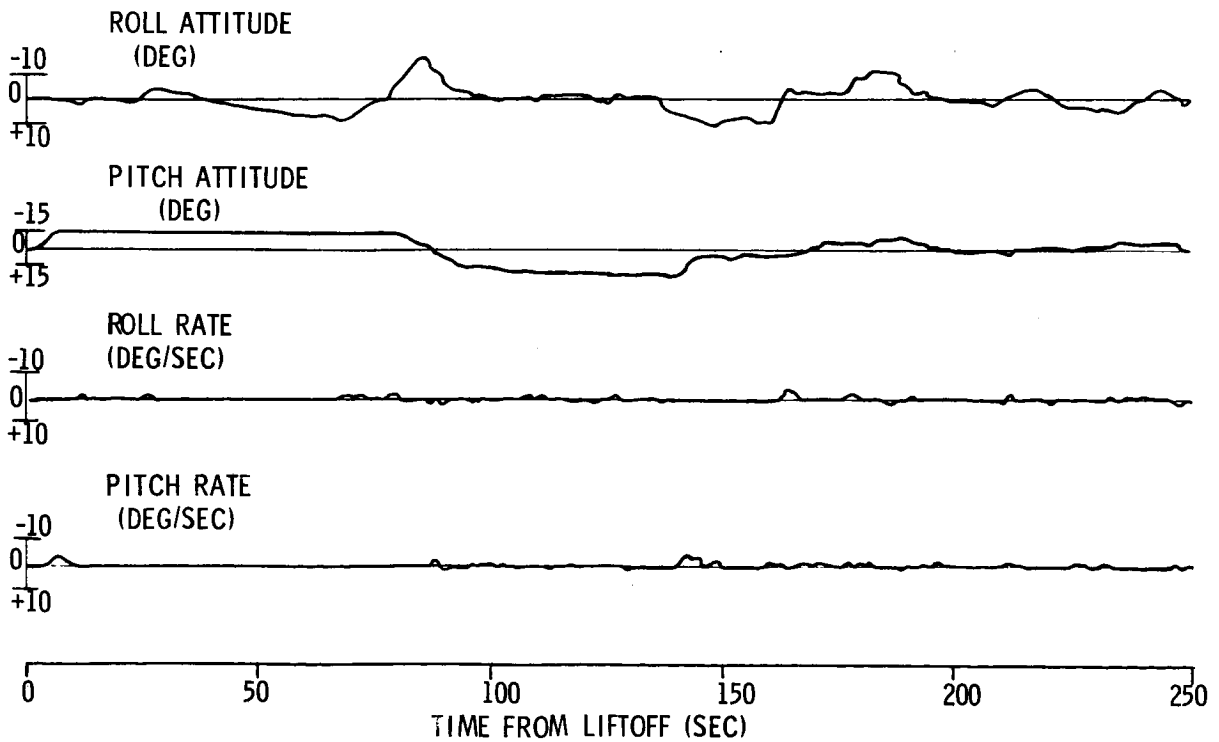


Figure 1-36. RCS Pitch and Roll Control Duty Cycle

Table 1-23. RCS System Weight Comparison

Configuration	System Weight (lb)		
	Bipropellant	Nitrogen	Helium
Four-thruster	15.6	46.4	73.9
Eight-thruster	27.9	53.3	80.8

Since the target weight of the LFV does not include an allowance for yaw RCS, the addition of even the lightest weight yaw RCS would incur some penalty. Also the RCS mode may be compared against alternative modes such as yaw jet vanes. The weight of any additional yaw control system would be a penalty for that particular configuration, such as a single main engine configuration (gimballed in pitch and roll), whereas the current base-line configuration has four gimballed main engines which include a yaw control capability.

#### Summary

As discussed in greater detail in the preceding paragraphs, the following conclusions provide a brief summary of the results.

1. The RCS system weight is decreased as the maneuvering times are increased (decreased yaw rates), although the main-engine hovering propellant increases greatly. Hovering propellant is a consideration for any other type yaw control, including main engine gimbaling.
2. The bipropellant RCS (either four-thruster or eight-thruster) using main-engine propellant is the lightest weight system, compared to the cold gas system.
3. The cold-gas RCS system weights (helium and nitrogen) are prohibitive, considering the total vehicle target weight of 180 lb. These weights were higher due to the relatively lower propellant specific impulse, and heavier additional tankage weights for the high-volume propellant gas storage (3,000 to 4,000 psi).
4. The lightest RCS weight configuration is the four-thruster (no redundancy) bipropellant RCS system, 23 lb at 5-sec maneuvering time (36-deg/sec yaw rate), or 10 lb at 20-sec maneuvering time (9-deg/sec yaw rate).

5. About 90 percent of RCS propellant is for yaw orientation maneuvers, and the remaining 10 percent for limit-cycle operation.
6. This analysis of yaw RCS is applicable for the stability augmented control mode where propellant-weight calculations include a nominal allowance for contingencies. However, further analysis can also yield yaw RCS system weights for use with the hardwire manual control mode and the kinesthetic control mode (where yaw control is also via hardwire manual). For these latter modes, increased propellant allowances would be necessary, based on results of prior simulation runs. Current simulation runs could provide updated criteria for these calculations. However, based on prior studies the yaw orientation propellant may require additions of 10 percent to 30 percent, depending in part on the selected yaw orientation angular rate, and the yaw stabilization propellant may require additions up to 100 percent.

### Three Axis RCS Requirements (Bipropellant)

Three-axis RCS is required for those vehicle concepts employing nonkinesthetic control with fixed main engines. Such a system, as a delta to the foregoing yaw RCS, is employed to maintain and change attitude during flight. Figure 1-36 presents a typical attitude and angular-rate time history taken from simulator data. Pitch-attitude changes are required for horizontal acceleration and deceleration. Roll-attitude changes together with yaw provide heading changes.

The major item of interest in Figure 1-36 is the total rate change required during the mission. This, based in the simulator data, is 220 deg/sec and 200 deg/sec for roll and pitch, respectively. Assuming that the optimum 5-lb thrusters of the yaw RCS analysis are employed for commonality, the required propellant is only 1.5 lb. This thrust level is compatible with the acceptable angular accelerations in pitch and roll.

Figure 1-37 illustrates the recommended three-axis RCS concept. Two independent sets of 5-lb thrusters mounted diametrically opposed provide roll and yaw torque. Ninety degrees from these quads, two sets of two 5-lb thrusters provide pitch torque. This thruster array operating in a pulse mode is fed directly from the main propellant tankage. Thruster-quad isolation valves are employed to provide for the possibility of a thruster control valve failure in the open position. The normal use of two thrusters in each control axis direction precludes loss of control should a valve fail to open on command. The weights of this three-axis RCS subsystem are 28.8 lb dry and 34.1 lb with propellant.



COMPONENT	WEIGHT (POUNDS)
THRUSTERS - 12 (5 LB F)	22.6
THRUSTER ASSEMBLY - 8 ISOLATION VALVES	3.2
LINES, FITTINGS, ETC.	3.0
USEABLE PROPELLANT P & R	1.5
RESIDUAL PROPELLANT	3.3
	0.5
TOTAL	34.1
ΔWEIGHT/MAIN SYSTEM	0.3
TOTAL WEIGHT PENALTY	34.4

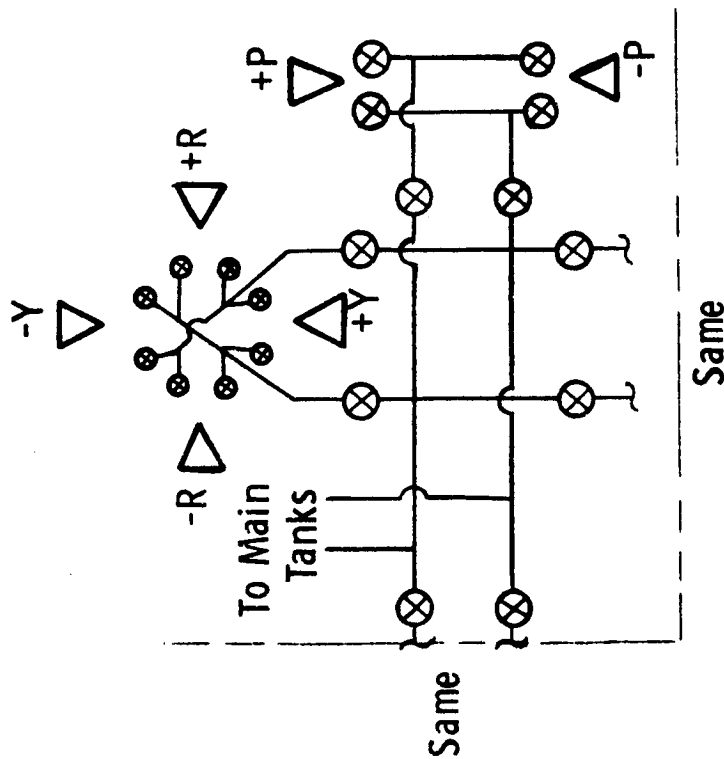


Figure 1-37. Combined Pitch, Yaw, and Roll RCS Characteristics

Table 1-24 presents a summary of RCS weight required for various control concepts. It will be noted that an additional propellant quantity has been added to the foregoing values. This is based on control simulation studies and includes the variabilities of engine misalignment and offset.

Table 1-24. RCS Control-Mode Weight Summary

Engine Configuration	Control Mode		
	Kinesthetic	Hard-Wire	Stability Augmented
Fixed engines	Yaw jets	Pitch, roll and yaw jets	Pitch, roll and yaw jets
Dry weight	11.7	28.8	28.8
Propellant	3.5	11.1	10.6
Total weight	15.2	39.9	39.4
Gimbaled engines	NA	Yaw jets	Yaw jets
Dry weight		11.7	11.7
Propellant		3.5	3.3
Total weight		15.2	15.0

\*Includes 5.3 lb propellant for main-engine(s) misalignment

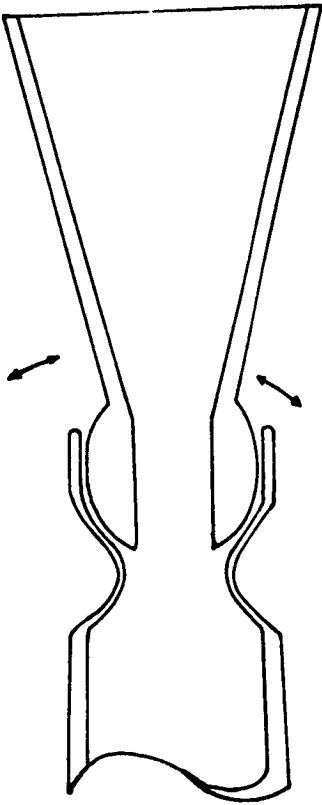
#### Non-RCS Thrust-Vector-Control Evaluation

A number of potential methods of TVC for use in the lunar flying vehicle as shown in Figure 1-38 were analyzed during this period. These included:

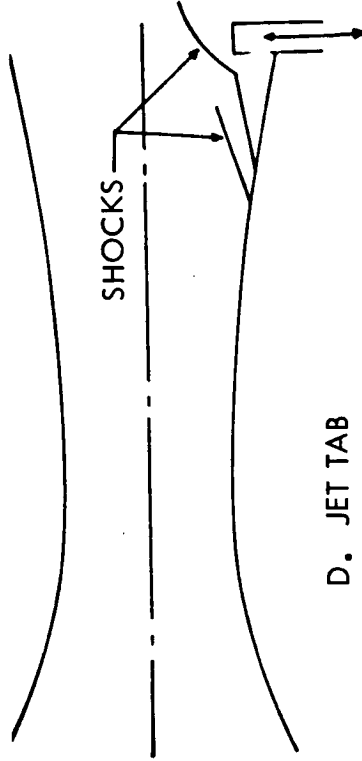
- Secondary injection
- Swiveled nozzles
- Engine gimbaling
- Jet tabs, vanes, and jetavators
- Differential throttling

#### Secondary Injection

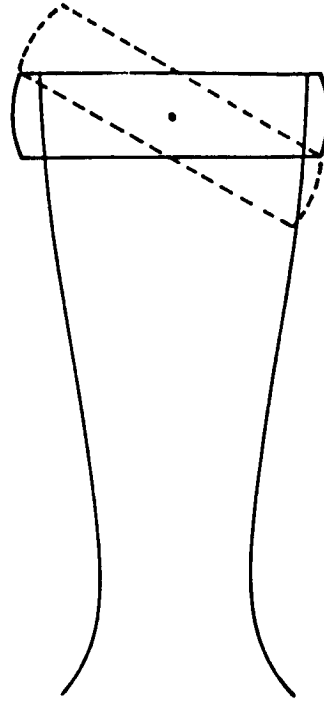
Secondary injection was shown to be a simple and compact system capable of very high frequency response. Additional advantages included no



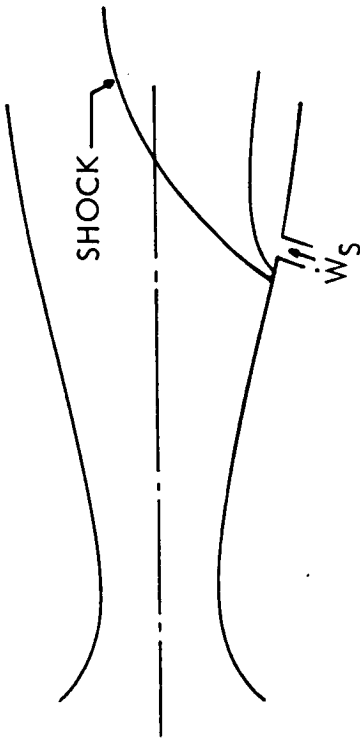
B. SWIVELED NOZZLE



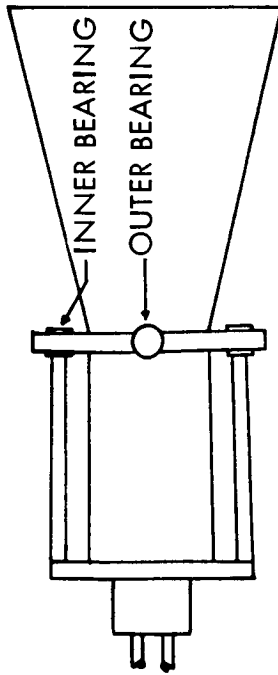
D. JET TAB



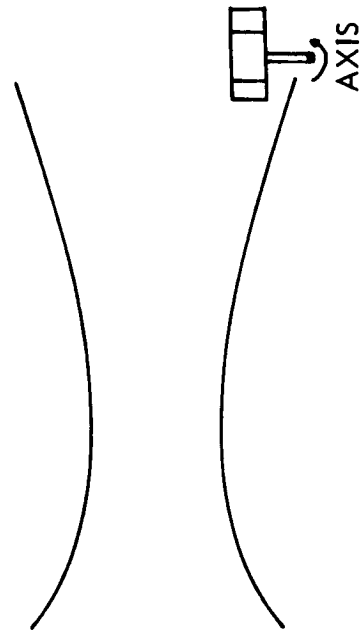
F. JETAVATOR



A. SECONDARY FLUID INJECTION



C. GIMBALED THRUST CHAMBER



E. JET VANE

Figure 1-38. Thrust Vector Control Concepts

additional flexible propellant lines and only a small drag penalty. The major disadvantage which caused the rejection of this system was the fact that for the gimbal angle range (8 to 10 degrees) of the lunar flying vehicle, at least 15 percent of propellant flow would be required as shown in Table 1-25.

Table 1-25. Secondary-Injection TVC Injectant Requirements

$w_s/w_p$ (percent)	Gimbal Angle (degree)		
	Freon 113	Cold Gas	Reactant Liquid N <sub>2</sub> O <sub>4</sub> )
0	0	0	0
1	0.4	0.9	1
2	0.6	1.9	2
4	1.2	3	3
7	1.6	4	4.4

(Ref. - Rocketdyne Data Supplied to NR SD)

Even the extrapolation of 15-percent side-injectant propellant required may be too low an estimate since performance decreases at high flow rates because there are cosine flow losses when the shock interactions distort the flow and intersect the bell. In addition there can be structural problems due to the fact that the side forces tend to distort the bell when the large leverage arm (3/4 of distance from throat to exit) of a high-area-ratio nozzle is used. In addition to this problem, tap-in in the nozzle for secondary injection would result in decreased reliability and interference with normal cooling techniques. Extra valving would also be required to introduce the auxiliary injected fluid.

#### Swivel Nozzle

This method was considered because:

The rigid mount provides the advantage of no flexible propellant lines.

Since only the nozzle was gimballed, the system will be lightweight.

The system provides sensitive response with low servo power.

This system was rejected on the basis of Space Division and subcontractor opinion because of the severe problems associated with the high



temperature sealed movable joint at the throat. In addition there is no known technology available for this size and class of engine.

### Engine Gimballing

This highly developed system used in many spacecraft was thoroughly explored with respect to its performance. In spite of the simplicity, compactness, and reliability of this system, its disadvantages included:

Requirements for gimbals and actuators add complexity and weight.

Systems with multiple actuators will require high servo power.

As a result of engine motion, propellant supply lines will have to be flexible. In spite of these disadvantages, this system emerged from the study as a key contender for the thrust-vector control on the basis of simplicity, reliability, and weight. Consequently, a survey of similar space systems was undertaken with respect to engine, vehicle, actuator, and gimbal characteristics. A summary of the survey results are shown in Table 1-26. The survey showed that all spacecraft of the general class of the LFV (same weight, moment of inertia, range, etc.) used electro-mechanical gimbals. The survey coupled with subcontractor discussions with TRW, Autonetics, and Cadillac Controls indicated that 2.5 lb per actuator was a good state-of-the-art weight for an LFV engine actuator. However, it was also found that 2.0 lb could serve as a reasonable design goal for a weight-reduction program. Some investigation was made into hydraulic actuators both open and closed loop. The open-loop system required a large amount of dumped propellant traceable to the relatively low ullage source-pressure available. The closed-loop systems were complex, and experience was lacking at LFV torque levels.

### Jet Tabs, Vanes, and Jetavators

These systems were considered because of their simplicity and compactness, their ability to affect torque about 3 axes, the low power servo system, and the fact that no flex lines are required.

It was apparent from the literature survey that this system was not well developed for bipropellant rockets. Severe erosion and high weight were generally regarded as system penalties. In addition, large equivalent  $I_{sp}$  losses would result from the requirement for gimbal angles of approximately 10 degrees. Figure 1-39 shows, for example, that with a requirement for a 10-degree vector angle, a 32-degree vane angle of attack is required for a typical jet vane design. In addition, the thrust of a typical 100-lb engine would be reduced to 82 lb with an equivalent loss of 47 sec of



Table 1-26. Summary of Applicable TVC Experience

System	Actuators						Gimbals		
	Force (lb)	Weight (lb)	Power	Velocity	Type	Weight (lb)	Angle (Deg)	Attachment	
Lunar orbiter	3	3.7	15.4 W at 28 V	1.04 in./sec 10 deg/sec	Kearfott EM	1.27	±2.82 (±0.293 in.)	Head end	
MMIII PBCS	100 max 62 min at stall	2.75	0.6 amps 25 VDC	0.3 in./sec	Autonetics EM	1.88	±13	2.5 in. above engine c. g.	
Mariner '71	20 to 30	2.5 - 3.0	0.6 amps at 25-31 VDC	0 to 0.39 in./sec for 62 to 0 lb load	Autonetics EM	1.88	±4.5 skewed Null 4 deg	Throat	
Classified military program (TRW)	5 max	2.0	28 VDC	5° at 10 cps sinusoidal	TRW EM	1.4 (2 rings)	±5 7-1/2 (diag)	Head end	
Surveyor	80 in. -lb	1.45		6 deg/sec	Hughes EM	Very low	One axis roll axis ±6	Trunnions near engine center	
Lunar flying vehicle	-	3 (1 eng) 2 (4 eng)	28 VDC	Not known	Not known (probably EM)	1.8 (1 eng) 1.2 (4 eng)	±10	Under evaluation	



Table 1-26. Summary of Applicable TVC Experience (Cont)

	Engines				Vehicle	
	Thrust (lb)	Weight (lb)	Type	$I_{sp}$ (lb-in. <sup>2</sup> )	Weight (lb)	$I$ (slug-ft <sup>2</sup> )
Lunar orbiter	100 (Apollo SMRCS)	5.1	Radiation cooled	p 9.5 y 49.9 r 54.0	850 full 576 empty	full p 123 y 82 r 132 empty 78 73 89
MMIII PBCS	316 (RS14)	19.31	Interregenerative buried	r 116 p 374 y 370	566 full	full r 168 p 663 y 631 empty 73 110 102
Mariner '71	300 (RS21)	15.9	Interregenerative	r 116 p 374 y 370	2120 full 1170 empty	full r 278.5 p 291.5 y 365.3 orbital 233.3 237.5 304.5
Classified military program (TRW)	100 (URSA 100)	4.85	Radiation	p 8 y 76 r 76	2000 full	
Surveyor	104 - 30	5.87	Regenerative plus radiation		2150	r 208 137
Lunar flying vehicle	360 - 74	5 (100# F) 15 (400# F)	Radiation or interregenerative	Similar to Lunar Orbiter (low thrust) or MIII (high thrust)	1200 full	full p 165 r 203 y 88 empty 112 117 29

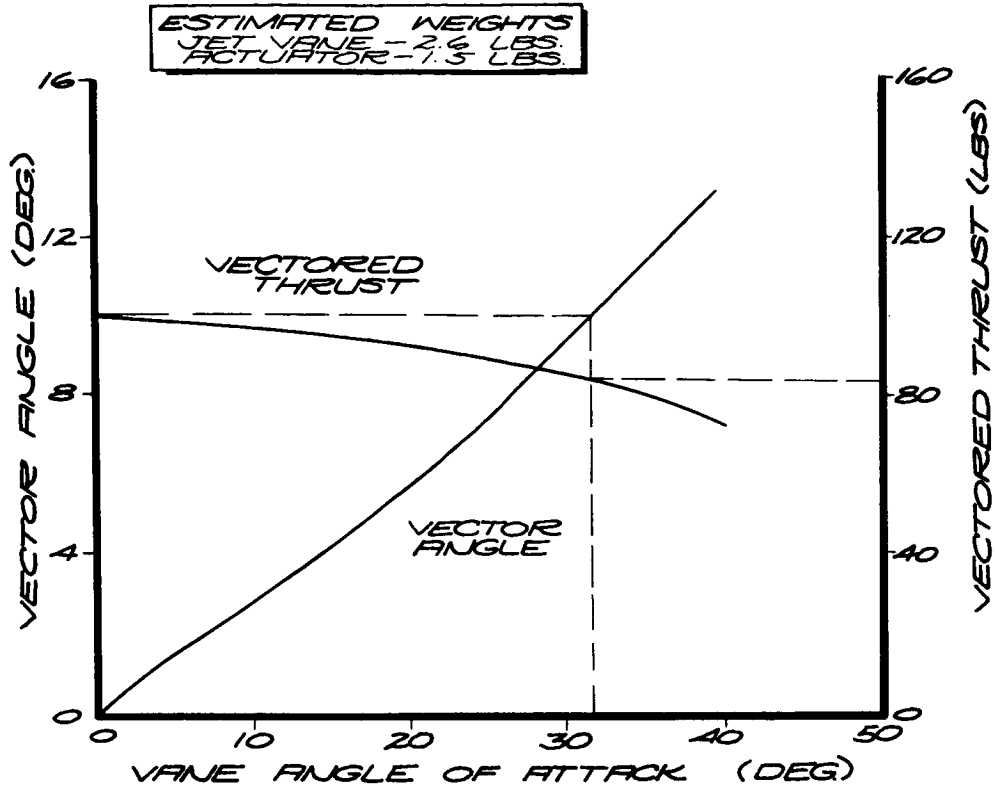


Figure 1-39. Jet Vane Thrust Vector Control

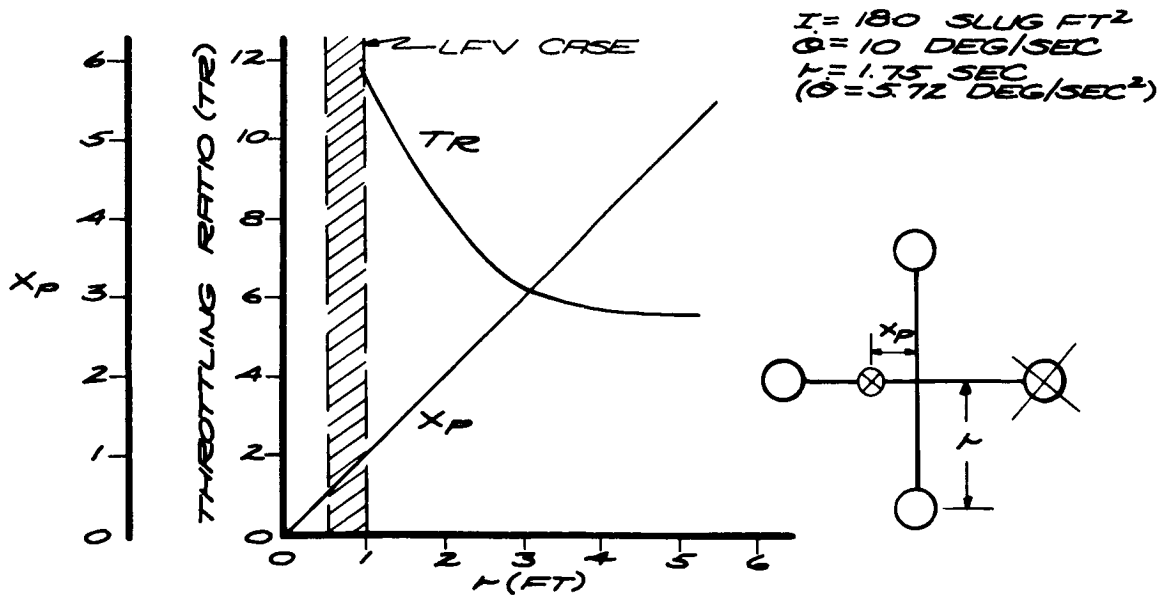


Figure 1-40. Thrust Ratio Requirements for Differential Throttling

specific impulse. As a result of this high  $I_{sp}$  loss, this system was rejected for pitch and roll control. Since the yaw requirements may be less severe than pitch and roll, further analysis on yaw vanes for the single engine case will be carried out.

### Differential Throttling

The differential throttling system was investigated because no additional hardware was required and because of its fast response.

A four-100-lb thruster system was investigated because of the requirement for multiple engines. The analysis showed that the nominal thrust of the engine must be oversized by  $\Delta T/2$  relative to the normal thrust produced from the design to thrust-to-weight ratio. ( $\Delta T$  is the thrust differential required for pitch or roll acceleration.) At low thrust, a very large throttling ratio (greater than 12) may be required. This disadvantage can be overcome by making the moment arms larger. However, as the moment arms increase in length, recovery from an engine failure by astronaut relocation becomes impossible. A typical analysis of thrust-ratio requirements and astronaut-position change requirement as a result of one engine out is shown on Figure 1-40. This system was rejected mainly because of the high throttling ratio requirements.

### Yaw Vanes

Two cases of yaw vanes for TVC were analyzed. These included four vanes in the form of a cruciform in a single 300-lb thrust engine and four vanes set on diagonals for the square-pattern four-engine case with one vane per engine. In both cases, columbium and hafnium/tantalum were used for the leading edge; columbium and titanium were used for structure and shaft components; in the single-engine case, titanium was used for the control yoke. In both cases a 20-ft-lb torque design point was chosen. This value is equivalent to two 5-lb thrusters on two-foot arms. The weight of the bipropellant yaw system was 15 lb.

In the single-engine case, each vane was assumed to have a 4-1/2-in. span and 9-in. chord. These dimensions were chosen to fill the exit plane and to keep the vane in the strongest aerodynamic influence zones. The analysis of the four-vane single-engine case showed that, at an angle of attack of 17 degrees, the 20-ft-lb torque was achieved with lift and drag (per airfoil) of 24 and 26 lb respectively. The dry weight of this system was as shown below:

Component	Weight, (lb)
Vane	11
Holding structure	8
Control yoke	3-1/2
Actuators	6
Total	28-1/2

With single-vane failure, the system would have to assume a very large angle of attack which, even under ideal conditions, would represent a marginal ability to produce the required torque. This system requires 17 lb of additional dry weight compared to the yaw RCS. The propellant requirement per sortie is approximately 2.3 lb. As a result of these disadvantages and the fact that there is little or no experience with this type of system, the four-vane system was considered unacceptable for TVC.

The vanes for the four-engine case are each 6 in. by 3 in. on a 12-inch moment arm. The results showed that the required torque could be achieved at approximately 20 degrees angle of attack. However, single-engine (or single-vane) failure would result in a situation where the design torque could not be achieved, since the maximum torque per pair is about 17 ft-lb at 40 degrees angle of attack. The system weight including vanes, actuators and propellant is 17.6 lb or approximately 3 lb heavier than the bipropellant yaw RCS system. Nominal engine thrust must be increased by 14 percent (at 20 degrees angle of attack) to account for drag losses. The disadvantages for the four-vane case, therefore, mitigate against its choice for a thrust-vector control.

#### Differential Throttling (8-engine case)

An eight-engine differential-throttling case was also analyzed during this period. In this configuration, four pairs of engines, each at one side of the platform, were used. The moment arm was 1 foot to the c.g. The system was required to yield 20 ft-lb torque for yaw in addition to the normal requirements for pitch and roll. The other basic assumptions used were: (1) engine-out capability, (2) lift-off T/W = 1.4, (3) landing T/W = 0.7. The results of the analysis showed that each engine size was required to be 72 lb for a total of 576 lb total thrust. The throttling ratio required was dictated by the T/W of landing. For all engines firing, the eight-engine system analyzed was not feasible with respect to throttling ratio. The throttling ratio for the six- and four-engine cases were 16.8 and 6.6, respectively. Only the latter case is within the range of the current state of the art. The analysis also showed that the average thrust for flight was 200 lb, which represents only 35 percent of nominal value.

This system was deemed unacceptable for TVC because (1) it violates the "all engine operating" rule, (2) sensing of the failed engine is required, and (3) the oversized engine requirement costs 21 lb in dry weight and 18 lb propellant per sortie. A separate study of a pulse-modulated, eight-engine concept was conducted, and the results are reported in the Configuration Design Volume. This study concludes that such a concept is competitive in weight with the design that was ultimately selected and may use the Marquardt R4D thrusters in pulse-mode. The engine development cost and schedule advantages are obvious. Utilization of such a concept results in a range penalty of about 1 n. mi.

#### Overall TVC Conclusions

The TVC analysis led to the conclusions that (1) with a single engine, a gimbaled system is acceptable for pitch and roll with bipropellant-yaw RCS for yaw control, or pitch, roll, and yaw RCS are acceptable for a fixed single engine, and (2) for multiple engines either gimbals or pitch, roll, and yaw RCS for fixed engines are acceptable.

The stability-augmented case represents the minimum-propellant required for either fixed or gimbaled engines for attitude control. Additions to the minimum value of propellant required in the stability augmented case, derived from simulator experience, were made for hardwire and kinesthetic control (see Table 1-24).

## PROPULSION SYSTEM DEFINITION

Tradeoffs in previous sections combined with vehicle controls considerations have optimized the LFV propulsion engine design to a set of four variable-thrust bipropellant engines of 100 lb maximum thrust each, having a maximum required thrust of 300 lb. If the engines are radiatively cooled, the desired propellant inlet pressure is 225 psia; if interregeneratively cooled, 285 psia. The next task is a logical development of the propellant supply, pressurization, and servicing system required to feed these engines.

First considered are the constraints created by servicing from the lunar module. Next, basic tradeoffs affecting propulsion system design are discussed, leading to a brief itemization of design requirements. Then the subassemblies and component required to produce the propulsion subsystem are discussed in some detail, with emphasis on the use of components already qualified for NASA programs. Finally, a preliminary servicing concept for the system is presented.

### ROCKET ENGINES

The LFV propulsion subsystem employs four 100-lb thrust, throttlable, bipropellant rocket engines. The following discussion describes the design criteria and characteristics recommended as the result of the LFV study.

The specific engine-design criteria selected as the result of detailed optimization and tradeoff studies are as given in Table 1-27.

Two thrust-chamber design concepts are considered applicable - radiation cooled and interregeneratively cooled. Both exhibit desirable features, provide approximately the same LFV performance, and are substantially developed. The final selection is considered to be a Phase C program decision based on the detailed evaluation of engine subcontractor proposals in response to a detailed procurement specification.

The radiation-cooled thrust chamber operates at 100 psia chamber pressure with a nozzle area ratio of 40:1. Either molybdenum or columbium are considered satisfactory as combustion-chamber construction materials. The nozzle extension, attached to the refractory metal chamber by a flange nut, is constructed either of L605 alloy, Haynes 25, or simply a monolithic

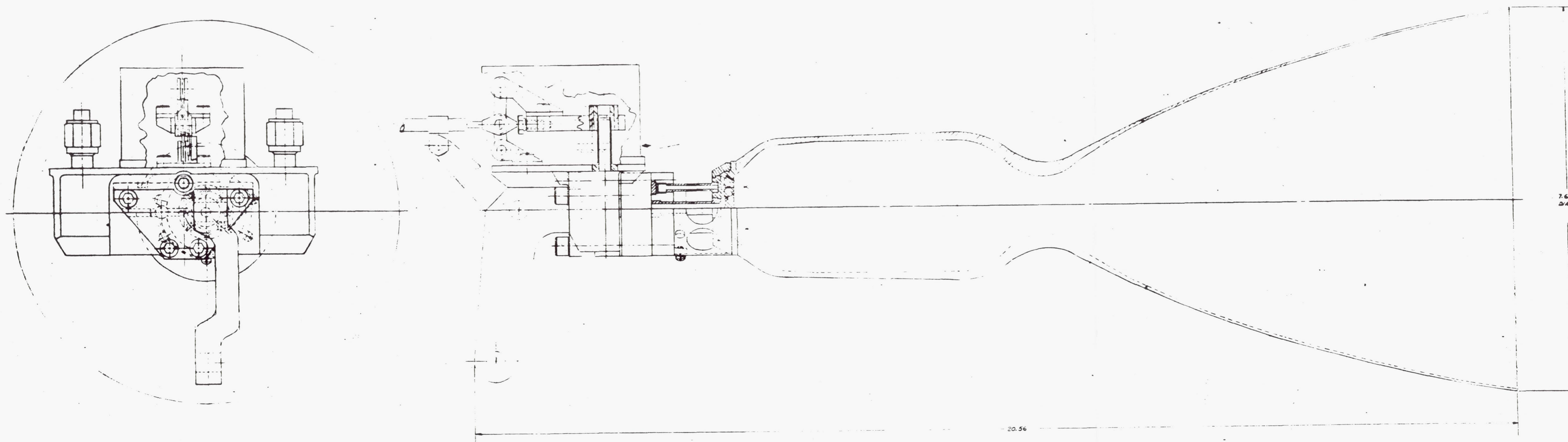


Table 1-27. LFV Engine-Design Criteria

Consideration	Criteria	
Number of Engines	4	
Thrust (lb)		
Maximum	100	
Minimum	16	
Throttle ratio	6:1	
Propellants	N <sub>2</sub> O <sub>4</sub> /A-50	
Mixture ratio	1.5 to 1.6	
Cooling method	Radiation	Interregenerative
Chamber pressure (psia)	100	140
Inlet pressure (psia)	225	285
Nozzle area ratio	35 to 40	
TVC	Gimbal	
Throttle method	Variable area (~ΔP) inlet valve	
Useful life (assuming 1000 seconds ground time and 500 seconds per sortie)	For 5-sortie requirement: 3500 sec  For 30-sortie requirement: 16,000 sec	
Reliability	0.999	

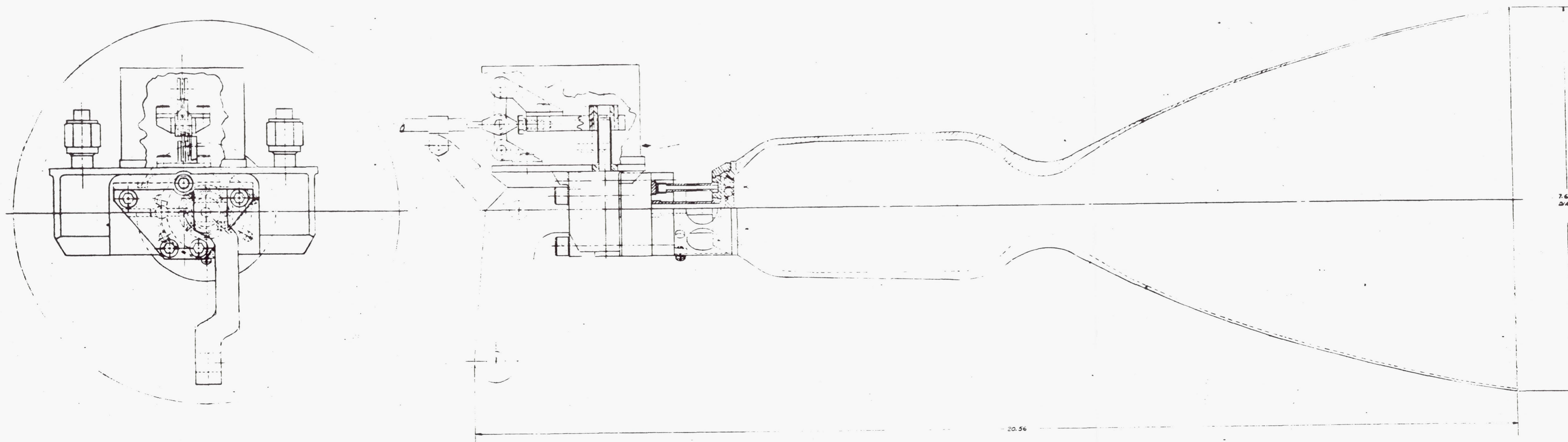
extension of the chamber, depending on specific subcontractor experience. Fuel-film cooling supplements radiant heat dissipation to provide a chamber with essentially unlimited life. Typical examples of this chamber type were illustrated in Figures 1-1 through 1-3. A preliminary design layout by Bell Aerosystems is shown in Figure 1-41.

The interregeneratively cooled thrust chamber operates at 140 psia chamber pressure with a 40:1 nozzle-area ratio. Beryllium is the combustion chamber material used by Rocketdyne in current systems. L605 is



ENGINE SPECIFICATION	
CHAMBER PRESSURE	80 PSIA
THROTTLE RATIO	8/1
NOZZLE EXPANSION RATIO	40/1

Figure 1-41. 150-Pound Thrust Throttleable Engine  
Manually Operated Valve



ENGINE SPECIFICATION	
CHAMBER PRESSURE	80 PSIA
THROTTLE RATIO	8/1
NOZZLE EXPANSION RATIO	40/1

Figure 1-41. 150-Pound Thrust Throttleable Engine  
Manually Operated Valve

used for nozzle extension. Head-end fuel-film cooling provides the primary heat removal mechanism as depicted in Figure 1-6. A typical example of this concept is illustrated in Figure 1-5. Figure 1-42 shows the preliminary-design layout conceived by Rocketdyne.

Throttling is accomplished by a variable area, cavitating venturi, bipropellant throttle valve for both thrust-chamber concepts. This valve is a development item. In one concept one throttle valve is employed for each of the four rocket engines. A direct, manually operated, hydraulic-throttle control subassembly provides the 5 to 8 in.-lb work required for full valve stroke actuation. The hydraulic system also incorporates provision for individual valve deactivation and spring powered closure in event of in-flight engine shutdown. The cavitating-venturi valve provides precise, predetermined flow-rate control. This allows the injector to be designed for optimum performance and thrust chamber life. The valve will be designed with the capability of operating with both propellants helium saturated over a 6:1 throttle range at a maximum inlet pressure of 225 psia and 285 psia for radiation and interregenerative chambers respectively. The throttle valve may be designed to provide propellant shutoff by pintle seating, or separate, mechanically linked shutoff valves may be required, depending on the final detailed design selected.

Thrust-vector control of  $\pm 7.5$  degrees is provided by a head-mounted, 2-axis, flexure-pivot gimbal using an electromechanical actuation system. Two-axis gimbals have been developed for the small-engine applications of Lunar Orbiter, Minuteman PBPS, and currently, Mariner 71. An engine characteristics summary is shown in Table 1-28.

## ENGINE DEVELOPMENT REQUIREMENTS

The LFV rocket engine development program schedule is a key element to timely LFV development. While many qualified 100-lb fixed thrust engines exist, a variable-thrust engine for manned flight must be developed and qualified. The variable thrust Bell 8414, and fixed thrust Marquardt R4D and Rocketdyne (P/N PD410770) engines represent the major initial building block alternatives for the LFV engine. Development schedule estimates by cognizant engine manufacturers range from 17 months to 20 months for delivery of qualified hardware. Figure 1-43 presents a representative radiation cooled LFV engine development schedule submitted to NR/SD by Bell Aerosystems and based on minimum modification to the Model 8414 engine.

While the foregoing engines now exist, they must be further developed and/or modified. One major development item is the close-coupled, cavitating-venturi throttling valve. Two similar valves have been developed

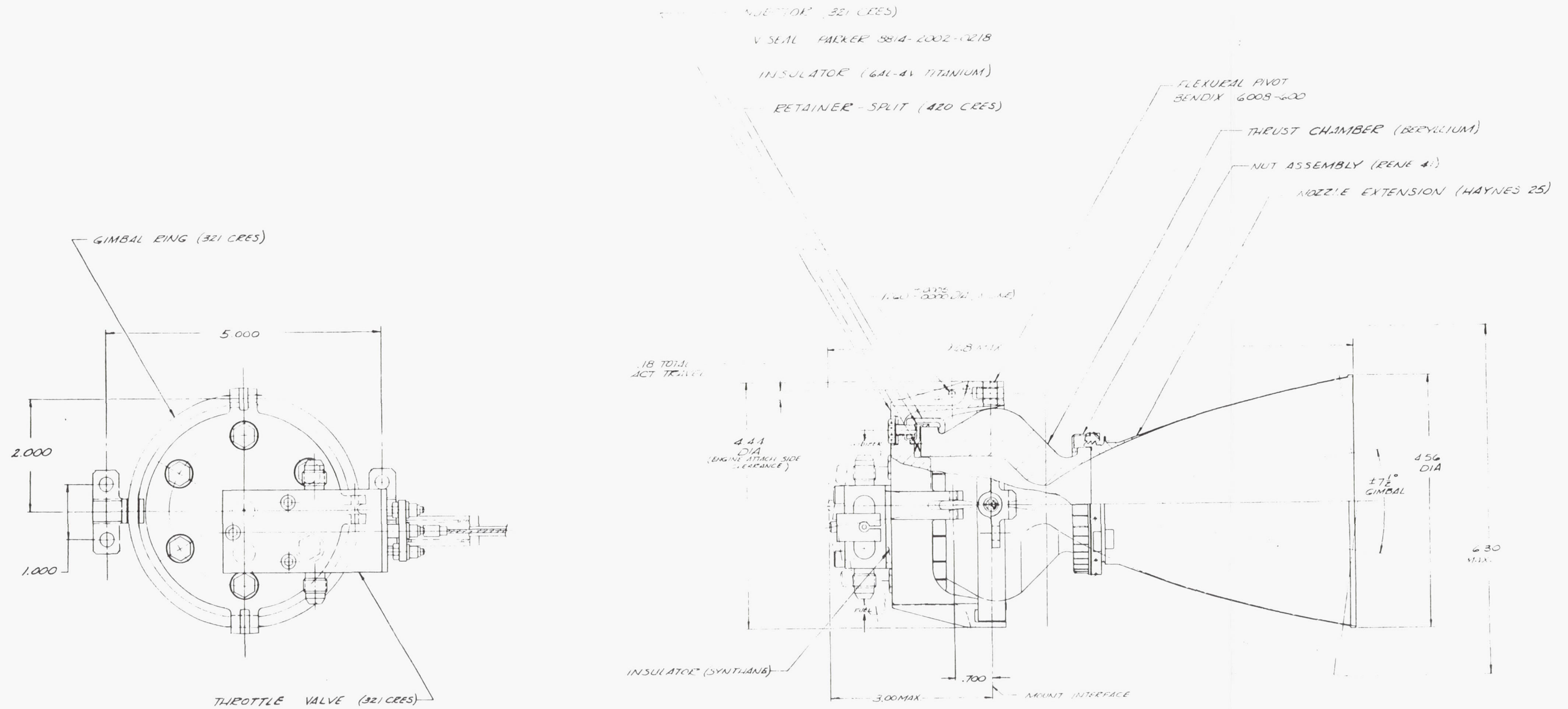


Figure 1-42. 150-Pound Thrust Throttleable Rocket Engine Assembly

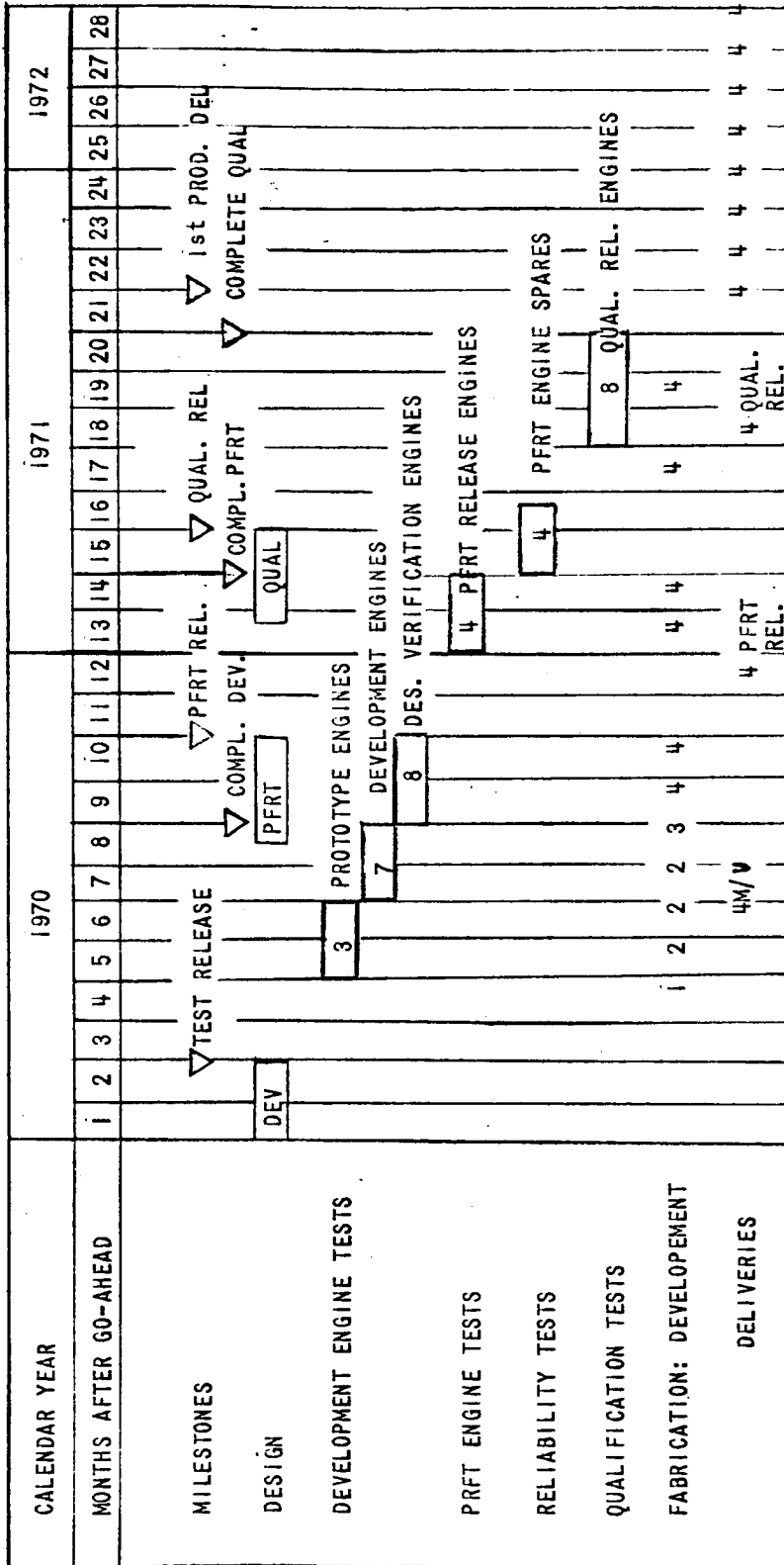


Figure 1-43. 100-Pound Thrust Model 8414 Engine Development Plan  
(Man-Rated)

Table 1-28. LFV Engine-Characteristics Summary

Parameter	Cooling System	
	Radiation	Interregenerative
Thrust (lb)		
Maximum	100	100
Minimum	16	16
Delivered specific impulse (sec)		
Maximum thrust	294	298
Minimum thrust	258	250
Chamber pressure (psia)	100	140
Valve inlet pressure (psia)	225	285
Valve stroke (in.)	0.5	0.75
Weight (lb)		
Thrust chamber	2.89	4.25
Throttling valve	1.10	1.68
Shutoff valve	1.78	(not required)
Gimbal	2.15	1.40
Total weight	7.92	7.33
Dimensions (in.)		
Overall length	14.8	9.68
Nozzle-exit diameter	5.4	4.56

as part of the LFV advanced engine-development programs at Bell and TRW. However, both were hydraulic powered by fuel system pressure. Neither incorporated provisions for propellant shutoff. Also, manual throttle force limitations will most probably require further redesign. In any event, the valve development should entail little risk.

The existing nonthrottling thrust chambers will most probably require some modification. While both TMC and Rocketdyne engines have demonstrated the capability to be line-throttled, specific LFV qualification

requirements, such as performance, installation environment, etc., will require some design modifications. As an example, the following paragraphs delineate in detail the Rocketdyne interregenerative engine development program and its attendant schedules submitted to NR SD.

Development of a candidate throttling engine for the LFV has proceeded through the feasibility demonstration phase in Rocketdyne IR&D programs. In these programs, throttling was simulated by orificing upstream of the injector and by varying supply tank pressure, which provided excellent steady-state data but no dynamic throttling data. Two of the prime objectives of the proposed program, therefore, are evaluation of a throttling valve as a component, and the effects of dynamic throttling as engine performance and stability. The other objectives are engine steady-state performance and stability demonstrations and qualification of the LFV rocket engine assembly for man-rated missions in a lunar environment.

Although Rocketdyne is designing and procuring a throttling valve for IR&D evaluation in support of the LFV Program, the status of this effort is somewhat behind that of the engine; development and qualification of the valve is expected to pace qualification of the complete REA. This LFV program is planned to take advantage of the valve lead time requirements by completing injector tuning, preliminary stability evaluation, performance demonstration, and mechanical assembly development testing in the early months of the program.

As shown in Figure 1-44, a six-task 17-month program to bring the LFV REA through man-rated lunar environment qualification has been planned. The plan includes the capability of beginning delivery of REA's of the qualification configuration in the 18th month. (Delivery of the flight weight prototype engines could be accomplished in the fourteenth month, if desired.) The seven tasks are:

1. Injector tuning
2. Valve development and qualification
3. Workhorse integration
4. Flightweight integration
5. PFRT
6. Qualification
7. Deliverables



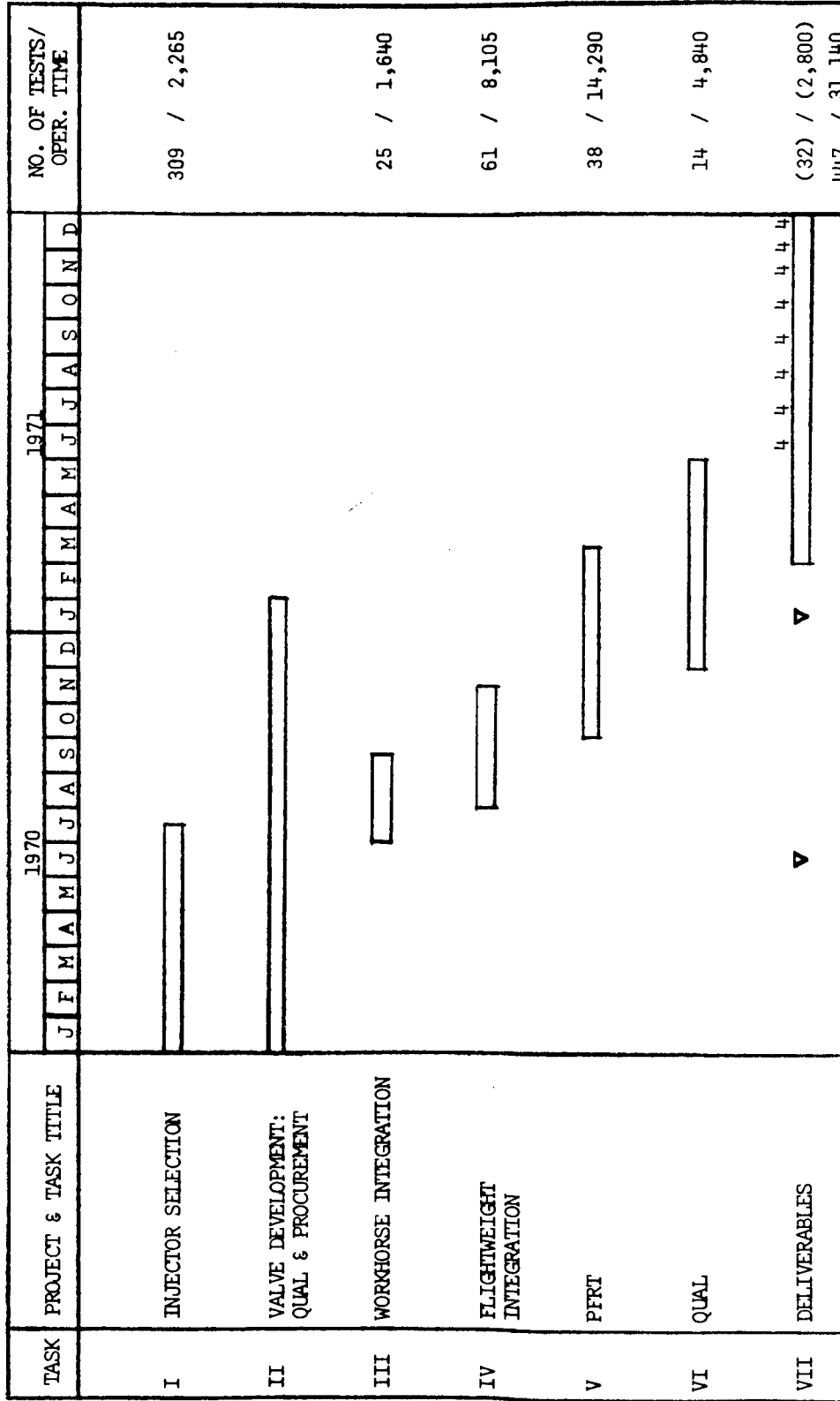


Figure 1-44. Six-Task, 17-Month Program to Bring the LFV Rocket Engine Assembly Through Man-Rated Lunar Environment Qualification

## Injector Tuning

A total of 309 tests and 2265 hot-fire seconds are planned for the injector tuning task. The prime objectives of the task will be to:

1. Optimize performance over the entire thrust range. This will be accomplished by steady-state firing at seven discrete thrust levels, using fixed orifices upstream of the injector to simulate throttling. The approach to optimization will be the achievement of maximum performance at about the 55-percent thrust level (predicted predominant level in MDC), which will minimize performance tail-off losses associated with throttling up and down.
2. Demonstrate injector and thrust-chamber compatibility at all thrust levels.
3. Demonstrate engine structural integrity under operating conditions.
4. Demonstrate injector steady-state stability over the required thrust levels. This demonstration will be accomplished by installing pulse valves up-stream of the injector and attempting to induce instability by firing the engine in the pulse mode. This demonstration method has been successfully used on previous small thrust man-rated engines, such as Apollo and Gemini.

An outline of the injector tuning task is as follows:

- A. Six injector design concepts will be evaluated; these concepts will include BLC variations.
- B. Unless otherwise stated, all testing will be conducted with beryllium chambers and L-605 skirts at altitude.
- C. Fabricate
  1. 1 each injector type
  2. 6 beryllium thrust chambers
  3. 6 nozzle extensions. The nozzle thrust chamber attach device may differ on these nozzles if there is a desire to evaluate alternate sealing approaches.
- D. Cold flow each injector at MR's 1.3, 1.6, 1.9; 18 cold-flow tests

E. Performance evaluation using fixed orifices for F level

1. Test as follows:

- a. 55-percent F level tests; five seconds each at MR's 1.6, 1.75, 1.9, 1.45, 1.3, 1.6, 1.9, 1.3

Eight tests each injector = 48 tests = 240 seconds

- b. Eight-test MR survey at 100-percent F level, each injector 48 tests = 240 seconds

- c. Eight-test MR survey at 16-percent F level, each injector 48 tests = 240 seconds

- d. Five-test MR survey at 30-percent F level, each injector

MR = 1.3, 1.45, 1.6, 1.75, 1.9; 30 tests = 150 seconds

- e. Five-test MR survey at 45-percent F level, each injector 30 tests = 150 seconds

- f. Five-test MR survey at 70-percent F level, each injector 30 tests = 150 seconds

- g. Five-test MR survey at 85-percent F level, each injector 30 tests = 150 seconds

2. During tests, measure performance parameters, radiation from nozzle, and injector, nozzle, and gimbal ring T. Gimbal ring may be mass-simulated, but injector attach should be flight type. Monitor for nozzle joint leakage.

- a. Parameters

(1) Chamber pressure

(2) Inlet pressures (2)

(3) Thrust

- b. Flow rates (dual flow meters each side)

c. Temperatures

- (1) Nozzle end
- (2) Nozzle joint
- (3) Chamber outside - 3 places
- (4) Injector attach ring
- (5) Injector outside
- (6) Injector/valve interface

d. Acceleration: 3 axes

3. Select three most promising injector designs
  4. Select nozzle-joint design
- F. Fabricate back-up injector for each selected design
1. Cold flow (3 injectors) at 3 MR's - 9 tests
- G. Fabricate 18 steel chambers for streak testing. Streak tests will be 30 seconds duration each, at sea level conditions
- H. Conduct streak tests
1. Fire each injector (3) at MR = 1.3, 1.6, 1.9 at F = 55 percent, using new chamber for each test - 9 tests = 270 seconds
  2. Fire each injector at 100-percent F and MR = 1.6 - 3 tests = 90 seconds
  3. Fire each injector at 15-percent F and MR = 1.6 - 3 tests = 90 seconds
  4. Modify injectors as required to correct streaking
  5. Refire each injector at 55-percent F, MR = 1.6 to verify modification - 3 tests = 90 seconds

### I. Steady-state stability

1. Fire each injector at 55-percent F and MR = 1.6, 1.9, 1.3; 15 seconds duration each test with pulse valve - 9 tests = 135 seconds
2. Fire each injector at 100-percent and MR = 1.6, 1.9, 1.3 - 9 tests = 135 seconds
3. Fire each injector at 16-percent F and MR = 1.6, 1.3, 1.9 - 9 tests = 135 seconds

### J. Select injector

## Valve Development and Qualification

The valve development task will consist of a prototype evaluation effort, a flight-weight qualification effort, and acceptance testing of all valves used in the program. The prototype valves are expected to differ from the flightweight only in external configuration, where no attempt will be made to optimize the body weight. Of the four prototype valves procured, three will be used in preliminary engine throttling tests and the fourth will be subjected to a complete engineering evaluation. This evaluation will culminate in a six-month propellant compatibility storage test which will qualify the flightweight valve for long term propellant exposure on the valve seats. Two flightweight valves will be submitted to a full component qualification program. This program will subject the valves to earth environment, lunar environment, launch boost and lunar descent vibration, shock, and functional evaluation. Each valve will be subjected to acceptance testing before qualification, as will all valves used in the remainder of the program.

An outline of the valve development and qualification task is as follows:

### A. Procure four prototype valves

1. Each valve:
  - a. Leak check seals, measure  $\Delta P$  and flow versus position with simulated propellants
2. Fourth valve

- a. Check internal and external leakage, response rates, resolution,  $\Delta P$  and flow versus position with line propellants, contamination, propellant compatibility and follow with 6-month storage with propellant on seals
- B. Procure lightweight valve (22)
1. Acceptance test all lightweight valves:
    - a. Proof and leak
    - b.  $\Delta P$  and  $\dot{w}$  (simulants) versus position
    - c. Vibration
  2. Qual two valves
    - a. Acceptance test per II. B. 1
    - b. Salt fog
    - c. Sand and dust
    - d. Humidity - 1 valve, lunar environment cycle for other valve.
    - e. Function test
    - f. Vibration; launch boost, lunar descent and shock
    - g. Functional test with line propellants
    - h. Decontaminate
    - i. Function test
    - j. Disassembly and inspection

Note: Prototype and lightweight valves should be sufficiently similar internally to negate need for propellant compatibility and storage tests with lightweight valve.

## Workhorse Integration

The workhorse integration task will combine the prototype valve with the thrust chamber assembly and evaluate the REA for performance with the valve, throttling and dynamic stability. Twenty-three tests and 1540 hot-fire seconds are planned during which four different throttling evaluation MDC's will be conducted (see Appendix A ). These MDC's will test for response, response rate, functional performance, gain, hysteresis, and repeatability.

Dynamic stability will be evaluated by subjecting the engines to functional/performance and sawtooth duty cycles with helium-saturated propellants. Tests will be conducted at nominal, low, and high mixture ratios.

An outline of the work horse integration task is as follows:

- A. Use three prototype valves from Task II
- B. Build back-up injector of selected design
  1. Cold flow at 3 MR's - 3 tests
- C. Conduct performance survey with valve at altitude
  1. 55-percent F level, 5 seconds each, MR = 1.3, 1.6, 1.9 - 3 tests = 15 seconds
  2. MR = 1.6, F = 16 percent, 30 percent, 45 percent, 70 percent, 85 percent, 100 percent - 6 tests = 30 seconds
- D. Throttling evaluation
  1. At MR = 1.6, conduct MDC's 1, 2, 3, and 4  
Four MDC's, approximately 1000 hot-fire seconds
  2. At MR = 1.3, conduct MDC's 2 and 3  
Two MDC's, approximately 100 seconds
  3. At MR = 1.9, conduct MDC's 2 and 3  
Two MDC's, approximately 100 seconds

E. Dynamic stability

1. Conduct MDC 2 at MR = 1.6, 1.3, 1.9; helium saturated  
3 MDC's, 195 seconds
2. Conduct MDC 3 at MR = 1.6, 1.3, 1.9; helium saturated  
3 MDC's, approximately 100 seconds

Flightweight Integration

During flightweight integration testing (61 tests, 8105 seconds), the flightweight valve and gimbal capability will be introduced to the REA. In addition, one REA will be subjected to vibration testing for an early assurance of the adequacy of the mechanical interface attachments of the assembly. The hot-firing tests will consist of performance and MDC testing, including stability, as in the previous task, with the addition of gimbal evaluation during the MDC's. A further addition will be worst-case MDC's; these MDC's will be determined primarily from the thermal analysis conducted throughout the program.

An outline of the flightweight integration task is as follows:

A. Fabricate five REA's

1. Freon-flow calibrate and clean each valve/injector assembly before engine assembly (to be accomplished on all REA's in remainder of program).

B. Structural evaluation

1. Subject one REA to launch boost and lunar descent vibration and shock
2. Subject engine to MDC 3

One vibration test series

One MDC, 70 seconds

C. Performance survey 4 REA's

1. At 55-percent F, MR = 1.3, 1.6, 1.9 - 12 tests, 60 seconds



2. At MR = 1.6, F = 16 percent, 30 percent, 45 percent, 70 percent, 85 percent, 100 percent - 24 tests, 120 seconds
  3. At MR = 1.6, MDC 3 - MDC's, 280 seconds
- D. Gimbal integration
1. MDC's 1, 2, 3, and 4; gimbal during each - four MDC's, approximately 1000 seconds.
- E. Performance evaluation
1. MDC 3, each engine (4) - four MDC's, 280 seconds
  2. MDC 4, each engine gimbaling - four MDC's, 2900 seconds
  3. Worst-case duty cycle (TBD), two engines - two MDC's, ~200 seconds
- F. Stability Verification
1. MDC 1 at MR = 1.6, 1.3, 1.9; helium saturated - three MDC's, 195 seconds
  2. MDC 2 at MR = 1.6, 1.3, 1.9; helium saturated - three MDC's, 100 seconds

### PFRT

The 38 tests (14,290 seconds) during PFRT will subject engines to all the requirements of the qualification test program. In addition, five REA's will be tested to provide statistical data for the reliability demonstration. These REA's will then be subjected to off-limits evaluation which will include endurance, fuel and oxidizer depletion, high and low inlet pressures, high and low mixture ratio, and helium saturation testing.

An outline of the PFRT task is as follows:

- A. Fabricate 10 REA's
- B. Acceptance test each REA
  1. Each valve acceptance tested per II. B. 1
  2. Freon flow clean and calibrate per IV. A. 1

3. MDC 3
4. Decontaminate and functional test (proof leak and valve actuation) 10 MDC's, 700 seconds

C. Pre-qualify five REA's

1. REA 1

- a. Acceptance test per V.B
- b. Vibration, launch boost and lunar descent
- c. Shock
- d. Function test
- e. MDC 2, helium saturated
- f. Decontaminate and functional test
- g. MDC 4 and gimbal
- h. Decontaminate and functional test
- i. Disassemble and inspect

Two MDC's  
795 seconds

2. REA 2

- a. Acceptance test per V.B.
- b. MDC 4, helium saturated
- c. Decontaminate and functional test
- d. Vibration, boost, and descent
- e. Shock
- f. Functional test
- g. MDC 4 and gimbal
- h. Decontaminate and functional test
- i. Disassemble and inspect

Two MDC's  
1450 seconds



3. REA 3

- a. Acceptance test per V.B
- b. Thermal vacuum (lunar cycles)
  - (1) Functional test
- c. MDC 4 and gimbal
- d. Decontaminate and functional test
- e. MDC 2 helium saturated
- f. Decontaminate and functional test
- g. Disassemble and inspect

Two MDC's  
760 seconds

4. REA 4

- a. Acceptance test per V.B
- b. Salt fog
- c. Sand and dust
- d. Humidity
- e. Functional test
- f. Vibration, launch boost, and lunar descent
- g. Shock
- h. Functional test
- i. MDC 4 and gimbal
- j. Decontaminate and functional test
- k. Disassemble and inspect

One MDC  
725 seconds



5. REA 5

- a. Acceptance test per V.B
- b. MDC 4 and gimbal
- c. Decontaminate and functional test
- d. MDC 2, helium saturated
- e. Decontaminate and functional test
- f. Disassemble and inspect

} Two MDC's  
760 seconds

D. Reliability demonstration

- 1. Test each of 5 REA's as follows:
  - a. Acceptance test per V.B
  - b. MDC 4 and gimbal
  - c. MDC 2 - 10 MDC's, 7600 seconds

E. Off-limits

- 1. Use REA's from D
- 2. Endurance test, MDC TBD - 1000 seconds minimum
- 3. Fuel depletion
- 4. Oxidizer depletion
- 5. High pressure
- 6. Low pressure
- 7. High MR
- 8. Low MR
- 9. Helium saturation



## Qualification

Five engines will be evaluated in a formal qualification test program. This program is based primarily on the program used to qualify the LM ascent engine injector for man-rating; modifications include the additional requirements of throttling, gimbaling, and lunar environment exposure.

An outline of the qualification task is as follows:

- A. Fabricate 5 REA's and acceptance test per V.B
- B. Test REA 1 per V.C.1 (two MDC's, 795 seconds)
- C. Test REA 2 per V.C.2 (two MDC's, 1450 seconds)
- D. Test REA 3 per V.C.3 (two MDC's, 760 seconds)
- E. Test REA 4 per V.C.4 (one MDC, 725 seconds)
- F. Test REA 5 per V.C.5 (two MDC's, 760 seconds)

## Deliverables

An outline of the deliverables task is as follows:

- A. Fabricate 32 engines, one per week
- B. Acceptance test each per V.B

## LUNAR MODULE CONSTRAINTS

Propellant for the LFV will be obtained from the lunar module descent propulsion system (DPS), so some of the parameters of that system must be considered as constraining the LFV propulsion design. First, the DPS employs nitrogen tetroxide and Aerozine 50 (50-percent hydrazine and 50-percent unsymmetrical dimethylhydrazine) at a 1.6:1.0 (equal volume) oxidizer fuel ratio. Some consideration has been given to providing a capability in the LFV to burn a range of O/F ratios to obtain complete use of residual DPS propellant, which may be available at some off-nominal mixture ratio. However, the problems of (a) determining with confidence exactly what the residual DPS O/F ratio is, with a gaging accuracy of  $\pm 55$  lbm oxidizer and  $\pm 35$  lbm fuel per tank, (b) decreased range in flying the LFV at off-nominal O/F ratio with fixed tankage, and (c) increased propulsion system complexity have caused this alternative to be rejected.

A more favorable approach is to match the LFV design to the expected residual mixture ratio. As noted in Reference 1 of Volume 4, Configuration Design, the ratio varies from 1.01 to 3.13 as the LM design limits on loading and velocity requirements are considered as variables. Most of the points, however, fall about a ratio of 1.5. This would indicate that the LM is loaded to a fuel bias away from the engine mixture ratio - a conventional procedure (based on a volumetric model) usually used to obtain the least outage weight penalty. It is considered that this practice would probably be maintained in future LM's even if the velocity and loading requirements evolved to new values. In any event, the LFV design mixture ratio can be adjusted in Phase C to the current expected residual value as long as a range of 1.4 to 1.8 is not exceeded (designs outside this range might be fundamentally different). At this time, the best data source (Reference 1, Volume 4) indicates that a value of 1.5 is expected. As noted in Volume 4, a ratio of 1.5 also has a favorable stowing advantage which, together with the residual-matching advantage, overcomes the performance loss of about three seconds in specific impulse. For those reasons, 1.5 is the value finally used in the selected preliminary design. Elsewhere in this volume, the earlier baseline value of 1.6 is used as the reference standard for trade studies.

The propellant temperature range in the LM DPS at lunar touchdown is estimated by Grumman (Reference 4, page 23) at between 50 and 90 F. Grumman also estimates this temperature may increase as much as 25 F in 60 hours stay time on the lunar surface, so that temperature at propellant transfer could be as high as 115 F. This could present a serious problem to the LFV oxidizer tank, which will probably be of titanium and constrained to 105 F oxidizer temperature from fracture mechanics considerations. Grumman suggests, however, that the LM glycol line from the batteries could be run around the bottom end-dome of each tank with valving to control flow through the lines, thereby maintaining propellant temperature in an acceptable region. It will, therefore, be assumed for this study that propellant is available from the LM between 50 and 90 F. If this proves too difficult, it may be necessary to cool the  $N_2O_4$  by vaporization to vacuum. Decreasing oxidizer temperature 25 F (13.9C) would require 472 cal/g. mol, which could be obtained by vaporizing about 5.2-percent of the oxidizer. Problems would be the loss of about 10-lbm oxidizer per 185-lbm cool oxidizer remaining, and the care necessary to prevent contamination of flight suits and equipment.

The LM DPS will be vented during post-landing checkout operations. According to Grumman (Reference 4, page 22), the venting can be monitored to provide an initial tank pressure of up to 150 psia if desired, and this may rise to 200 psia as helium warms. It will therefore be assumed that any DPS pressure up to 150 psia can be made available for propellant transfer.

## BASIC DESIGN TRADEOFFS

Certain basic design criteria must be established before developing the propulsion system design. These include the LFV placement before fueling, the basic pressurization concept and use of refillable or replaceable propellant tanks.

### LFV Placement

The basic concept for LFV removal from stowage and preparation for flight is that one astronaut will be capable of transporting an empty LFV a reasonable distance to a takeoff pad, but that carrying the added mass of 300-lbm propellant is not feasible for pressure-suited personnel even under lunar gravity conditions. The LFV must therefore be fueled at the point of landing and takeoff. Grumman has estimated (see Table 1-29 and Reference 4) that lunar ejecta from a single 125-lbf engine firing 3 feet above the lunar surface will not damage the LM, since it is protected by a 0.004-inch thick aluminum bumper. However, the LFV engines will have 300-lbf thrust at liftoff, and the nozzle exit will only be about 1 foot above the surface. Provision of a landing and takeoff pad will minimize ejecta in liftoff, but failure to hit the pad in landing must be considered (Table 1-29). Therefore, NR SD operations analysis recommended a 40-foot separation in order to minimize the precision needed in landing. With provision for vertical runs and non-radial misalignment, this leads to a desired servicing hose length of 50 feet.

### Basic Pressurization Concept

Two basic types of pressurization are conventionally used with liquid propulsion systems: pump fed and pressure fed systems. For a system as small as the LFV, pump-fed concepts offer no real weight advantage and add unacceptable disadvantages of complexity, cost, and development time. The LFV has therefore been specified as a pressure-fed system. Since the propellant is already available saturated with helium, helium will be used as the pressurant to avoid introducing new problems.

### Propellant Tankage

Several techniques may be considered for providing propellant tankage. Earth-loaded propellant tanks that might be attached to the LFV by quick disconnects are not really a consideration, since the basic concept of the LFV is to use contingency propellant available without further tank weight penalty in the LM DPS tanks. No capability of carrying any substantial amount of propellant beyond that in a fully loaded DPS is assumed. LFV propellant tanks used for only one LFV flight would carry an unnecessary weight penalty of at least 20-lbm hardware per LFV flight.

Table 1-29. Lunar Ejecta From LFV Engine Exhaust

Particle Diameter	Particle Velocity		Required Single Skin Thickness
	Ft/Sec	Km/Sec	
Inches			Inches
0.0002	5806	1.77	0.000156
0.002	663	0.202	0.000202
0.02	149	0.0455	0.000456
0.2	40	0.0122	0.00122
2.0	11.7	0.0036	0.0036

Assumptions

## 1. Engine Characteristics:

$$F = 125 \text{ lb} \quad O/F = 1.6$$

$$p_c = 80 \text{ psia} \quad \epsilon = 40 \text{ (80-percent Bell)}$$

 2. Propellants:  $N_2O_4/A-50$ 

## 3. Engine Exit Plane 3.0 ft above lunar surface

## 4. Surface particle density - 100 lb/cu ft

## 5. For ejecta Ref. ATAA Paper No. 63-199

## 6. For required skin thickness, Ref. LED-520-1F, p. 44 (Figure 9)

It does seem feasible to provide a set of LFV tanks with quick disconnects that could be carried to the LM for filling and then carried back to the LFV and installed for each mission. However, additional mass would be required to beef up the tanks against accidental damage and provide refueling cradles of some type at the LM. Additional leakage problems would be created at the quick disconnects on the LFV, since there would be flow through them during flight. Most important, this concept appears to require greater amounts of the short EVA time the Astronauts will have available for servicing.



The best solution therefore appears to be refillable tanks permanently attached to the LFV and serviced from the LM through flexible hoses. As we will see when components are discussed, the weight penalty for this approach is not excessive.

### Helium Tankage

Helium in the LM DPS tank is available at touchdown at about 400 psia at -340 F, or can be heated to 1010 psia at 70 F. Only about 6.0-lbm helium is available at an unacceptably low pressure, so LFV helium must be supplied from an external source. One alternative would be to provide helium in a high-pressure tank on the LM and use it to repeatedly service a lower pressure tank on the LFV. The high-pressure tank should not be much above 6000 psi in today's state-of-the-art, nor the LFV tank much below 3000 psia for efficiency and compactness. With these constraints, helium tankage for five LFV flights would weigh about 151-lbm plus the weight of a high-pressure servicing line, twice the estimated 77 lbm for replaceable helium tank assemblies, one each for five flights. Moreover, the 6000-psia working pressure tank and new GSE to fill it would have to be developed. Within the constraints of available GSE, the high-pressure tank would be pressurized to only 4500 psia, and a refill system would weigh about three times the weight of a replaceable tank system. Replaceable tanks, therefore, will be used.

### DESIGN REQUIREMENTS

Based on the foregoing considerations, on criteria developed under the engine tradeoff, and on other system considerations, requirements for the propulsion subsystem design may now be developed. They are discussed below and summarized on Drawing 2230-102A (Figure 1-45). Pressure requirements must be shown for two types of engines, radiative and regenerative cooling. The second pressure will be shown in parentheses, as: Radiative (regenerative) psia.

### Propellant Tankage

Tankage should be provided for 300-lbm propellant at 1.6:1.0 O/F ratio (about 185-lbm  $N_2O_4$  and 115-lbm Aerozine 50). Fuel temperature can range from 25 to 120 F, but if titanium is used for the tanks, the oxidizer temperature should not exceed 105 F from fracture mechanics considerations. Design limit pressure of the tanks should be about 300 (360) psia. The logic optimizing tankage to one oxidizer and one fuel tank has already been discussed. Internal capillary screens and close baffles will be required for slosh and location control, and external insulation will be needed to keep propellant temperature within acceptable limits.

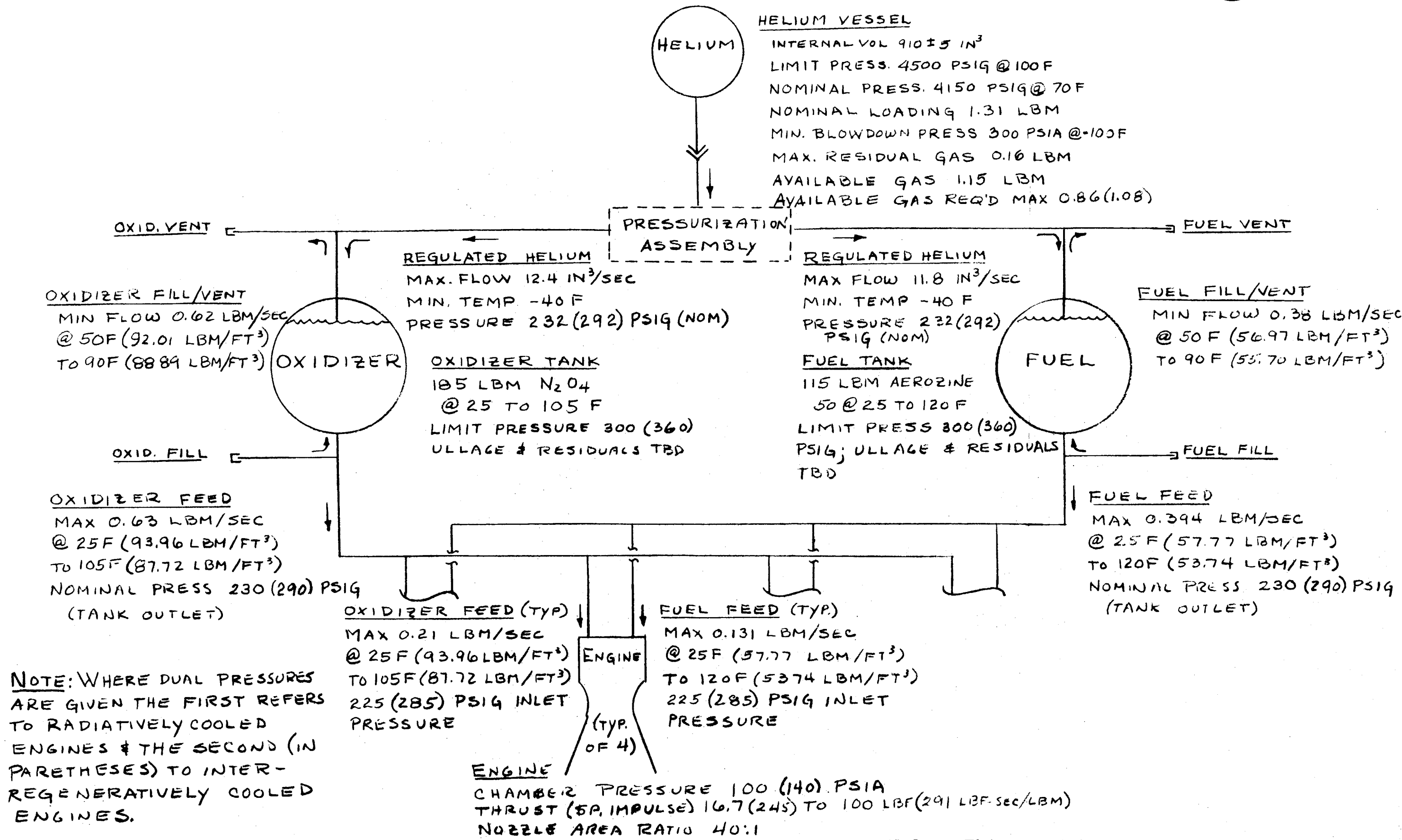


Figure 1-45. Lunar Flying Vehicle Propulsion Subsystem System Diagram

### Propellant Fill

As an initial criterion, five minutes was established as the maximum flow time that could be permitted for servicing each propellant. Minimum servicing flow should therefore be 0.62 lbm/sec oxidizer and 0.35 lbm/sec fuel. As previously stated, propellant is assumed available from the LM at 50 to 90 F. Venting provisions are required for the servicing operation.

### Propellant Feed

In order to provide propellant for a total thrust of 300 lbf, propellant flow of 0.63 lbm/sec oxidizer and 0.39 lbm/sec fuel is required. One-third this amount should be delivered to each of any three engines at an inlet pressure of 225 (285) psia.

### Helium Supply

Helium requirements depend on ullage, blowdown rate, leakage, and other considerations. To fill two 20-inch diameter propellant spheres (which permit about 14 percent ullage) with helium at 25 F and 232 (290) psia requires about 0.86 (1.08) lbm helium.

### Pressurization System

A pressurization system must be provided to reduce helium from tank pressure to about 232 (292) psia, check backflow to prevent intermixing of oxidizer and fuel vapors and provide pressure relief.

### Propulsion Components (Tables 1-30 and 1-31)

Once propulsion system design requirements are defined, it becomes possible to define criteria for individual components. Where possible, components are desired that have already been qualified on NASA programs and can be used with a minimum of modification and testing. Components described below are keyed to the item numbers found on the LFV Propulsion System Schematic-Drawing 2230-101C (Sheet 1, attached as Figure 1-46, and Sheet 2, attached as Table 1-30). It seems most convenient to discuss these components as part of subassemblies, which in turn are keyed to the work breakdown structure (WBS) of the resources plan under which they would be developed as follows:

Engine, gimbal, and thrust mount (WBS 3.3.1 and 3.3.2) have already been described

Propellant tanks (WBS 3.3.3)

Helium tank assembly (WBS 3.3.4)

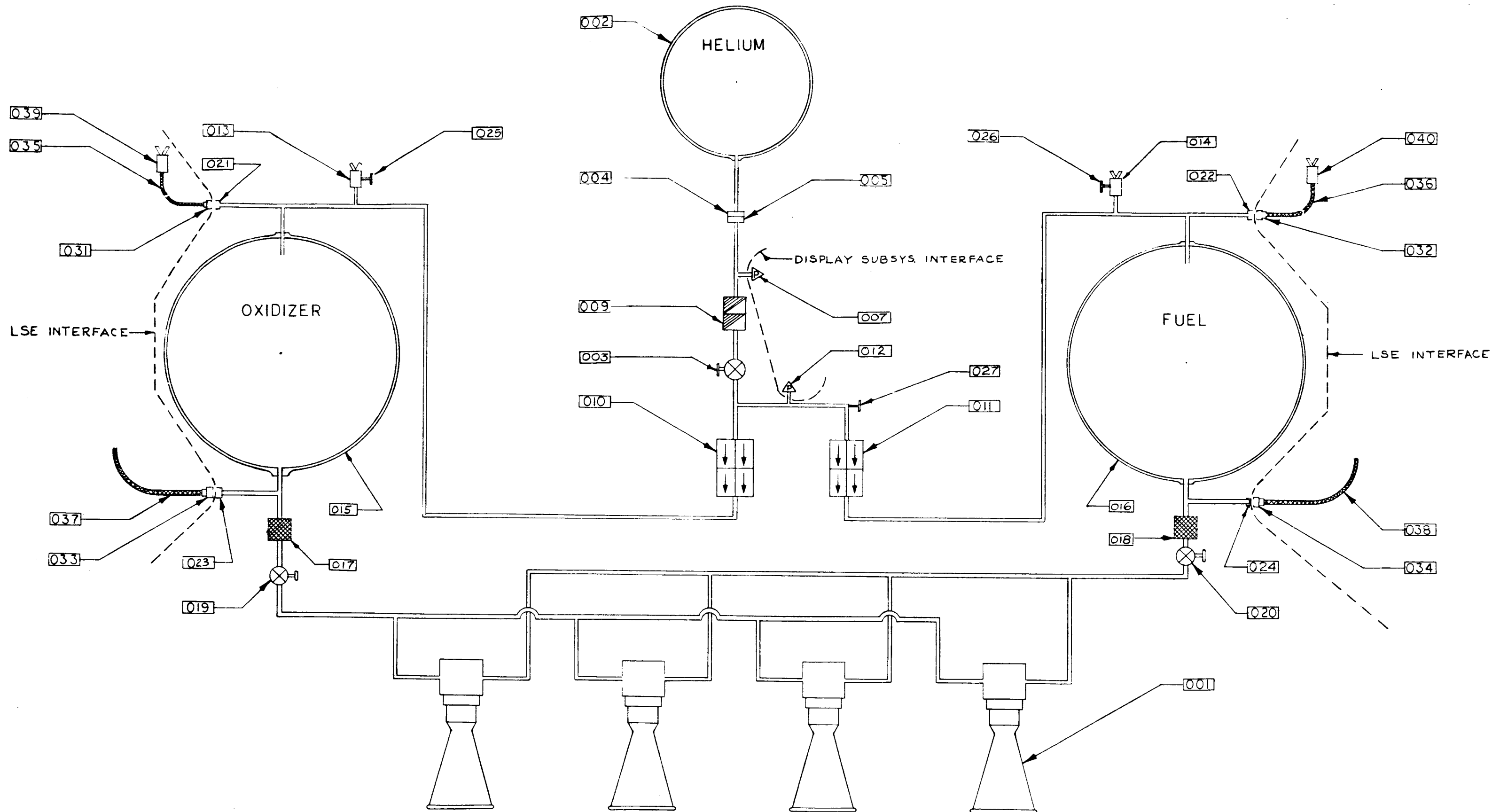


Figure 1-46. Lunar Flying Vehicle Propulsion Subsystem Schematic

**Table 1-30. LFV Propulsion Subsystem and Related Components\***

WES No.	Subsystem Assembly	Item No. <sup>1</sup>	Qty	Description	Candidate Part No.
3.3	Propulsion				
3.3.2	Engine and gimbal	001	4	Engine and gimbal	TBD
3.3.3	Propellant tanks	015	1	Tank, oxid	Make from 20 Gemini     OAMS tank shell
		016	1	Tank, fuel	
3.3.4	Helium vessel assembly	002	1	Helium vessel	ME282-0051-0001
		004	1	Helium coupling, tank 1/2	ME273-0010-0001
3.3.5	Pressure regulator assembly	003	1	Manual valve, helium	New part
		005	1	Helium coupling, LFV 1/2	ME273-0010-0002 <sup>2</sup>
		009	1	Pressure regulator	ME284-0021-0005 <sup>3</sup>
		010	1	Check valve assembly, oxidizer	ME284-0024-0001
		011	1	Check valve assembly, fuel	ME284-0024-0002
		013	1	Relief valve, oxidizer	ME284-0062-0002 <sup>3</sup>
		014	1	Relief valve, fuel	ME284-0062-0012 <sup>3</sup>
		021	1	Vent coupling, oxidizer, LFV 1/2	ME273-0011-0001
		022	1	Vent coupling, fuel, LFV 1/2	ME273-0024-0001
		025	1	Test point coupling, oxidizer	ME144-0023-0011
		026	1	Test point coupling, fuel	ME144-0023-0031
		027	1	Test point coupling, helium	ME144-0023-0051
3.3.6	Propellant manifold	017	1	Filter, oxidizer	ME286-0039 Type
		018	1	Filter, fuel	ME286-0039 Type
		019	1	Manual valve, oxidizer	New part
		020	1	Manual valve, fuel	New part
		023	1	Fill coupling, oxidizer, LFV 1/2	ME273-0019-0001
		024	1	Fill coupling, fuel, LFV 1/2	ME273-0021-0001
3.6	Display				
3.6.8	Pressure measurement	007	1	Pressure sensor, He, high	TBD
		012	1	Pressure sensor, He, regular	TBD
4.1	Lunar support equipment				
4.1.1	Propellant servicing	031	1	Vent coupling, oxidizer, ground 1/2	ME273-0011-0002 <sup>2</sup>
		032	1	Vent coupling, fuel, ground 1/2	ME273-0024-0002 <sup>2</sup>
		033	1	Fill coupling, oxidizer, ground 1/2	ME273-0019-0002 <sup>2</sup>
		034	1	Fill coupling, oxidizer, ground 1/2	ME273-0021-0002 <sup>2</sup>
		035	1	Vent hose, oxidizer	New part
		036	1	Vent hose, fuel	New part
		037	1	Fill hose, oxidizer	New part
		038	1	Fill hose, fuel	New part
		039	1	Vent relief, oxidizer	New part
		040	1	Vent relief, fuel	New part

**Notes:**
<sup>1</sup>Reference sheet 1 of schematic.

<sup>2</sup>Redesign for pressure suit use and space qualification required.

<sup>3</sup>Redesign to new system pressure and redesignation may be required.

\*Sheet 2 of Drawing 2230-1010, LFV Propulsion Subsystem Schematic, revised 5 June 1969.

Pressure regulation assembly (WBS 3.3.5)  
Propellant manifold (WBS 3.3.6)  
Propellant servicing equipment (WBS 4.1.1)  
Propellant quantity measurement (WBS 3.6.1)  
Pressure measurement (WBS 3.6.8)

### Propellant Tanks (Items 015 and 016 on Figure 1-46 and Table 1-30)

Propellant tank volume (not including ullage) must be at least equivalent to 185 lbm oxidizer at 105 F (3644 in.<sup>3</sup>) and 115 lbm fuel at 120 F (3700 in.<sup>3</sup>). With this volume requirement, costs can be minimized by selecting the 20.03 inch I.D. spherical tank shell employed on the Gemini OAMS tanks. This shell was built by Airtek Division, Fansteel Corporation, to Rocketdyne Division, North American Rockwell Drawing 103177. Airtek advises they still retain the key tooling for this shell. The tank has a minimum internal volume of 4180 in.<sup>3</sup>, which permits a generous (but not excessive) 15 percent and 13 percent ullage over the oxidizer and fuel volumes above. The tank is welded of 0.022 inch minimum wall 6Al4V titanium, weighing about eight pounds, and has maximum operating, proof, and burst pressures of 300/500/700 psig. This is entirely suitable for the LFV application if a radiatively cooled engine is chosen: for a regeneratively cooled engine, the minimum wall thickness would be increased to be consistent with a 360 psig maximum operating pressure.

The Gemini OAMS tank was designed for positive expulsion using a Teflon bladder. As described in the tank concept tradeoff elsewhere in this report, a bladder tank is unsuitable for the LFV application because of the time and care required in reservicing, cycle life problems, and the entrapment caused by permeability. Using technology pioneered by NR/SD on the Apollo CSM Service Propulsion System tank screens, a simple screen system can be confidently designed which will provide slosh control, prevent helium from entering the propellant feedline, and minimize residuals.

### Helium Tank Assembly (Items 002, 004, 005 on Figure 1-46 and Table 1-30)

Previous sections have defined the requirement for a replaceable helium tank assembly supplying at least 0.86 (1.08) lbm helium for a radiative (regenerative) engine system. The 12.3 inch diameter ME282-0051-0001 helium pressure vessel used on the Block II Apollo Service Module Reaction Control System (SM RCS) seems most attractive for this application. It is loaded at 4150 psia and 70 F with 1.31 lbm helium, and retains 0.16 lbm at -100 F and 300 psia. The minimum 1.15 lbm of helium supplied should therefore be adequate. The tank is fully qualified as shown on Table 1-31.

Table 1-31. LRV Component Capabilities

Component	Part No.	Used on Apollo	Drawing Ref. No.	Previous Test Limits													Failure Summary	Remarks	Apollo Design Life	NR (Apollo) References
				Temperature	Pressure	Humidity	Fluid Resistance	Vibration	Shock	Acceleration	Acoustical Noise	Leakage	Other	Leakage	Other					
Helium pressure vessel	ME282-0051-0001	SM RCS	002	Ambient: +30 to +100 F Fill: -150 to +114 F Blowdown: -65 to +80 F	External: 10 <sup>-6</sup> mmHg Proof: 6000 psia for 15 min	Not tested	Not tested	Not tested	From 0.04 g <sup>2</sup> /cps at 20 cps to 0.15 g <sup>2</sup> /cps at 80 cps Constant to 1000 cps to 0.075 g <sup>2</sup> /cps at 2000 cps (15 min/axis, press. to 4500)	Not tested	Not tested	Not tested	156 db/10 sec 152 db/80 sec 144 db/60 sec	< 5 x 10 <sup>-6</sup> sec/sec at 4500 psig and room temp		None reported	Suitable for LRV (thru-drilled fill port might be replaced by weld)	720 hours	Certif test reqt (CTR) 14316005 and 14312003, test agency repr (TAR) 48163	
Helium pressure regulator unit	ME284-0021-0005	CM RCS	009	1 x 10 <sup>-6</sup> torr external, 2000 psig inlet at 0 and 150 F, 5000 psig inlet at -65 and 150 F	Proof: 6750 psig Burst: 9000 psig	MLL-STD 810, method 507	124-day exposure on similar ME284-0022 SM RCS regulator	As above plus 5 to 2000 cps resonant search at min 0.086-in. D.A., 3 axes	Not tested	Not tested	Not tested	Similar Apollo regulator Tested as above	Internal < 20 sec/hr at 4500 and 425 psig; external < 5 x 10 <sup>-5</sup> sec/sec at 540 psig		23 leakage failures caused procedure and equipment changes 7 contamination and stock-piston failures caused redesign	Suitable for LRV with shim adjustment to modify output pressure.	4000 cycles	CTR 00913307 TAR SR 466, SR 470		
Helium check valve assembly (series-parallel quad)	ME284-0357 -0001 (oxidizer) -0002 (fuel)	CM RCS and SM RCS	010 011	Ambient: +30 to +150 F Fluid: -65 to +110 F	Proof: 540 psig Burst: 720 psig Pressure drop max 4 psi at 0.12 lbm/min	Not tested	103-day test (NR Apollo CCA 1968) being analyzed	As above (both resonant and random)	Not tested	20 g/10 min each of 3 axes	As above	Internal < 10 <sup>-4</sup> sec/sec helium; external < 5 x 10 <sup>-6</sup> sec/sec at 540 psig	Filter surge, dirt retention, strength, cracking pressure max 4 to 5 psi/element.	8 leakage, 7 pressure drop, 3 cracking pressure caused by contamination, seal deterioration.	Suitable for LRV.	4000 cycles	CTR 01213701 and 14316010, TAR 393, 396, 4524-1 and 5087			
Helium pressure relief valve	ME284-0062 -0002 (oxidizer) -0011 (fuel)	CM RCS	013 014	Ambient: +30 to +150 F Helium: -65 to +80 F Propellant: to +105 F	Burst: 720 psig Diaphragm rupture 340 psig, reseal < 327	Not tested	103-day test (CCA 1968) on similar ME284-0026 SM RCS valve	As above on ME284-0026, reduced levels on -0062. Both included resonant and off-limit random.	Not tested	20 g/10 min each of 3 axes	Not tested	< 5 x 10 <sup>-6</sup> sec/sec at 520 psig (external); and 327 psig (diaphragm); relief valve < 20 sec/hr	Pressure cycling at ambient and extreme temperatures.	37 failures, including premature burst-disc rupture and leakage have resulted in specification and procedure changes.	Suitable for LRV if 340 psig diaphragm burst suitable; poppet spring and disc support change required for 280-psig burst.	336 hours; 1500 diaph, 600 vent; 4000 poppet cycles	CTR 00913309, TAR CM240B, CM 249			
Oxidizer vent coupling, flight 1/2	ME273-0011-0001	CM RCS	021		Proof: 540 psig Burst: 720 psig	Not tested	19-day exposure N <sub>2</sub> O <sub>4</sub> /MMH at 360 psig plus CCA 1968 test	As above (both resonant and random)	30 g for 10-msec rise, 1-msec decay	Not tested	156 db/10 sec 152 db/80 sec 144 db/60 sec	< 5 x 10 <sup>-6</sup> sec/sec he at 0 to 360 and 540 psig		1 nut seized; 3 contamination leakage due to poor cleaning.	Suitable for LRV. Ground half (-0002) of each component requires space rating	400 ground engagement cycles	CTR 00913304 and 012280B, TAR 3534-2			
Fuel vent coupling, flight	ME273-0024-0001	SM RCS	022		Proof: 375 psig Burst: 500 psig Specified (3400 to 3600 psig actual)	Not tested	103-day test (NR Apollo CCA 1968)	From 0.02 g <sup>2</sup> /cps at 10 cps to 1.8 g <sup>2</sup> /cps at 100 cps Constant to 400 cps to 0.36 g <sup>2</sup> /cps at 2000 cps	Not tested	6 g/5 min each of 3 axes	Not tested	External < 5 x 10 <sup>-6</sup> sec/sec		None reported	Suitable for LRV (acceptance proof pressure would be increased).	14-day flow cycle	CTR 01214703 TAR TRI174, 125			
Fuel fill coupling, flight	ME273-0021-0001	SM RCS	024		Proof: 7500 psig Burst: 15,400 psig (engaged and separate halves)	Not tested		Same as pressure regulator	30 g for 10-msec rise, 1-msec decay	Not tested	156 db/10 sec 152 db/80 sec 144 db/60 sec	< 10 sec/min engaged at 5000 psig; airborne half < 5 x 10 <sup>-6</sup> sec/min		4 excessive leakage (mostly contamination)	Attractive for LRV subject to confirmation of ease and safety of astronaut operation and reduction of engaged leakage	13 days active with 400 engagement cycles	CTR 00913303 TAR 1112A, 1114			
Propellant in-line filter	ME286-0039 -0001 (oxidizer) -0011 (fuel)	SM RCS	017 018			Not tested														
Helium fill disconnect coupling	ME273-0010 -0001 (airborne) -0002 (ground)	CM RCS and SM RCS	004 005			Not tested														

165, 166 (1)

165, 166 (2)

165, 166 (3)

An available quick-disconnect helium coupling (Items 004 and 005) exists in the ME273-0010 fill-disconnect coupling qualified for the Apollo CM and SM RCS. The "airborne half" weighs only one-quarter pound with pressure cap installed and has negligible leakage; it would be employed on the helium tank during storage (Item 004). The "ground half" would become part of the LFV (item 005). Since the two halves are engaged on Apollo only during servicing, leakage of up to 10 standard cc per minute (0.11 lbm per hour) was permitted by specifications in the engaged condition. (Although it seldom comes close to this and then only at -150 F). The supplier, On-Mark Couplings Division of Purolator, advises that with rather modest seal modifications, this engaged leakage could be reduced drastically. The component has a desirable dual action in that the first four turns in engagement provide coupling and the next four turns open poppet valves. Actuation tests with space-suited personnel would be required to demonstrate the ease and safety of engaging the helium tank under simulated lunar conditions. The "ground half" proposed for use on the LFV would also require space rating.

Pressure Regulation Assembly (Items 009, 010, 011, 013, 014 in Figure 1-46 and Table 1-30)

The pressure regulation assembly will consist of the components required for helium pressure control mounted in a compact assembly and checked out as an assembly before installation in the LFV. The components involved are the helium pressure regulator unit (item 009), the helium valve (003), the check valve assemblies (010 and 011), and the relief valves (013 and 014). The system will be brazed together with one-quarter inch CRES tubing using the procedures proven on the Apollo CSM program.

Pressure Regulator Unit. Two qualified regulator units are available, the ME284-0021 used on the Apollo CM RCS and the ME284-0022 used on the SM RCS. The supplier (Stratos-Western Division of Fairchild Hiller Corporation) advises that the units are identical except for shims under the bellows spring which change the output pressure from the  $181 \pm 3$  psig on the -0022 unit to the  $291 \pm 4$  psig produced by the -0021 unit. A simple shim change and confirming test should be suitable to adjust this already qualified unit to the 235 or 295 psig range being considered for the LFV.

This regulator unit consists of two pressure regulators in series, which is desirable because the "normal failure mode" is an open failure. The Apollo CM and SM RCS (pressurization assemblies) employ two of these series regulator units in parallel to guard against regulator failure closed. In order to assess the need for parallel regulation on the LFV, the following reliability analysis was made:



In accordance with Reference 1-4, the allocated failure modes for an Apollo RCS regulator are as follows:

	<u>Failures Per Hour</u>
Failure open (of two regulators in series)	Negligible
Failure closed (either of two series regulators)	$2.0 \times 10^{-6}$
Leakage failures:	
External	1.0
Lockup Leak	0.75
Bellows (either of 2)	4.0
	$5.75 \times 10^{-6}$

The failure rate of a series regulator unit is therefore allocated as 7.8 per million hours. If two regulator units are placed in parallel, the failure closed problem becomes negligible, but the leakage failures are additive for a total allocated failure rate of 11.5 per million missions. (See Figure 1-47).

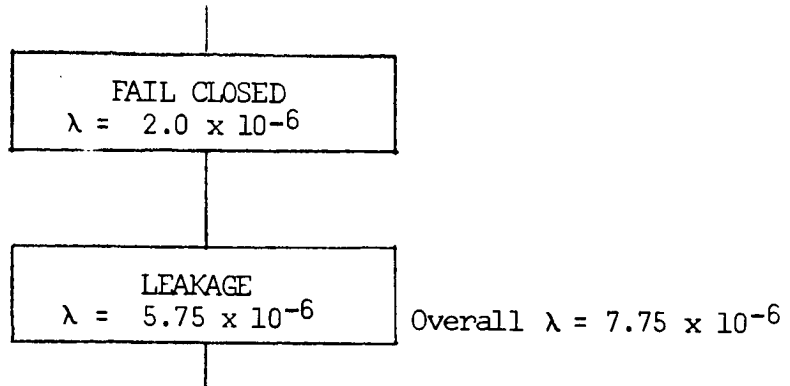
One should not place excessive dependence on these figures, except to note that the reliability justification for parallel regulator units is weak. Each regulator unit weighs about 3.0 pounds, and because of the desirability to keep the LFV light and simple, it is recommended that only a single series regulator unit be employed on the LFV pressurization system.

Helium Valve. The Apollo CM/SM/LM RCS employ remotely operated solenoid valves for propellant and pressurant control, but the weight, complexity, and power drain associated with them are both unnecessary and undesirable in the LFV. Manual valves exist off-the-shelf that should be qualifiable to LFV conditions. For example, the Jamesbury Valve Company makes a stainless steel ball valve with dual teflon seals on both the ball and the valve stem that requires only a 90° turn of a projecting lever to actuate from full-closed to full-open. This valve series has been used extensively by NR/SD in helium, N<sub>2</sub>O<sub>4</sub>, and Aerozine 50 service in RCS breadboard tests under conditions approximately those of the LFV propulsion with excellent results.

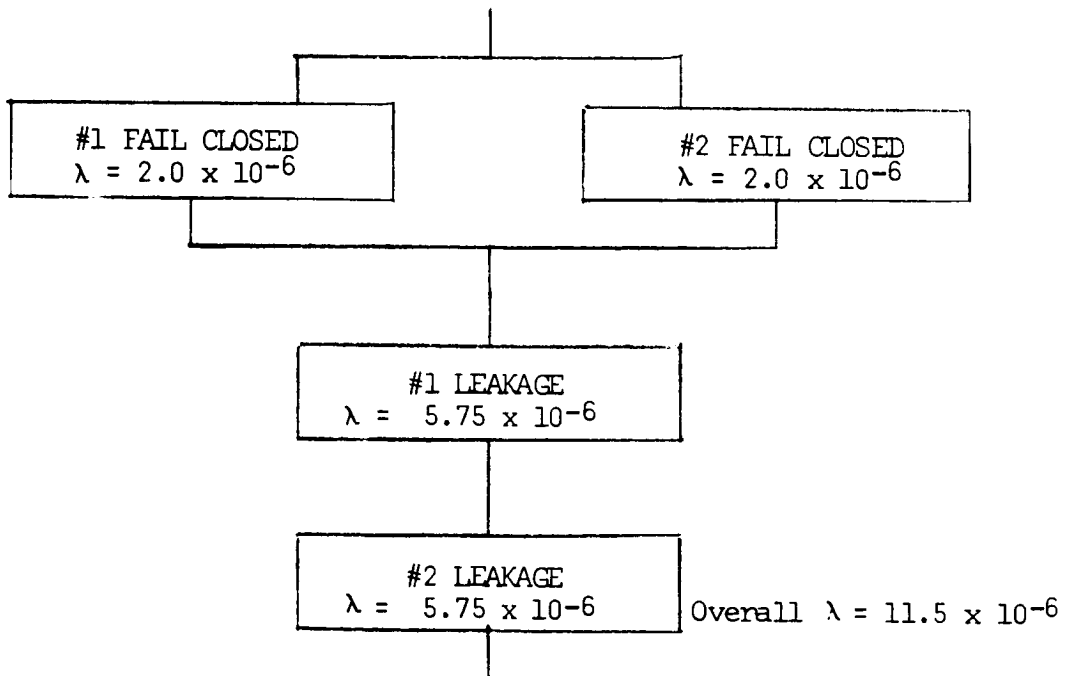
Check Valves. The ME284-0357 series-parallel quad check valve assemblies used on the Apollo CM and SM RCS are fully qualified (Table 1-31) and appear entirely suitable for the LFV.

Relief Valves. The ME284-0062 helium pressure relief valve, fully qualified for the Apollo CM RCS (Table 1-31), consists of a burst diaphragm bursting at 340 psig backed up by a downstream check valve flowing at 346 psig. If a regeneratively cooled engine is used, this pressure would be quite appropriate. To make the relief valve consistent with the lower system pressure associated with a radiatively cooled engine, the poppet spring and

SINGLE SERIES REGULATOR



SERIES - PARALLEL REGULATOR



(  $\lambda$  = Failures per Hour)

Figure 1-47. Regulator-Failure Logic Diagram

the disc support which determines the effective area on the Belleville spring would have to be changed and a modest requalification conducted.

### Propellant Manifold

The propellant manifold will include propellant filters (items 017 and 018), manual propellant valves (019 and 020), and brazed tubing. The ME286-0039 propellant filters qualified for Table 1-31 and used on the Apollo SM RCS will filter out particles above 15 microns, and should be suitable for the flow rates and propellant quantity of the LFV. Although only specified for proof/burst pressures of 350/500 psig, the unit actually bursts well above 3000 psig, and a higher proof requirement for the LFV use would be no problem. Manual propellant valves exist off-the-shelf that should be qualifiable for LFV use as already discussed for helium valves under the pressure regulation assembly.

The propellant manifold would be of brazed CRES tubing with the same type of elbows and tees used on the Apollo RCS. To obtain a first estimate of line sizes, the following pressure drops were calculated for 105 F oxidizer and 120 F fuel flow from tanks to the point at which flow to individual engines begins (Table 1-32).

Table 1-32. Line-Flow Pressure Drops for Oxidizer and Fuel

Nominal Line O. D. (in.)	T. D. (in.)	$\Delta P$ Oxidizer		$\Delta P$ Fuel	
		1-Ft	3-Ft	1-Ft	4-Ft
1/4	0.210	9.0	27.0	8.7	34.8
5/16	0.272	2.45	7.35	2.37	9.48
3/8	0.335	0.87	2.62	0.85	3.38
1/2	0.450	0.198	0.595	0.192	0.770
5/8	0.575	0.058	0.175	0.057	0.226

The calculation assumes 300 lbf total engine thrust and friction factors of  $(4f) = 0.021$  (oxidizer) and  $0.027$  (fuel). No elbows, tees, filters or valves were included.

For the estimated lengths, one-half-inch tubing seems desirable, although the pressure drop associated with 3/8-inch tubing could be accepted

if it has clear design advantage. Since flow lines to individual engines will have a  $\Delta P$  nominally 1/16 (and in three-engine use 1/9) as great, use of 5/16-inch tubing to individual engines seems appropriate.

### Propellant Servicing Equipment

The propellant servicing equipment includes fill/vent couplings, flexible hose, and vent relief valves. The ME273-0011, -0019, -0021 and -0024 fuel and oxidizer fill and vent couplings are qualified for the Apollo CM and SM RCS (Table 1-31) and can be easily adapted to LFV use. The "flight halves" (items 021 through 024) which would be brazed to the LFV, are light weight and have a pressure cap as a secondary seal. The "ground halves" (items 031 through 034), which would terminate the 50-foot fill hoses from the LM and the detachable vent hoses used to vent propellant away from the LFV, would require some delta qualifications for lunar surface use. The ground halves, their dust caps, and the pressure caps for the flight halves would require special design consideration and evaluation by space-suited personnel to assure ease of operation under lunar conditions, but any external modifications required should not affect the integrity of the internal design.

For the propellant fill and vent hose (items 035 through 038), a simple, yet apparently satisfactory solution is a Teflon hose covered with stainless steel wire braid for strength (type T-1). It is available from several suppliers, including Preece, Inc., and Anaconda Metal Hose Division. The effect of external vacuum on the Teflon has been investigated briefly and does not appear to be serious unless it occurs simultaneously with temperatures above 350 F. Properties of representative hose sizes (from Anaconda) are shown on Table 1-33. Since it is expected that driving forces of up to 150 psia will be available from the LM DPS for propellant servicing, the 85 psig pressure drop associated with filling an oxidizer tank in five minutes through a 3/8-inch hose seems acceptable, and the 0.12 lbm/ft (plus 10 feet) hose weight is quite attractive. Providing a 40-foot fueling radius/rather than 20 feet carries only a 4.8 lbm weight penalty, and appears worth this penalty from system considerations.

The vent lines also contain sight glasses (not shown on drawing) and vent relief valves (items 039 and 040) to provide back pressure during servicing. No effort has been expended to find candidate designs for these applications, but they are relatively simple and noncritical in operation and are considered well within the state of the art.

Table 1-33. Properties of T-1 Hose

Nominal Tube Size (in.)	Minimum Hose I. D. (in.)	Rated Burst Pressure (psi)	Minimum C/L Bend Radius (in.)	Weight Per Foot (lbm)	Pressure Drop Per Foot (psi)*	
					Oxidizer	Fuel
5/16	0.335	10,000	2	0.10	5.44	3.44
3/8	0.298	9,000	4	0.12	1.69	1.22
1/2	0.391	8,000	4-5/8	0.14	0.427	0.309
5/8	0.485	7,000	5-1/2	0.19	0.145	0.105
3/4	0.605	6,000	6-1/2	0.23	0.043	0.035

\*Assuming servicing 185 lbm NTO and 115 lbm A-50 in 5 minutes each at 70F.  
 Halving servicing time quadruples pressure drop.

## Propellant Quantity Gaging

In order to operate in a safe and efficient manner, the LFV pilot must have an accurate propellant-quantity gaging system. Such a system would provide the needed in-flight planning information, aid in propellant servicing, and facilitate preflight checkout. Seven specific concepts were considered before the selection of a specific propellant quantity gaging system. Several of these are currently employed in manned or unmanned spacecraft and launch vehicles. Table 1-34 presents a comparison of the characteristics of each of these candidate concepts.

Desirable features which must be exhibited by the selected concept include good accuracy, minimum power consumption, simplicity and its attendant reliability and little or no required development. The Apollo program employs in its various vehicles and stages the PVT, capacitance probes, and electrical point sensors. When designed with appropriate redundancy and using computer processing (onboard and ground), these systems fulfill their accuracy requirements. The PVT system employed in the Apollo SM/RCS is adequate for its intended use. Capacitance probes and electric point sensors are used in both the SM SPS and preceding booster stages. They are accurate, but require substantial electronic signal processing and a computer readout. Other gaging concepts, such as the measurement of tank inlet to outlet pressure differential, using measured values of thrust and/or vehicle acceleration to infer propellant quantity or integrated propellant flow rate are considered relatively unproven and also require electronic signal processing. Those systems using a thrust measurement depend on a widely varying parameter. All of the previous systems require to some degree the use of electronic sensors, transducers, and a logic processor to define the propellant quantity remaining. The remaining gaging concept, an NR SD-conceived approach derived from previous well proven launch vehicle point sensor technology, is considered to be the most desirable for this application. Its only competitor from the accuracy viewpoint is the electrical point sensor concept. From the simplicity viewpoint, it has no competition.

The selected propellant quantity gaging concept, as noted in Figure 1-48, uses prisms as point sensors to indicate propellant level within the LFV tanks. A direct reading control panel mounted indicator requires no electronic signal processing and provides an absolute indication of liquid level within system accuracy.

Figure 1-48 illustrates the detailed conceptual design of the prism/fiber optic gaging device. In this concept, many optical prisms are suspended within the tank at specific levels. The prism, held by a support



Table 1-34. Gaging Concept Comparison

Consideration	PVT	$\Delta P$ Head	Thrust Weight	Thrust	Prism and/or Fiber Optic	Capacitance Probe	Electrical Point Sensors
Measured or inferred variable	Ullage	Liquid level	Weight	Flow rate	Liquid level	Liquid level	Liquid level
Electronic required	Yes	Yes	Yes	Yes	No	Yes - complex	Yes - moderately complex
Valid during flow	No	Yes	Yes	Yes	Yes	Yes	Yes
Affected by: Vehicle acceleration	No	Yes	Yes	No	No	No	No
Slosh	No	Yes	No	No	Yes	Yes	Yes
Temperature	Yes	No	No	No	Slight	Yes	Slight
Required transients	Yes	Yes	No	No	No	No	No
Sensor	P, T	P	F, a	F	Prism	Capacitance	Conductance
Accuracy (percent)	7 to 10	Very poor in flight	6 to 10	4 to 7	.2 to 3	4 to 6	2 to 3

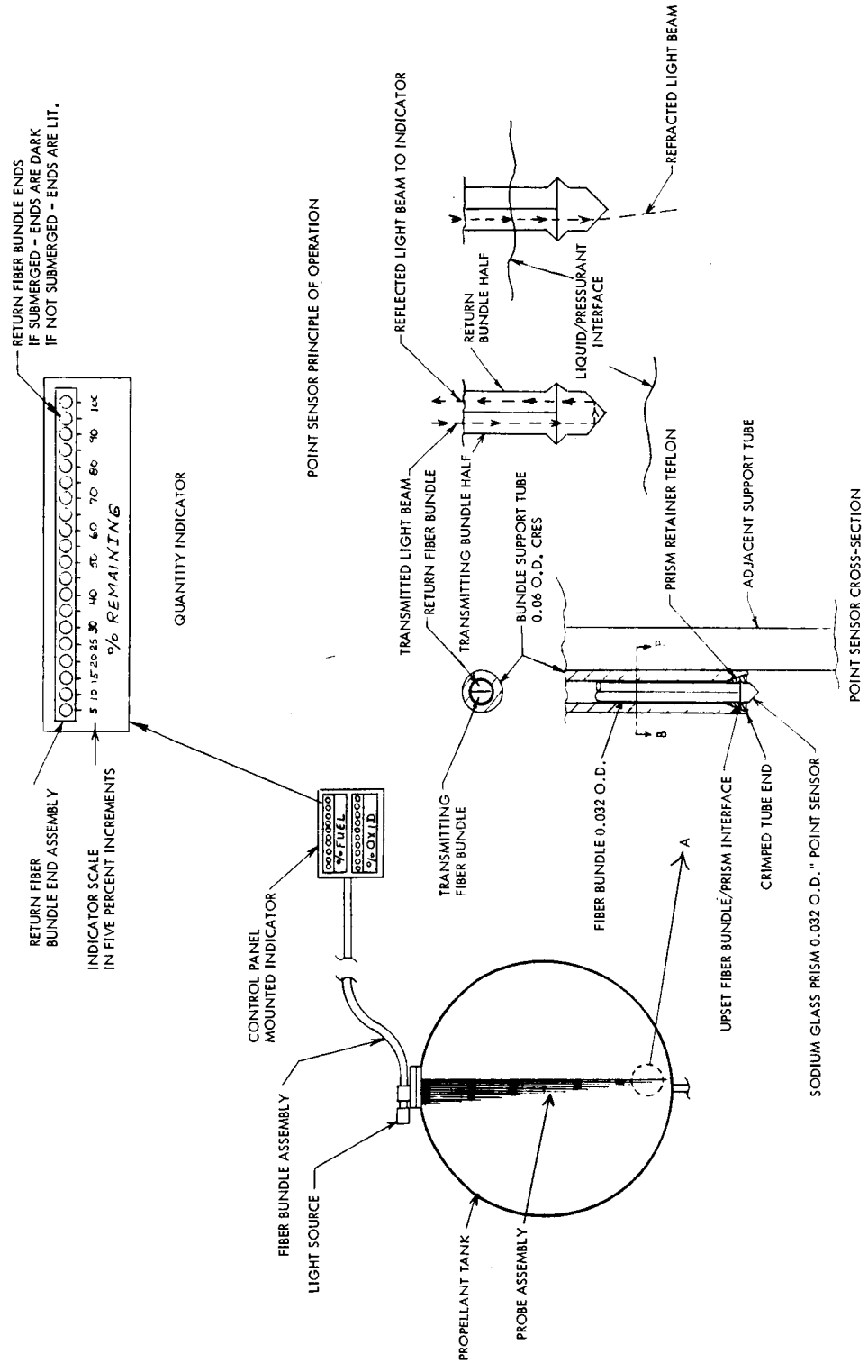


Figure 1-48. LfV Propellant Quantity Indicator Conceptual Design





tube, interfaces with a small two-path fiber-optic bundle. This bundle, as noted in Figure 1-48 may be as small as 1/32 inch in diameter. The fiber-bundle support tube is approximately 1/16 inch in diameter. An externally mounted light source illuminating all transmitting fiber bundle halves is mounted in close proximity to, but external from the propellant tank. The light rays are transmitted through the fiber optics to the prism within the tank. If the specific prism is submerged within propellant, the resultant effect of the prism and propellant indices of refraction are such as that no light is reflected. It is transmitted into the propellant and diffused. If the prism is above the propellant level, the differences in indices of refraction between the prism and pressurant are such that the light rays are totally reflected into the return fiber bundle half and transmitted to the propellant quantity indicator on the control panel.

Noting Figure 1-48, it is seen that 20 prism/fiber-optic point sensors are employed. This provides sensing at 5-percent increments and yields an accuracy of  $\pm 2\frac{1}{2}$ -percent. The indicator illustrated in this figure is composed of the return fiber half ends which glow if above the propellant level. Fiber optic end covers consisting of colored glass or Lucite may be employed to distinguish between fuel and oxidizer on adjacent quantity indicators. In this fashion, the LFV pilot is provided with an accurate and readily readable indication of propellant quantity. The ability to read the sensors in sunlight can be enhanced by several methods, such as cover shields.

A feasibility test model incorporating five point sensors and their attendant prisms and fiber optics has been constructed and successfully tested at Space Division. While this concept is not thoroughly developed for the LFV application, its inherent simplicity promises a short, low-risk development program. Point sensors of this type have been used for the Titan II, Tian I and Saturn 1B. In these applications employing both cryogenic and earth storable propellant combinations, fiber optics were not employed due to the length of signal transmission and subsequent telemetry. In those applications, a photocell was used to transmit an electronic signal.

#### Pressure Measurement (items 007 and 012)

A wide range of pressure transducers has been qualified for the Apollo propulsion systems. When more exact design requirements exist, there should be no problem obtaining suitable helium pressure measurement systems for the LFV.

## Propulsion System Servicing

The following procedure has been developed as a tentative concept for LFV propellant servicing. First discussed is the assumed propulsion-system status before servicing, then the conceptual procedure for initial servicing, and finally the differences between the first and subsequent servicing operations. Item numbers shown in parentheses as (001) are keyed to Figure 1-46 and Table 1-30.

### Preservicing Status

As it is loaded on the LM before launch and offloaded on the lunar surface, the LFV propulsion system is assumed to be in the following condition:

- a. Helium tank assembly (002 through 004) installed.
- b. Dust caps installed on fill-vent connectors, both LFV halves (021 through 024) and ground halves (031 through 034).
- c. Manual propellant valves (019 and 020) closed.
- d. Engine valves closed.
- e. Nominal (50 psia) helium pressure in system (higher than servicing pressure, yet substantially lower than normal operating pressure).

### Initial Servicing

- a. Observe that system pressure (012) is within allowable limits of preflight pressure.
- b. Close manual propellant valves (019 and 020).
- c. Open engine valves to remove helium from propellant manifold. Close engine valves.
- d. Obtain oxidizer vent hose assembly from LM storage, remove dust caps (021 and 031) and connect oxidizer vent. Observe stabilization of oxidizer pressure (012).
- e. Uncoil oxidizer fill line from LM and remove dust caps on (023 and 033). Attach oxidizer fill line to LF and observe oxidizer pressure (012) still stable.

- f. Actuate oxidizer fill system open in LM. (Note: It is assumed either that this is a one-time action, or that some other provision in the LM system assures that the fill hose, once filled with oxidizer, always has provision for expansion.)
- g. The oxidizer tank will now fill automatically at a speed regulated by:
  - 1. The system pressure provided by the LM
  - 2. Orifices and/or other line losses
  - 3. Back pressure provided by the vent relief (039)
- h. Monitor oxidizer fill by observing the sight glass in the vent line (035).
- i. When bubble-free liquid appears in the line (035), turn the fill coupling (033) closed.
- j. When vent flow ceases, turn the vent coupling (031) closed, but do not remove it.
- k. Detach the oxidizer fill line, replace dust caps on the coupling halves (023 and 033), and stow the oxidizer fill line.
- l. Repeat the equivalent of steps d through k to service the fuel tank.
- m. Remove pressure-tight dust cap from helium connector tank half (005) and discard.
- n. Crack helium valve (003) slightly to raise system pressure (012) to nominal. Close helium valve.
- o. Open oxidizer vent coupling (031) to vent excess oxidizer and assure proper ullage.
- p. When sight glass in vent line (035) shows essentially liquid free flow, close vent coupling (031). Remove oxidizer vent hose assembly, install dust caps on (021) and (031), and stow oxidizer vent hose assembly.
- q. Repeat steps (o) and (p) for the fuel system.
- r. Open helium valve (003) until the pressure sensors (012) indicate proper pressure.

- s. Close helium valve (003) and observe that helium system pressure is maintained (012).
- t. Open propellant valves (019 and 020). Observe that helium pressure (012) decreases and stabilizes.
- u. Open helium valve (003) and observe proper helium pressure (012).
- v. Test fire engines at low thrust level. (Engine bleed is obtained at this time.)

### Subsequent Servicing

Servicing for subsequent missions would be about the same as the initial servicing above, except that:

- a. At step a under initial servicing, the observed pressure would be full system pressure, and it would be necessary to close the helium valve (003).
- b. Since the propellant lines would already be filled, steps c, f, and m under initial servicing should not be required.
- c. Steps n through g precede helium vessel replacement (d and e below) to utilize residual helium in the spent tank.
- d. Obtain replacement helium vessel from LM stowing compartment. Remove and discard dust cap from (004).
- e. Attach helium vessel to LFV connecting (004) to (005). Observe that pressure (007) stabilizes at nominal level.
- f. The pressure decrease in step t would not occur, since the propellant lines are already filled with liquid.



APPENDIX A  
ROCKET ENGINE SUBCONTRACTOR  
PARAMETRIC DESIGN DATA

## APPENDIX A

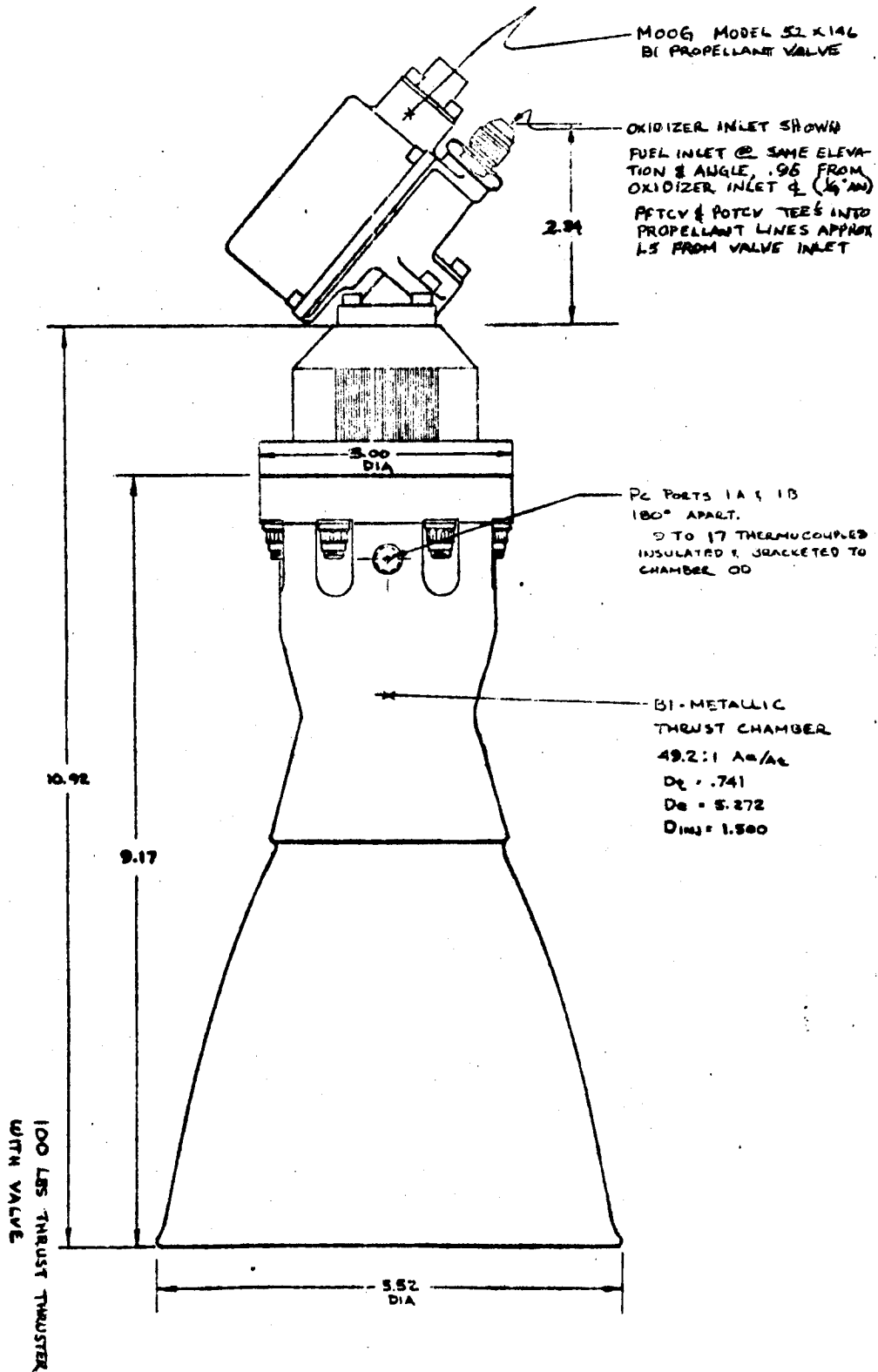
### ROCKET ENGINE SUBCONTRACTOR PARAMETRIC DESIGN DATA

The following appendix presents rocket engine parametric design data formulated by the various cognizant rocket engine manufacturers and submitted to NR-SD during the LFV study. These data were used extensively during both the propulsion subsystem optimization study and the subsequent concept trade-off studies. The Space Division wishes to express its thanks to these companies who participated on an unfunded basis in a very complete and timely fashion.

Aerojet General Corporation  
Bell Aerosystems  
Rocketdyne Division, North  
American Rockwell  
The Marquardt Corporation  
TRW Systems

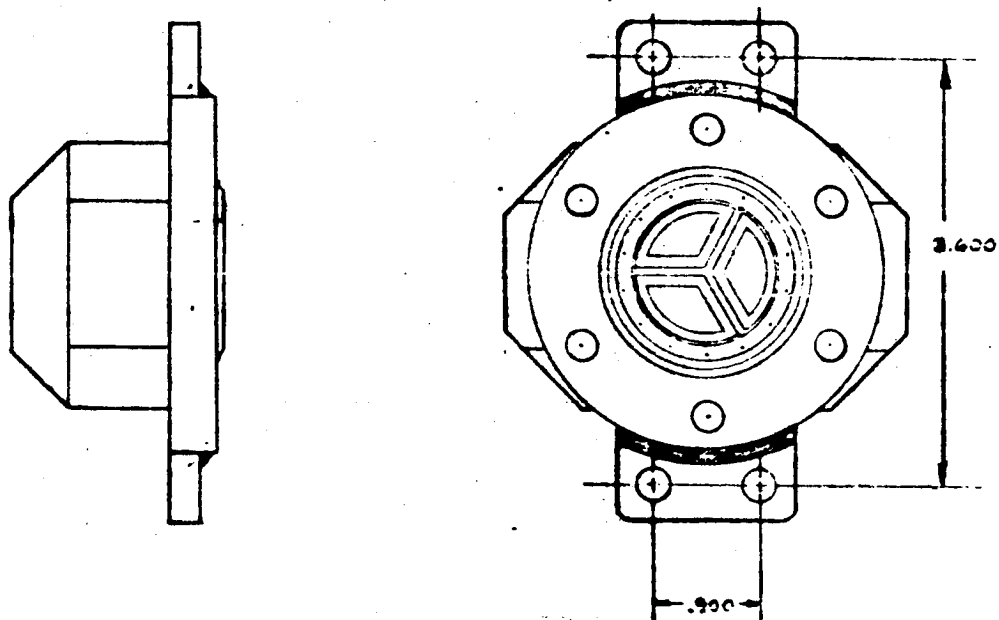
AEROJET GENERAL  
LIQUID BIPROPELLANT ROCKET ENGINE DATA  
PREPARED FOR  
NORTH AMERICAN ROCKWELL CORPORATION

AEROJET-GENERAL CORPORATION  
PROPULSION SYSTEMS DEPARTMENT  
SACRAMENTO, CALIFORNIA

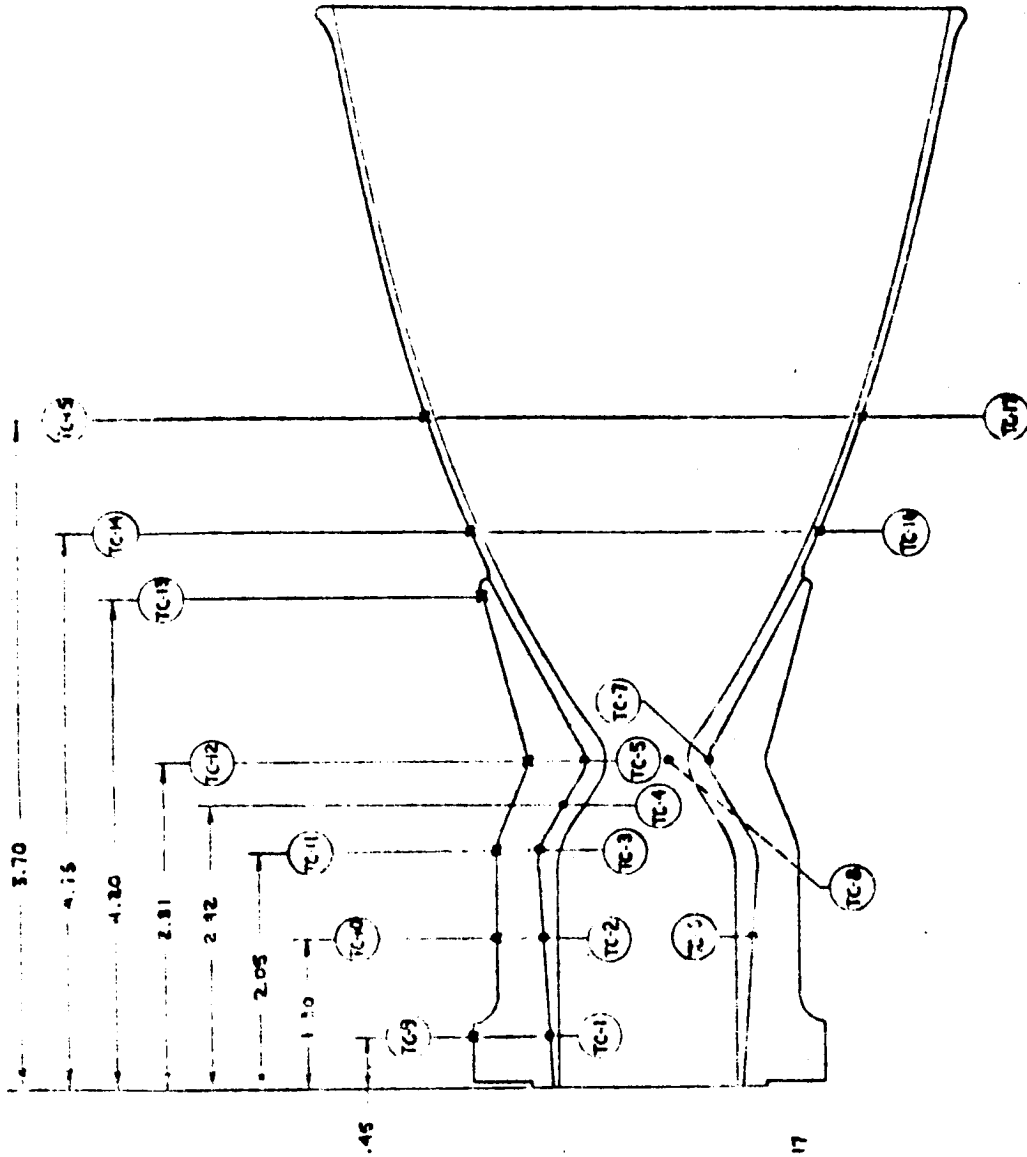


A-1

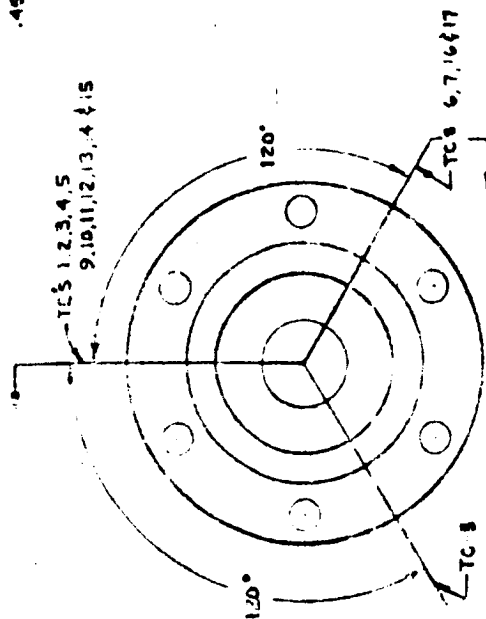




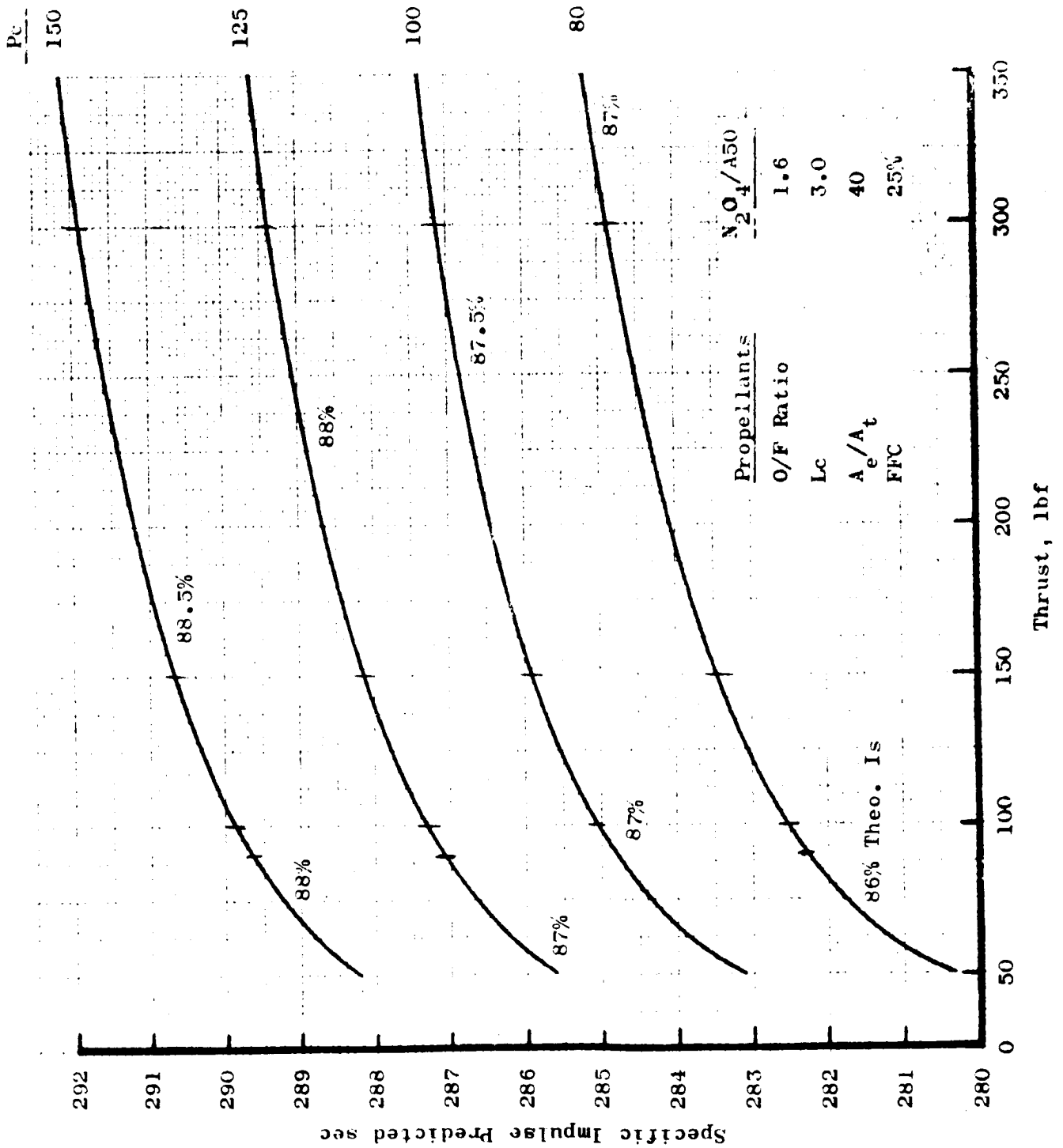
INJECTOR WITH THRUST MOUNT LUG



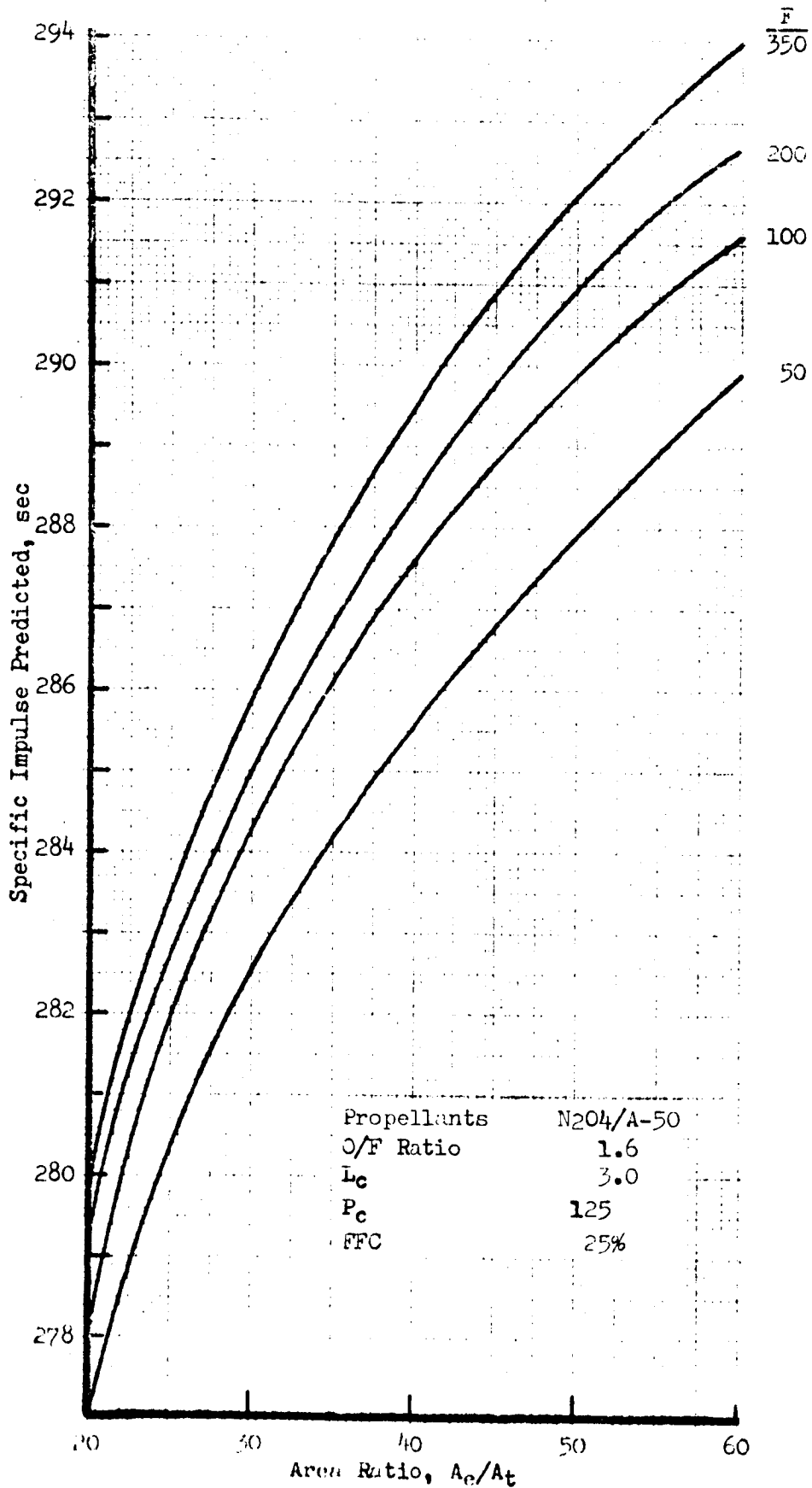
THEMOCOUPLE LOCATIONS  
100% THRUST ENGINE  
S/A 001  
TEST NO 3292-A01-0M-001



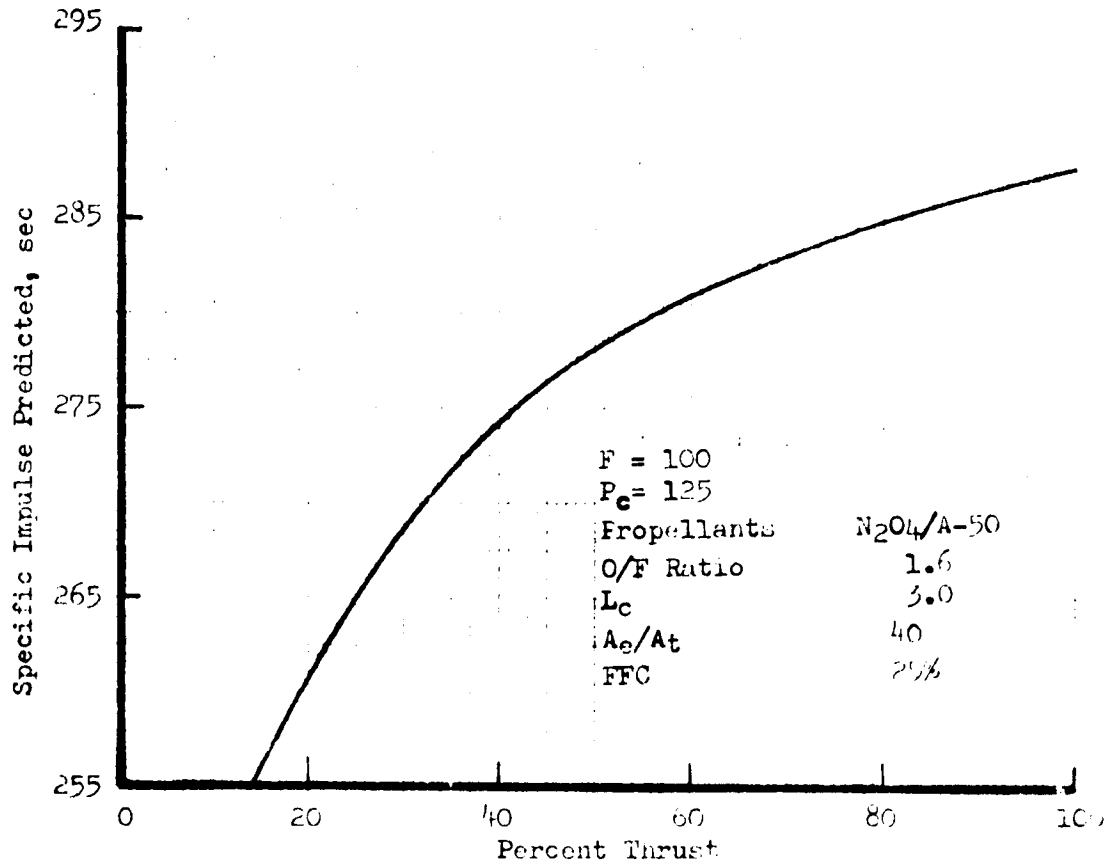
X INTERNAL (SKIN) THEMOCOUPLE  
O INTERNAL (BETWEEN COPPER & INCOMEL) THEMOCOUPLE



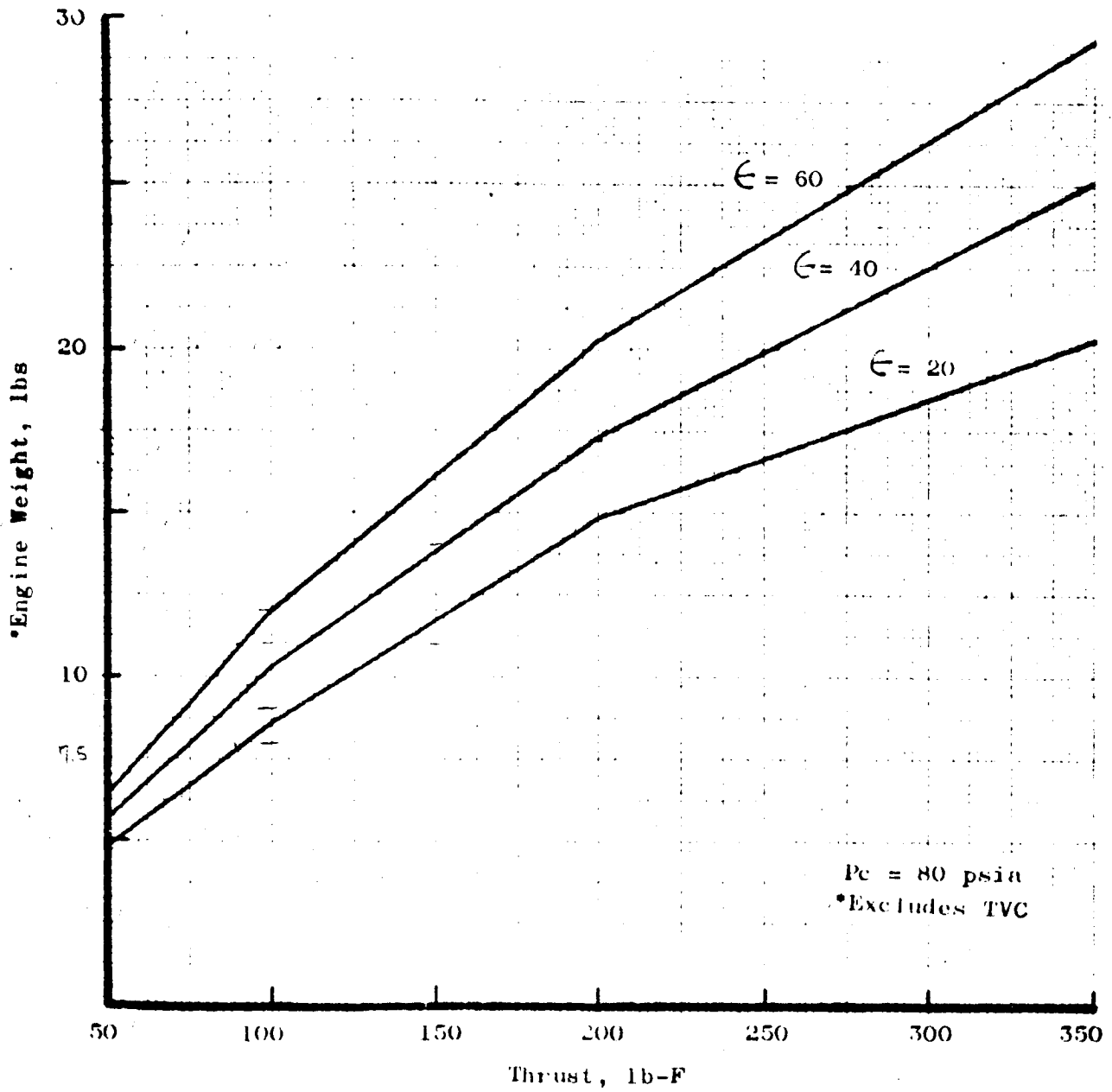
Engine Performance, Specific Impulse Versus Thrust



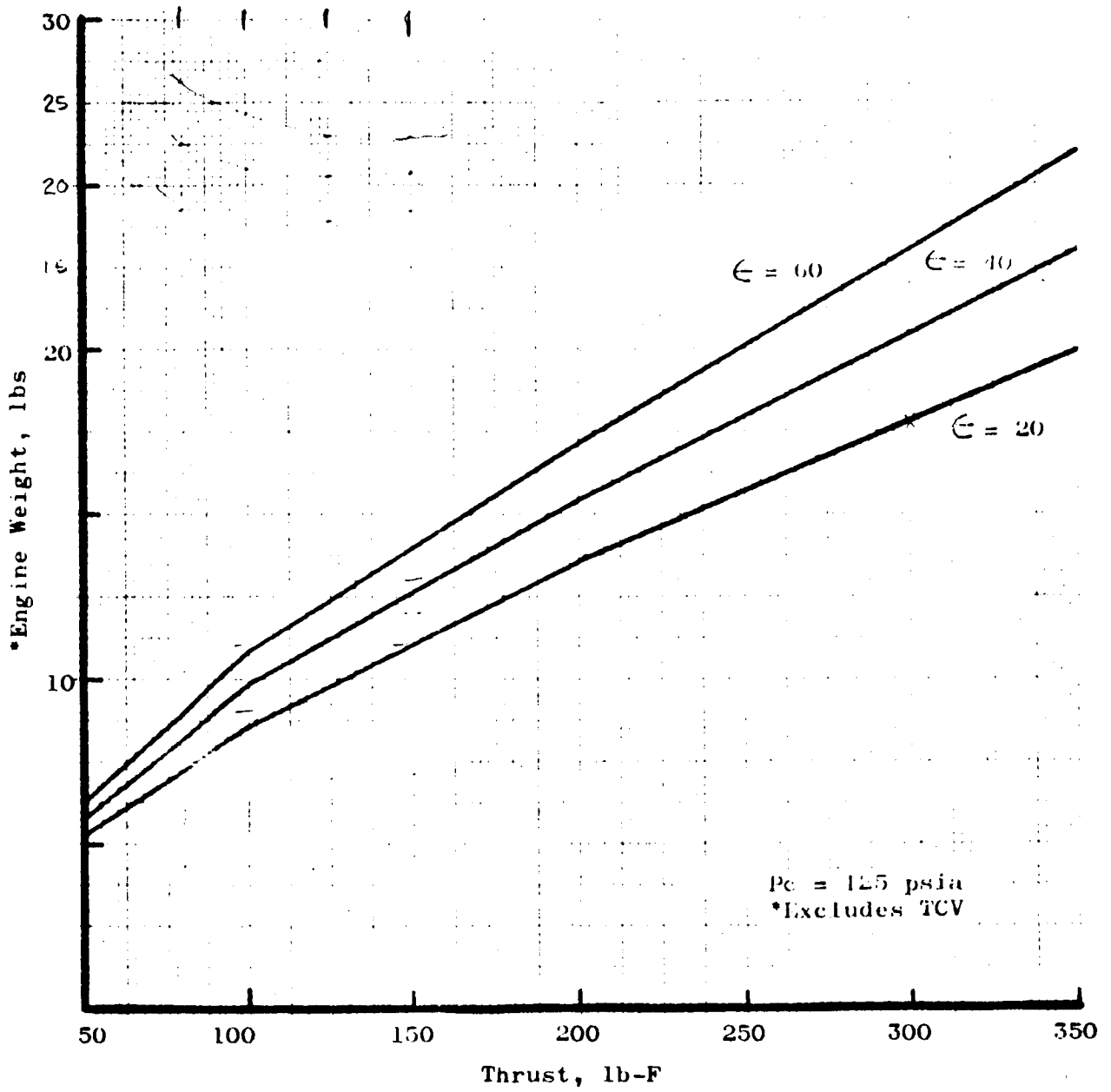
Engine Performance, Specific Impulse Versus Area Ratio



Engine Performance, Specific Impulse Versus Percent Thrust

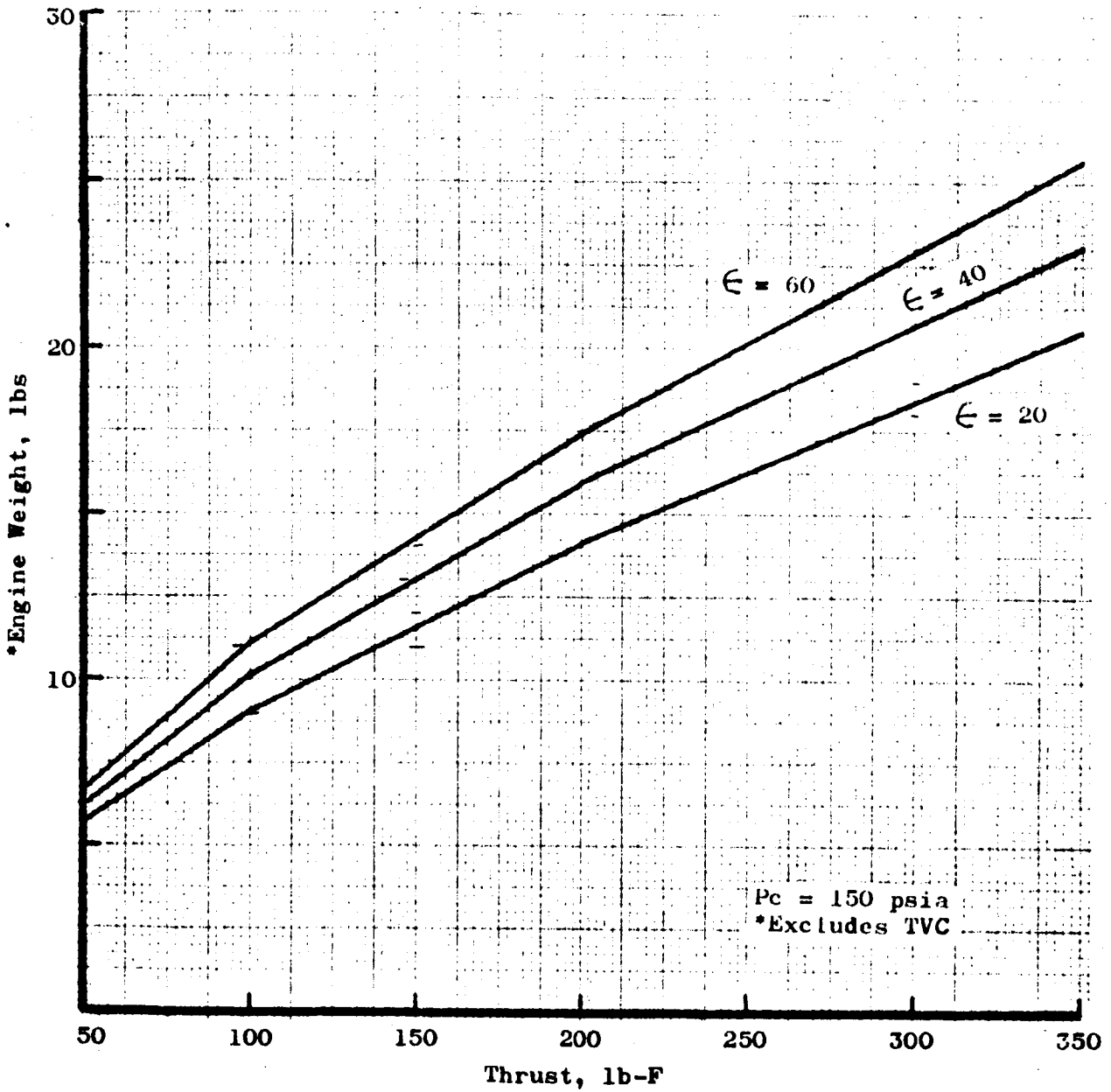


Throttling Engine Length,  $P_c = 80$  psia



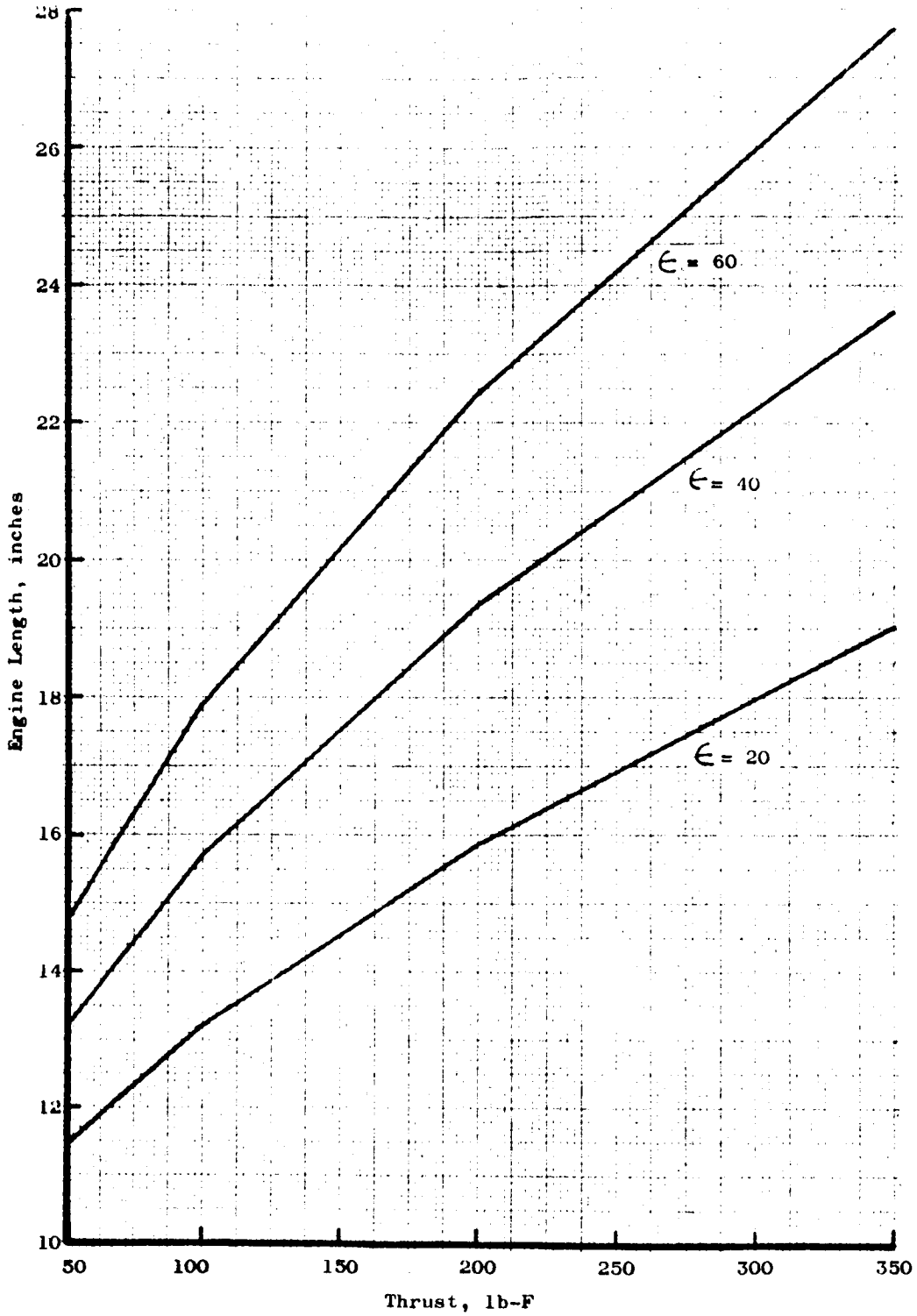
Throttling Engine Length,  $P_c = 125$  psia

A-8

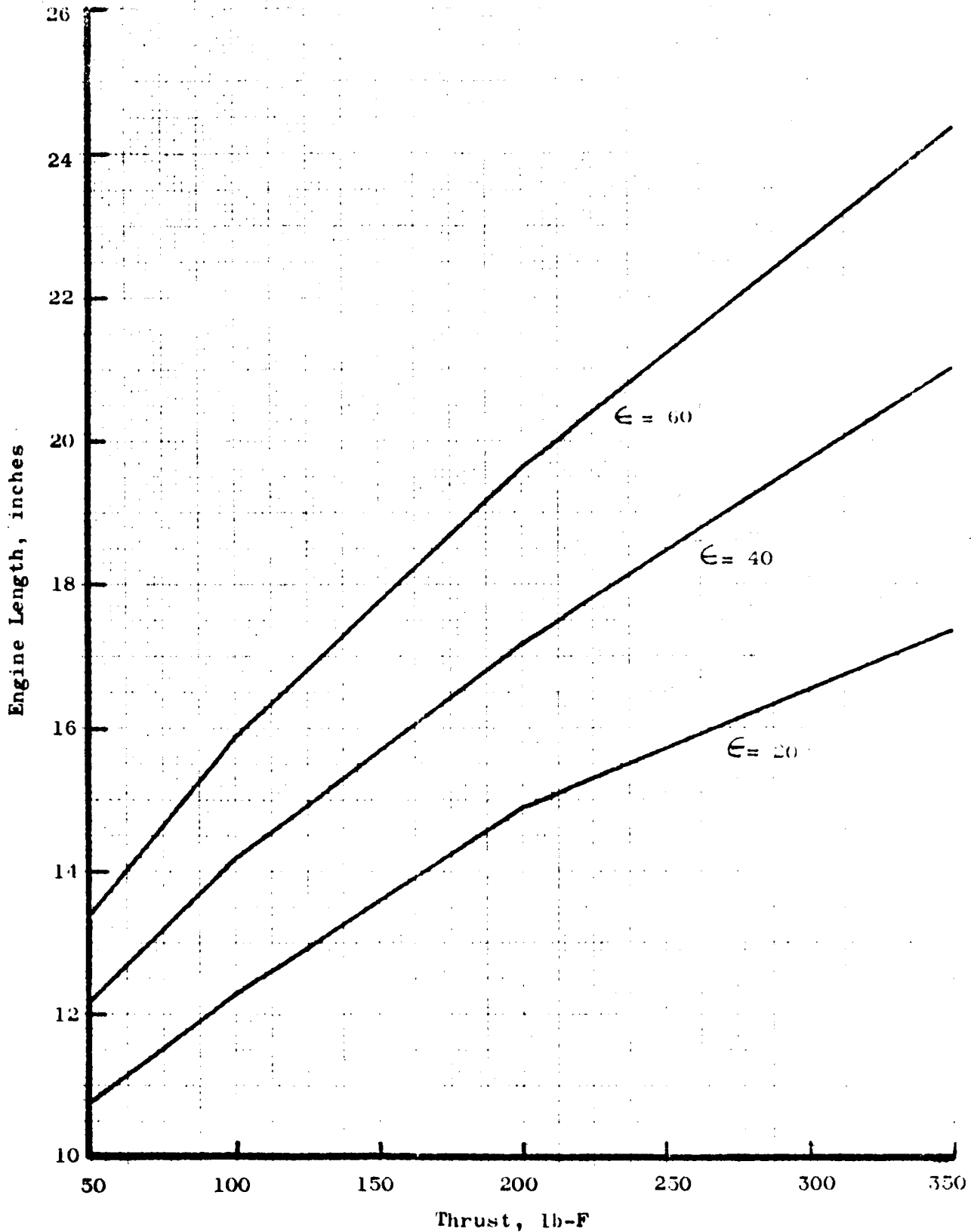


Throttling Engine Length,  $P_c = 150$  psia



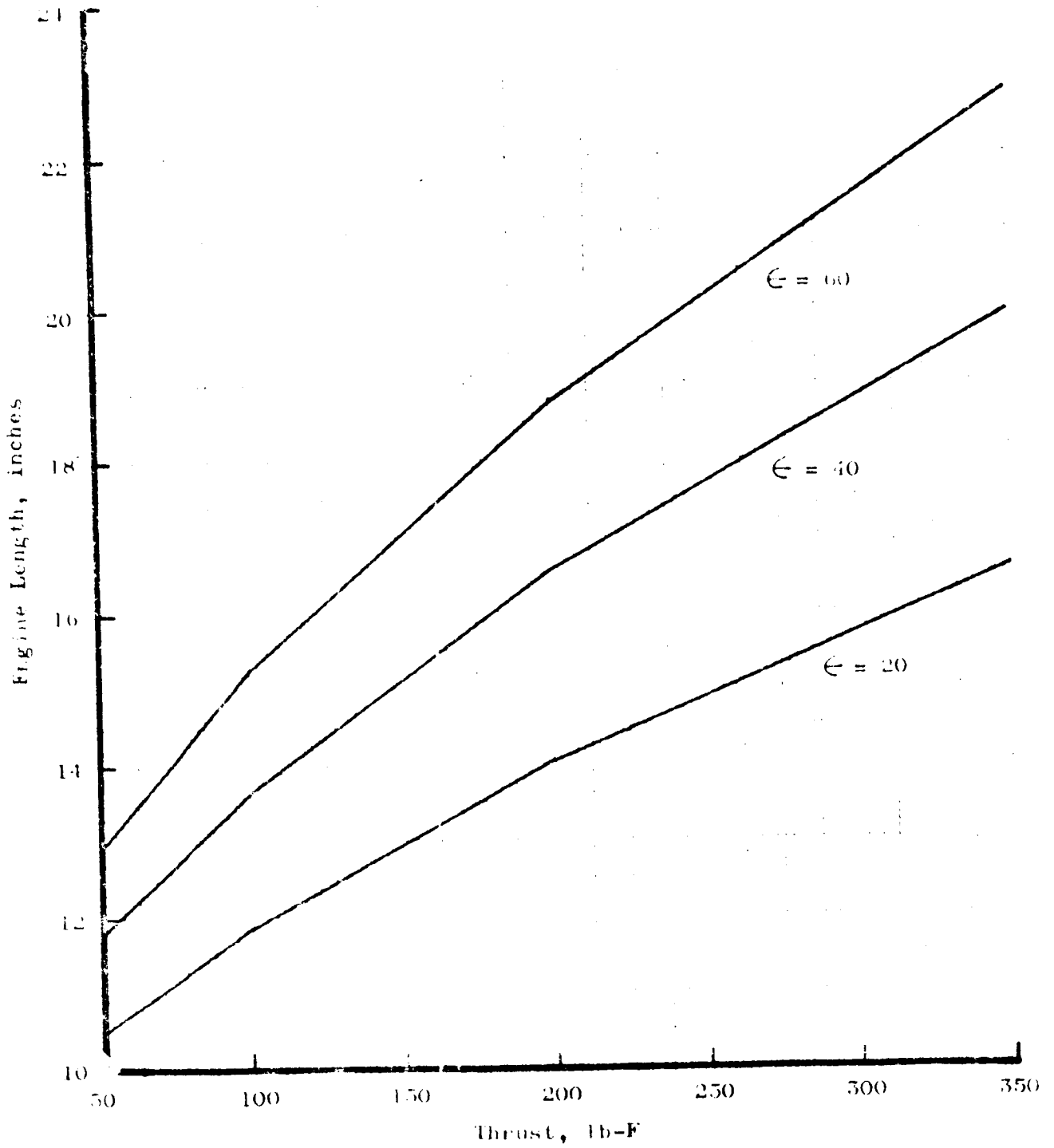


Throttling Engine Envelope,  $P_c = 80$  psia



Throttling Engine Envelope,  $P_c = 150$  psia

A-11

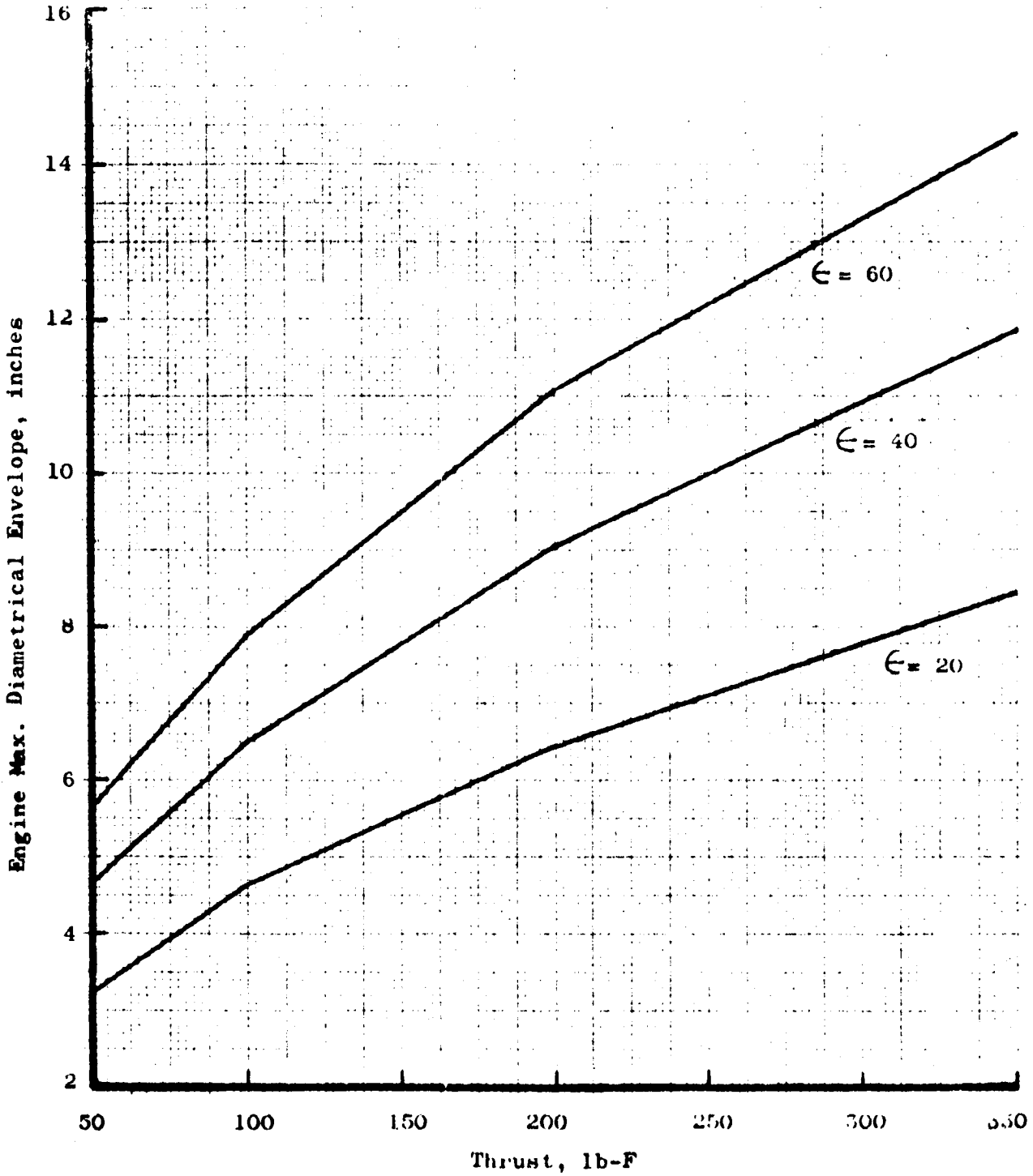


Throttling Engine Envelope,  $P_c = 125$  psia

A-12

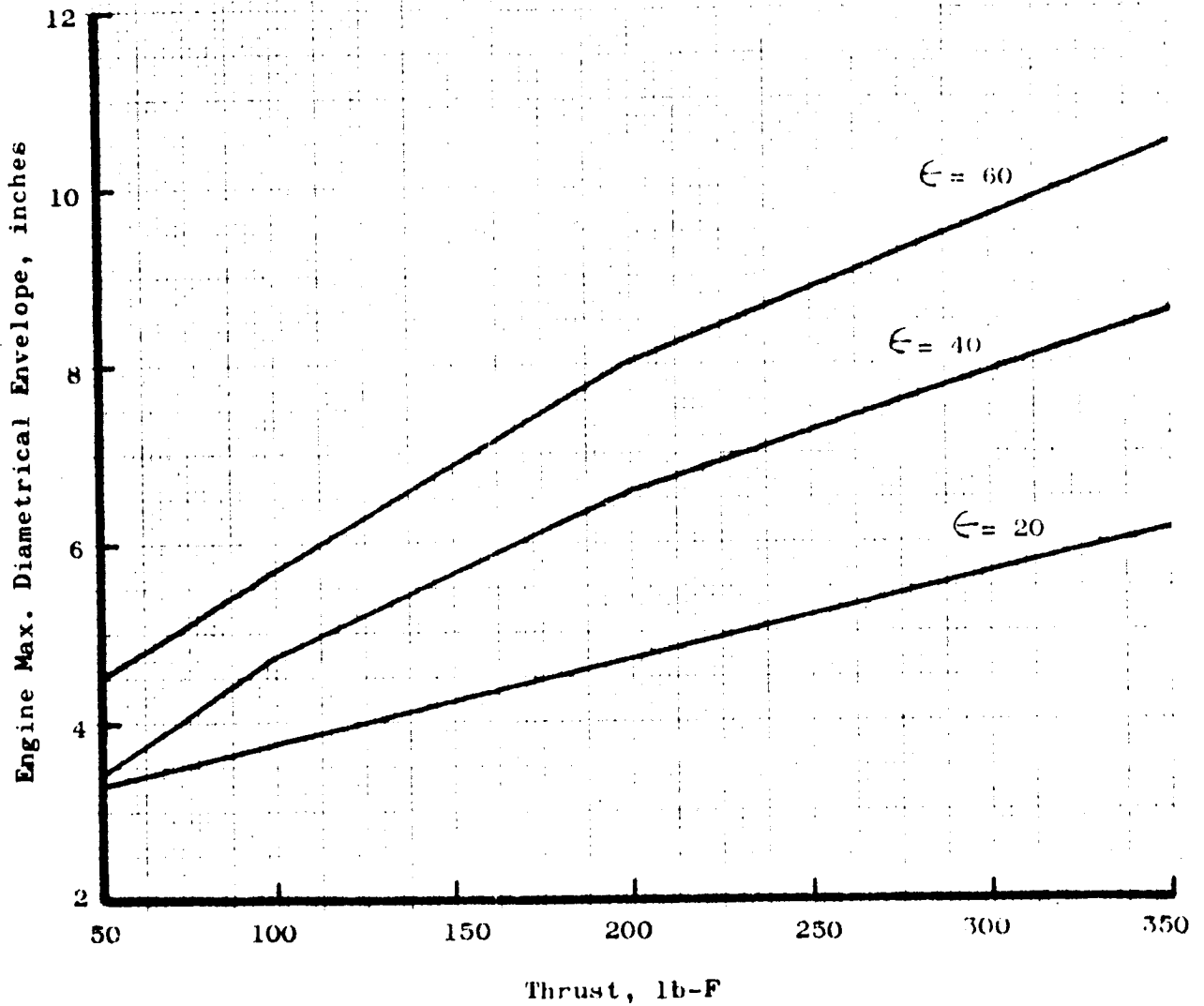
- 198 -

SD 69-419-3

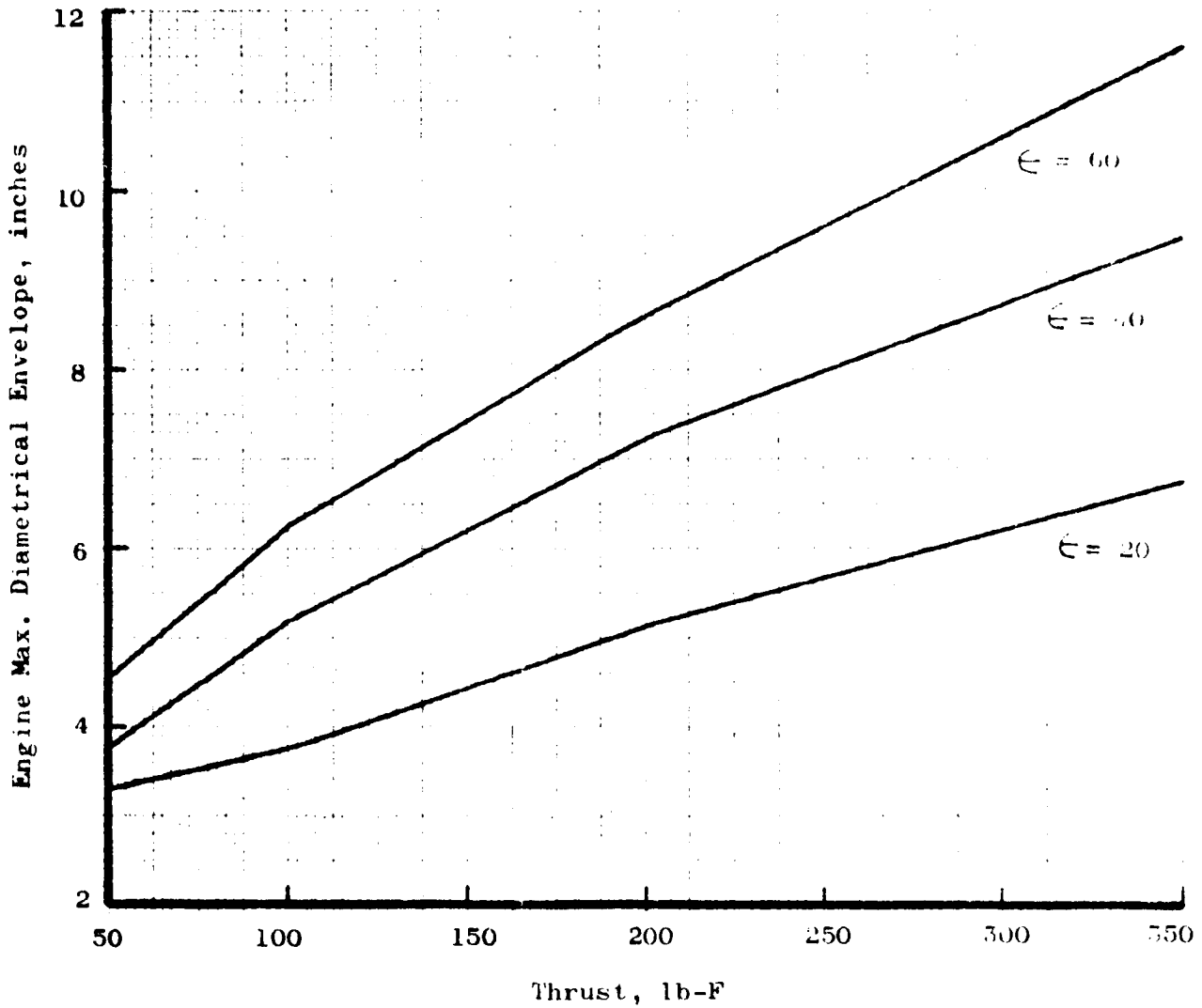


Throttling Engine Envelope, Pc = 80 psia

A-13



Throttling Engine Envelope,  $P_c = 150$  psia



Throttling Engine Envelope,  $P_c = 125$  psia

BELL AEROSYSTEMS

THROTTLEABLE ENGINES FOR THE  
NORTH AMERICAN ROCKWELL  
LUNAR FLYING VEHICLE STUDY

REPORT NO. D8414-953003

February 1969

## THROTTLEABLE ENGINES FOR THE NORTH AMERICAN-ROCKWELL LUNAR FLYER

### INTRODUCTION

The nature of the lunar flying vehicle (LFV) mission places a premium on engine reliability. Engine performance and weight may be traded off against other measures of merit. Reliability, however, is not negotiable. The LFV engine(s) must provide lift, acceleration, attitude control, safe deceleration and soft landing for a manned vehicle.

The redundancy approach to high reliability is feasible for this mission, but this can be compromised by any resulting requirement to detect failures and initiate corrective action before critical LFV attitudes or flight paths are reached.

The best approach to high reliability is intrinsic engine design reliability. High intrinsic reliability is achieved by minimizing the number of components that must operate successfully and by providing large operating margins on the design capabilities of these components (design simplicity and design margin).

### ENGINE DESIGN

This design simplicity and design margin approach to high intrinsic reliability was successfully employed by Bell in the design and development testing of a 100-pound throttleable engine for the Lunar Manned Flying System under NASA contract NAS8-20086 with the Marshall Space Flight Center. The major design features of this engine (Model 8414) are as follows:

1. A mature silicide coated columbium thrust chamber technology-operating in the radiation cooled mode at a maximum temperature of 2600 F to provide a minimum design margin of 500 F on the 3100 F material and coating capability (with  $N_2O_4/0.5 N_2H_4 + 0.5$  UDMH propellants)
2. Fixed injection geometry with some compromise in throttling performance to avoid the degraded reliability inherent in variable injection geometry





3. Separate propellant shutoff valve to capitalize on existing proven valves from fixed thrust engines and eliminate the need to compromise throttle valve design to provide this feature
4. Variable area cavitating venturi throttle valves for thrust modulation control. The bipropellant venturis decouple the flow control, by variable cavitation, and from injection and combustion variations
5. Thrust vector control can be provided by differential throttling and/or single axis or two axis gimbaling, depending on the number and location of engines in the LFV, or by jet vanes, jetavators, secondary injection, or additional attitude motors

The validity of this intrinsic reliability design approach was demonstrated by four engines of the 100-pound Model 8414 design which were built and tested. From the first to the last test, 72 runs were completed without engine failure or malfunction of any kind.

The engine designs proposed for the North American-Rockwell LFV are the basic Model 8414 engine scaled through the thrust and throttle ratio range of interest to NR. Extensive design and test data for the 100-pound engine can be found in References 1, 2 and 3. Discussion here will therefore be concerned with design and performance changes with thrust, rated chamber pressure, nozzle expansion ratio and method of valve actuation and gimbaling.

The basic 150-pound engine design is given in Figure A-16. The design incorporates a single axis gimbal mount that is integral with the valve body. The propellant valve shown is a normally closed Moog torque-motor-operated bipropellant shutoff valve design that has been space qualified on the engines of the Minuteman III program. The opening power requirement of this valve is 1.05 amp at 28 vdc. The throttle valve (not shown) for this engine can be remotely located on a LFV pilot control quadrant and connected to the propellant valve inlet ports by flexlines. The electron beam welded assembly of 8 triplet capillary manifold injector and columbium thrust chamber is bolt mounted to the valve body with an omega seal downstream of the propellant valve seats. The 8-triplet injector has been throttle tested at sea level.

A remotely located, manually operated modification of the Fox variable area cavitating venturi throttle valve is given in Figure A-17. The configuration shown is only typical of several possible arrangements to permit rod, cam or cable positioning of the throttling pintles, normally open or normally closed force balance, or provision for differential throttling among 2 or more valves.



Bell 150-Pound-Thrust Throttleable Engine,  
Single-Axis Gimbal Mount

(Figure omitted. Copy - not suitable for  
reproduction - is on file with contractor.)

A-16

Bipropellant Throttling Valve, Bell  
150-Pound-Thrust Engine

(Figure omitted. Copy - not suitable for  
reproduction - is on file with contractor.)

A-17



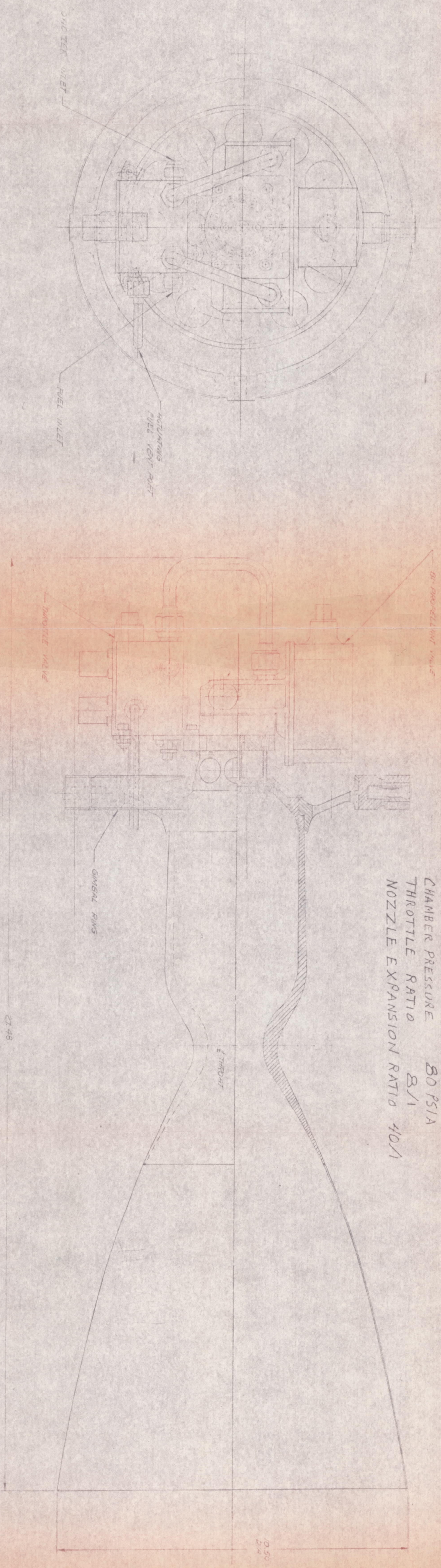
The basic 300-pound engine design is given in Figure A-18. This design incorporates a two-axis gimbal mount and a 16 triplet injector that has been throttle tested at sea level. The valve arrangement is identical with the demonstrated 100-pound engine and the propellant valve is a minor modification of the Moog valve developed for the axial engine of the Minuteman III Post Boost Propulsion System.

The bipropellant throttle valve was developed by the Fox Valve Development Company. It is designed for 87 percent maximum venturi pressure recovery at rated thrust flows. The valve is driven by a double-acting hydraulic piston operated by fuel pressure and piloted by two normally closed solenoid valves. The control piston is liquid locked in position when the pilot solenoid valves are deenergized. The throttle valve (TV) is opened by the differential area of the control piston when the TV opening solenoid valve is opened to equalize pressure on both sides of the piston. The power requirement of the pilot solenoid valves is 1.0 Amp at 28 vdc. The TV is closed by differential pressure when the TV closing solenoid is opened to bleed the high-area side of the control piston. The opening and closing times are 300 msec for full stroke in either direction. Throttle-valve operation is completely independent of propellant valve operation.

All the engine designs can meet the following table of NR requirements for LFV engines:

Operational date	Mid-1972
Propellants	$N_2O_4/A-50$
Nominal mixture ratio	1.6
TVC Angle (maximum)	$\pm 10$ degrees
Max TVC rate	10 deg/sec
Max TVC acceleration	50 deg/sec <sup>2</sup>
Number of firings	60
Engine life maximum burn	10,000 sec
Mission burn time	1,500 sec
Typical thrust time	
Nominal sortie - 2 firings, 416 sec total duration	

ENGINE SPECIFICATION  
 CHAMBER PRESSURE 80 PSIA  
 THROTTLE RATIO 8/1  
 NOZZLE EXPANSION RATIO 40/1



① 209, 210

② 209, 210

A-18  
- 209, 210 -

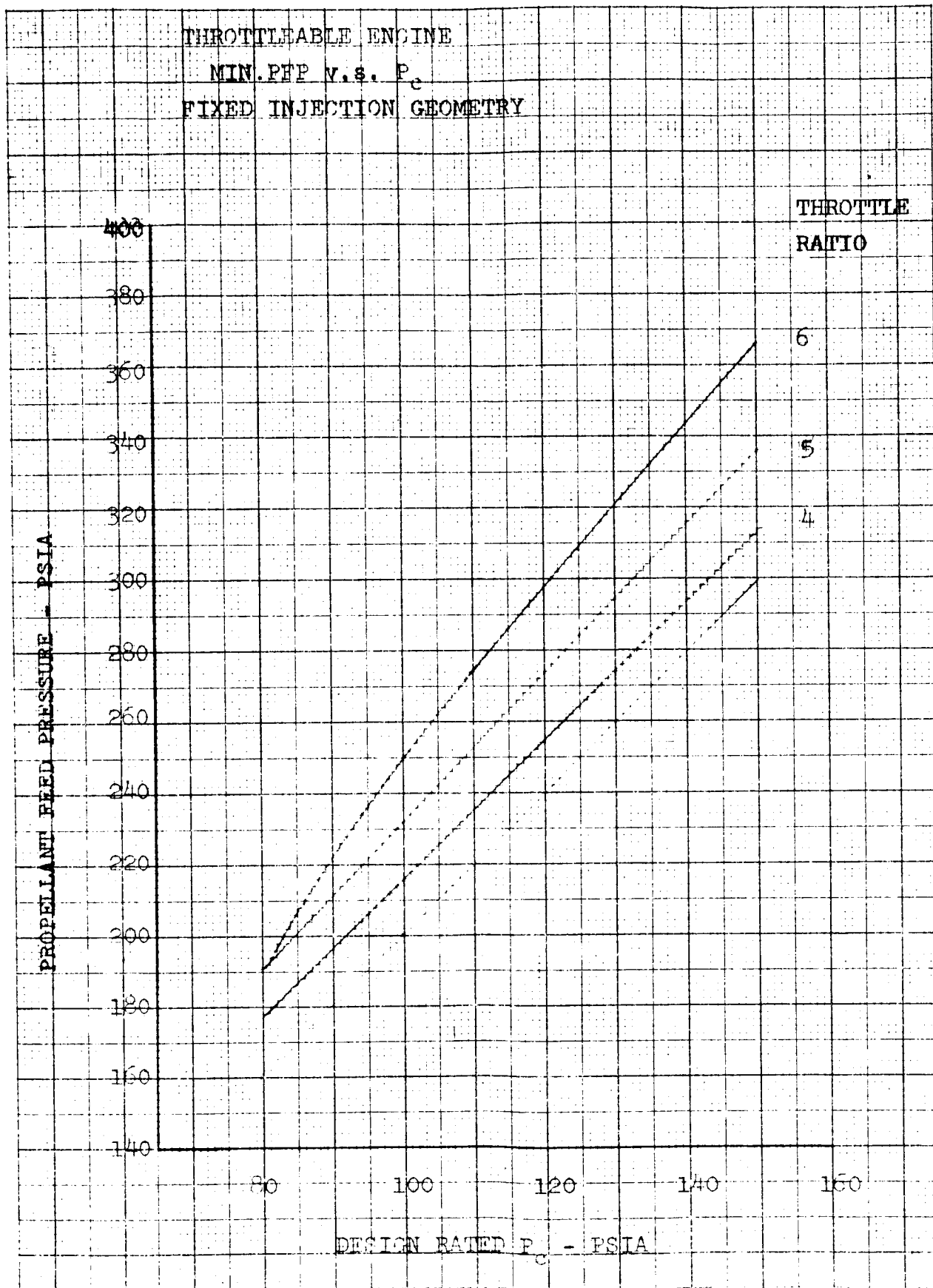
SD 69-419-3

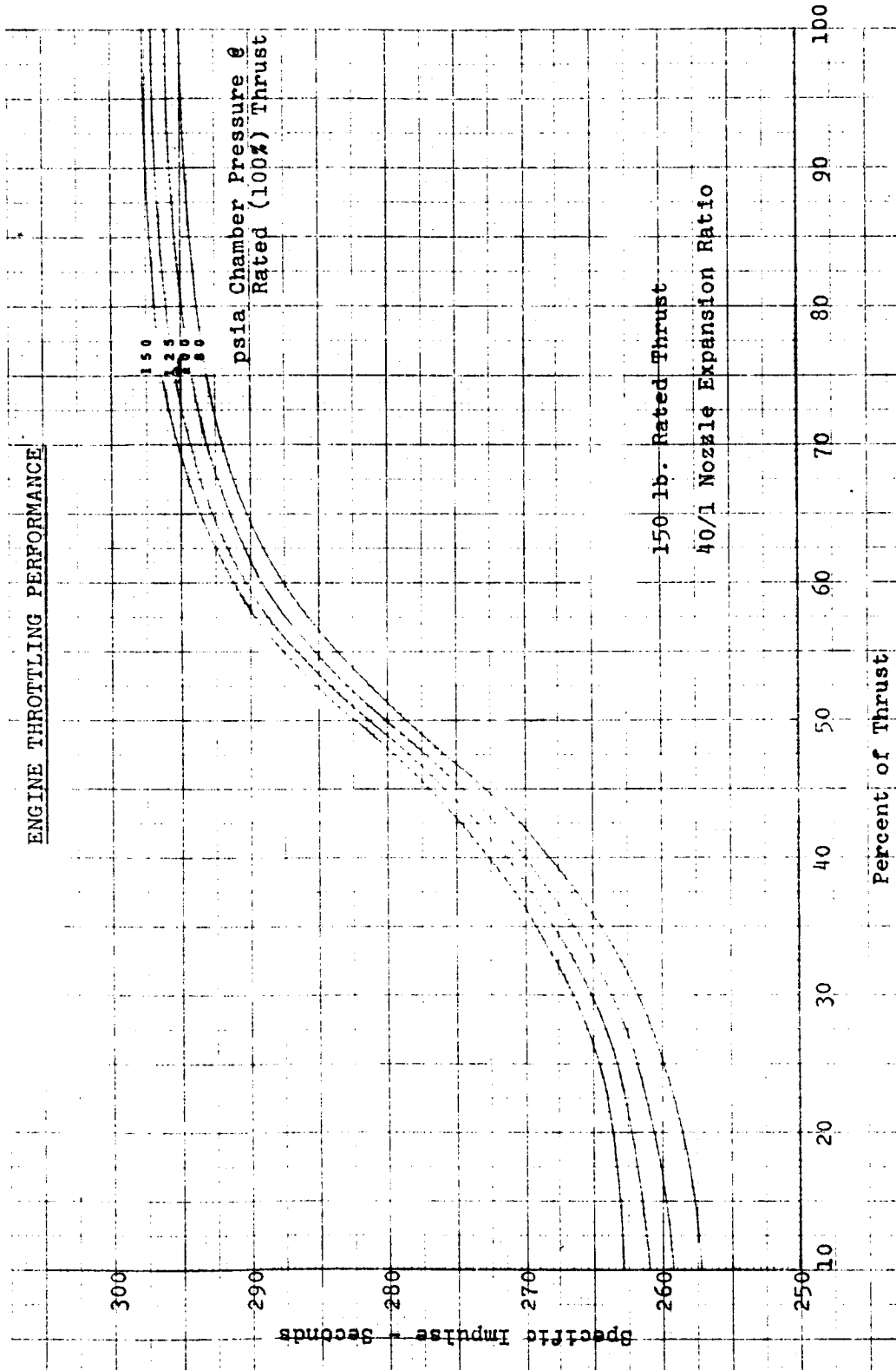
	Percent (maximum thrust)	Duration (seconds)
a. First Firing (208 seconds)	95 - 89	80
	62	42
	86 - 81	76
	57	10
		<hr style="width: 50px; margin: 0 auto;"/>
b. Second Firing (208 seconds)	81 - 77	80
	43	42
	59 - 57	76
	39	10
		<hr style="width: 50px; margin: 0 auto;"/>

#### PERFORMANCE AND PROPELLANT FEED PRESSURE

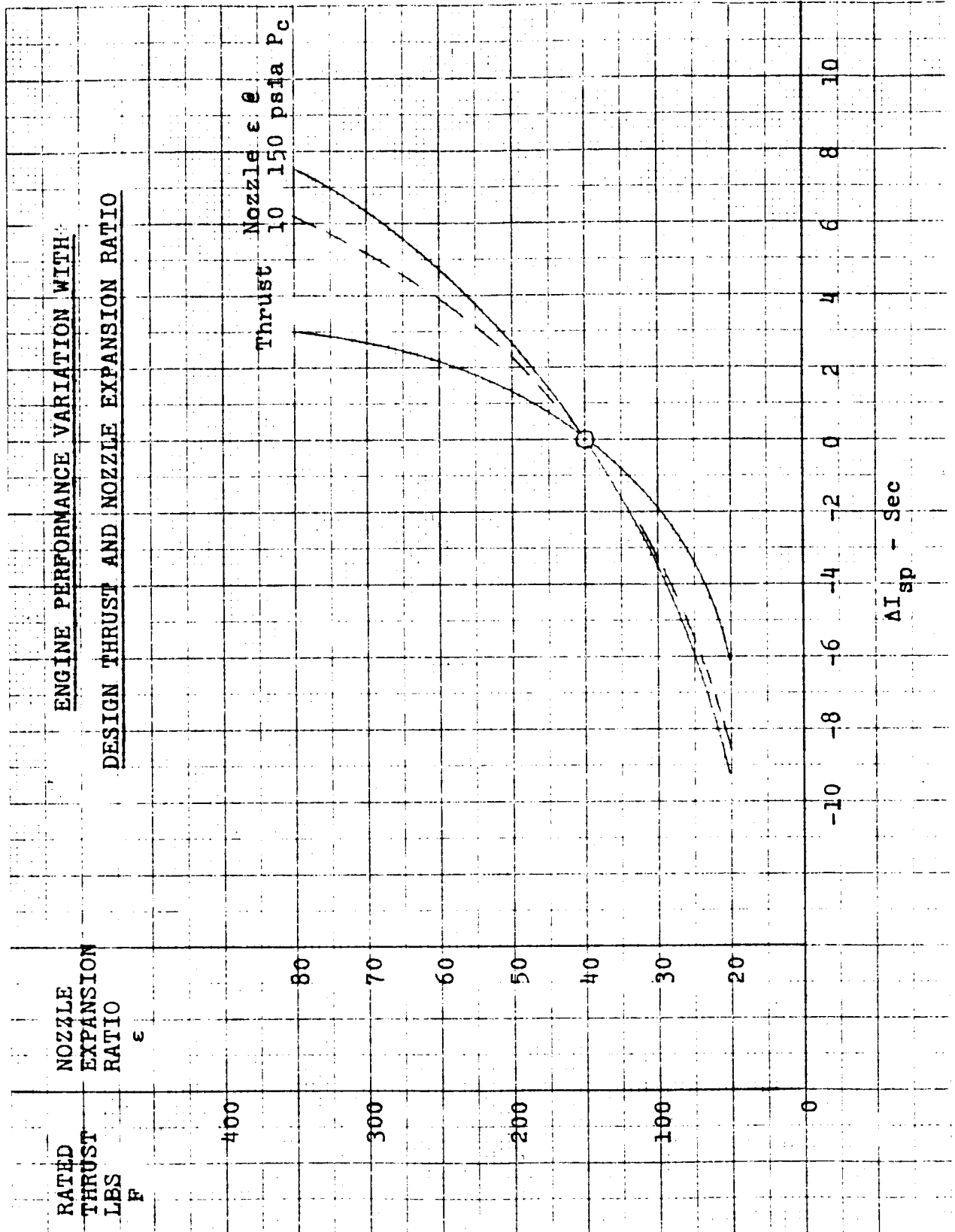
The baseline engine designs discussed in section II were designed to develop rated thrust at 80 psia chamber pressure. This value was selected to minimize the propellant feed pressure requirements for these engines. At higher design chamber pressures a small performance improvement and a significant reduction in engine weight and envelope can be achieved. These advantages will be offset by propellant supply system weight (and gas tank envelope) increases resulting from the attendant increases in propellant feed pressure shown in Figure A-19. The optimum engine design chamber pressure can be identified by tradeoff study for each LFV system concept.

The engine performance variations with design thrust and nozzle expansion ratio must also be included in the optimization tradeoff studies. The basic engine performance variation with design chamber pressure and throttling ratio are given in Figure A-20 for a 150-pound engine with a nozzle expansion ratio of 40:1. This data is based on measured performance throughout the chamber pressure range from 10 to 150 psia. The change in engine performance (with respect to Figure 20) resulting from variations in design thrust and nozzle expansion ratio are given in Figure A-21. The performance change with thrust is a combustion efficiency change due to an increase in the number of injector triplets with thrust. The performance change with nozzle expansion ratio is based on Bray non-equilibrium flow analysis.





A-20





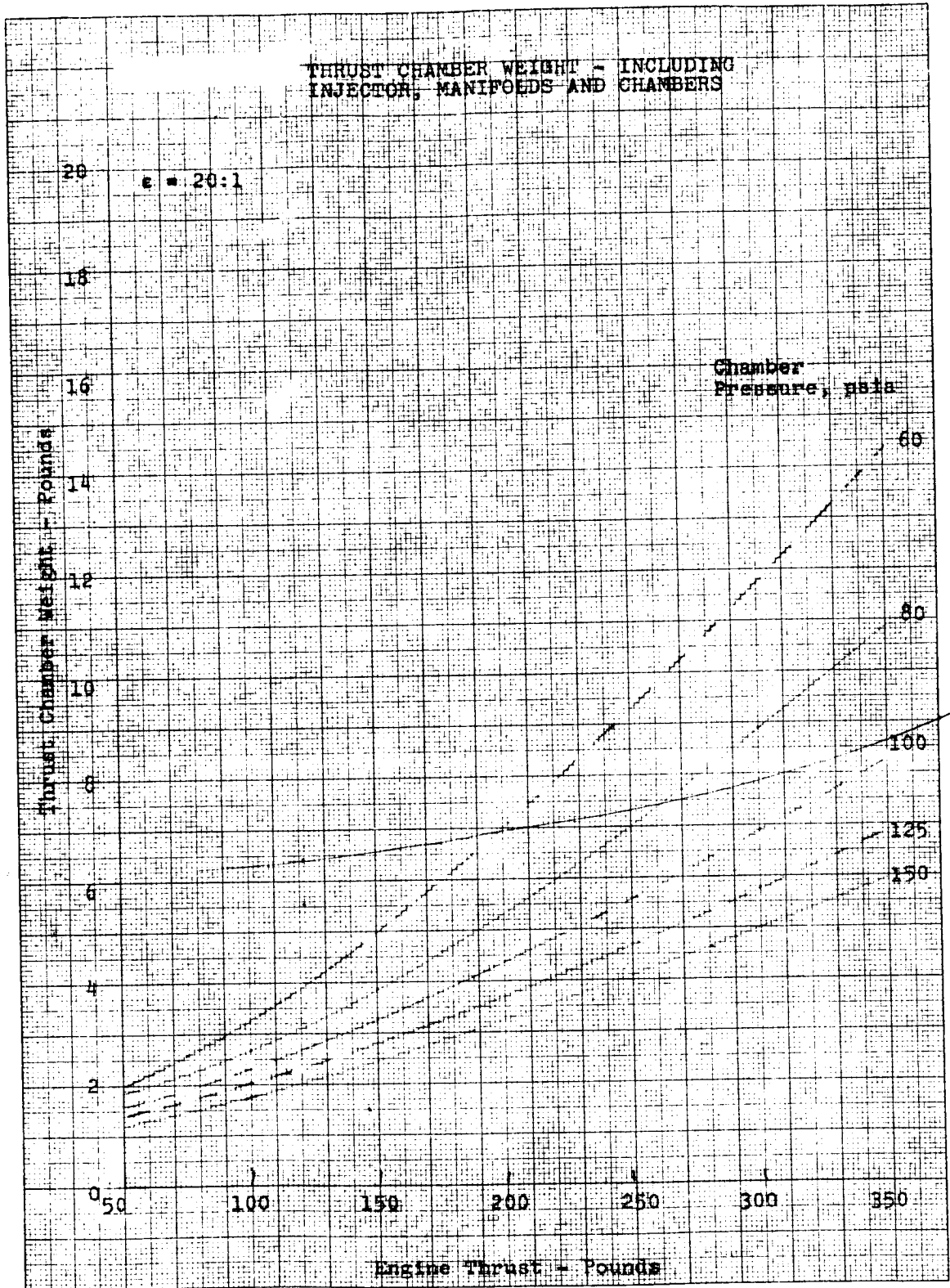
One dimensional exact kinetic performance calculations are currently in work for the  $N_2O_4$  - 50 percent— $N_2H_4$  + 50 percent UDMH propellants in the 10 to 150 psia chamber pressure range to confirm the performance data given in Figures A-20 and A-21.

## WEIGHT AND ENVELOPE

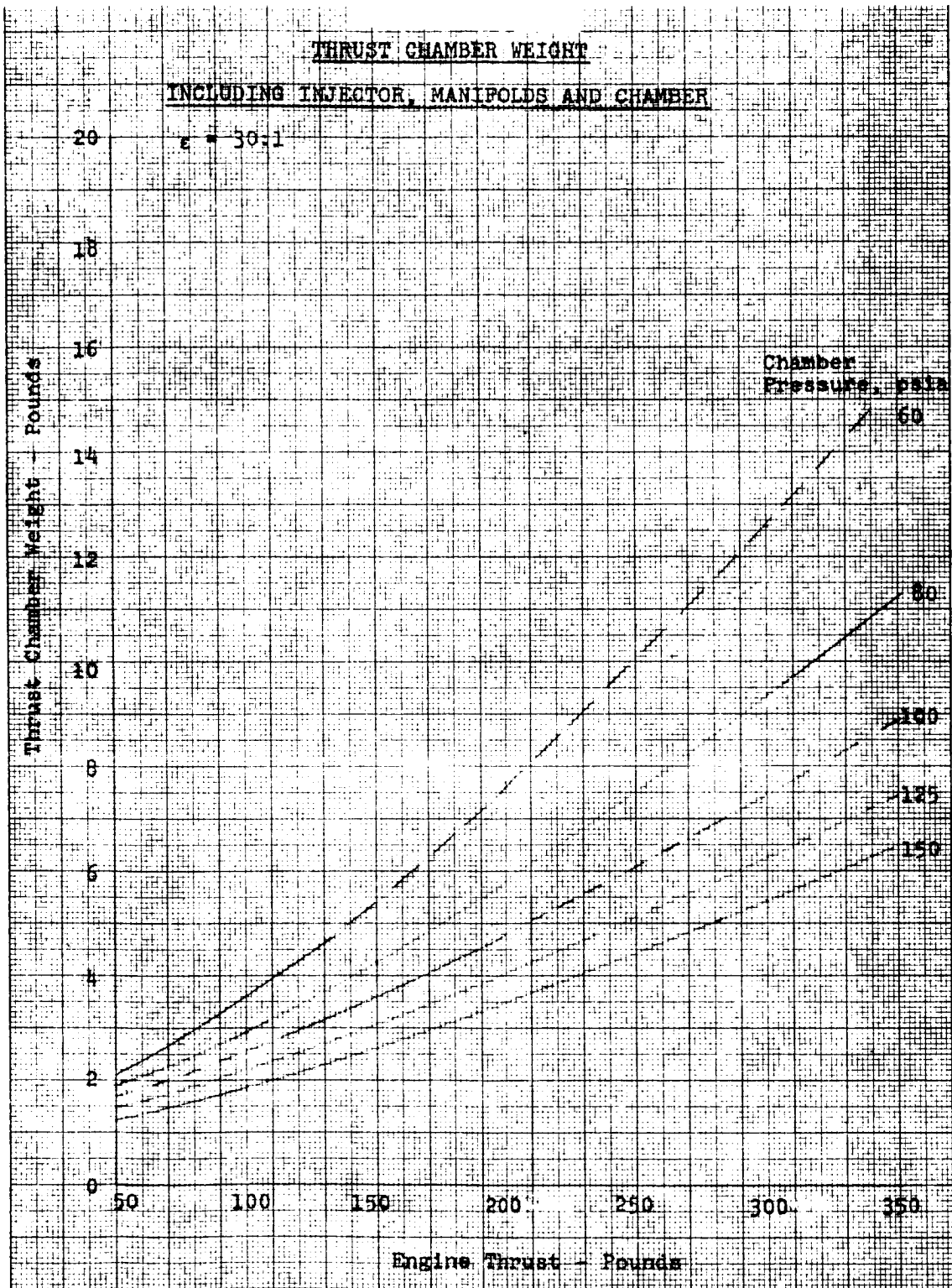
The large number of possible engine configurations—including single and two axis gimbaling, fixed mounting, remote and integrated throttle valves, electrically and manually operated propellant and throttle valves, single and multiple engine installations and inboard or outboard mounting—indicated that the most useful engine weight data would be major engine component weight, rather than engine assembly weight for one or two hypothetical configurations.

The weight of the thrust chamber is given as a function of rated thrust and chamber pressure in Figures A-22 through A-25 for nozzle expansion ratios from 20: to 60:1. The weight and envelope of the throttle valve is given as a function of thrust in Figures A-26 and A-27 respectively for electrically and manually operated units. The weight and envelope variation of the propellant shutoff valve with engine rated thrust is shown in Figures A-28 and A-29 respectively for electrically and manually operated valves. Engine mount weight for fixed, single axis gimbaling and two axis gimbaling is given in Figure A-30 as a function of engine design thrust and chamber pressure.

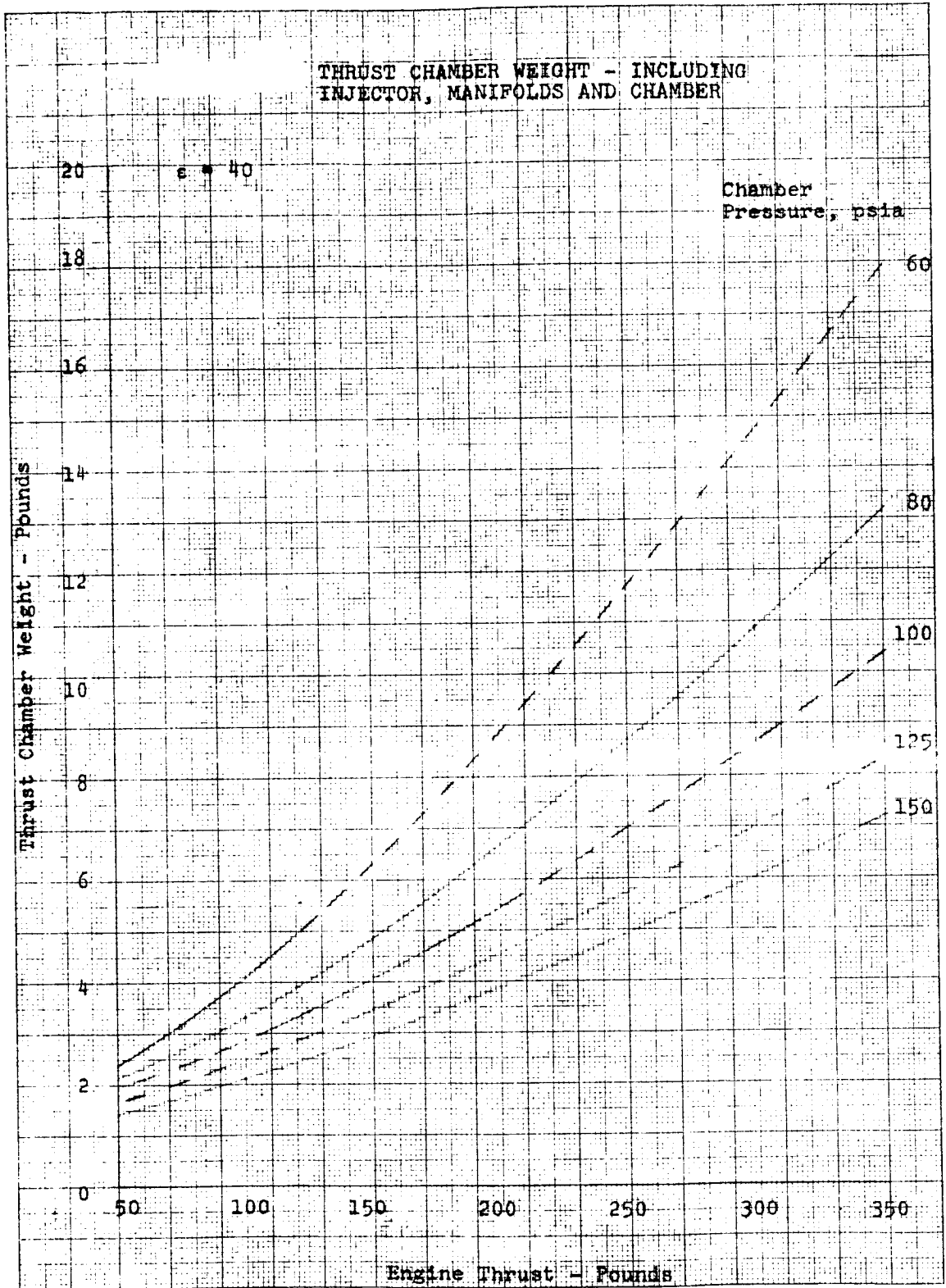
The propellant valve is flush mounted on the injector manifold in all the proposed designs and, in cases where the throttle valve is integrated in the engine assembly, the throttle may be located in parallel with the propellant valve such that it does not increase engine assembly length. This permits definition of a minimum engine length equal to the length of the thrust chamber with flush mounted propellant valve. This minimum engine length, together with the nozzle exit diameter are given as a function of design thrust, chamber pressure and nozzle expansion ratio in Figures A-31 through A-34.

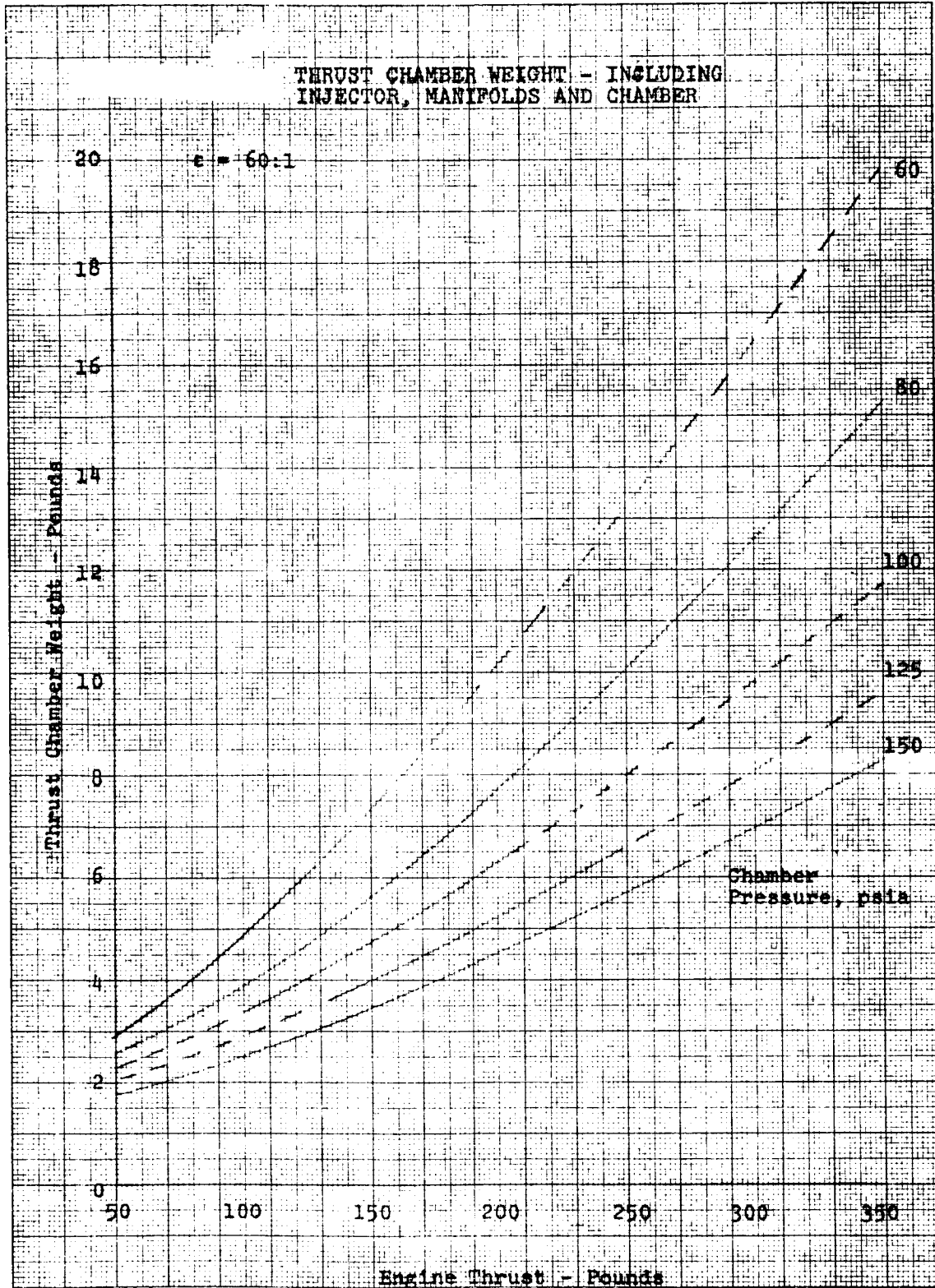


A-22

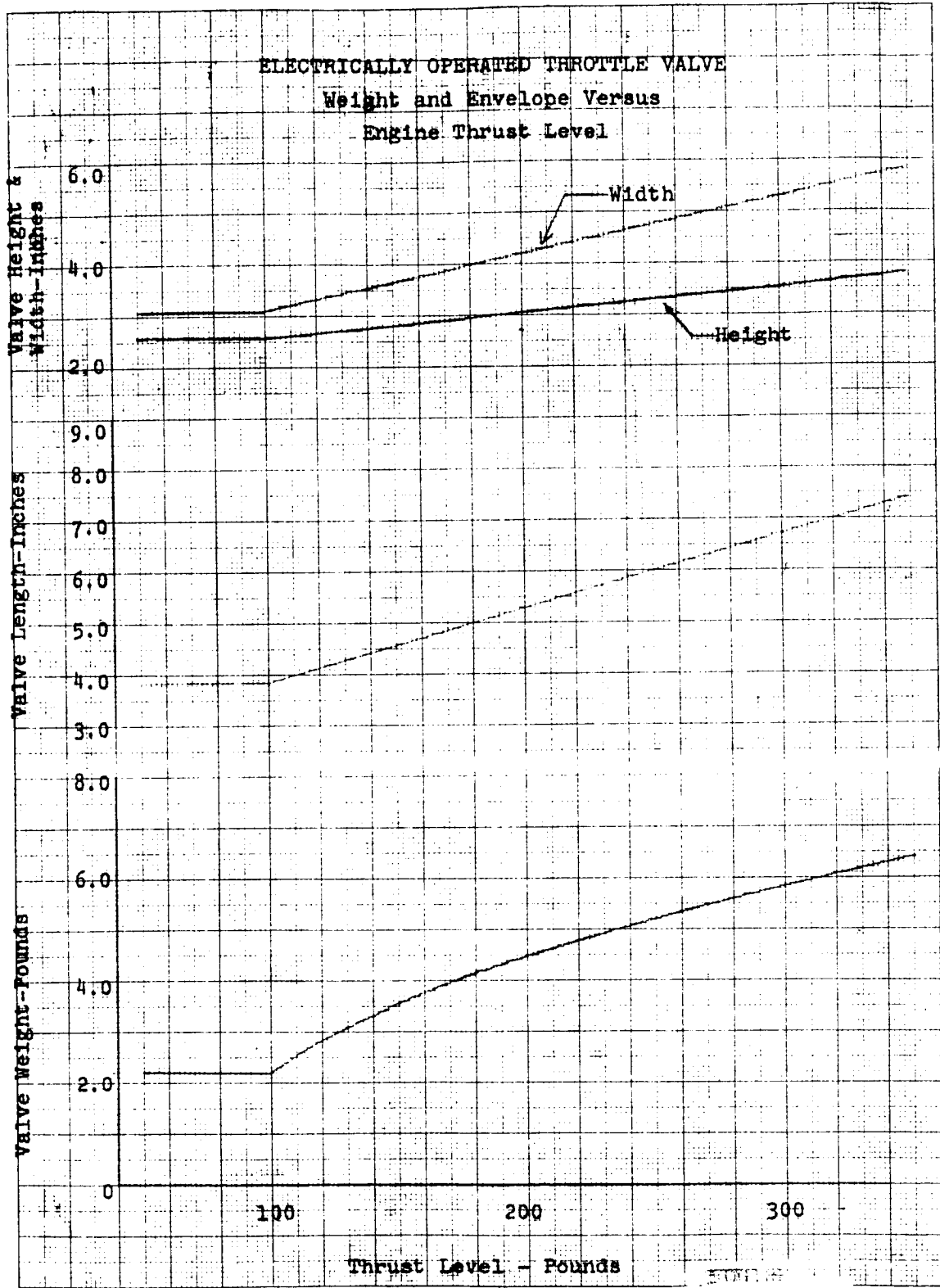


A-23

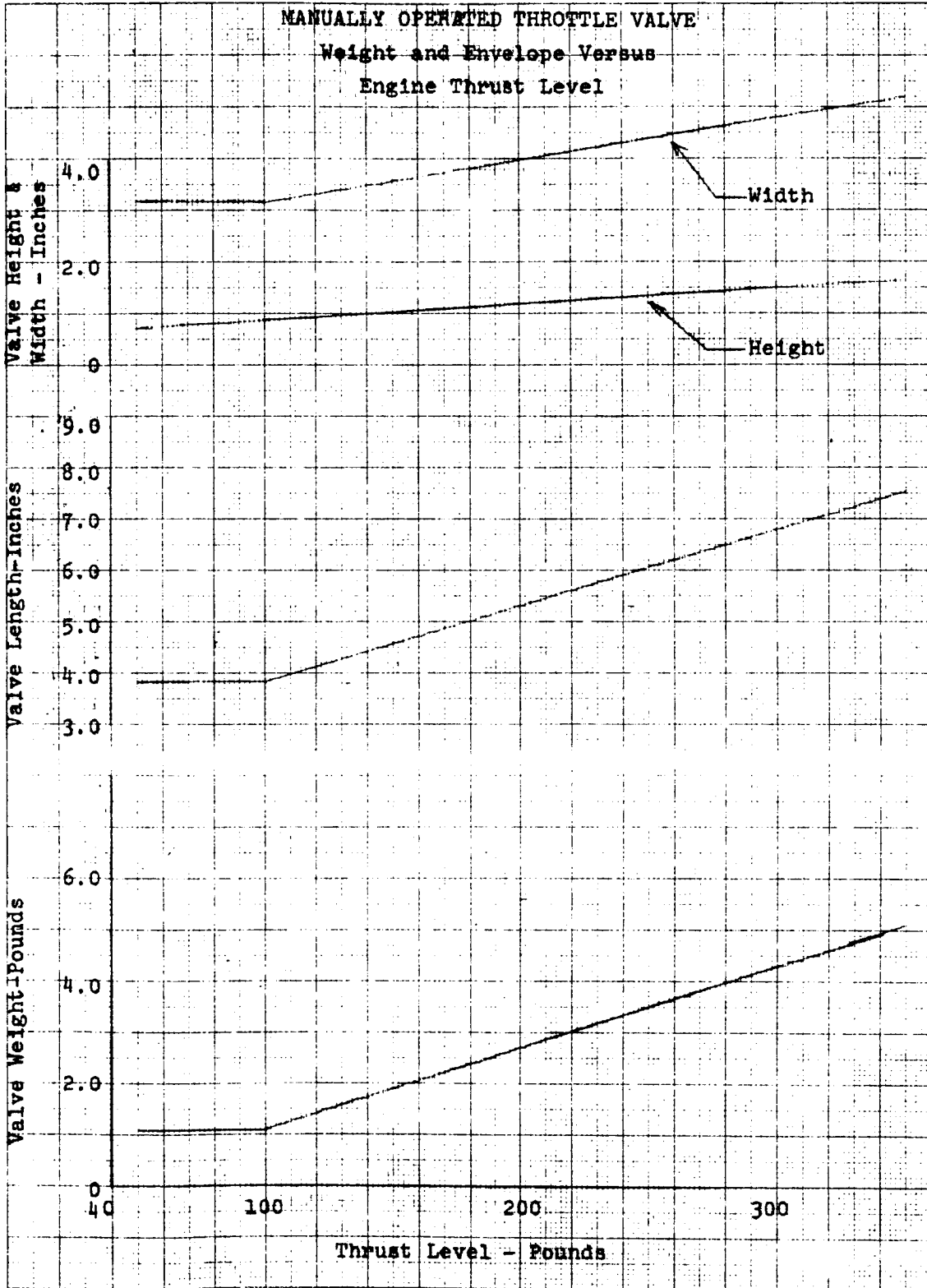




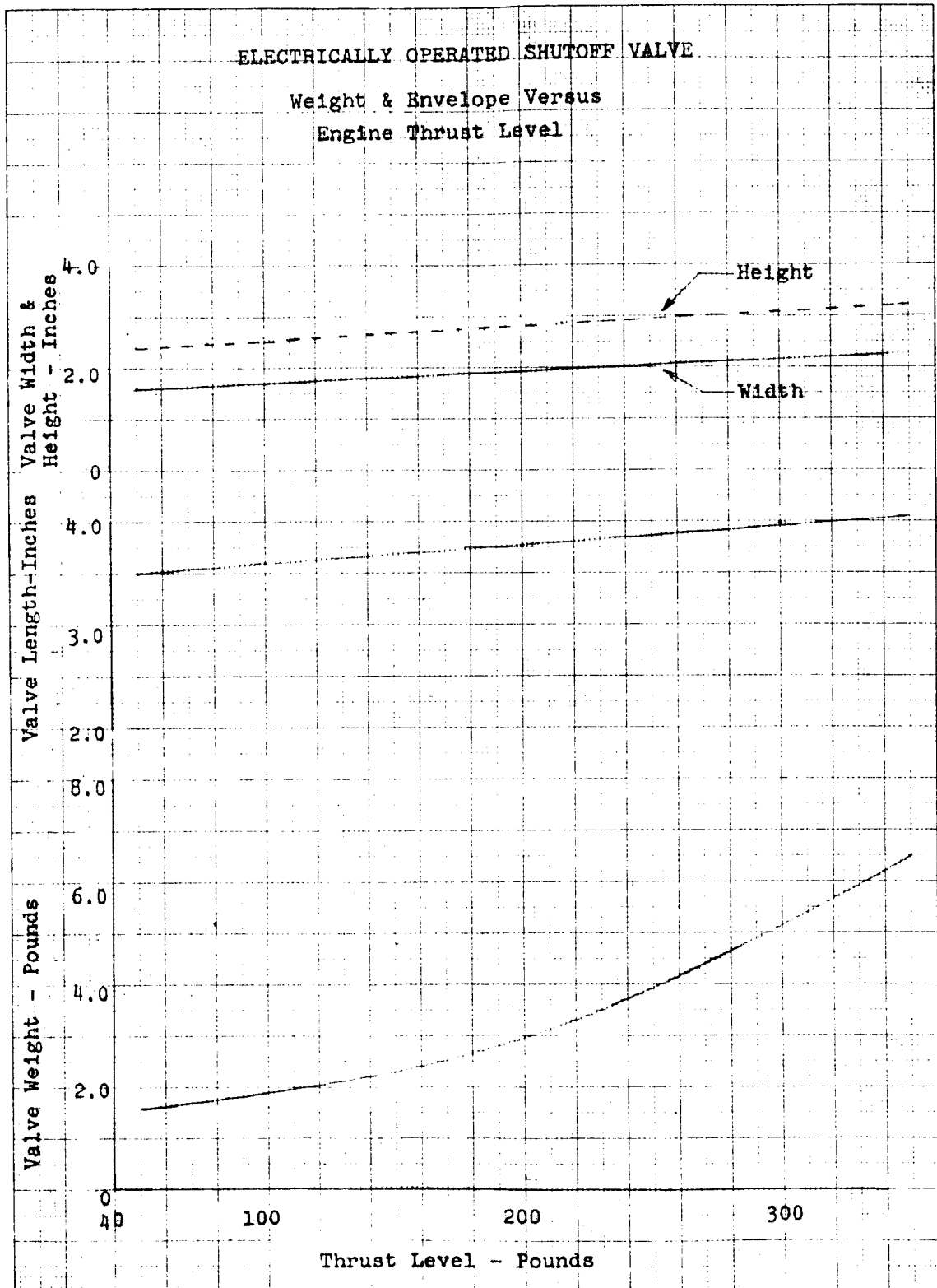
A-25



A-26

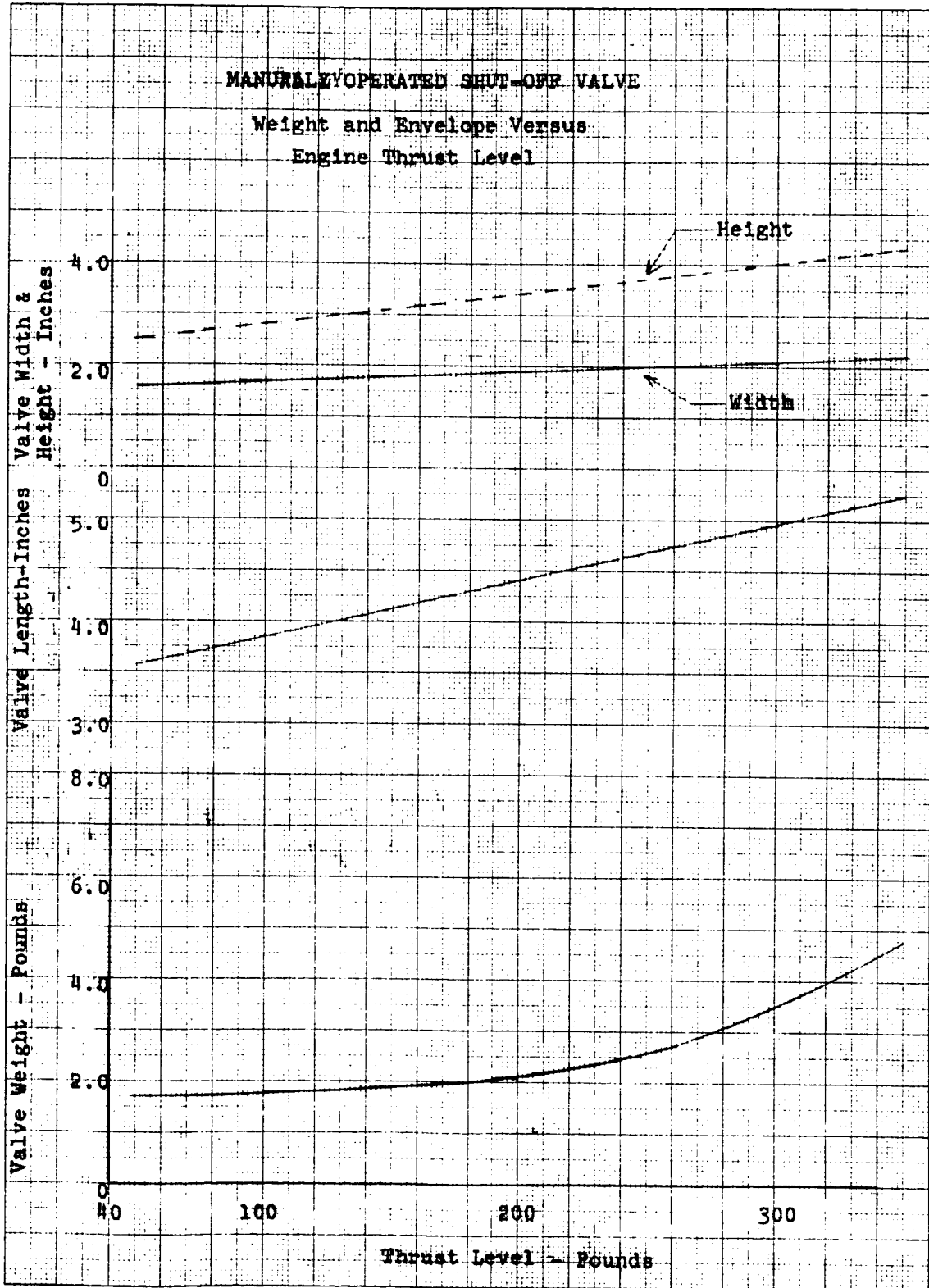


A-27

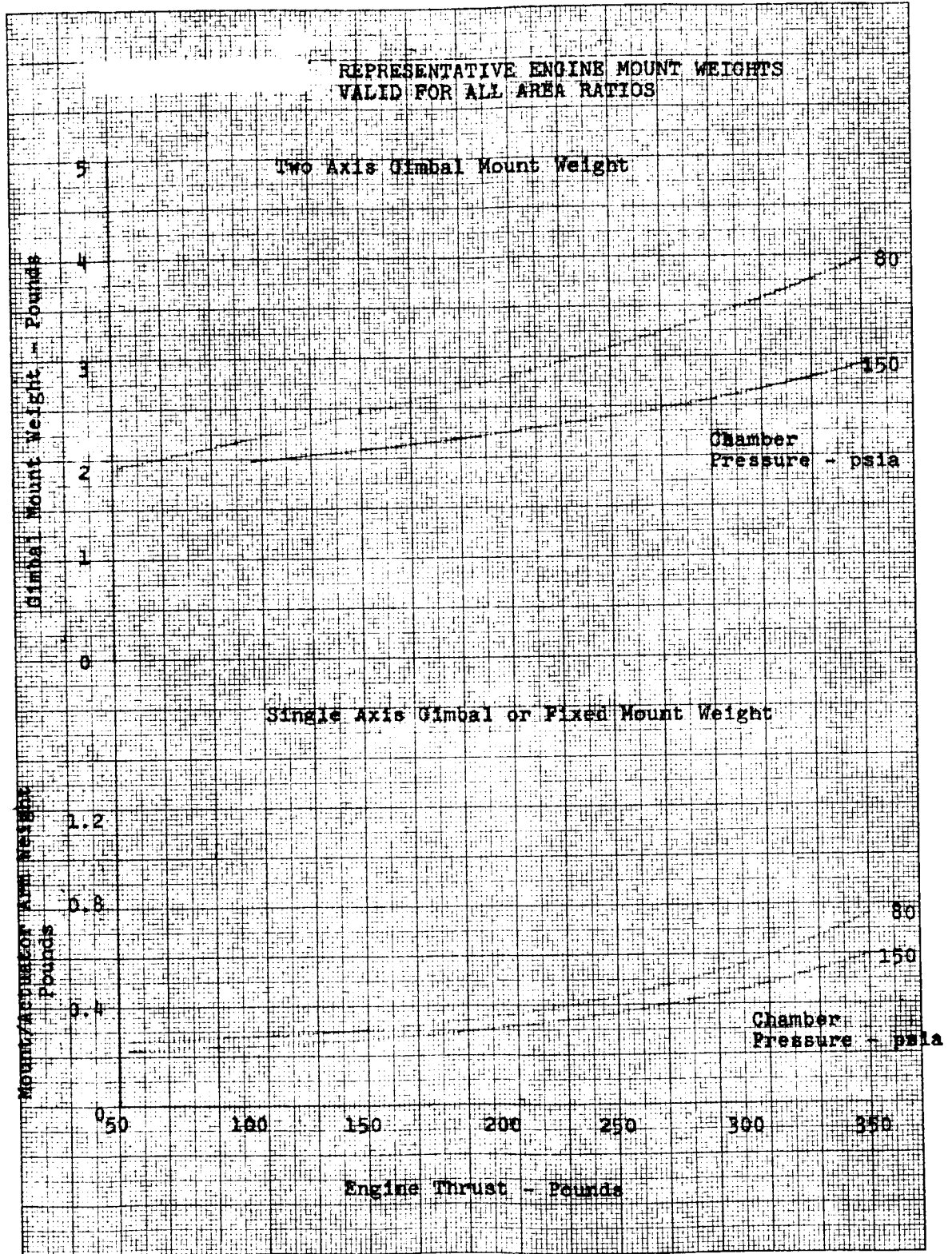


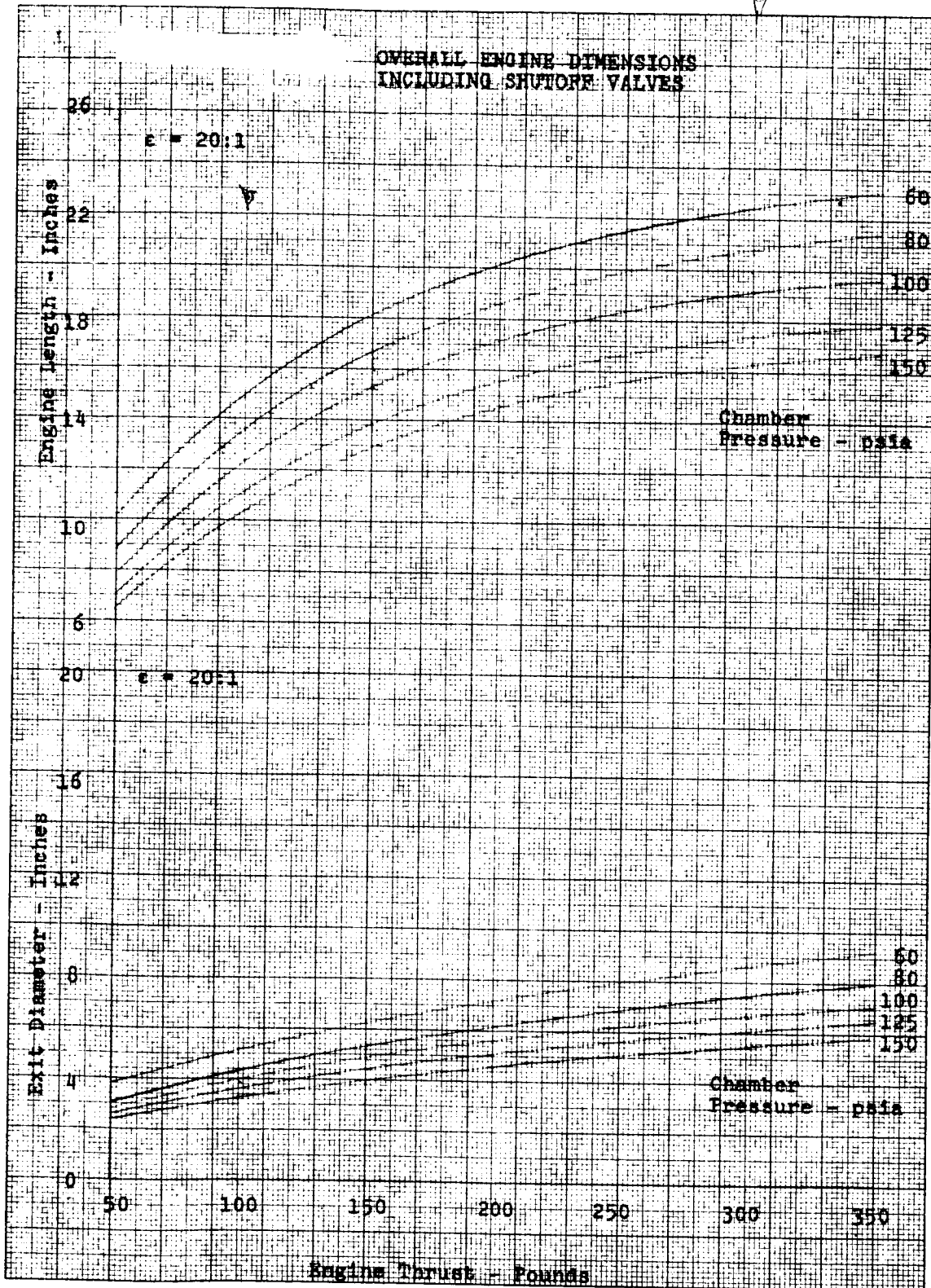
A-28



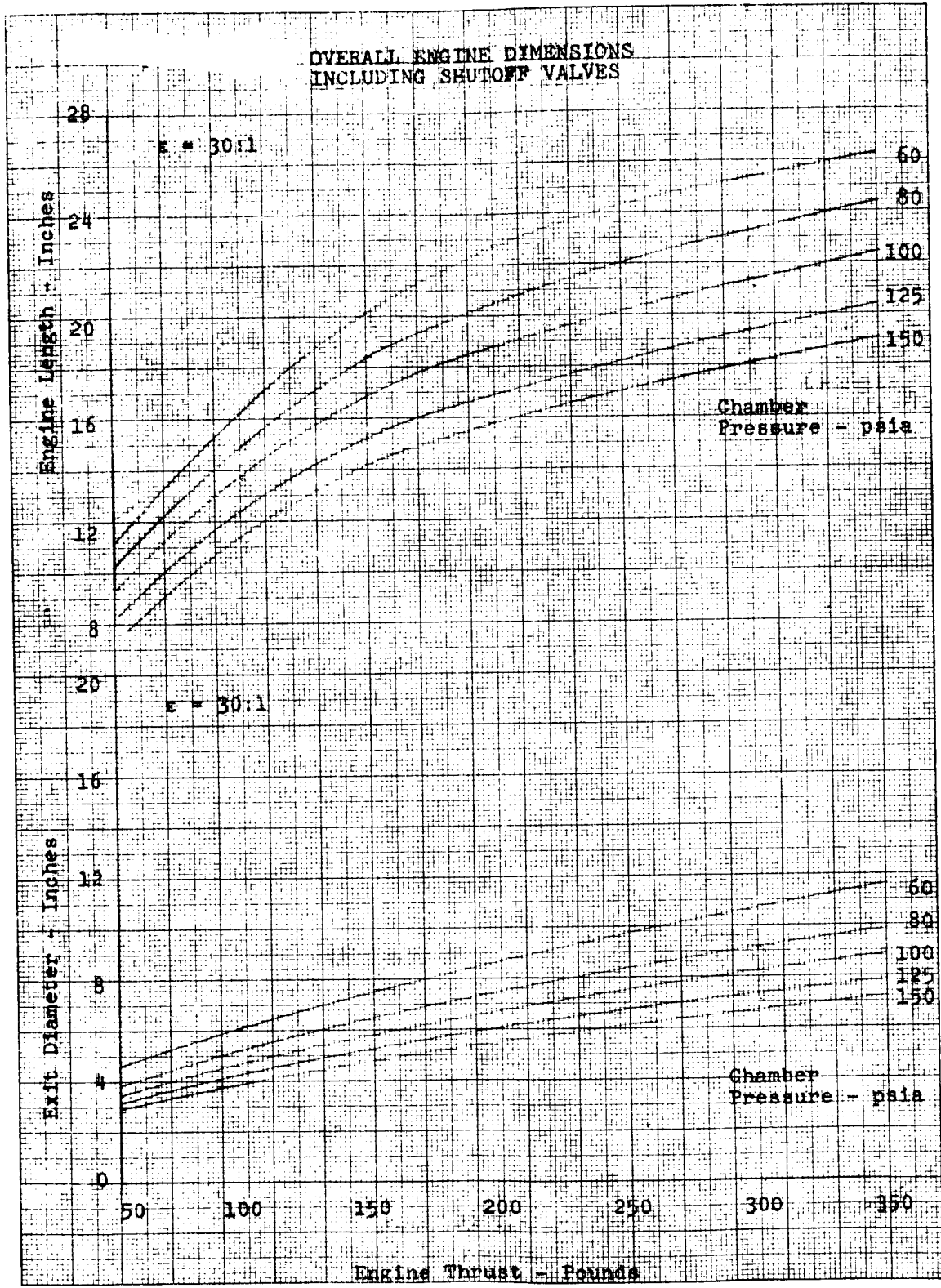


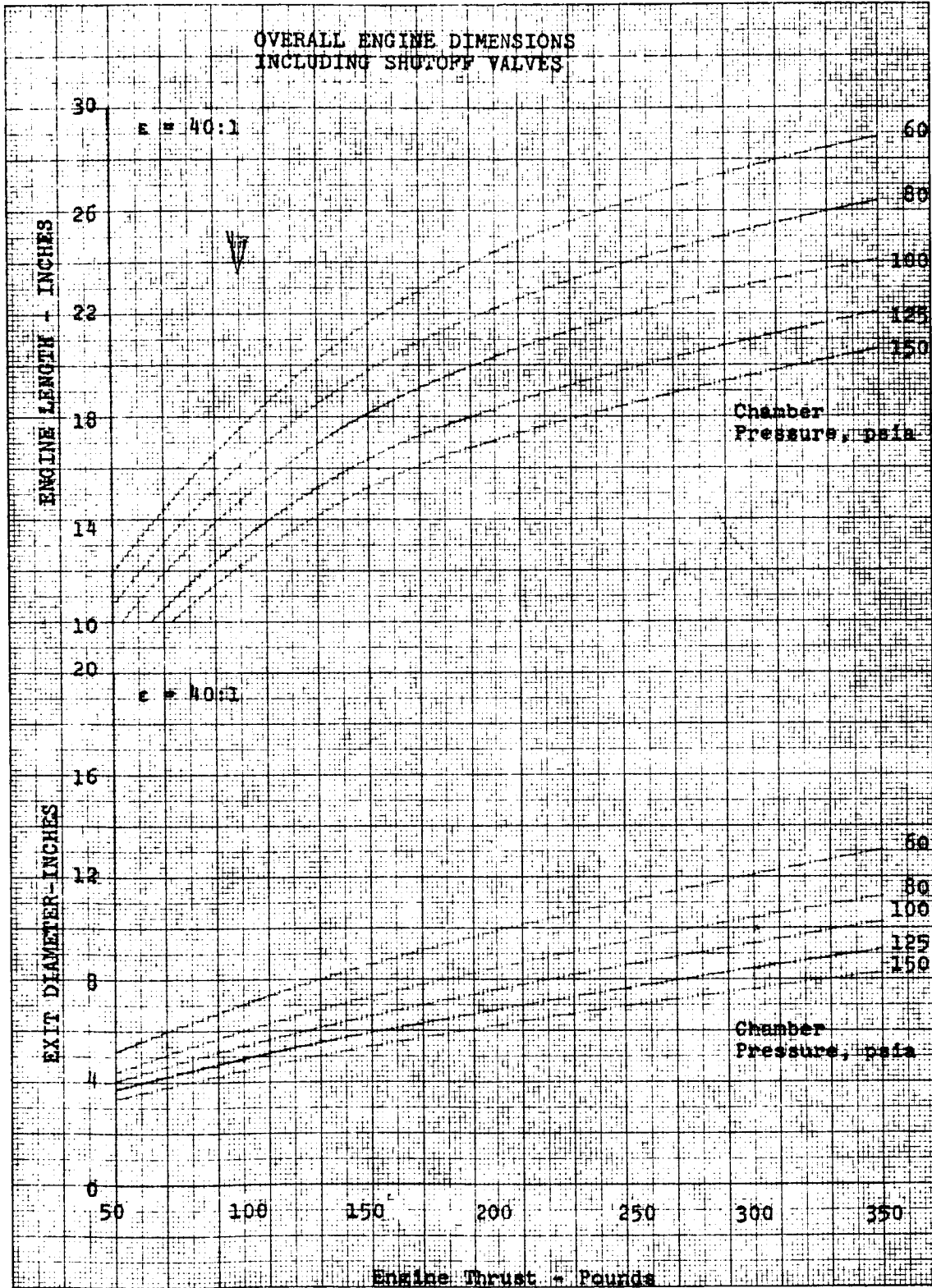
A-29

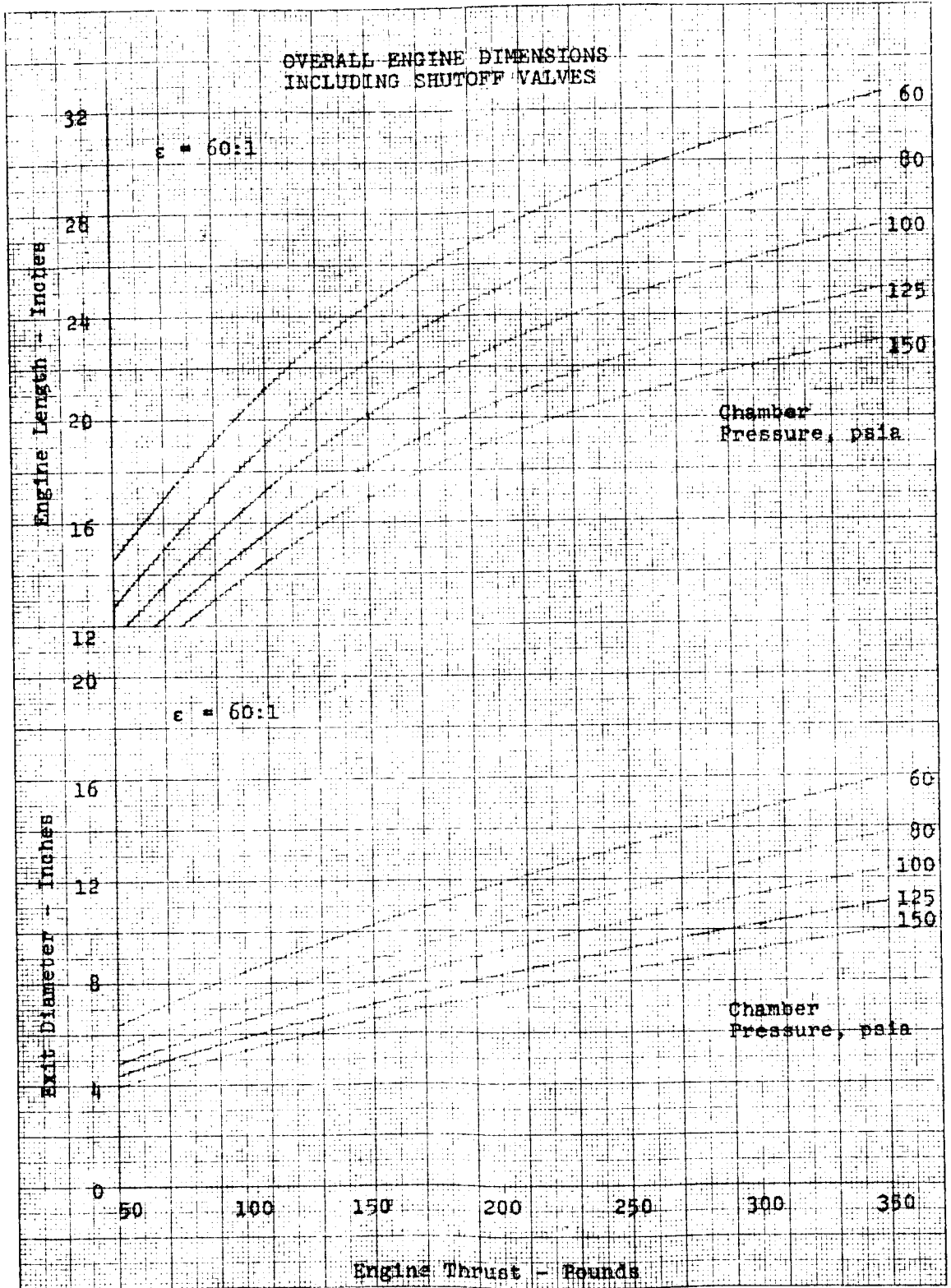




A-31







A-34



Space Division  
North American Rockwell

MARQUARDT CORPORATION  
PRELIMINARY DESIGN STUDY  
THROTTLING AND THRUST VECTOR CONTROL  
OF  
ROCKET ENGINES

## INTRODUCTION

Several future space missions require the use of reliable, proven precision control rocket engines of 1000 pounds thrust or less that have essentially unlimited life in terms of combustion time, number of space restarts, and space exposure time. These engines will be required to provide precise impulse bits ranging from less than one pound-second to possibly several million pound-seconds. The engines will be required to provide variable thrust over a range of possibly 10 to 1. Variable propellant mixture ratios may also be required and the engines may need to be operable with several propellant combinations, such as A-50/N<sub>2</sub>O<sub>4</sub>, MMH/N<sub>2</sub>O<sub>4</sub>, and N<sub>2</sub>H<sub>4</sub>/N<sub>2</sub>O<sub>4</sub>. Thrust vectoring control will be required with most of these space engines.

The existing Marquardt R-4D, R-4B, and R-23B rocket engines will be directly applicable to most of these future space missions. They also represent a firm design base from which other specific design engines can be obtained to meet specialized requirements. Up to the present time, these engines have been operated primarily at specific design thrust and mixture ratio levels in steady state or ON-OFF pulsing mode. However, in ground tests they have been thoroughly evaluated over wide ranges of mixture ratio and thrust levels. The results of these investigations have been utilized to obtain the performance levels presented.

This design study presents Marquardt's presently existing capability in the field of throttleable rocket engines to cover the thrust range from about 20 to 600 pounds. Performance characteristics are presented for existing designs (including the qualified R-4D engine) and weight and dimensional estimates are given as a function of nominal design thrust. Design schematics are given to illustrate throttling and thrust vectoring techniques that are applicable to these rocket engines. Estimates of weight, actuation forces, and actual thrust vectoring capabilities for each technique are discussed and development difficulties are indicated.



## DISCUSSION

### GENERAL ENGINE DESCRIPTION

The Marquardt R-4D rocket engine is a qualified engine presently being used for attitude control on the Apollo service and lunar modules. This engine was also used for velocity control on the lunar orbiter vehicle and will be qualified for use on the manned orbital laboratory and a classified program. The R-4D is nominally a 100-pound thrust engine, but has been operated over a thrust range from 15 to 300 pounds. All flight engines to date have been operated at a nominal mixture ratio of about 2.05, but the engine is equally capable of operation over a range from 1.0 to 2.4. The engine operates on MMH/N<sub>2</sub>O<sub>4</sub> on the Apollo service module and A-50/N<sub>2</sub>O<sub>4</sub> on the Apollo lunar module.

The R-4D engine has a refractory metal combustion chamber which is fuel film cooled to provide low operation temperatures and essentially unlimited combustion life. Continuous engine firings up to two hours in length have been conducted with no engine degradation. A total combustion time of about 10 hours has been accumulated on one combustion chamber with no degradation.

A sketch showing the exterior dimensions and primary characteristics of the R-4D engine is given in Figure A-35.

The Marquardt R-4B engine is a high performance design improvement engine based on the R-4D technology. This engine has the same long life capabilities as the R-4D and the same capability of operating with several propellants and at various mixture ratios.

The Marquardt R-23B engine (Figure A-36) is a nominal 300-pound thrust engine designed from the R-4D technology. The same chamber materials and injector cooling techniques were employed to give the same long life capability as the R-4D. This has been demonstrated with continuous firings up to 2000 seconds in duration and a total accumulated combustion time up to 6,391 seconds on a single engine. The engine has been tested with A-50/N<sub>2</sub>O<sub>4</sub>, MMH/N<sub>2</sub>O<sub>4</sub>, and N<sub>2</sub>H<sub>4</sub>/N<sub>2</sub>O<sub>4</sub> over wide mixture ratio and thrust ranges.



ROCKET SYSTEMS DIVISION  
THE MARQUARDT CORPORATION



# MODEL R-4D ROCKET ENGINE

## 100 POUNDS THRUST

### GENERAL DESCRIPTION

Total Weight - 4.9 lbs.  
Electrically Linked Propellant Valves.  
Extended Pulse Width Injector.  
Fuel Film Cooled Combustor.  
40:1 Expansion Bell.  
Valves can be furnished with pigtails  
or mechanical connector as required.

### RATING CONDITIONS

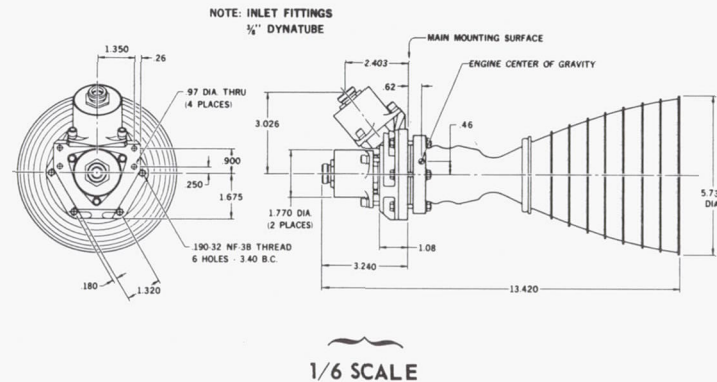
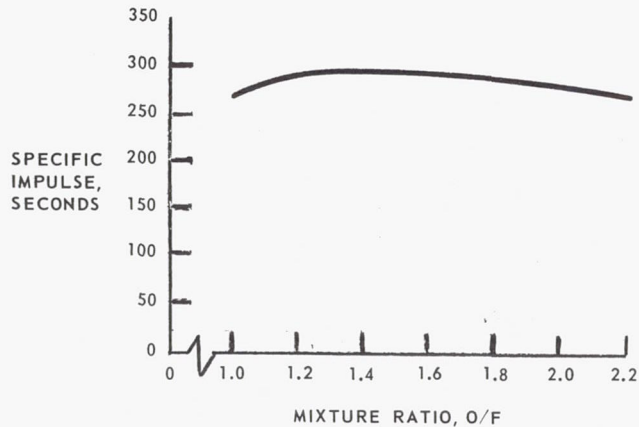
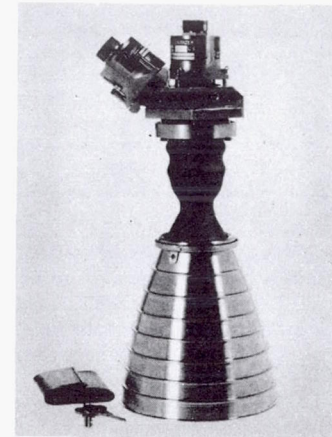
Propellant Pressures: 170 psia @ 100 lbs. Thrust @ O/F = 2.0  
Propellant Temperatures: 30 - 110° F  
Valve Voltage: 21 - 32 Volts DC  
Valve Power:  
(Primary Coil) 102 Watts @ 27 Volts DC  
(Redundant Coil) 26 Watts @ 27 Volts DC

### PERFORMANCE

Operating Life: Unlimited  
Pulse Width Range: 0.010 sec. to Continuous  
Thrust Operating Range: 40 - 200 lbs.  
O/F Operating Range: 1.0 to 2.2  
Minimum Impulse: 0.51 lb-sec.

### PROPELLANTS

Oxidizer: N<sub>2</sub>O<sub>4</sub>  
Fuels: MMH or A-50  
Pressurants: N<sub>2</sub> or He



A-35

- 234 -

SD 69-419-3



ROCKET SYSTEMS DIVISION  
THE MARQUARDT CORPORATION

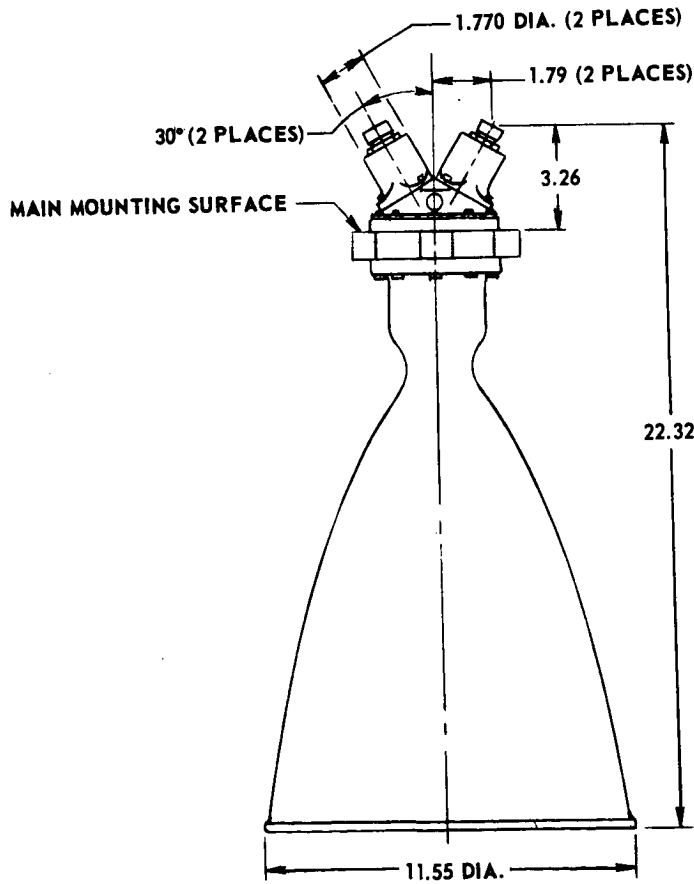
# MODEL R-23B ROCKET ENGINE

S 922



3/8 IN. DYNATUBE  
INLET FITTINGS

.250 - 28 NF-3B THREAD  
6 HOLES, 5.00 B.C.



1/5 SCALE

A-36

## PERFORMANCE CHARACTERISTICS

The following discussion on engine performance characteristics is based upon a combination of actual test data and analysis. All of the test data have been obtained with the R-4D, R-4B, and R-23B engines, described above. The tests on the R-4D engine have been the most extensive and have all been conducted at high altitude conditions. The tests on the R-23B engine have been less extensive and have all been conducted at sea level pressures. Altitude performance values have been calculated by application of thrust coefficient values obtained from the tests on the R-4D engine. Tests on the R-4B engine indicate that performance gains could be realized with current design technology, although the tests are not as extensive as on the R-4D. The more conservative R-4D performance levels are used for most of the following discussion.

Specific impulse as a function of percent design thrust is shown in Figure A-37 for the R-4D engine and R-23B engine. The design point specific impulse for the R-4B engine is also shown, but this engine has not been tested over a wide thrust range. The performance is for a propellant combination of A-50/N<sub>2</sub>O<sub>4</sub> at a mixture ratio of 1.6 and nozzle area ratio of 40:1 exhausting to vacuum. Both the R-4D and R-23B have been tested over the thrust range shown, although actual data points are not shown for the R-4D for the sake of clarity. The thrust range indicated for the R-4D is from 25 percent to 175 percent of nominal thrust which is a throttling ratio of 7:1. As shown, the specific impulse over the range from 60 percent to 100 percent of design thrust is equal or greater than the design point  $I_{sp}$  for both the R-4D and the R-23B.

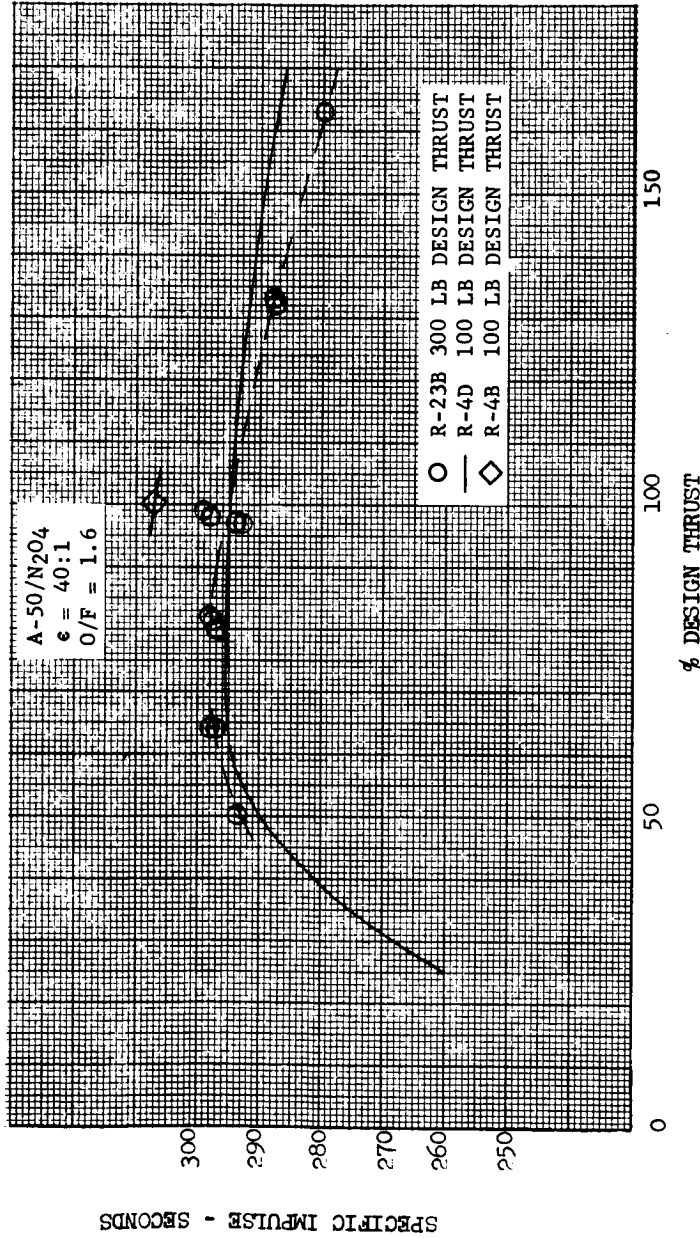
As proven by the R-23B development, the technologies learned during development of the R-4D can be utilized to develop long life, reliable engines which have other design thrust levels. For preliminary design studies, the actual performance level of the R-4D and R-23B (Figure A-37) can be used for any design thrust in the range of 50 to 350 pounds.

The change in vacuum specific impulse with nozzle area ratio as obtained in tests with the R-4D engine is shown in Figure A-38. The figure is presented in terms of a change in specific impulse (both positive and negative) from that obtained at a nominal area ratio of 40:1. The data are in good agreement with the theoretical relationship based upon equilibrium flow to the nozzle throat and frozen flow downstream of the throat.

Test data on performance effects of changes in design chamber pressure,  $P_c$ , are not available for the R-4D or R-23B. From considerations of fixed injector characteristics, it is assumed that the impulse efficiency (similar to a combustion efficiency) remains constant over the design  $P_c$  range of this study. However, the theoretical specific impulse



SPECIFIC IMPULSE vs DESIGN THRUST

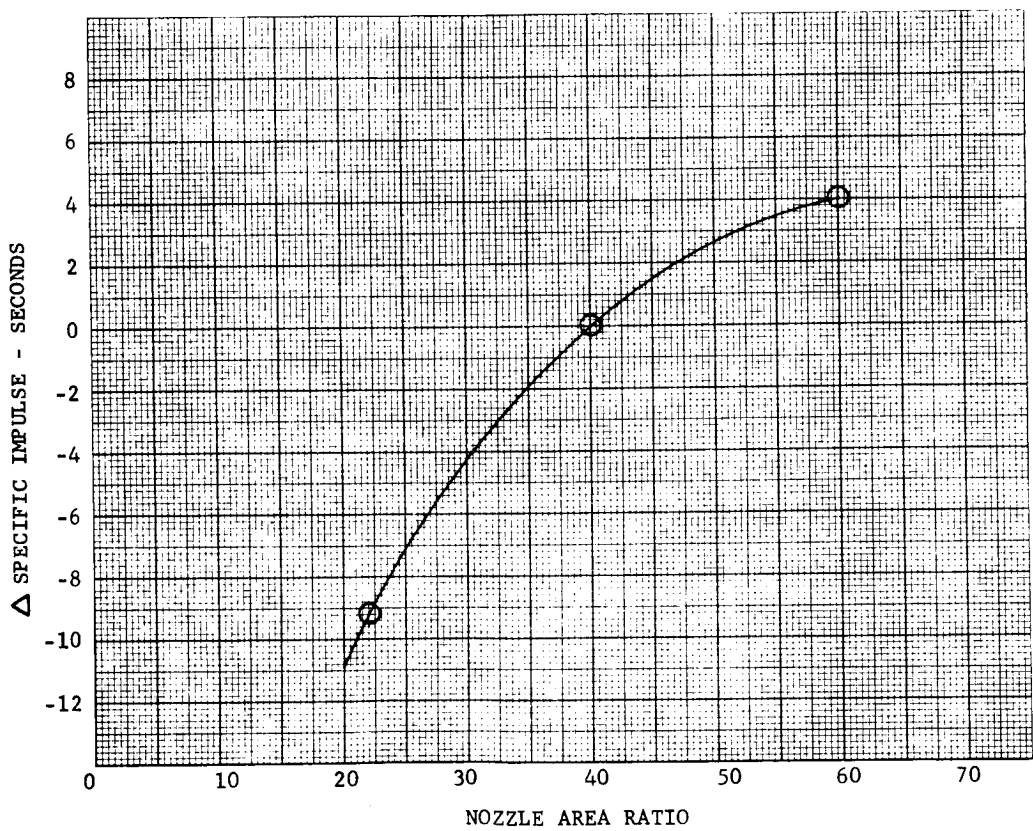


A-37



ENGINE MODEL R-4D  
SPECIFIC IMPULSE vs NOZZLE AREA RATIO

A-50/N<sub>2</sub>O<sub>4</sub>  
O/F = 1.6



A-38

does increase slightly as  $P_c$  increases (Figure A-39). This theoretical change in  $I_{sp}$  with  $P_c$  was applied to the R-4D data at a design  $P_c$  of 100 psia to obtain the performance prediction shown in Figure A-40. A specific impulse increase of about one second is expected as the design  $P_c$  is changed from 80 to 100 psia or from 100 to 150 psia.

Design chamber pressure does have a significant effect upon the required engine inlet pressure. The relationship between engine inlet pressure and percent design thrust for the R-4D engine operating at design point chamber pressures of 80, 100, 125, and 150 psia are shown in Figure A-41. These curves are calculated using presently existing propellant valve pressure losses. Marquardt is confident that throttling valves as described in Section D can be designed with equal or lower pressure losses at equivalent flow rates. Marquardt is also confident that engines with any maximum design thrust levels between 50 and 350 pounds can be designed with injector and throttling valve pressure losses equal or less than those in the present R-4D.

Figure A-41 indicates that the R-4D engine can be throttled to a lower thrust level if the chamber pressure is increased. This is the result of the fact that engine ignition and continued combustion are both enhanced by higher chamber pressures. This has been shown to be true during testing where the reliable occurrence of ignition has been correlated with a flow rate per throat area ( $\dot{w}/A_t$ ) parameter.

An analysis of the specific impulse that can be expected at the lower thrust levels shown in Figure A-41 was conducted. In addition to the effects discussed earlier, the specific impulse efficiency of a given injector design can be affected by self-induced separation of the two propellants at the point of propellant impingement. The analysis indicates that such separation should not be expected with the R-4D, R-4B, or R-23B engines over the entire throttling range shown in Figure A-41. Therefore, the specific impulse values in Figure A-40 have been extended to include these thrust ranges.

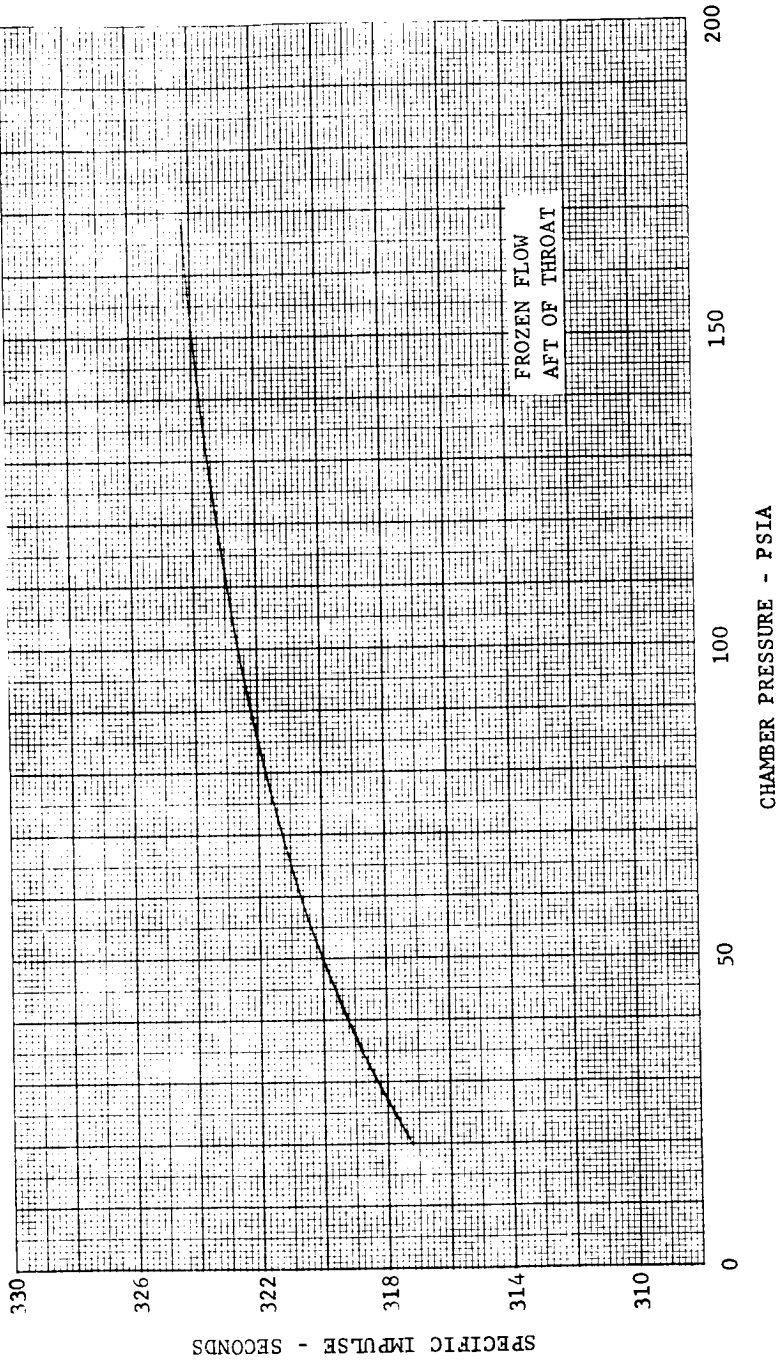
## ENGINE WEIGHT AND SIZE ESTIMATES

Estimates of engine weights, diameters and lengths have been prepared as functions of engine design thrust levels and nozzle area ratios, and are presented in Figures A-42 through A-47. These estimates are based upon the use of externally controlled throttling valves on the engines, as discussed: the weights of the presently used ON-OFF solenoid valves have been subtracted and the weight estimates of throttling valves have been included. The weight and dimensions of the present R-4D engine are included in each figure for comparison.



THEORETICAL SPECIFIC IMPULSE  
vs. CHAMBER PRESSURE

A-50/N<sub>2</sub>O<sub>4</sub>  
 $\epsilon = 40:1$   
O/F = 1.6

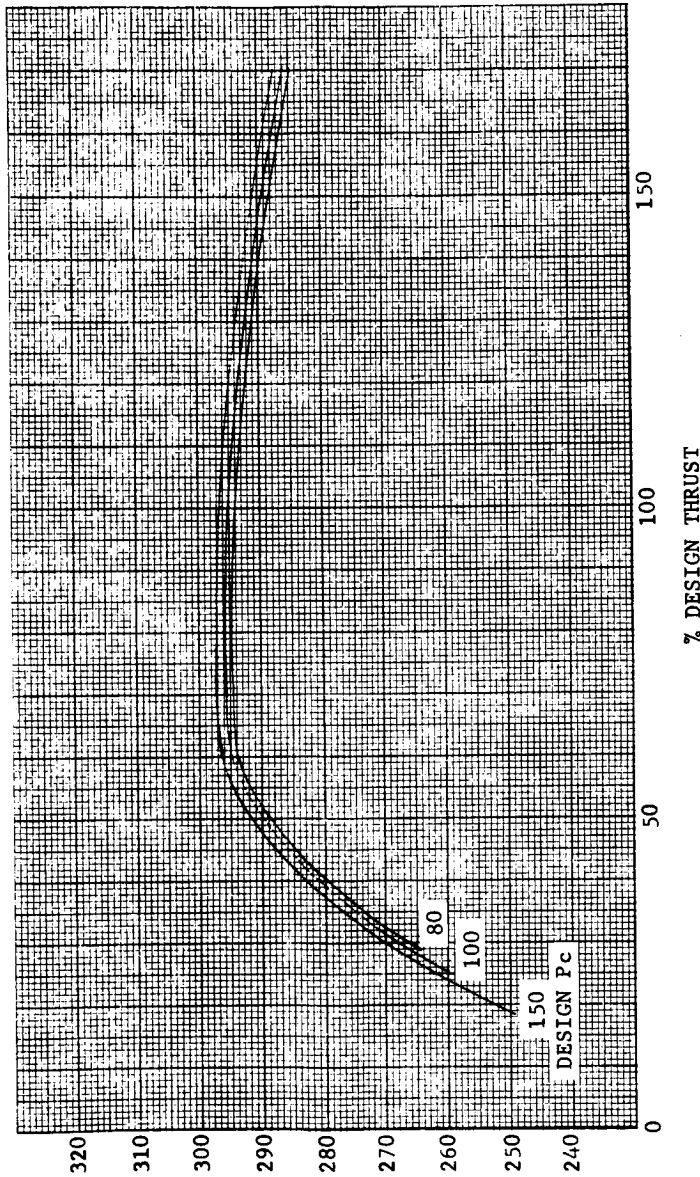


A-39



SPECIFIC IMPULSE vs. DESIGN THRUST

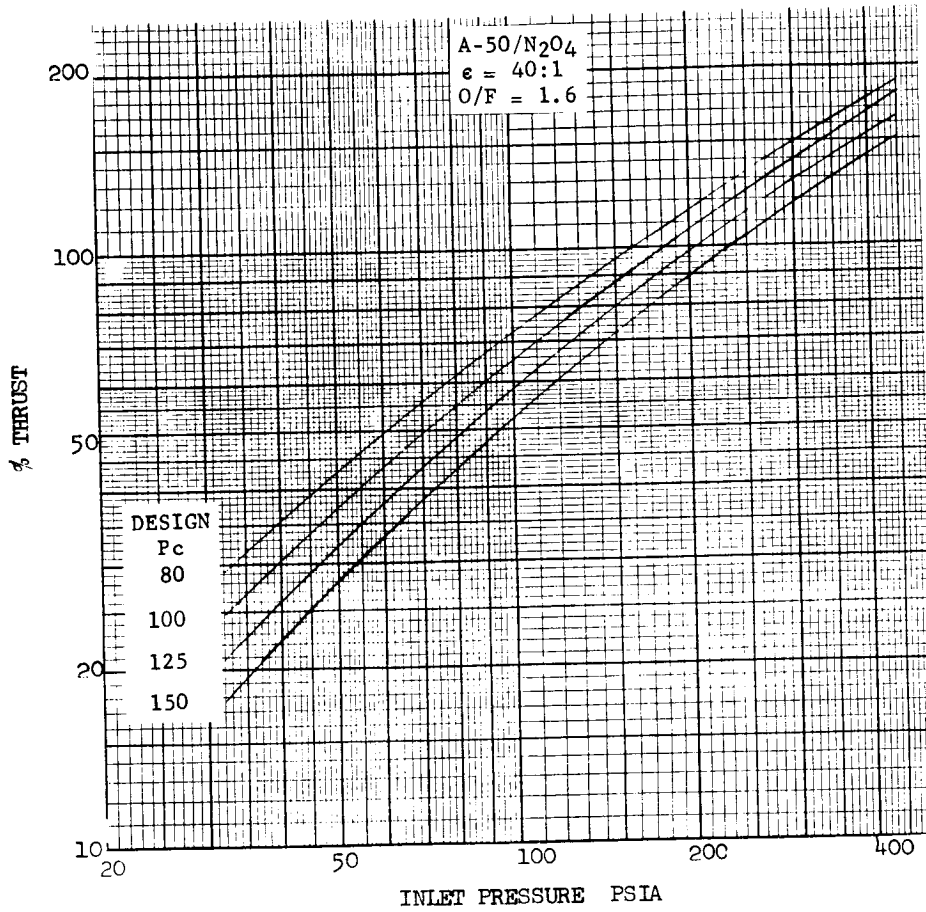
R-4D  
A-50/N2O4  
 $\epsilon = 40:1$   
O/F = 1.6



A-40

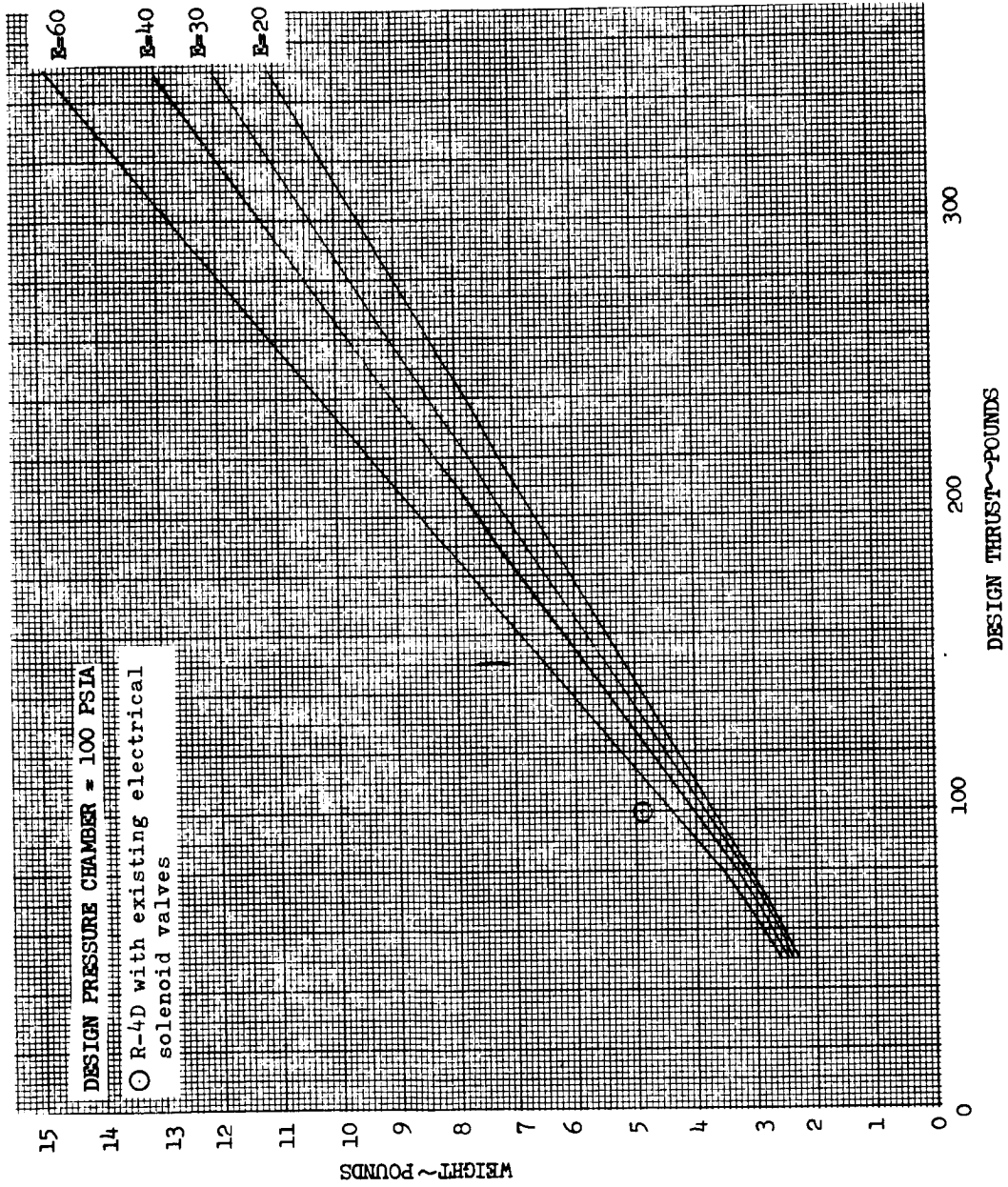


PERCENTAGE THRUST vs INLET PRESSURE



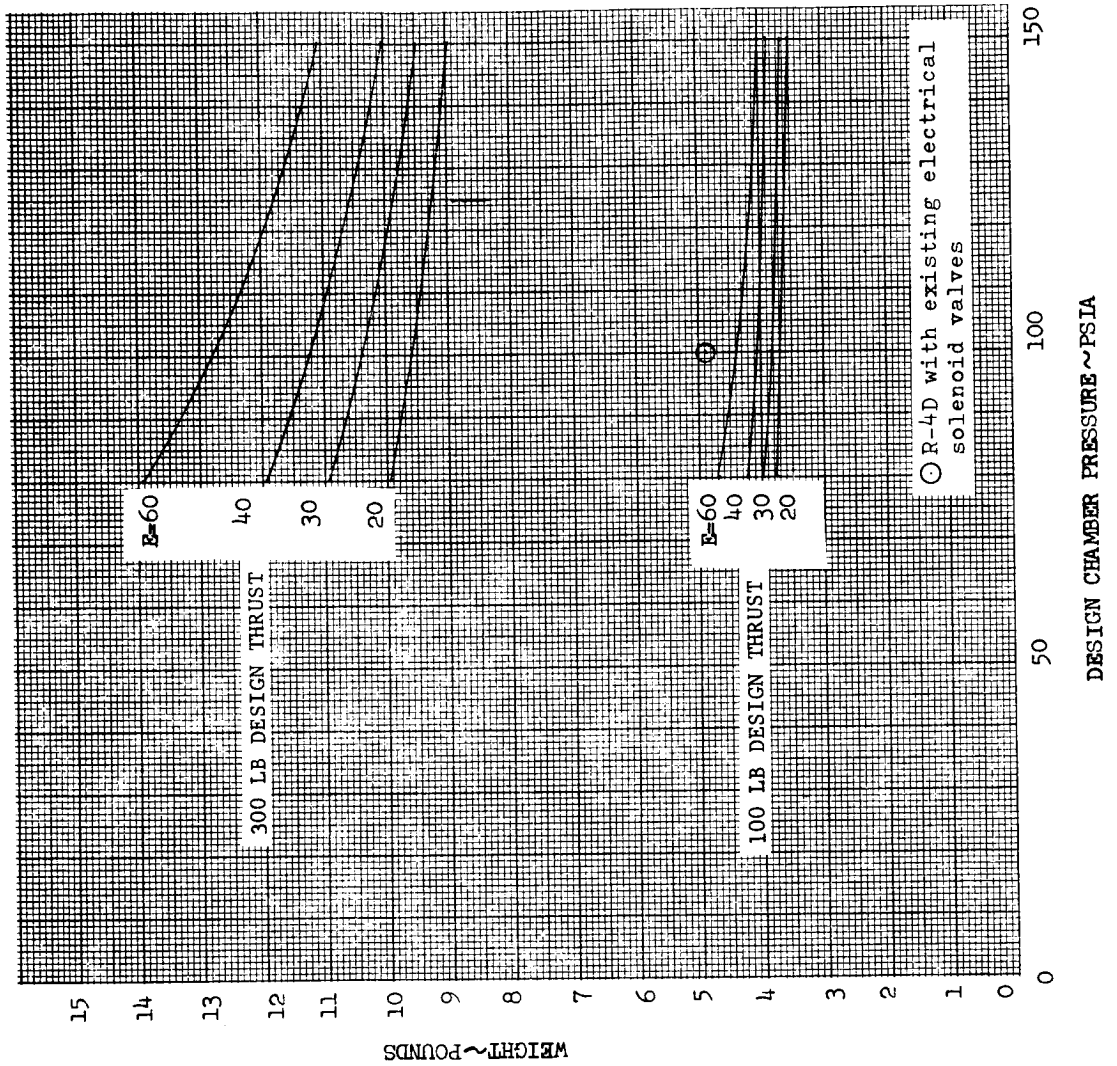
A-41

ENGINE WEIGHT vs DESIGN THRUST

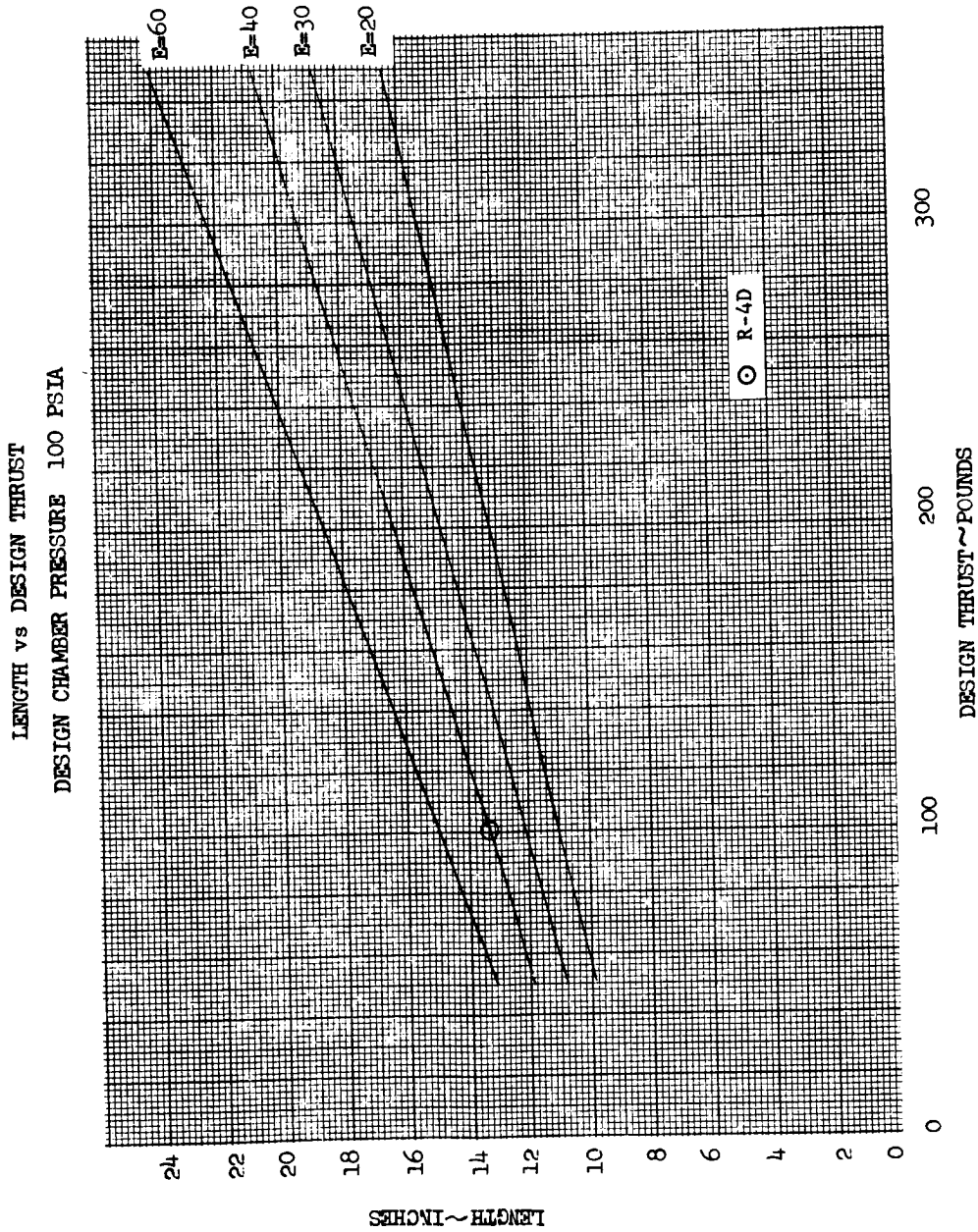


A-42

WEIGHT vs DESIGN CHAMBER PRESSURE



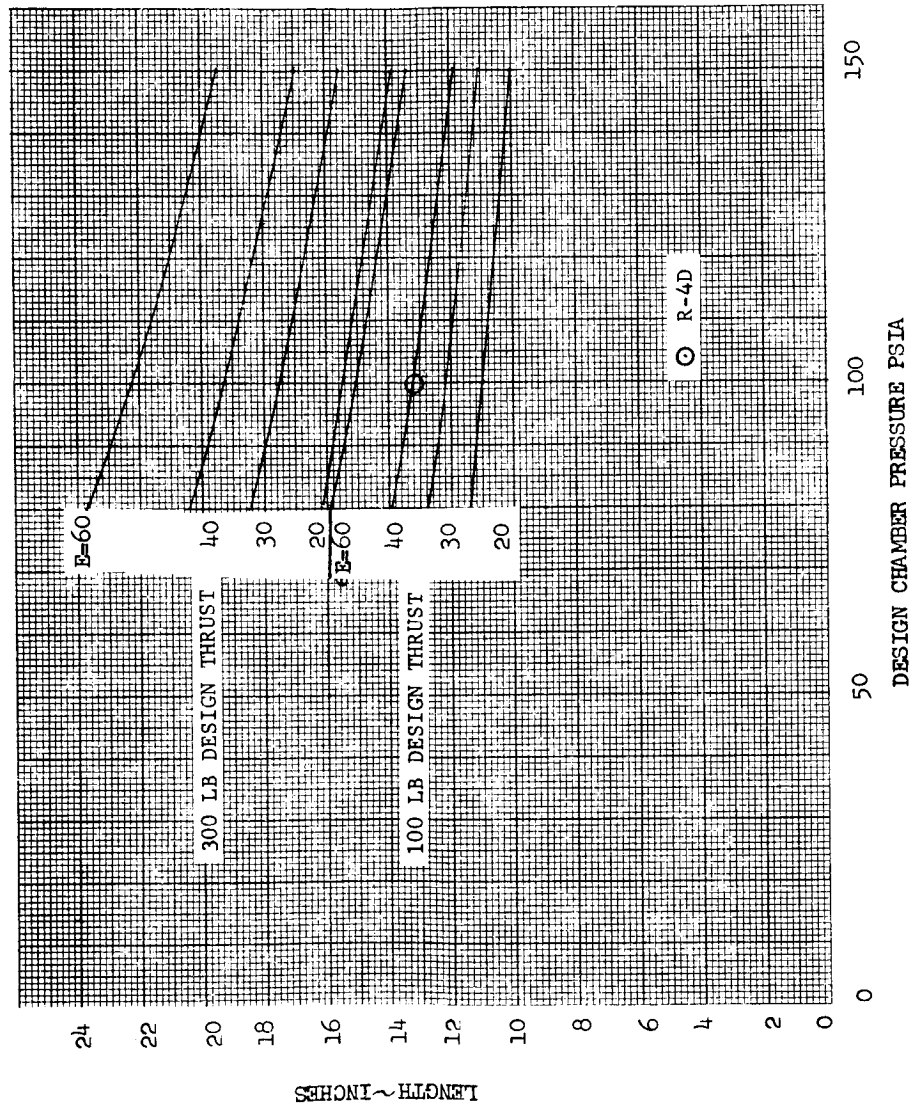
A-43



A-44

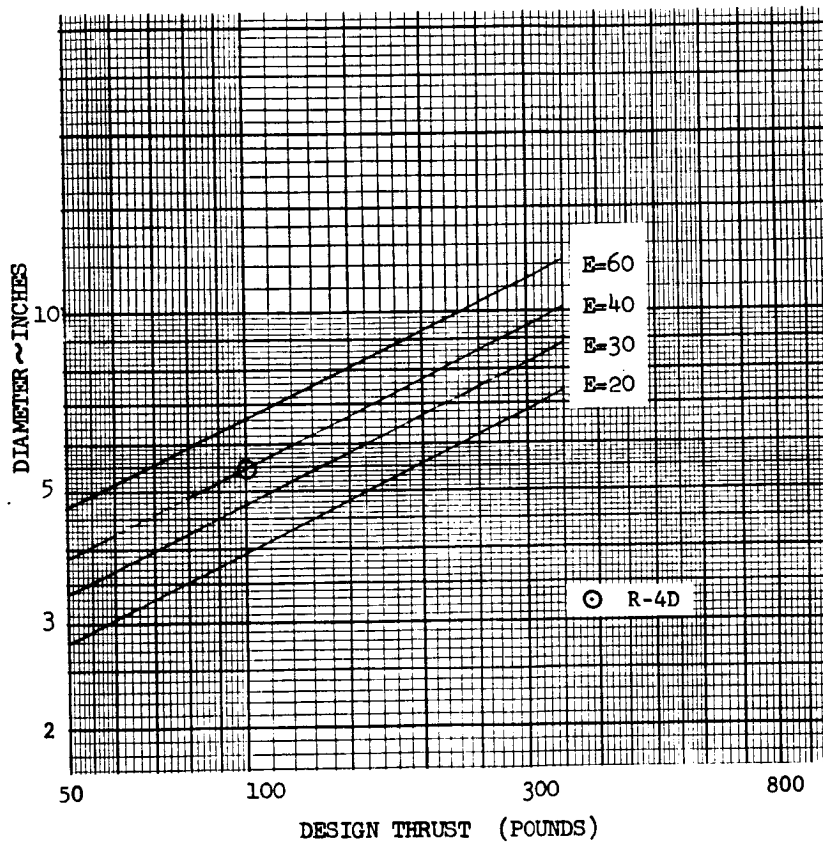


LENGTH vs DESIGN CHAMBER PRESSURE



A-45

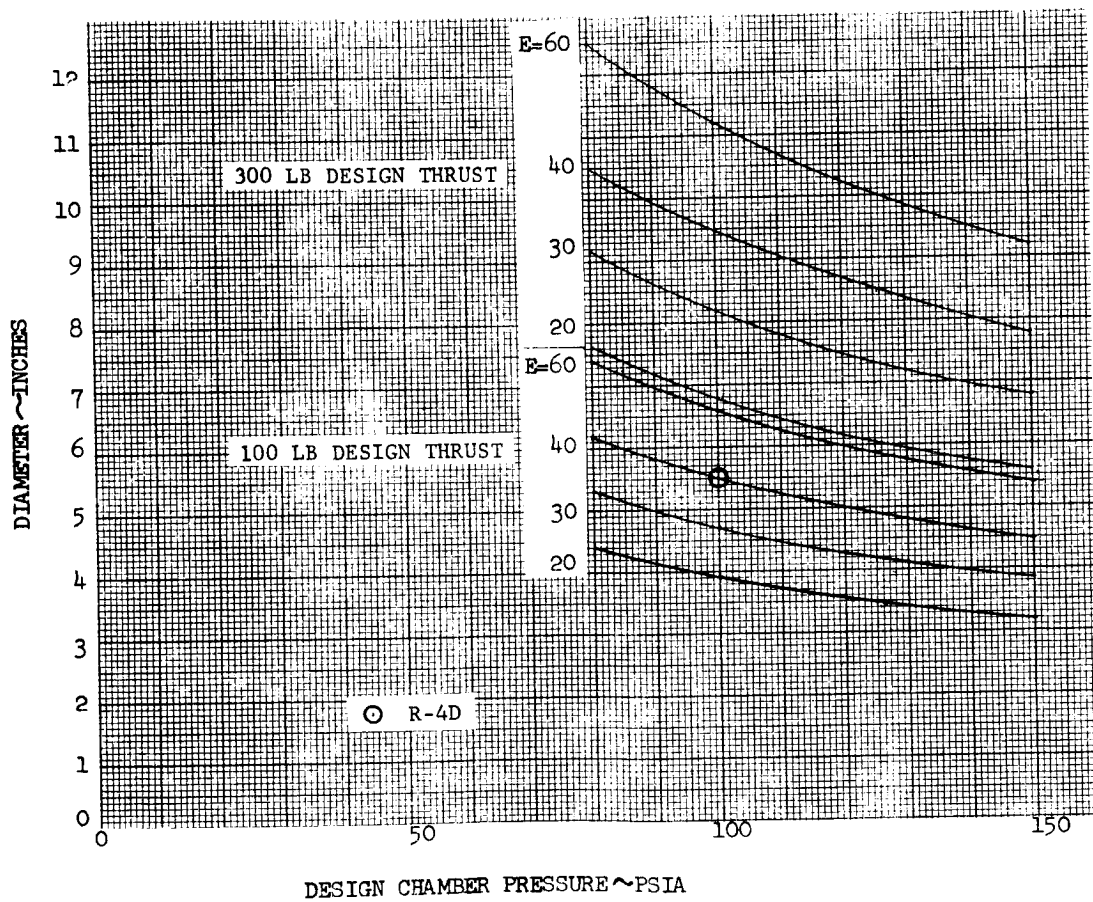
DIAMETER vs THRUST  
DESIGN CHAMBER PRESSURE 100 PSIA



A-46



DIAMETER vs DESIGN CHAMBER PRESSURE



A-47



These weight and dimension estimates do not include the thrust vectoring control system. The additional weight increments and engine envelope dimensions for various TVC methods are included below.

Engine design weight estimates as a function of nominal design thrust levels and chamber pressures are presented in Figure A-42 and A-43. The effects of changes in nozzle area ratio are shown in both figures.

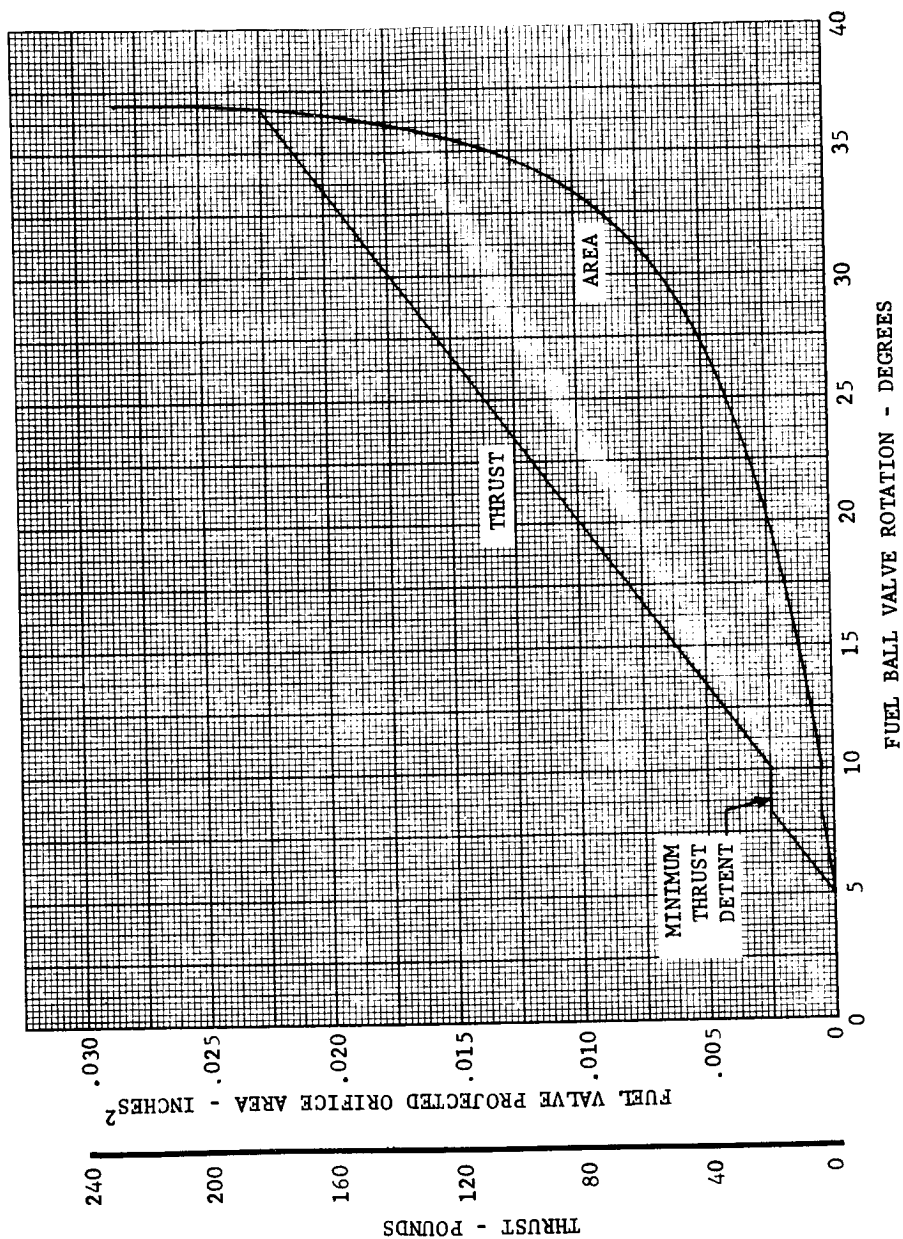
Engine design lengths as a function of nominal design thrusts and chamber pressures are presented in Figures A-44 and A-45. Engine design diameters as a function of nominal design thrusts and chamber pressures are presented in Figures A-46 and A-47.

### THRUST THROTTLING CONTROL

Preliminary design studies of methods of accomplishing thrust control of the Marquardt R-4D, R-4B, and R-23B engines have been conducted. The basic design approach has been to leave the engine injector head unchanged and accomplish the desired thrust variation by means of flow area variation in the engine propellant valves. This will require removal of the present solenoid valves and the installation of valves with a controlled variable area. The engine performance with this type of valve approach will be as given above. All of the test data discussed were obtained with the present modified engines with changes in propellant supply pressure.

The primary valve design approach considered has a pair of mechanically linked ball valves to replace the current solenoid valves on the R-4D. The valves will be simultaneously actuated (manually or remotely) by a single motion and will schedule orifice area to give the desired thrust versus deflection characteristic. The ball valves will provide positive shut off of the engine without leakage, which is a well-proven characteristic of this type of valve in rocket propellant service. The contour cut in the face of the valves will be slightly different for oxidizer and fuel to maintain constant oxidizer to fuel ratio over the thrust range. It would be possible to schedule oxidizer to fuel ratio with thrust level by controlling the contours if that should be desired. As an example of this design concept, a one-inch diameter ball valve in a 3/8-inch diameter line has been considered. Thrust and area schedules for the fuel valve are presented in Figure A-48. The area schedule would be projected area normal to the flow stream and assumes a constant  $C_D = 0.65$ . The thrust schedule is based upon 5 degree rotation beyond cut off for positive sealing. Throttling is not intended below a minimum thrust, which is shown as twenty pounds.

THRUST AND FUEL VALVE FLOW AREA  
vs. THROTTLE VALVE ROTATION

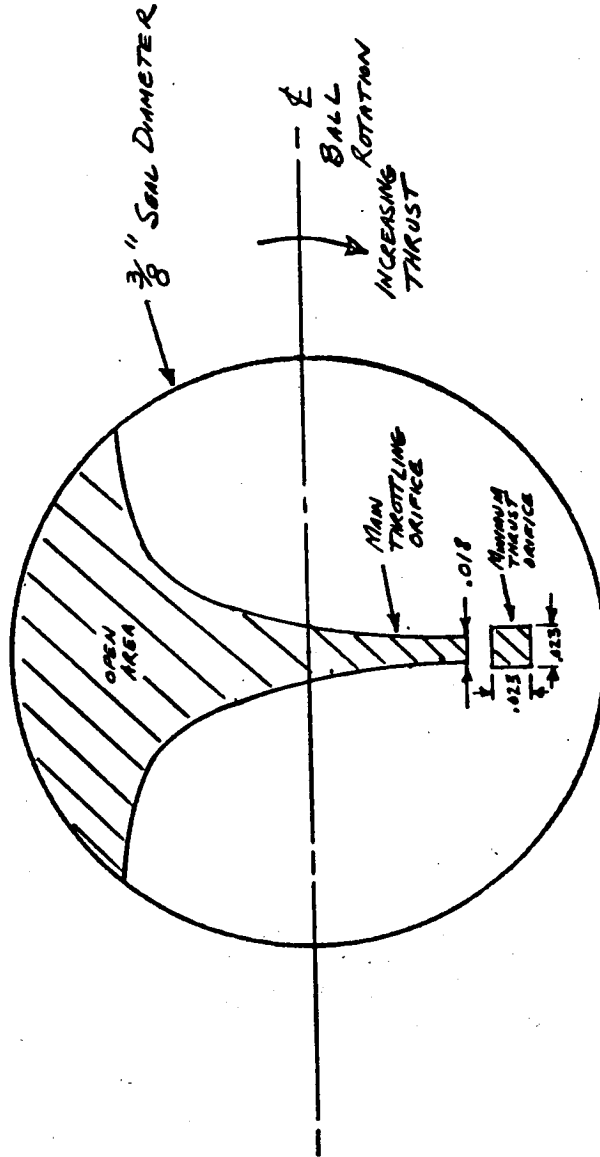


A-48

An approximate two-dimensional contour of the fuel ball valve window is illustrated in Figure A-49. Minimum thrust is achieved by a square hole orifice, 0.023 inch on a side. Opening this orifice requires 3-1/4 degree ball rotation. Then 1-3/4 degree has been left blank with no opening before the main orifice starts. This is intended to allow incorporation of a detent to prevent inadvertently going below minimum thrust when throttling back. At 10 degree rotation, the main orifice of the ball begins to open, as shown in Figure A-48. The thrust schedule selected is 6 pounds per degree of valve rotation which will be constant up to 160 pounds thrust. Beyond that the area increase required is so rapid that the thrust change per degree of rotation may diminish slightly.

Preliminary design sketches of the ball valve concept on the R-4D and R-23B engines are shown in Figures A-50 and A-51. Figure A-52 is an artist's sketch of the valve on the R-4D engine.

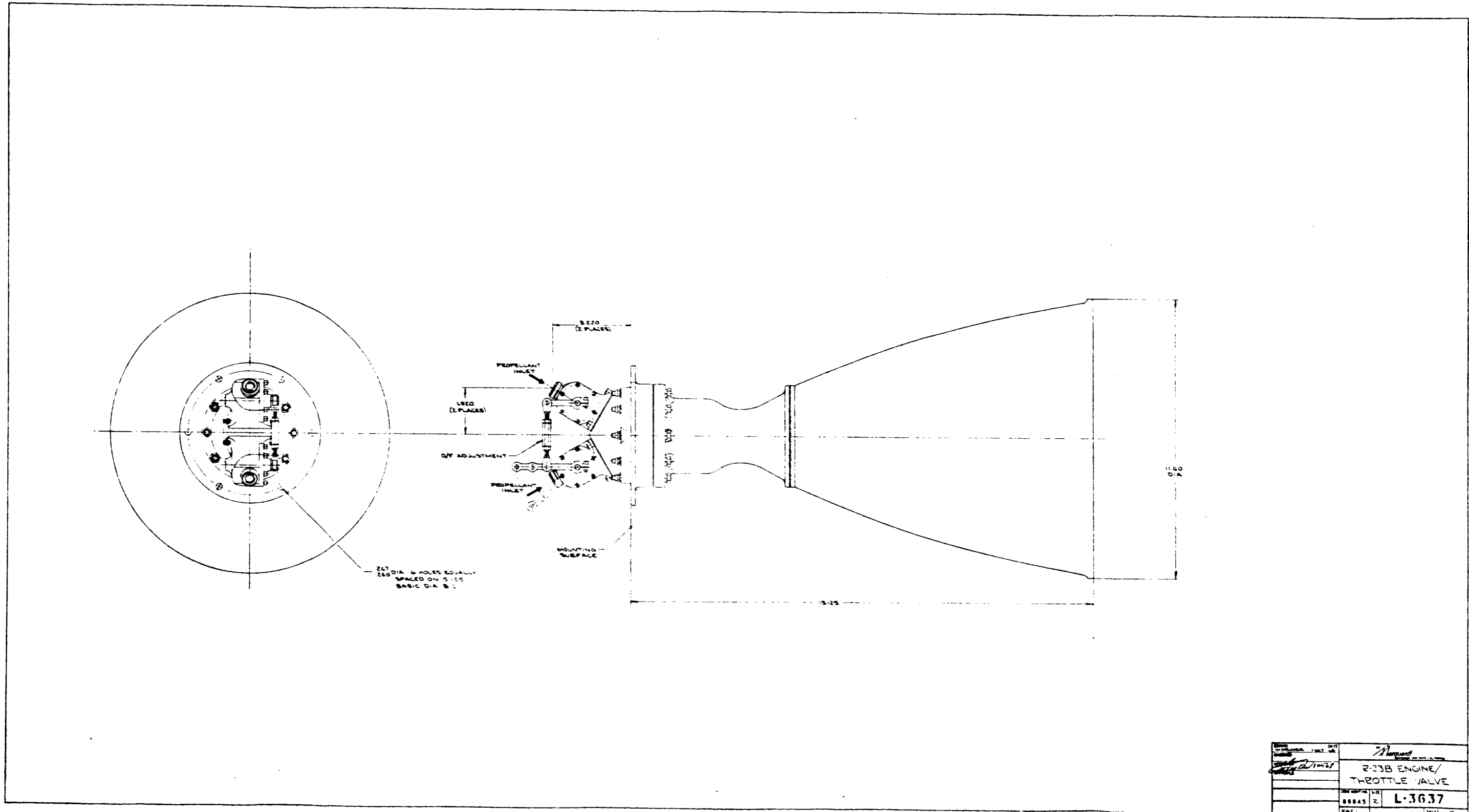
APPROXIMATE FLOW PASSAGE CONTOUR  
FOR FUEL THROTTLE VALVE



A-49

REVISIONS DATE APPROVED		PART OR IDENTIFYING NO. CHECKED APPROVED DATE	MANUFACTURE OR SOURCE OF MATERIAL OR PART LINE DATE	SPECIFICATION MATERIAL OR NOTE DATE
		MARQUARDT ROCKET ENGINE, VARIABLE THRUST, MODIFIED RAD	MARQUARDT ROCKET ENGINE, VARIABLE THRUST, MODIFIED RAD	MARQUARDT ROCKET ENGINE, VARIABLE THRUST, MODIFIED RAD
		00043 D L3122 PART 1 OF 1		

A-50



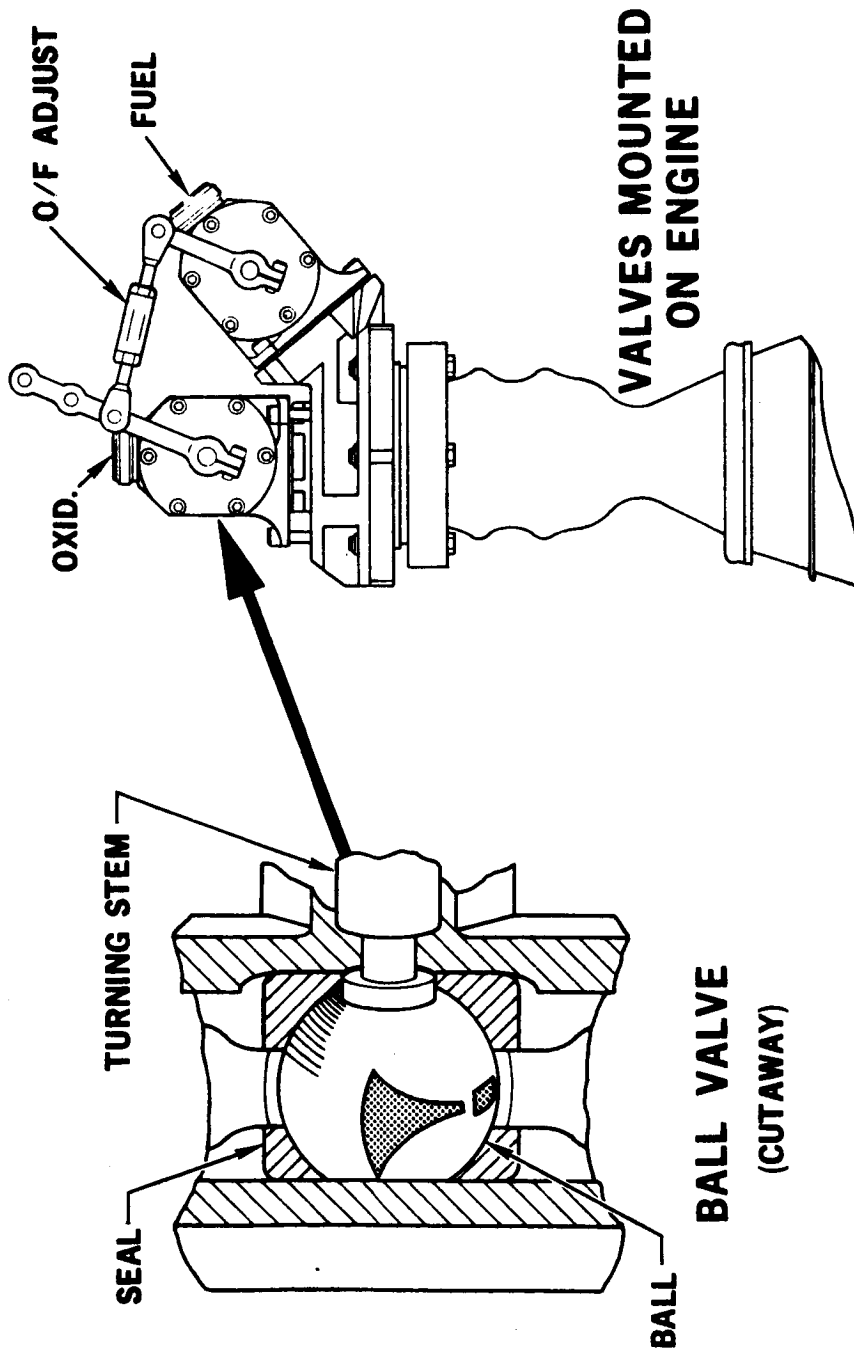
REV.	DATE	BY	CHKD.	APP'D.
1				
2-3B ENGINE / THROTTLE VALVE				
REV.	DATE	BY	CHKD.	APP'D.
1				
L-3637				

A-51

- 255,256 -

SD 69-419-3

# THROTTLE VALVE CONCEPTS



A-52



Space Division  
North American Rockwell

ROCKETDYNE

LAP 69-201 (RC)

21 MARCH 1969

LUNAR FLYING UNIT

PROPULSION STUDY

Prepared By:

Advanced Systems

Rocketdyne



## INTRODUCTION AND SUMMARY

The Space Division of NR was recently awarded a study contract for a Lunar Flying Vehicle. A generalized parametric study of performance and descriptive data has been compiled by Rocketdyne. These data were generated from Rocketdyne contract, development, and technology programs.

Efficiency factors are presented to permit realistic estimates of thrust chamber performance. Basic component parameters, such as weights and envelopes, are shown as composite curves and nomographs. Sectional views and drawings are presented to clarify the construction features and details of the system elements.

## ENGINE TYPE DESIGNS

A number of methods have been used for cooling small thrust chambers. The selection of the most suitable method depends on operating parameters of the thrust chambers; duty cycle, operating mode, chamber pressure, thrust range, total burn time, operating duration, propellant combination, allowable chamber surface temperatures, injector and valve soak back temperatures, allowable adjacent component temperatures, envelope, and weight limitations. This discussion will be limited to a comparison between radiation cooling and interregenerative cooling with a radiation skirt.

### RADIATION COOLING

For a "true" radiation-cooled thrust chamber, the critical parameter is the chamber wall temperature. The inherent limitation on radiation cooling is the availability of materials that can operate in the combustion environment at high wall temperatures. Therefore, the chamber is usually made of a refractory metal with an oxidation resistant coating. The coatings and wall materials limit the wall temperature to approximately 3000 F, which limits the chamber pressure to approximately 100 psia. Therefore, close control of the operating temperature must be maintained to keep the chamber wall temperature below the critical value. Radiation-cooled thrust chambers are being used in man rated space systems and other important system applications. They have demonstrated their applicability, in unburied configurations, to various mission duty cycles, restart conditions, and long life operation.

Some practical limitations and reliability problems associated with radiation-cooled thrust chambers are described below. Many of the problem areas presented are discussed more fully by Coulbert<sup>1</sup>.

1. A thin chamber wall is usually required because of weight considerations from high-density refractory metals and also to minimize the inside to outside temperature difference and maximize radiation heat loss. This puts limits on the structural strength of the chamber
2. The high operating wall temperature is generally above the recrystallization temperature of most refractory metals. Grain

---

<sup>1</sup>Coulbert, C. D., "Selecting Cooling Techniques for Liquid Rockets for Spacecraft," Journal of Spacecraft, Vol. 1, No. 2, 129-139, (March-April 1964).

growth and brittleness of metal greatly reduce the reliability with the presence of high-ignition pressure spikes

3. Unless assisted by film cooling or other methods, radiation-cooled chambers are not adaptable to buried installation. Reflective shielding has been tried with limited success. A large shield enclosure is needed to obtain large view angles for reradiation. Active methods of cooling radiation shields would require heavy cooling jackets
4. High thermal diffusivity and temperature of the chamber presents a "thermal management" problem for the propellants and vehicle structure
5. Disilicide is probably the best overall oxidation-resistant coating known to date. It forms a protective layer in an oxidizing atmosphere. Good adhesion and graded silicide structure can be obtained with molybdenum because of the formation of a number of silicides:  $\text{MoSi}_2$ ,  $\text{MoSi}_3$ , and  $\text{Mo}_3\text{Si}$ . However, at high temperatures, and in hard space vacuum, the vaporization of Si or  $\text{SiO}_2$  from the coating becomes appreciable, and the life will then be limited by the coating thickness. For such extended durations as this application, the coating life will be a major concern. To provide for adequate adhesion with the substrate material, the coating thickness is usually limited to below 0.002-inch. Nonuniformity of coating thickness and imperfections (such as pinholes) are potential problems of quality control and reliability. Clad coating of tantalum-tungsten shows some promise, but is still very much in the experimental research phase
6. Because of the high chamber operating temperature, the chamber-to-injector seal and the propellant valve heat soakback are critical problems
7. A radiation engine designed to operate with film coolant will be quite sensitive to perturbation in flow from the coolant orifices. Because of the relatively poor conductivity of refractory alloys, a restricted coolant orifice could result in local temperatures above the coating capability.

## INTERREGENERATIVE COOLING (TWO-PIECE DESIGN)

The internal-regeneration (interegen) thrust chamber cooling concept utilizes injection of a liquid coolant on the internal surface of the thrust chamber to remove heat from the thrust chamber wall. This function is in addition to the more familiar film-cooling technique: reduction of heat transfer rate from the combustion gases to the thrust chamber wall by providing a heat transfer barrier.

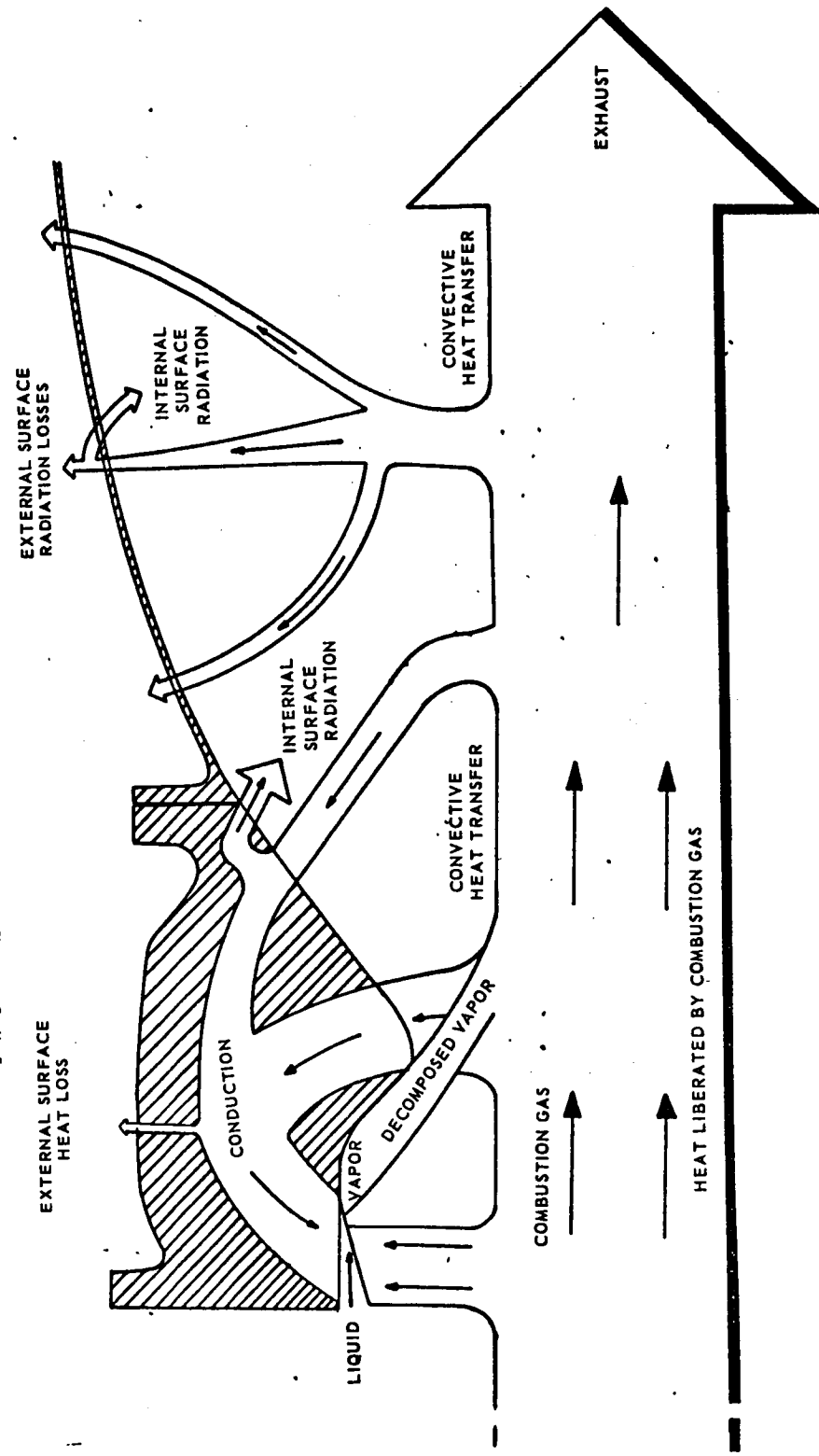
To accomplish the interegen mode of energy transfer, the thrust chamber is fabricated of high-thermal-conductivity material and uniquely contoured. The heat generated in the high heat flux regions of the nozzle is conducted through the walls and absorbed by the liquid coolant on the combustion wall. This energy transfer process uses both the sensible and latent heat of the fuel to cool the thrust chamber. Thus, the cooling effect of the film coolant is extended beyond the throat region, and much lower temperatures can be maintained in the chamber than is possible in many other cooling techniques. Beryllium is uniquely suited for this concept, being one of the lightest materials known (density - 0.067 lb/in<sup>3</sup>), and has a high thermal conductivity. These physical properties give a thrust chamber many desirable features, including lightweight, thick-walled, and rugged construction, low temperature, low cost, duty cycle insensitive, and infinite life potential.

The two-piece design feature of the thrust chamber incorporates an L-605 (cobalt alloy) skirt attached at an appropriate axial location (optimum interegen-skirt temperature trade) to minimize high heat flux from the skirt region to the combustion zone during operation and, more importantly, during soakout. The two-piece design minimizes the total stored thermal energy and results in lower equilibrium temperatures. Because of the optimized attachment location of radiation skirt to beryllium chamber and choice of material, the radiation skirt does not require the use of oxidation-resistant coatings. As a result of the reduced total stored thermal energy of the interegen two-piece engine, it has been shown that a low valve soak-back temperature is achievable by incorporating insulation between the thrust chamber and injector.

Figure A-53 presents an interegen heat flow schematic with a radiation skirt attached. A graphic representation of beryllium chamber thermal data is shown in Figure A-54 to illustrate the interegen concept. Isothermal and heat flux lines are plotted showing the internal conduction from the throat region to the coolant film in the chamber wall. Figure A-55 illustrates the equilibrium temperature distribution of a 300-pound-thrust beryllium engine with a L-605 nozzle skirt.



TWO-PIECE INTEREGEN HEAT FLOW SCHEMATIC

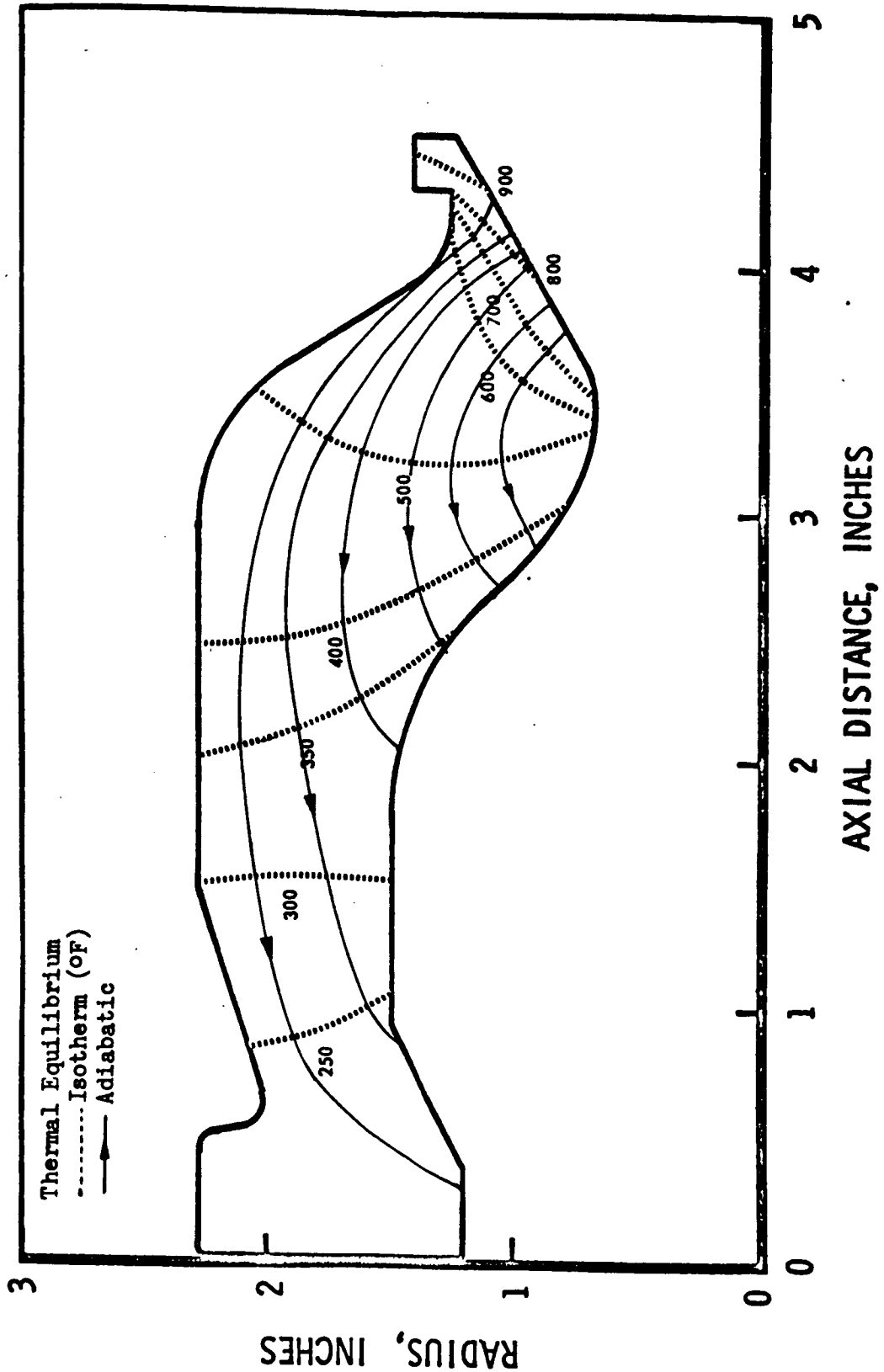


**ROCKETDYNE**  
A DIVISION OF NORTH AMERICAN ROCKWELL CORPORATION  
4813 CANOGA AVENUE CANOGA PARK, CALIFORNIA 91304

A-53



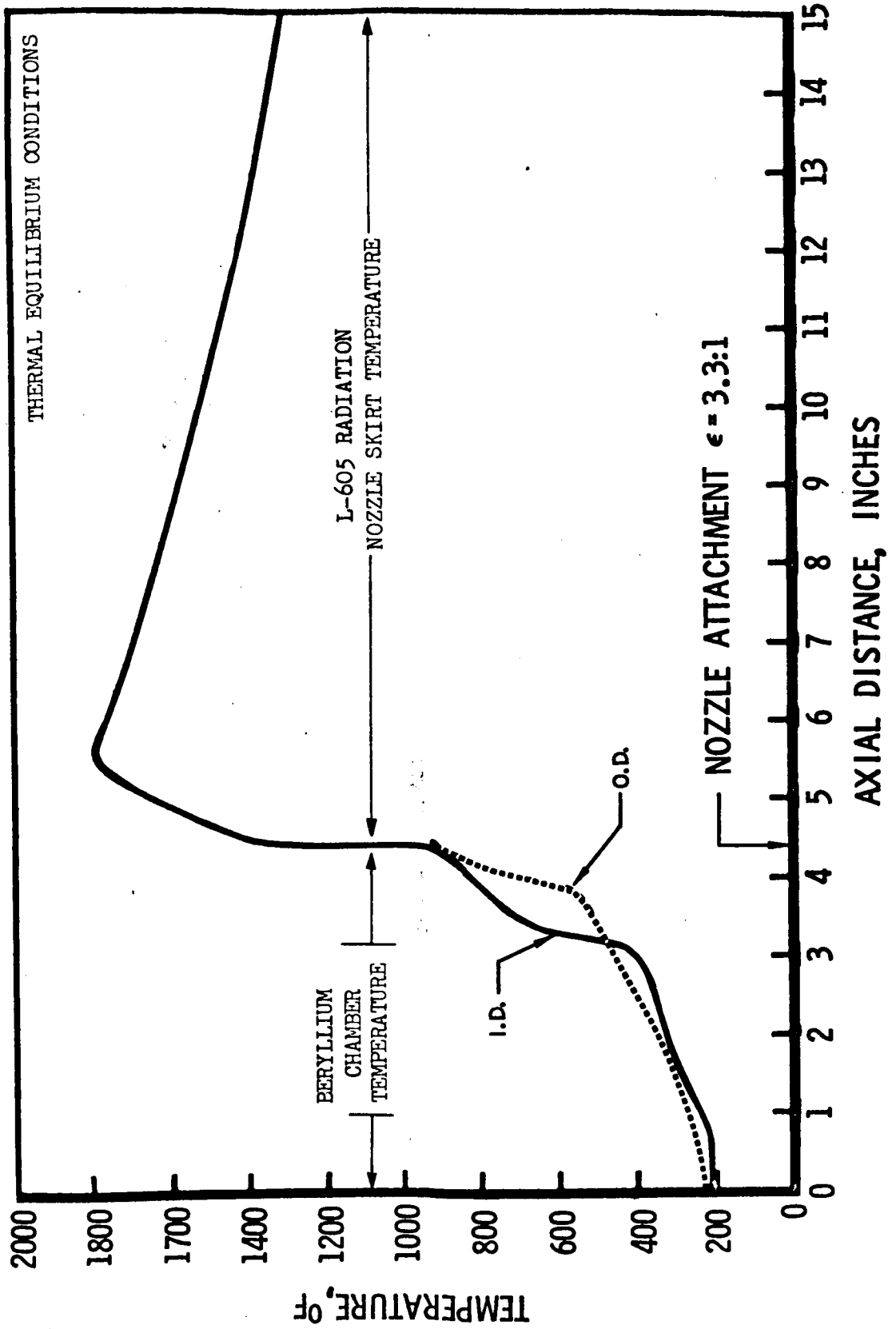
300 - POUND - THRUST  
BERYLLIUM CHAMBER  
POTENTIAL PLOT



A-54



300-POUND-THRUST INTERGEN ENGINE



A summary of the interegen cooling concept discussion is as follows:

1. This concept features inherent reliability, ease of manufacturing, and maintenance simplicity
2. Current basic designs will meet the LFV TCA requirements
3. Lightweight assemblies of rugged chamber construction are capable of withstanding severe vibration and shocks, repeated ignition pressure spikes, and thermal cycles
4. Such a chamber can be insensitive to duty-cycle changes and can exhibit infinite life potential
5. Inherent high thermal capacity minimizes "thermal management" problems
6. No hazard of heterogeneous decomposition of the coolant, and no cooling jacket propellant boiling problems are encountered
7. No oxidation-resistant coating is required
8. Low injector valve soak back temperature can be maintained by unique interface design between the chamber, the injector, and the valves
9. The concept lends itself to high performance, which can result in considerable saving in propellant weight.



## THROTTLING TECHNIQUES

Liquid rockets are readily adaptable to thrust modulated modes of operation with numerous concepts having been developed for successful throttling. The propellant flowrate equation

$$\dot{W} = \rho A V$$

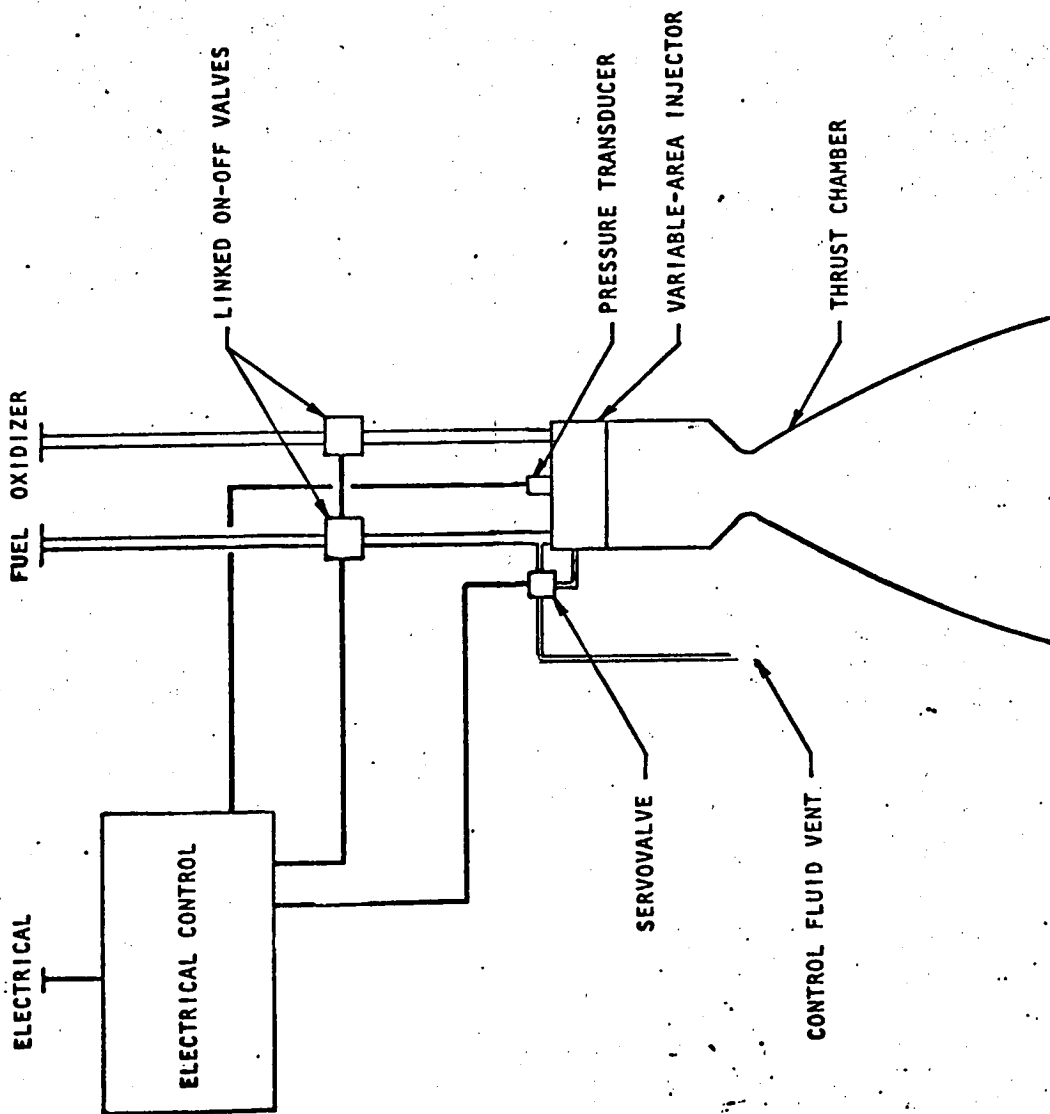
shows that fluid flow ( $\dot{W}$ ), and, therefore, thrust, may be controlled directly by varying density ( $\rho$ ), total injector orifice area ( $A$ ), or injection velocity ( $V$ ). Although most real systems actually modulate more than a single variable, they may be generally categorized as variable-area, variable velocity, or variable-density propellant throttling. These three thrust modulating techniques, each of which is encompassed by Rocketdyne Small Engine Division experience, are examined in detail and evaluated in terms of the environment and functional requirements.

### VARIABLE-AREA THROTTLING

Thrust variation with the variable-area injector concept is achieved by positioning a throttling pintle to vary propellant flow areas at the injector orifices. This method is used on the Lance missile sustainer engine developed by Rocketdyne under contract to Ling-Temco-Vought Corporation for the United States Army. In the missile application, the sustainer engine has a maximum thrust in excess of 4000 pounds. The chamber pressure is at a sufficiently high level that the actual injector is essentially the correct size for the engine.

A schematic representation of a variable-area engine assembly is shown in Figure A-56. The assembly incorporates solenoid-operated on-off valves and normally open, squib-actuated shutoff valves to seal all propellant lines at the mission terminus. Throttling is achieved through use of a torque motor controlling a servovalve in response to a command signal. The servovalve provides hydraulic pressure (fuel propellant) positioning the injector pintle to meter the requirement propellant flowrate. This simplified control concept has been developed for ease in achieving a high missile production rate, and is a fully proved system.

The performance of the variable-area concept is characterized by a progressively higher delta pressure across metering pintle as the injector orifices are closed. The Lance injector operates over a range of 50:1, indicating a high degree of flexibility.



Variable-Area Injector Schematic (Hydraulic Actuation)

A-56

Figure A-57 illustrates an alternate control system to the hydraulic servo used in the Lance sustainer, employing an electromechanical actuator to operate both the injector and the on-off valves.

#### VARIABLE VELOCITY - SINGLE MANIFOLD

Velocity variation as a primary throttling technique can be successfully used with a simple fixed-geometry injector to achieve a throttling range of about 4:1. The limitation results from injection velocity variance in proportion to the square root of the injector differential pressure. The concept attractiveness stems from the capability of accomplishing a moderate degree of thrust modulation by varying the injector supply pressure. The thrust modulation range can be extended significantly by segmenting the injector and varying the supply pressure progressively to the entire injector area and then to the injector individual sectors.

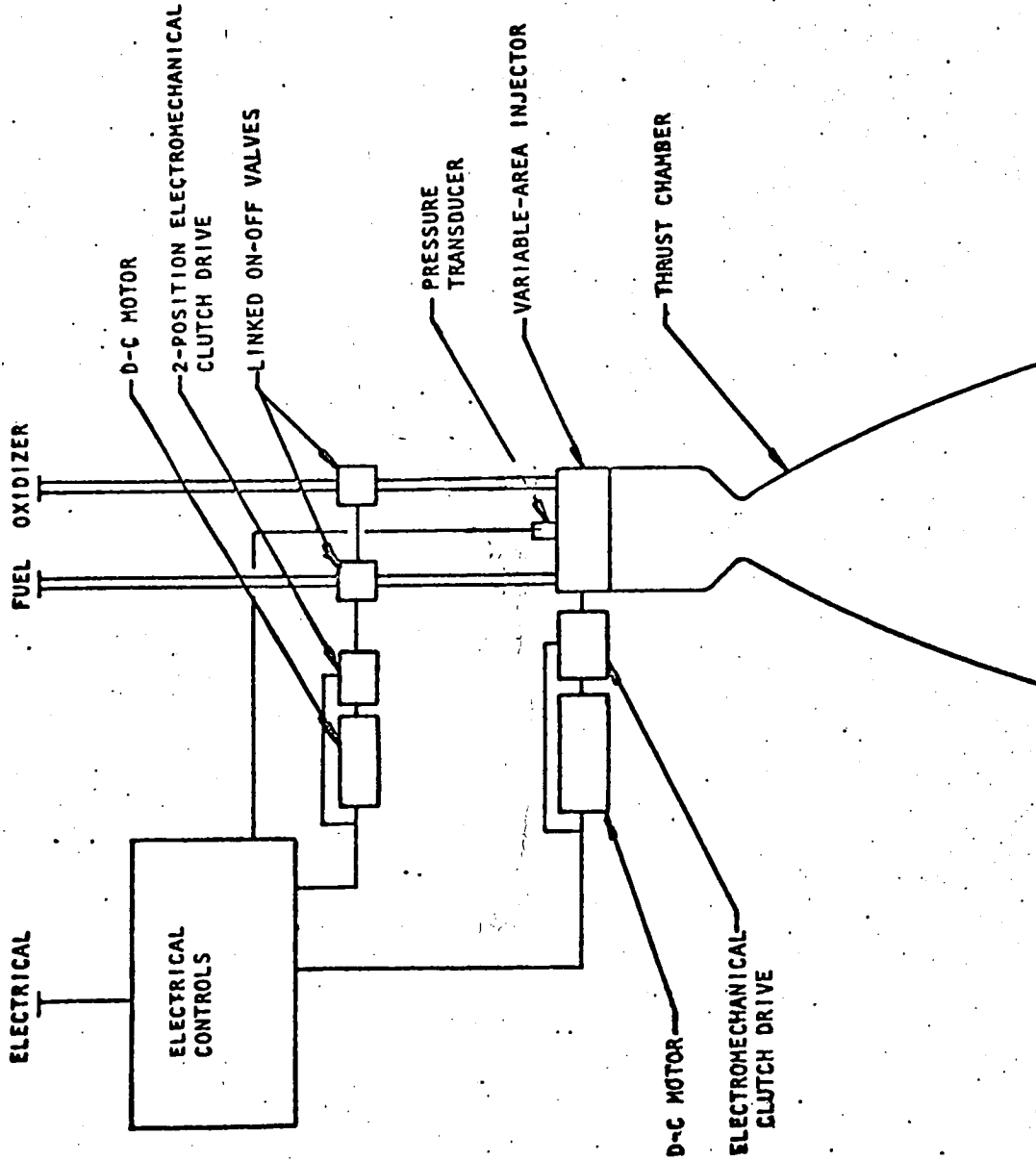
#### VARIABLE VELOCITY - DUAL MANIFOLD

A dual manifold concept was developed (NASA Contract NAS7-304) which has a capability of 10:1 thrust modulation by means of a two-segment injector. The injector is supplied by a dual manifold system which permits a portion of the injector to be shut off at an established level while operation is continued on the remaining sector. In this manner, pressure throttling can be accomplished from maximum thrust to some intermediate point while supplying the propellant to the entire injector and then, by closing one manifold set, throttling can be continued from the intermediate level to minimum thrust. A system diagram is shown in Figure A-58.

The dual manifold concept is more suitable for throttling operation at thrust levels away from the transition point for full injector area operation to partial area injection. The transition point is characterized by an abrupt change in injector differential pressures and is susceptible to hysteresis in the  $k$  thrust level response to a command signal due to manifold priming. Demonstrations of throttling from maximum to minimum power over a 10:1 range have been smooth and stable. A rapid transit from minimum power to maximum thrust would be less predictable, and could involve a delayed response unless proper valve timing is accomplished. As part of the NASA-JPL program, a small metered flow of propellant was maintained through the shutoff valves of the segmented injector to cool the inoperative injector section and to maintain fully primed manifolds. As a result, a more nearly linear transition through the point of discontinuity was made possible.



ROCKETDYNE • A DIVISION OF NORTH AMERICAN AVIATION, INC.

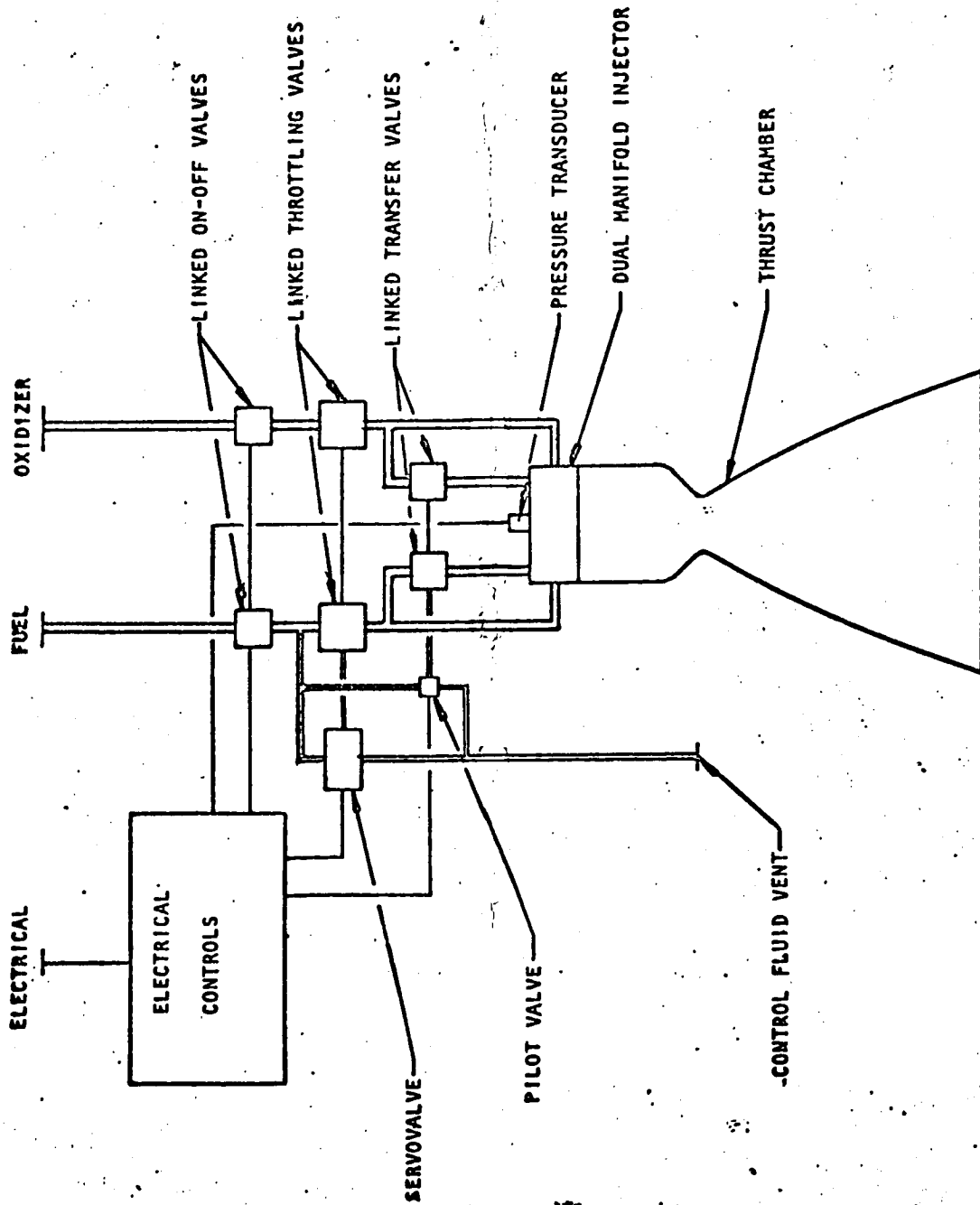


Variable-Area Injector Schematic (Electromechanical Actuation)

A-57



ROCKETDYNE • A DIVISION OF NORTH AMERICAN AVIATION, INC.



Dual Manifold Schematic

A-58

## VARIABLE-DENSITY THROTTLING

A successful concept of variable-density throttling has been developed at Rocketdyne by means of helium aeration of the propellants. As part of the lunar module program, several injectors were designed for use with helium injection. While the injector development was not completed, sufficient data were obtained to demonstrate the concept feasibility with reasonably high efficiencies over the 10:1 throttling range. A diagram of the helium injection system is shown in Figure A-59.

The system throttling operation from maximum thrust to 50 percent of maximum is accomplished by simple propellant pressure modulation. At the mid-thrust point, helium is injected into the propellants causing a decrease in density and consequently an injection velocity increase. Throttling is then continued by further reducing the propellant pressures to the injector to achieve thrust variance. The helium flowrate is constant and creates little interference with the normal combustion process.

The helium injection concept is attractive because it permits extending the normal 4:1 throttling range of a fixed-geometry injector to greater than a 10:1 range by modulating only the propellant flowrate. A major limitation of the concept is the relatively slow response inherent in the helium aerated propellants which are moderately compressible. This is amplified at the low-thrust point where a substantial percentage of the manifold volume is helium. While the helium injection concept was carried well into the development of an operational system, the final injector development phases were not completed. The feasibility of the concept was thoroughly demonstrated, however. One characteristic noted during the lunar module program was the sensitivity of the engine system to the facility feed system dynamics.

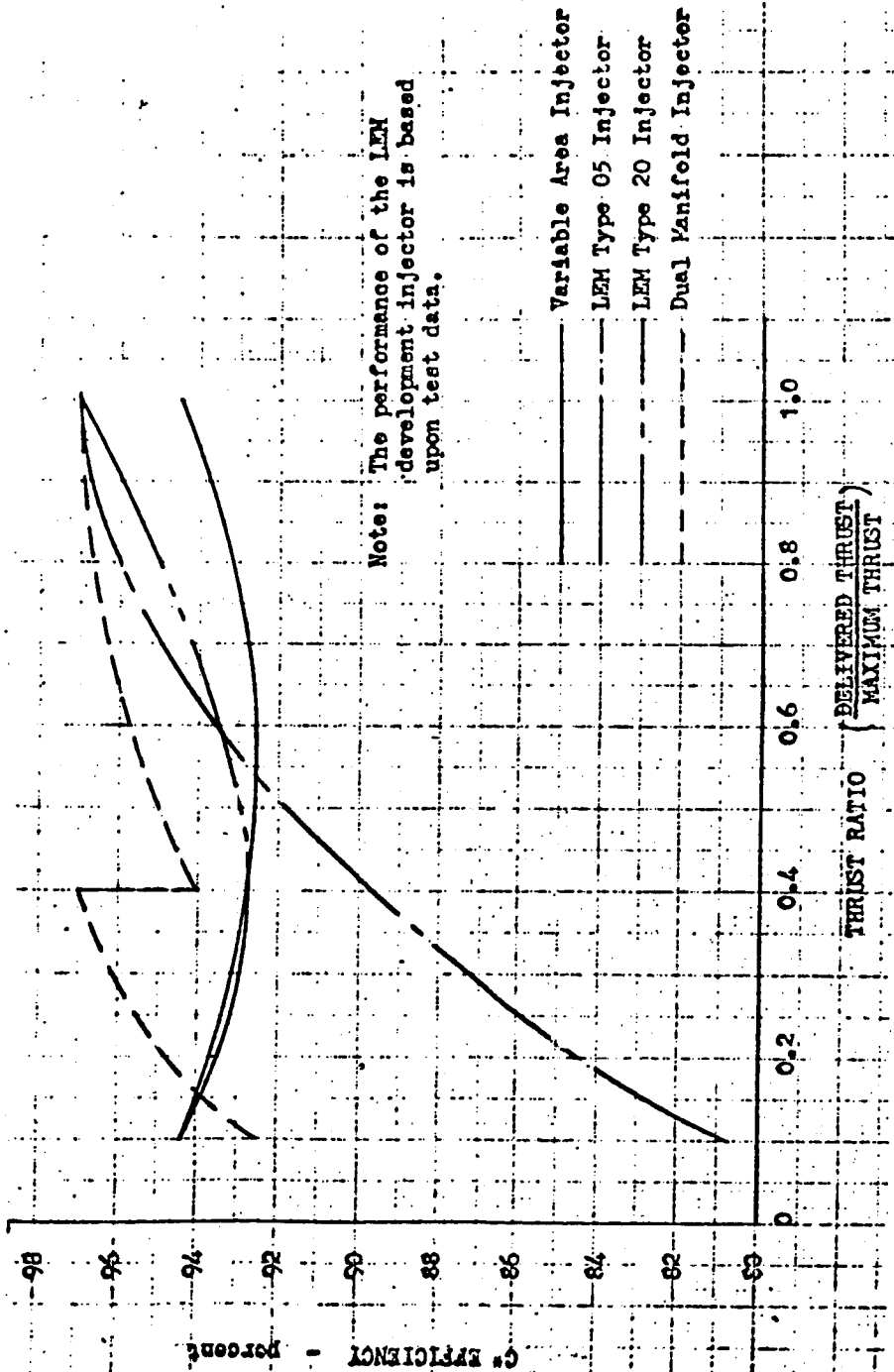
## THROTTLING PERFORMANCE

A comparison of the throttling performance of the three throttling concepts is presented in Figure A-60. The performance of the lunar module injectors (types 05 and 20) is based upon test data. The type 05 injector was devised early in the program and type 20 was designed near the end of the program. The performance of the variable-area injector is based on the injector developed for the Lance missile sustainer engine. This engine is designed for high production rather than maximum performance. Consequently, the Lance data do not typify performance for a close-tolerance, high-efficiency space engine. An estimate of the improvement that should be available with precision hardware and with  $N_2O_4$  as an oxidizer is included in the performance prediction. The dual-manifold injector performance is based on the work done under NASA Contract NAS7-304. This program was conducted to advance and extend chamber technology for the space storable  $OF_2/MMH$  to estimate the throttling performance shown.



HR

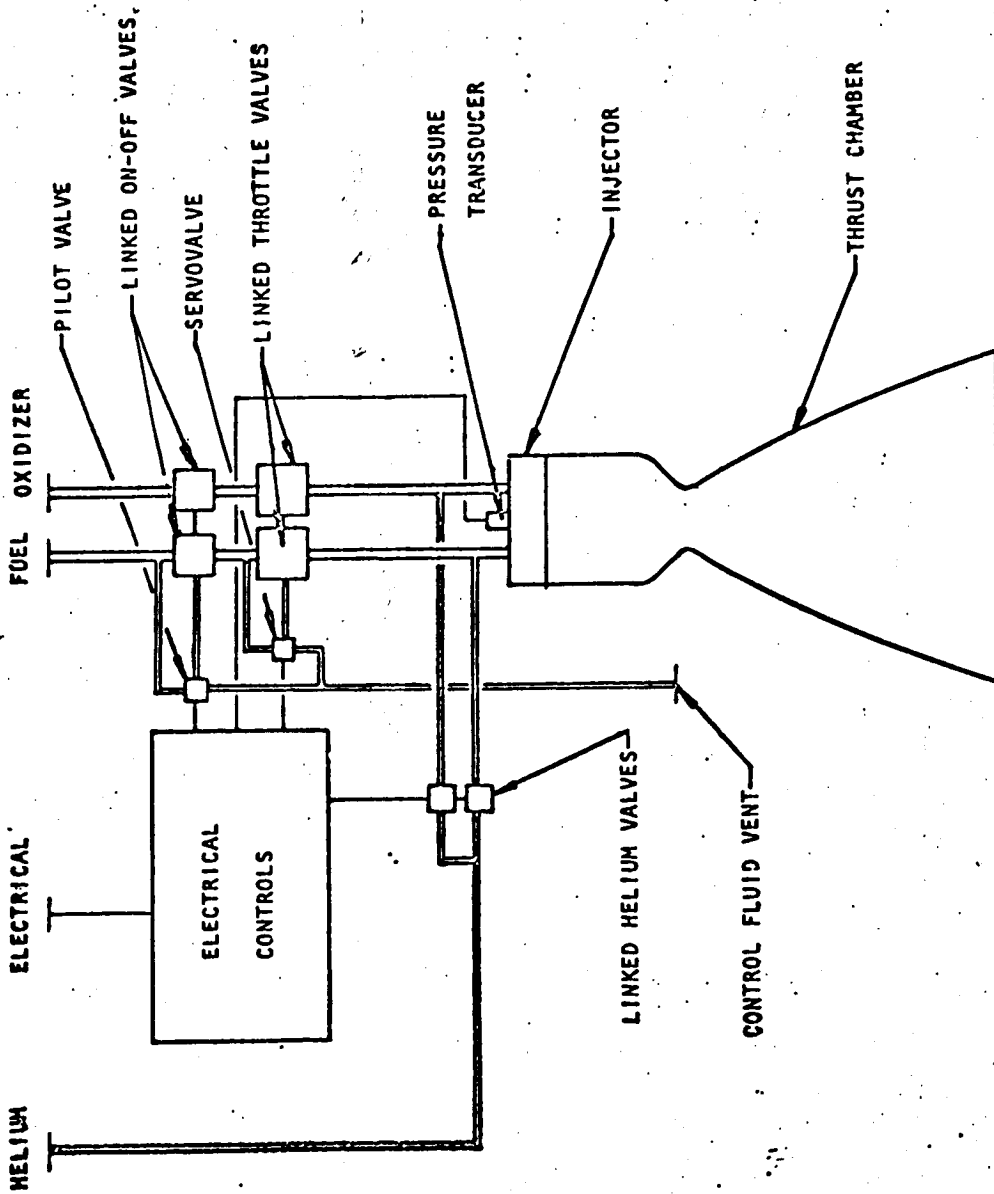
ROCKETDYNE • A DIVISION OF NORTH AMERICAN AVIATION, INC.



Predicted Throttling Performance With No Film Cooling

A-59

ROCKETDYNE • A DIVISION OF NORTH AMERICAN AVIATION, INC.



Helium Injection Schematic

A-60



The effect of film cooling on the throttling performance of the dual-manifold and variable-area injector is shown in Figure A-61. A 7.5-percent, boundary-layer cooling (BLC) was selected for the study comparison. The percent of BLC is defined as the ratio of fuel coolant flow to total propellant flow, and is considered constant throughout the operation.

As shown in the dual-manifold injector curve, a 40-percent (of full thrust) transition point was used for this application. Higher combustion efficiencies are realized at this transition point due to the higher pressure drop across the injector upon closing off one manifold set while maintaining constant tank pressure and utilizing only 40 percent of the total flowrate. However, the transition point can be repositioned on any given design to be more compatible with any desired duty cycles.

#### MIXTURE RATIO VARIATION

The mixture ratio tolerance band typical of space engine specifications is approximately  $\pm 3$  percent. This limit would be maintained at the maximum thrust level for the engines. However, as the thrust is modulated, mechanical tolerances become more critical, and the mixture ratio cannot be maintained as closely. Figure A-62 was generated from experience gained from the Lance program and from other throttling injector programs. A range of mixture ratio variation versus thrust is provided rather than a precise curve.

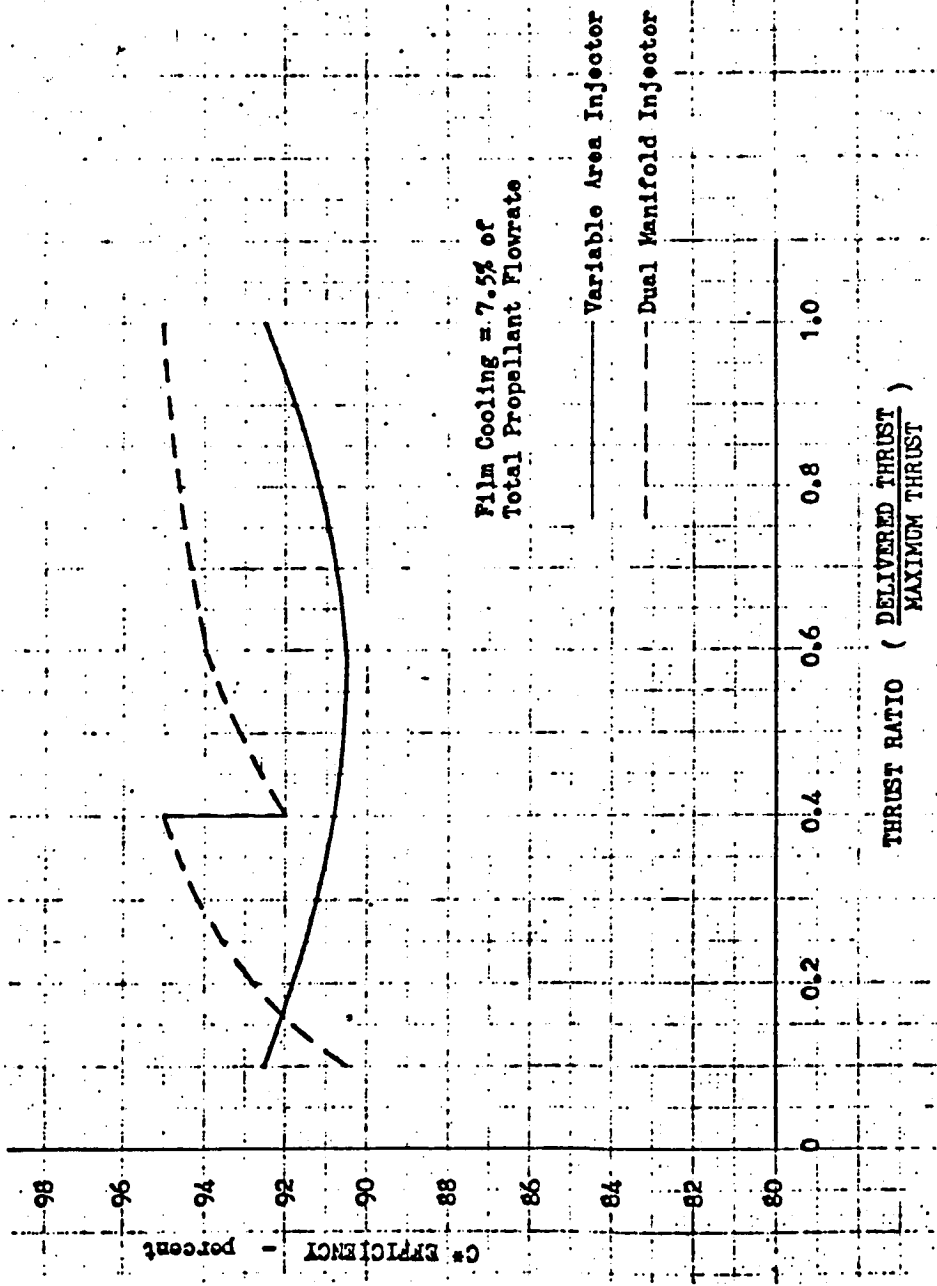
Figure A-62 shows a reasonable estimate of the mixture ratio variation for any of the above throttling injector concepts. Test firings and a trade study involving complexity and part tolerances as a function of cost are required to establish the exact mixture ratio variation.

#### CORRECTED SPECIFIC IMPULSES

Predicted deliverable specific impulse, identified as corrected specific impulse, is presented in Figures A-63 through A-66. The independent variables are chamber pressure, thrust, and expansion area ratio. Characteristic velocity efficiency at full thrust was selected as a constant value of 0.93, representative of the range of performance expected from the several injector types being considered. Variations as a function of individual injector design could be as great as  $\pm 2$  percent. Thrust coefficient efficiency was computed accounting for geometric, friction, and kinetic losses. Comparing these losses to those actually determined from testing of the 100-pound and 300-pound engines illustrated that the actual losses are 0.7 of the computed values.



ROCKETDYNE • A DIVISION OF NORTH AMERICAN AVIATION, INC.

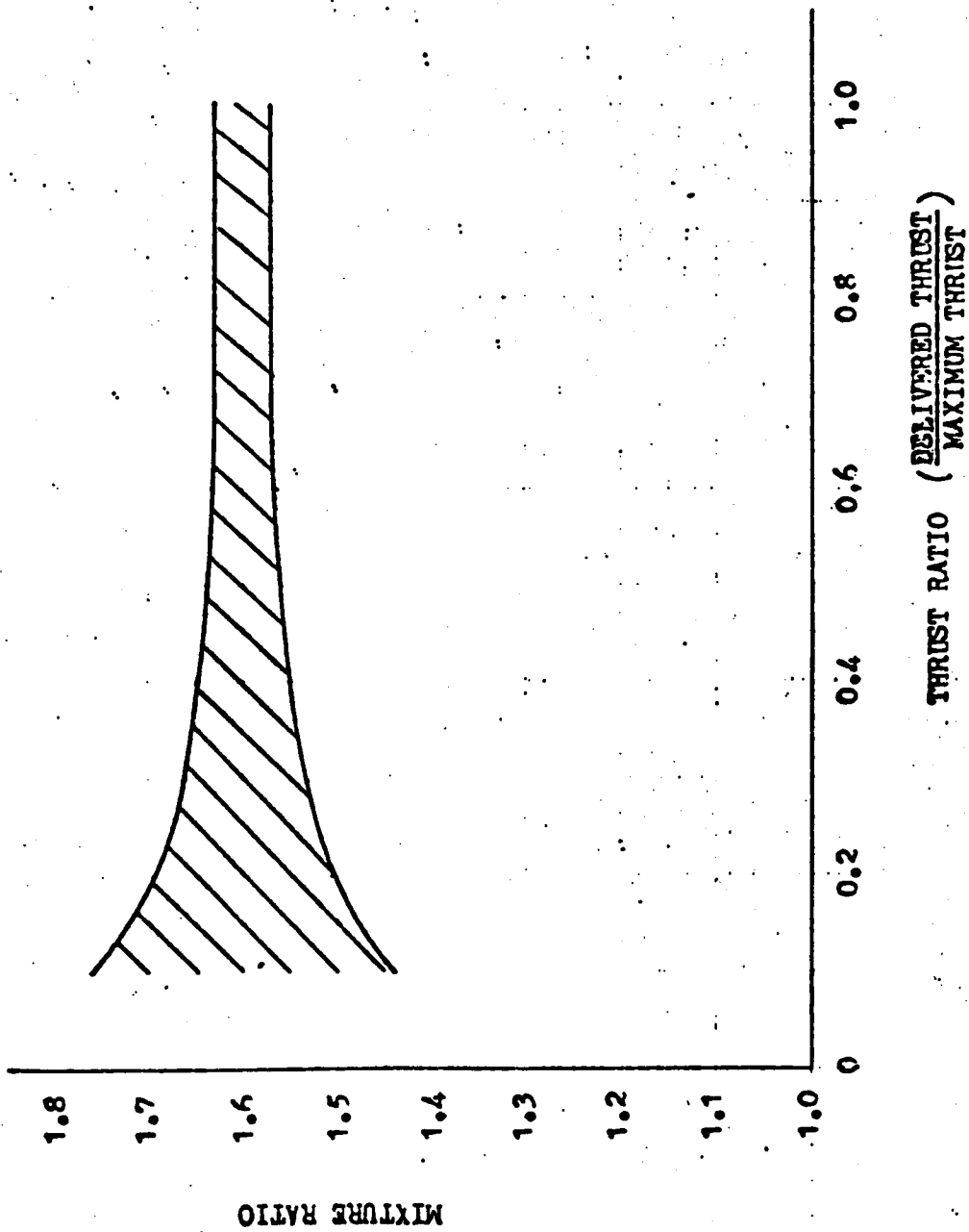


Predicted Throttling Performance With Film Cooling

A-61



ROCKETDYNE • A DIVISION OF NORTH AMERICAN AVIATION, INC.



Estimated Mixture Ratio Variation For Throttling

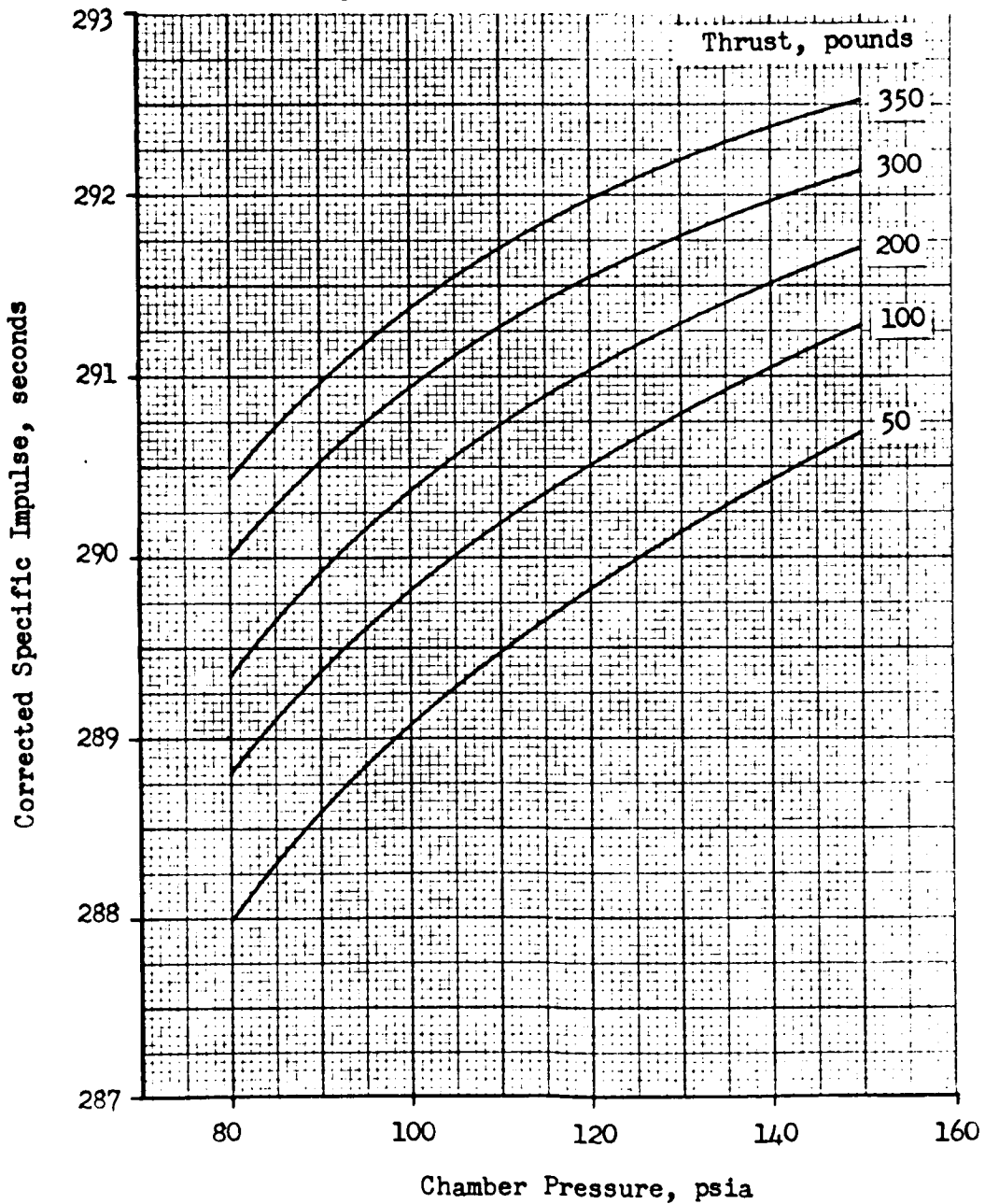
A-62

Corrected Specific Impulse  
vs. Chamber Pressure

Propellants =  $N_2O_4/N_2H_4$  - UDMH (50-50)

Mixture Ratio = 1.6 o/f

Expansion Area Ratio = 20



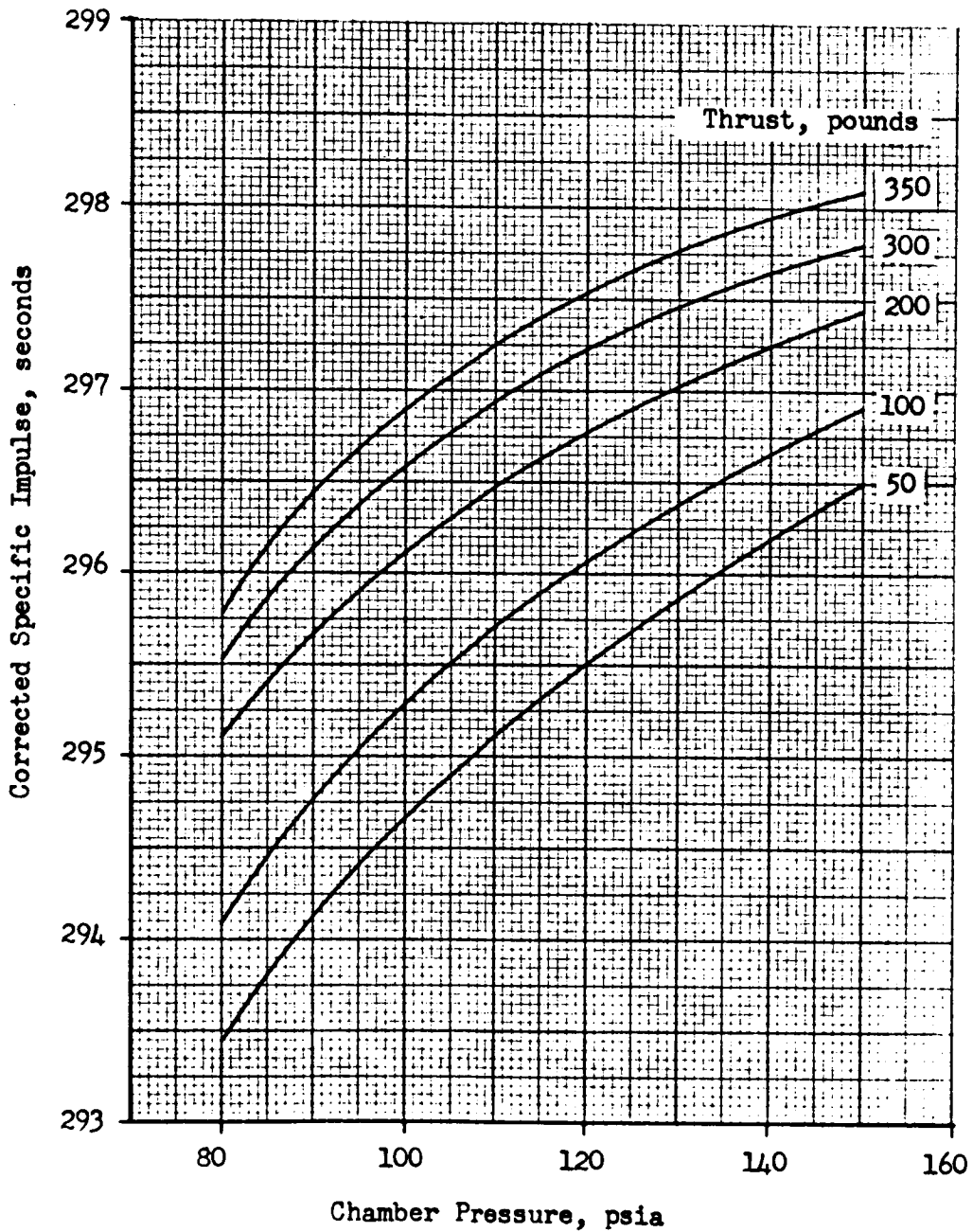
A-63

- 282 -

SD 69-419-3

Corrected Specific Impulse  
vs. Chamber Pressure

Propellants -  $N_2O_4/N_2H_4$  - UDMH (50-50)  
Mixture Ratio = 1.6 o/f  
Expansion Area Ratio = 30

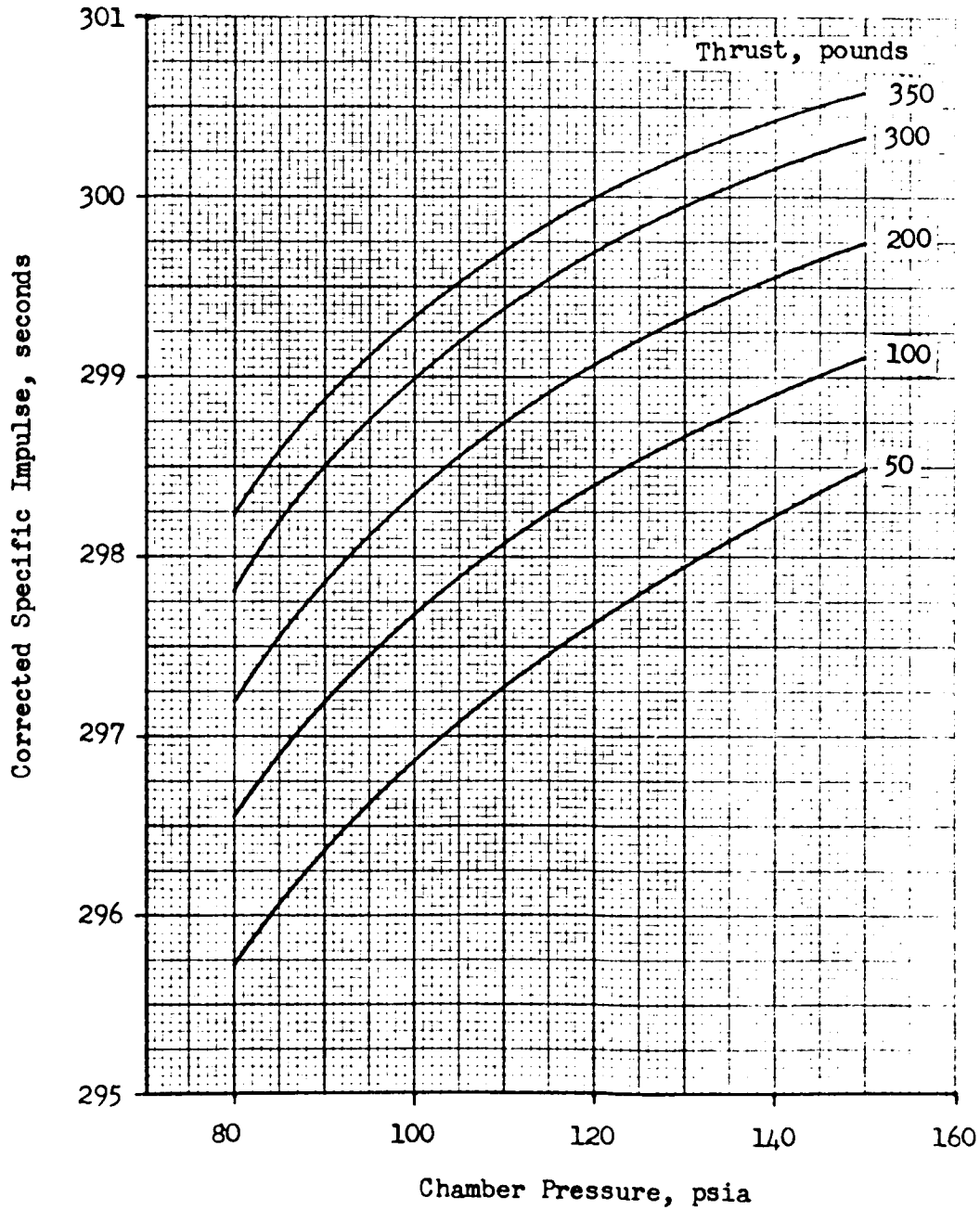


Corrected Specific Impulse  
vs. Chamber Pressure

Propellants =  $N_2O_4/N_2H_4$  - UDMH (50-50)

Mixture Ratio = 1.6 o/f

Expansion Area Ratio = 40



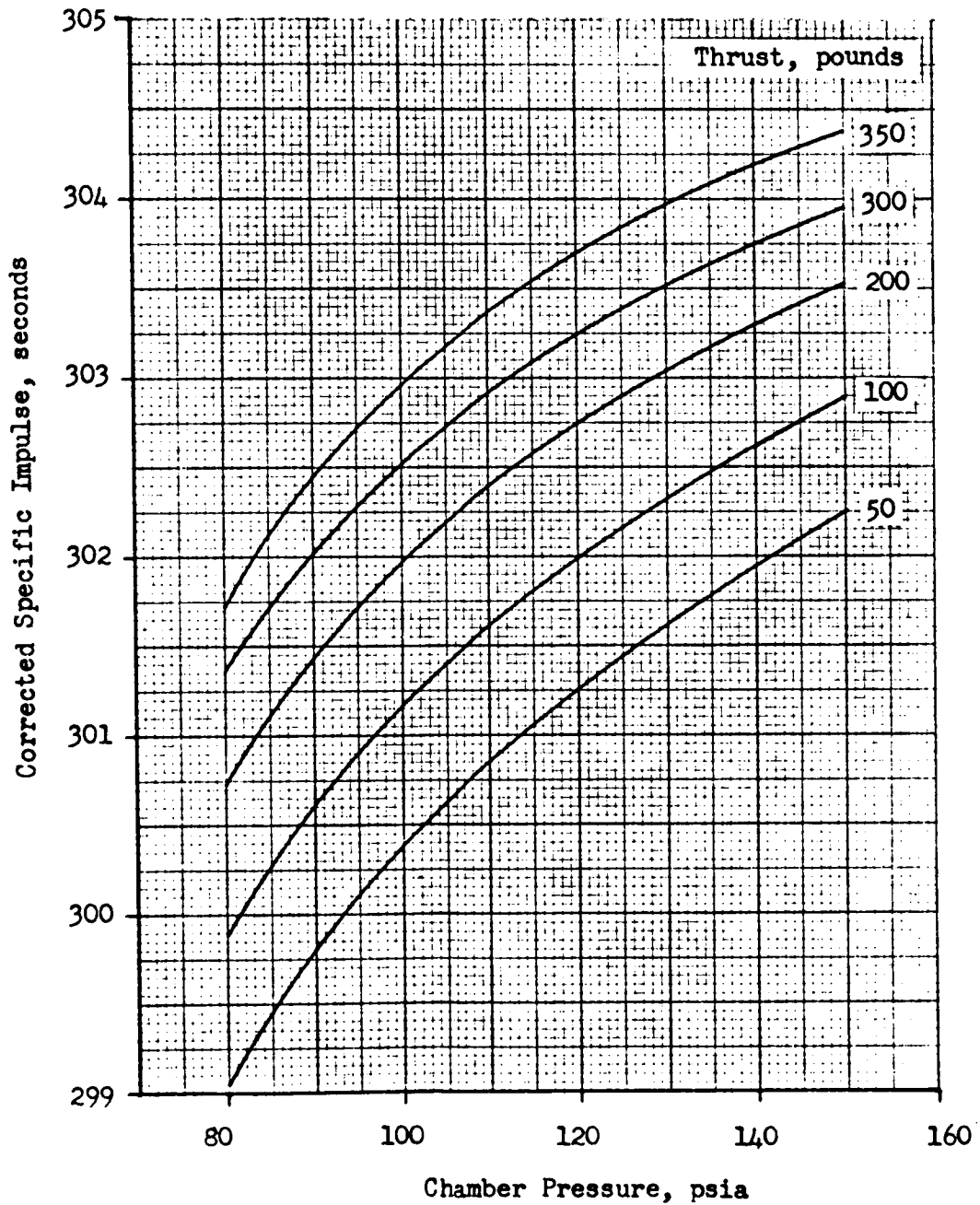
A-65

- 284 -

SD 69-419-3

Corrected Specific Impulse  
vs. Chamber Pressure

Propellants =  $N_2O_4/N_2H_4$  - UDMH (50-50)  
Mixture Ratio = 1.6 o/f  
Expansion Area Ratio = 60



$$\frac{1 - \eta C_F \text{ test}}{1 - \eta C_F \text{ computed}} = 0.7$$

This 0.7 factor was used in the final computation of all corrected specific impulse presented in this report, whether at full thrust or throttled.

#### THROTTLED ENGINE PERFORMANCE

Throttled engine performance predictions are shown for two discrete engine designs, essentially the RS-2101 300-pound-engine and the 100-pound two-piece engine. Characteristic velocity efficiency for each was changed to be 93 percent at full thrust to coincide with the full-thrust performance data presented herein. Injection pressure drop was increased to 100 psia on the oxidizer side and 53 psia on the fuel side. Rocketdyne experience in throttling engines has led to a correlation of characteristic velocity with throttling. The correlation parameter is the square root of the fuel orifice diameter-to-velocity ratio  $(D_f/V_f)^{1/2}$ . Experience was gathered for:  $N_2O_4$ /MMH throttled 3:1 single manifold, an interhalogen oxidizer/hydrazine base fuel throttled 3:1 single manifold,  $OF_2/B_2H_6$  throttled 10:1 dual manifold. In the later engine, the secondary manifold was completely shut off during low thrust operation. No problems occurred reinitiating flow through the secondary, such as contamination, injector burnout, or instability.

Predicted performance of the single manifold configurations is presented on Figures A-67 and A-68. Low thrust (6:1) oxidizer manifold pressures are 23 and 35 psia for the 300-pound and 100-pound thrust engines, respectively. Predicted performance of arbitrary dual manifold configurations is presented on Figures A-69 and A-70 (arbitrary in the sense of throttle ratio split between the manifolds). Low thrust (6:1) oxidizer manifold pressures are 51 and 47 psia (target value was 50 psia) for the 300-pound engine (secondary throttled 2.5:1) and the 100-pound engine (secondary throttled 2.1:1), respectively.



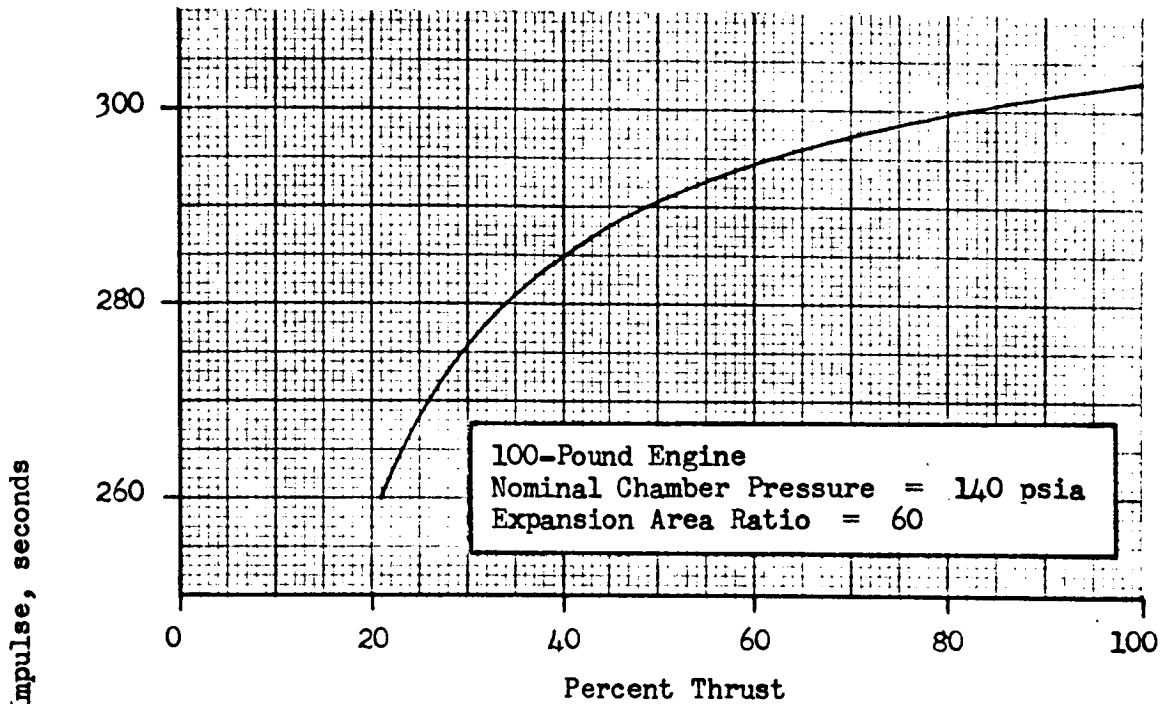
Throttled Performance

Single Manifold Injector

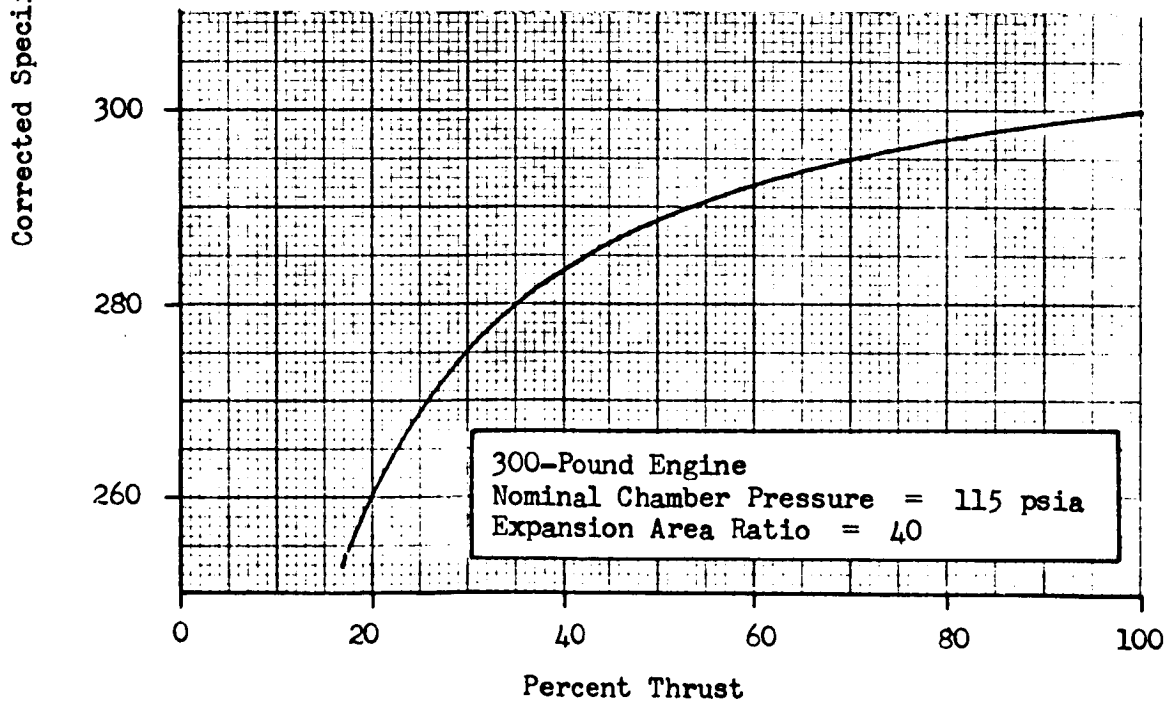
Propellants =  $N_2O_4/N_2H_4$  - UDMH (50-50)

Supply Pressure = 280 psia

Mixture Ratio = 1.6 o/f



A-67



A-68



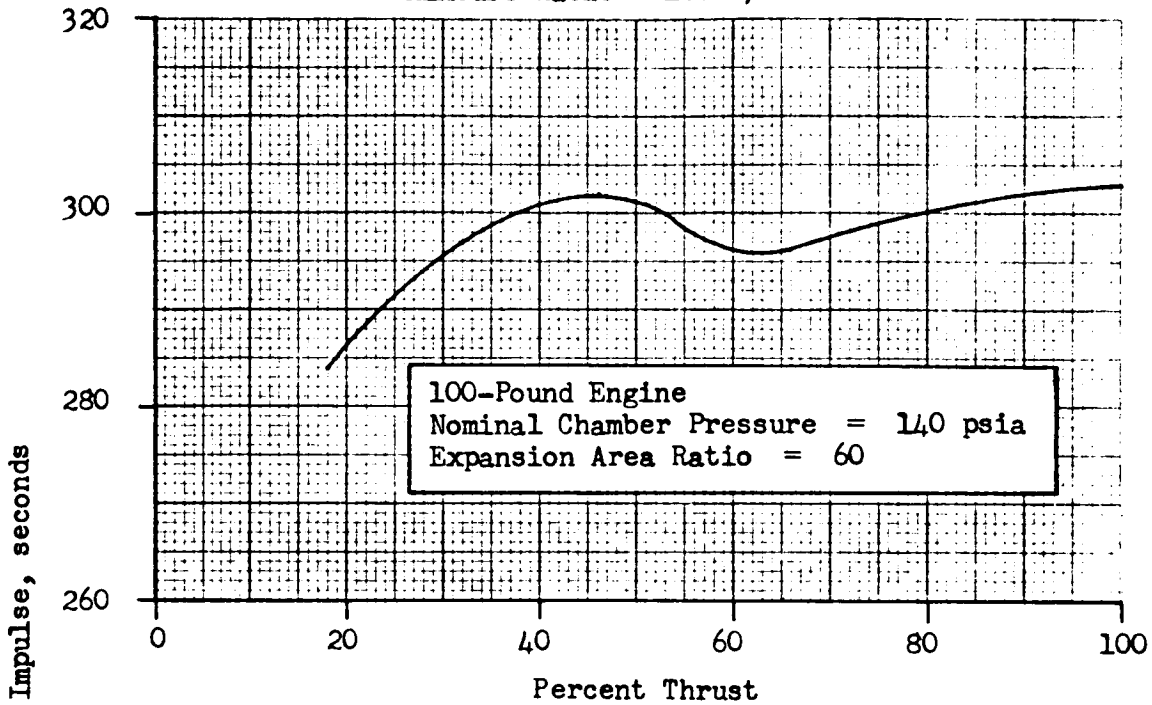
### Throttled Performance

#### Dual Manifold Injector

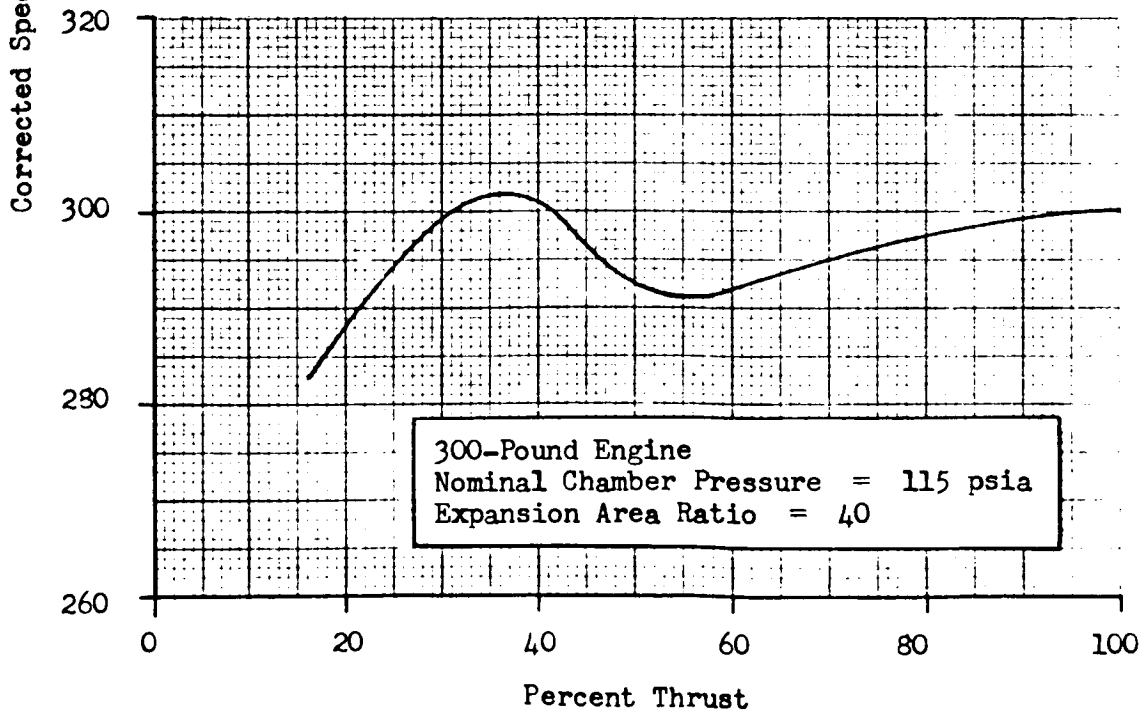
Propellants =  $N_2O_4/N_2H_4$  - UDMH (50-50)

Supply Pressure = 280 psia

Mixture Ratio = 1.6 o/f



A-69



A-70



Interregenerative Engine Performance History

	25-lb Thrust	100-lb Thrust	300-lb Thrust	1000-lb Thrust
Program	Advanced technology (IR&D)	Duradyne (NASA/Houston Contract)	RS-1401	Advanced technology (NASA/JPL contract)
Design Goal	Unlimited life	Unlimited life interegen engine	197-sec burn with $(I_s)_{min}$ = classified at $\epsilon = 30$	Unlimited life
Demonstrated	Unlimited life with $I_{sp} = 285$ sec at $\epsilon = 60$	Unlimited life with $I_s = 285$ sec at $\epsilon = 30$	197 sec burn with $(I_s)_{min}$ = met reqmt at $\epsilon = 30$	Unlimited life with $I_s = 275$ sec at $\epsilon = 60:1$
Program	Advanced technology (IR&D NASA demonstration)	Advanced technology (for NASA/Huntsville)	RS-2101	Advanced technology follow-on (NASA/JPL contract)
Design Goal	Unlimited life detonation insensitivity	Unlimited life, high performance	Unlimited life with $(I_s)_{goal} = 285$ sec at $\epsilon = 40$	Unlimited life, high performance
Demonstrated	Unlimited life $\eta C^* 92\%$ , M.R. 1.59	Unlimited life with $I_s = 301$ sec at $\epsilon = 60:1$	Unlimited life with $I_s = 285$ sec at $\epsilon = 40$	Unlimited life with $I_s = 297$ sec at $\epsilon = 60:1$
Program			Advanced technology	
Design Goal			Unlimited life	
Demonstrated			High performance	
			Program in progress	

## THRUST CHAMBER ASSEMBLY WEIGHT AND DIMENSION

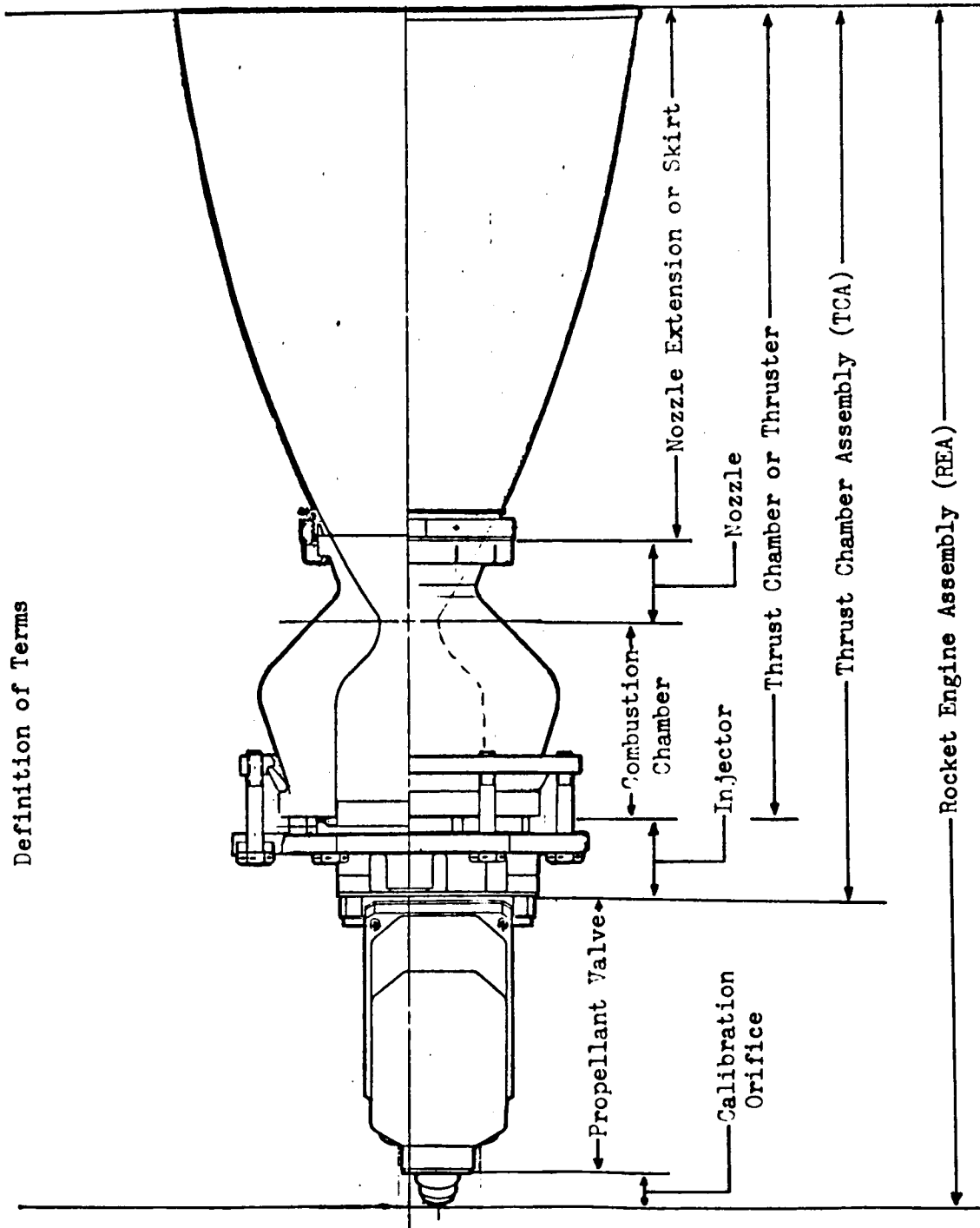
Thrust chamber assembly weight and size data are presented for radiation-cooled, beryllium interegen, and beryllium interegen two-piece configuration. Figure A-71 presents the standard definition of engine terms used in this report. Related component weights for each thrust chamber configuration are also presented. Thrust chamber diameters and lengths may vary little for chamber type presented. Therefore, one set of dimension curves is shown. Diameter and length nomographs for thrust levels of from 50 to 350 pounds are presented in Figures A-72 and A-73. Nozzle length data are presented for thrust levels of from 25 to 500 pounds in Figure A-74. The length data are based on use of bell-contoured nozzles, 80-percent of the length of 15-degree conical nozzles. The nozzle lengths are shown separately in Figure A-74 to permit computing nozzle lengths other than 80 percent by use of length ratios. The following parameters were used to establish the thrust chamber assembly dimension and weight data:

Propellant	N <sub>2</sub> O <sub>4</sub> /N <sub>2</sub> H <sub>4</sub> -UDMH (50-50)
Mixture ratio, o/f	1.6:1
Characteristic Length (L*)	11
Contraction Ratio	4:1
Nozzle contour, percent bell	80
Convergence angle, degrees	
Beryllium chambers	45
Radiation chamber	30
Beryllium chamber radiation	L605
Skirt material	0.025-inch-thick
Radiation chamber material	90-10 Ta/W
	0.050-inch-thick

Parametric weight estimates (injector weight included) for beryllium thrust chambers up to 350 pounds thrust are shown in Figure A-75. Beryllium thrust chambers configured with radiation-cooled nozzle extensions at area expansion ratio,  $\epsilon = 8$ , are presented in Figure A-76. Typical thrust chambers for full beryllium and beryllium with radiation-cooled skirt are shown in Figures A-76 and A-77, respectively. Valve and injector weights used with beryllium thrust chambers are given in Figure A-78.

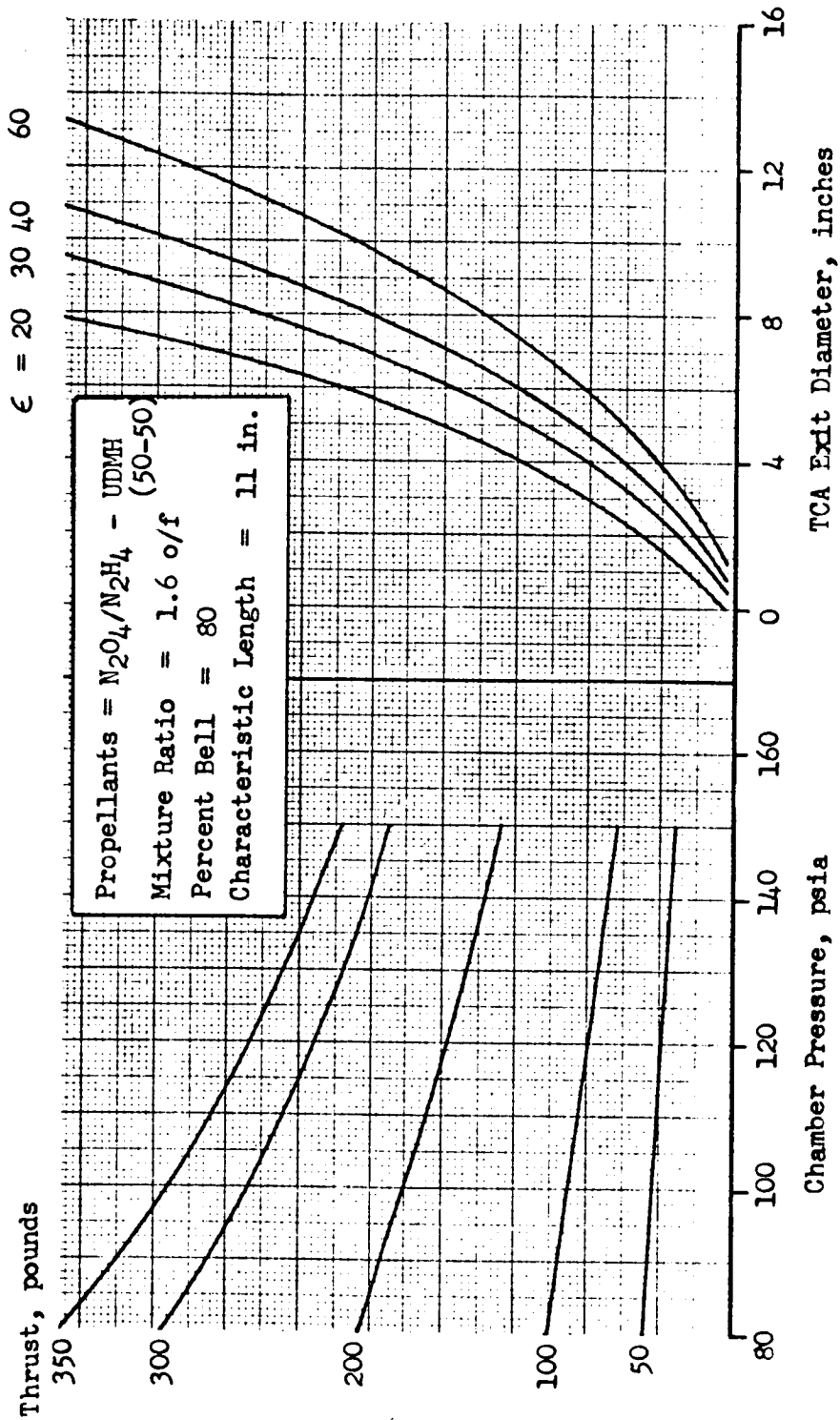
Weight estimates for radiation thrust chambers are presented in Figure A-79. The thrust chamber weight data include the weight of the injector.

Definition of Terms



A-71

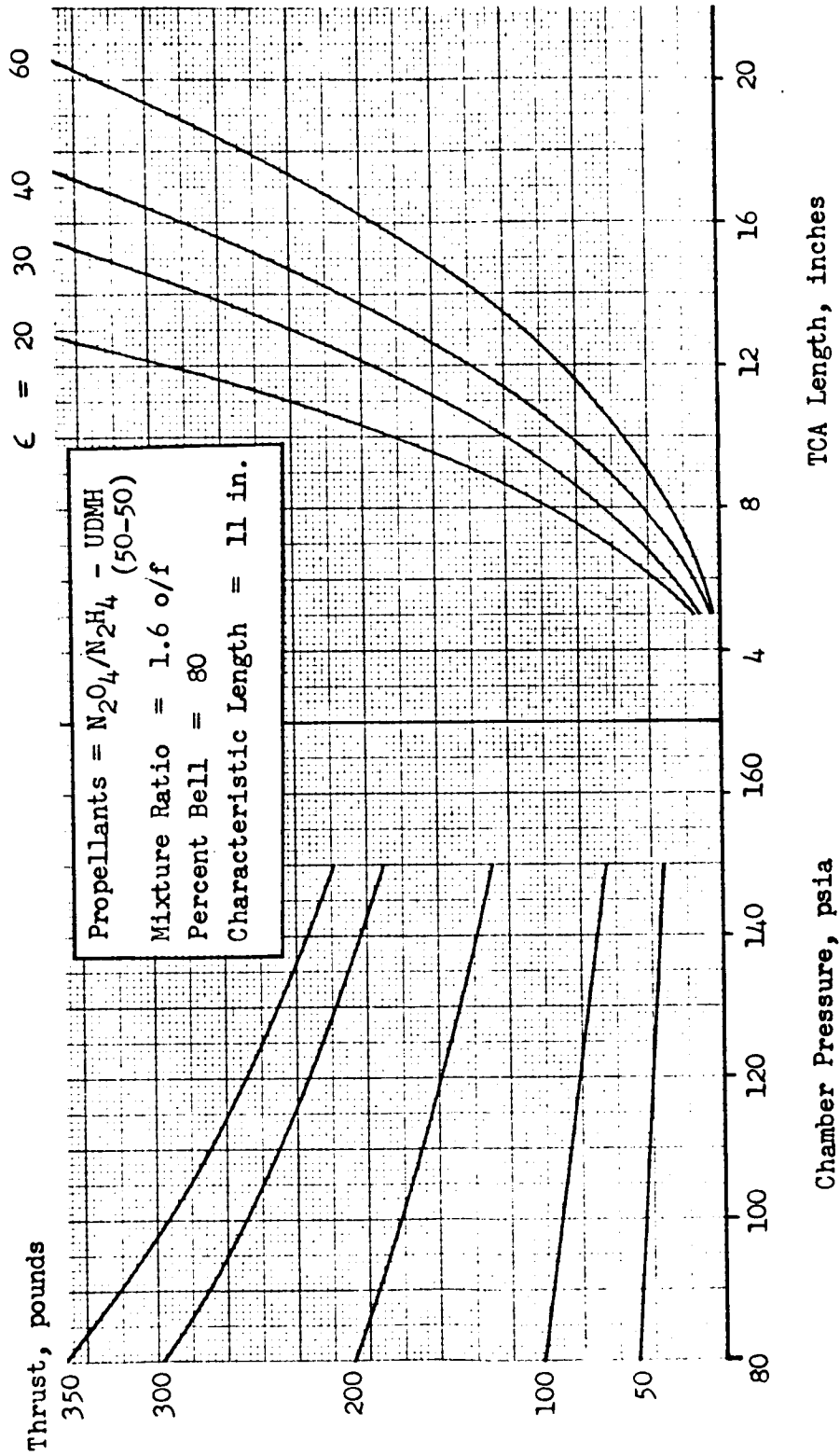
TCA Diameter Envelope Nomograph



A-72



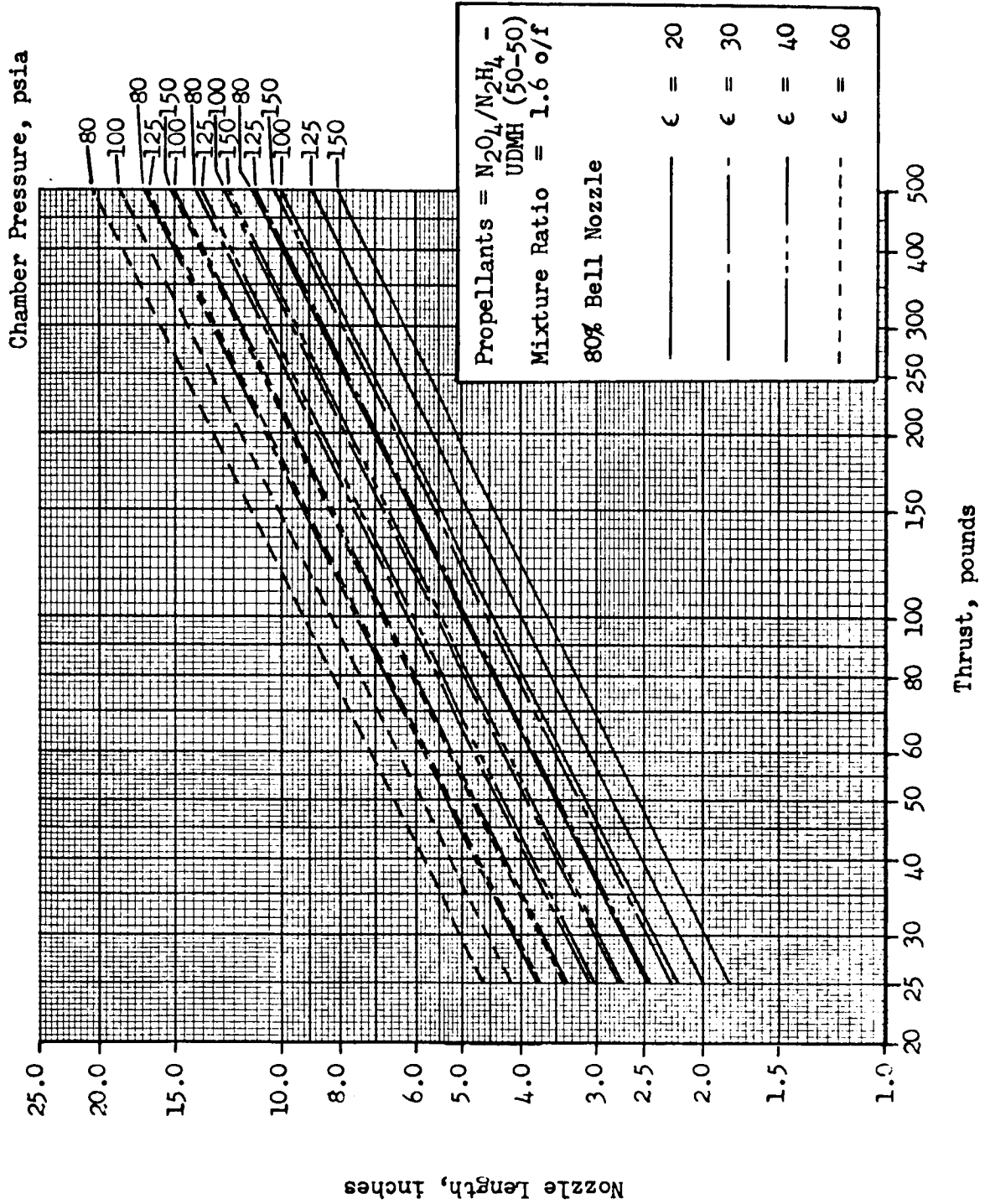
TCA Length Envelope Nomograph



A-73

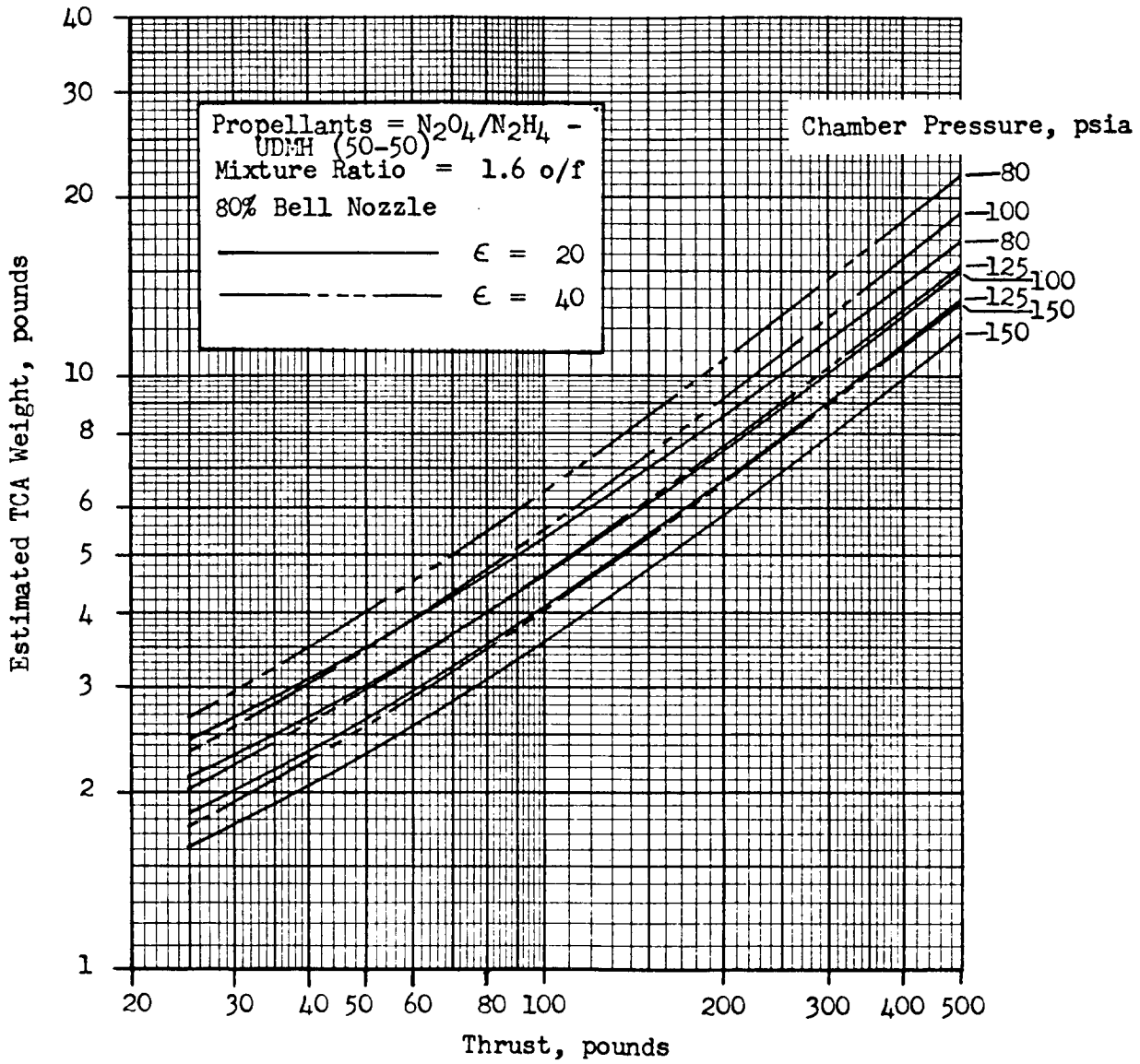


Nozzle Length

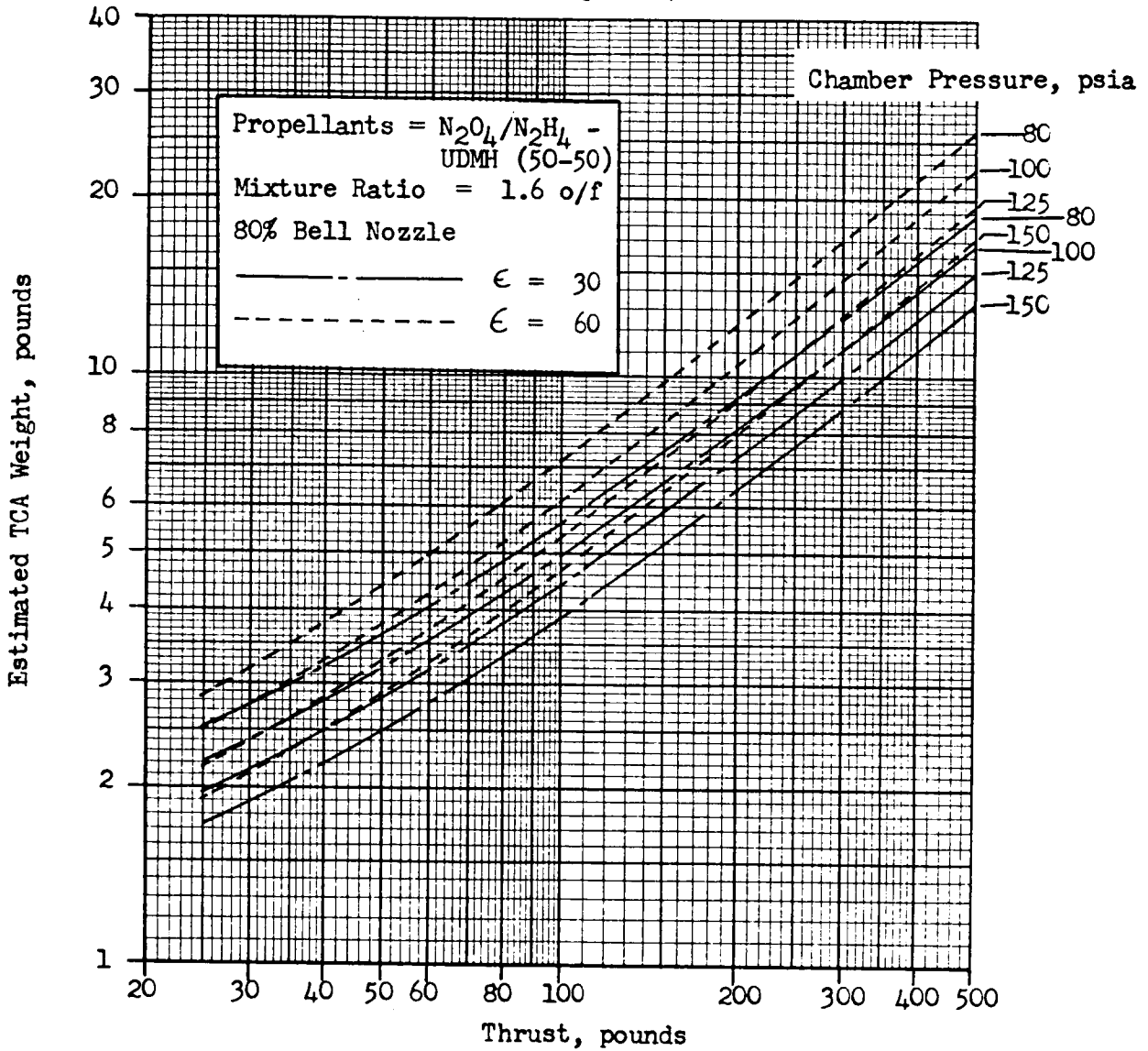




Beryllium TCA Weight  
(Includes Injector)



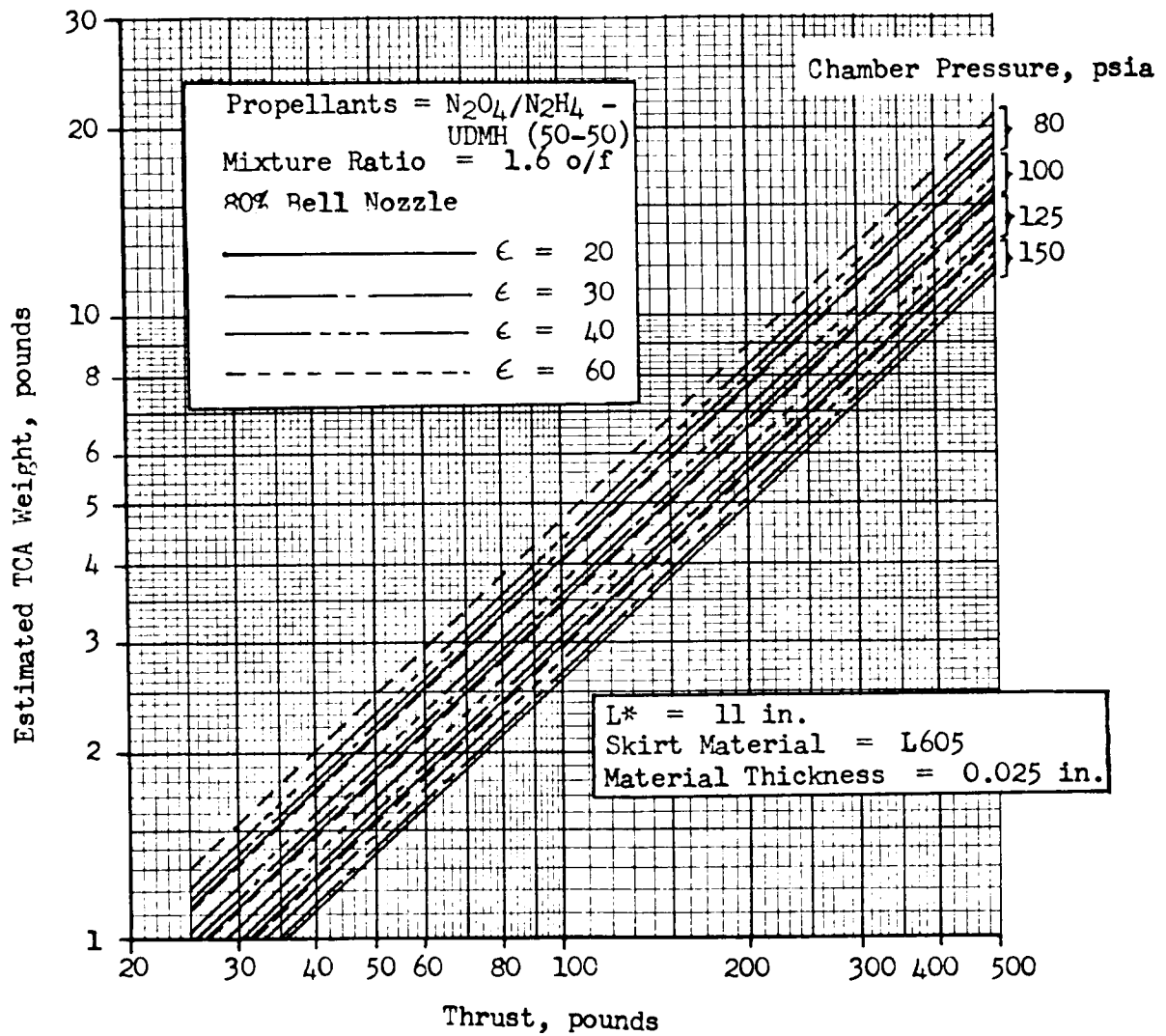
Beryllium TCA Weight  
(Includes Injector)





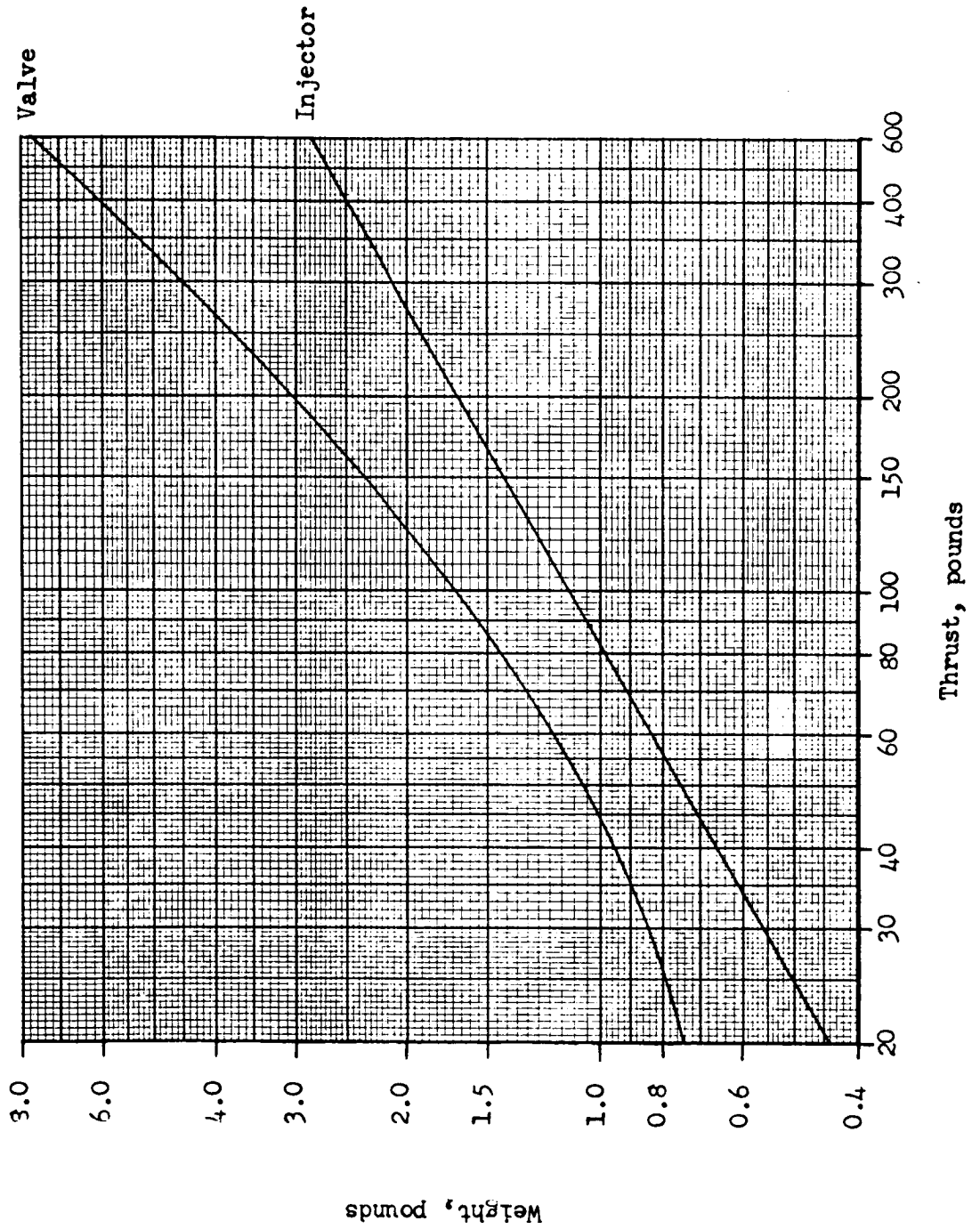
### Beryllium TCA Weight with Radiation Skirt

(Skirt Attached at  $\epsilon = 8$ )



Bipropellant

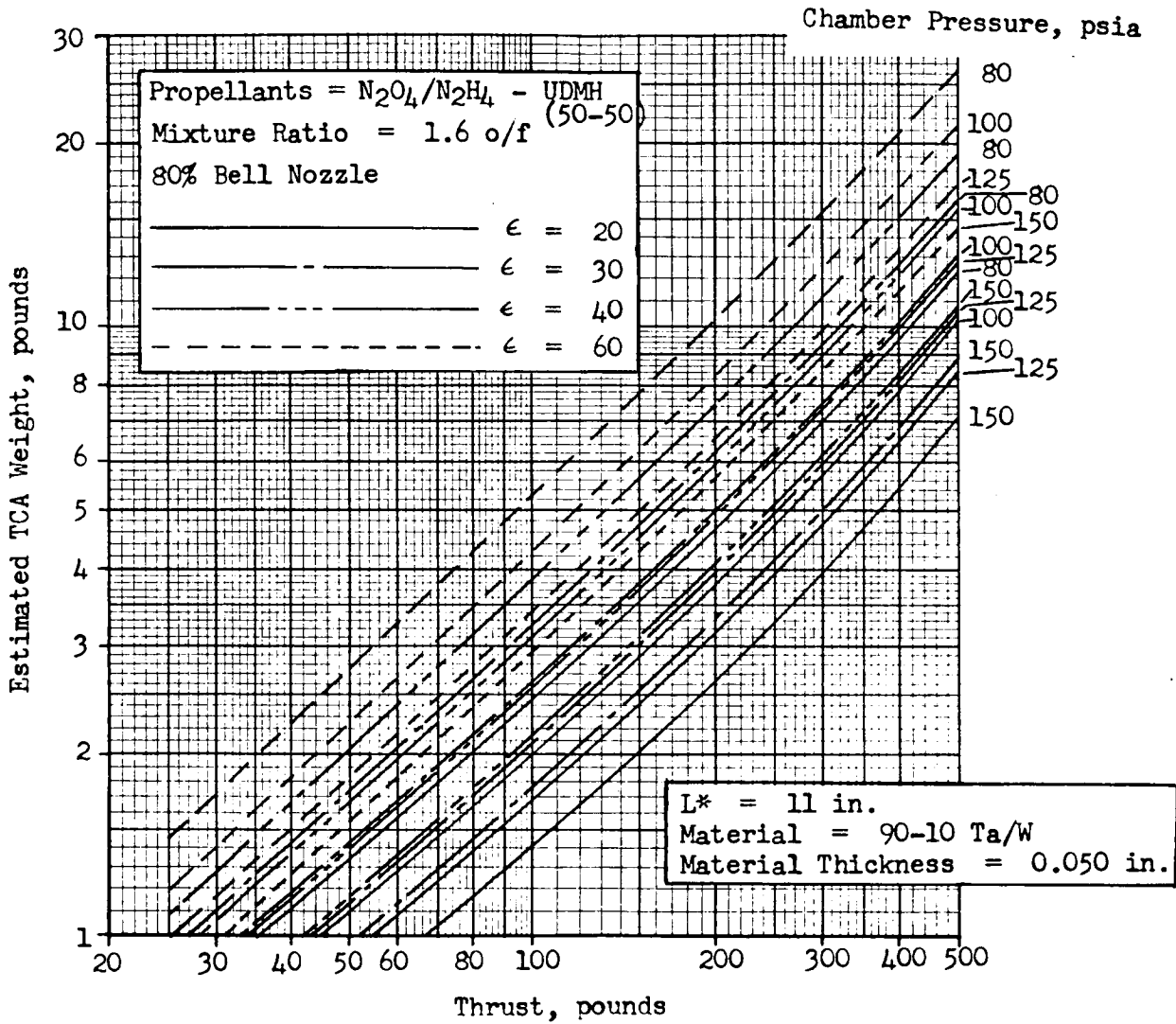
Valve and Injector Weights



A-78



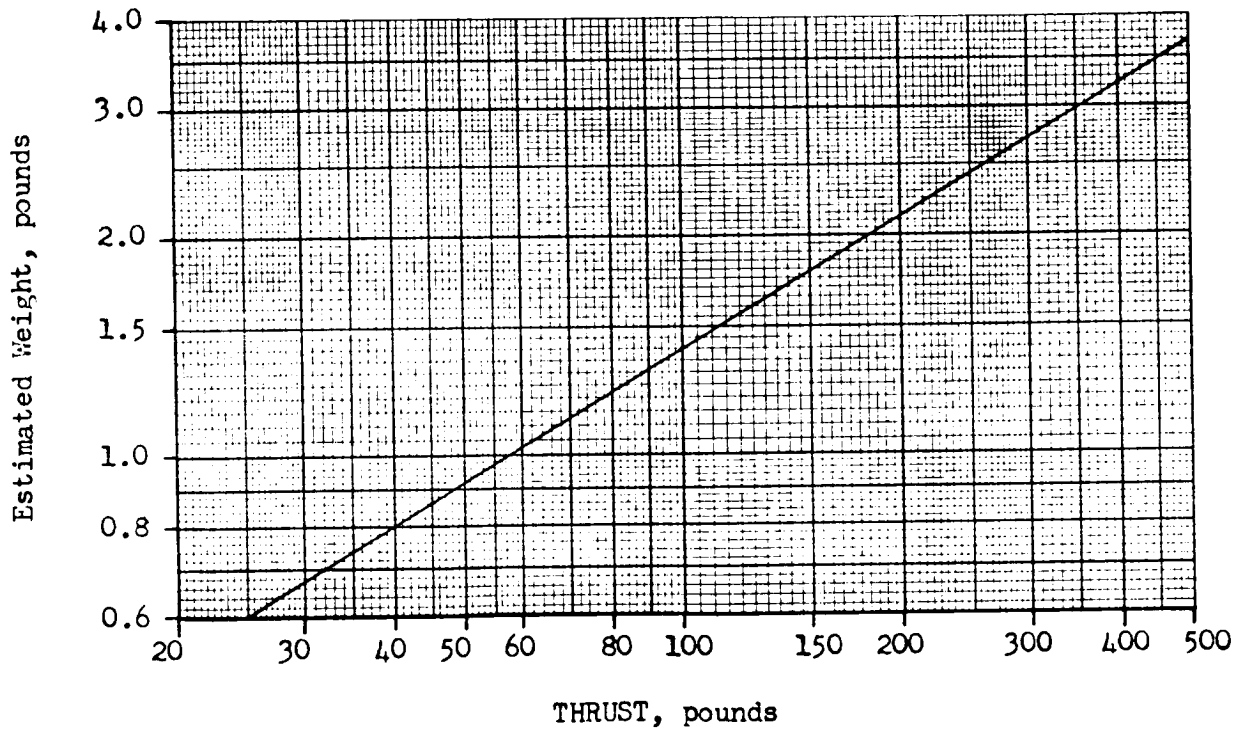
Radiation TCA Weight with Injector



At present there is little basis for size or weight correlations of the array of possible thrust vector control arrangements. However, throat mounted gimbal weights may be estimated reasonably well with the curve shown in Figure A-80.



Throat Gimbal Assembly Weight  
(Includes Gimbal, Ring, Bearings and Bolt)



A-80

- 302 -

SD 69-419-3

## TRW SYSTEMS

TRW Systems provided NR/SD with briefing chart material indicating the performance and development requirements of the Mira 150R during the LFV study. These data were not directly applicable to the parametric phase of the study and are not presented in this appendix. To represent parametrically the variable area injector design and performance characteristics adequately, two data points were employed. One was that of the Mira 150R and the other was representative of a 400-pound thrust engine employing the same design concepts. Such data were utilized to estimate the head-in assembly weights (injector, flow control valves, etc.). The radiation cooled thrust chamber characteristics employed were those furnished by Bell Aerosystems. In effect, for parametric study purposes, the TRW injector was synthesized with the Bell Aerosystems combustion chamber and nozzle.



APPENDIX B

PROPULSION SUBSYSTEM OPTIMIZATION PROGRAM

## APPENDIX B

### PROPULSION SUBSYSTEM OPTIMIZATION PROGRAM

During the LFV study, an IBM 360-65 program was developed to aid in the comparative analysis of various design alternatives and criteria. It was specifically aimed at defining propulsion component and subsystem weight, resupply weight, and LFV range as functions of the variables delineated in Table 1 of the Propulsion section. This appendix documents the IBM program by defining program nomenclature, input and output data, and presenting a listing of the compiled source deck.

The LFV propulsion analysis program employs an incremented thrust versus time input, corresponding to a specific flight profile, coupled with specific impulse versus percent thrust table to compute the propellant required. Specific impulse data are a function of chamber pressure, nozzle area ratio, and thrust level for each specific engine type. This propellant quantity may be more, or less, than the usable tanked value. To accommodate this probable difference, the analysis employs the delta propellant at a predesignated thrust level (cruise thrust) to either add or detract from the range of the specific flight profile. For those cases where tanked propellant is considered a dependent variable, range is held constant.

The size of propellant tankage is then computed based on propellant density, mixture ratio, ullage fraction, residuals, and number of tanks. Subsequent tank weight calculations are based on material strength, density, factor of safety, minimum acceptable wall thickness, and a multiplier to account for penetration fittings and mounting provisions. The usable pressurant required is based on desired propellant tank pressure, volume, and minimum operating temperature and corresponding pressurant density. The pressurant tank characteristics are computed in a similar fashion. Component weights, including regulators, valves, lines and fittings are computed based on empirical data of Reference 1.5.

Rocket engine weights were obtained from the respective engine suppliers as functions of nozzle area ratio, chamber pressure and thrust level. Such data combined with the number of engines results in engine assembly weight. Engine geometry effects on installation weight are computed as deltas from a baseline engine length and diameter and a corresponding vehicle structure weight. Engine length and diameter are input. Gross vehicle weight is held constant for this calculation.

The resultant program output consists of major component sizes: and burned propellant, subassembly, dry, burnout, total loaded, and resupply weights, and LFV range. Pertinent output data is plotted by CRT as functions of chamber pressure and nozzle area ratio as required.

The following program nomenclature defines input and output data in program notation.

Symbol	Definition	Units
FD	Total design thrust	lb
FE	Individual engine design thrust	lb
WE	Individual engine weight	lb
WEH	Individual engine hardware weight (flex lines, gimbal, etc.)	lb
XNE	Number of engines	--
XPT	Propellant tank pressure	psia
XPC	Chamber pressure	psia
XK1	Specific impulse multiplier	--
XK2	Propellant residual factor	--
XK3	Tank line constant	<u>lb/lbF</u>
XK4	Engine hardware constant	<u>lb/lbF</u>
F(I)	Required thrust for each mission time increment - up to 20 inputs	lb
FOU	Outbound cruise thrust	lb
FIN	Inbound cruise thrust	lb
TI	Number of time increments	(integer)
XPERF	Percent thrust	--
SI	Specific Impulse	sec

Symbol	Definition	Units
THRT		
EPS	Nozzle area ratio	--
DE	Nozzle exit diameter	in.
XLE	Engine length	in.
WPL	Payload Weight	lb
FPLT	Plot control	(integer)
FTYP	Plot control	(integer)
XL	Plot dimension	--
XR	Plot dimension	--
YR	Plot dimension	--
YT	Plot dimension	--
XLB	Baseline engine length	in.
DEB	Baseline engine diameter	in.
RB	Nominal mission range	NM
XNT	Number of tanks/propellant	--
XNP	Number of pressurant tanks	--
XOF	Mixture ratio (o/f)	--
RHOF	Fuel density	lb/ft <sup>3</sup>
RHOX	Oxidizer density	lb/ft <sup>3</sup>
RHOP	Pressurant density (storage)	lb/ft <sup>3</sup>
RHOT	Propellant tank material density	lb/in <sup>3</sup>
RHOH	Pressurant tank material density	lb/in <sup>3</sup>



Symbol	Definition	Units
SFT	Propellant tank factor of safety	--
SIT	Propellant tank material strength	PSI
SFP	Pressurant tank factor of safety	--
SIP	Pressurant tank material strength	PSI
XMG	Tank minimum gauge	in.
BF	Propellant tank weight multiplier	--
BFP	Pressurant tank weight multiplier	--
XPPR	Maximum storage pressure	psia
XPR	Pressurant residual factor	--
XNF	Number of flights	--
UF	Propellant tank ullage factor	--
DT(I)	Time increment at each thrust level - up to 20 inputs	sec
WGB	Gross vehicle weight	lb
XKL	Structure weight sensitivity to engine length	lb/in.
XKD	Structure weight sensitivity to engine length	lb/in.
WVB	Baseline structure weight	lb
VC	Cruise velocity	ft/sec

The following listing outlines the specific analytical procedure equations employed in the LFV propulsion system analysis, Program XH0099. The program is written in Fortran IV 6 for use with the NR IBM 360-65 installation. The program output is in printed form as shown in Figure B-1. CRT output is tailored to the specific form required as illustrated in the main body of the report.

```

0001 DIMENSION Y(10)
0002 DIMENSION XX(10),YY(10),ZX(10,10),ZY(10,10)
0003 DIMENSION DATA(120),DT(20),F(20),TAB2(21),TITLE(18)
0004 EQUIVALENCE (FD,DATA(1)),(FE,DATA(2)),(WE,DATA(3)),(WEH,DATA(4)),
X(XNE,DATA(5)),(XPT,DATA(6)),(XPC,DATA(7)),(XK1,DATA(8)),
X(XK2,DATA(9)),(XK3,DATA(10)),(XK4,DATA(11)),(XNT,DATA(12)),
X(XNP,DATA(13)),(XOF,DATA(14)),(RHOE,DATA(15)),(RHOX,DATA(16)),
X(XPHOP,DATA(17)),(RHOT,DATA(18)),(RHOH,DATA(19)),(SFT,DATA(20)),
X(SIT,DATA(21)),(SFP,DATA(22)),(SIP,DATA(23)),(XMG,DATA(24)),
X(BF,DATA(25)),(BFP,DATA(26)),(XPPR,DATA(27)),(XPR,DATA(28)),
X(XNF,DATA(29)),(LUF,DATA(30)),(LDT(1),DATA(31)),(F(1),DATA(51)),
X(FGJ,DATA(56)),(FIN,DATA(54)),
X(TL,DATA(71)),(TAB2(1),DATA(72)),(THRT,DATA(93)),(EPS,DATA(94)),
X(DE,DATA(95)),(XLE,DATA(96)),(WPL,DATA(97)),
X(FPLT,DATA(98)),(FTYP,DATA(99))
X , (XL,DATA(100)), (XR,DATA(101)), (YB,DATA(102)), (YT,DATA(103))
X, (XKL,DATA(104)), (XKD,DATA(105)), (RB,DATA(106)), (WGB,DATA(107)),
X(WV3 ,DATA(108)), (VC,DATA(109)), (DEB,DATA(110)), (XLB,DATA(111))
DATA M/38,63,16,55,44,19,24,52,17,18 /
1 ICP=1
0006 IAR=1
0007
0008 READ(5,5) TITLE
0009 5 FORMAT(18A4)
0010 2 CALL DECRD(DATA)
0011 WPU=0
0012 NL=TL
0013 DO 10 I=1,NL
0014 XPERF=100.* F(I)/FD
0015 SI=XK1*ENTERP(XPERF,TAB2)
0016 WP = F(I)*DT(I) / SI
0017 WPU=WPU+WP
0018 10 CONTINUE
C
0019 VF=3805.4
0020 VQ=3805.4
0021 RTF={.239*VF}*(1./3.)
0022 TF=(XPT*RTF*SFI)/(2*SIT)
0023 IF(TF.LT.XMG) TF=XMG
0024 DTF=2.*(RTF+TF)
0025 WTF=BFB*RHOT*4.199*((RTF+TF)**3.)-(RTF**3.)

```

0005  
0006  
0007  
0008  
0009  
0010  
0011  
0012  
0013  
0014  
0015  
0016  
0017  
0018

00000005  
00000010  
00000020  
00000030  
00000040  
00000050  
00000060  
00000070  
00000080  
00000090  
00000100  
00000101  
00000110  
00000111  
00000120  
00000122  
00000123  
000001231  
00000124  
00000130  
00000140  
00000142  
00000144  
00000150  
00000160  
00000170  
00000180  
00000190  
00000200  
00000210  
00000220  
00000230  
00000235  
240  
250  
00000260  
00000270  
00000280  
00000290  
300

```

0024 RTQ=(.230*V0)**(1./3.)
0027 TO=(XPT*RTQ*SFI)/(2*SII)
0028 IF(TO.LT.XMG) TO=XMG
0029 TO=2.0*(RTQ+TO)
0030 NTO=BE#RHOT*4.188*((RTQ+TO)**3.1-(RTQ**3.1))
0031 WPR=XPT*(VF+V0)*XPR*(1/2455000.)
0032 VPR=(1728*WPR)/(XNP*RHDP)
0033 RPT=(.239*VPR)**(1./3.)
0034 TPR=(XOPR*RRPT*SFP)/(2*SIP)
0035 DHT=2.0*(RPT+TPR)
0036 WHT=BFP*RHUH*4.188*((RPT+TPR)**3.1-(RPT**3.1))
0037 WRV=1.18*(FD*.C014)
0038 WHI=XNP*(.3+(FD*.0055))
0039 WRG=4.8*(FD*.005)
0040 WFW=1.5
0041 WPI=1.4*(FD*.003)
0042 WL=(XK3*FD)+(XK4*XNE*EE1)
0043 WC=WRV+WHI+WRG+WFW+WPI+WL
0044 WET=XNE*(WE+WEH)
0045 WD=(XNT*(WTF+WTO))+(XNP*WHT)+WET+WC
0046 DMV=XK0*(DEB-DE)+XKL*(XLB-XLE)
0047 WPT=WRG+WVB-WD-WPL-DMV-WPR-(300.*(XK2-1))
0048 WPIW=300./XK2
0049 IF(WPTM.LT.WPT) WPT=WPTM
0050 DWP=WPT-WPU
0051 XPERF=100.*FOU/FD
0052 SIO=XK1*ENTERP(XPERF,TAR2)
0053 XPERF=100.*FIN/FD
0054 SII=XK1*ENTERP(XPERF,TAR2)
0055 Y=DWP/((FOU/SIO)+(FIN/SII))
0056 RC=RB+(VC*T/12152.)
0057 WBO=WD+WPR+(300.*(XK2-1))
0058 WT=WBO+WPT
0059 WTS=XNE*(WHI+(XNP*WHT))+WPR+WPU+DWP
0060 WRITE(6,50) TITLE
0061 50 FORMAT(1H,36X,'LUNAR FLYING UNIT PROPUSSION',14X,18A4 / )
0062 XNTE,WTO,WHT,WPR,WC,WET,WD,WBO,WT,WTS
X,RC,WPL
0063 55 FORMAT(15X,'DESIGN THRUST',I35,F14.2,' LB*/15X,'CHAMBER PRESSURE',00000590

```

310  
00000320  
00000340  
00000350  
360  
00000370  
00000380  
390  
00000400  
00000410  
420  
00000430  
00000440  
00000450  
00000460  
00000470  
00000480  
00000490  
00000500  
00000510  
00000531

236  
00000237  
00000238  
00000239  
00000240  
00000241  
00000242  
520  
530  
00000533  
00000550  
00000560  
00000570  
00000580  
00000581  
00000590

B-1 (Continued)

```

0064      XT36,F14.2,' PSIA',/15X,'TANK PRESSURE',T36,F14.2,'PSIA',/15X,'HE TAN00000600
0065      XK PRESSURE',T36,F14.2,' PSIA',/15X,'FUEL TANK DIA',T36,F14.2,'IN',/ 00000610
0066      X15X,'OXID TANK DIA',T36,F14.2,'IN',/15X,'HE TANK DIA',T36,F14.2,'IN00000620
0067      X1/15X,'FS PROP TANK',T36,F14.2,'/15X,'FS HE TANK',T36,F14.2/ 00000630
0068      X15X,'MIXTURE RATIO',T36,F14.2,'/15X,'NUMBER OF ENGINES',T36,F14.2// 00000640
0069      X18X,'WEIGHTS',T40,'LB',/15X,'USEABLE PROP',T36,F14.2/ 00000650
0070      X15X,'TANKED PROP',T36,F14.2,'/15X,'FUEL TANK',T36,F14.2/ 00000660
0071      X15X,'OXIDIZER TANK',T36,F14.2,'/15X,'HE TANK',T36,F14.2,'/15X,'HELIUM',T36,F14.2// 00000670
0072      X,T36,F14.2,'/15X,'COMPONENTS',T36,F14.2,'/15X,'ENGINES',T36,F14.2// 00000680
0073      X15X,'DRY',T36,F14.2,'/15X,'BURNDUT',T36,F14.2,'/15X,'TOTAL LOADED',T36,F14.2// 00000690
0074      X6,E14.2,'/15X,'PRE-SUPPLY',T36,F14.2,'/15X,'RANGE',T36,F14.2,'NM',/ 00000700
0075      X15X,'PAYLOAD',T36,F14.2,'LB',) 00000701
0076      XX(ICP) =XPC 00000710
0077      YY(IAR) =EPS 00000720
0078      ZZ(ICP,IAR) = RC 00000730
0079      ZY(IAR,ICP) = RC 00000740
0080      JELEBJJ 300,350,400 00000750
0081      HERE IF NO PLOT 00000760
0082      C 350 IF(FTYP.NE.0.) GO TO 360 00000770
0083      IAR =IAR+1 00000780
0084      GO TO 2 00000790
0085      360 IAR=1 00000800
0086      ICP=ICP+1 00000810
0087      GO TO2 00000820
0088      C 300 PLOT RC VS CP 00000830
0089      CALL SETMIV(50,24,84,24) 00000840
0090      CALL LIMITI(XL,XR,YB,YT) 00000880
0091      K=1 00000890
0092      DO 310 J=1,IAR 00000900
0093      CALL GRAPH(K,M(J),ICP,XX,ZX(1,J),'CHAMBER PRESSURE PSIA@', 'RANGE 00000910
0094      *NM@',TITLEF) 00000930
0095      K=0 00000940
0096      GO TO 420 00000950
0097      C 310 CONTINUE 00000970
0098      PLOT RC VS AR 00001010
0099      CALL SETMIV(60,24,84,24) 001020
0100      CALL LIMITI(XL,XR,YR,YT) 001020
0101      K=1 001020
0102      DO 410 J=1,ICP 001020
0103      CALL GRAPH(K,M(J),IAR,YY,ZY(1,J),'NOZZLE AREA RATIO@', 'RANGE NM@', 001020

```

B-1 (Continued)



12/46/31

DATE = 69104

MAIN

FORTRAN IV G LEVEL 1, MOD 2

```

0088      *TITLF)
0089      K=0
0090      410 CONTINUE
0091      420 CALL PRINTV(19, 'NUMBER OF ENGINES =', 300, 3)
0092      CALL LABLV(XNE, 448, 3, 4, 1, 3)
0093      CALL PRINTV(17, 'NUMBER OF TANKS =', 300, 15)
0094      CALL LABLV(XNT, 448, 15, 4, 1, 3)
0095      CALL PRINTV(20, 'NUMBER OF HE TANKS =', 300, 27)
0096      CALL LABLV(XNP, 448, 27, 4, 1, 3)
0097      CALL PRINTV(19, 'TANKED PROPELLANT =', 300, 39)
0098      CALL LABLV(WPT, 448, 39, 4, 1, 3)
0099      CALL PRINTV(37, 'DESIGN THRUST =
          CALL LABLV(FD, 448, 51, 4, 1, 3)
          LBS., 300, 51)
0100      GO TO 1
0101      END
00001030
00001040
00001060
00001070
00001090
00001090
00001100
00001110
00001120
          1130
          1140
00001142
/C001143
00001150
00001160
00001990

```

B-1 (Continued)

RADIATION ENGINE, C.V. INLET THROTTLING, GIMBALLED, NOMINAL TRAJECTORY

DESIGN THRUST	400.00 LB
CHAMBER PRESSURE	100.00 PSIA
TANK PRESSURE	232.00 PSIA
HE TANK PRESSURE	4450.00 PSIA
FUEL TANK DIA	19.43 IN
OXID TANK DIA	19.43 IN
HE TANK DIA	11.84 IN
FS PROP TANK	1.50
FS HF TANK	1.50
MIXTURE RATIO	1.60
NUMBER OF ENGINES	4.00

WEIGHTS

USEABLE PROP	262.26
TANKED PROP	272.60
FUEL TANK	5.68
OXIDIZER TANK	5.68
HE TANK	10.10
HELIUM	1.14
COMPONENTS	20.47
ENGINES	29.64
DRY	71.56
BURNOUT	36.20
TOTAL LOADED	358.90
RE-SUPPLY	1431.59
PANGL	5.25 MM
PAYLOAD	370.00 LB

B-1 (Continued)

## CONTROL SYSTEMS STUDIES

### SUMMARY

The controls studies were conducted for two primary purposes: (1) to provide a source of handling qualities data for use in comparing results from the visual simulation and tethered flight vehicle and (2) establish the simplest, most reliable control system design. To accomplish the first objective, dynamic equations of motion were developed and used with a mathematical model of the pilot and with performance requirements to determine whether kinesthetic or hardwire controls would suffice or whether the complexity of a stability augmentation system was necessary. These data were compared with visual and flight simulation data to form a final conclusion on handling qualities. The second objective was achieved by conducting control feasibility and failure modes analyses of candidate configurations. After the major design features were established, subsystem and component studies defined configuration details.

### ANALYTICAL STUDIES OF HANDLING QUALITIES

When dissected and investigated in detail, a kinesthetic maneuver is found to be composed of several parts. To begin the maneuver, the pilot, desiring to translate, tilts forward on the platform to move the total center of gravity forward. In doing so, he generates an angular acceleration tending to pitch the vehicle nose down. This position produces the constant forward acceleration needed for travel. In the pilot's action of tilting forward, however, the vehicle initially reacts by rotating in the opposite direction and momentarily accelerates rearward until the nose-down orientation is reached. Each time the pilot starts or stops an angular acceleration, the reaction occurs, resulting in a wavering flight path. If the combined moment of inertia of the pilot and the vehicle is small, responses to balancing inputs are rapid and the path reversal, or wavering effect, is negligible, but higher moments of inertia allow longer periods for reverse velocity to grow and result in large path reversal amplitudes. The optimum vehicle size for kinesthetic control is, therefore, one which is large enough to respond slowly, but not so large as to undergo dangerous oscillations. From tethered flight vehicle tests at 1-g conditions the optimum range lies between 100 and 200 slug-ft<sup>2</sup>, depending on the pilot's characteristics. The corresponding lunar flying vehicle (LFV) moment of inertia range (1/6-g) is from 35 to 77 slug-ft<sup>2</sup>. At best, however, the vehicle would be unsatisfactory to the pilot.

Hardwire control represents an improvement over kinesthetic in that the pilot may control by hand motions rather than by body motions, and may, therefore, be either seated or standing. Even with kinesthetic control, hand motions are required for yaw axis inputs. A hand controller with three-axis command capability is familiar to the pilot and seems to be less confusing than commanding by combining hand controller and body motions. Hardwire control permits adjustment of angular acceleration sensitivity independently of the vehicle size. The benefits of this control method, however, are not sufficient to endow it with better than unsatisfactory handling qualities, as described by analytical, visual simulation, and tethered flight vehicle results.

The path reversal effect is also inherent in hardwire control. The nearer the pivot is to the total center of gravity, the larger the amount of transient horizontal acceleration generated with control torque. As long as the pivot is below the total center of gravity, the transient horizontal acceleration is always in the wrong direction. Moving the pivot to a point above the total center of gravity gives the right sign to the acceleration.

As a special case, the pivot may be located at the total center of gravity and the vehicle flies with the platform level, rather than by tilting in the direction of travel. This method, referred to as the neutral gimbal configuration, effectively decouples the rotational and translational vehicle dynamics and permits the pilot to provide more precise vehicle position and velocity control during flight. The resulting enhancement of handling qualities introduces design problems, since larger engine gimbal angles are required, a center-of-gravity tracking method is necessary, and a platform leveling method is needed. The first two problems present severe design constraints, while the third requires either that the pilot take on the additional task of leveling the platform manually, or that an automatic means be devised.

Another approach to improving the handling qualities of the hardwire control method was studied. It involved the addition of simple compensation networks between the rotational controller and the pivot to produce an effect similar to rate command. With the network, a step rotational controller input produces a transient engine rotation which results in a net change in rotational velocity. It was soon discovered, however, that the system was unable to cope with steady-state disturbance torques which realistically are present. To add this control capability meant to mix a small amount of acceleration command with the rate command. A step rotational controller input would then result in a net change in rotational velocity and an additional change in angular acceleration. This system give the pilot no means of properly mixing angular velocity and acceleration to combat a given combination of angular rate error and disturbance torque; thus it does not represent an improvement over the basic hardwire system.

To summarize the hardwire cases, the basic uncompensated hardwire control method, with pivot below the total center of gravity, was found to be unsatisfactory. Candidate improvement methods tested spanned from relocation of the pilot, to center-of-gravity tracking, to the addition of compensation networks — all of which resulted in unsatisfactory or unacceptable handling qualities.

The use of either kinesthetic or several forms of hardwire control does not appear to be feasible from a handling qualities standpoint, thus ruling out the two simplest methods. Attitude rate stabilization by automatic means was considered to be the next system in order of increasing complexity. The system was mechanized in a manner similar to that of the Apollo SCS, in which rate gyros are used to produce compensating feedback. The pilot is essentially removed from the rotational stability loop but retains the task of command generation. Rotational controller deflections, acting as command inputs, produce proportional vehicle angular rates. When no commands are given, the rate gyro signals are additionally switched to integrators which produce incremental attitude feedbacks to damp the angular rates to zero. This system effectively slows the actions required of the pilot, lowers his control workload portion, and permits him to concentrate on conducting precise maneuvers. Thus, the additional weight introduced by the stability augmented control method is partially compensated for by a reduction in propellant consumption. Analysis and visual simulation studies show the control method to have acceptable handling qualities.

#### SIMULATION STUDIES OF HANDLING QUALITIES

Both a visual simulation and a tethered flight vehicle program were conducted during the contract effort to assess the characteristics of the various control methods. The simulations, together with the analytical studies, provided a three-pronged approach which produced high confidence answers.

The visual simulation consisted of a transparent scene, capable of motion in six degrees-of-freedom, which was illuminated by a point light source. The scene was projected on a screen which wrapped part way around the pilot. The peripheral view afforded near the pilot's feet was especially important for landing cues. Three sections of an analog computer contained the dynamic mathematical model which drove the scene motion and the instrument panel. Inputs to the analog consisted of rotational controller and throttle-setting commands, and two-axis pilot body position measurements from the platform.

Data from more than 500 flight conducted with the visual simulator, including kinesthetic and several versions of hardwire and stability-augmented control modes, showed that the stability-augmented control mode

was the only acceptable one from all aspects. This conclusion was reached by comparing handling qualities ratings given by the pilots, who had performed many successful runs.

More than 100 tethered vehicle flights were conducted to assess kinesthetic and hardwire control methods at different values of pitch and roll moments of inertia. The vehicle was powered by a nitrogen exhaust nozzle and was confined to a limited flight volume by a system of tethers. The pilot controlled five degrees-of-freedom, yaw being damped by the nitrogen inlet hoses. Use of the vehicle allowed realistic exploration of handling qualities over a range of moment of inertia from 105 to 600 slug-ft<sup>2</sup>.

With kinesthetic control on the tethered vehicle, the pilot was typically able to stabilize attitude, but had difficulty maintaining a fixed translational position. Response decreased as moment of inertia increased. The pilot was forced to use his predictive abilities to a greater extent with high inertias to damp oscillations. At any inertia value, large transients seem to be an inherent part of the takeoff phase. Hardwire control flights on the tethered vehicle were not accomplished as well as kinesthetic control. Both control methods had unsatisfactory to unacceptable handling qualities.

#### THRUST VECTOR CONTROL CONFIGURATION ANALYSIS

Although all known engine and gimbaling system configurations which would be compatible with stability augmented control were considered, only 13 of these were considered sufficiently promising to be used in a tradeoff study. The constraints of the study were that crew safety would not be impaired as a result of a single engine or actuator failure, and that such a failure would not require time-critical action by the crew. The study shows that the configuration with four engines arranged in a square pattern, each with two gimbal actuators, is the most feasible.

#### CONTROL SYSTEM FAILURE MODE ANALYSIS

In a tradeoff study separate from the thrust vector configuration analysis, failure modes of the entire stability augmentation system were examined. The study considered three engine actuation systems and possible failures in the electrical power system, the stability augmentation system, including the actuators, and the engines. The first of the three configurations was a translating TVC system in which four engines were mounted on a sliding plate so that all engines moved together in pitch or roll control. Each engine was gimballed to provide yaw control. With the second configuration, each engine gimballed in only one axis, but had two redundant actuators. The actuators, referred to as "two in a can," were contained in the same housing

and shared a common bull gear and engine link. The third configuration used two separate orthogonally-mounted actuators on each of the four engines.

From an electrical power system standpoint, sufficient reliability for any of the three systems means redundant power supplies, each capable of operating independently. Circuit protection devices prevent proliferation of failures through the system. To avoid time-critical switching problems after a failure, the two power systems would share loads under normal operation.

The operation of each of the engine actuation systems was analyzed for engine thrust failure and hardover actuator conditions. The results of the engine thrust failure analysis showed that all configurations were controllable and were not time critical, but the eight-actuator case required the least actuator travel to stabilize. Both the translating TVC and the four actuator cases had time-critical pilot action requirements associated with actuator hardover failures.

On the basis of this analysis, the four-engine, eight-actuator configuration with redundant load-sharing power systems is recommended.

#### SYSTEM MECHANIZATION

Up to this point, the actual details of the control system have not been discussed. Studies of each of the subsystems were conducted to determine the best mechanizations. During the studies, numerous suppliers were consulted to obtain state-of-the-art concepts. The resulting study efforts and recommended mechanization for each subsystem are described in the following paragraphs.

The pilot will control engine thrust level by a throttle which is rotated by his left hand. A tradeoff study was conducted to select the linkage best suited for throttle valve operation. Ground rules for the study included 150 degrees of throttle rotation range, rotation torque not to exceed 10 inch-pounds, and individual engine cutoffs using prevalves. Although the engines are normally shut down together using the main valves, the possibility of a valve sticking requires an alternate means of turning an engine off. Three concepts were considered for the linkages between the throttle controller and the valves: cables within sleeves, electrical power, and hydraulic power.

The cable would actually be a stiff wire, suitable for compression and tension forces. Each cable would be disconnected at the controller if an engine, a main valve, or the cable fails. The electrical power method uses proportional transducers at the controller to develop signals for throttle valve actuators. Individual engine cutoffs consist of manually-operated



circuit breakers. Three versions of the hydraulic method were considered; all required pressure transducers at both the controller and valve ends of the line. After consideration of the problems associated with each concept, the cable system was recommended because it is the simplest, requires few undeveloped parts, and requires no electrical power.

The rotational hand controller was selected based on consideration of Apollo similarity and was not subjected to tradeoff analyses. Minor redesign is necessary to prepare it for lunar flying vehicle use. Because of changes, however, a complete qualification program is required.

A survey of engine gimbals led to the recommendation of the Minuteman III P106A actuator. It is electromechanical and has a completely geared system, but required certain modifications for LFV use. It has clear advantages over electromechanical clutch systems, and hydraulic or pneumatic systems.

The display panel recommendations combine the requirements derived from design, reliability, and the best estimates of pilot needs. Included in the panel are the following functions: roll, pitch, yaw attitude, thrust-to-weight ratio setting, fuel and oxidizer levels, high and low pressurant readings, electrical power status, and individual engine cut-off controls and lights.

Part of the display panel functions are driven directly from sensors. Three functions, thrust-to-weight ratio, attitude, and individual engine failure lights are driven by sensor-fed logic in the control unit. Thrust-to-weight ratio uses an amplified measurement from an accelerometer mounted along the thrust axis. Attitude meters are driven by Euler angle logic within the control unit which transforms and integrates three-axis rate gyro signals. The engine failure lights are energized because of voting logic which determines engine status from strain gauge measurements.

The control unit performs stability augmentation functions, as well as operating part of the display panel. The heart of the stability augmentation system is the summing of rate gyro outputs with rotation controller commands. These commands are positively indicated by a separately generated signal indicating breakout from the controller null position. When the controller is in the null position in any axis, the attitude hold portion of the control system is energized. Total gimbal error signals are the results of summing. These signals generate servo amplifier commands through the actuator logic transformation. Within each servo amplifier, the driver voltage is generated for each actuation by summing the command with the negative position and rate actuator pickoff voltages.



Reliability within the system is obtained by dual-control channels from the rotational controller and the gyros to the servo amplifiers. The pilot may select one of the two channels by using the system select switch located in the press-to-talk position on the rotation controller. The channel-select switch and its related wiring is itself redundant. Each servo amplifier is redundant based on the selection of the four-engine, eight-actuator configuration. The channel not in use at any one time is in standby status, ready for instant use.

## SYSTEMS ANALYSIS

The controls studies were conducted for two primary purposes: (1) to provide a source of handling qualities data for comparing results from the visual simulation and the tethered flight vehicle, and (2) to determine the simplest, most reliable control system design. To accomplish the first objective, dynamic equations of motion were developed and used with a mathematical model of the pilot and with performance requirements to determine whether kinesthetic or hardwire controls would suffice or whether the complexity of a stability augmentation system were necessary. The second objective was achieved by conducting control feasibility and failure modes analyses of candidate configurations. After the major design features were established, subsystem and component studies defined configuration details.

A major question which was investigated early in the program was whether an overhead pivot location had inherent advantages. Analysis showed that no significant advantages over the conventional (nozzle below center of gravity) case were realized. Therefore, the overhead pivot configuration was not recommended from a controls standpoint.

Intensive handling qualities analyses of the kinesthetic, hardwire, and stability-augmented control modes were performed. Gimbal below center of gravity and neutral pivot cases were included. Dynamics mathematical analyses were supported by simulator studies. Special attention was paid to developing analyses for hardwire cases, with and without spring and dashpot shaping networks. The conclusions reached by these studies and tests are as follows:

1. Kinesthetic control of the lunar flying vehicle will be rated by a pilot as unacceptable even for emergency operations.
2. Hardwire control of the LFV will be rated as unacceptable for normal operations by a pilot. A compensation network with separate trimming inputs shows promise of improving this rating. Further investigation is recommended.
3. The stability-augmented LFV will be given a Cooper rating of 3 (satisfactory) by the pilot, and is therefore acceptable from a handling qualities standpoint.

4. A neutral cg control system received a Cooper rating of 2 (good) on the NR visual simulator, and an estimate of 1 (optimum) with throttle modification. This was the highest rating given any LFV control system. The system may be difficult to mechanize; however, further study was recommended.
5. Results of the analyses agreed with findings from the LFV visual simulator and flight vehicle investigations.

The first step in establishing a configuration which is acceptable for control purposes was to perform an analysis to determine engine configurations which would continue to operate satisfactorily with either engine out or actuator hard over failures. One-, two-, three-, and four-engine configurations were studied. The three- and four-engine cases were studied with one or two actuators per engine or combinations of both cases. The only cases which operated satisfactorily with failures were the four-engine, eight-actuator cases. These cases were retained for further study. The single-engine case was also retained because of its simplicity. Final choice of the four-engine (square pattern), eight-actuator case was based on an overall vehicle evaluation procedure.

Failure mode analyses of three promising configurations were completed. The configurations were: (1) four engines mounted rigidly to a sliding plate, (2) four-engine and four dual-(two-in-a-can) actuators, and (3) four engines and eight actuators. The failures investigated were single engine out and actuator failed hard over. The results showed that the sliding plate and the four dual-actuator cases were subject to time-critical failures. The eight-actuator case was chosen as the final configuration based on this analysis and overall vehicle considerations of weight and reliability.

Company-sponsored simulations included a six degree-of-freedom visual simulation and a five degree-of-freedom tethered flight vehicle program. The visual simulation was concerned with all control modes as applied to realistic vehicle configurations. Flight maneuvers and navigational problems were studied in detail. Only the kinesthetic and hardwire control modes were studied with the tethered flight vehicle. The major conclusion from the Company sponsored simulations, as expressed previously, is that the kinesthetic and hardwire control modes are not satisfactory for use with the lunar flying vehicle. The stability-augmented system was shown to have satisfactory handling qualities.

## HANDLING QUALITIES ANALYSIS

### Dynamic Equations of Motion

The equations of motion required to analyze the five proposed LFV configurations, delineated on page 52 of the NR-SD LFV proposal, and shown in Figure 2-1, were derived and are shown in Appendix C. The five configurations, extensively analyzed in this report, are as follows:

1. Kinesthetic, pivot below center of gravity
2. Hardwire, pivot below center of gravity
3. Stability augmented, pivot below center of gravity
4. Manually directed, inertial mass is pilot only, pivot above center of gravity
5. Manually directed, inertial mass is pilot and lunar flying vehicle, pivot above center of gravity.

The pitch and roll axes have identical dynamic relationships, thereby allowing the equations to accommodate analysis of either axis by modifying the values of a few constants. The equations of motion which will be employed to obtain transfer functions in stability analysis and parameter sensitivity studies are linearized, planar (no cross-coupling terms included) differential equations and are summarized in matrix form at the end of Appendix C, Parts 1 and 2.

Part 1 of Appendix C presents the kinesthetic equations required for analysis of Case 1 of the five configurations. The diagrams and nomenclature for the analyses are also shown in Appendix C. For the proposed LFV configuration,  $F_{T2}$ ,  $m_{v2}$ ,  $I_2$ ,  $B$ ;  $K$ ,  $l_3$ ,  $l_4$ , and  $\rho$  can be taken as zero.

The equations of Part 2 of Appendix C provide the vehicle dynamic relationships (including pilot) for analysis of Cases 2 through 5. In each of these cases, the pilot is assumed part of the platform rigid body with no kinesthetic contribution to control stability (or instability). Fuel slosh, mechanical shaping of the input command for hardwire systems, and other disturbance or compensatory considerations can be added to the equations with relative ease as the situation demands. Case 2 is the hardwire configuration studied by NR in the past. It uses an engine which gimbals below the total center of gravity in proportion to the amount of stick deflection provided by the pilot.

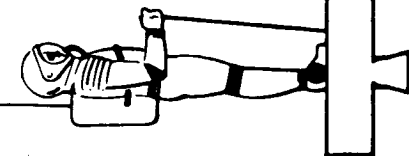
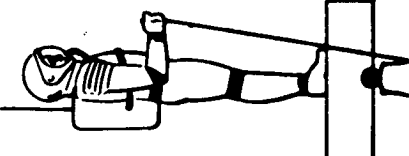
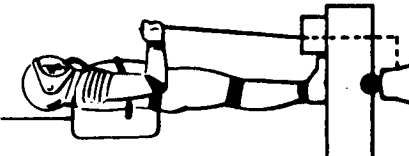
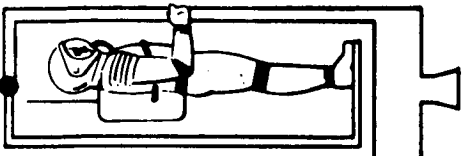
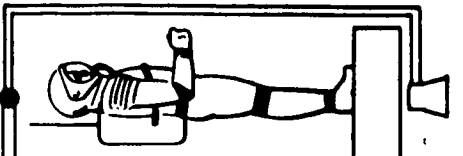
TYPE	GEOMETRY & STUDY STATUS	CONTROL ACTUATOR	INERTIAL MASS	PIVOT LOCATION FROM INERTIAL MASS C.G.	STUDY STATUS
1		BODY MOTION	PILOT	BELOW C.G.	STUDIED CONCLUSIVELY AT NR/SD
2		MANUAL DIRECT OR BOOSTED	PILOT & LFV LESS ENGINES	BELOW C.G.	STUDIED CONCLUSIVELY AT NR/SD
3		CLOSED-LOOP SERVO	PILOT & LFV LESS ENGINES	BELOW C.G.	STUDIES
4		MANUAL DIRECT OR BOOSTED	PILOT	ABOVE C.G.	CONCLUSIVE STUDY PROPOSED
5		MANUAL DIRECT OR BOOSTED	PILOT & LFV LESS ENGINES	ABOVE C.G.	CONCLUSIVE STUDY PROPOSED

Figure 2-1. Pitch and Roll Controls Mechanization Concepts

Case 3 is basically the same as Case 2, except that stability augmentation about a given operating point is automatically provided. In all but Case 3, the dynamics of human reaction must be considered in the stability loop.

Case 4 is identical to Case 5, except that the gimballed engine mass is not negligible because of the different mass distribution of the configuration. In Cases 4 and 5, the engine is gimballed above the total center of gravity (overhead pivot), giving dynamic effects which differ slightly from the other cases. Although the equations in Part 2 of Appendix C may be used for overhead pivot analysis simply by making  $l_2$  more negative than the total center of gravity position, a separate derivation is provided in Part 3.

In all but Case 4, the mass of the engines may be neglected, if desired, because the tail-wags-dog effect is negligible. The actual number of engines may be represented by one engine for most of these studies.

### Analytical Studies

This section discusses handling qualities of the lunar flying vehicle under kinesthetic, hardwire and stability-augmented control modes. The basic question is, whether a pilot can sufficiently stabilize the LFV by himself (hardwire or kinesthetic), or whether a stability-augmentation system is necessary. This problem is amenable to the techniques of aircraft handling qualities analysis and is approached by using test data and mathematical models developed by McRuer, Ashkenas, Bergeron, et al, (Reference 2-1), as well as lunar flying vehicle flight test and visual simulator experience. These data will be used to predict pilot opinion ratings for the various LFV control modes, and to identify tasks which impose maximum work load on the pilot.

From a mechanization standpoint, kinesthetic and hardwire control systems are appealing because of their extreme simplicity, inherent reliability, light weight, and low cost. These advantages are overridden if the pilot cannot satisfactorily control the vehicle. Astronauts are heavily scheduled in the months before a flight and an LFV possessing marginal handling qualities would require an additional intensive flight training program, with proficiency maintenance flights scheduled right up to launch. This is unattractive, and motivates the use of a highly stable flight control system. A stability augmentation system will yield satisfactory handling qualities, but it carries some penalties in terms of weight, cost, and complexity.

Of the three types of control, hardwire appeared to be the most promising system in the early phases of this work in the tradeoff between system weight/complexity and good handling qualities. For this reason, hardwire control systems, with and without compensation networks, received considerable attention in this study.

## Mathematical Modeling of the Human Pilot

If kinesthetic control is to be satisfactorily achieved, the LFV must be dynamically matched to the pilot's sensing and control force capabilities in much the same way an actuator/gyro package is matched to an airframe flight control system. Extensive tests with human subjects have revealed that pilots performing tracking tasks will assume transfer functions of the form:

$$\frac{\delta}{\theta_\epsilon} = K_{\rho\theta} e^{-\tau s} \frac{\left(S + \frac{1}{T_L}\right)}{\left(S + \frac{1}{T_N}\right)} \quad (1)$$

where  $S$  is the Laplace transform variable. The transport delay,  $\tau$ , represents two components: an inherent neuromuscular system delay which is relatively fixed, and a mental computation time delay that depends on pilot work load. A pilot will adjust his gain,  $K_{\rho\theta}$ , and his lead time constant,  $1/T_L$ , as necessary to obtain satisfactory kinesthetic control. That is, he will adjust  $K_{\rho\theta}$  and  $1/T_L$  such that the system is suitably stable and well damped, with sufficient bandwidth to meet performance requirements. His pilot opinion is closely related to the values of  $T_L$  and  $K_{\rho\theta}$  and to the resulting airframe closed loop performance. A vehicle requiring a  $T_L$  of zero for satisfactory stabilization would be rated good if the gain  $K_{\rho\theta}$  were not required to be too low (touchy vehicle) or too high (not enough control authority). A  $T_L$  of 2 is difficult to maintain and would earn the vehicle a poor rating. Similarly, very low or very high vehicle gains require values for  $K_{\rho\theta}$  which would earn a poor rating, while intermediate values earn good ratings.

These transfer functions suffice for steady-state tracking tasks involved in maneuvering the LFV, but do not, of course, represent pilot characteristics under stress situations such as engine failure.

Assessing whether or not a vehicle has satisfactory handling qualities is a process conducted during test flights by engineering test pilots. It has been found through experience that test pilots comprise a highly trained group, and their ratings of a given vehicle are reasonably consistent. The standard method used for a number of years to rate airframe handling qualities is the Cooper Rating scale (Reference 2-3). The Cooper scale forms the basis for a quantified weighting of a test pilot's evaluation. The basic Cooper scale is shown in Table 2-1 and an expanded, somewhat more useful version is shown in Table 2-2. Cooper ratings for a given vehicle depend upon the workload imposed on the pilot. Thus, deficiencies not especially objectionable when only pitch, yaw, and roll attitude are to be controlled might

Table 2-1. Pilot Opinion Rating System for Universal Use

	Adjective Rating	Numerical Rating	Description	Primary Mission Accomplished?	Can be Landed
Normal Operation	Satisfactory	1	Excellent, includes optimum	Yes	Yes
		2	Good, pleasant to fly	Yes	Yes
		3	Satisfactory, but with some mildly unpleasant characteristics	Yes	Yes
Emergency Operation	Unsatisfactory	4	Acceptable, but with unpleasant characteristics	Yes	Yes
		5	Unacceptable for normal operation	Doubtful	Yes
		6	Acceptable for emergency condition only*	Doubtful	Yes
No Operation	Unacceptable	7	Unacceptable even for emergency condition*	No	Doubtful
		8	Unacceptable - dangerous	No	No
		9	Unacceptable - uncontrollable	No	No
		10	Motions possibly violent enough to prevent pilot escape	-	-
*Failure of a Stability Augmenter					



Table 2-2. Expanded Cooper Rating Scale

Rating	Adjective	Expanded Description
1	<p style="text-align: center;">←</p> <p style="text-align: center;">Satisfactory</p> <p style="text-align: center;">→</p>	Excellent, highly desirable
2		Good, pleasant, well behaved
3		Fair, some mildly unpleasant characteristics Good enough for task or flight phase without improvement
4	<p style="text-align: center;">←</p> <p style="text-align: center;">Unsatisfactory</p> <p style="text-align: center;">→</p>	Some minor but annoying deficiencies
5		Effect on performance is easily compensated for by pilot Improvement is requested
6	<p style="text-align: center;">←</p> <p style="text-align: center;">Unsatisfactory</p> <p style="text-align: center;">→</p>	Moderately objectionable deficiencies
		Reasonable performance requires considerable pilot compensation Improvement is needed
		Very objectionable deficiencies Require best available pilot compensation to achieve acceptable performance Major improvements are needed

Table 2-2. Expanded Cooper Rating Scale (Cont.)

Rating	Adjective	Expanded Description
7	<p style="text-align: center;">←</p> <p style="text-align: center;">Unacceptable</p> <p style="text-align: center;">→</p>	<p>Major deficiencies but controllable</p> <p>Performance inadequate or pilot compensation</p> <p>Required for minimum acceptable performance in task or flight phase is too high</p> <p>Requires mandatory improvement for acceptance</p>
8		<p>Controllable with difficulty in task and flight phase</p> <p>Requires substantial pilot skill to retain control and continue mission</p>
9		<p>Marginally controllable in task or flight phase</p> <p>Requires maximum available pilot skill to retain control</p>
10		<p>Uncontrollable in task or flight phase</p>

become very objectionable if altitude and translational variables also must be closely controlled. Failure to meet performance requirements despite intensive efforts will cause degraded opinion.

This implies that the Cooper rating is decremented by additional tasks in this fashion:

$$R = R_{\text{best}} - \sum \Delta R_{\text{tasks}}$$

For example, the Cooper rating is heavily influenced by the value of pilot lead required (Figure 2-2), and the rating for a vehicle is decremented for each axis of  $T_L$  the pilot must generate.

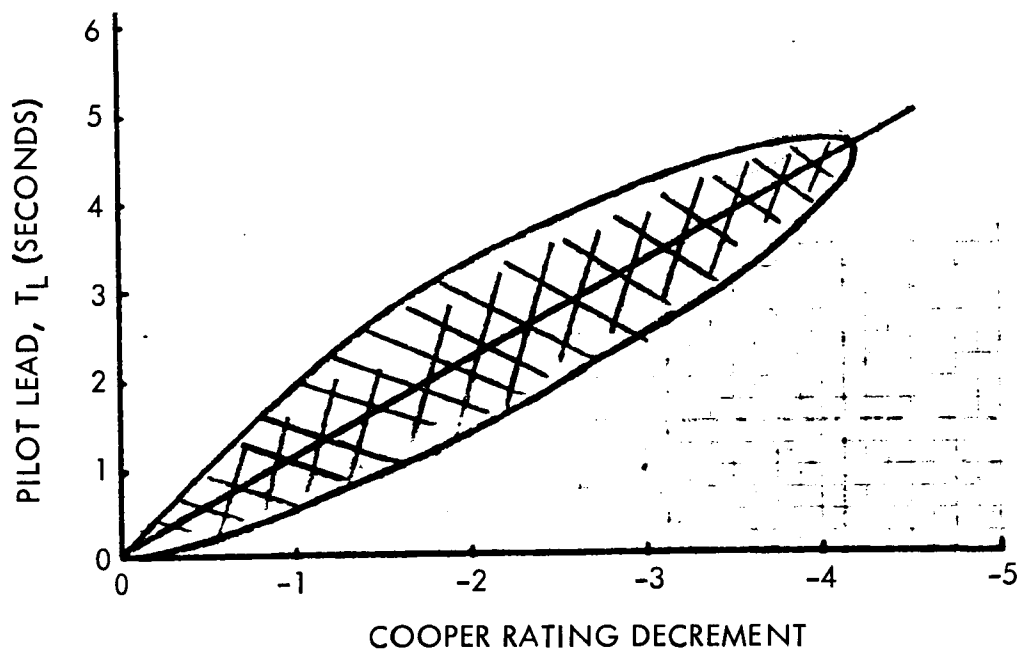


Figure 2-2. Degradation of Cooper Ratings Due to Pilot Lead Requirements

#### Stability and Control Performance Requirements

The notion of acceptable handling qualities for a vehicle is heavily dependent on the tasks expected of it. For LFV, probably the most demanding task is that of descent and landing. In doing this, the pilot must accurately control 12 variables: three-axis attitude and angular rates, as well as three-axis positions and velocities.

As pointed out in Reference 2-4, high-performance aircraft are considered marginal when the dominant closed loop natural frequency is less than about 0.8 rad/sec. It also has been found that acceptable high-performance aircraft must have a closed loop damping ratio of 0.35 or greater. The LFV basic vehicle transfer function consists simply of poles at the origin, and hence, the pilot must always supply equalization to force the system to meet basic response requirements.

Table 2-3 lists these parameters for various aircraft in the landing configuration. It is noted the damping ratios always exceed 0.3 and the natural frequencies lie in the range 0.76 - 2.6 rad/sec. Thus, aircraft experience indicates that the LFV must satisfy the following requirements during the landing phase:

$$\begin{aligned} \omega_N &\geq 0.76 \\ \zeta &\geq 0.3 \end{aligned} \quad (2)$$

Taking another approach, the maximum LFV tilt angle anticipated is  $\pm 45$  degrees, and simulator experience has shown that pilots are willing to pitch over at about a maximum of 10 deg/sec. The maneuver therefore takes 4-1/2 seconds. Using the 50-percent delay time criterion, we have:

$$T_{\text{delay}} = 2.25 = \frac{1 + 0.7\zeta}{\omega_N} \quad (3)$$

Table 2-3. Dominant Natural Frequencies and Damping Ratios of Various Acceptable Handling Qualities Aircraft During Land Phase (Reference 2-4)

Aircraft	Dominant Natural Frequency (rad/sec)	Dominant Damping Ratio
F6A	2.6	0.31
F106B	0.87	0.69
F94C	1.3	0.5
A3J-3	0.91	0.46
Boeing 727	0.9	0.5
Boeing 727-320	0.76	0.39
C5A	0.81	0.61
B52	1.4	0.58
SST-Delta Wing	0.68	1.0

Considering that  $\zeta$  must exceed 0.3 for human factors reasons we have for this approach:

$$\omega_N \geq 0.55 \text{ rad/sec} \quad (4)$$

Therefore, the range of closed loop natural frequencies must range from 0.55 rad/sec to 2.6 rad/sec. A reasonable performance requirement on the system is estimated to be:

$$\begin{aligned} \omega_N &\geq 1 \text{ rad/sec} \\ \zeta &\geq 0.3 \end{aligned} \quad (5)$$

Thus, in the following analyses, a vehicle will be downgraded if its characteristics fail to meet the above requirements, and upgraded if it is capable of exceeding these requirements.

#### Kinesthetic Control Analysis

Equations of Motion. Although the kinesthetic equations derived in Appendix C, Part 1, are valid for this analysis, their generality is larger than necessary. It is felt, therefore, that the simpler derivation provided in this section is appropriate.

For this stability analysis, moments of inertia, masses, and lever arms are assumed to be constant. The model is shown in Figure 2-3. The kinetic energy of the system is:

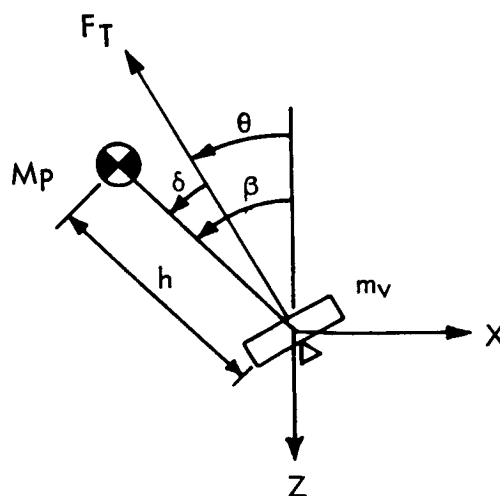


Figure 2-3. LFV Kinesthetic Dynamics Model

$$T = 1/2 \left\{ m_p v_p^2 + m_v v_v^2 + I_p \dot{\beta}^2 + I_v \dot{\theta}^2 \right\} \quad (6)$$

And the potential energy of the system is:

$$V = -g \left\{ m_v z + m_p (z - h \cos \beta) \right\} \quad (7)$$

where h is taken positive as shown. Forces and torques not derivable from a potential are:

$$Q_x = -F_T \sin \theta \quad (8)$$

$$Q_z = -F_T \cos \theta \quad (9)$$

$$Q_\theta = F_T h \sin \theta \quad (10)$$

The velocities of the particles are:

$$v_v^2 = \dot{x}^2 + \dot{z}^2 \quad (11)$$

$$v_p^2 = v_{p_x}^2 + v_{p_z}^2 = \left[ \dot{x} - h \dot{\beta} \cos \beta \right]^2 + \left[ \dot{z} + h \dot{\beta} \sin \beta \right]^2 \quad (12)$$

The Lagrangian L is:

$$L = T - V = \frac{1}{2} m_p \left[ \dot{x}^2 + \dot{z}^2 - 2h \dot{\beta} \dot{x} \cos \beta + 2h \dot{\beta} \dot{z} \sin \beta + h^2 \dot{\beta}^2 \right] \quad (13)$$

$$+ \frac{1}{2} \left[ I_p \dot{\beta}^2 + m_v (\dot{x}^2 + \dot{z}^2) + I_v \dot{\theta}^2 \right] + m_v g z + m_p g z - m_p g h \cos \beta$$

Using Lagrange's equation and performing the required operations:

$$\frac{d}{dt} \left( \frac{\partial L}{\partial \dot{q}_i} \right) - \frac{\partial L}{\partial q_i} = \sum_i Q_i \quad (14)$$

$$(I_p + m_p h^2) \ddot{\beta} + m_p h (\ddot{z} \sin \beta - \ddot{x} \cos \beta) - m_p h g \sin \beta = 0 \quad (15)$$

$$I_v \ddot{\theta} = F_T h \sin \delta \quad (16)$$

$$(m_p + m_v) \ddot{x} - m_p h \ddot{\beta} \cos \beta + m_p h \dot{\beta}^2 \sin \beta = -F_T \sin \theta \quad (17)$$

$$(m_p + m_v) \ddot{z} + m_p h \dot{\beta} \sin \beta + m_p h \dot{\beta}^2 \cos \beta - (m_p + m_v) g = -F_T \cos \theta \quad (18)$$

The equations may be linearized by using an expansion including the first two terms of a Taylor's series. This represents small perturbations about a fixed operating point. All operating points are assumed zero except for:

$$\theta \rightarrow \theta_o + \theta \quad (19)$$

$$\ddot{x} \rightarrow -\frac{F_T}{m_T} \sin \theta_o + \ddot{x} \quad (20)$$

$$\ddot{z} \rightarrow \left( g - \frac{F_T}{m_T} \cos \theta_o \right) + \ddot{z} \quad (21)$$

$$\sin \theta \rightarrow \sin \theta_o + (\cos \theta_o) \theta \quad (22)$$

$$\cos \theta \rightarrow \cos \theta_o - (\sin \theta_o) \theta \quad (23)$$

$$\sin \beta \rightarrow \sin \theta_o + (\cos \theta_o) \beta \quad (24)$$

$$\cos \beta \rightarrow \cos \theta_o - (\sin \theta_o) \beta \quad (25)$$

$$\sin \delta \rightarrow \delta \quad (26)$$

Two definitions aid in the linearization:

$$\theta = \beta - \delta \quad (27)$$

$$m_T = m_p + m_v \quad (28)$$

If small angle perturbations are made about an operating point and the unperturbed equations are subtracted, the following linear differential equations occur:

$$(I_p + m_p h^2) \ddot{\beta} - \frac{m_p h F_T}{m_T} \cos^2 \theta_o \beta + m_p h \sin \theta_o \ddot{z} - \frac{m_p h F_T}{m_T} \sin^2 \theta_o \beta \quad (29)$$

$$- m_p h \cos \theta_o \ddot{x} = 0$$

$$I_v \ddot{\theta} = F_T h \delta \quad (30)$$

$$m_T \ddot{x} - m_p h \cos \theta_o \ddot{\beta} = -F_T \theta \cos \theta_o \quad (31)$$

$$m_T \ddot{z} + m_p h \ddot{\beta} \sin \theta_o = F_T \theta \sin \theta_o \quad (32)$$



Finally, Laplace transforming and casting into matrix format we have:

$$\begin{bmatrix}
 (I_v + I_p + m_p h^2) s^2 & -m_p h \cos \theta_o s^2 & m_p h \sin \theta_o s^2 \\
 -\frac{m_p}{m_T} h F_T & & \\
 \hline
 -m_p h \cos \theta_o s^2 & m_T s^2 & 0 \\
 + F_T \cos \theta_o & & \\
 \hline
 m_p h \sin \theta_o s^2 & 0 & m_T s^2 \\
 - F_T \sin \theta_o & & 
 \end{bmatrix}
 \begin{bmatrix}
 \beta \\
 \\
 \\
 \\
 \\
 \end{bmatrix}
 =
 \begin{bmatrix}
 I_v s^2 + F_T h \\
 \\
 F_T \cos \theta_o \\
 \\
 - F_T \sin \theta_o
 \end{bmatrix}
 \begin{bmatrix}
 \delta \\
 \\
 \\
 \\
 \end{bmatrix}
 \quad (33)$$

The matrix equation is solved in standard fashion to yield the transfer function:

$$\frac{\beta}{\delta} = \frac{\left[ \frac{I_v}{I_p + I_v + \frac{m_p m_v}{m_p + m_v} h^2} \right]}{\left[ \frac{s^2 + \frac{F_T h}{I_v} \left( \frac{m_p}{m_p + m_v} + 1 \right)}{s^2} \right]} \quad (34)$$

Action - Reaction Effect. The equations developed in the previous section showed the vehicle transfer function to be of the following form:

$$\frac{\beta}{\delta} = \frac{K (s^2 + \omega^2)}{s^2} = \left\{ \frac{I_v}{I_T} \right\} \left[ \frac{s^2 + \frac{F_T h}{I_v} \left\{ \frac{m_p}{m_T} + 1 \right\}}{s^2} \right] \quad (35)$$

This section is intended to discuss the meaning of this transfer function, and to point out the ways in which it imposes performance limitations on the LFV.

A typical attitude maneuver sequence is shown in Figure 2-4. To generate a pitchover moment, the pilot must pull the handlebars towards him (or alternatively lean toward the handlebars). By Newton's Law of action and reaction, the platform rotates in a direction opposite to that in which the pilot moves. When in this position (Figure 2-4b), the momentary horizontal component of thrust causes a small velocity to build up in the wrong direction. Called path reversal, this effect is discussed in more detail in the Hardwire Analysis section.

The thrust vector, acting through the displaced center of mass, causes the vehicle to rotate to its desired attitude. Once there, as in Figure 2-4e, the pilot must push backward (or lean backward) to stop his angular rate. The action reaction effect again comes into play, and the system finally comes to equilibrium as in Figure 2-4f. The effect occurs in proportion to the ratio of pilot to vehicle inertias, and is identical to the tail-wags-dog effect found in launch vehicle control systems. It is important here because it sets the maximum stabilization and control system performance limitation on the LFV. That is, as will be seen in a later section, the frequency

$$\omega = \left[ \frac{F_{Th}}{I_v} \left\{ \frac{m_p}{m_T} + 1 \right\} \right]^{1/2} \quad (36)$$

sets the basic system achievable bandwidth. This, in large part, determines pilot handling qualities opinion, ability of the system to reject oscillatory center of gravity shifts (e. g., inadvertent pilot motion), and overall maneuverability.

Stability Analysis. The equations of motion of LFV were developed earlier and now will be used for analysis. The pitch plane block diagram is shown in Figure 2-5. The inner loop represents the attitude loop, with dynamics closed through the pilot's vestibular, visual, and proprioceptive sensory capabilities. Tilt angle,  $\theta$ , is proportional to linear acceleration by the factor  $g \sin \theta$ , or  $g\theta$  in the linear sense. Two integrations, represented in Laplace notation by  $1/s^2$  convert the linear acceleration into a translation,  $x$ . Thus the block diagram as shown represents the LFV in a path control task, usually a landing or hovering operation. Because the pilot is controlling four integrations (two for  $\theta$ ; two for  $x$ ) in addition to two more for altitude control, this block diagram represents the most demanding workload to the pilot.

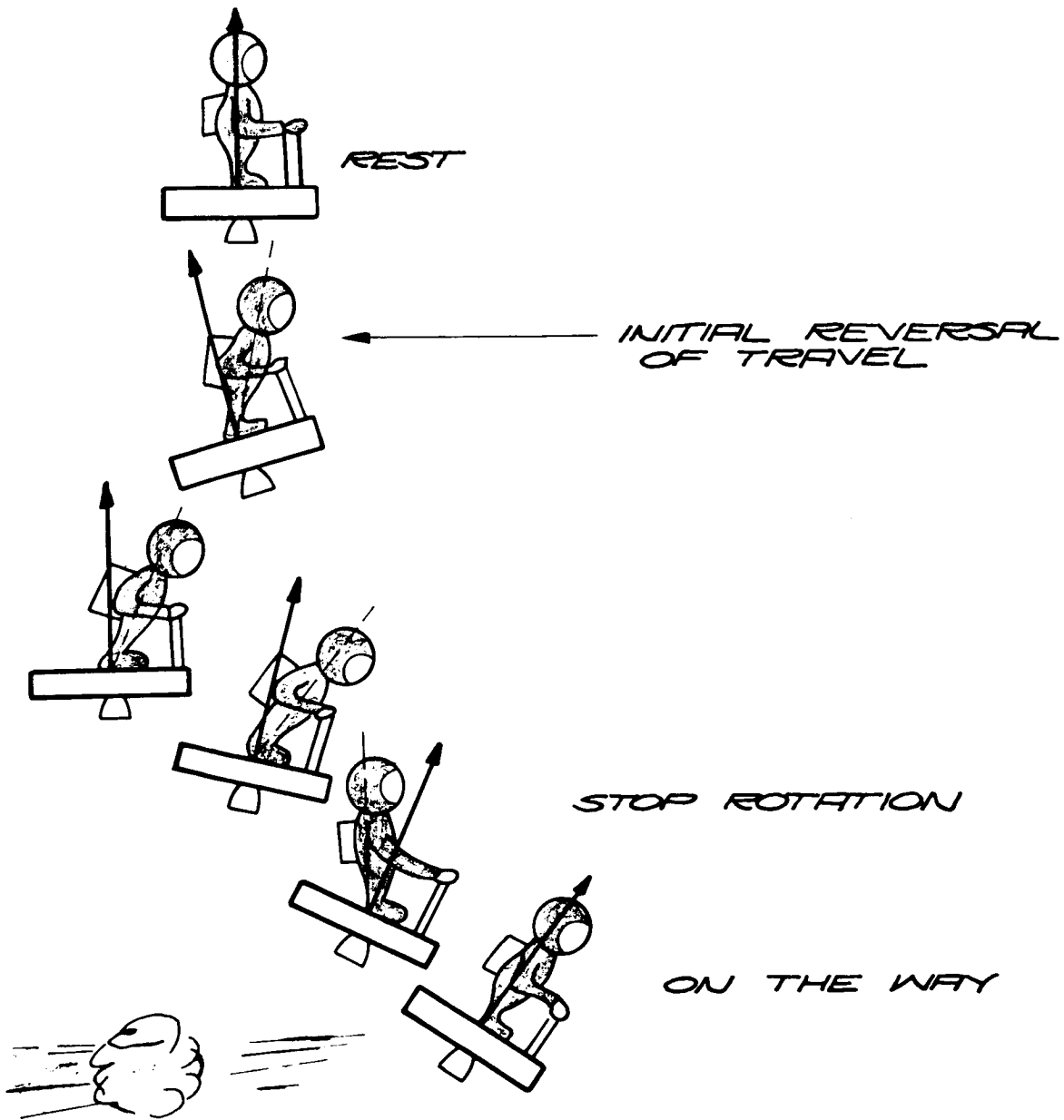


Figure 2-4. Lunar Flying Vehicle Response

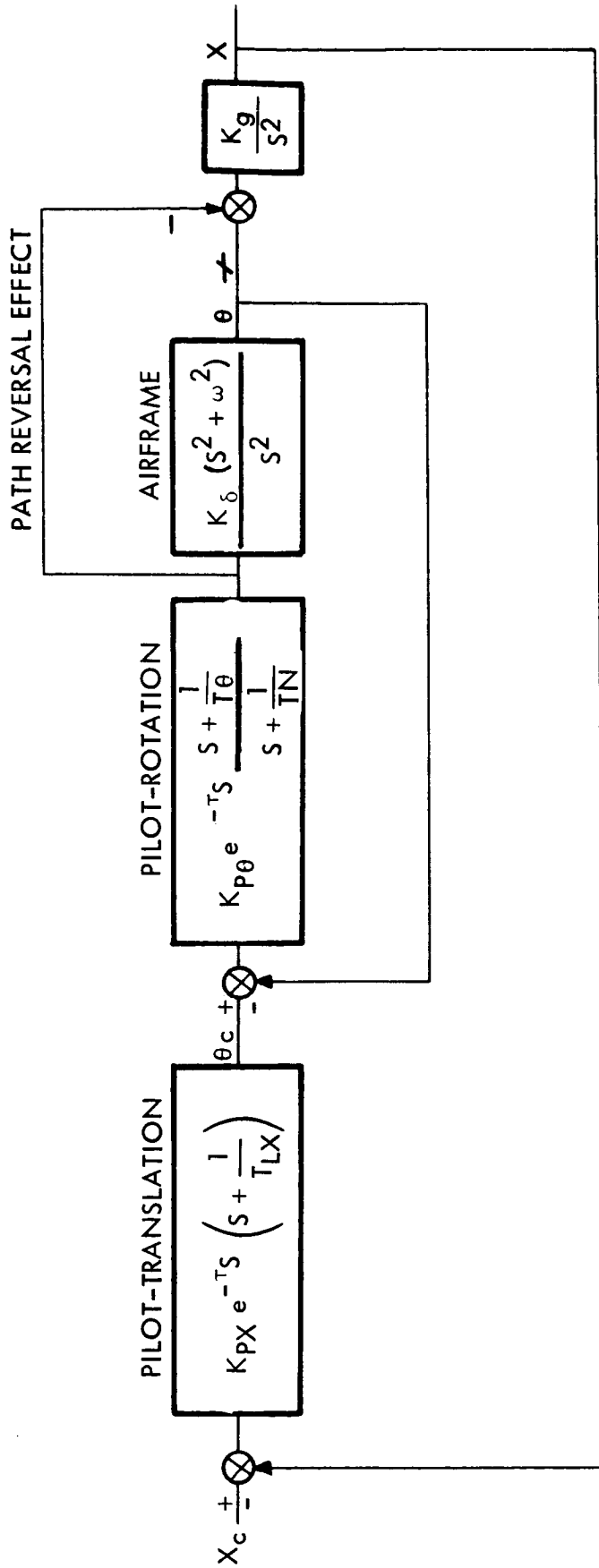


Figure 2-5. Kinesthetic Attitude and Path Control Block Diagram

The pilot time constants shown in Equation 76 were taken from actual data (Reference 2-8) and modified in accordance with References 3, 4 to account for the full 6DOF control task. The pole at  $S = -3$  represents the pilot's neuromuscular lags. The translation pilot math model has no such pole because the process is purely sensory and computational. The feed-forward path from  $\delta$  to  $\theta$  represents the path reversal effect discussed previously. Lunar thrust, moments of inertia, and weights used for the vehicle were essentially the configuration of Reference 2-9.

The approach to be taken here will be to first close the system inner loop, determining pilot gain and lead required to meet performance requirements. Next, the outer, path-loop will be closed and an attempt made to predict pilot opinion of the vehicle's handling qualities. Finally, comments will be made on possible vehicle design changes required to improve the system handling qualities.

Performance requirements dictate that the overall closed-loop system bandwidth exceed 1 rad/sec, with damping of 0.3 or better. The inner (i. e., attitude) loop root locus is shown in Figure 2-6. Using the block diagram in Figure 2-5, the characteristic equation is:

$$1 + \frac{K_{p\theta} (0.69) (S + 0.5) (S^2 + \overline{2.74}^2) (S - 6.66)}{S^2 (S + 3) (S + 6.66)} = 0 \quad (37)$$

and the attitude loop closure yields the following transfer function:

$$\frac{\theta}{\theta_c} = \frac{-0.789 (S + 0.5) (S^2 + \overline{2.74}^2) (S - 6.66)}{(S + 1) (S + 16) (S^2 + 0.6 S + 1)} \quad (38)$$

The criterion of closure was maximum system bandwidth while maintaining 6 db gain margin. The gain margin constraint was imposed by the Padé pole at  $S = -6.6$ . Doubling loop gain would drive this pole unstable. Therefore, the maximum attitude loop bandwidth achievable for this system is 1 rad/sec, barely meeting attitude loop requirements. The system is conditionally stable, and inadvertent raising of loop gain by the pilot will cause instability.

The outer loop (path) closure, also shown in Figure 2-6, is also conditionally stable. Achievable system bandwidth ( $< 0.5$ ) is very poor with no path loop lead compensation by the pilot. Addition of a moderate amount of pilot translation lead ( $1/T_{Lx} = 1$ ) yielded good damping, but the bandwidth remains very poor. Additions of more translation lead yielded little improvement.

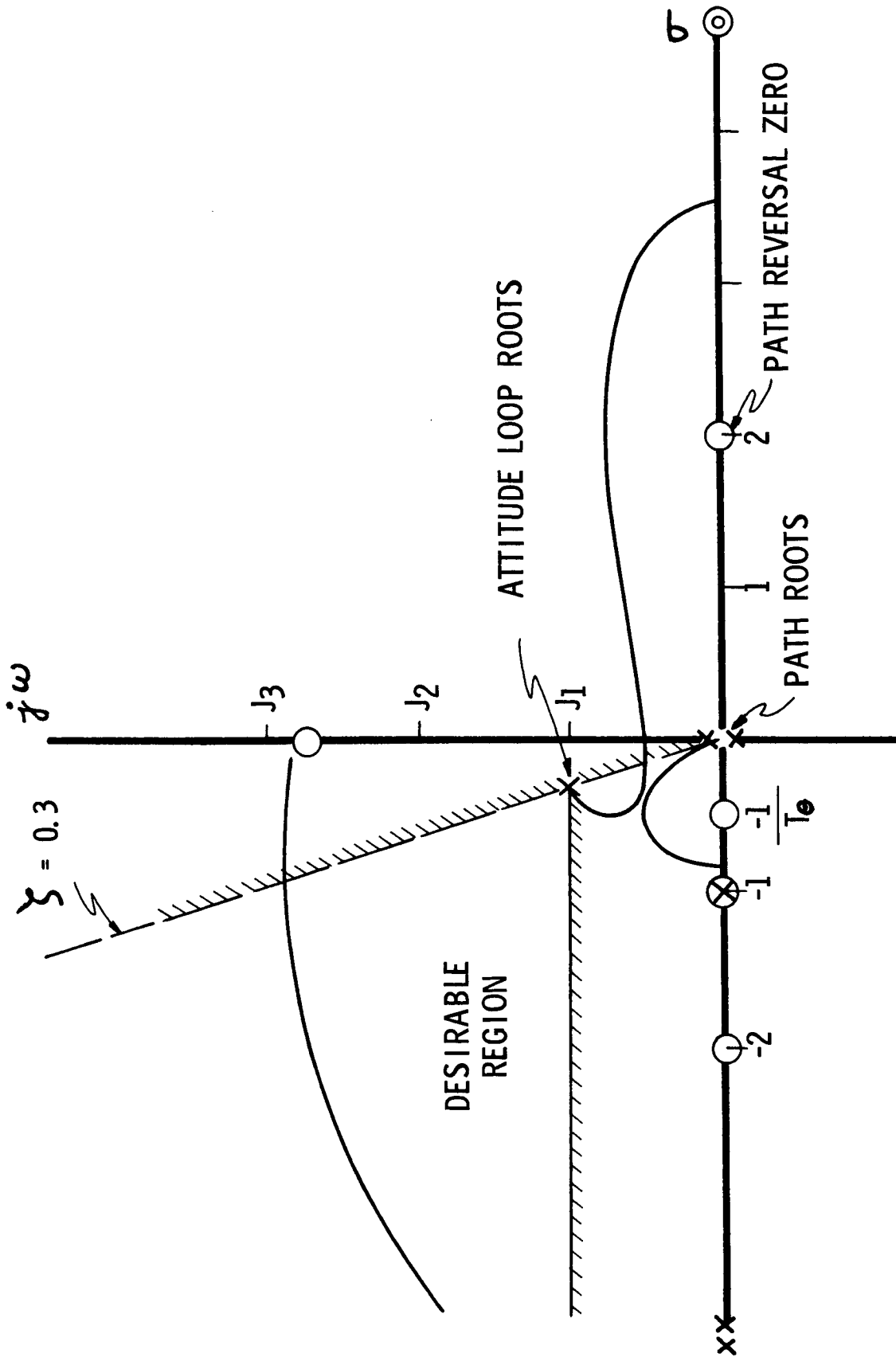


Figure 2-6. Kinesthetic Control of Lunar Flying Vehicle

It therefore may be concluded that kinesthetic control is incapable of providing adequate system response to permit landings (i. e., path control) to be achieved. Maximum attitude lead generation is required of the pilot in order to achieve, at best, very poor performance. Consequently, it is estimated that a test pilot would give this vehicle a 7 to 8 rating. Table 2-1 shows that this ranges from "unacceptable even for emergency use" to "unacceptable-dangerous".

In assessing inertias over a wide range at low values, the vehicle is far too lively for comfortable control, correspondingly degrading the pilot's rating. As more and more inertia is added to the vehicle, it becomes more stable, although further inertia makes the vehicle sluggish to a point where loop gains required to achieve bandwidth requirements cause instability.

### Conclusions for Kinesthetic Control Analysis

1. A kinesthetic control system is conditionally stable. "Over-control", "rough control", etc. will cause loss of control.
2. LFV kinesthetic control suffers from the path reversal problem.
3. Achieved closed-loop damping is adequate, although bandwidth is far below the requirements. The system path control will appear sluggish even though the pilot exerts maximum lead control. Workload is at or near maximum pilot capability.
4. Cooper rating, estimated at 7 to 8, is unacceptable even for emergency operation and is dangerous.

### Hardware Controls Analysis

The Path Reversal Problem. Previous sections have discussed the attitude sequence required to initiate or terminate an LFV translation maneuver. Geometrical relationships between the nozzle gimbal and system center of gravity give rise to the so-called path reversal problem illustrated in Figure 2-7. Initial displacements of the nozzle (to produce pitching moments) cause a momentary velocity buildup in the wrong direction, an undesired velocity that is rapidly nulled and the correct velocity achieved as the pitch angle increases. This effect was very objectionable to pilots flying the NR tethered flight vehicle at high inertias when the gimbal axis was located below and close to the center of gravity.

In the S-plane, this phenomena shows up as a right half plane real zero. Three schemes for overcoming the path reversal effect are shown in Figure 2-8. These methods overcome the unfavorable gimbal geometry of Figure 2-7 by placing the gimbaling point above the system center of gravity, permitting initial velocity buildup to occur in the proper direction. All of these schemes, considered in the LFV system selection tradeoffs, were rejected primarily on the basis of design complexity. Therefore, all the following analyses include path reversal dynamics.

System Analysis of the LFV Hardwire Control Mode. Hardwire control systems use a mechanical linkage between the hand controller and the rocket engine. In common with the kinesthetic control method, the pilot's visual, vestibular, and proprioceptive capabilities are used for sensing while his neuromuscular system is used for actuation.

The hardwire system, very similar to kinesthetic control, has an advantage in that thrust vector control is achieved by gimbaling small engines rather than by using pilot center of gravity movement for tilting the vehicle. Intuitively, one would expect hardwire control to be preferable to kinesthetic for large moment of inertia vehicles. The primary advantage of hardwire control is related to the larger control bandwidths that are achievable when the gimbaled mass is kept small. The system block diagram (Figure 2-9) is similar to that for kinesthetic control. However, because the gimbaled mass is small, the quadratic zero pair discussed earlier is not considered. The gimbal center of gravity geometry is the same as for kinesthetic control when the gimbal pivot is below the center of gravity; hence the path reversal problem remains. Using the same vehicle parameters as before, we have for the inner, attitude loop closure:

$$1 + \left( \frac{2.56K_{P\theta}}{S^2} \right) \frac{S-6.66}{(S+6.66)(S+10)} \left( S + \frac{1}{T_{LA}} \right) = 0 \quad (39)$$

The neuromuscular pole at -3 for kinesthetic control has been moved to -10 for the wrist and hand motions required in hardwire control (References 2-1 and 2-5). The zero degree root locus is shown in Figure 2-10, and the closed-loop poles are found at -2.2, -14,  $\omega_N = 2$  and  $\zeta = 0.3$ . A  $T_L = 1$  was required to achieve these characteristics. Thus the attitude loop, by itself, would probably earn a Cooper rating of 3 to 4. Addition of the path control task, with its two additional integrations, will degrade this rating.

The outer loop closure characteristic equation is,

$$1 - \frac{K_{PX}(S-6.66)^2 \left( S + \frac{1}{T_{LX}} \right) (6.44)(S+1)(S+1.6)(S-1.6)(5.3)}{S^2(S+6.66)(S^2+1.2S+4)(S+2.2)(S+14)} = 0$$



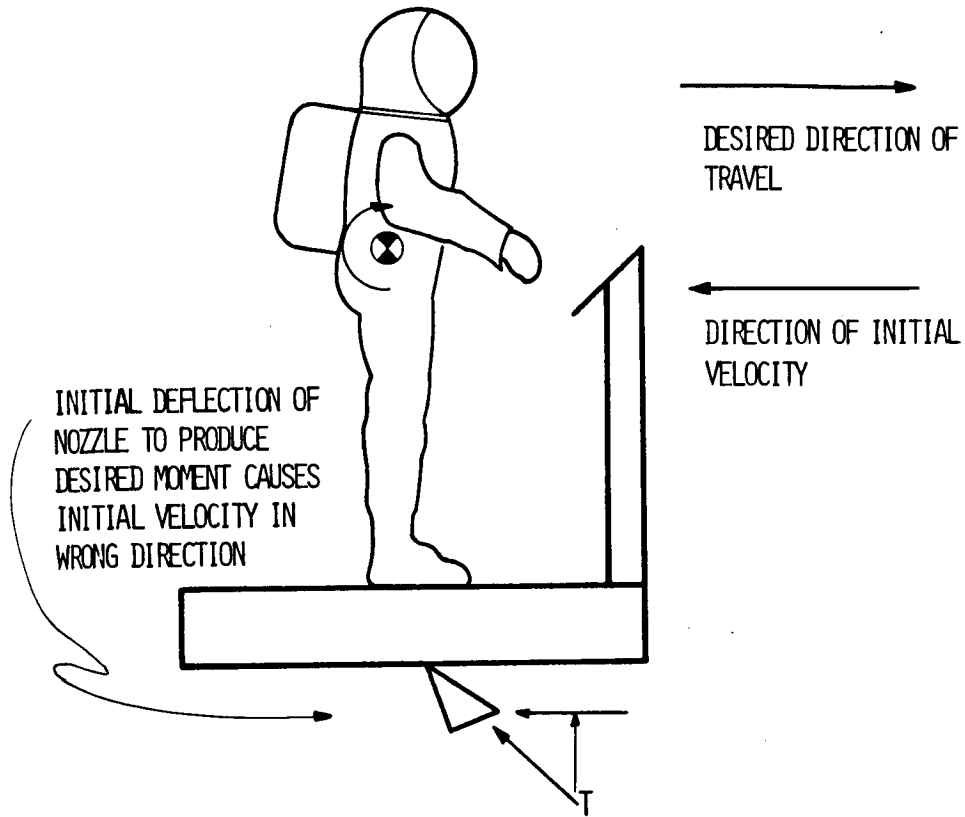


Figure 2-7. Path Reversal Problem

TRANSLATING PLATE

VIRTUAL PIVOT POINT

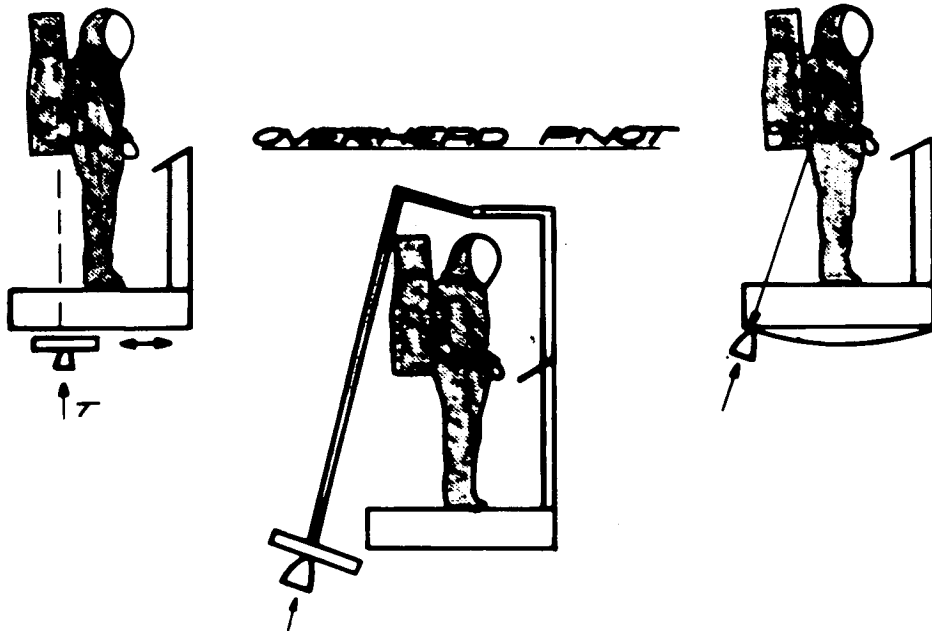


Figure 2-8. Three Solutions to the Path Reversal Problem

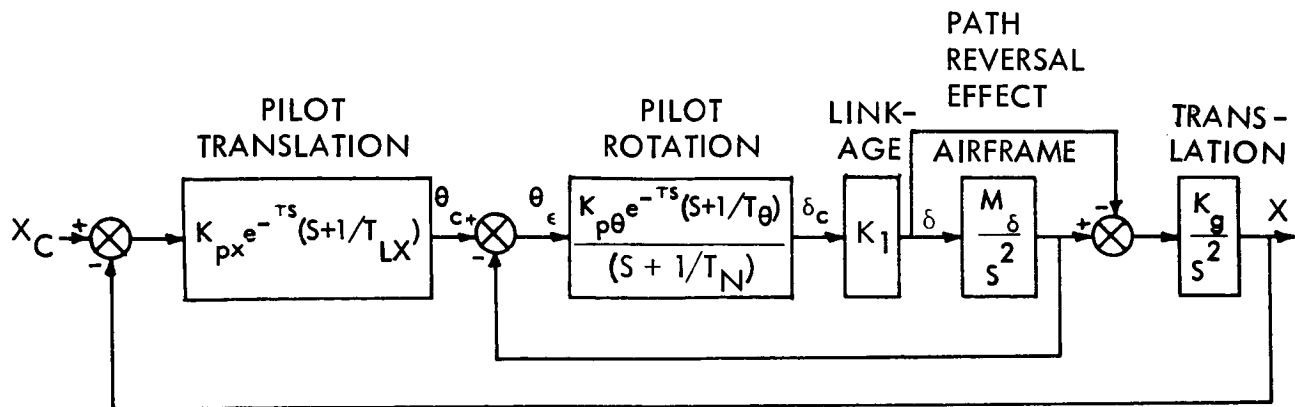


Figure 2-9. Hardware Path Control System Block Diagram

The root locus for this closure is shown in Figure 2-11. Loci are shown with and without pilot translation lead,  $1/T_{Lx}$ . The plot shows that a  $1/T_{Lx}$  of one allows the system to meet performance requirements. Basic system natural frequency is 0.9 rad/sec with a damping ratio of 0.3. Achieving this involved generating two lead-time constants of 1.0 for each channel, a total of 6. Therefore, the basic Cooper rating is downrated 1.5 points, as shown in Figure 2-2. The acceleration control throttle causes an additional degradation of 1 point for an overall airframe rating of 5.5 to 6.5 on the Cooper scale. From Table 2-2 this earns the vehicle an "unsatisfactory" rating, rating of 4 or better being required for an operational vehicle.

This rating was earned primarily because of the requirement for pilot lead generation. The next section explores methods for improving basic hardware handling qualities.

Stability and Control Aspects of the Overhead Pivots. By locating the engine gimbal pivot above the total center of gravity, one of the objectionable features of hardware control may be removed: that of the path reversal effect. At the initiation of a translation maneuver using an overhead pivot vehicle, the engines are gimballed in a direction that produces an initial velocity in the desired direction. From a controllability standpoint, this represents a potential advantage over the underneath gimbal configuration during hovering or landing. It does not, however, allow the pilot to hold a horizontal position more precisely since the gimballed engine produces a horizontal force component regardless of where it is located.

In this section, the stability aspects of the overhead pivot will be analyzed for comparison with the underneath pivot investigated previously (Figure 2-12).

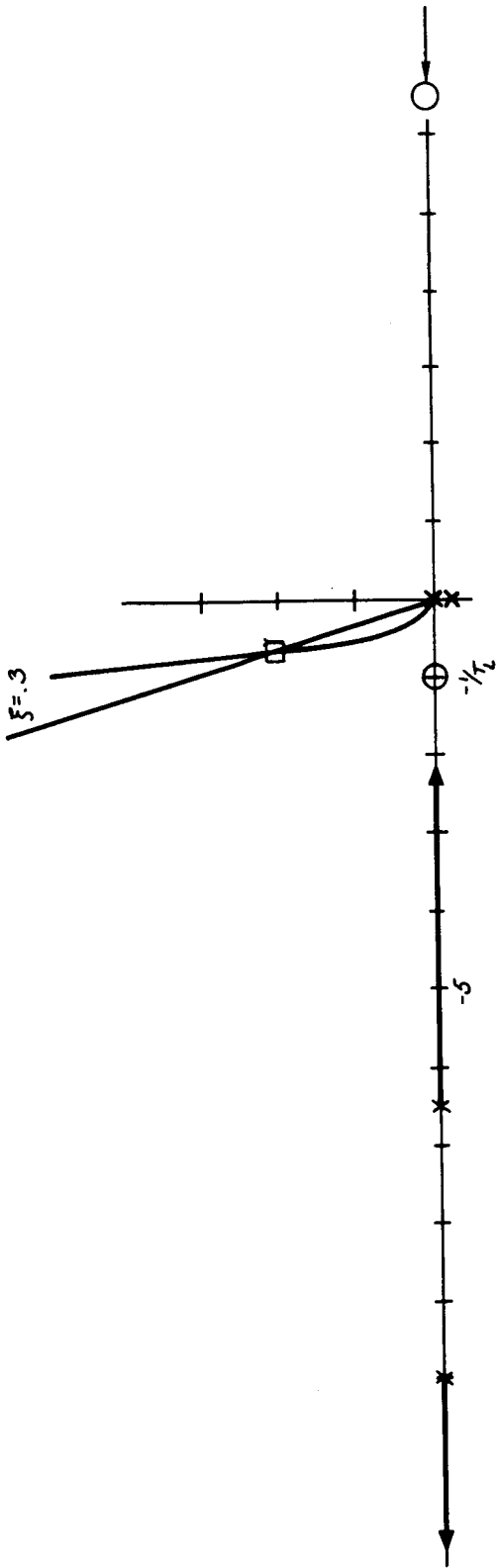


Figure 2-10. LFV Hardwire Control, Attitude Closure

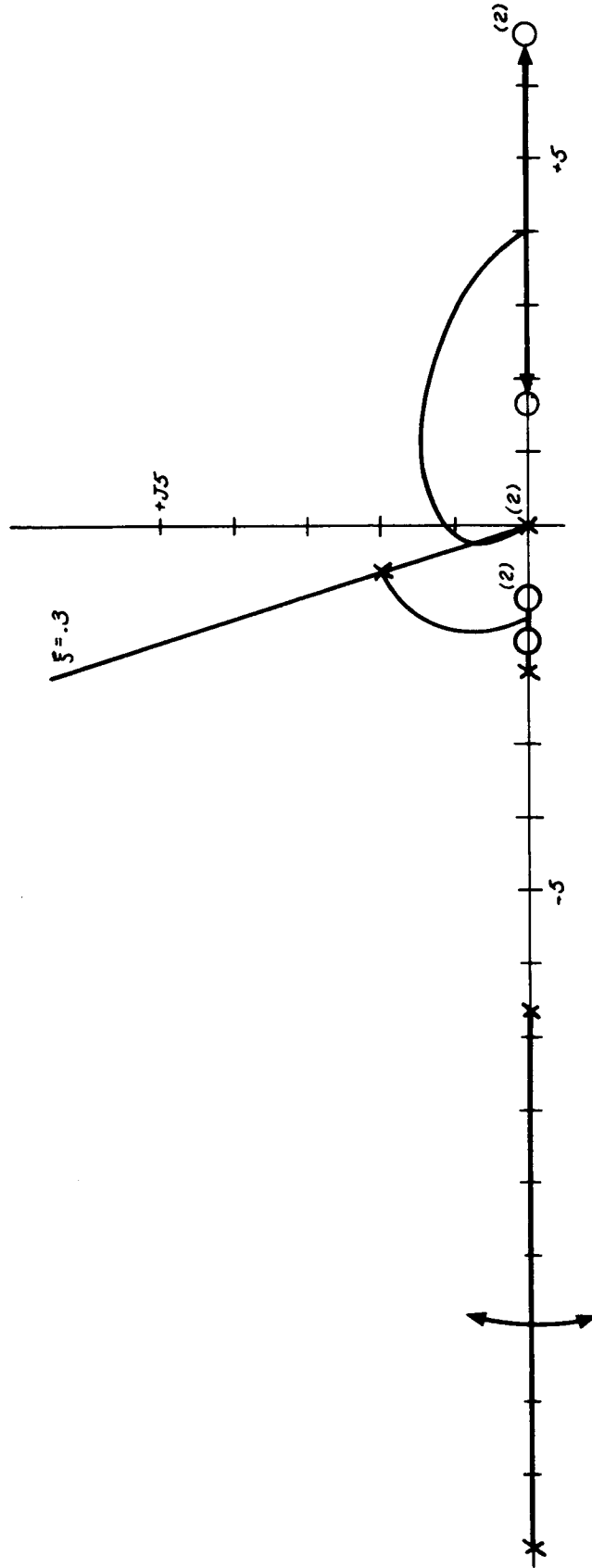


Figure 2-11. LFV Hardwire Control, Path Closure

Defined here, a stable system is one that returns to rest when perturbed, whereas an unstable system is one that diverges when perturbed. A neutrally stable system has no preferred orientation. Figure 2-13 gives examples of these phenomena. For an inertially fixed condition, the underneath pivot may be likened to the unstable case where the pilot and vehicle are balanced atop the gimbal. Also, the overhead gimbal, if inertially fixed, compares to the stable case. Because of gravity, small perturbations from the balanced position cause diverging moments with an underneath pivot and converging moments with an overhead pivot.

This is not true, however, if the pivot is free to translate, as may be intuitively seen. Mathematical proof that the overhead pivot is not inherently stable may be obtained by using the equations derived in Appendix C, Part 3.

Although control differences exist between the overhead and underneath pivot configurations, the actual position of the engine along the line of action does not affect control. Thus, the vehicle with engines located below the center of gravity but gimbaling through a point above the center of gravity will have handling qualities identical to the vehicle that has engines physically located at the overhead pivot.

Equations C-31 and C-32 in Appendix C, Part 3 may be now transformed to the time domain for interpretation of their meaning.

Consider the forcing function  $F_A$  to be a delta function,  $\delta(0)$ . The time response of Equation C-32 is:

$$\theta(t) = \mathcal{L}^{-1} \left[ \frac{Kb\omega_1^2 \left\{ S^2 + \frac{1}{b} \right\}}{S^2 \left\{ S^2 + \omega_1^2 \right\}} \right] \quad (41)$$

which transforms to:

$$\theta(t) = K \left\{ t + \left[ b\omega_1 - \frac{1}{\omega_1} \right] \sin \omega_1 t \right\} \quad (42)$$

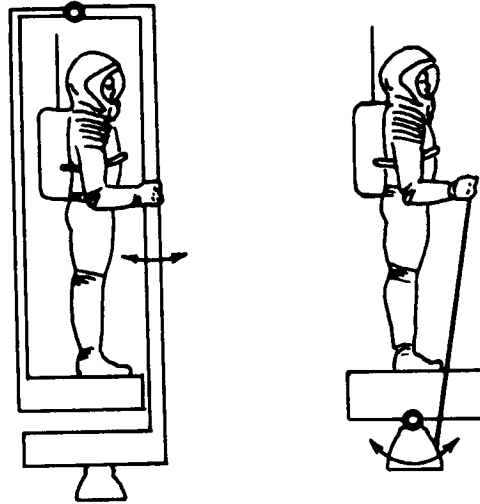


Figure 2-12. Overhead Pivot and Nozzle Beneath Configurations

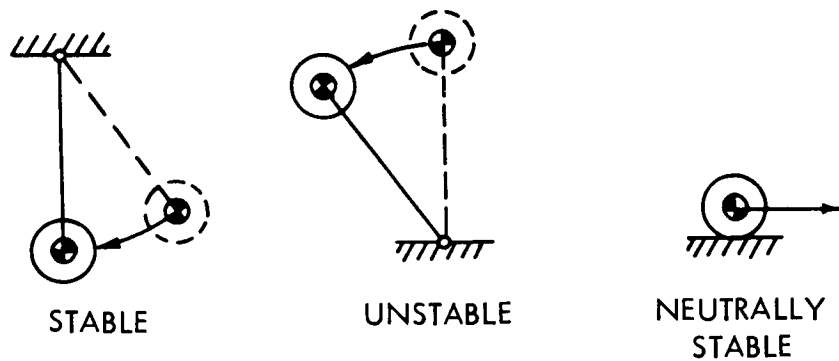


Figure 2-13. Stability Cases

The transform of Equation C-31 to a delta function is a simple sine wave. The coefficients  $b$ ,  $\omega_1$ ,  $K$  are obtained from inspection of Equation C-32. Equation C-34 shows fixed amplitude oscillatory terms  $K \sin \omega_1 t$ , and a secular term,  $Kt$  that grows without bound with time.

Given a perturbation force,  $F_A$ , the overhead pivot configuration LFV will therefore rotate indefinitely. It will not come to rest at a trimmed position as would, say, a trimmed airplane momentarily disturbed by a gust. Consequently, the term "pendulous stability" is a misnomer according to the definitions of FIGURE 2-13.

Analysis of Hardwire Control with Neutral Stability. All of the control systems discussed previously require a pitchover maneuver to allow a component of the main thrust vector to build up translational velocities. It is this requirement that gives rise to one of the major handling qualities problems.

This section discusses a concept that shows promise of avoiding this problem by placing the thrust vector gimbal through the system center of gravity, thereby decoupling translation dynamics from rotation dynamics. The requirement for pitchover to attain translation velocities disappears and the handling qualities problem is improved since the vehicle remains horizontal throughout the flight. Two neutral stability configurations are shown in FIGURE 2-14. A small bang-bang RCS is required to trim out residual drifts and center-of-gravity misalignments during flight. Gross center-of-gravity (addition of payload, etc.) changes are compensated by changing the pilot's seat adjustment before flight.

To perform a translation, the pilot rotates the engines to the required angle with respect to his centerline. He uses RCS jets to trim out residual drift rates caused by center-of-gravity misalignments. The main engines are returned to neutral when proper velocity is achieved. Various features, such as RCS jet weight, fuel consumption and engine out, weigh against the scheme. However, a feasible vehicle with hardwire control and superior handling qualities has much to recommend it.

This vehicle received limited testing on the NR visual simulator, the NR test pilot giving it a Cooper rating of 2 (good, pleasant to fly). The pilot indicated that improvements to the throttle would upgrade the rating to 1 (optimum). The simulator mechanization configuration automatically leveled the platform, relieving the pilot of that task. These were the best ratings given any LFV control system, indicating that further investigations of this configuration are well warranted.

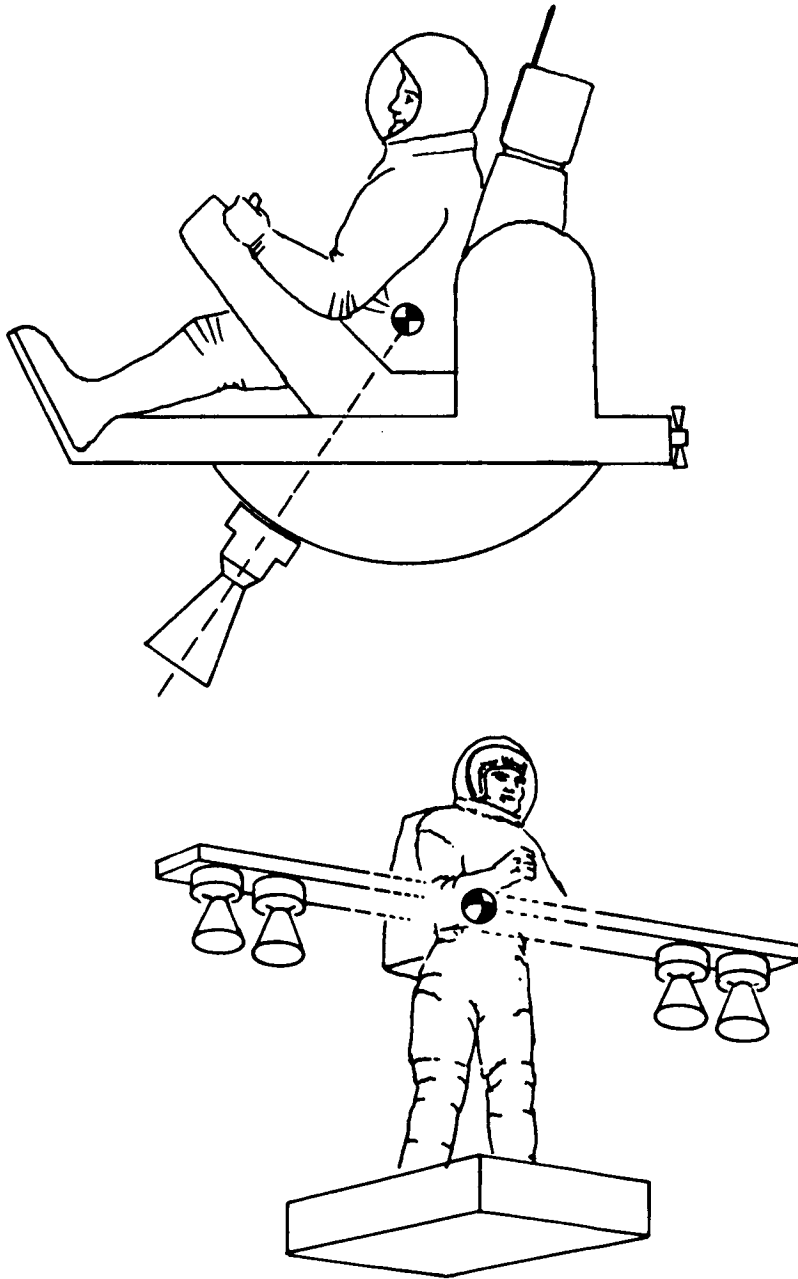


Figure 2-14. Two-C.G. LFV Configurations

The neutral stability concept may be analyzed, based on the special case of the overhead pivot equations derived in Appendix C, Part 3. Equation 30 indicates that the forcing function lever arms of Equations 31 and 32 are equal. Therefore, Equations 31 and 32 are rewritten as:

$$\frac{\phi}{F_A \ell^*} = \frac{A^* + C^*}{(A^* D^* - E^* C^*) S^2 + A^* \ell_p^* T} \quad (43)$$

$$\frac{\theta}{F_A \ell^*} = \frac{-(D^* + E^*) S^2 - \ell_p^* T}{S^2 \left[ (A^* D^* - E^* C^*) S^2 + A^* \ell_p^* T \right]} \quad (44)$$

Consequently, Equations 25 to 29, set  $\ell_B = \ell_p = 0$ . In effect, this puts the engine pivot point at the system center of mass. The transfer of functions of Equations 43 and 44 [ using Equations 25 to 29 ] become:

$$\begin{aligned} A^* &= I_B & \frac{\phi}{F_A \ell^*} &= \frac{I_B + I_p}{I_B I_p S^2} \\ D^* &= I_p \\ E^* &= 0 \\ C^* &= I_p = D^* & \frac{\theta}{F_A \ell^*} &= -\frac{I_p S^2}{S^2 (I_p I_B S^2)} \end{aligned} \quad (45)$$

Pilot attitude with respect to the ground is:

$$\begin{aligned} \frac{\theta + \phi}{F_A \ell^*} &= \left[ \frac{I_B + I_p}{I_B I_p} - \frac{1}{I_B} \right] \left[ \frac{1}{S^2} \right] \\ &= \left[ \frac{I_B + I_p - I_p}{I_B I_p} \right] \left[ \frac{1}{S^2} \right] = \frac{1}{I_p S^2} \\ \frac{\theta + \phi}{F_A \ell^*} &= \frac{1}{I_p S^2} \end{aligned} \quad (46)$$



Engine deflection with respect to inertial space yields

$$\frac{\theta}{F_A \ell^*} = \frac{-1}{I_B S^2}; \quad \frac{\theta + \phi}{F_A \ell^*} = \frac{1}{I_p S^2} \quad (47)$$

Since  $I_B$  is very small ( $\sim 0.1$  slug  $\text{ft}^2$ ) compared to  $I_p$  ( $\sim 150$  slug  $\text{ft}^2$ ) it is easy to see from Equations 46 and 47 that action-reaction forces will not move the pilot appreciably from the vertical when the engine is swung to accelerate the vehicle translationally.

Hence, the requirement to swing the entire vehicle to gain translational force disappears. Since this requirement increased the difficulty of flight control, an improvement in handling qualities is expected. A small RCS system, manually actuated, would probably be required to trim out residual thrust unbalance and trim disturbances. Sizing of this system remains to be accomplished.

In conclusion, therefore, this section indicated that placing the engine gimbals at the system center of gravity decouples the rotational dynamics from the translation problem. The handling qualities problem is improved, but the problem of controlling a small RCS system to trim out residual drift rates due to center-of-gravity misalignments, thrust unbalances, etc, remains.

Use of Compensation Networks to Improve Hardware Control. As seen in the preceding section, hardware attitude and path control required the pilot to generate 4 lead zeros at  $\sigma = 1.0$ . Each degrades the vehicle 1/2 Cooper point, the acceleration control throttle degrading it another point. Therefore, as it stands, the basic vehicle rating is penalized 3 Cooper points, making an "acceptable" rating impossible.

This section considers a method for improving the hardware Cooper rating by relieving the pilot of attitude lead generation requirements, and by improving the throttle. The use of gyros for this purpose would amount to stability augmentation by introducing complex components. This section will consider only mechanical compensation networks (consisting of springs and dashpots) to improve matters. The network is inserted between the hand controller and nozzle, as shown in Figure 2-15. Its function will be discussed in general terms, after which a servo analysis will be performed to synthesize the desired network.

The basic hardwire network uses a straight link between engine and hand controller. A steady hand controller displacement produces steady engine displacement and constant angular acceleration. Vehicle angular velocity will increase until the hand controller is neutralized. Figure 2-16 illustrates how the achievement of proper pitchover rates involves accurately timing (mentally) controller displacements. Such pilot lead generation causes the vehicle to be downrated.

Suppose a clock spring were placed around the engine gimbal to ensure a centering force, and a dashpot placed in the hand controller link, as shown in Figure 2-17. A hand controller displacement would cause the engine to momentarily displace, although the clock spring would return it to center. LFV angular velocity is proportional to the integral of engine displacements, hence the controller displacement commands angular rate. This behaves like a rate-damped stability augmented system, and pilot's opinion of it improves since he no longer must generate an attitude lead (mental timing).

In this way, the spring-dashpot combination of Figure 2-17 promises to obtain a rate command system without use of gyros. With a similar improvement in the throttle, this shows promise of elevating the Cooper rating by 2 1/2 points, to the "acceptable" range. Since the hardwire system is very simple, lightweight, and inexpensive compared to the stability augmented system, this would greatly simplify the LFV control system.

It must, however, be noticed that since the engine always returns to neutral, a constant external disturbing torque would require repeated hand controller inputs, eventually causing saturation. Whether or not this will occur depends on the nature of the pilot's inadvertent center of gravity, a question that can be settled only by simulator runs.

Figure 2-18 shows a method for combatting steady-state disturbance torques. The dashpot B of Figure 2-17 is paralleled with a spring,  $K_2$ . This, in effect, allows steady-state engine displacements for disturbance suppression. Step response wave forms for this network are shown in Figure 2-18 and its transfer function in Figure 2-19. A step hand-controller displacement causes an initial engine deflection that subsides to a steady-state displacement proportional to a ratio of  $K_2$  to  $K_1$ . Vehicle rate, the integral of the engine displacement, is also shown. The steady-state  $\delta$  yields a  $\theta$  that increases with time; therefore, this system is a hybrid between a straight hardwire system and the straight dashpot system.

**OBJECTIVE:**  
- TO UPGRADE HANDLING QUALITIES OF BASIC HARDWARE SYSTEM

**TECHNIQUE:**  
- INTRODUCE A MECHANICAL COMPENSATION NETWORK TO DYNAMICALLY "MATCH" AIRFRAME DYNAMICS TO PILOT CAPABILITIES

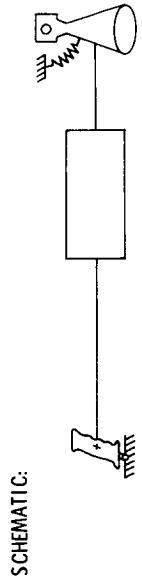
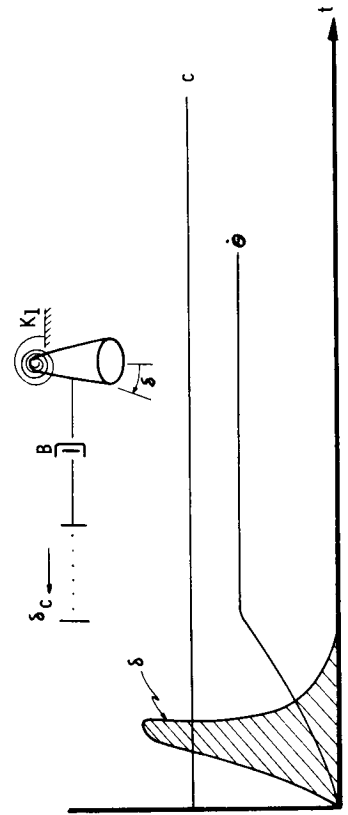


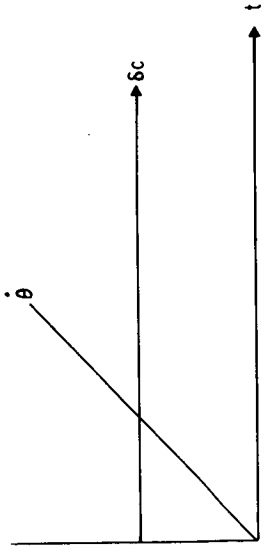
Figure 2-15. Improvements to Basic Hardware System



STICK DISPLACEMENT COMMANDS VEHICLE RATE - HANDLING QUALITIES ARE IMPROVED OVER ACCEL. COMMAND SYSTEM

SYSTEM SATURATES IF SUBJECTED TO STEADY STATE DISTURBANCE TORQUES (C.G. SHIFTS, ETC.)

Figure 2-17. Hardware Control System Compensation Network

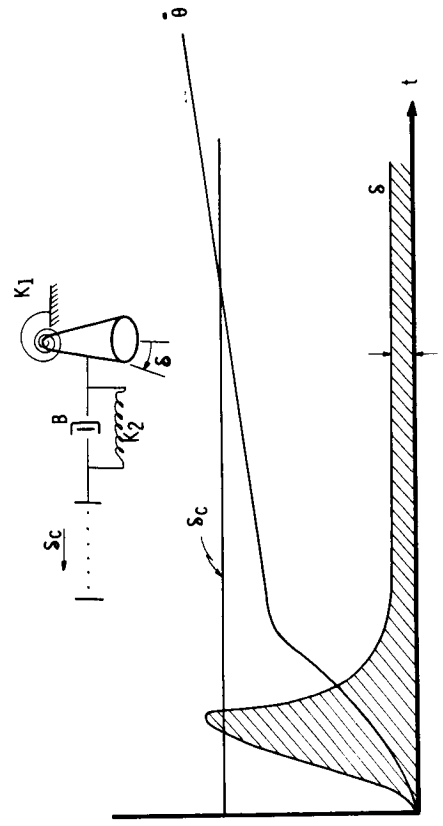


ACHIEVING DESIRED PITCHOVER RATE REQUIRES ACCURATE TIMING OF STICK DISPLACEMENT

POOR HANDLING QUALITIES

MAXIMUM RESISTANCE TO DISTURBANCE TORQUES

Figure 2-16. Basic Hardwire Control System



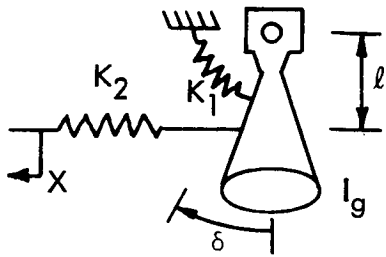
ADDITION OF SPRING INCREASES SYSTEM D. C. GAIN TO FINITE VALUE - RESISTANCE TO STEADY STATE DISTURBANCE TORQUES IMPROVED

HANDLING QUALITIES DEGRADED

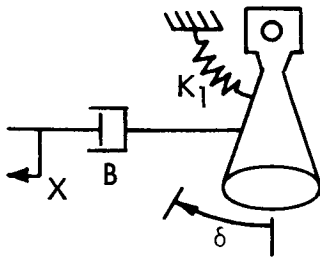
Figure 2-18. Revised Hardware Control System Compensation Network

CONFIGURATION

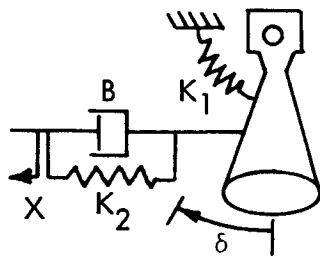
TRANSFER FUNCTION



$$\frac{\delta}{X} = \frac{K_2 / l_g}{s^2 + \frac{K_1 + l^2 K_2}{l_g}}$$



$$\frac{\delta}{X} = \frac{(Bl/l_g) s}{s^2 + \frac{Bl^2}{l_g} s + \frac{K_1}{l_g}}$$



$$\frac{\delta}{X} = \frac{Bl/l_g (s + K_2/B)}{s^2 + \frac{Bl^2}{l_g} s + \frac{K_1 + K_2 l^2}{l_g}}$$

$$\approx \frac{1}{l} \frac{(s + K_2/B)}{(s + K_2/B + K_1/Bl^2)} \text{ for } l_g \approx 0$$

Figure 2-19. Mechanical Hardwire Compensation Networks

In conducting a system analysis, first consider the simplified LFV attitude control system with disturbing inputs shown in Figure 2-20. The dashpot compensation network is shown. The closed-loop system transfer function is, by inspection:

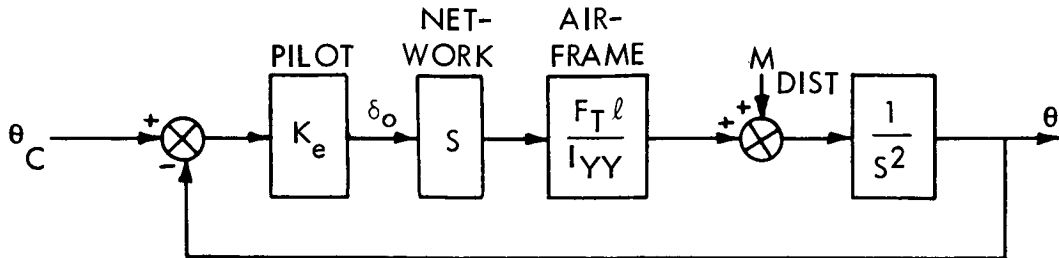


Figure 2-20. Simplified LFV Attitude Control System

$$\frac{\theta}{\theta_C} = \frac{\frac{K_{\theta} F_T l}{I_{yy}}}{S + \frac{K_{\theta} F_T l}{I_{yy}}} \quad (48)$$

which shows good stable characteristics. However the system response to a disturbance input,  $M_D$ , is:

$$\frac{\theta}{M_D} = \frac{1}{S \left( S + \frac{K_{\theta} F_T l}{I_{yy}} \right)} \quad (49)$$

Equation 49 contains a free integration yielding unbounded  $\theta$  in response to a constant disturbance input,  $M_D$ . This is an unsatisfactory condition.

If a constant term is added to the compensator, the block diagram of Figure 2-21 results.

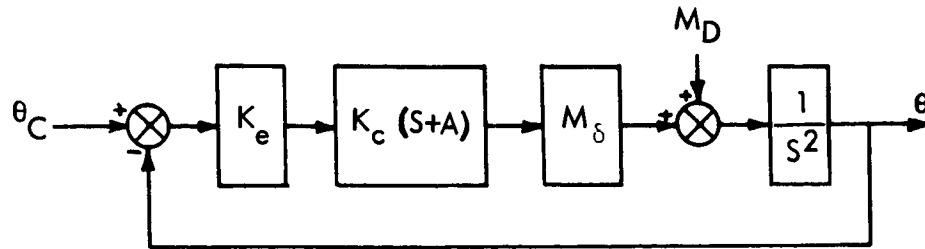


Figure 2-21. Simplified LFV Attitude Control System With Lead Compensation

Again, the closed-loop transfer function is:

$$\frac{\theta}{\theta_c} = \frac{K_{\theta} K_c M_{\delta} (S + A)}{S^2 + K_{\theta} K_c M_{\delta} S + K_{\theta} K_c M_{\delta} A}, \quad (50)$$

where

$$M_{\delta} = \frac{T l}{I_{yy}}$$

and the system disturbance input transfer function is:

$$\frac{\theta}{M_D} = \frac{1}{S^2 + K_{\theta} K_c M_{\delta} S + K_{\theta} K_c M_{\delta} A} \quad (51)$$

System closed loop natural frequency and damping ratio are, by inspection:

$$\omega_N = \sqrt{K_{\theta} K_c M_{\delta} A} \quad (52)$$

$$\zeta = \frac{1}{2} \sqrt{\frac{K_{\theta} K_c M_{\delta}}{A}}$$

and the disturbance rejection quotient:

$$\frac{M_D}{\theta_c} = \frac{M_D/\theta_c}{\theta/\theta_c} = \frac{1}{K_{\theta} K_c M_{\delta} A} \quad (53)$$

Thus, a tug-of-war between stability and noise rejection capability becomes apparent. High natural frequency and good noise rejection ability require  $A$  to be a large number, while good damping ratio requires  $A$  to be a small number. Because the network is passive,  $K_C A \leq 1$ . Too large a requirement for  $K_\theta$  degrades pilot opinion. Therefore, the degrees of freedom available to the network have been mapped out. Compensation network configurations and transfer functions for several networks are shown in Figure 2-19.

Rather than specifying a network for this simplified system, an analysis was conducted for the entire two-loop path control system to see if the network can be optimized to improve overall handling qualities. A sliding plate gimbal will be used to eliminate the path reversal problem. The overall block diagram is shown in Figure 2-21. Higher-order lags have been neglected for the moment. The approach is to break the loop at  $x$  in Figure 2-22, then manipulate the characteristic equation so as to place the shaping network as a multiplier, and synthesize the network. The characteristic equation is:

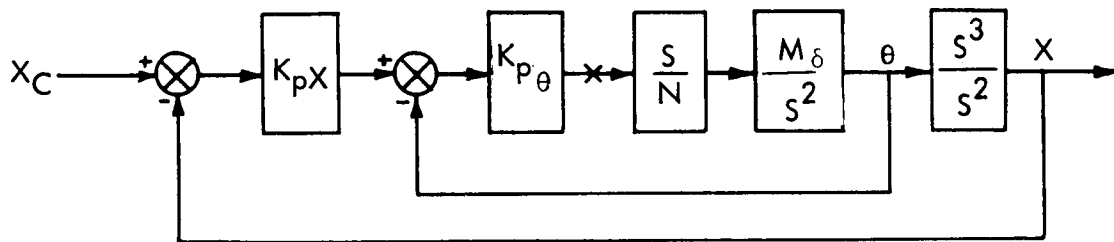


Figure 2-22. Two-Loop LFV With Shaping Network

$$1 + \left(\frac{S}{N}\right) \left(\frac{K_{p\theta} M_\delta}{S^2}\right) \left(\frac{S^2 + 5.3 K_{px}}{S^2}\right) = 0 \quad (54)$$

The root locus for this system with a simple lead network is shown in Figure 2-23. By the rules of S-plane geometry, the root locus must leave the fourth order origin poles at multiples of 45 degrees, hence the system is unconditionally unstable at low gain which is unacceptable. Pilot lead is required to stabilize the system, and therefore a more complicated network is required to relieve the pilot of this task. A third attempt, using  $T_{LX} = 0.33$  and including transport delays, yielded the root locus shown in Figure 2-24.

These networks were evaluated on the NR visual LFV simulator. Disturbing moments caused the hand controller to saturate; therefore, DC

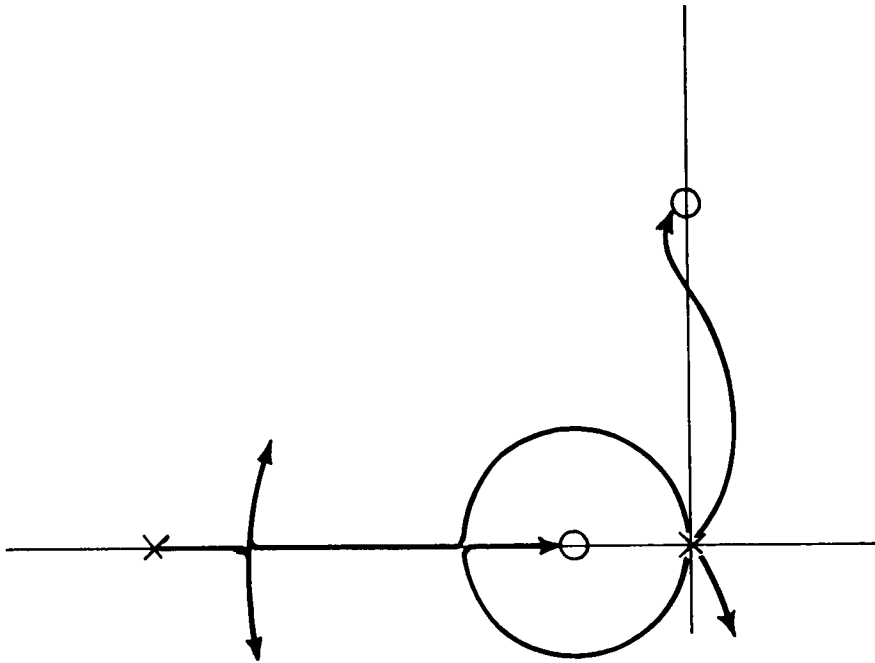


Figure 2-23. Generic Two-Loop Root Locus,  
Simple Lead Network

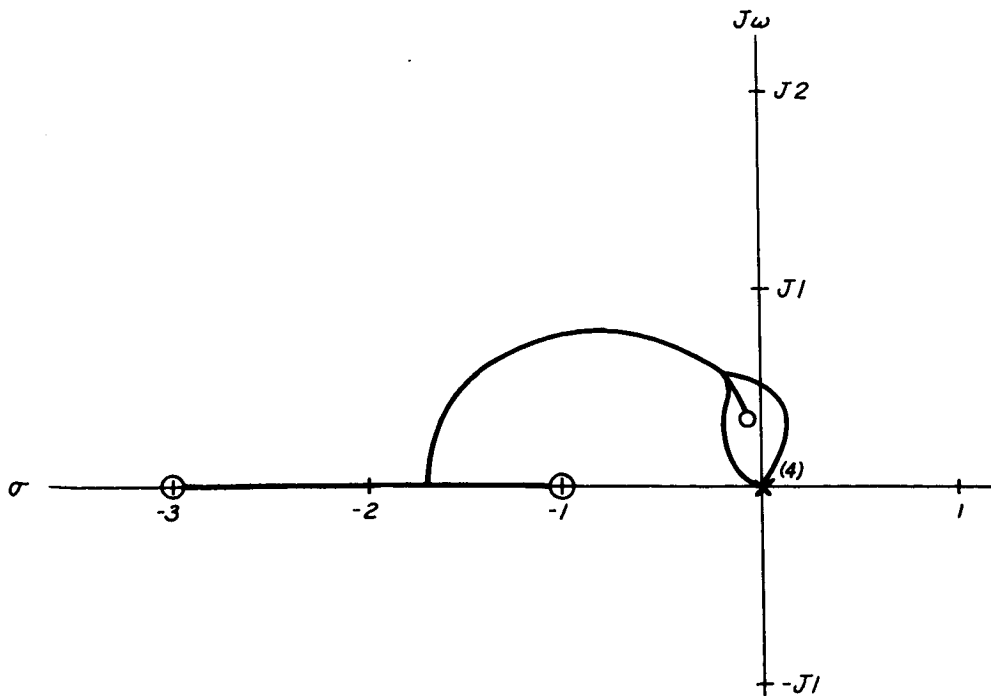


Figure 2-24. Two-Loop Root Locus,  $T_{LX} = 0.33$





gain was added to the network to assist in rejecting the disturbing torques. When sufficient gain was added to successfully combat the disturbance torques, the test pilot remarked that the system was indistinguishable from a straight hardwire system. Several runs verified this finding. It was consequently concluded that this type of network was incapable of upgrading hardwire LFV handling qualities.

A different sort of network uses a separate trim input (like an airplane) to zero the steady-state disturbing torques. Although time constraints prevented investigation of this type of network, it is recommended that such an approach be evaluated in future activity.

### Conclusions for Hardwire Control Analysis

1. Hardwire control with the pivot below the center of gravity and no compensation has an estimated Cooper rating of 5.5 to 6.5, caused primarily, by the requirement for pilot lead generation.
2. Moving the pivot to a position above the total center of gravity does not change the stability, although it does solve the path reversal problem.
3. Neutral stability, obtained by pivoting the engine through the total center of gravity, allows thrust vector control while maintaining a level platform. With vehicle rotation and translation dynamics thus decoupled, hardwire control Cooper ratings may be increased. Platform leveling may be accomplished by either hardwire or stability-augmented control of reaction jets.
4. Various compensation networks, placed between the rotation hand controller and the pivot, have not improved handling qualities over those of basic hardwire control.

### Stability Augmented Controls Analysis

System Analysis. The stability augmented system discussed here is similar to the Apollo SCS. The system provides rate damping and attitude hold. When the astronaut moves the hand controller, attitude feedback from the gyros is inhibited, while angular rate damping is maintained. The attitude loop is then closed through the astronaut, as is the translation loop.

Attitude hold with this system poses no workload to the pilot. A rate-damped maneuver with path control is the most difficult task to perform with this system, and this is the situation to be analyzed. The block diagram is shown in Figure 2-25, along with the same vehicle constants previously used. The path reversal problem is included. The task of the rate gyro is to

suppress disturbance moments automatically, while also relieving the pilot of his lead generation task in attitude. A rate gyro gain of two was used to split the rigid body integration pole pair at the origin into a real pole at  $-M_{\delta}K_{\theta}$  and one at the origin. The pilot, acting as a gain only (which earns favorable opinions), closes the loop to drive the poles together to form a dominant pair at  $\zeta = 0.4$ ,  $\omega_N = 2$ . This is considerably in excess of that achievable with hardwire or kinesthetic control. It is interesting to note that system bandwidth is basically set by the pilot's neuromuscular pole,  $-1/T_N$ , and his transport delay. Figure 2-26 shows these effects in the attitude loop closure root locus. The rate gyro/airframe pole is also seen to interact with the Padé pole at  $-6.7$  to form a second highly damped pole pair. The path closure is shown in Figure 2-27. As before, the right and left half plane path reversal zeros interact with the pilot's transport delays to yield a conditionally stable system. The closed-loop system dominant roots lie at slightly below one radian per second. In order to gain this bandwidth, the pilot is forced to generate a translation lead zero at  $-1/2$ , which degrades the basic Cooper rating by one point, as before. Thus, it is estimated that using a rate-damped path maneuvering mode, the vehicle would be rated 4. However, if landing is performed by leaving the system in attitude hold and controlling sink rate with throttle, the Cooper rating will improve to 3, or "acceptable."

Conclusions for the Stability Augmented Control Mode. The convenience and performance capabilities of the stability-augmented system will yield acceptable ratings from pilots. Thus the system is acceptable from a handling qualities standpoint for LFV. Use of stability augmentation should reduce the scope and intensity of the LFV flight training program from that required for a hardwire or a kinesthetic system. This savings in effort and cost deduct from the basic system costs.

### Simulation Studies

#### Visual Simulator

The visual simulation was conducted at the Los Angeles Division of NR using the hover and transition simulator (HOTRAN) facility. The HOTRAN consisted of a transparent scene, capable of motion in six degrees of freedom, which was illuminated by a point light source. The scene was projected on a spherical screen 12 feet in radius. Located near the center of the screen, the pilot's eyes viewed from 25 degrees above the horizon to 65 degrees below and 100 degrees of azimuth on each side. Near the pilot's feet, the peripheral view was especially important. The pilot stood on a platform which was mounted on a hydraulically supported base gimballed for small motions in pitch and roll. When operating, the motion base rotated to give the pilot motion cues without rotating through large angles.

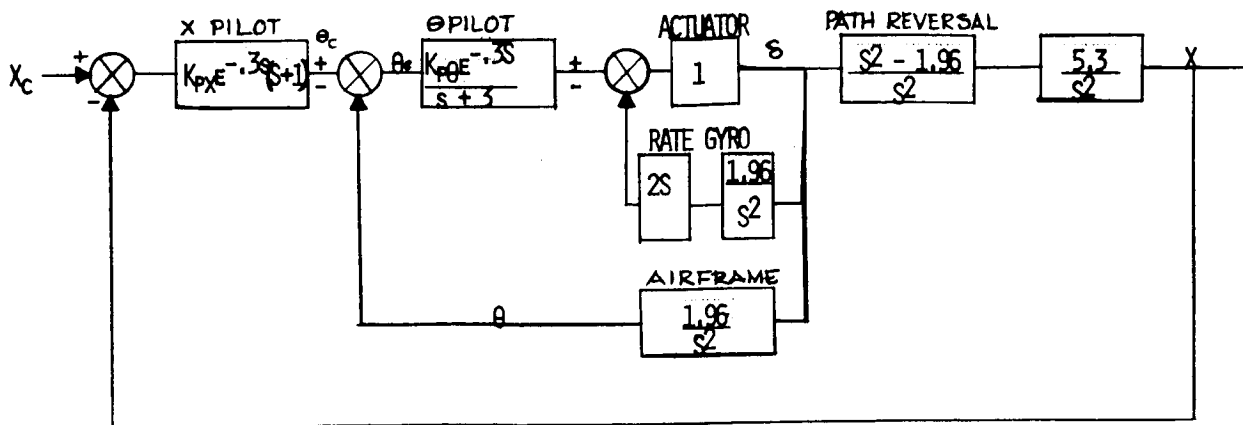


Figure 2-25. Stability-Augmented LFV Block Diagram

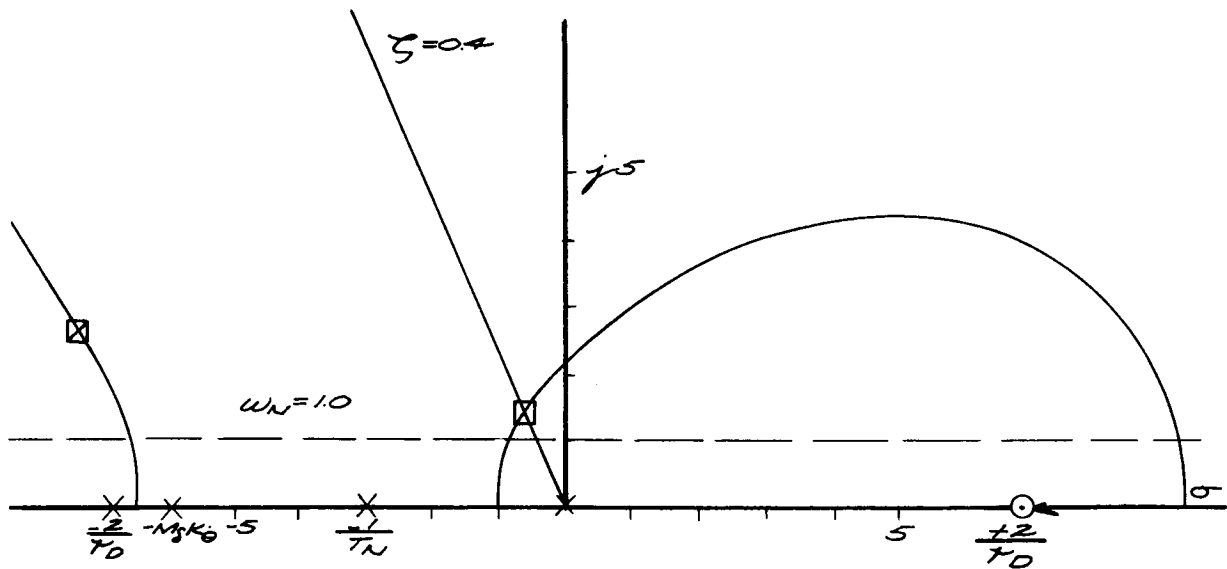


Figure 2-26. Attitude-Loop Root Locus for LFV Stability Augmentation System

**"Page missing from available version"**

**"Page missing from available version"**

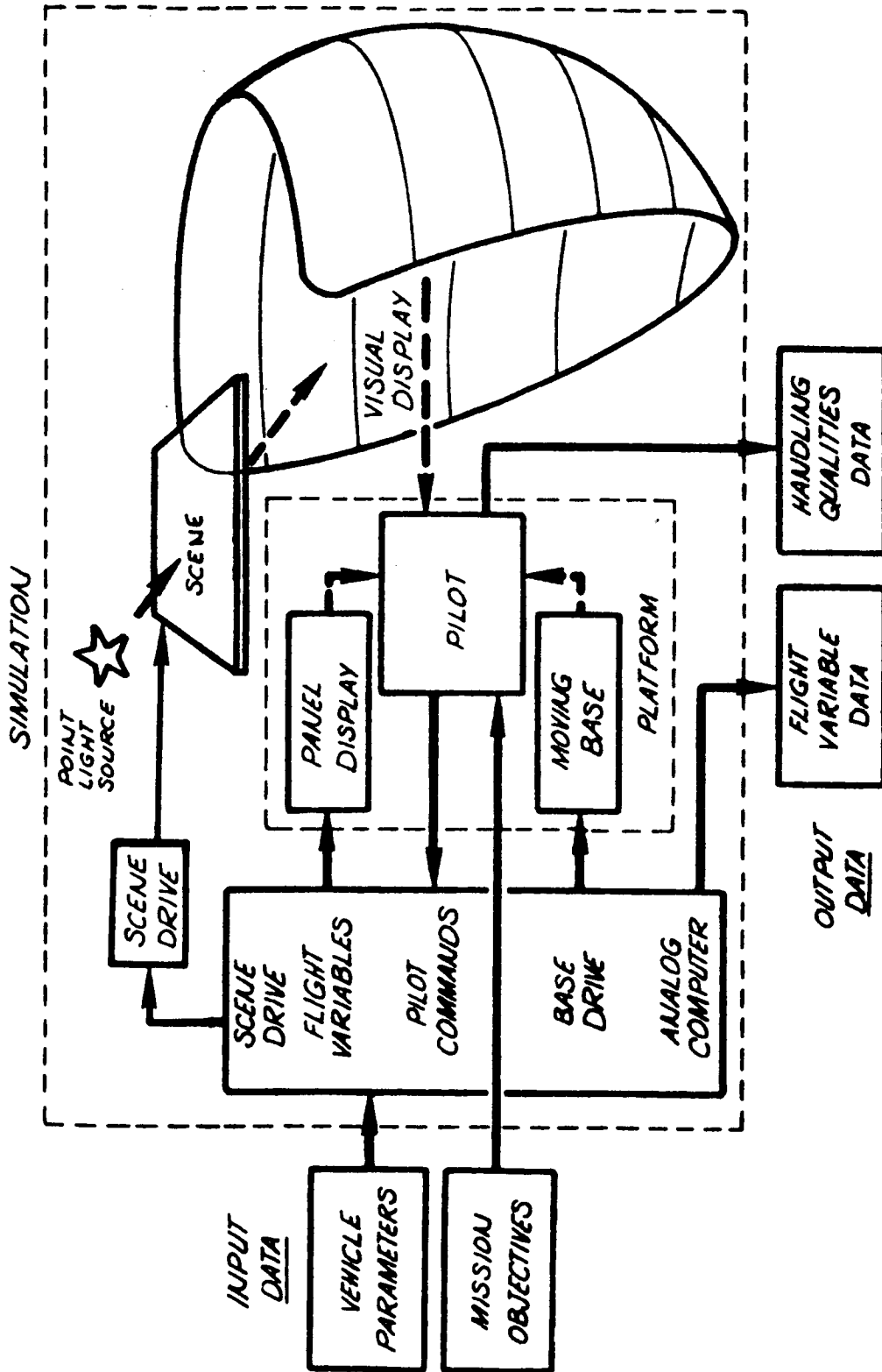
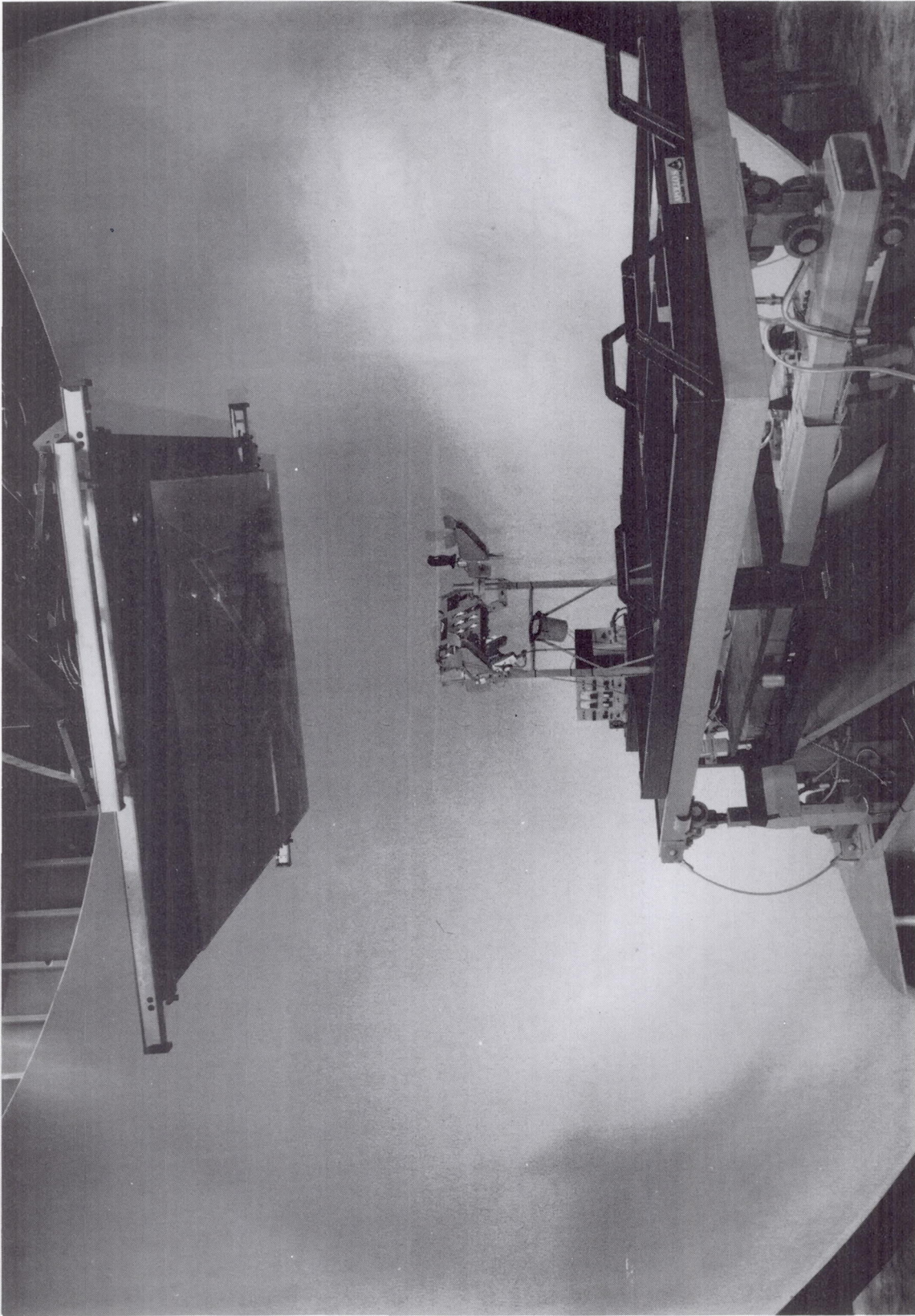


Figure 2-28. Visual Simulator Functional Flow Diagram



7279-851-1A

Figure 2-29. HOTRAN Simulation Facility

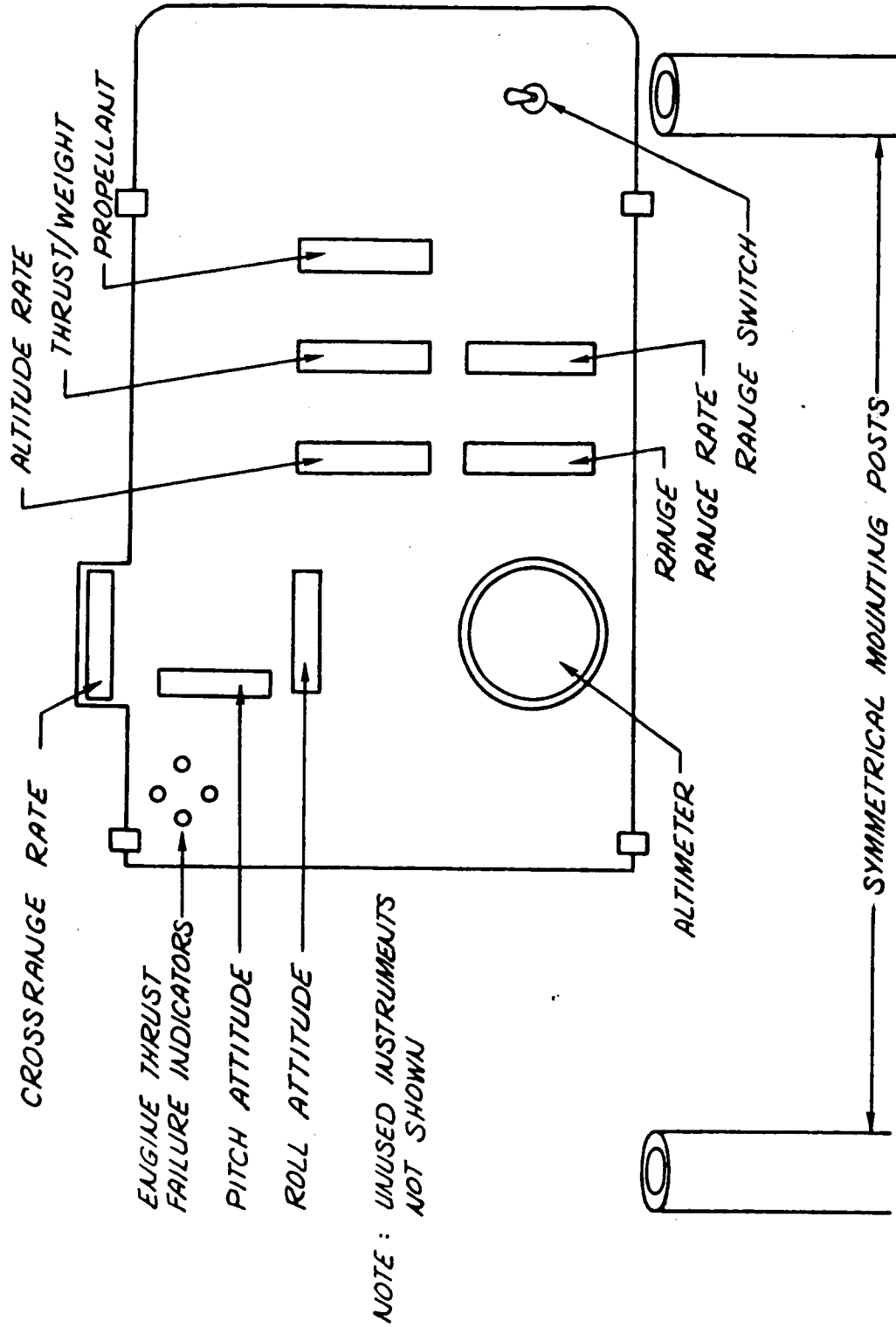


Figure 2-30 • Simulator Display Panel



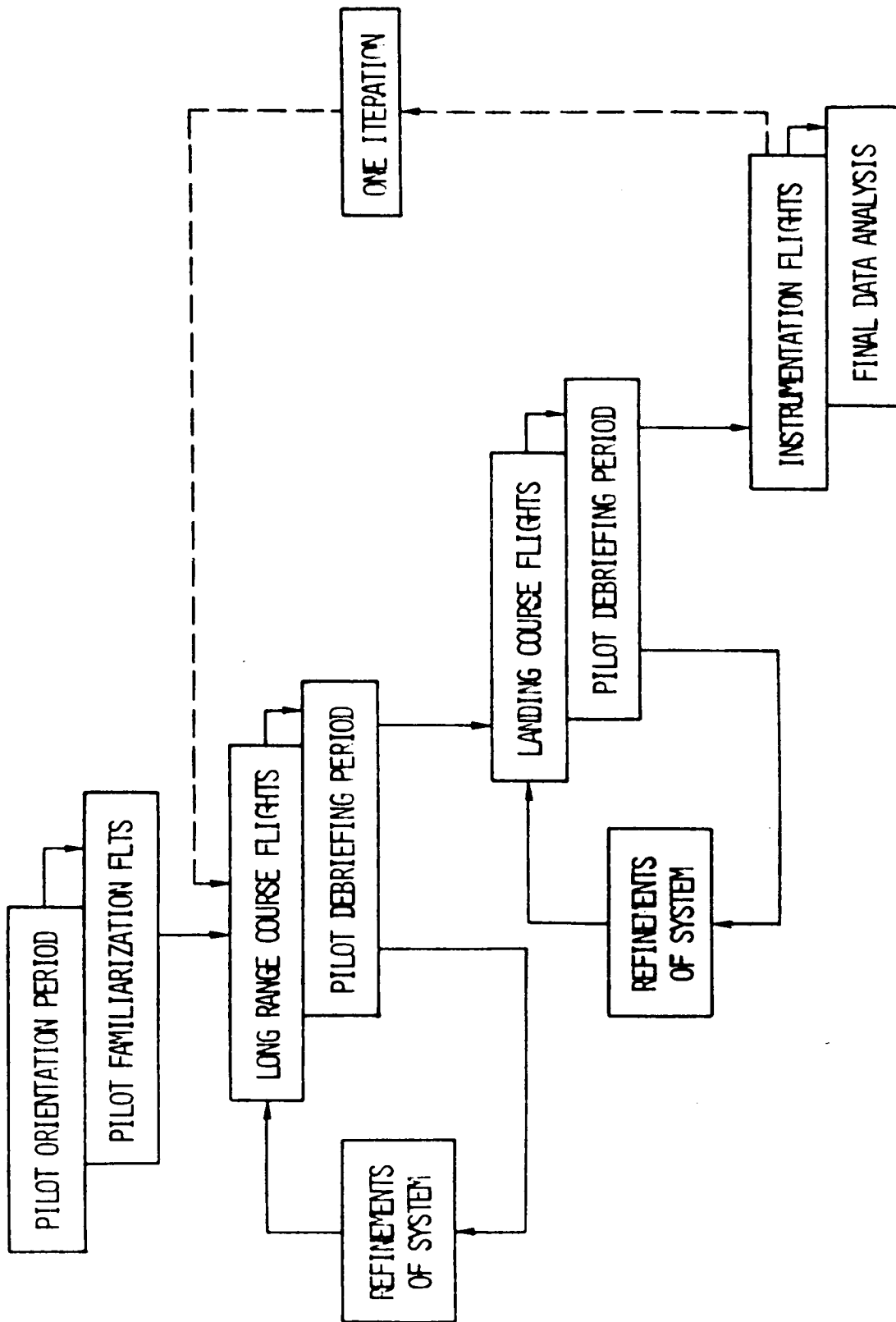


Figure 2-31. Visual Simulation Approach

Table 2-4. Summary of Visual Simulation

<p>6-Degrees-of-Freedom</p> <p>Man-In-Loop Interfacing With Mathematical Model of Vehicle on Moon</p>	<p>Control concepts include:</p> <ul style="list-style-type: none"> <li>- Kinesthetic control</li> <li>- Hardwire hand control (gimbal above or below center of gravity)</li> <li>- Hardwire with mechanical shaping network</li> <li>- Hardwire hand control (translating engines)</li> <li>- Hardwire gimbal at center of gravity (stabilized platform)</li> <li>- Stability augmented angular control</li> </ul>
<p>Output data include:</p> <ul style="list-style-type: none"> <li>- 31 strip chart channels</li> <li>- Flight log</li> <li>- Pilot opinion ratings</li> </ul>	<p>Operating tasks include:</p> <ul style="list-style-type: none"> <li>- Fly long-range course (7.67 miles)</li> <li>- Precision landing</li> </ul>
<p>Objective</p> <ul style="list-style-type: none"> <li>- To determine feasibility of control concepts</li> </ul>	



The pilots also attempted to land on target, but the visual cues were not proper with the long-range course scaling. A summary of information on the long-range course is given in Table 2-5.

As an example of long-range course runs, traces of kinesthetic, hardwire, and stability augmented flight are presented in Figure 2-32. Only pitch attitude and downrange velocity variables are shown. The wavy oscillations of both the kinesthetic and the hardwire attitude traces are indicative of the pilot workload to maintain stabilization. Greater controllability, an inherent factor in the stability augmentation system, allowed the pilot to reach a larger horizontal velocity than with the other systems and thus to complete the mission sooner. These comments, and others, are summarized in Table 2-6.

A complete summary of control configurations is graphically portrayed in Figure 2-33. The abscissa shows a performance rating based on observer decisions as to whether a flight was or was not well controlled. These numbers are divided by the total number of flights attempted using each control configuration. The ordinate shows the controllability decision given by the pilot using the standard pilot opinion rating system.

The landing course represented a special scaling to provide the pilot with visual cues at altitudes down to as low as 6 feet. Landing runs were begun from 400 to 1200 feet away from the target and 100 feet above. It was left to the pilot to determine the compromise between the time duration of the landing operation, the landing accuracy, and the inclination and velocity of the vehicle at touchdown. Frequently, large amounts of propellant were expended to position the vehicle near target and set it down within the structural bounds on translational velocities and rotational angles and rates. FIGURE 2-34 shows a pictorial representation of the compromise problem.

Analog computer strip chart recording of hardwire and stability-augmented landings are presented in Figure 2-35. Pitch attitude, horizontal velocity, and altitude variable are shown. The difference between the pilot workloads for the two control methods is more pronounced for landing than it was for the long-range flight task. Other comments are given in Table 2-7. A graphical performance presentation is shown in Figure 2-36. Kinesthetic landings were not attempted. Hardwire control performance and opinion rating are degraded for landing. A new configuration using hardwire control of engines gimballed at the total center of gravity and a stabilized platform is shown to be competitive with stability-augmented control.

Summary. A general statement may be made about controlling the LFV by the methods studied: The greater the amount of concentration required for stability, the less feasible the method. If the pilot is required

Table 2-5. Long-Range Course

Task	To fly 7.67 miles down a straight runway
Flight Phases	Launch, ascent, pitchover, boost, level, cruise, pitchback, deboost, descend
Difficult aspects of flight	
Timing for end of boost	Used range meter, range rate, Visual scene cues
Timing for end of deboost	Visual scene cues
Engine thrust failure control	Trimmed with hand controls and pilot position.
Throttle control throughout level flight	Used T/W, Z, and Z meters
Flight data	
	22 flight variables charted - 3 attitudes, 3 translations, 6 rates kin, inputs (2 axis), 3 gimbal angles thrust, prop. wt. pilot workload (3)
	Pilot comments
	Flight log

- KINESTHETIC INPUTS IN ALL RUNS

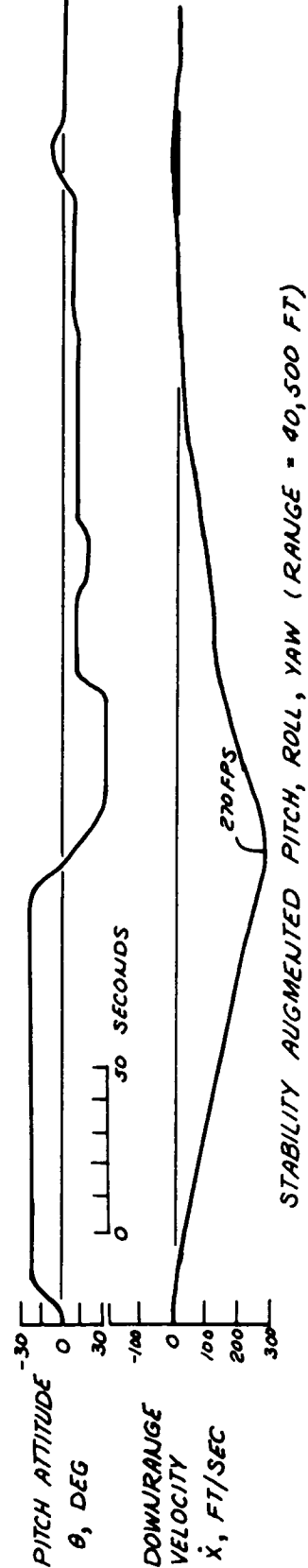
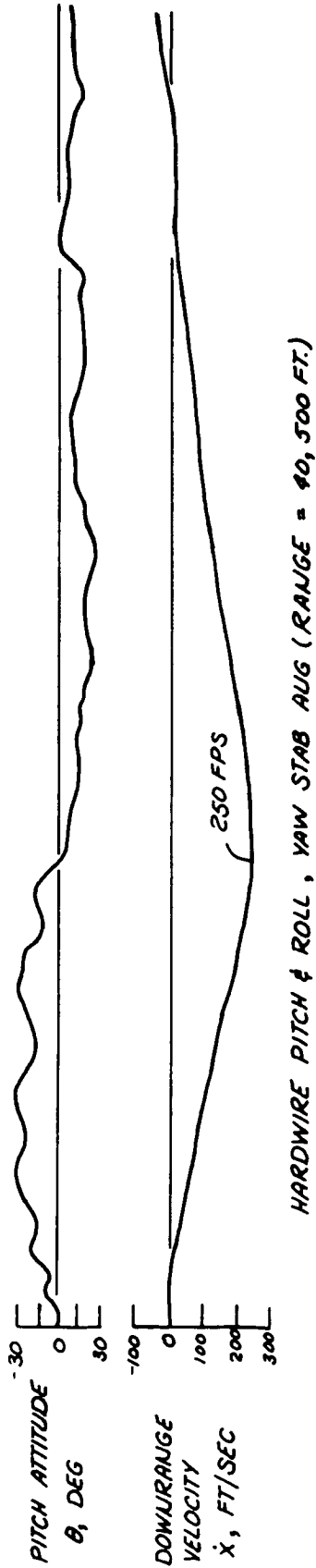
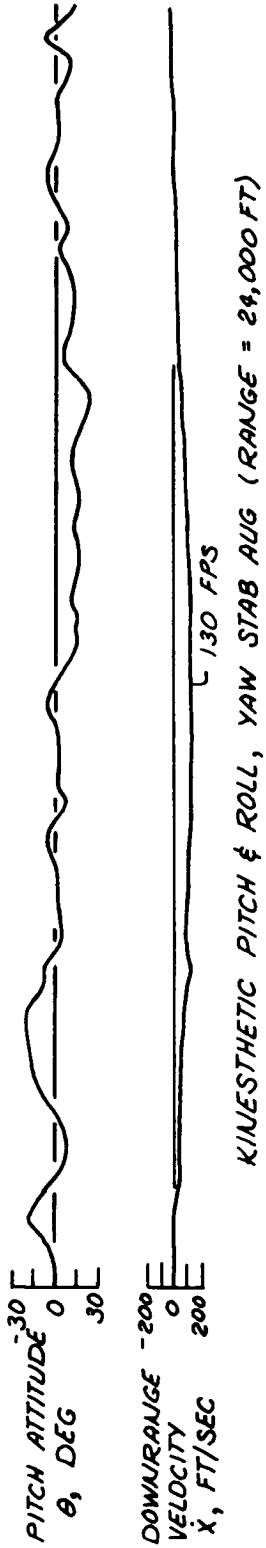


Figure 2-32. Comparison of Simulator Recordings for Three Control Modes



Table 2-6. Long-Range Course Data

Pitch Attitude Comparison
Kinesthetic and Hardwire Control
<ul style="list-style-type: none"><li>● Pilot has difficulty maintaining attitude hold, especially during boost</li><li>● Precise descent not feasible</li></ul>
Stability Augmentation
<ul style="list-style-type: none"><li>● Pilot relieved from attitude maintenance task can concentrate on precise maneuvers</li><li>● Precise descent difficult</li></ul>
Horizontal Velocity Comparison
Kinesthetic and Hardwire
<ul style="list-style-type: none"><li>● Non-precision boost prevents large velocities</li><li>● Difficult to zero velocity over target</li></ul>
Stability Augmentation
<ul style="list-style-type: none"><li>● Large velocities easily controlled</li><li>● Difficult to zero velocity over target</li></ul>



- NOTES:
1. 1969 VISUAL SIMULATOR DATA
  2. KINESTHETIC DISTURBANCES IN ALL DATA
  3.  $\Delta$  = TOTAL NUMBER OF APPLICABLE FLIGHTS, AND CONTAINS COMPLETE LEARNING CURVE

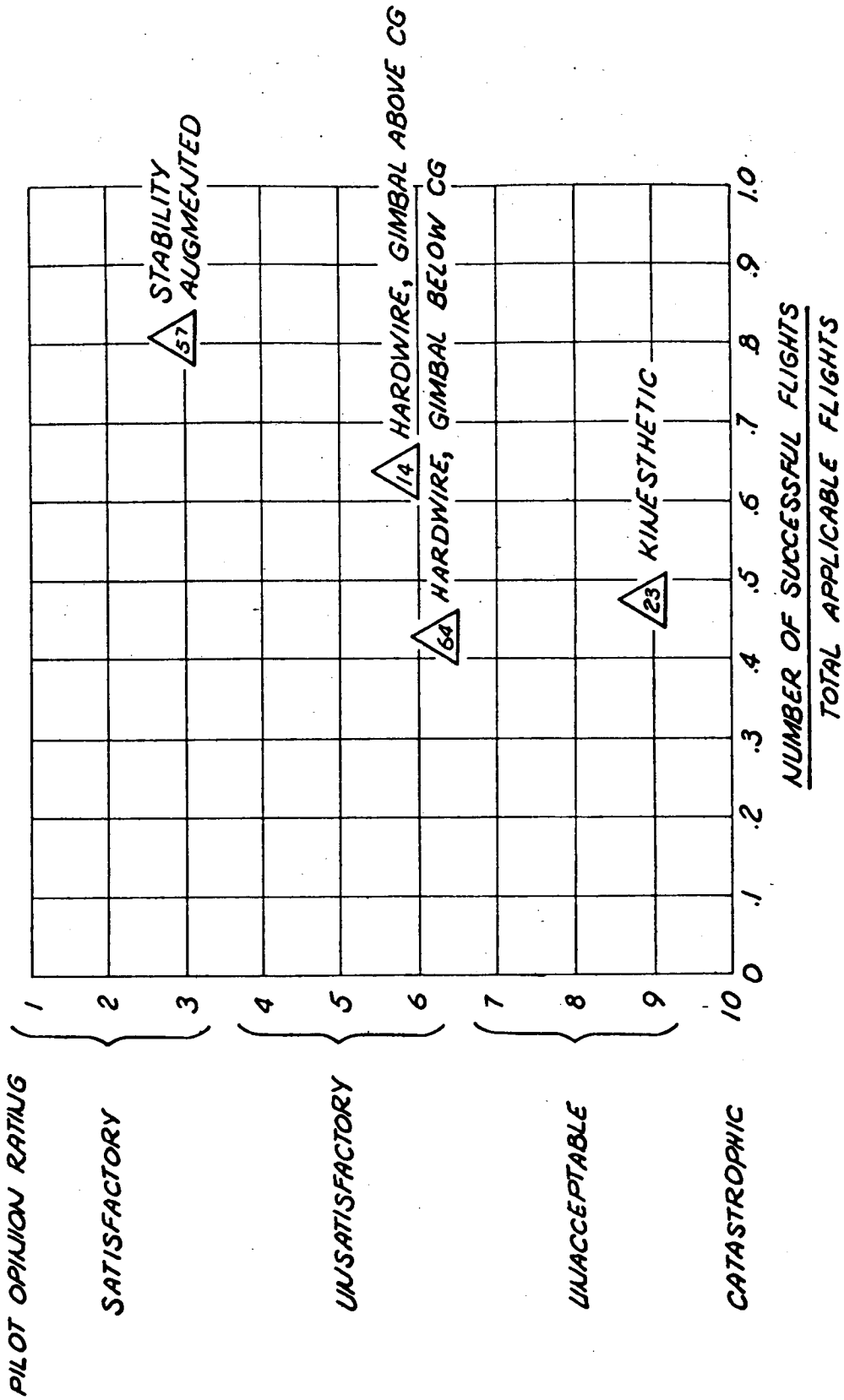


Figure 2-33. Status of Control Configurations Based on Long-Range Course

TASK

TO FLY FROM I.C.'S TO TARGET

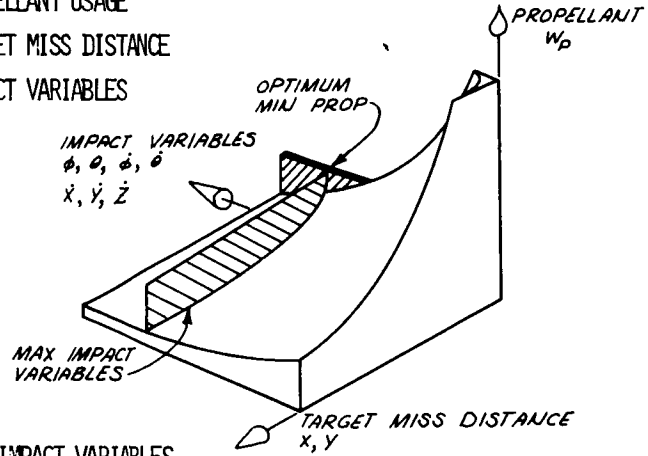
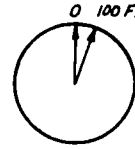
400-TO 1200-FT RANGE, 100-FT ALTITUDE

DIFFICULT ASPECTS OF LANDING

ALTIMETER NOT SENSITIVE TO SMALL ALTITUDE CHANGES

PILOT MUST CHOOSE COMPROMISE BETWEEN LANDING WITH

- MINIMUM PROPELLANT USAGE
- MINIMUM TARGET MISS DISTANCE
- MINIMUM IMPACT VARIABLES



FLIGHT DATA

SAME AS LONG RANGE COURSE + IMPACT VARIABLES

Figure 2-34 . Landing Course

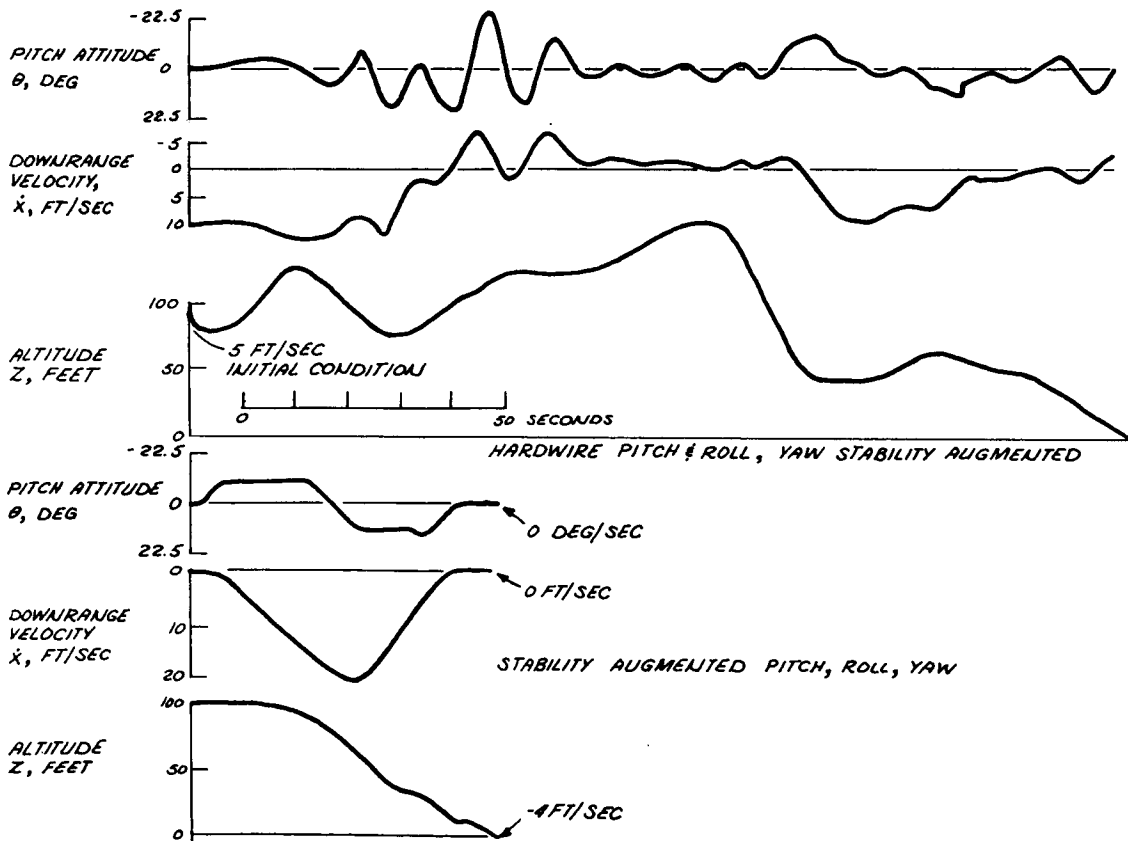


Figure 2-35. Comparison of Simulator Recordings for Two Control Modes





Table 2-7. Landing Data

<p>Pitch Attitude Comparison</p> <p>Hardware Control</p> <ul style="list-style-type: none"><li>- Pilot has difficulty maintaining attitude hold</li><li>- Large touchdown pitch rate</li></ul> <p>Stability Augmentation</p> <ul style="list-style-type: none"><li>- Attitude under complete control</li></ul>
<p>Horizontal Velocity Comparison</p> <p>Hardware Control</p> <ul style="list-style-type: none"><li>- Attitude instability prolongs landing task</li><li>- Difficult to zero velocity at touchdown</li></ul> <p>Stability Augmentation</p> <ul style="list-style-type: none"><li>- Precise boost and deboost profile possible</li></ul>
<p>Altitude Comparison</p> <p>Hardware Control</p> <ul style="list-style-type: none"><li>- Attitude maintenance task prevents precise altitude control</li></ul> <p>Stability Augmentation</p> <ul style="list-style-type: none"><li>- Perfect landing possible even with hardware throttle</li></ul>

- NOTES : 1. 1969 VISUAL SIMULATOR DATA  
 2. KINESTHETIC DISTURBANCES IN ALL DATA.  
 3.  $\Delta$  = TOTAL NUMBER OF APPLICABLE FLIGHTS, AND CONTAINS COMPLETE LEARNING CURVE

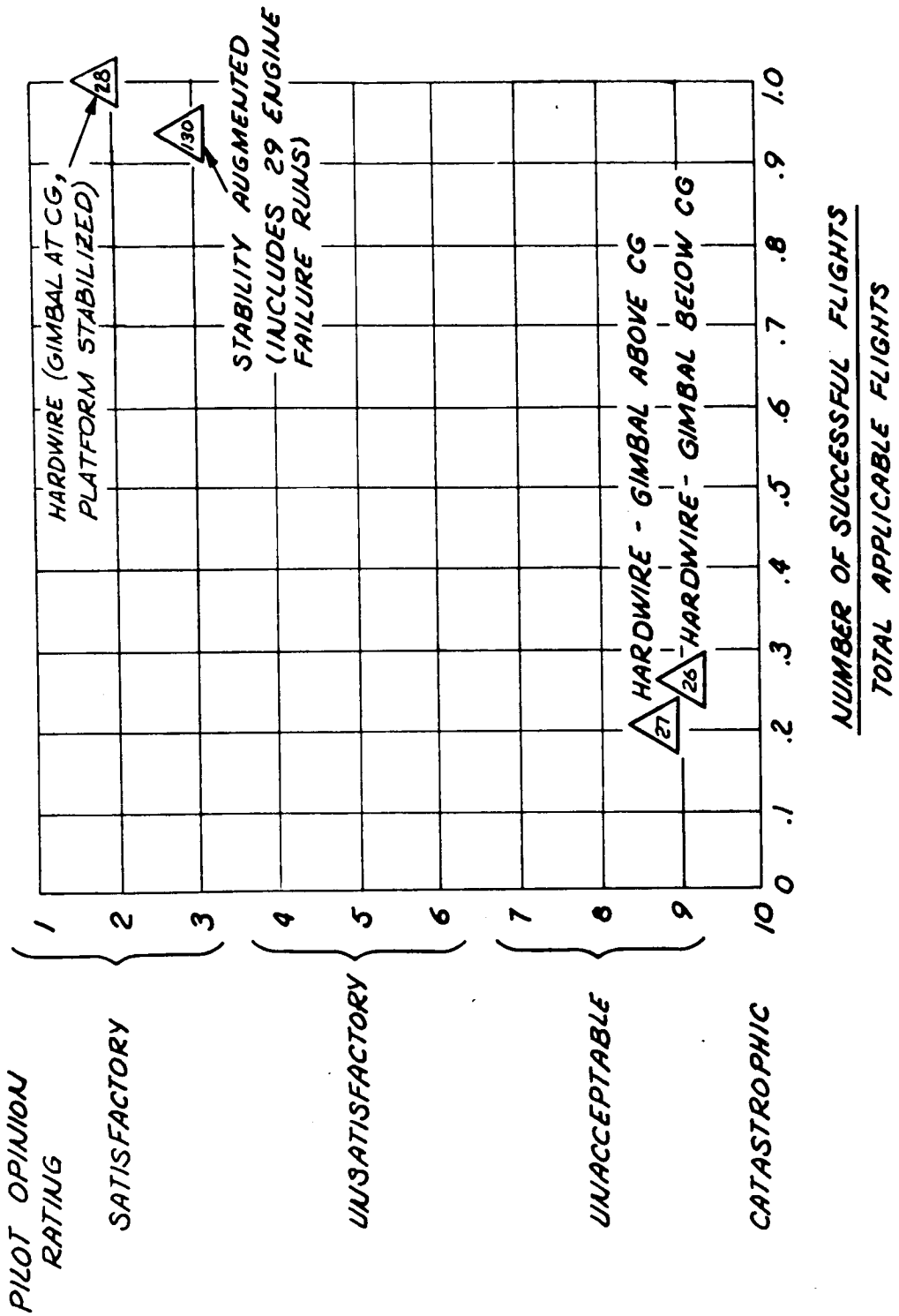


Figure 2-36. Status of Control Configurations Based on Landing Course

to spend all his time maintaining the desired vehicle attitude, he cannot navigate. All the control methods required greater concentration for stability than such standard transportation devices as automobiles, boats, and airplanes. Each of the standard devices, however, rely on inherent damping characteristics for much of their stability. Lacking a simple and natural means of providing the stability, other approaches must be taken.

Recognizing that the kinesthetic and hardwire methods of control have no inherent damping, but are the simplest conceivable configurations, they were used as a basis for more complicated, but stable, vehicles. From a servomechanisms standpoint, the straightforward solution was to synthesize a compensation network to be inserted between the rotational controller and the engine gimbals. Networks of varying complexity were studied, all with the objective of increasing system damping. All the networks, however, required large amounts of gain to enable the pilot to counteract disturbances. With the necessary levels of gain, the system reacted much like ordinary hardwire control, and the advantages of the network were lost.

Another attempt to lessen the pilot's stability task, and thus his workload, came with the study of overhead engine gimbals. By changing the gimbals from below the total vehicle center of gravity to above, the horizontal force component from a gimballed engine produces horizontal velocity in the desired direction. If the pilot desires to translate in a certain direction, he must first tilt the vehicle in that direction to aim the thrust vector. With gimbals below the center of gravity, the tilting moment involves engine deflections which initially reverse the direction of translation. Gimbals above the center of gravity produce an initial translation in the desired direction; however, flights with gimbals above showed a negligible increase in stability. Further study using translating engines which produced no initial vehicle translation in either direction was conducted. This attempt also revealed no appreciable increase in stability over the basic hardwire method of control.

The stability-augmented system utilized feedback signals from rate gyros in three axes to provide rate command capability for the pilot. Attitude hold is accomplished by an integrated rate feedback for zero rate command. The total effect of the system is to give the pilot more time to interpret visual and display cues, and to make decisions. The control method greatly decreased the concentration required for stability and thus increased the pilot's capability for precise navigation.

A final type of control, using an automatically stabilized platform, was studied. The vehicle configuration involved hardwire-controlled

engine gimbals at the vehicle center of gravity. Thus, gimbaling did not torque the vehicle. A separate reaction control system, driven by an undefined stabilizing system, kept the platform level. The vertical thrust component was automatically compensated for gimbale angle. The control method proved to be slightly better than the stability augmented system, principally due to the lack of tilting motions which require interpretation by the pilot.

Although the latter two systems represent a rather large departure from the kinesthetic and hardware concepts, the results of the study show that this departure is necessary for adequate inherent stability.

The control methods discussed in this section may be compared from another viewpoint. With the kinesthetic and hardware control methods, the pilot has only angular acceleration at his disposal, yet he must use it to produce a translation in order to reach his destination. The procedure involves a prediction, on the part of the pilot, as to the propagated results of each of his commands. As seen in Figure 2-37, his predictions are necessary to control a variable which is four integrations removed. The task is difficult at best, but is greatly magnified if it must be simultaneously carried out in three axes. With the use of a shaping network, the task was slightly simplified by eliminating one of the integrals part of the time. The stability augmentation system completely eliminates one of the integrals for commands, and eliminates one more for stability. With the control method involving a stabilized platform and hardware control to engines gimbaled at the center of gravity, only two integrals remain — a system comparable to driving an automobile.

A hardware throttle control proved difficult to operate when most of the pilot's attention was required for attitude stability. Typically, a flight includes a nearly sinusoidal altitude time history, with a frequency of one-half the pilot's instrument scan frequency. The pilot manipulates the throttle to check an ascending rate and then returns his attention to other aspects of flight. Later, he again manipulates the throttle to check the descending rate resulting from the previous correction.

The first attempt to correct the problem resulted in the development of the thrust-to-weight ratio tracker. Assuming that the throttle is initially adjusted correctly, the tracker will automatically change the throttle setting as propellant is used, thereby relieving the pilot of the task. The tracker, while nullifying a source of long-term error, did nothing to alleviate the original problem; hence it was unsuccessful.

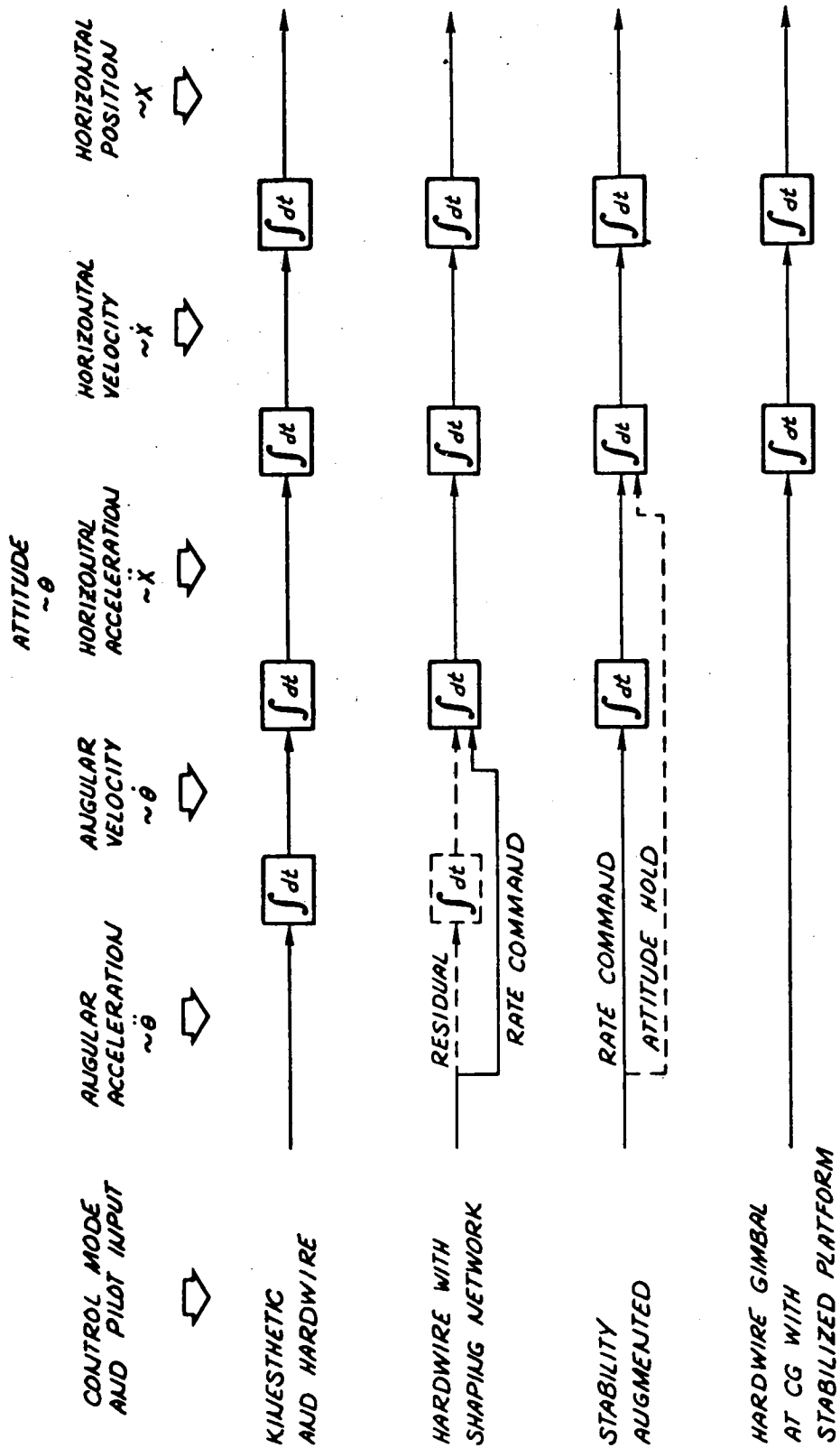


Figure 2-37. Comparison of Prediction Tasks for Various Control Methods

The only other attempt to improve the throttle control method resulted in a shaping network. Theoretically, the throttle would consist of two segments: a hardwire segment for gross corrections and a network to provide vernier control. Time and funding did not permit its full implementation; however, the network portion was mechanized for use during landing. The network provided all the throttle range necessary during this phase of flight, unless engine thrust failure occurred. An insufficient number of runs using the throttle network were obtained to allow a statistical evaluation, but pilot comments indicate the network greatly improves altitude control.

Conclusions. The general conclusion from the study is that small, manned propulsion devices are feasible from the standpoints of stability, control, and flight performance. Further development of control methods must be undertaken, however, prior to establishing the optimum system. The following paragraphs in this section discuss detailed conclusions. These conclusions are summarized in Table 2-8.

Based on the pilot opinion rating and success ratio data contained in the report, the kinesthetic control mode and all versions of the hardwire control mode are unacceptable. The methods using stability-augmented and hardwire gimbal control with stabilized platform are satisfactory. Ratings for the system potentially could be improved if

- a. Improved throttle characteristics are implemented
- b. A method could be devised to simplify the landing task: specifically, to minimize landing impact variables and translational position errors without large expenditures of propellant

The simulation results showed that a vast improvement in flight performance and control is possible over a short training period. These characteristics do not, however, closely approach the theoretical optimum. Trained pilots still required approximately 33 percent more propellant to complete a long-range flight than that required by the theoretical optimum.

With the conditions studied, the pilot is fully capable of recovery from an engine thrust failure. The conditions are summarized as follows:

- a. Stability augmented control
- b. Standing pilot who is sufficiently unrestrained to change platform position to retrim engines
- c. Visual display of failed engine location

Table 2-8. Visual Simulation Conclusions

- Hardwire and kinesthetic control modes are unacceptable
- Stability augmented and stable platform with gimbal at center of gravity are satisfactory control modes but with mildly unpleasant characteristics
  - Hardwire throttle requires excessive attention
  - Horizontal landing translational position errors difficult to null
- Landing impact structural limits may be met consistently at the cost of excess propellant and positional errors
- Vehicle control learning curves indicate vast improvement during short training periods
- Engine thrust loss can be adequately controlled by pilot using stabilized control modes
- Average simulator flight requires one-third more round trip propellant than an optimum trajectory
- In order of importance, most necessary pilot display variables are:
  - Thrust-to-weight
  - Propellant remaining
  - Engine failure indication

Based on pilot comments, the required panel displays for safe flight are thrust-to-weight ratios, propellant remaining, and thrust-failure indication. Additional displays, as listed in Table 2-9, are necessary for maximum performance.

Recommendations. With confidence that the visual simulation conditions were sufficiently near to physical reality to use as a basis for control method recommendation, the choice is the stability augmentation system. All hardwire and kinesthetic methods have proved to be overly difficult to control. The complexity of the system using hardwire gimbals at the center of gravity and stabilized platform is felt to be unnecessary; however, it is recommended as an alternate choice. The stability-augmented and stable platform control methods may require more equipment redundancy than kinesthetic or hardwire methods to reach the same hardware reliability; however, the reliability of the pilot, in a sense, has been improved with the recommended control methods.

Sufficient data were generated during the study to show that the hardwire throttle was not desirable but not enough data were generated to define an improved throttle control method. Future effort on this area should include throttle control investigations.

#### Tethered Flight Vehicle

The tethered flight vehicle was designed by the Research, Engineering, and Test Division at the Space Division and was fabricated and tested by the Laboratory and Test Department, also of the Space Division. As part of a continuing series of studies directed toward small manned propulsion devices, the tethered flight vehicle program represents an advancement in the state of the art and drew upon technology from the previous studies.

In an effort to establish an upper bound on controllable moment of inertia, the most recent flight vehicle program was initiated involving the tethered flight vehicle discussed in this section. The vehicle extends the moment-of-inertia range of the total airborne system to approximately 600 slug-feet squared.

The purpose was to investigate the influence of moment of inertia, as a parameter, on two types of acceleration systems: kinesthetic and hardwire. The kinesthetic configuration was essentially the same as that studied with the one-man propulsion device in 1968 - the pilot standing and the total system center of gravity located about the lower part of the pilot's body. Hardwire control, also with the pilot standing, used a gimballed engine located below the total system center of gravity and operated in pitch and roll by a two-axis rotational controller.



Table 2-9. Onboard Display Requirements Based on Pilot Preference

<ul style="list-style-type: none"> <li>• Visual simulation and tethered flight vehicle experience</li> <li>• Stability augmentation with attitude hold</li> </ul>			
Category	Pilot A	Ranking Pilot B	Pilot C
<b>Mandatory for safe flight:</b> <ul style="list-style-type: none"> <li>• Short Range</li> <li>• Low Altitude</li> <li>• Low Velocity</li> </ul>	T/W $W_p$ Fail Ind	T/W Fail Ind $W_p$	T/W $W_p$ Fail Ind
<b>Desirable:</b> <ul style="list-style-type: none"> <li>• Mandatory for maximum performance</li> <li>• 45-degree pitch angle</li> <li>• 8-mile range level flight</li> <li>• 10-percent fuel reserve</li> </ul>	$\dot{Z}$ $\theta$ $\dot{X}$ $\phi$ X Z $\dot{Y}$	$\dot{Z}$ $\theta$ $\dot{X}$ X Z $\phi$ $\dot{Y}$	$\theta$ $\dot{Z}$ $\dot{X}$ X Z $\phi$ $\dot{Y}$
Unnecessary	$\dot{\theta}$ $\dot{\phi}$ $\dot{\psi}$ $\psi$ Y	$\dot{\theta}$ $\dot{\phi}$ $\dot{\psi}$ $\psi$ Y	$\dot{\theta}$ $\dot{\phi}$ $\dot{\psi}$ $\psi$ Y

Before conducting the tests, it was expected that radical changes in controllability would be seen as moment of inertia was increased. The tests proved this to be true.

Figure 2-38 shows the major features of the vehicle structure. The booms shown could carry weights up to 15 pounds each, at which the equivalent moment of inertia was approximately 500 slug-feet squared above the bare vehicle and pilot, or 604 slug-feet squared total.

Initial tests employed an engine position two inches below the pilot's feet. Later, because of adverse translation effects with engine gimbaling, the engine was lowered to the base of the vehicle. Figure 2-38 shows details of the engine in its lower position. The throttle and two-axis rotational controller details are also shown.

Up to the time the tethered vehicle was designed and tested, the Space Division had not investigated in actual flight the full range of possible control sensitivities using the kinesthetic control method. Neither had it flown a gimballed engine system. The vehicle was thus developed to fill a gap in our knowledge of handling qualities over the complete spectrum of sensitivities. Very little information was available at the onset to indicate how far in moment of inertia it was necessary to go in order to obtain the complete picture; the maximum of 604 slug-feet squared was felt to be sufficient, however.

The major objective of the program, therefore, was to determine the stability bounds over the inertia range capability of the vehicle. The bounds were to be determined by use of a hovering task. A second objective was to determine the probable values of flight variables during landing for comparison to the data obtained from the visual simulation. A comparison of sorts for the second objective was derived from the tests in that the pilot was not able to hold the vehicle in most cases within the limits of the the tethers over an adequate period of time. This result could have been predicted from visual simulation data had it been available earlier.

A brief summary of the tethered flight vehicle is given in Table 2-10. In addition to the data presented in the table, motion pictures were taken of many of the flights.

**Design Procedure.** A large number of changes have been made to the tethered flight vehicle since the basic production drawings have been completed. The drawings do, however, give a general idea of the configuration. The most recent sketch showing major dimensions appears in FIGURE 2-39. Supports and constraints are shown schematically in FIGURE 2-40.



Figure 2-38. Bottom View of the Tethered Flight Vehicle

Table 2-10. Tethered Flight Vehicle

5-degrees-of-freedom: 3 translation, pitch and roll rotation

Parametric moment of inertia investigation from 100 to 600 slug-ft<sup>2</sup>

Pitch and roll control torques by

- Kinesthetic inputs, or
- Hardwire hand control

Output data include:

- Pilot opinion ratings
- Pitch and roll rate and attitude time histories
- Pitch and roll hand control deflection time histories

Objectives

- To determine stability bounds parametric in moment of inertia
- To determine probable flight variables at landing

From weights analysis conducted on the tethered flight vehicle, detailed subsystem lists were prepared which include pilot, vehicle structure, controls, propulsion, and the effect of tethers, gas lines, and supports. Summary data from the analysis are presented in TABLE 2-11.

Additional mass properties data, dealing with center of gravity position, are shown in FIGURE 2-41. As is seen in the figure, very little change in center of gravity position results when weights are added to increase the total moment of inertia. The two positions of the engine are shown on the accompanying vehicle profile sketch for reference.

The total capability of investigation may be understood by referring to FIGURE 2-42 where a complete picture of the moment of inertia range is given, from the bare vehicle to the configuration resulting when booms and weights are added. Weight variations at nearly constant moment of inertia are possible if the weights are added at the boom roots. Large increases in moment of inertia result when the weights are added to the boom tips.

For reference, the moment of inertia values of the one-man propulsion device flown in 1968 are also presented in FIGURE 2-42. The highest value of inertia for that vehicle is larger than the lowest tethered flight vehicle inertia, providing a continuous and overlapping region. Also shown on the figure is the inertia range of the visual simulation mathematical model as translated to Earth conditions.

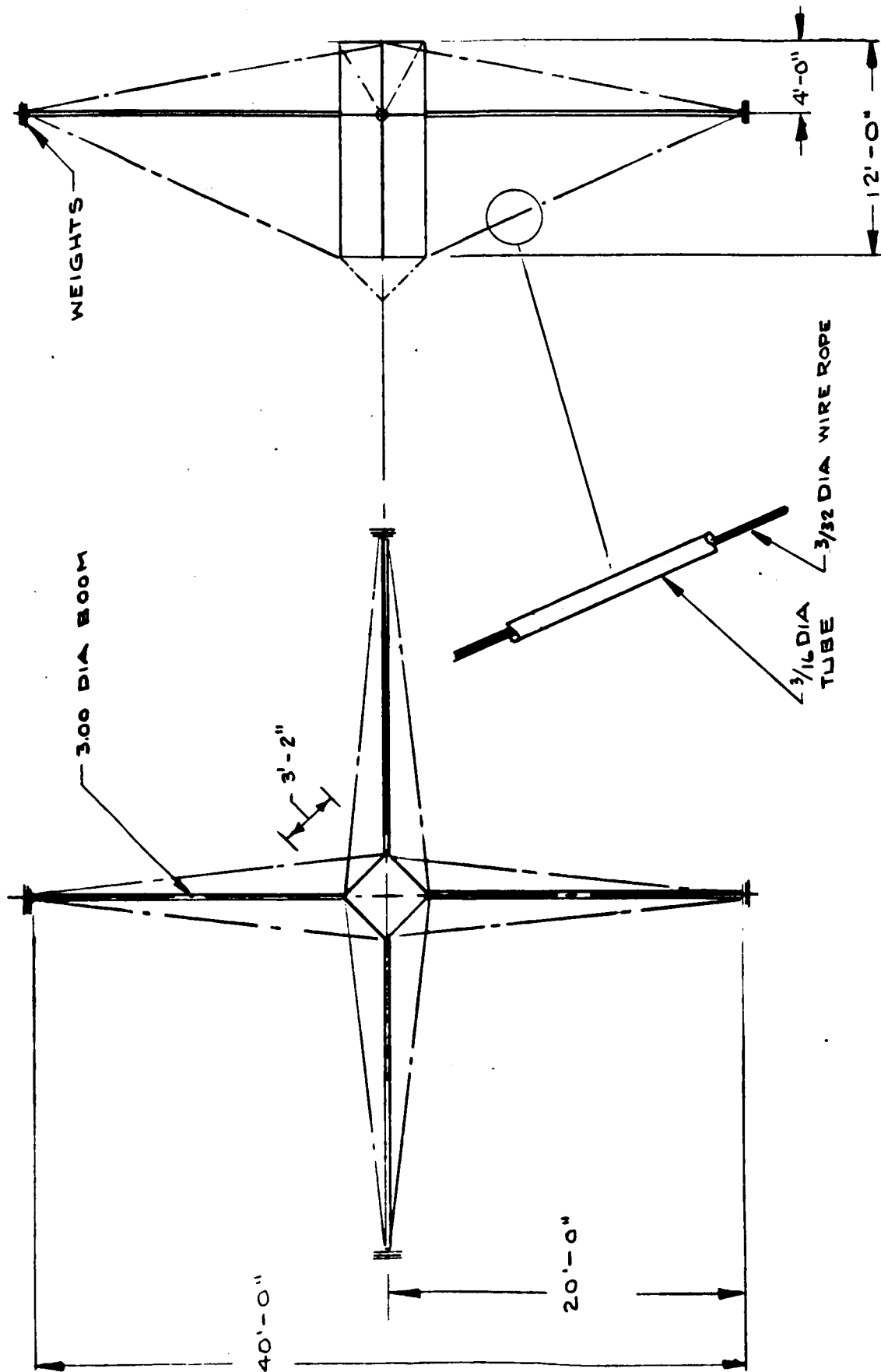


Figure 2-39. Tethered Flight Vehicle

Operational Procedure. The vehicle was supported prior to each flight by a tether attached to a 110-foot-high crane. From the vehicle, extending upward for 38 feet, the tether was composed of nylon for shock absorption. At the end of the nylon section a mechanical shock absorber was inserted to provide additional safety to the pilot. Above the shock absorber, a 400-pound weight held the crane cable taut.

To limit the vehicle range to the available space, another tether was added. Attached to the bottom of the vehicle, the second tether extended to the ground where it was held by another weight. The limits of the two tethers provided a saucer-shaped volume, 10 feet in altitude and 32 feet in range, within which the vehicle could fly unrestrained. Details of the tethers are shown in FIGURE 2-40.

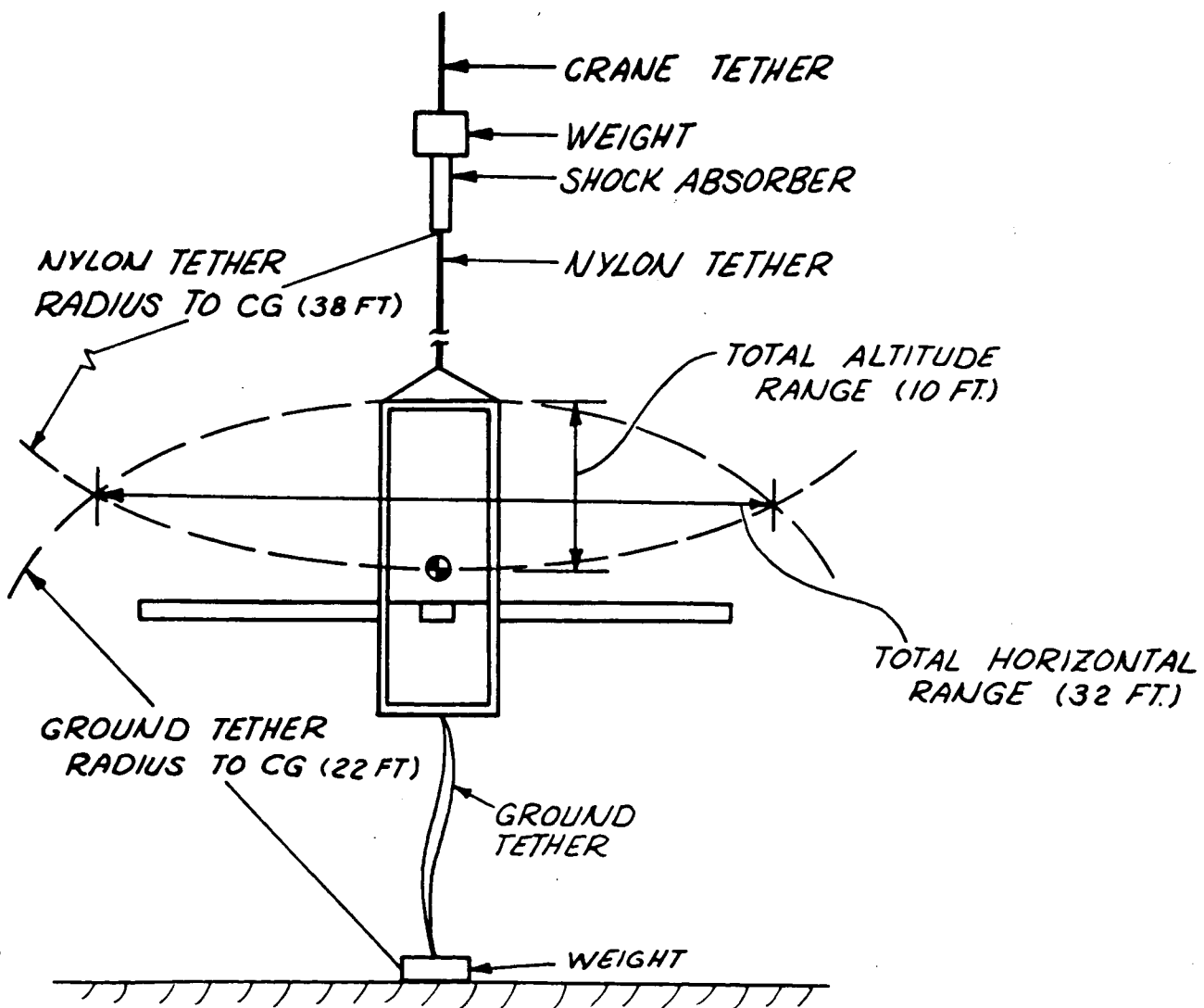


Figure 2-40. Tethered Flight Vehicle Constraints

Table 2-11. Tethered Flight Vehicle Mass Properties

Weight Statement		
Group	Weight (lb)	
Propulsion system	20.0	
Controls	5.0	
Structure	107.0	
Tethers and supports	15.0	
Empty weight		147.0
Pilot (90 percentile)		192.6
Total minimum weight		339.6
Four 20-foot booms and associated supports		53.3
Fifteen pound weights		60.0
Total maximum weight		452.9
Moment of Inertia Ranges		
Configuration (including pilot):	Total Weight (lb):	Total Moment of Inertia (slug-ft <sup>2</sup> ):
Without booms or weights	339	105
With booms, without weights	393	220
3-pound weights on boom tips	405	297
6-pound weights on boom tips	417	373
9-pound weights on boom tips	429	450
12-pound weights on boom tips	441	527
15-pound weights on boom tips	453	604

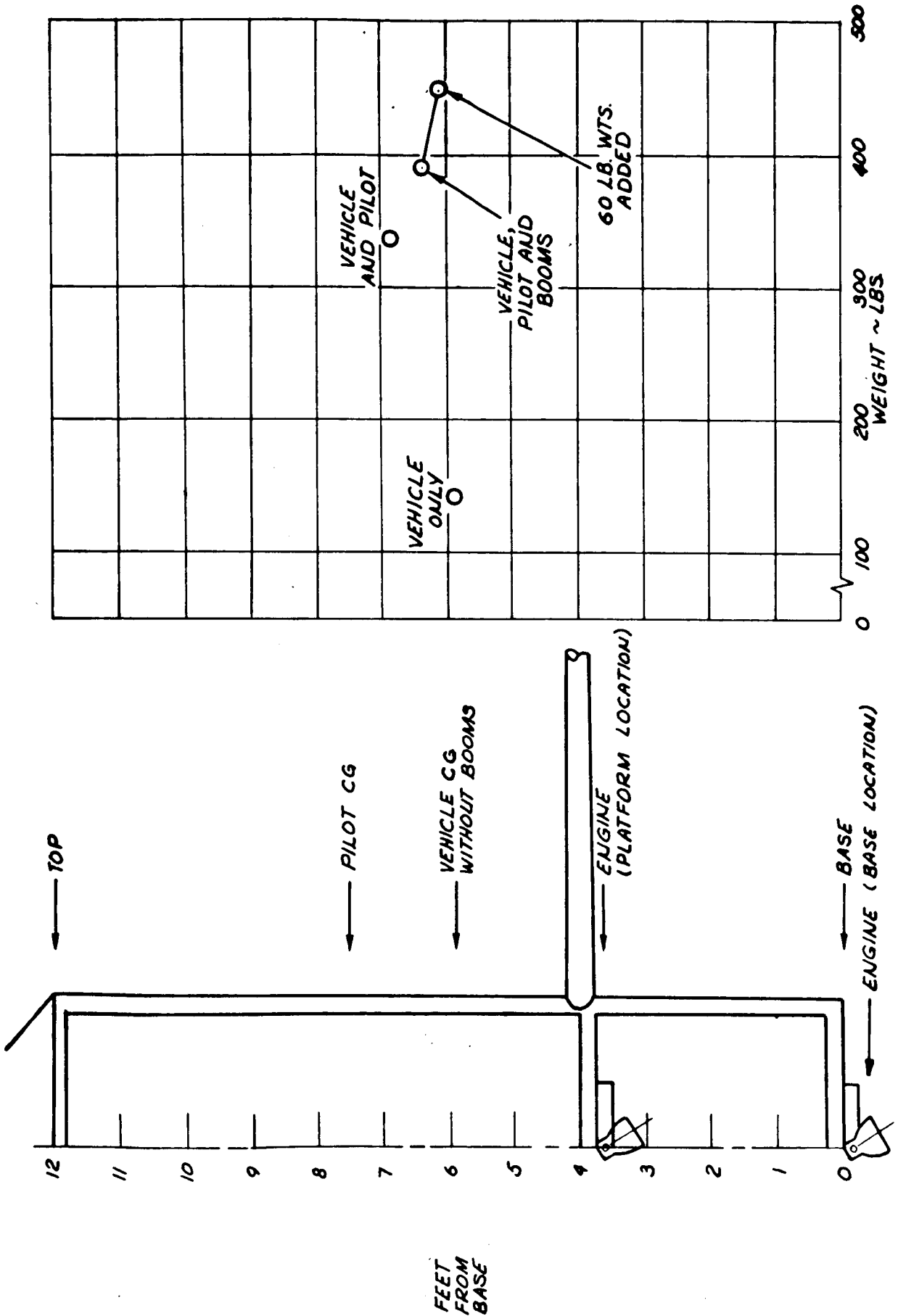


Figure 2-41. Tethered Flight Vehicle Center-of-Gravity Ranges



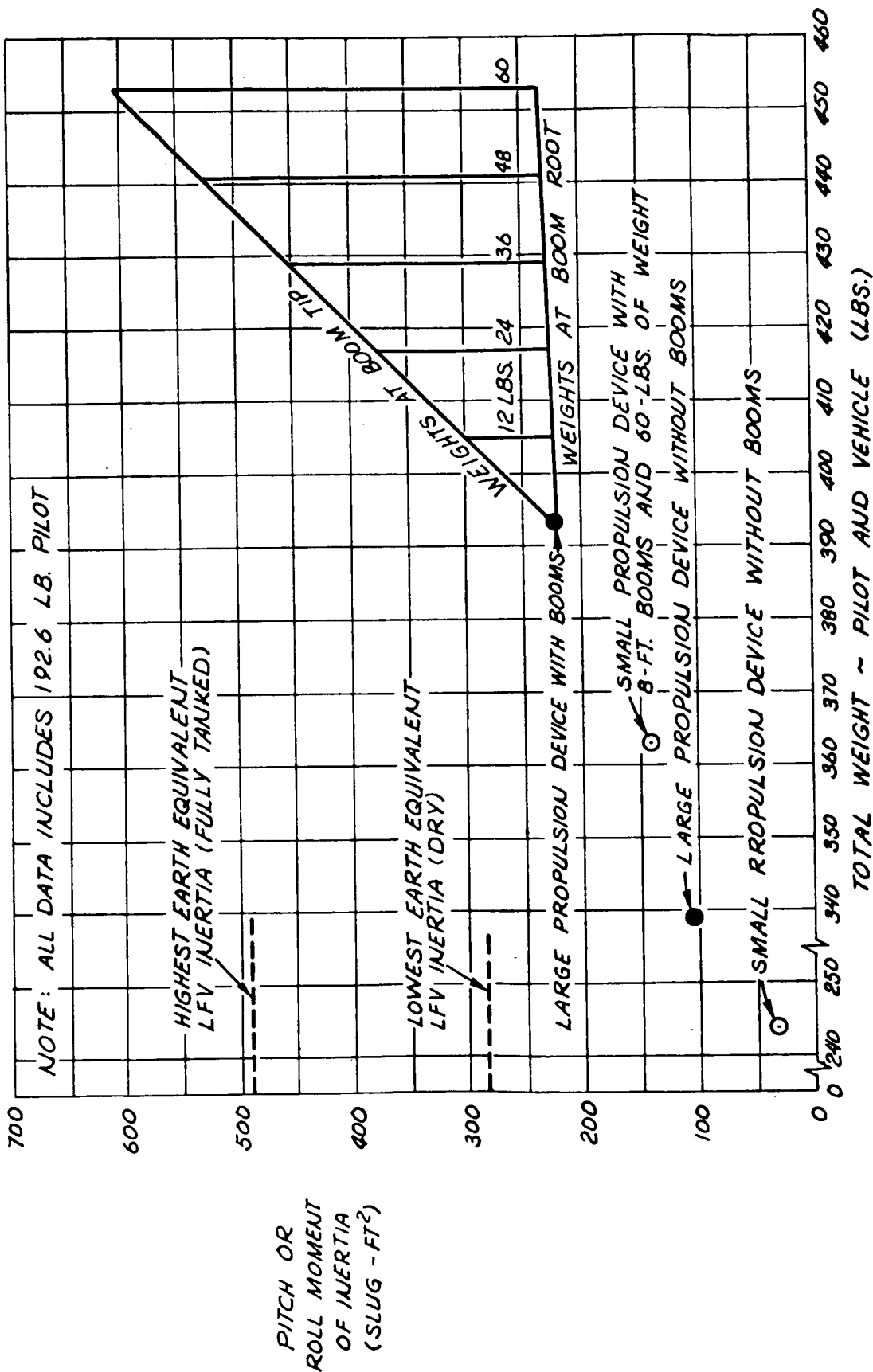


Figure 2-42. Tethered Flight Vehicle Moment-of-Inertia Ranges

The total flight schedule for the tethered vehicle was completed in eight days of flying and a total of 101 separate flights. Each day of flying incorporated improvements in the vehicle hardware, flight procedures and data recording methods.

Usually, the first flight of the day was with low-inertia characteristics, so that the pilot could get the feel of the vehicle with the sensitivity he could more confidently control. If larger inertias were to be flown that day, they were flown in the next few flights, since the nitrogen pressure and the thrust dropped lower with each flight and eventually would not support the additional weight. A flight would begin with the pressure control attendant gradually increasing nitrogen pressure until the pilot, with low throttle, was able to control altitude. During the pressure buildup period, wind and thrust disturbances caused the vehicle to swing on the crane tether. The pilot could often damp the oscillation kinesthetically but had no success in damping with the hardware control. After it was airborne, the pilot was required to hold the vehicle within the tether limits on altitude and range in order to hover. When a tether limit was reached, a large disturbance torque was applied to the vehicle by the tether. Control was rarely recovered after a tether limit had been reached.

During the last three days of tests, a light was installed on the vehicle which indicated when the crane tether was slack. The light also served to key the strip recorder data, separating areas of free flight from those inhibited by the tethers.

Although a large number of flights were conducted, a statistical analysis as was used in displaying visual simulator data is not appropriate for the tethered flight vehicle program. Neither control mode contained a sufficiently large sample of flights without major changes affecting the characteristics of the flight to apply statistics.

Since nearly every flight continued until control was lost by reaching a tether limit, quantitative data on handling qualities for complete flights were not obtained. Rather, a qualitative evaluation of the vehicle handling qualities was obtained. Although control was only necessary in five of the six degrees of freedom (yaw motion is damped by the tethers and nitrogen supply hoses) the effect of small disturbances from wind and the tethers tended to provide a pilot workload level equivalent of six degrees of freedom.

At the lowest moment of inertia, the vehicle was easily stabilized using kinesthetic control reflecting experiences at nearly the same inertia with the one-man propulsion device in 1968. When the booms were added, horizontal

oscillations at the start of flight were noticeably increased. As weights were added to the boom tips, fewer and fewer flights lasted beyond the initial transient motions, which swept the vehicle into the tethers.

To start a flight using hardwire control, the pilot would first attempt to damp the initial oscillations kinesthetically; then when the flight was quiescent, switch to hardwire control. This procedure was followed because it was obviously easier to control by the kinesthetic mode. With each gimbal deflection, a large horizontal acceleration appeared, followed by a slow and belated angular acceleration. Usually, the final result was a violent, pendulous motion of the vehicle as it oscillated between the tethers.

When the engine was lowered, the ratio of translational to rotational acceleration was decreased and the controllability was slightly improved. On one flight day, the engine was unintentionally misaligned and went undiscovered throughout the day. When the pilot stood in his usual position on the platform, the increased distance to the gimbal created a large disturbance torque which made control impossible. However, the problem was corrected before the next flight day.

A summary of the flight results, as discussed in the preceding three paragraphs, is shown in Table 2-12. A curve of pilot opinion rating versus moment of inertia is shown in Figure 2-43. The curve reflects kinesthetic flight only, since insufficient hardwire control flights were conducted to produce a curve. It is generally felt, however, that the hardwire handling qualities curve falls below the kinesthetic curve.

One of the two objectives of the tests was to determine the probable values of flight variables for landing. It was intended at the beginning of the program to have the pilots perform a task in which they would slowly descend over a marker while minimizing pitch and roll attitudes and rates, and horizontal velocity. Although the vehicle would not actually touch the ground, the flight variable during descent would be typical of the impact.

This task was not purposefully conducted, because the first task, that of determining the stability bounds parametrically in moment of inertia, utilized nearly all the flying time. Furthermore, the pilot could not react with the accuracy necessary to stay within the free flight envelope defined by the tether limits.

#### Summary, Conclusions, and Recommendations

Although a large number of flights were performed using the tethered flight vehicle, numerous changes were made, and an insufficient number of flights were conducted with a single configuration to form a statistical base. If more flights are approved in the future, there will undoubtedly be additional



Table 2-12. Tethered Flight Vehicle Results

Moment of Inertia (slug-ft <sup>2</sup> )	Comments
Kinesthetic flight	
105	Several successful flights, easily stabilized
220	Large horizontal oscillations, difficult to stabilize
297	Increased horizontal oscillations, more difficult to stabilize
373	Oscillations reach tether limits
450	Unstable interaction with tethers
Hardwire flight - engine at pilot platform	
105	Combined kinesthetic and hardwire for stabilization
220	Unable to control within tether limits
Hardwire flight - engine at vehicle base	
220	Control marginal, unacceptable for landing

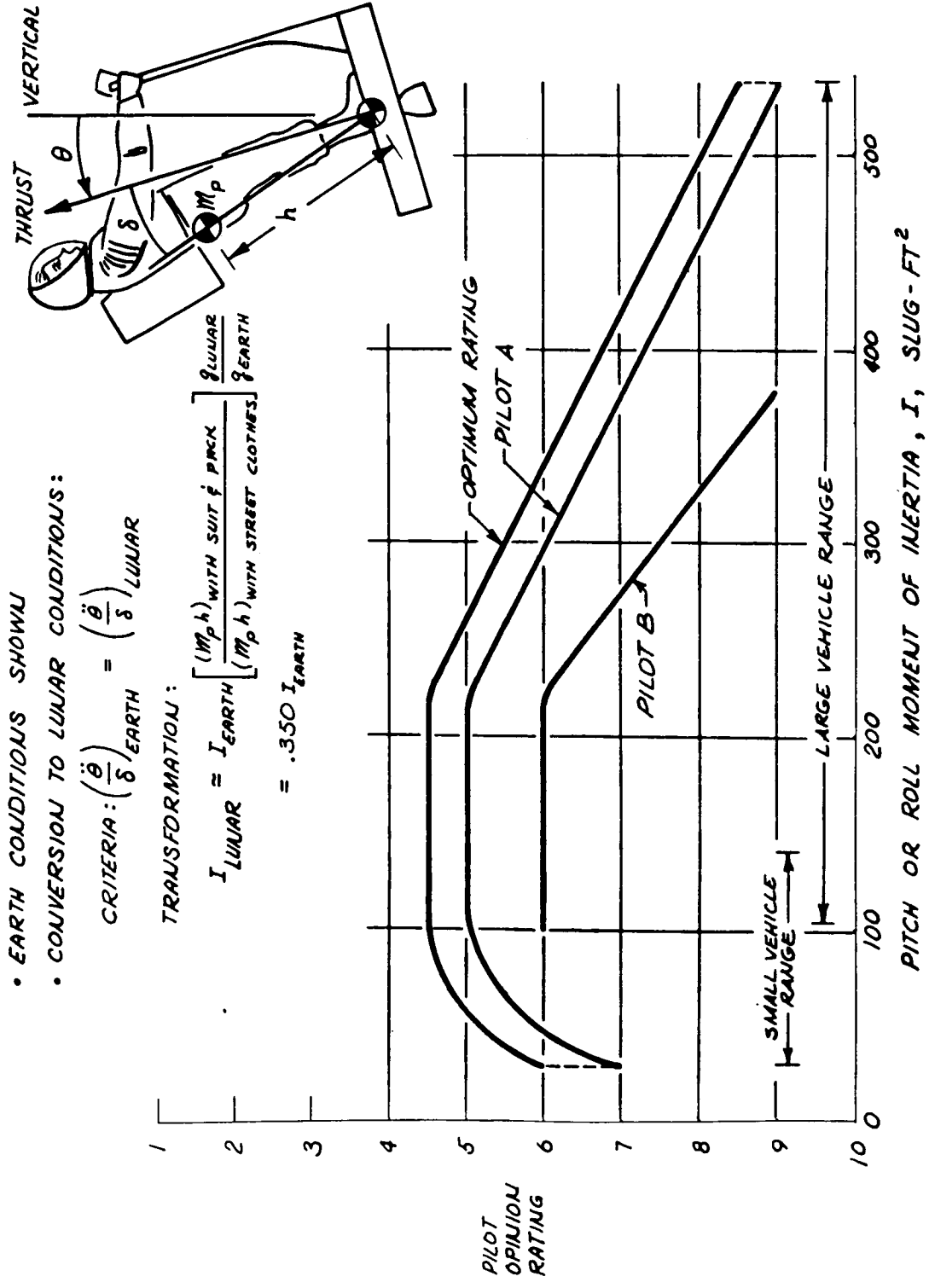


Figure 2-43. Tethered Flight Vehicle Kinesthetic Results

changes to improve the configuration. It is felt, however, that the latter flights displayed the conditions of kinesthetic and hardwire control sufficiently near their optimums to allow conclusions to be drawn.

With kinesthetic control, the pilot was typically able to stabilize the vehicle attitude, but had difficulty maintaining a fixed translational position. Response decreased as moment of inertia was increased. The pilot was forced to use his predictive abilities to a greater extent with high inertias in order to damp oscillations. At any inertia, large transients seem to be an inherent part of the take-off phase. If a control input is improperly managed, a great deal of effort must be expended to recover control. In view of these comments and because no means of improving kinesthetic control is now foreseen, the method is not recommended for moon flight.

Although hardwire control did not fare as well as kinesthetic using the tethered flight vehicle, more opportunities for improvement may be seen. A more thorough investigation of rotational controller sensitivities, for example, may produce higher handling qualities. Various center-of-gravity-to-gimbal distances may be used, other than the two that were studied, to find a manageable combination of translational and rotational accelerations produced by the gimbaled engine. Even with possible improvements, the method will still require the constant attention of the pilot to control three axes of rotation without making costly mistakes and misjudgments. Only a small part of the pilot's concentration span will be left to handle the translational tasks. This fact alone precludes a recommendation of the hardwire control concept.


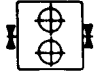


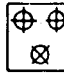

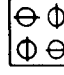
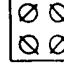

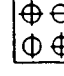



In summary, therefore, neither the kinesthetic nor the hardwire control method, as they were defined in this study, is considered feasible for use with a moon vehicle.

Future studies using the tethered flight vehicle may consider more complex control methods, such as the hardwire shaping network which was discussed earlier. These studies should also assure a larger flight envelope than was afforded by the tether limits used in the present study.

#### THRUST VECTOR CONTROL CONFIGURATION ANALYSIS

Analysis and tradeoff evaluations were made of 13 proposed thrust vector control configurations listed in Table 2-13. Candidate actuation systems include one-, two-, three-, and four-engine arrangements with various combinations of single- and dual-axis actuators employed on each engine.

Table 2-13. Candidate Engine Gimbal Configurations

Configurations	Engines	Actuators No.	Control Planes	Physical Considerations	Engine Out	Actuator Hardover Failure
1 	Does not allow engine-out failure	Two	Requires aux yaw control		(1) No control in any plane	(6) Loss of control
2 	Requires 2 engines, each with full thrust	Four	3-axis control 2-2-2		(1) Requires external yaw control	(6) Loss of control, saturates control in pitch. Loss of control in roll and yaw
3 	Heavier than 4-engine case	Six	3-axis control 3-3-2		(1) Yaw control avail with relocation and change of yaw logic	(6) Loss of control in roll and yaw
4 	Heavier than 4-engine case	Five	3-axis control; roll, pitch, yaw control available		(3), (1) Yaw and pitch control avail with severe relocation	(6) Produces pitch-axis saturation before shutoff
5 	Heavier than 4-engine case	Six	3-axis control 3-3-5		(1), (2) Marginal stability (further analysis required)	(6)
6 	Minimum weight T/C	Four (lightest wt for 4 engines)	3-axis control 2-2-2 or 2-2-4		(1), (2) Produces 3-axis saturation before shutoff	(4), (6)
7 	Minimum weight T/C	Four	3-axis control 2-2-4		(1), (2) Produces 3-axis saturation before shutoff	(5)
8 	Minimum weight T/C	Four	3-Axis control 4-4-4	(5)	(1), (2) Saturates control in pitch, yaw and roll	(6)
9 	Minimum weight T/C	Four (lightest wt for 4 engines)		(5)	(1) Marginal stability (further analysis required)	(6)
10 	Minimum weight T/C	Six	3-axis control, 2-2-4 (11 other combinations available)		(1), (2) Will maintain 3-axis control after one random failure	(6)
11 	Minimum weight T/C	Eight	3-axis control, 4-4-8 (15 other combinations available)	(5)	(1), (2) Will maintain 3-axis control after one random failure	(6)
12 	Minimum weight T/C	Eight	3-axis control, 4-4-8 (15 other combinations available)	(5)	(1), (2) Full 3-axis control with any one random failure	(6)
13 	Minimum weight T/C	Eight (heaviest actuator wt for 4 engines)	3-axis control, 4-4-4, 4-4-8 (14 other combinations available)		(1), (2) Full 3-axis control with any one random failure	(6)

(1) Pilot relocates for engine-out to trim vehicle  
 (2) Change in yaw logic may be required if using 2-engine yaw control  
 (3) Yaw and pitch control may yield high extraneous moments  
 (4) Engine or failed actuator must be shutdown  
 (5) These configurations interfere with physical placement of fuel tanks that minimize weight, breadth and vehicle MOI  
 (6) Time-critical failure--hardover failure impairs mission success and/or crew safety--stability doubtful

## Constraints

The particular selected thrust vector control configuration is based on set system requirements, some of which create tradeoff conditions between themselves. The selection criteria applied to the lunar flying vehicle, and their assigned priorities, in descending order, are as follows:

1. Crew safety shall not be impaired as a result of one random engine failure or one random actuator failure.
  - a. Full nominal thrusting capability shall be available, by additional manual throttling, after one engine-out failure or when one engine is turned off because of failure of another mode.
  - b. A first actuator or engine failure shall not create a time-critical recovery condition. Three-axis control will be maintained until back-up procedures can be implemented.
  - c. The pilot may be required to relocate his position with one engine out to restore trim to the vehicle, but shall not be required to move in order to maintain 3-axis stability.
2. The gimbal configuration shall be conducive to minimizing total vehicle size and weight.

## Analysis

Table 2-13 delineates the 13 candidate gimbal configurations considered most feasible. The detailed analysis associated with actuator hardover failures and engine out are shown in Appendix D. From the sixth column in the table, it is seen that numbers 1 through 9 of the thirteen candidate approaches fail to meet the actuator hardover requirements. That is, the first random hardover actuator failure will create a time-critical condition that must be corrected (possibly faster than human reaction time allows) before vehicle stability is lost. While there are many systems that will withstand certain selected failures without catastrophe, these will not accommodate random (worst-case) failures, which is sufficient to disqualify these geometries. Furthermore, configurations 1 through 4 do not respond adequately under engine-out conditions, an absolute criterion for rejection in this analysis.

The stability of configurations 5 and 10 is marginal after one hardover failure. Control authority still exists in all three axis, although the ability to provide torque as a "couple" is some axis is highly attenuated or completely eliminated. This implies that a high degree of cross-coupling develops when attempting to correct about an axis for which a torque couple is not



available. If the cross-coupling is induced into another axis in which a corrective torque couple is not available, further cross-coupling will result. The perpetuation of this phenomenon can lead to a divergent limit cycle in one or more axis under the influence of a small external disturbance. An initial translational velocity will probably also be generated at the time of hardover failure, requiring negation as soon as the induced acceleration is cancelled. This necessitates additional control authority. Dynamic stability analyses must be employed to determine the capacity of these systems to control after hardover failure.

Configuration 11 is unsuitable because the fuel tanks must be placed farther away from the center of gravity in the roll plane (implying a higher mass due to additional lengths for tank support equipment), higher moment of inertia in the roll axis, and greater breadth. The width of the LFV is an important consideration since a serious space limitation exists in the lunar excursion module in which the LFV will be transported.

Configurations 12 and 13 satisfy all high-priority constraints with some sacrifice in weight, power and MTBF. The only functional difference between 12 and 13 is that all eight actuators control pitch and roll and 4 actuators control yaw in case 12, whereas in 13, pitch and roll are aligned so that pitch and roll are four-actuator control systems, and yaw has eight-actuator control. Configuration 12 is more subject to a plume impingement problem with one of the fuel tanks than is 13. Since there is no advantage of configuration 12 over 13, and because 12 may cause plume impingement, 13 becomes the preferred configuration.

## Conclusions

Of the thirteen engine/actuator geometries analyzed, eight configurations suffered loss of attitude control authority under worst-case, single-actuator, hardover failure conditions. Additionally, four of these configurations could not maintain three-axis stability under engine-out conditions. All eight configurations were judged unacceptable because crew safety and/or mission success were greatly jeopardized by a single-point failure.

Of the remaining five, two were rejected because engine location and/or gimbal axis orientation gave rise to fuel tank/plume impingement problems. Solutions to this problem involved either moving the tanks outward for clearance or employing heatshields. However, this is undesirable since vehicle size would be increased, creating an interface problem with the lunar excursion module. There is no operational capability or weight compromise made in excluding these candidates, since others that do not cause plume impingement are equally effective in every way.

Three candidate configurations remain at this point, one of which is completely operationally acceptable under the failure constraint applied; however, a weight penalty is involved, since it requires four engines and eight actuators. The two remaining configurations are three-engine/six actuator, and four-engine/six-actuator systems that do not completely saturate control authority after one hardover actuator failure, but which one or more key actuators do saturate. The small amount of remaining control authority is very marginal. With these configurations, a realistic appraisal of continued attitude control stability after one failure must be made by additional nonlinear analysis and/or simulation.

The preferred configuration, therefore, is a four-engine/eight-actuator system--provided the required weight penalty can be endured. Two other candidate systems (six-actuator configurations) may provide a compromise selection based on additional stability analyses.

## CONTROL SYSTEM FAILURE MODE ANALYSIS

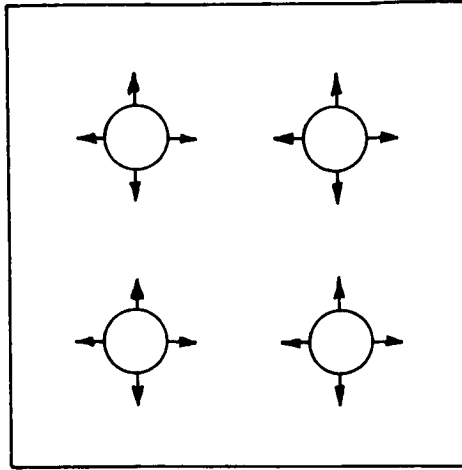
### Introduction

The capability to accept single failures in (1) the electrical power system, (2) the engine gimbal actuators, or (3) the engines, was analyzed for three candidate configurations shown in Figure 2-44. The translating TVC configuration was studied since it was capable of control with pure torque commands, rather than the combination of torque and horizontal force inherent in the gimbal engine systems. The second configuration shown in Figure 33 used a minimum number of actuators, although they were of the two-in-a-can variety. This was an attempt to reduce weight and further simplify the system as compared to the eight actuator case. The third configuration used eight single actuators which had no time-critical failures. The eight actuator case was the result of an engine/actuator geometry study discussed earlier.

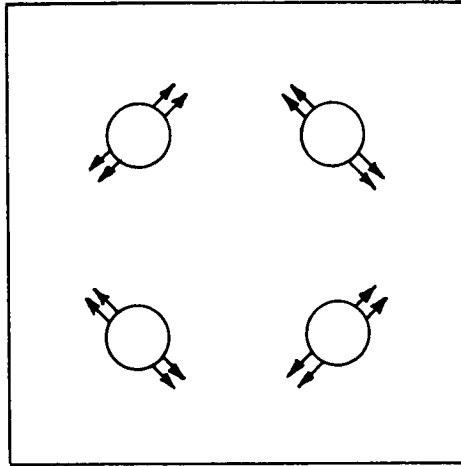
### Electrical Power System Analysis

The translating TVC system uses each power source to operate alternate motors in X and Y translating two-in-a-can actuators. Each source also provides power to a yaw actuator. The result is two completely separate gimbaling systems from a power source through the actuators. In event of failure in one of the gimbaling systems, either the pilot or an automatic sensing mechanism would switch from operating to standby system. The flow diagram of the translating TVC power system is shown in Figure 2-45. The second configuration resembles the first, except that the electrical power sources energize more actuators. In keeping with the automatic failure mode recovery characteristics of the third configuration, another method of computing the power sources to the actuators was used.

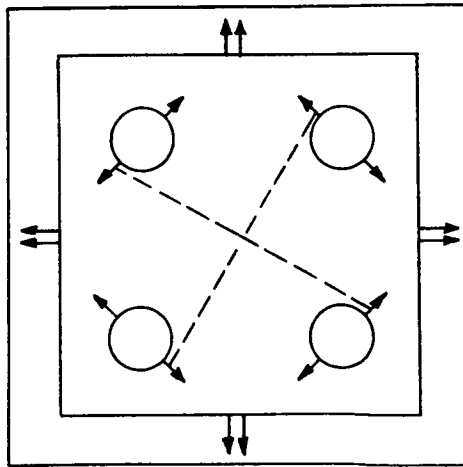
GIMBALED ENGINES  
PITCH, ROLL, AND YAW:  
8 SINGLE ACTUATORS



GIMBALED ENGINES  
PITCH, ROLL, AND YAW:  
4 2-IN-A-CAN ACTUATORS



TRANSLATING TVC  
PITCH AND ROLL:  
2 2-IN-A-CAN ACTUATORS  
YAW: 2 SINGLE ACTUATORS



FAILURE MODES:

- ELECTRICAL SYSTEM LOSS
- ACTUATOR HARDOVER
- ENGINE THRUST LOSS

Figure 2-44. Failure Mode Analysis for Three Configurations

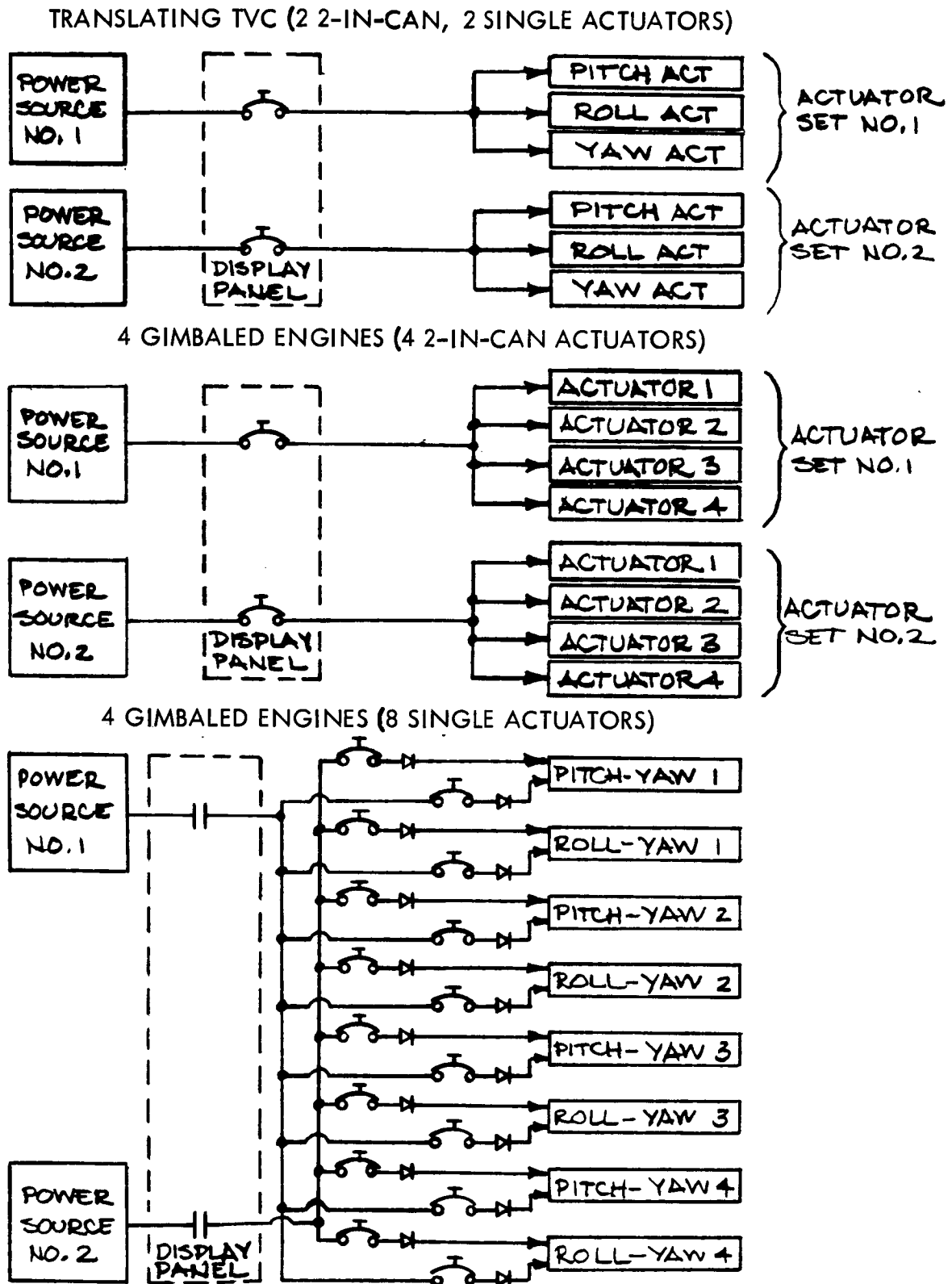


Figure 2-45. Gimbal Actuation Power-Flow Diagram

Each power source provides half the power to each actuator. If one of the sources or its associated wiring fails, the other source supplies all the power to the actuators. Since the pilot is commanding all eight actuators continuously, no time-critical switching in the entire system is necessary. A disadvantage of this method is the requirement for more electrical components to properly isolate each power source and each failure.

Failure rates associated with the electrical components are compared in Table 2-14. These rates, taken from the AVCO data, contain the factor of 30 necessary to reflect space applications. Even with the relatively high number of components used in the electrical power systems of the eight actuator configuration, the high reliability of the electrical components does not appreciably affect mission success. Therefore, the electrical power system was not considered a key factor in selecting one of the three configurations for further study.

Table 2-14. Electrical System Failure Mode Results

Component	Failure Modes	Failure Rate
Circuit Breakers	Open, Closed, High Res	$9/10^6$ hours
Diodes	Open, Short	$6/10^6$ hours
Switches	Open, Closed, High Res	$1.8/10^6$ cycles
Connectors	Open, Short to Ground, Short Between Pins	$0.15/10^6$ hours
Batteries	Low Voltage	$45/10^6$ hours
Conclusions: Reliability of electrical components relatively high Electrical system is not a deciding factor		

#### Engine Thrust Failure Analysis

The worst failure from the stabilization point of view is that which causes the migration of the actuator rod to either full extension or full retraction. The larger the allowable excursion of the actuator, the worse this type of failure becomes. A minimum excursion for the two gimbaled

configurations would include a small control margin past the gimbal angle necessary to trim for one engine out.

Figure 2-46 shows the three configurations to be studied, the engines numbered according to the left-hand rule around a mounting circle with radius  $r$ , beginning with the one nearest the  $+x$  vehicle axis. Positive actuator motion (independent of extension-retraction signs) is signified by arrows attached to the engines; the greek letter  $\delta$  is the actuator motion variable. Subscripts  $\phi, \theta, \psi$  indicate roll, pitch, and yaw signals. In two of the three configurations, the engines are mounted in a canted position ( $\delta_c$ ), reducing failure disturbances. The distance from the total center of gravity to the gimbal plane is  $lg$ . Standard actuation system logic is used on all three configurations.

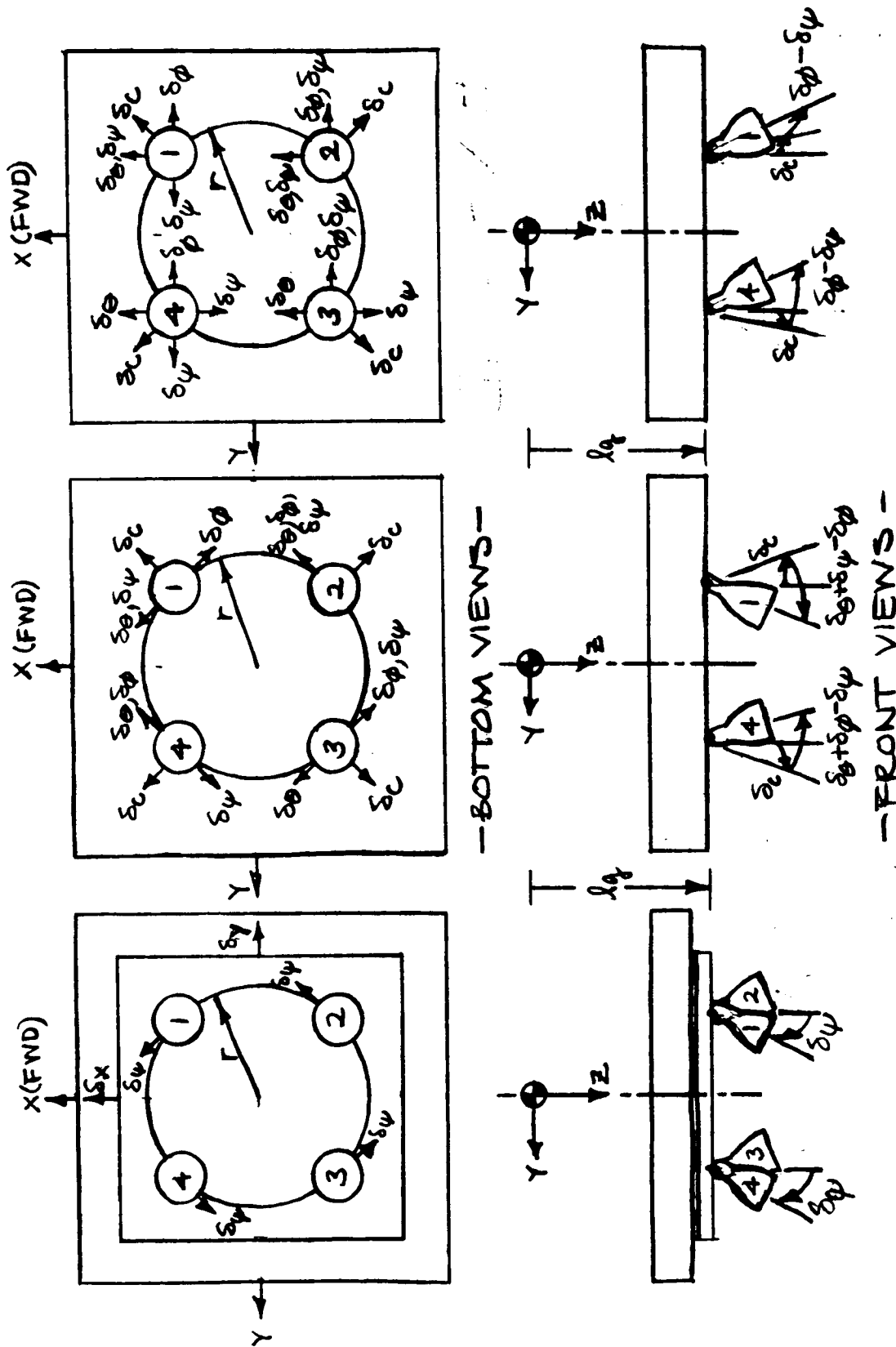
The algebraic equations for thrust forces and moments resulting from an actuator motion and cant angles are given in Table 2-15. The translating motion of the longitudinal and lateral actuators in the first configuration may be considered an equivalent gimbaling motion for moments, thereby providing a basis for comparison.

The equations in TABLE 2-15 may be used to express engine thrust failure conditions. As an example, assume that Engine 2 fails in all three configurations. The remaining engines have sufficient thrust to provide full nominal thrust by increasing the throttle setting. When the transients have damped, the steady-state trim conditions for gimbal angles and platform tilt to zero horizontal forces are as shown in Table 2-16. Added to the steady state trim gimbal angles are the requirements needed for transient conditions. This angle may be calculated by dividing the required angular acceleration of 0.15 radians/per second squared by the factor  $(Tl/I)$ , the vehicle sensitivity to control moment. The angular acceleration requirement is explained in the gimbal command histogram study described in the next section. For the eight actuator case, 4.3 degrees are needed. Accounting for the gimbaling arrangement of the four actuator case, its requirement is 6.1 degrees. Assuming a 10-inch moment arm for gimbaling, the translating TVC case requires 0.75 inches for transient control.

Comparative data for total actuator travel and platform tilt attitude are given in TABLE 2-17.

#### Actuator Hardover Failure Analysis

Using the worst case of actuator failure, one which causes the rod to fully extend or retract, the resulting vehicle conditions will be shown. At failure onset, initial conditions were assumed where the pilot is initiating the boost phase of flight by pitching to 45 degrees. Just before ending the pitch maneuver, the failure occurs. Since the translating TVC configuration is obviously disastrous if the actuator is allowed to go the full extension



TRANSLATING TVC FOUR 2-IN-A-CAN ACTUATORS EIGHT SINGLE ACTUATORS

Figure 2-46. Engine and Actuator Configurations

**Table 2-15. Thrust Force and Moment Equations**

Assumptions
1. Pilot and cargo perfectly positioned 2. Zero structural misalignments 3. Gimbal angles, cant angles, and displacements small 4. Four-engine control in each plane
Translating TVC
$F_{T_x} \cong \frac{1}{\sqrt{2}} (-T_1 - T_2 + T_3 + T_4) \delta_\psi$ $F_{T_y} \cong \frac{1}{\sqrt{2}} (-T_1 + T_2 + T_3 - T_4) \delta_\psi$ $F_{T_z} \cong -(T_1 + T_2 + T_3 + T_4)$ $L_T \cong T_1 \left( \frac{r}{\sqrt{2}} + l_g \delta_\phi + \frac{l_g}{\sqrt{2}} \delta_\psi \right) + T_2 \left( \frac{r}{\sqrt{2}} + l_g \delta_\phi - \frac{l_g}{\sqrt{2}} \delta_\psi \right)$ $+ T_3 \left( -\frac{r}{\sqrt{2}} + l_g \delta_\phi - \frac{l_g}{\sqrt{2}} \delta_\psi \right) + T_4 \left( -\frac{r}{\sqrt{2}} + l_g \delta_\phi + \frac{l_g}{\sqrt{2}} \delta_\psi \right)$ $M_T \cong T_1 \left( \frac{r}{\sqrt{2}} + l_g \delta_\theta - \frac{l_g}{\sqrt{2}} \delta_\psi \right) + T_2 \left( -\frac{r}{\sqrt{2}} + l_g \delta_\theta - \frac{l_g}{\sqrt{2}} \delta_\psi \right)$ $+ T_3 \left( -\frac{r}{\sqrt{2}} + l_g \delta_\theta + \frac{l_g}{\sqrt{2}} \delta_\psi \right) + T_4 \left( \frac{r}{\sqrt{2}} + l_g \delta_\theta + \frac{l_g}{\sqrt{2}} \delta_\psi \right)$ $N_T \cong -(T_1 + T_2 + T_3 + T_4) \delta_\psi$ <p style="text-align: center;">EQUIVALENT GIMBAL ANGLES --</p> $\delta_\phi = \frac{1}{l_g} \delta_y$ $\delta_\theta = \frac{1}{l_g} \delta_x$



**Table 2-15. Thrust Force and Moment Equations (Cont)**

FOUR 2-IN-A-CAN ACTUATORS	
$F_{T_x} \cong \frac{T_1}{\sqrt{2}} (\delta_\phi - \delta_\theta - \delta_\psi - \delta_c) + \frac{T_2}{\sqrt{2}} (-\delta_\phi - \delta_\theta - \delta_\psi + \delta_c)$ $+ \frac{T_3}{\sqrt{2}} (\delta_\phi - \delta_\theta + \delta_\psi + \delta_c) + \frac{T_4}{\sqrt{2}} (-\delta_\phi - \delta_\theta + \delta_\psi - \delta_c)$	
$F_{T_y} \cong \frac{T_1}{\sqrt{2}} (\delta_\phi - \delta_\theta - \delta_\psi + \delta_c) + \frac{T_2}{\sqrt{2}} (\delta_\phi + \delta_\theta + \delta_\psi + \delta_c)$ $+ \frac{T_3}{\sqrt{2}} (\delta_\phi - \delta_\theta + \delta_\psi - \delta_c) + \frac{T_4}{\sqrt{2}} (\delta_\phi + \delta_\theta - \delta_\psi - \delta_c)$	
$F_{T_z} \cong -T_1 - T_2 - T_3 - T_4$	
$L_T \cong \frac{l_g}{\sqrt{2}} T_1 (-\delta_\phi + \delta_\theta + \delta_\psi - \delta_c + \frac{r}{l_g}) + \frac{l_g}{\sqrt{2}} T_2 (-\delta_\phi - \delta_\theta - \delta_\psi - \delta_c + \frac{r}{l_g})$ $+ \frac{l_g}{\sqrt{2}} T_3 (-\delta_\phi + \delta_\theta - \delta_\psi + \delta_c - \frac{r}{l_g}) + \frac{l_g}{\sqrt{2}} T_4 (-\delta_\phi - \delta_\theta + \delta_\psi + \delta_c - \frac{r}{l_g})$	
$M_T \cong \frac{l_g}{\sqrt{2}} T_1 (\delta_\phi - \delta_\theta - \delta_\psi - \delta_c + \frac{r}{l_g}) + \frac{l_g}{\sqrt{2}} T_2 (-\delta_\phi - \delta_\theta - \delta_\psi + \delta_c - \frac{r}{l_g})$ $+ \frac{l_g}{\sqrt{2}} T_3 (\delta_\phi - \delta_\theta + \delta_\psi + \delta_c - \frac{r}{l_g}) + \frac{l_g}{\sqrt{2}} T_4 (-\delta_\phi - \delta_\theta + \delta_\psi - \delta_c + \frac{r}{l_g})$	
$N_T \cong rT_1 (\delta_\phi - \delta_\theta - \delta_\psi) + rT_2 (-\delta_\phi - \delta_\theta - \delta_\psi) + rT_3 (-\delta_\phi + \delta_\theta - \delta_\psi)$ $+ rT_4 (\delta_\phi + \delta_\theta - \delta_\psi)$	

**Table 2-15. Thrust Force and Moment Equations (Cont)**

## EIGHT ACTUATORS

$$F_{T_x} \cong T_1 \left( -\delta_\theta - \delta_\psi - \frac{1}{\sqrt{2}} \delta_c \right) + T_2 \left( -\delta_\theta - \delta_\psi + \frac{1}{\sqrt{2}} \delta_c \right) \\ + T_3 \left( -\delta_\theta + \delta_\psi + \frac{1}{\sqrt{2}} \delta_c \right) + T_4 \left( -\delta_\theta + \delta_\psi - \frac{1}{\sqrt{2}} \delta_c \right)$$

$$F_{T_y} \cong T_1 \left( \delta_\phi - \delta_\psi + \frac{1}{\sqrt{2}} \delta_c \right) + T_2 \left( \delta_\phi + \delta_\psi + \frac{1}{\sqrt{2}} \delta_c \right) \\ + T_3 \left( \delta_\phi + \delta_\psi - \frac{1}{\sqrt{2}} \delta_c \right) + T_4 \left( \delta_\phi - \delta_\psi - \frac{1}{\sqrt{2}} \delta_c \right)$$

$$F_{T_z} \cong -T_1 - T_2 - T_3 - T_4$$

$$L_T \cong T_1 \ell g \left( -\delta_\phi + \delta_\psi - \frac{1}{\sqrt{2}} \delta_c + \frac{1}{\sqrt{2}} \frac{r}{\ell g} \right) + T_2 \ell g \left( -\delta_\phi - \delta_\psi - \frac{1}{\sqrt{2}} \delta_c + \frac{1}{\sqrt{2}} \frac{r}{\ell g} \right) \\ + T_3 \ell g \left( -\delta_\phi - \delta_\psi + \frac{1}{\sqrt{2}} \delta_c - \frac{1}{\sqrt{2}} \frac{r}{\ell g} \right) + T_4 \ell g \left( -\delta_\phi + \delta_\psi + \frac{1}{\sqrt{2}} \delta_c - \frac{1}{\sqrt{2}} \frac{r}{\ell g} \right)$$

$$M_T \cong T_1 \ell g \left( -\delta_\theta - \delta_\psi - \frac{1}{\sqrt{2}} \delta_c + \frac{1}{\sqrt{2}} \frac{r}{\ell g} \right) + T_2 \ell g \left( -\delta_\theta - \delta_\psi + \frac{1}{\sqrt{2}} \delta_c - \frac{1}{\sqrt{2}} \frac{r}{\ell g} \right) \\ + T_3 \ell g \left( -\delta_\theta + \delta_\psi + \frac{1}{\sqrt{2}} \delta_c - \frac{1}{\sqrt{2}} \frac{r}{\ell g} \right) + T_4 \ell g \left( -\delta_\theta + \delta_\psi - \frac{1}{\sqrt{2}} \delta_c + \frac{1}{\sqrt{2}} \frac{r}{\ell g} \right)$$

$$N_T \cong \frac{r}{\sqrt{2}} T_1 \left( \delta_\phi - \delta_\theta - 2\delta_\psi \right) + \frac{r}{\sqrt{2}} T_2 \left( -\delta_\phi - \delta_\theta - 2\delta_\psi \right) \\ + \frac{r}{\sqrt{2}} T_3 \left( -\delta_\phi + \delta_\theta - 2\delta_\psi \right) + \frac{r}{\sqrt{2}} T_4 \left( \delta_\phi + \delta_\theta - 2\delta_\psi \right)$$

Table 2-16. Steady-State Gimbal Angle Trim and Platform Tilt Requirements for Single Engine Thrust Failure

Steady-State Angular Requirement Engine Actuation System Configuration	Gimbal Trim Angle (degrees)	Zero Horizontal Force Vehicle Tilt Angle (degrees)
Translating TVC	* $\frac{1}{3\sqrt{2}} \frac{1}{\ell g}$	none
Four two-in-a-Can Actuators	$\frac{57.3}{2} \left( \frac{r}{\ell g} - \frac{\delta_c}{57.3} \right)$	$\frac{57.3}{3} \frac{r}{\ell g}$
Eight Single Actuators	$\frac{57.3}{3\sqrt{2}} \left( \frac{r}{\ell g} - \frac{\delta_c}{57.3} \right)$	$\frac{57.3}{3} \frac{r}{\ell g}$
Notes: Small Angles Assumed * Translating TVC equivalent gimbal angle equations shown in Table 2-15		

Table 2-17. Actuator Requirements for Engine Thrust Failure

Input Data	Translating TVC	4 Actuators 2-in-a-can	8 Single Actuators
Distance from Center Gravity to gimbal	NA	10 inches	10 inches
Engine mounting circle radius	5.5 inches	5.5 inches	5.5 inches
Engine cant angle	0	15 degrees	15 degrees
Actuator Requirements			
Realignment Trim	1.3 Inches	8.3 Degrees	3.9 Degrees
Margin needed for control	0.75 Inches	6.1 Degrees	4.3 Degrees
Total Actuator Requirement	2.05 Inches	14.4 Degrees	8.2 Degrees
Vehicle attitude trim Requirements	0	10.5 degrees	10.5 degrees

distance, an intermediate stop was assumed available at the range  $\pm 0.75$  inches. The stop prevented the actuator from extending or retracting the full distance, although it did insert a second time-critical failure into the configuration. The pilot is required to pull the stop when an engine thrust failure occurs.

After failure has occurred, the actuator extends or retracts to the stop and stays there. The system stays failed until the pilot or an automatic sensing device reacts by switching the failed actuator out and an unused actuator into operation. The pilot reaction time, based on Apollo CSM simulator studies, may be as long as 1.5 seconds.

When the previously unused actuator is operating, the stability augmentation system automatically corrects to the commanded vehicle rate. Assuming the pilot uses the rotational controller to command the opposing rate until the vehicle is level, the correcting actuator must swing the engine through its entire range. All actuator motion in response to a command, and in failure condition, was assumed to be initially 25 degrees per second, or its equivalent for the translating TVC actuator. After the gyros sense vehicle response to the command, the actuators gimbal exponentially with time. The vehicle and actuator data and the vehicle initial conditions are summarized in TABLE 2-18.

Taking the translating TVC configuration first, FIGURE 2-47 shows the time history of the failed actuator. In the first moment after the failure, the actuator migrates to its stop, 0.75 inches. During the intervening time period, and until the pilot activates the alternate actuator, the vehicle angular rate continues to increase. Equations for angular rate and vehicle attitude were generated by integrating the moment equation, including the actuator time history. The vehicle attitude passes that point where the vertical component of thrust is able to compensate for gravitational acceleration, even with full throttle, and the vehicle begins to accelerate downward. After the pilot reacts (1.5 seconds), switching to the alternate two-in-a-can actuator, the new actuator follows the command signal and therefore the translating plate at an equivalent 25 degrees per second in the opposite direction. The actuator again limits until its command signal is nulled by the stability augmentation system. By now, the vehicle is rotating back towards a level attitude after nearly 100 degrees of travel. When the attitude is nearly level, the pilot commands attitude hold and the actuator limits for the third time. The vehicle continues to fall, however, since the acceleration inflection point occurred at approximately 10 seconds. The next graph, FIGURE 2-48, repeats the vehicle attitude time history, showing that the resulting net altitude loss approximates 380 feet. It is not certain that the pilot could safely negotiate a nearly inverted attitude without becoming disoriented; certainly, the resulting altitude loss would, in some cases, be

Table 2-18. Actuator Hardover Analysis

<p>Vehicle Data</p> <ul style="list-style-type: none"> <li>- Weight = 1373 pounds</li> <li>- Max. thrust = 420 pounds</li> <li>- Distance from cg to gimbal plane = 10 inches</li> <li>- Nominal angular acceleration = 0.15 rad/sec<sup>2</sup></li> </ul>
<p>Initial Conditions (at failure onset)</p> <ul style="list-style-type: none"> <li>- Pitch angle = 40 degrees</li> <li>- Pitch rate = 10 degrees/second</li> </ul>
<p>Conditions After Failure</p> <ul style="list-style-type: none"> <li>- Max. actuator rate = 25 degrees/second</li> <li>- Pilot reacts to fail indicator at <math>\tau = 1.5</math> seconds</li> <li>- Actuator limits set for <ul style="list-style-type: none"> <li>translating TVC:      0.75 inches</li> <li>4 actuators:            14.4 degrees</li> <li>8 actuators:            8.2 degrees</li> </ul> </li> </ul>



ALTERNATE 2-IN-A-CAN ACTUATOR ENERGIZED AT 1.5 SECONDS

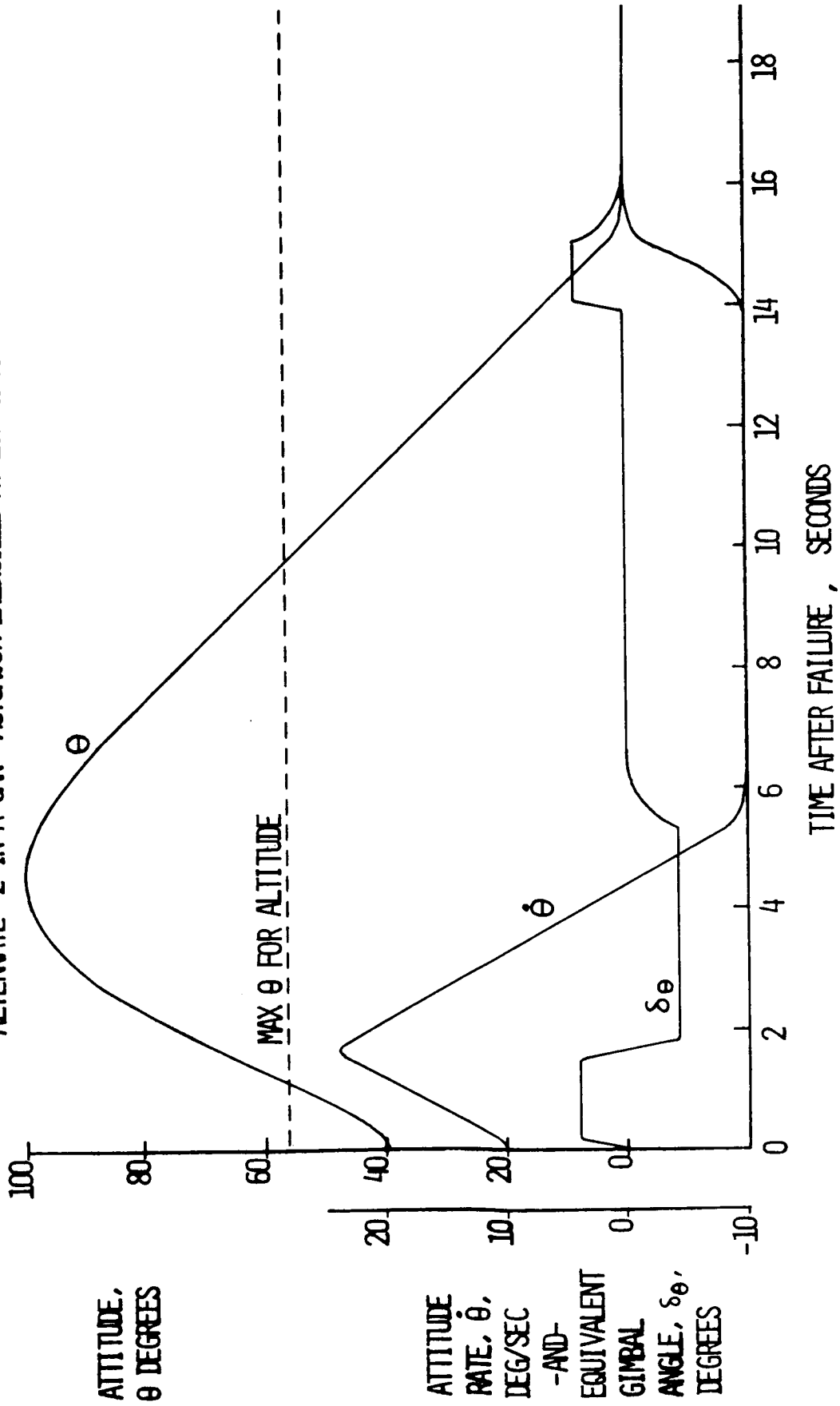


Figure 2-47. Actuator Hardover Failure of Translating TVC

• ALTERNATE 2-IN-A-CAN ACTUATOR ENERGIZED AT 1.5 SECONDS

• MAX THRUST = 420 LBS.

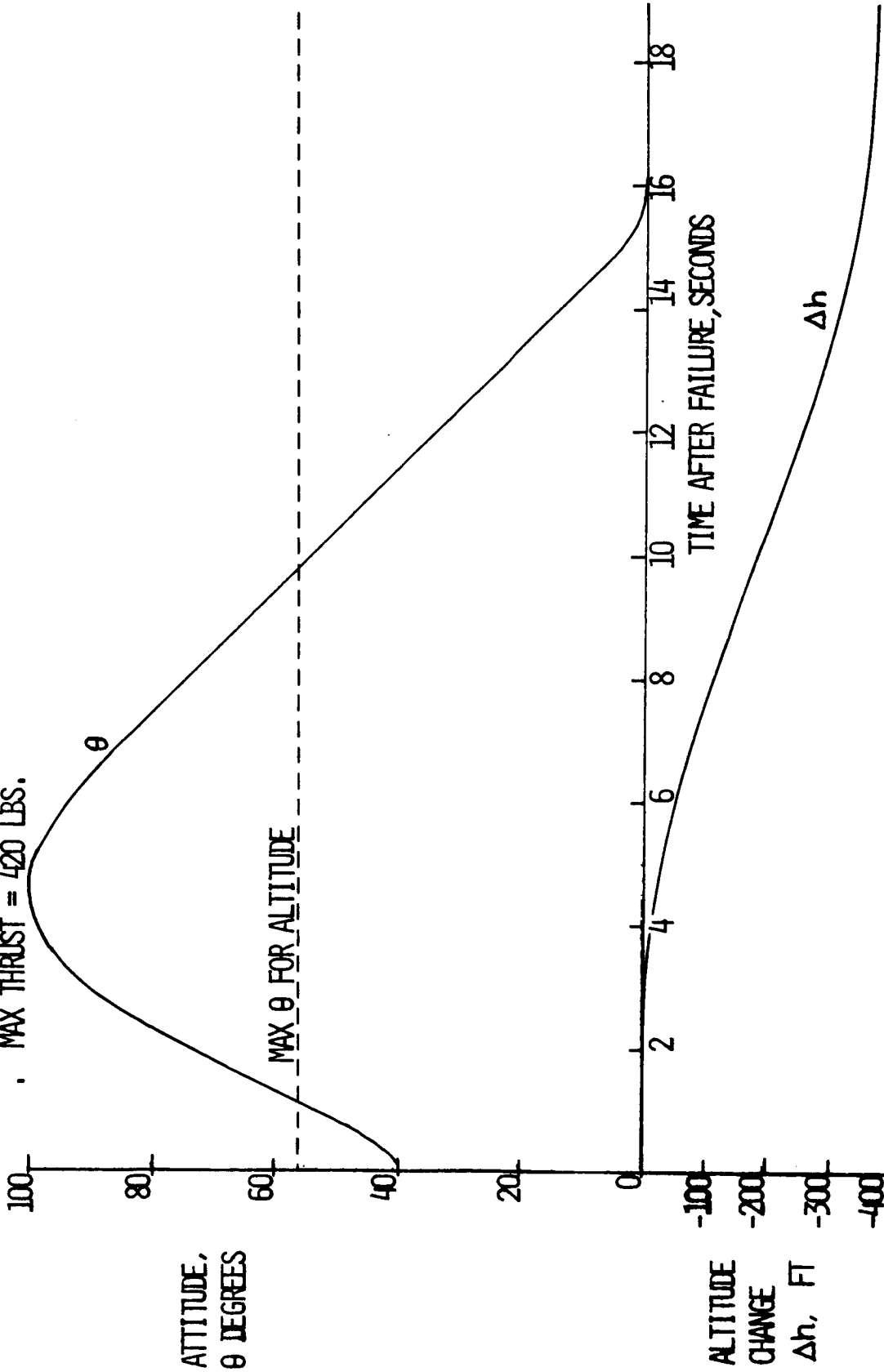


Figure 2-48. Altitude Loss From Actuator Hardover Failure of Translating TVC





catastrophic. On this basis, plus that of a double time-critical failure, the translating plate configuration may be eliminated.

The second configuration, using four two-in-a-can actuators, is a less severe case. Where an actuator fails hardover, the other three operative actuators are driven to their limits by the stability augmentation system, effectively stopping angular acceleration of the vehicle. Since all actuators are then hardover, no control margin remains and the system is unable to damp small disturbances. Furthermore, there is no response to the pilot's commands. FIGURE 2-49 shows the resulting time histories. For the particular conditions given the case, which are the same as those for the translating TVC configuration, the attitude excursion barely exceeds the attitude for altitude maintenance, and recovery is swift. The configuration contains a time-critical failure, however, in that either the pilot or an automatic system must switch the alternate actuator into operation.

The third configuration, using eight single actuators, requires no switching by the pilot. An actuator hardover failure does not force all other actuators to their limits, and adequate control may be retained.

Actuator hardover failure results are summarized in TABLE 2-19. The conclusion drawn from the analysis is that the translating TVC configuration is not feasible. Furthermore, the four two-in-a-can actuator case is marginal.

#### Results of Failure Mode Analysis

TABLE 2-20 summarizes the failure mode analysis results for the three configurations studied. Conclusions indicate that the electrical power system shows no discriminating difference between the configurations. The actuator hardover failure is probably catastrophic with the translating TVC configuration, having an associated time-critical failure. The hardover failure is probably not catastrophic with the four actuator configuration, and the time criticality of the failure is not severe. No time-critical failure is associated with the eight actuator configuration.

The engine thrust failure analysis showed only small differences between the three configurations, except that the translating TVC configuration has a second time-critical failure. The gimbaleed configurations both require that either the vehicle be landed at a 10.5 degree inclination to null horizontal acceleration or that the center of gravity be retrimmed following the thrust failure.

• ALTERNATE 2-IN-A-CAN ACTUATOR ENERGIZED AT 1.5 SECONDS

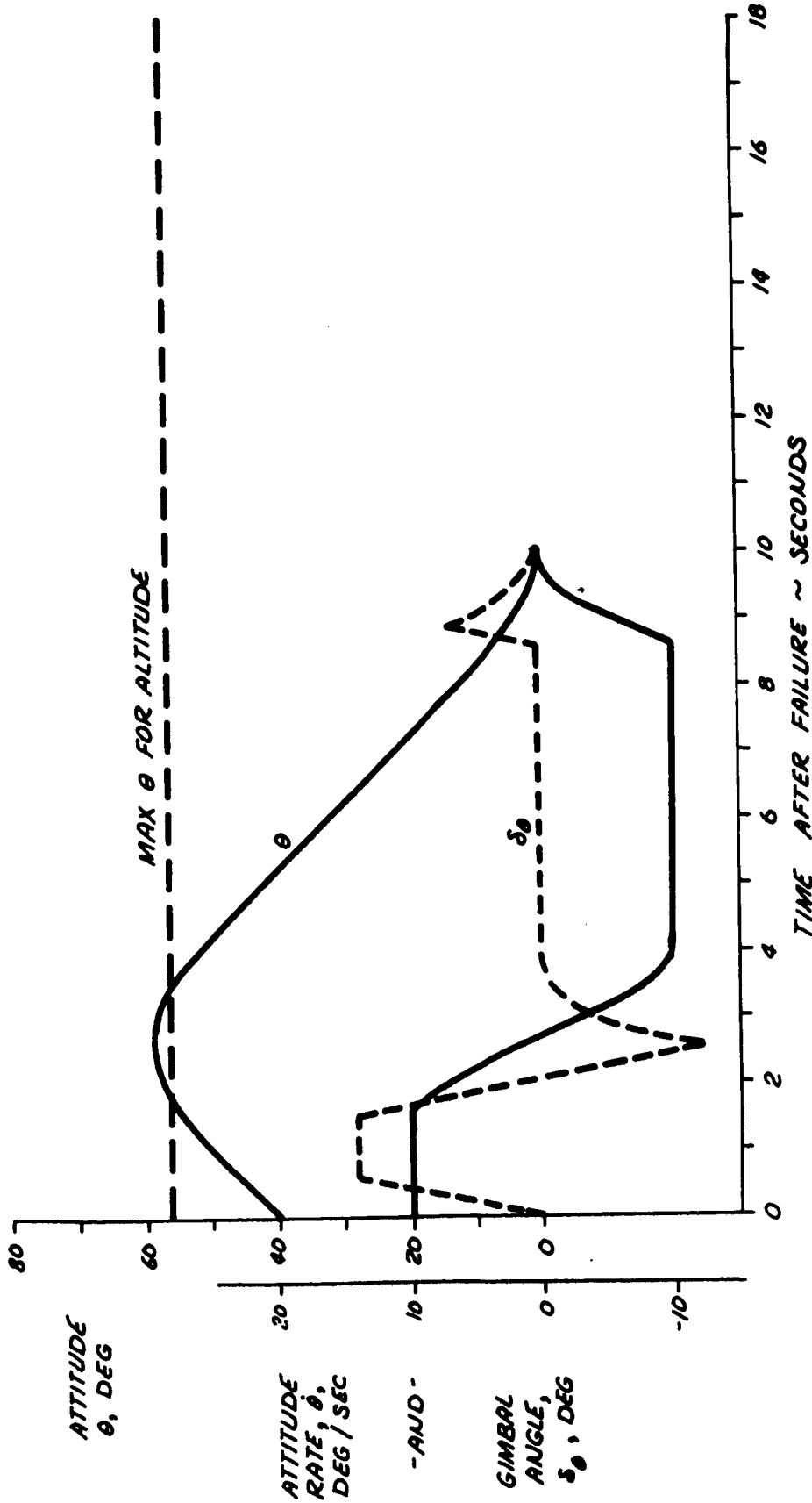


Figure 2-49. Actuator Hardover of Four Two-in-a-Can Actuators

Table 2-19. Results of Actuator Hardover Failure Analysis

<p>Translating TVC</p> <ul style="list-style-type: none"> <li>- Extreme attitude excursion results from assumed conditions</li> <li>- Large altitude drop results</li> <li>- Time-critical failure</li> </ul>
<p>Four 2-in-a-can actuators</p> <ul style="list-style-type: none"> <li>- Small attitude excursion results from assumed conditions</li> <li>- Negligible altitude drop results</li> <li>- Time-critical failure</li> </ul>
<p>8 single actuators</p> <ul style="list-style-type: none"> <li>- No attitude excursion</li> <li>- No altitude drop</li> <li>- No time-critical failure</li> </ul>
<p>Conclusion: Translating TVC configuration not feasible</p>

Table 2-20. Results of Failure Mode Analysis

Item	Translating TVC	4 Actuators 2-in-a-Can	8 Single Actuators
Electrical power system	No discriminating difference		
Actuator hardover	large	small	none
Attitude change	large	small	none
Altitude change	yes	yes	no
Pilot-initiated action			
Engine thrust failure			
Maximum gimbal angle	2.05 inches	14.4 degrees	8.2 degrees
Vehicle attitude trim	0	10.5 degrees	10.5 degrees
Pilot-initiated action	yes <sup>1</sup>	yes <sup>2</sup>	yes <sup>2</sup>

<sup>1</sup> Adjust actuator stops

<sup>2</sup> Retrim vehicle center of gravity



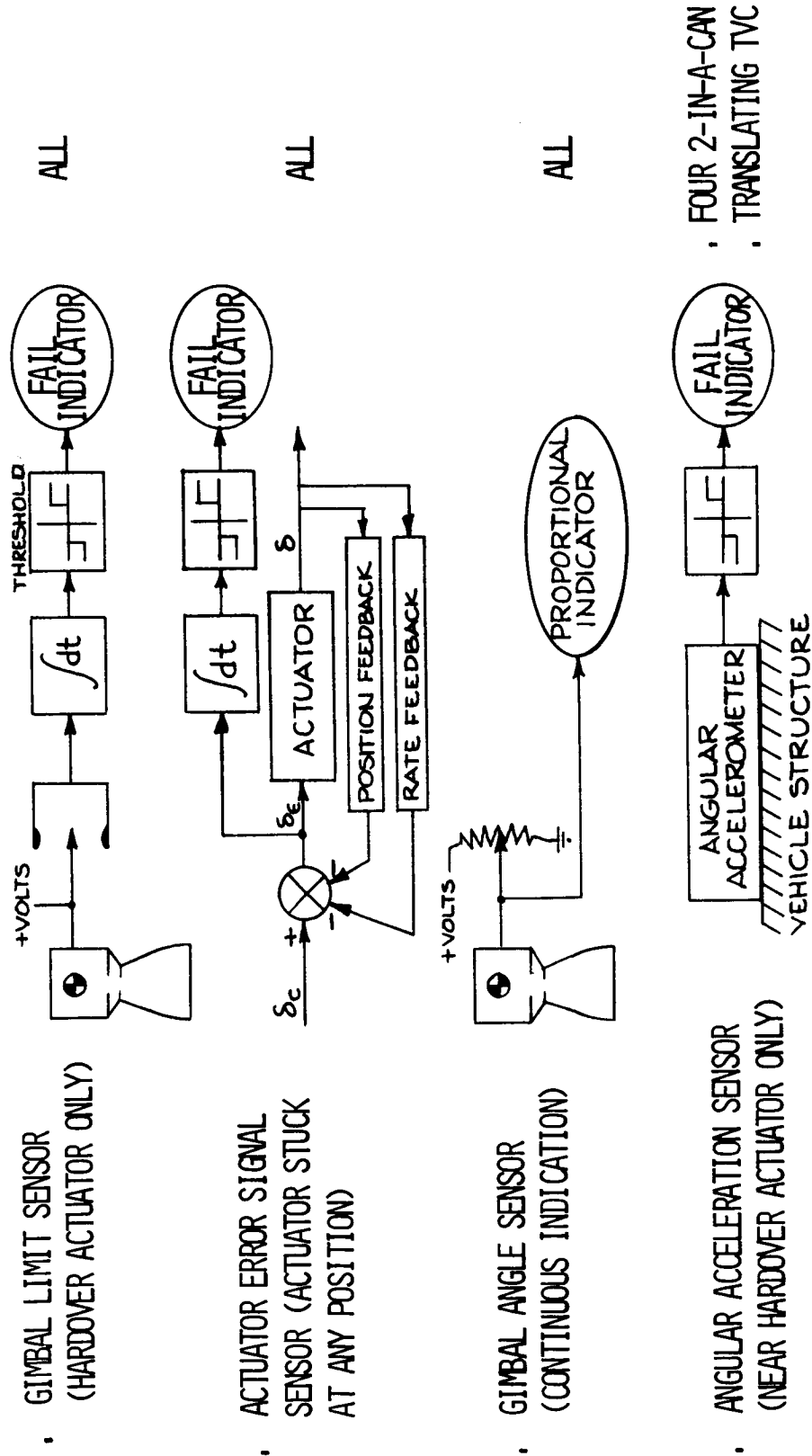
## Hardover Actuator Failure Sensors

In either a case, where the pilot must react to a hardover actuator failure or where an automatic system is available to switch to a new actuator, the failure must be sensed. Four types of sensing mechanisms are shown in Figure 2-50. Two of these measure gimbal excursion directly; a third measures the actuator error signal (comparing command and response); and a fourth method measures the vehicle angular acceleration resulting from an uncorrected failure. All the sensors degrade system reliability, and all require a time period to fully verify a true failure. Because the actuator sensor is highly sensitive to system biases, it could give a false failure indication. The angular accelerometer sensor would not produce a failure indication for the eight actuator configuration, since the system automatically corrects. The two gimbal angle sensors may produce many false failure indications during the course of normal flight. For this reason, it was concluded that the pilot would provide the best failure sensor system.

EFFECTIVE FOR WHICH  
ACTUATOR CONFIGURATION?

DIAGRAM

DESCRIPTION



GIMBAL LIMIT SENSOR  
(HARDOVER ACTUATOR ONLY)

ACTUATOR ERROR SIGNAL  
SENSOR (ACTUATOR STUCK  
AT ANY POSITION)

GIMBAL ANGLE SENSOR  
(CONTINUOUS INDICATION)

ANGULAR ACCELERATION SENSOR  
(NEAR HARDOVER ACTUATOR ONLY)

ALL

ALL

ALL

FOUR 2-IN-A-CAN  
TRANSLATING TVC

Figure 2-50. Actuator Failure Sensors

## SYSTEMS MECHANIZATION

### INTRODUCTION

During control system mechanization studies, the characteristics and availability of components were investigated. The results are summarized below.

1. Throttle hand controller - After a tradeoff study was performed between hardwire, hydraulic, and electrical systems, a hardwire system was chosen that combined simplicity and minimum weight.
2. Rotational hand controller - The Apollo Command Module and Lunar Module hand controller was chosen because it was quite suitable for the LFV functions and because it represented minimum development cost and time.
3. Actuators - Electromechanical actuators were chosen as a result of a vehicle survey. The Minuteman III P106A actuator was considered a good candidate with certain modifications to increase response and for man-rated applications.
4. Control unit - The control unit functions follow the general concept developed for Apollo. The stability augmentation system has redundancy features to provide adequate reliability.
5. Other electrical components - These include rate gyros for use both in the stability augmentation system logic and in attitude displays. An accelerometer, strain gauges, optical pickup, and pressure transducers are used for display sensors.

### GIMBAL COMMAND HISTOGRAM

FIGURE 2-51 represents a histogram of LFV gimbal actuator activity taken from LAD visual simulator runs. A total of thirty-two runs were used. Three ATO pilots participated in testing the stability augmented control system. Since the objective was to determine large excursion



32 RUNS USED  
3 PILOTS  
 $0.55 \leq \frac{\ddot{\theta}}{I} \leq 3.6 \frac{\text{RAD}}{\text{SEC}^2\text{-RAD}}$   
TWO PITCH PLANE ENGINES FOR CONTROL

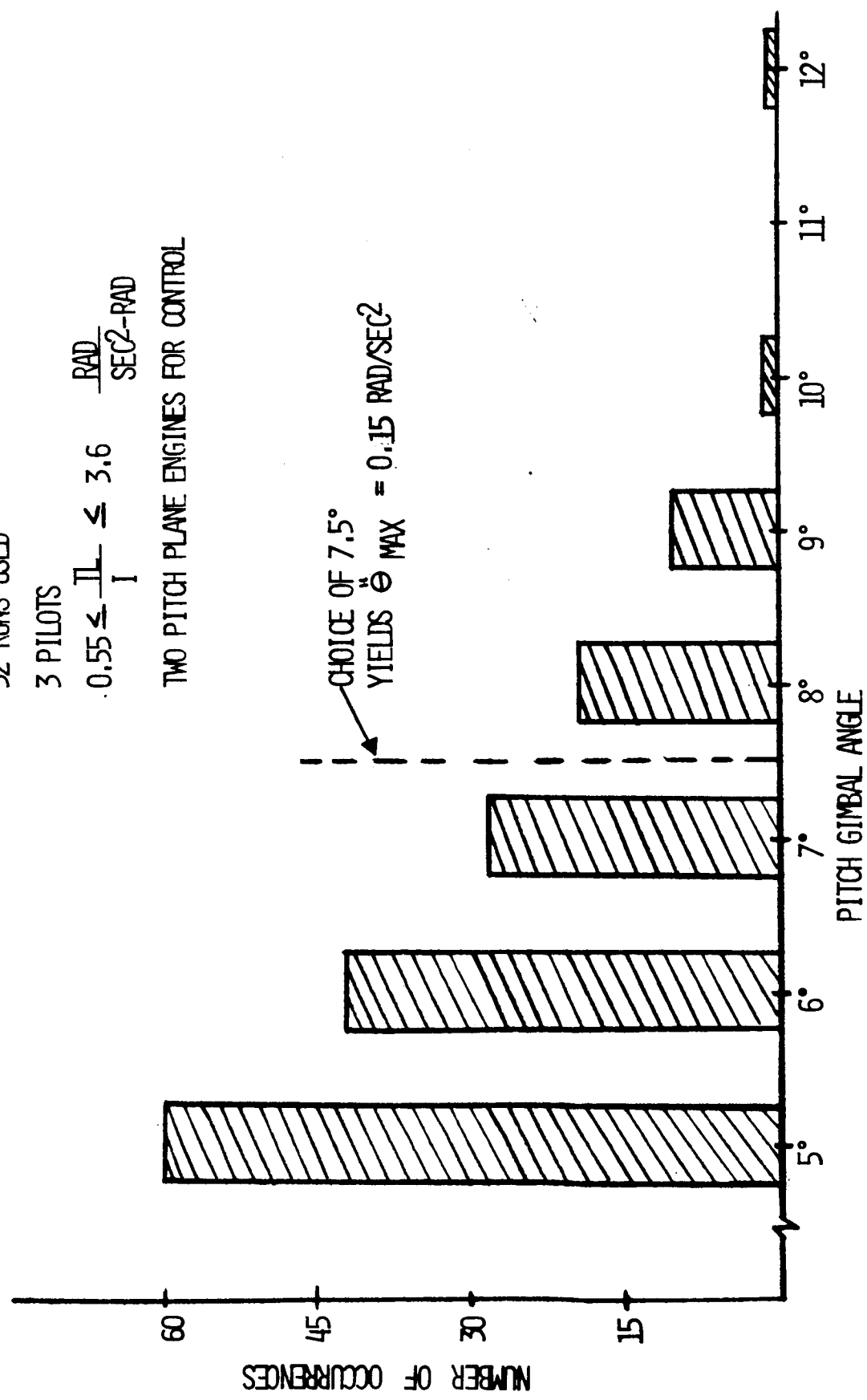


Figure 2-51. Histogram of LfV Gimbal Requirements From LAD Flight Simulator



gimbal activity, data under 5 degrees was not recorded. The data presented here is for the LFV pitch plane, employing two gimbal engines. The runs reduced are tabulated in TABLE 2-21, while ranges of thrust, moment of inertia, and the center-of-gravity lever arm used on the simulator are shown in TABLE 2-22.

Determination of gimbal-angle excursion requirements for a manned vehicle requires extensive simulation data with heavy emphasis on failure conditions. The simulator data available for this study involved nominal flight (with the exception of one engine failure run) and FIGURE 2-51 should be interpreted in that vein.

It will be noted that 7.5 degrees of gimbal angle includes virtually all of the commands encountered. Should the gimbal be limited at 7.5 degrees, no adverse effects will be seen since higher demands are met by limiting the gimbals over a short time period. An angular acceleration corresponding to the maximum gimbal angle is obtained from the moment equation. Simulator thrust and moment arm data combined with the 7.5 degrees results in a value of 0.15 radians per second squared.

## SUBSYSTEM STUDIES

### Throttle Hand Controller

The pilot will control the thrust level of the engines by rotating a throttle with his left hand. It is important that the throttle design does not include a single-point failure. To ensure proper design, there must be individual engine shutoffs at the hand controller plus a method for ensuring that the failure does not prevent the fuel and oxidizer flow to the engine from being shut off. Data from the visual simulation shows that a throttle hand controller which rotates 150 degrees will provide adequate sensitivity if the throttling ratio is 5.3:1. The maximum controller torque that can comfortably be accepted by the pilot is approximately 10 inch-pounds. A summary of those ground rules is given in TABLE 2-23.

Several mechanization approaches for the throttle and linkage are possible, all employing an ability to shut off all engines simultaneously by rotating the throttle past a detent on the minimum thrust end of the range. All approaches similarly require prevalves for cutoff of individual engines, since the main valve may be jammed in the open position. The prevalves and the main valves may, however, be contained in a single package.

The first mechanization approach considered used a cable within a sleeve to transmit commands from the controller to the valves. The stiff-wire cable accommodated compressive motions as well as tensive.

Table 2-21. LFV Simulation Runs Used for Histogram Compilation

Run	3-13-11	2-25-3	2-25-28
	3-13-6	2-25-4	2-19-19
	3-13-7	2-25-5	2-19-20
	3-13-8	2-25-6	2-19-21
	3-13-9	2-25-7	2-19-22
	3-13-10	2-25-8	2-19-26
	2-28-14	2-25-23	2-19-27
	2-28-15	2-25-24	2-19-28
	2-28-16	2-25-25	2-19-29
	2-25-1	2-25-26	2-19-30
	2-25-2	2-25-27	

Table 2-22. LFV Parameters Used on LAD Visual Simulator

	Full	Empty
Weight (Earth lb)	907.5	597.8
$l_{cg}$ (ft)	1.57	2.357
$I_{Roll}$ , slug ft <sup>2</sup>	194.7	117.3
$I_{Pitch}$ , slug ft <sup>2</sup>	150.3	112.0
$I_{Yaw}$ , slug ft <sup>2</sup>	77.6	29.4
Thrust, Max. #	360	360
Thrust, Min. #	68	68

Table 2-23. Throttle Hand Controller

Groundrules
1. Single hand controller only
2. No single point failure past hand controller
3. Individual linkage shutoffs required at hand control
4. Propellant shutoff required (prevalves) to guarantee engine shutoff
5. Actual torque requirements dependent on test Apollo system requires 10 to 11 in. /lb with spring-loaded system
Simulator requirements very low, <1 in. /lb
6. Required sensitivities available in 150 to 180 degrees

FIGURE 2-52 schematically shows that rotary motion of the controller produces translational motion of four cables within sleeves. The main valves are located at the other end of the cables. Each cable may be disconnected at the controller if an engine fails or if the main valve or cable fails. Not shown is the connection between the individual cutoffs and the prevalves. Operating an individual engine cutoff therefore removes a complete control link from the system.

The throttle may also be mechanized using electrical power. FIGURE 2-53 shows the electrical schematic, including four proportional transducers at the controller, individual engine cutoffs (manually operated circuit breakers), and valve actuators to move the main fuel and oxidizer valves. The prevalves are also operated by the circuit breakers in a manner similar to that described for the cable system.

A third mechanization of the throttle employs hydraulic pressure to transmit the controller signals. Three versions of the hydraulic method are shown in FIGURE 2-54, the first of which uses spring bellows with two completely isolated hydraulic systems. When the throttle is rotated once, the master bellows is compressed, the other expanded. Compression or expansion of a master bellows causes expansion or compression of a slave bellows at the main valve. At any steady-state position, the combination of throttle hand controller force and master bellows spring force is balanced

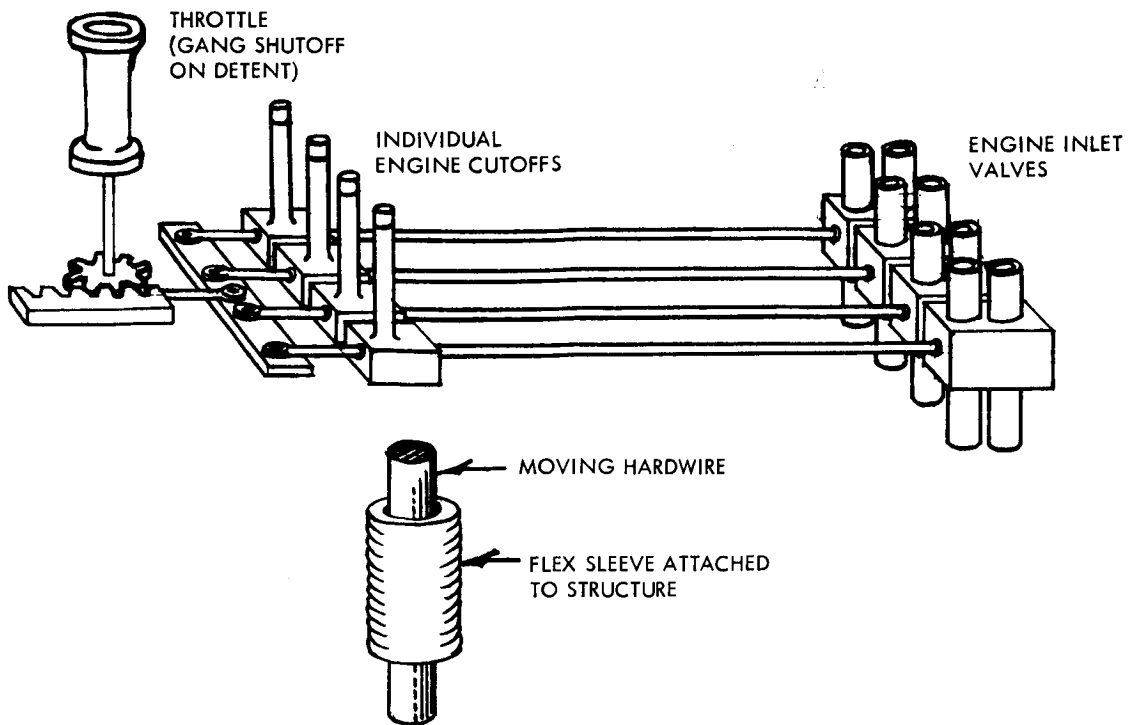


Figure 2-52 . Cable Mechanization of Throttle

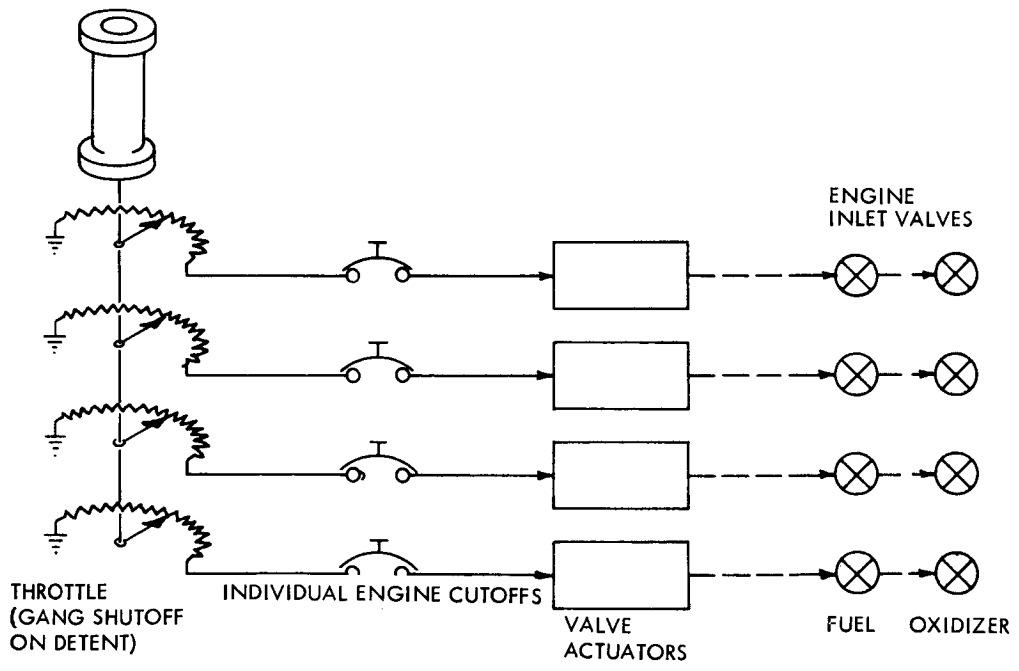


Figure 2-53 . Electrical Mechanization of Throttle

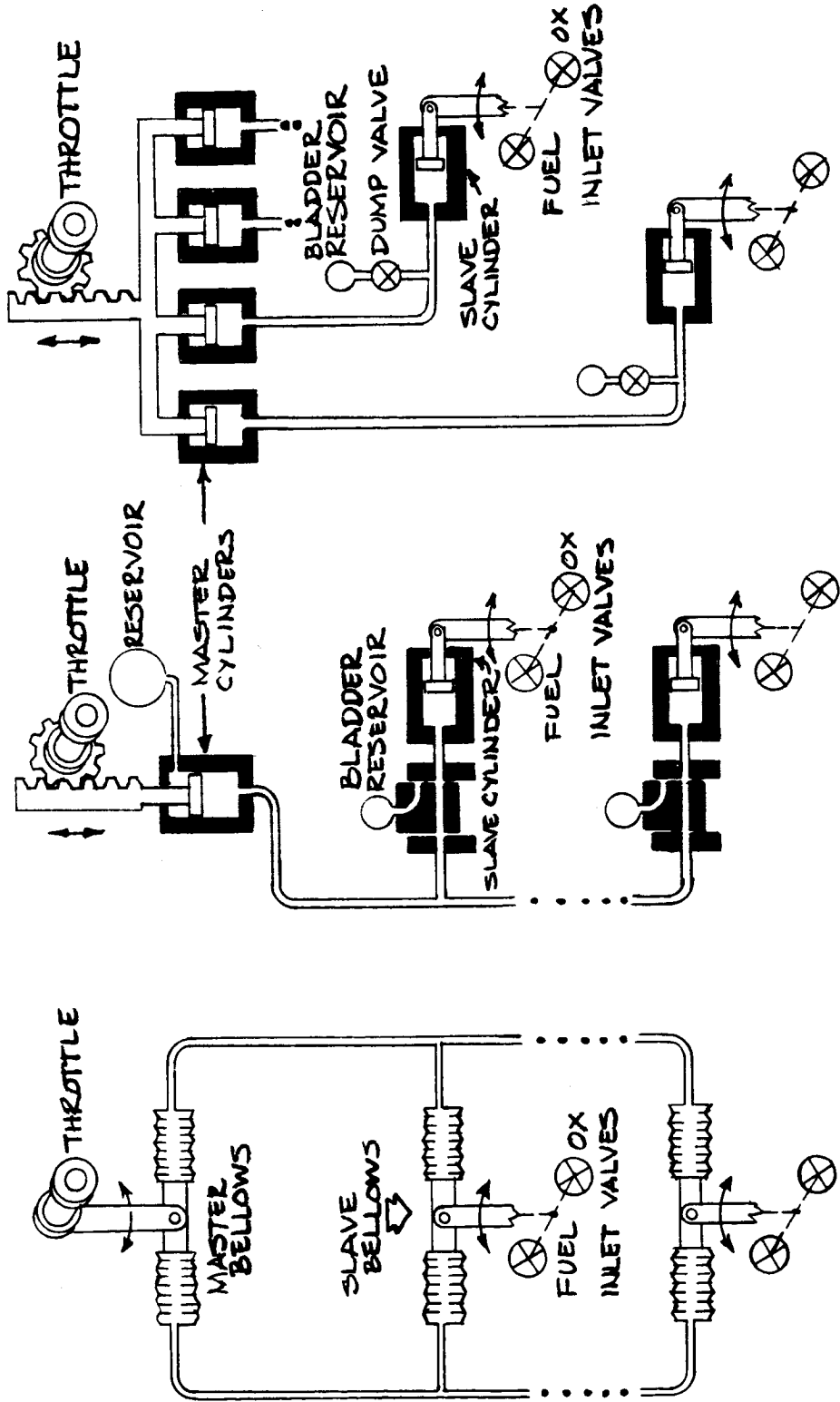


Figure 2-54. Hydraulic Mechanization of Throttle, Gang Shutoff on Throttle

by the combined inlet valve force and slave bellows spring force. If a leak appears in one hydraulic line, a bias force is applied to the controller by the remaining operative line and the spring of the failed line master bellows. The system would be designed to minimize such bias force. Prevalves for individual engine shutoff are operated by a separate system.

The second hydraulic system uses one master cylinder and four slave cylinders, one for each engine set of main valves. Operation of the controller allows additional fluid to flow into the lines from a reservoir, maintaining constant pressure against leakage. If a slave cylinder fails in any manner, an individual engine cutoff is provided, relieving the pressure on the slave cylinder and plugging the line upstream of the cylinder. Operation of a cutoff would also close the prevalves of that engine. A single-point failure exists in that the main hydraulic line may leak.

The third hydraulic system employs four master cylinders and four slave cylinders. Each main valve is controlled by a separate hydraulic line operated by its own master cylinder. A failure of any type will not change the remaining system. In case of a failure, the individual line is dumped into a bladder reservoir and the prevalves are closed.

Each of the five mechanization methods discussed allow the pilot to attempt using the failed system on the return flight by simply resetting the cutoff switch.

The major differences between the three types of systems are summarized in TABLE 2-24. The electrical system, although readily adaptable to shaping network compensation should this appear feasible in the the future, is much heavier than either the cable or the hydraulic systems. Advantages and disadvantages of the cable and hydraulic methods are nearly equal. However, the cable method is recommended, since it offers a slightly simpler and more commonly used state-of-the-art for space use than does the hydraulic method.

#### Rotation Hand Controller

The LFV stability augmentation system requires a hand controller to permit attitude command inputs by the astronauts. Functional requirements for this hand controller are very similar to those for Apollo, making it reasonable to recommend the Apollo hand controller, modified for LFV use. The most important advantage of this controller is that extensive human engineering design effort to assure satisfactory operation by pressure-suited astronauts has already been accomplished.

Table 2-24. Throttle Hand Controller Major Differences

<ul style="list-style-type: none"> <li>● Electrical           <ul style="list-style-type: none"> <li>Requires external power</li> <li>Requires actuators — heavy (2 pounds each)</li> <li>— development program</li> </ul> </li> <li>Most adaptable for use of shaping networks</li> </ul>	<ul style="list-style-type: none"> <li>● Hydraulic           <ul style="list-style-type: none"> <li>Earth systems well developed</li> <li>Temperature problems possible with fluid and lines</li> </ul> </li> </ul>	<ul style="list-style-type: none"> <li>● Cable           <ul style="list-style-type: none"> <li>Simple mechanical linkage</li> <li>Effects of space environment must be incorporated — cold welding, lubricant vaporization, thermal expansion</li> </ul> </li> </ul>	<ul style="list-style-type: none"> <li>● Conclusion:           <ul style="list-style-type: none"> <li>Hydraulic and cable systems equivalent (power, weight)</li> <li>Cable system chosen because of simplicity</li> </ul> </li> </ul>
--	---	---	--

The unit, as shown in FIGURE 2-55, has an acceptable mean time between failures (83,000 hours) for LFV and is dynamically balanced. The following modifications will be required to adapt the Apollo hand controller to LFV use:

1. Rework bracketry and repackage for lunar flyer mounting
2. Remove RCS "Direct" switches
3. Redesign and requalify the interior of the Apollo command module to accommodate difference in the LFV environments. These differences include temperature, solar radiation, and dust. Changed solar radiation environment would require changes in the elastomeric materials.
4. Modify existing RCS control switches deadband width for LFV attitude/attitude rate switching functions.
5. Install redundant press-to-talk switching function in existing location.

The controller is described in the NR-Honeywell Apollo SCS Procurement Specification, NR-SD Specification No. MC901-0594, "Stabilization and Control Subsystem," 25 May 1967, pages 39-40, 100-101, 135-138, PDC No. 1, pp 18, 28, and in FIGURE 2-55. Additional governing MIL specifications, quality assurance provisions and packaging, are called out in the specification, and should be used until suitable LFV exceptions have been established.

The Rotation controller is a spring-restrained hand grip that moves in either direction about each of three orthogonal axis corresponding to pitch, roll and yaw of the vehicle. Each axis includes the switches and transducers necessary to initiate such control commands as acceleration and attitude rate.

Proportional control is provided by rotational variable differential transformers (RVDT's) in each axis that generate an output voltage proportional to the angular displacement of the grip. Depending on the direction of grip displacement from neutral, this output voltage is either in-phase or out-of-phase with the reference excitation voltage.

Detent switches located at discrete points within the grip's range of rotation provide auxiliary control functions. At a deflection of about one and one-half degrees is a detent switch used to switch the mode of operation of the control system during maneuvers.



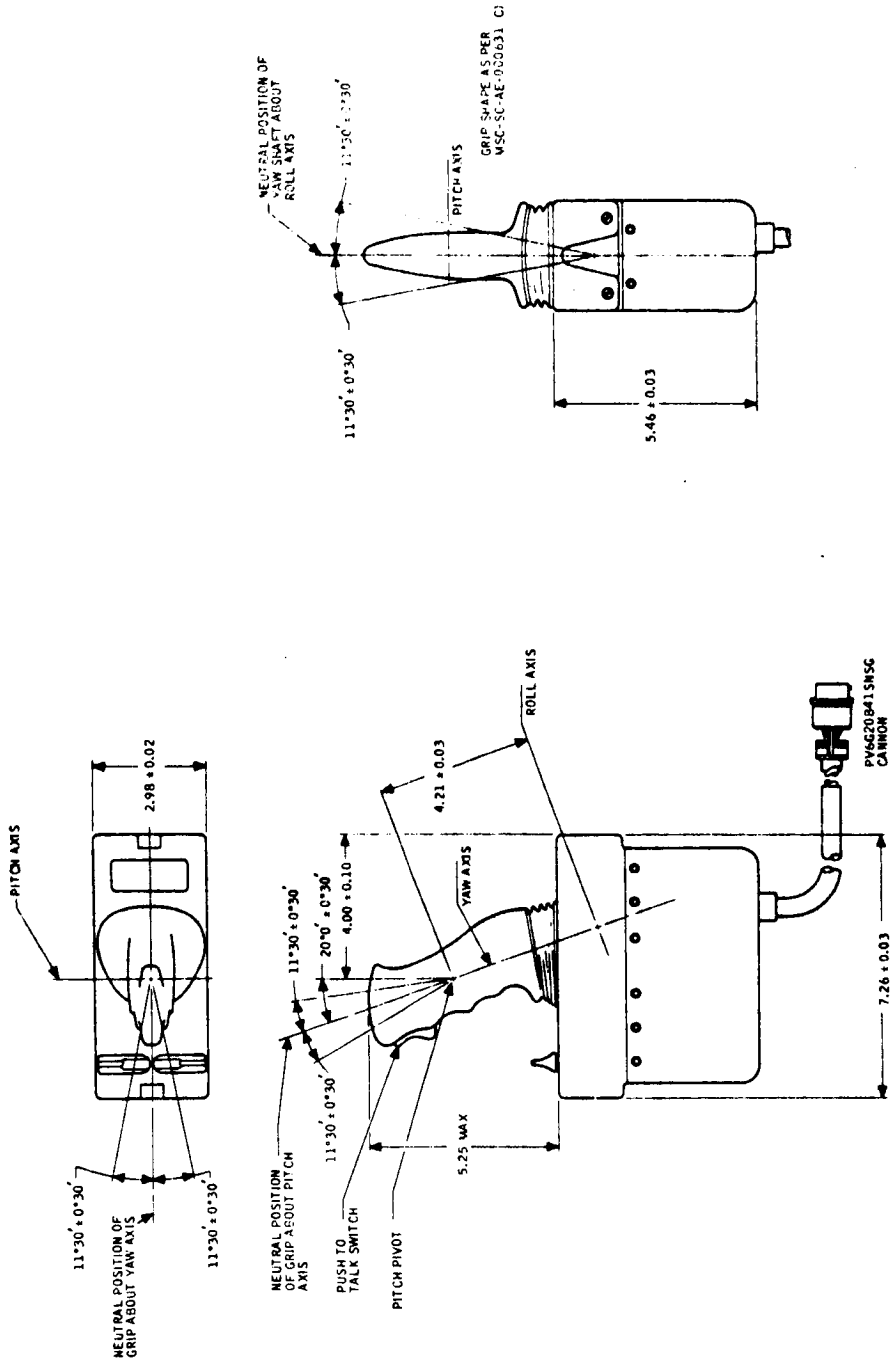


Figure 2-55 . Apollo Rotation Hand Controller

Beyond the soft stops that define the normal limit of proportional control, additional switches may be actuated for emergency control. A trigger switch operated by the index finger is also included on the hand grip for control of such auxiliary systems as communications.

Typical characteristics of force versus displacement are shown in TABLE 2-25. The rotation controllers, developed and tested to meet the stringent requirements of the Apollo Block II Lunar Mission, are designed to withstand and operate in the following environments:

- Temperature - 0 to 150F
- Shock - 20g, 11 milliseconds
- Vibration - Random profile  $0.06g^2/cps$  76 to 2000 cps
- Acceleration - 20g any axis
- Humidity - 95 percent
- Pressure -  $10^{-4}$  min Hg

Table 2-25. RHC Characteristics

Axis	Pitch	Roll	Yaw
Break-out Torque (lb-in)	7.0	5.0	4.5
Torque to reach soft stop (lb-in)	23.5	14.0	13.0
Torque to leave soft stop (lb-in)	38.5	25.0	18.5
Torque to reach hard stop (lb-in)	43.5	28.0	20.0
Soft stop displacement (degree)	10	10	10
Hard stop displacement (degree)	11.5	11.5	11.5

## Actuator Requirements

An analysis of thrust vector control methods was conducted to determine its applicability to the LFV. The results, detailed in the propulsion section, showed that bipropellant reaction control systems and gimballed systems were both acceptable. However, from the standpoint of overall vehicle reliability, controlability, and weight minimization, the system with four engines and eight actuators was chosen for the final vehicle configuration. A survey of actuators for vehicles having roughly the same control parameters was completed and is also contained in the propulsion section. This survey revealed that all previous similar vehicles on which data was available used electromechanical actuators, and subcontractor discussions with Cadillac Controls, TRW, and Autonetics confirmed this choice. A brief calculation of system requirements for open-loop hydraulic actuators revealed that an excessive dumping of fuel would be required attributable mainly to the relatively low pressure available in the ullage and to the leakage required by normal system design. Additional plumbing would also be required to bring the fuel to the actuators. Closed-loop actuators, using an independent working fluid, would be heavy and would require considerable time and resources for space qualification.

The actuator survey showed that an existing actuator in use on the P106A Minuteman III could be modified for use on the LFV. This actuator and its major components are shown in Figure 2-56. Its characteristics for LFV use are shown in Table 2-26, as worked out by Space Division and Autonetics in discussions during the Resource Planning phase of the contract. The specific modifications for LFV use are shown in Table 2-27. Since the P106A is a completely geared system, it was also desirable to investigate a clutch-type system. The development of a service module SPS-type actuator was discussed with Cadillac Controls of Costa Mesa, California, the same company that developed the SPS actuator system. These discussions revealed that (1) a clutch-type system was within the state-of-the-art; (2) its weight would roughly equal that of the geared system (P106A); (3) the clutch system could be built with a higher response rate than the P106A; and (4) the cost and development time for a clutch system was far greater than the P106A because the system program would essentially develop an entirely new system.

For the foregoing reasons, and, especially because of reason 4, the geared system (P106A modified) was chosen.

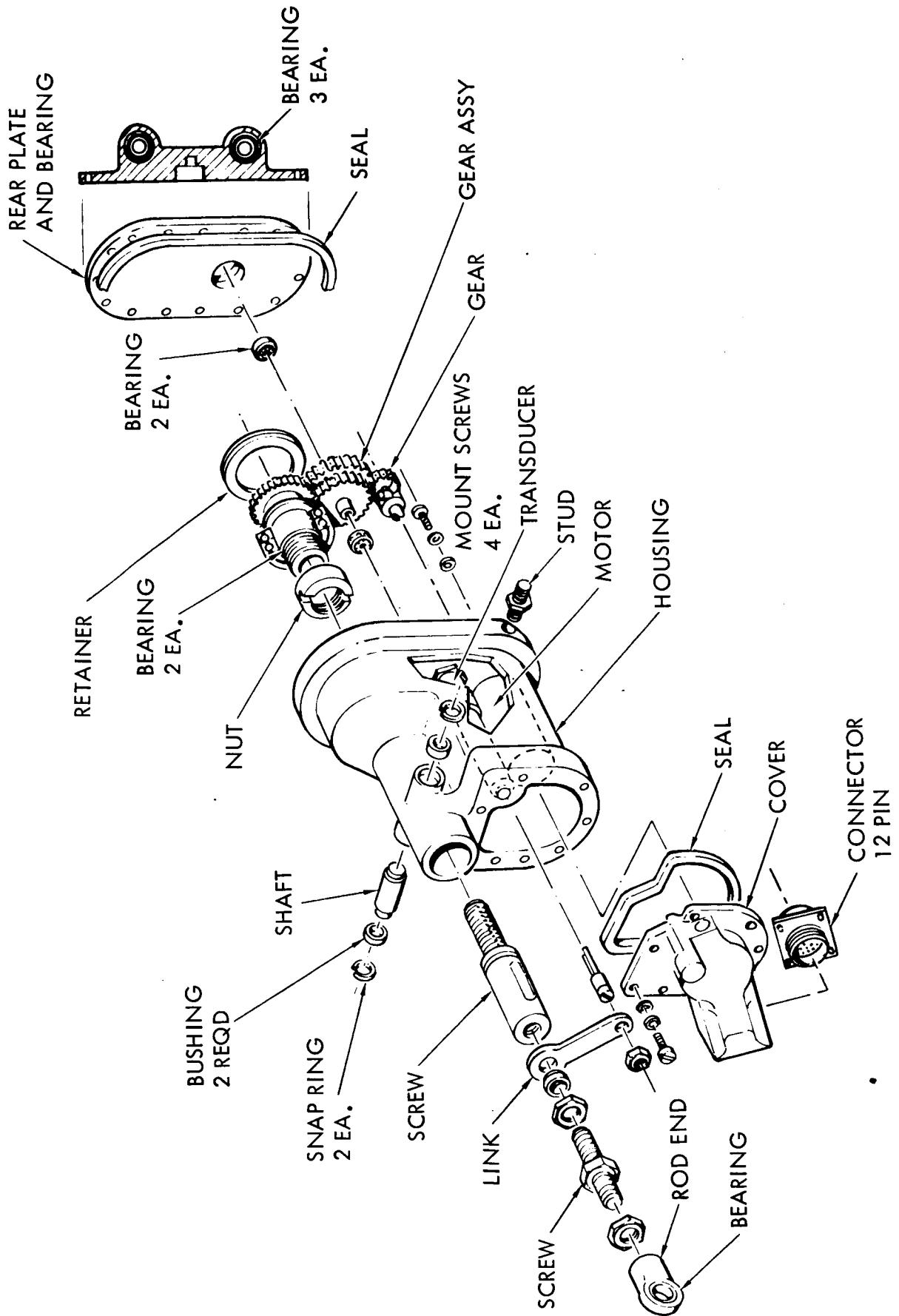


Figure 2-56 . Minuteman II (P106A) Actuator

Table 2-26. Actuator Characteristics

Characteristics	Limits
<p>Electrical requirements</p> <p>Motor</p> <ol style="list-style-type: none"> <li>1. Actual voltage, rated</li> <li>2. Actual voltage, starting</li> <li>3. Current, locked rotor at <math>25.4 \pm 0.1</math> V dc.</li> <li>4. Current, locked rotor at <math>31.1 \pm 0.1</math> V dc</li> <li>5. Input resistance</li> <li>6. Insulation resistance               <ul style="list-style-type: none"> <li>Motor leads to</li> <li>Chassis at <math>50 \pm 5</math> V dc</li> <li>Transducer leads to</li> </ul> </li> </ol> <p>Linear position transducer</p> <p>Excitation voltage</p> <p>Frequency power consumption</p> <p>Output load resistance</p> <p>Scale factor</p> <p>Linearity</p> <p>Null voltage</p> <p>Null position</p>	<p>0 to +31 V dc each coil</p> <p>17 V or less over operating range</p> <p>1.30 ampere, max</p> <p>1.62 ampere, max</p> <p>20 ohms minimum locked rotor</p> <p>&gt;25 megohms</p> <p>&gt;100 megohms</p> <p>Linear variable differential (transformer type)</p> <p><math>26.0 \pm 1.3</math> V peak sinusoidal or square wave</p> <p><math>400 \pm 2</math> cps</p> <p>2.0 volt-amp maximum</p> <p><math>4000 \pm 40</math> ohms, 5% change of scale factor at <math>2000 \pm 20</math> ohms</p> <p><math>0.877 \pm 0.009</math> V per volt per inch</p> <p><math>\pm 1.0</math> percent of <math>\pm 0.05</math> vac., whichever is greater</p> <p>0.025 vrms maximum</p> <p>Within <math>\pm 0.002</math> in. of actuator inner stroke</p>

Table 2-26. Actuator Characteristics (Cont.)

Characteristics	Limits
Mechanical output requirements	
General	Unit sealed for 7 days of vacuum operation design goal - available for reuse after 6 months lunar storage.
Stroke	1.000 ± 0.01 in. limited by mechanical steps
Length	The overall length of the equipment, from center of rear mounting hole to center of operating rod mounting hole, when fully retracted against the mechanical stop shall be capable of adjustment to any dimension within the range of 5.680 ± 0.100 in. with an adjustment accuracy of +0.0025 in. The adjustment of the overall length shall not effect the adjustment of the position transducer.
Boost phase holding load	(TBD) pounds
Maximum load torque	100 in.-lb with 3.5 in. moment arm
Backlash	The equipment backlash shall not exceed 0.004 in. of stroke. The maximum change of actuator length due to the effects of loads shall not exceed the backlash value.
Dynamic response	5 cps - min 10 cps - design goal
Attachment bearing torque	0.5 in.-lb, maximum in any direction
Flight duty cycle	2 hours total operation. No single continuous use greater than 400 sec
Weight, including loose equipment	2.5 lb max 2.0 lb design goal

Table 2-27. Proposed Modification to MMIII Actuator

<ul style="list-style-type: none"> <li>● Response Rate Increase</li> </ul> <p>Replace dc split-series motor with dc torque motor</p> <p>Decrease gear ratio from motor to acme screw</p>
<ul style="list-style-type: none"> <li>● Sealing for Space Use</li> </ul> <p>Add o-ring and silicon grease groove to acme screw</p> <p>Replace butyl seals with viton A for seals and o-rings</p> <p>Shorten stroke from 1.2 inch to 0.90 inch to accommodate seals</p> <p>Add gas filler screw for addition of 10% He and 90% N<sub>2</sub> @ 16 psia</p> <p>Seal transducer internally</p> <p>Change rubber grommated connector to glass bead</p>
<ul style="list-style-type: none"> <li>● Cold Welding Prevention</li> </ul> <p>Apply lub-lok 4306 to metal-to-metal surfaces</p> <p>Add lubeco liner to end bearings</p>
<ul style="list-style-type: none"> <li>● Weight Reduction</li> </ul> <p>Replace steel (-71) covers with aluminum (-61) covers</p>

### System Functional Flow Description

In the process of analyzing failures, functional flow diagrams for the controls, displays, propellant, and propulsion subsystems were generated in preliminary form. These were later finalized to the degree necessary for specifying the subsystems to prospective subcontractors. Figure 2-57 shows the total electrical power and signal distribution system. In addition to the electrical inputs to the display panel, there are also mechanical individual engine shutoff switches and optical fuel and oxidizer meters.

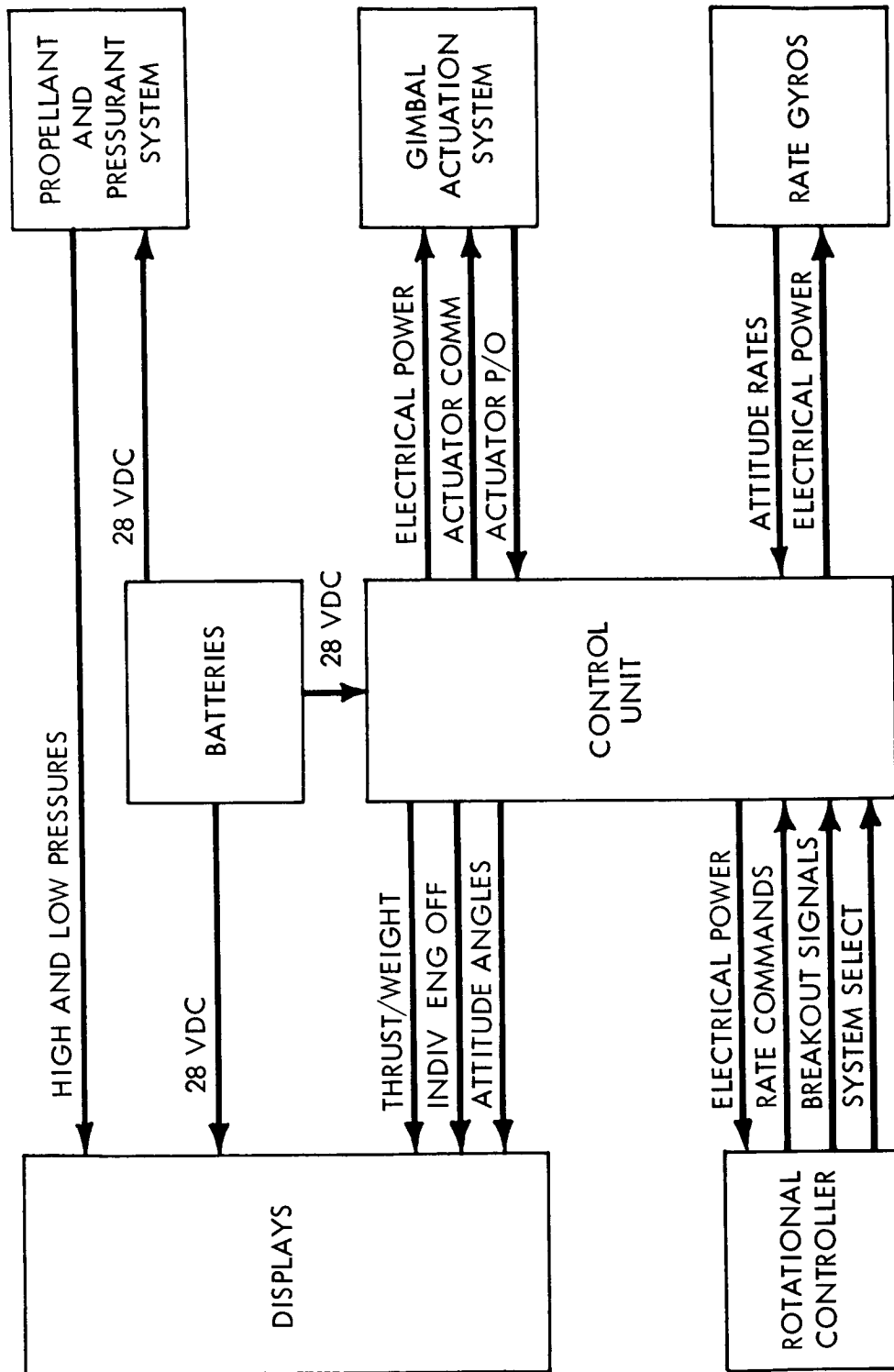


Figure 2-57. Electrical Power and Signal Flow Diagram



## Control Unit

The functional flow diagram for the control unit is shown in Figure 2-58. Roll, pitch and yaw rate commands and their redundant counterparts are produced by the modified Apollo rotation controller. Electrical characteristics of these signals are the same as used for Apollo. The maximum signal in any axis is  $\pm 10$  degrees per second. Roll, pitch, and yaw breakout commands and their redundant counterparts are also produced by the modified Apollo rotation controller, and have the same electrical characteristics as for Apollo. Breakout signals are constant voltage indications of controller deflections greater than  $\pm 0.25$  degrees. The "press-to-talk" trigger on the Apollo rotation controller has also been modified for use in redundant mode switching, allowing the pilot to switch a complete three-axis stability augmentation system out of the control loop and to switch the standby system in.

Figure 2-59 shows that the mode switch gives the pilot a completely redundant control system, from the rotation controller through to the engines. Each of the stability augmentation systems will command all of the eight servoactuators, any one of which is redundant. Any single engine is also redundant.

The extension or retraction position of each of the eight actuators is measured by a position pickoff transducer and summed with the actuator command signal at the driver amplifier. The maximum pickoff voltage is 1 volt. Depending on the type of actuator selected for production, a rate feedback pickoff may also be necessary.

Equations for the internal logic of the control unit are given in Table 2-28, and nomenclature list is presented in Table 2-29. It may be noted that the stability augmentation system used an attitude-hold circuit that is de-energized by the breakout signals. Complete logic diagrams of the control unit down to component level, are given in Figures 2-61 and 2-62.

## Rate Gyro Packages

Figure 2-58 also indicates that roll, pitch, and yaw rate gyro signals and their redundant counterparts are produced by the rate gyro packages. The two redundant sets supply separate stability augmentation systems with feedback signals. The rate gyros also supply signals to the Euler angle logic that drives the display panel attitude indicators. Maximum nominal angular rates expected of the vehicle are  $\pm 10$  degrees per second about any axis.

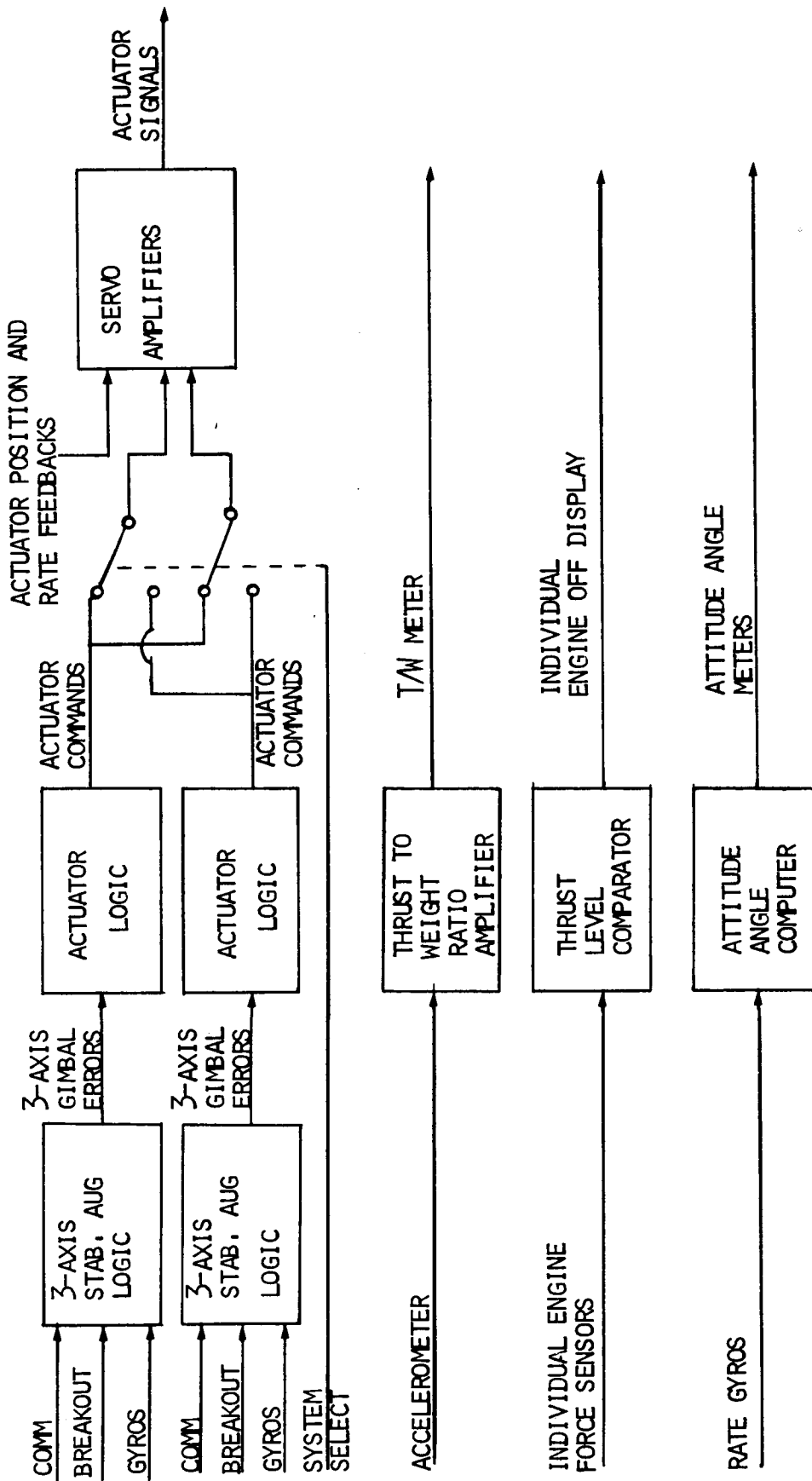


Figure 2-58. Control Unit Flow Diagram

ELECTRICAL ATTITUDE LOOPS  
 ELECTRICAL AND OPTICAL DISPLAYS  
 HARDWARE (MECHANICAL) THROTTLE  
 ELECTRICAL REDUNDANCY WHERE FEASIBLE TO ELIMINATE  
 SINGLE POINT FAILURES  
 TIME CRITICAL FAILURES

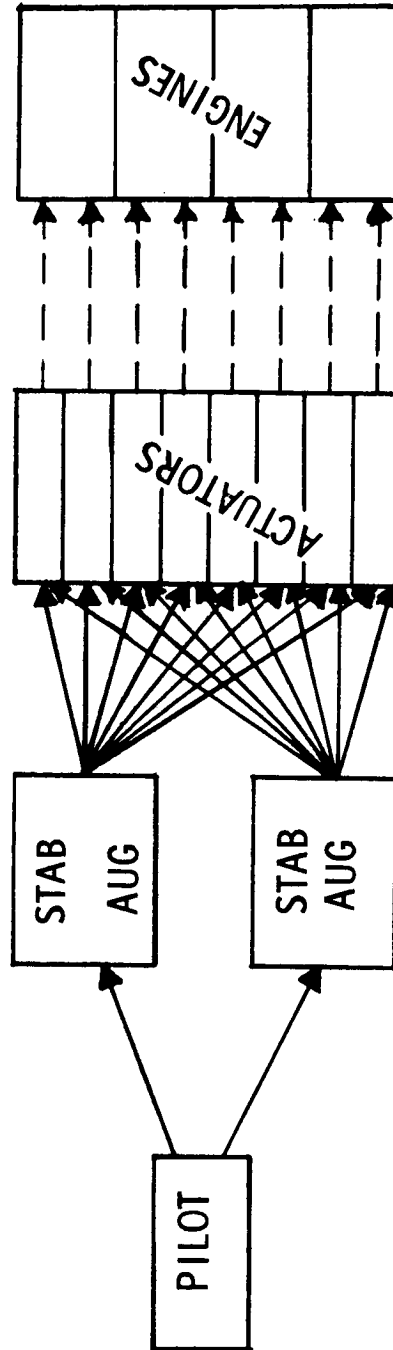


Figure 2-59. LFV Power and Signal Flow

**Table 2-28. Matrix of Linearized, Pitch/Roll Plane Equations of Motion for Hardwire Geometry**

Stability Augmentation:

$$\delta \phi = \begin{cases} \delta \phi_c - K_\phi p, & \delta \phi_c \neq 0 \\ -K_\phi p - K_\phi \int_0^t p dt, & \delta \phi_c = 0 \end{cases}$$

$$\delta \psi = \begin{cases} \delta \psi_c - K_\psi r, & \delta \psi_c \neq 0 \\ -K_\psi r - K_\psi \int_0^t r dt, & \delta \psi_c = 0 \end{cases}$$

$$\delta \theta = \begin{cases} \delta \theta_c - K_\theta q, & \delta \theta_c \neq 0 \\ -K_\theta q - K_\theta \int_0^t q dt, & \delta \theta_c = 0 \end{cases}$$

Actuator Logic:

$$\begin{aligned} \delta \phi_1 &= \delta \phi - \delta \psi & \delta \theta_1 &= \delta \theta + \delta \psi \\ \delta \phi_2 &= \delta \phi + \delta \psi & \delta \theta_2 &= \delta \theta + \delta \psi \\ \delta \phi_3 &= \delta \phi + \delta \psi & \delta \theta_3 &= \delta \theta - \delta \psi \\ \delta \phi_4 &= \delta \phi - \delta \psi & \delta \theta_4 &= \delta \theta - \delta \psi \end{aligned}$$

Thrust-to-Weight Ratio Meter Drive:

$$\frac{T}{W} = \left( \frac{1}{g_L} \right) \frac{T}{m_T}$$

Thrust Failure Indication Signals:

$$T_{AVE} = \frac{1}{4} \sum_{i=1}^4 T_i$$

$$T_{\epsilon_i} = T_{AVE} - T_i, \quad 1 \leq i \leq 4$$

$$T_{FAIL_i} = \begin{cases} 1, & T_{\epsilon_i} > \Delta T, \quad 1 \leq i \leq 4 \\ 0, & T_{\epsilon_i} < \Delta T, \quad 1 \leq i \leq 4 \end{cases}$$

Three-Axis Attitude Angle Drives:

$$\phi = \int_0^t \left[ p + \frac{\sin \theta}{\cos \theta} (q \sin \phi + r \cos \phi) \right] dt$$

$$\theta = \int_0^t [q \cos \phi - r \sin \phi] dt$$

$$\psi = \int_0^t \left[ q \frac{\sin \phi}{\cos \theta} + r \frac{\cos \phi}{\cos \theta} \right] dt$$

Table 2-29. Control Unit Logic Nomenclature List

Symbol	Description
$g_L$	Lunar gravitational acceleration
$K_{\phi, \theta, \psi}$	Attitude hold feedback gains in roll, pitch, and yaw axes
$K_{\dot{\phi}, \dot{\theta}, \dot{\psi}}$	Attitude rate feedback gains in roll, pitch, and yaw axes
$M_T$	Total mass of pilot and vehicle
$p, q, r$	Roll, pitch, and yaw body axis rates
$T$	Total thrust
$T_{AVE}$	Average thrust of one engine
$T_{FAIL_i}$	Thrust failure indication
$T_i$	Thrust of $i$ th engine ( $i = 1, 2, 3, 4$ )
$T_{\epsilon_i}$	Deviation of one engine thrust from average
$W$	Total lunar weight of vehicle and pilot
$\delta\phi, \theta, \psi$	gimbal angle commands
$\delta\phi_B, \theta_B, \psi_B$	Rotation controller breakout signals
$\delta\phi_C, \theta_C, \psi_C$	Rotation controller rate commands
$\delta\phi_{1, 2, 3, 4}$	Roll actuator commands for engines 1, 2, 3, 4
$\delta\theta_{1, 2, 3, 4}$	Pitch actuator commands for engines 1, 2, 3, 4

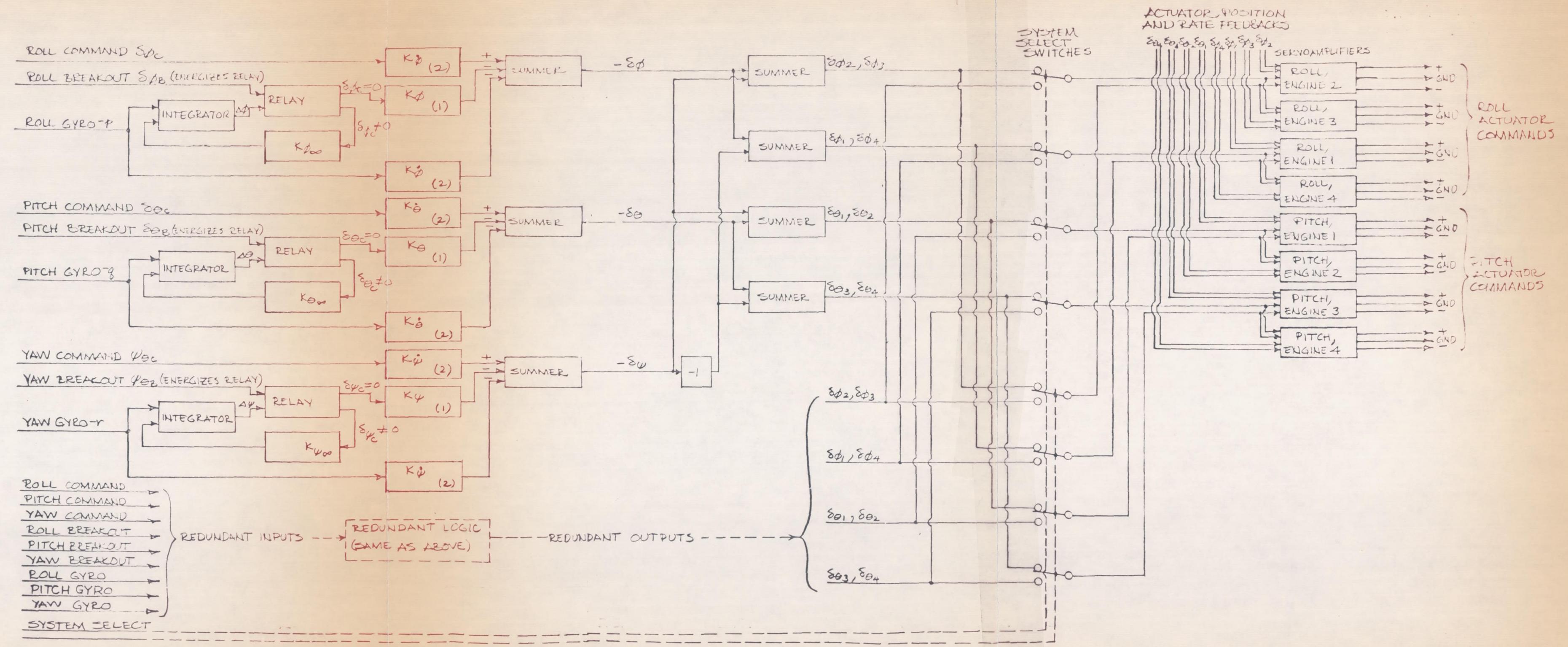


Figure 2-61. LFV Control Unit Flow Diagram, Engine Actuation System Commands

451, 452  
(1)

(2)

## Body-Mounted Accelerometer

The body-mounted accelerometer produces a signal proportional to linear acceleration along the vehicle centerline. When divided by the lunar value of gravity, the drive for the thrust-to-weight ratio meter is developed. Expected values of acceleration for the vehicle lie between 1.2 and 19 feet per second squared.

## Engine Thrust Sensors

Strain gauge sensors located on the mounting rings of each engine produce signals proportional to individual engine thrust. The signals vary as a group according to the thrust level, 17.5 to 115 pounds, and may also vary as a group or individually with gimbal angle. When one engine fails and produces an abnormally high or low thrust compared to the others, the resulting change in the force sensor is used in the control unit to drive displays.

## Electrical Power Distribution

The electrical power distribution from the dual batteries described in Figure 2-57 follows the shortest cabling path. Where other than 28 volts dc is used, power conversion units within the control unit are the distribution points. Complete wiring diagrams, suitable for wire counts, are presented in Figure 2-63 through 2-68.

## Display Panel

As stated in the contract proposal, final decisions on display panel requirements must await further tests. Insufficient data now exists on visual cues obtained from the lunar terrain during various flight phases and differing lighting conditions. The most pertinent data available at the present time is drawn from the visual simulation, data that consists of a priority list of flight variables and vehicle status indications assembled by trained test pilots. Heading the list is the thrust-to-weight ratio meter, as shown in Table 2-9. Fuel and oxidizer meters follow. During the simulation, the only fail mode tested was that of engine thrust loss. Thus, the pilots listed the failure indicators. Other indicators must be provided to permit onboard analysis, including helium bottle pressure and ullage pressure, dual electrical power level and attitude indicators. Attitude indicators also aid in performing more precise maneuvers and in helping the pilot perform his navigational task. This list of displays represents the minimum now considered necessary for safe flight. A preliminary layout of the display panel, located on the left of the pilot slightly beyond the throttle control, is presented in Figure 2-69.

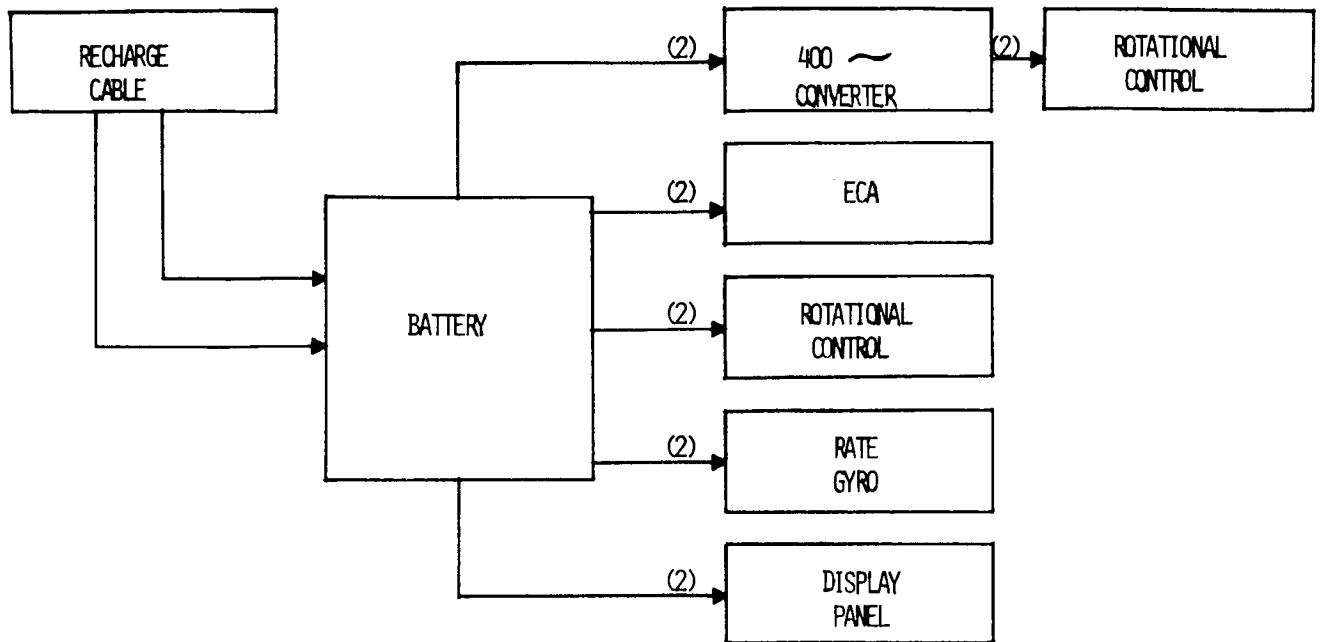


Figure 2-63. Electrical Power Flow Diagram, One Battery

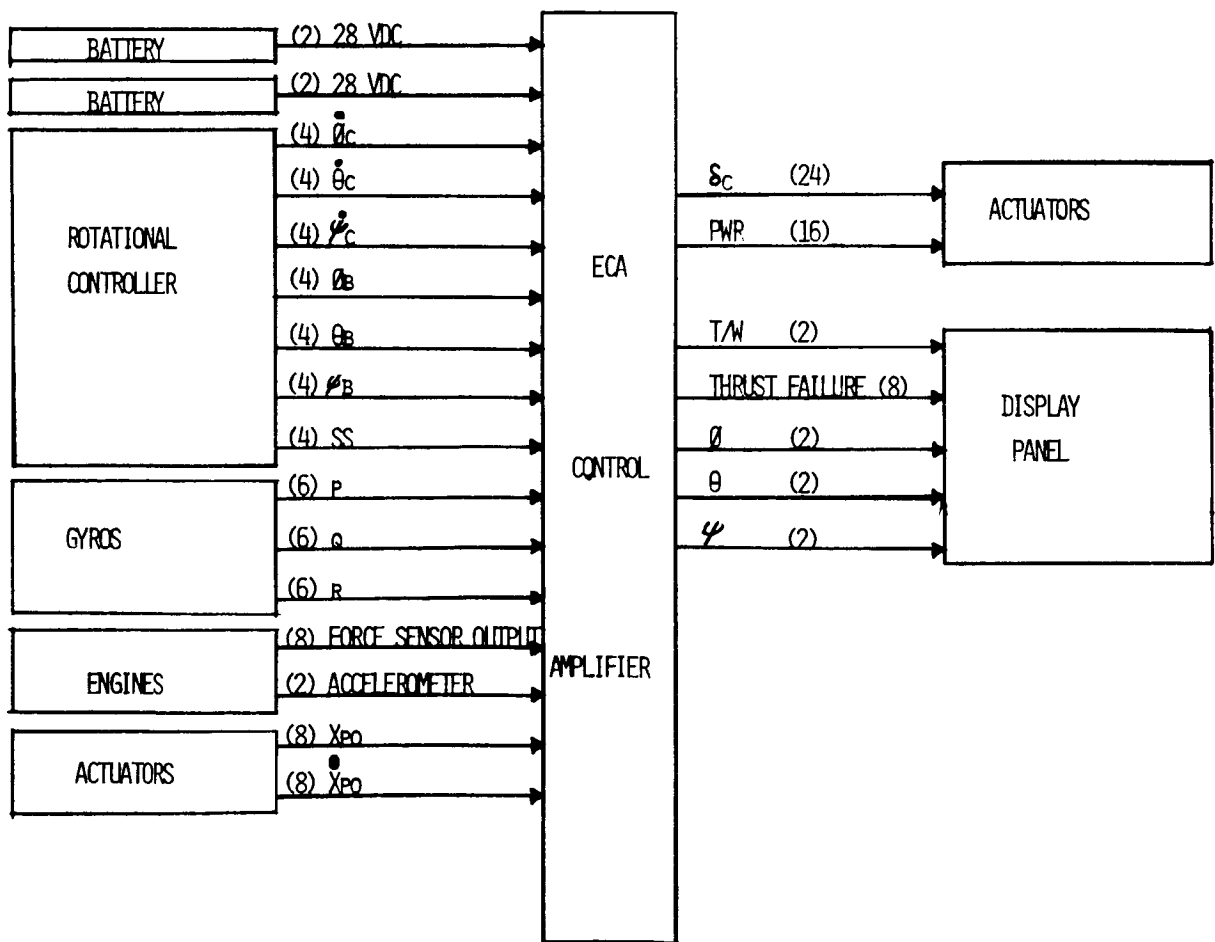


Figure 2-64. ECA Wiring Diagram



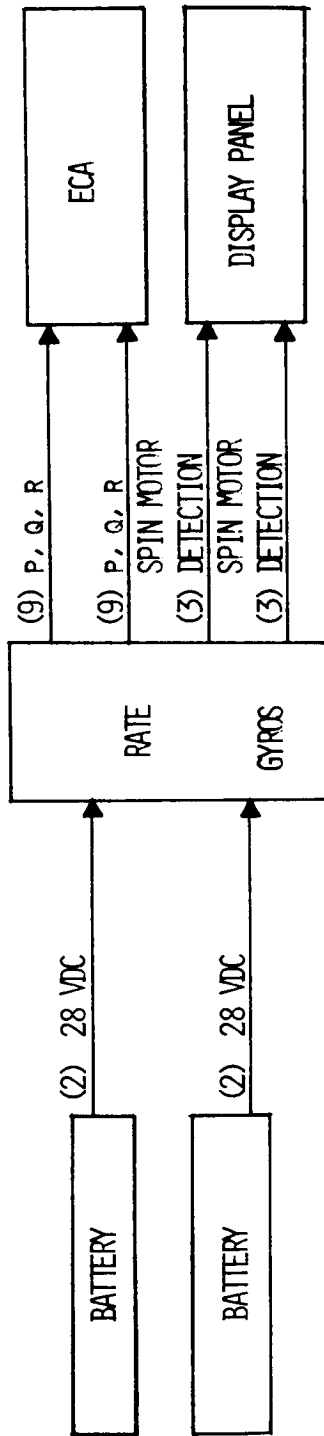


Figure 2-65. Rate Gyro Wiring Diagram

1 ACTUATOR (TYPICAL)  
(EIGHT REQUIRED)

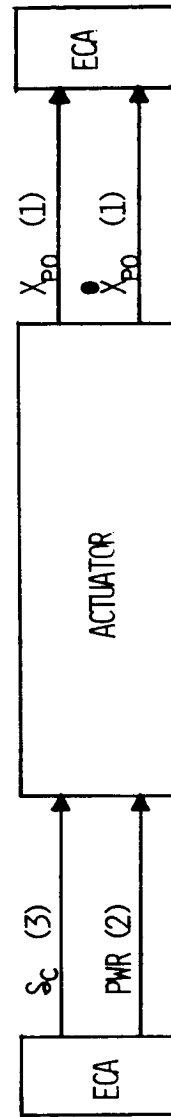


Figure 2-66. Actuator Wiring Diagram

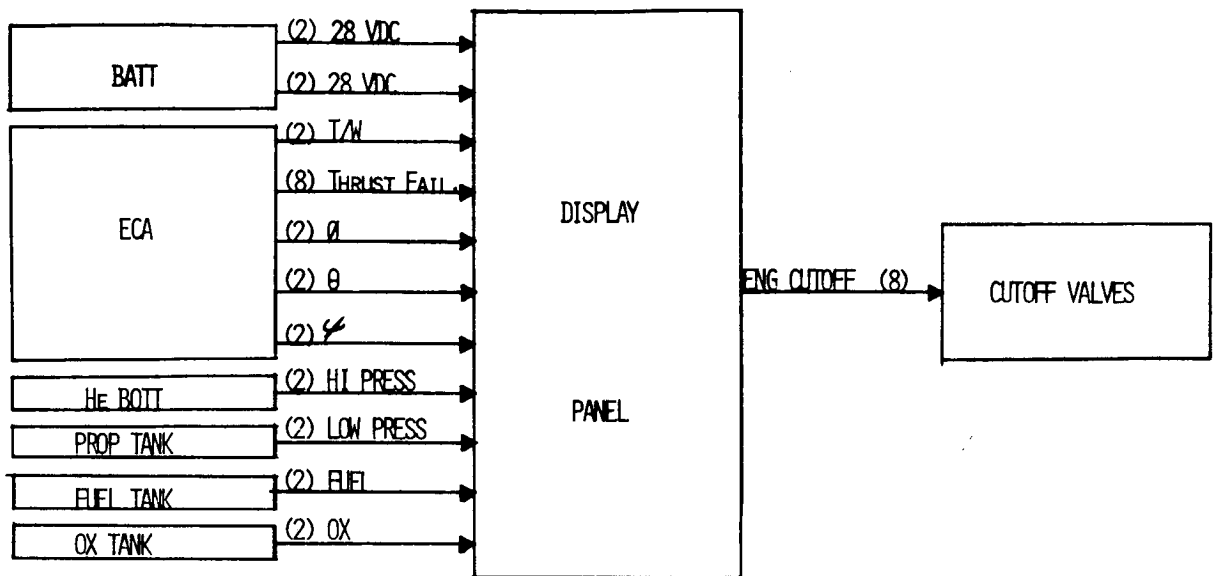


Figure 2-67. Display Panel Wiring Diagram

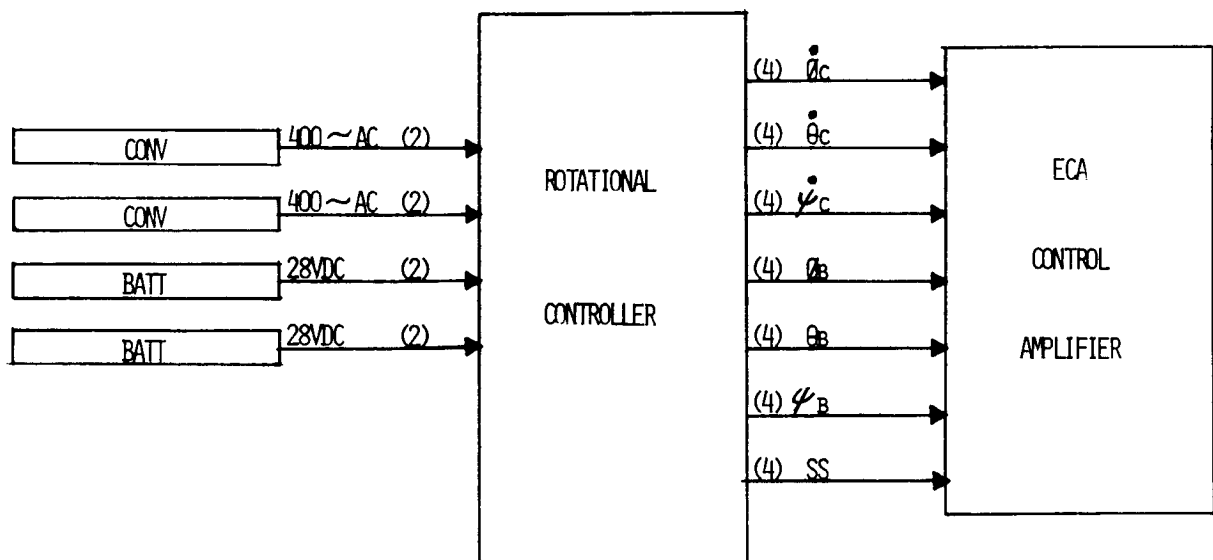


Figure 2-68. Rotational Hand Controller Wiring Diagram

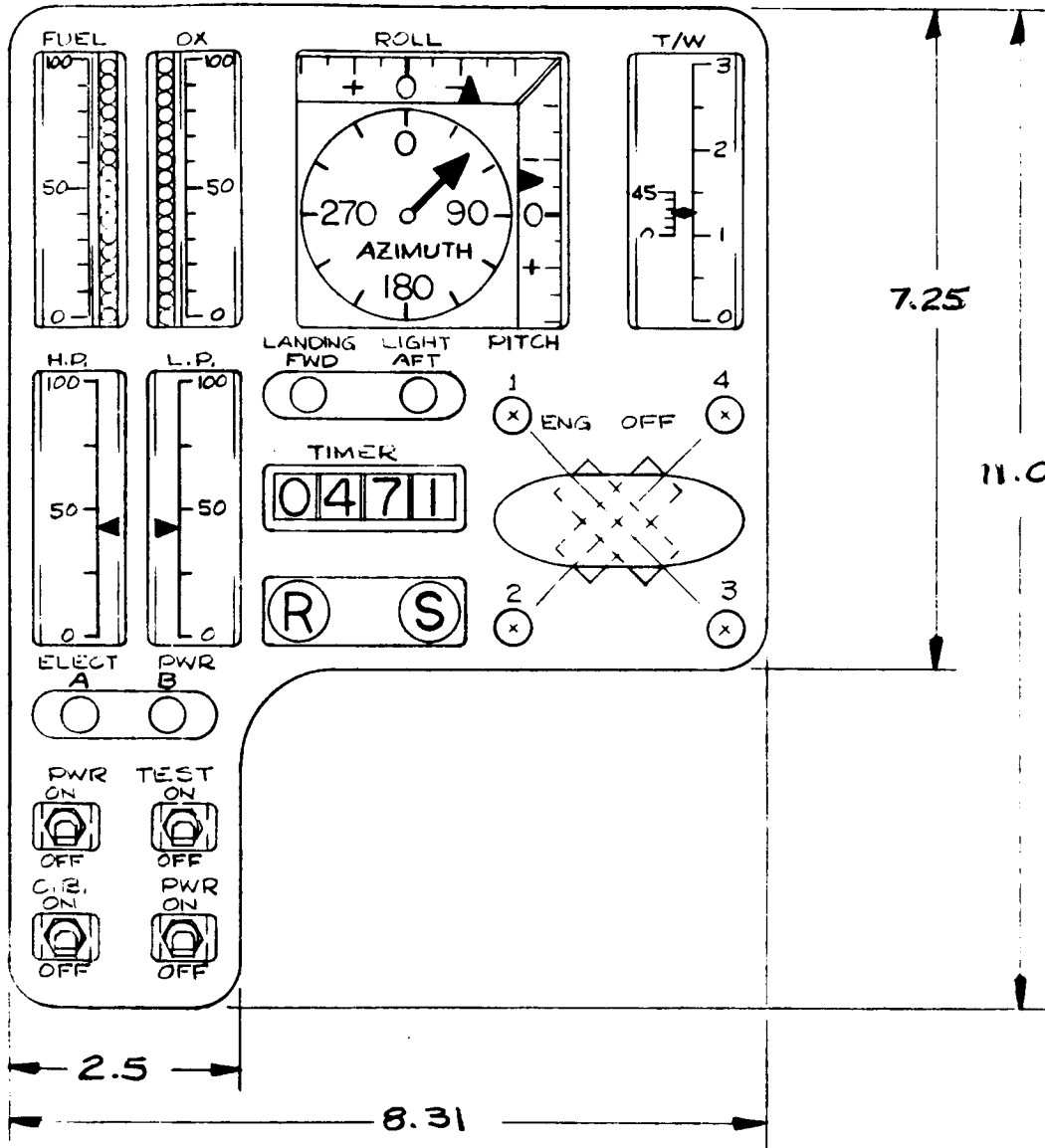


Figure 2-69. Preliminary Display Panel Layout

APPENDIX C, PART 1

KINESTHETIC EQUATIONS OF MOTION

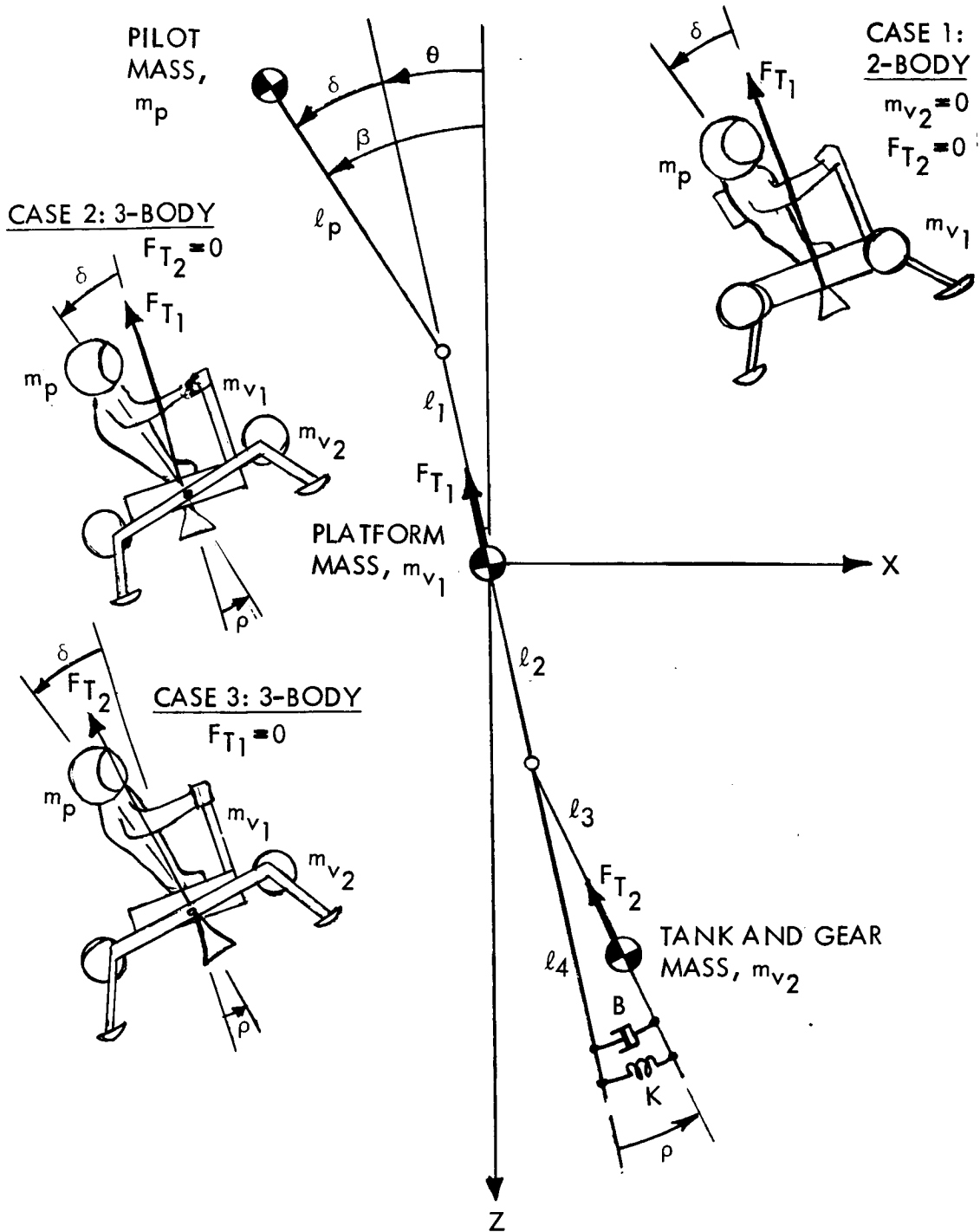


Figure C-1. Kinesthetic Pitch Plane General Geometry

## PLANAR EQUATIONS FOR KINESTHETIC MOTION

### Definitions

$I_p, I_1, I_2$  are MOI about  $m_p, m_{v_1}, m_{v_2}$

$$\beta = \delta + \theta$$

$$m_T = m_p + m_{v_1} + m_{v_2}$$

$\bar{r}_p, \bar{r}_1, \bar{r}_2$  are vector positions of  $m_p, m_{v_1}, m_{v_2}$  from origin

$\bar{F}_p, \bar{F}_1, \bar{F}_2$  are vector thrust forces on  $m_p, m_{v_1}, m_{v_2}$

### Kinetic Energy

$$T = \frac{1}{2} m_p v_p^2 + \frac{1}{2} I_p \dot{\beta}^2 + \frac{1}{2} m_{v_1} v_1^2 + \frac{1}{2} I_1 \dot{\theta}^2 + \frac{1}{2} m_{v_2} v_2^2 + \frac{1}{2} I_2 (\dot{\theta} + \dot{\rho})^2$$

### Potential Energy

$$V = -m_T g z + m_p g (\ell_1 \cos \theta + \ell_p \cos \beta) - m_{v_2} g [k \cos \theta + \ell_3 \cos (\theta + \rho)] + \frac{1}{2} k \rho^2$$

### Forces Not Derivable From a Potential

$$Q_x = -F_{T_1} \sin \theta - F_{T_2} \sin (\theta + \rho)$$

$$Q_z = -F_{T_1} \cos \theta - F_{T_2} \cos (\theta + \rho)$$

$$Q_\theta = \sum_{i=1}^n F_i \cdot \frac{\partial \bar{r}_i}{\partial \theta}$$

$$\bar{r}_p = [-l_1 \sin \theta - l_p \sin \beta] \bar{i} + [-l_1 \cos \theta - l_p \cos \beta] \bar{k}$$

$$\bar{F}_p = \left[ -F_{T_1} \sin \theta - F_{T_2} \sin (\theta + \rho) \right] \bar{i} + \left[ -F_{T_1} \cos \theta - F_{T_2} \cos (\theta + \rho) \right] \bar{k}$$

$$\bar{r}_1 = 0$$

$$\bar{F}_1 = \bar{F}_p$$

$$\bar{r}_2 = [l_2 \sin \theta + l_3 \sin (\theta + \rho)] \bar{i} + [l_2 \cos \theta + l_3 \cos (\theta + \rho)] \bar{k}$$

$$\bar{F}_2 = \bar{F}_p$$

$$\therefore \sum_{i=1}^n \bar{F}_i \cdot \frac{\partial \bar{r}_i}{\partial q_r} = \bar{F}_p \cdot \left( \frac{\partial \bar{r}_p}{\partial q_r} + \frac{\partial \bar{r}_1}{\partial q_r} + \frac{\partial \bar{r}_2}{\partial q_r} \right), \quad r = \theta, \beta, \rho$$

$$\begin{aligned} \therefore Q_\theta &= \left[ -F_{T_1} \sin \theta - F_{T_2} \sin (\theta + \rho) \right] \left[ -l_1 \cos \theta + l_2 \cos \theta + l_3 \cos (\theta + \rho) \right] \\ &\quad + \left[ -F_{T_1} \cos \theta - F_{T_2} \cos (\theta + \rho) \right] \left[ l_1 \sin \theta - l_2 \sin \theta - l_3 \sin (\theta + \rho) \right] \\ &= -F_{T_1} \left\{ \sin \theta [(\cancel{l_2} - l_1) \cos \theta + l_3 \cos (\theta + \rho)] \right. \\ &\quad \left. - \cos \theta [(\cancel{l_2} - l_1) \sin \theta + l_3 \sin (\theta + \rho)] \right\} \\ &\quad - F_{T_2} \left\{ \sin (\theta + \rho) [(l_2 - l_1) \cos \theta + l_3 \cos (\theta + \rho)] \right. \\ &\quad \left. - \cos (\theta + \rho) [(l_2 - l_1) \sin \theta + l_3 \sin (\theta + \rho)] \right\} \end{aligned}$$

$$= -F_{T_1} l_3 [\cancel{\sin \theta \cos \theta \cos \rho} - \sin^2 \theta \sin \rho - \cancel{\cos \theta \sin \theta \cos \rho} - \cos^2 \theta \sin \rho]$$

$$- F_{T_2} (l_2 - l_1) [\cancel{\sin \theta \cos \theta \cos \rho} + \cos^2 \theta \sin \rho - \cancel{\cos \theta \sin \theta \cos \rho} + \sin^2 \theta \sin \rho]$$

$$= F_{T_1} l_3 \cos(\theta - \theta) \sin \rho - F_{T_2} (l_2 - l_1) \cos(\theta - \theta) \sin \rho$$

$$= \left[ l_3 F_{T_1} + (l_1 - l_2) F_{T_2} \right] \sin \rho$$

$$Q_\beta = \left[ -F_{T_1} \sin \theta - F_{T_2} \sin(\theta + \rho) \right] \left[ -l_p \cos \beta \right]$$

$$+ \left[ -F_{T_1} \cos \theta - F_{T_2} \cos(\theta + \rho) \right] \left[ l_p \sin \beta \right]$$

$$= F_{T_1} l_p (\sin \theta \cos \beta - \cos \theta \sin \beta)$$

$$+ F_{T_2} l_p \left[ \sin(\theta + \rho) \cos \beta - \cos(\theta + \rho) \sin \beta \right]$$

$$= -F_{T_1} l_p \sin \delta - F_{T_2} l_p \sin(\delta - \rho)$$

$$Q_\rho = \left[ -F_{T_1} \sin \theta - F_{T_2} \sin(\theta + \rho) \right] \left[ l_3 \cos(\theta + \rho) \right]$$

$$+ \left[ -F_{T_1} \cos \theta - F_{T_2} \cos(\theta + \rho) \right] \left[ -l_3 \sin(\theta + \rho) \right]$$

$$+ \text{DASHPOT} \quad (\text{DASHPOT TERM} = -B l_4^2 \dot{\rho})$$



$$\begin{aligned}
 &= F_{T_1} l_3 [-\sin \theta \cos (\theta + \rho) + \cos \theta \sin (\theta + \rho)] \\
 &+ F_{T_2} l_3 [-\sin (\theta + \rho) \cos (\theta + \rho) + \cos (\theta + \rho) \sin (\theta + \rho)] - B l_4^2 \dot{\rho} \\
 &= F_{T_1} l_3 \sin \rho - B l_4^2 \dot{\rho}
 \end{aligned}$$

### Velocities

$$\begin{aligned}
 v_p^2 &= [\dot{x} - l_1 \dot{\theta} \cos \theta - l_p \dot{\beta} \cos \beta]^2 + [\dot{z} + l_1 \dot{\theta} \sin \theta + l_p \dot{\beta} \sin \beta]^2 \\
 &= \dot{x}^2 - 2 l_1 \dot{x} \dot{\theta} \cos \theta - 2 l_p \dot{x} \dot{\beta} \cos \beta + l_1^2 \dot{\theta}^2 \cos^2 \theta \\
 &\quad + 2 l_1 l_p \dot{\theta} \dot{\beta} \cos \theta \cos \beta + l_p^2 \dot{\beta}^2 \cos^2 \beta + \dot{z}^2 + 2 l_1 \dot{z} \dot{\theta} \sin \theta \\
 &\quad + 2 l_p \dot{z} \dot{\beta} \sin \beta + l_1^2 \dot{\theta}^2 \sin^2 \theta + 2 l_1 l_p \dot{\theta} \dot{\beta} \sin \theta \sin \beta + l_p^2 \dot{\beta}^2 \sin^2 \beta \\
 &= \dot{x}^2 + \dot{z}^2 + 2 l_1 (\dot{z} \sin \theta - \dot{x} \cos \theta) \dot{\theta} + 2 l_p (\dot{z} \sin \beta - \dot{x} \cos \beta) \dot{\beta} \\
 &\quad + l_1^2 \dot{\theta}^2 + 2 l_1 l_p \dot{\theta} \dot{\beta} \cos (\beta - \theta) + l_p^2 \dot{\beta}^2
 \end{aligned}$$

$$v_1^2 = \dot{x}^2 + \dot{z}^2$$

$$\begin{aligned}
 v_2^2 &= [\dot{x} + l_2 \dot{\theta} \cos \theta + l_3 (\dot{\rho} + \dot{\theta}) \cos (\theta + \rho)]^2 \\
 &\quad + [\dot{z} - l_2 \dot{\theta} \sin \theta - l_3 (\dot{\rho} + \dot{\theta}) \sin (\theta + \rho)]^2
 \end{aligned}$$

$$\begin{aligned}
 &= \dot{x}^2 + 2l_2 \dot{x} \dot{\theta} \cos \theta + 2l_3 \dot{x} (\dot{\rho} + \dot{\theta}) \cos (\theta + \rho) + l_2^2 \dot{\theta}^2 \cos^2 \theta \\
 &+ 2l_2 l_3 \dot{\theta} (\dot{\rho} + \dot{\theta}) \cos \theta \cos (\theta + \rho) + l_3^2 (\dot{\rho} + \dot{\theta})^2 \cos^2 (\theta + \rho) \\
 &+ \dot{z}^2 - 2l_2 \dot{z} \dot{\theta} \sin \theta - 2l_3 \dot{z} (\dot{\rho} + \dot{\theta}) \sin (\theta + \rho) + l_2^2 \dot{\theta}^2 \sin^2 \theta \\
 &+ 2l_2 l_3 \dot{\theta} (\dot{\rho} + \dot{\theta}) \sin \theta \sin (\theta + \rho) + l_3^2 (\dot{\rho} + \dot{\theta})^2 \sin^2 (\theta + \rho) \\
 &= \dot{x}^2 + \dot{z}^2 + 2l_2 (\dot{x} \cos \theta - \dot{z} \sin \theta) \dot{\theta} + 2l_3 [\dot{x} \cos (\theta + \rho) - \dot{z} \sin (\theta + \rho)] \\
 &\quad \dot{\rho} + l_2^2 \dot{\theta}^2 + 2l_2 l_3 \cos \rho \dot{\theta} \dot{\rho} + l_3^2 \dot{\rho}^2 \\
 &+ 2l_3 [\dot{x} \cos (\theta + \rho) - \dot{z} \sin (\theta + \rho)] \dot{\theta} + 2l_2 l_3 \cos \rho \dot{\theta}^2 \\
 &+ 2l_3^2 \dot{\rho} \dot{\theta} + l_3^2 \dot{\theta}^2
 \end{aligned}$$

### Lagrangian

$$\begin{aligned}
 L = T - V &= \frac{1}{2} m_p v_p^2 + \frac{1}{2} m_{v_1} v_1^2 + \frac{1}{2} m_{v_2} v_2^2 + \frac{1}{2} I_p \dot{\beta}^2 \\
 &+ \frac{1}{2} I_1 \dot{\theta}^2 + \frac{1}{2} I_2 (\dot{\theta} + \dot{\rho})^2 + m_T g z - m_p g (l_1 \cos \theta + l_p \cos \beta) \\
 &+ m_{v_2} g [l_2 \cos \theta + l_3 \cos (\theta + \rho)] - \frac{1}{2} K \rho^2
 \end{aligned}$$

### Lagrange Equations of Motion

$$\frac{d}{dt} \left\{ \frac{\partial L}{\partial \dot{q}_r} \right\} - \frac{\partial L}{\partial q_r} = Q_r$$



$$\frac{\partial L}{\partial \dot{x}} = \frac{1}{Z} m_p \left\{ Z \dot{x} - Z l_1 \dot{\theta} \cos \theta - Z l_p \dot{\beta} \cos \beta \right\} + \frac{1}{Z} m_{v_1} (Z \dot{x})$$

$$+ \frac{1}{Z} m_{v_2} \left\{ Z \dot{x} + Z l_2 \dot{\theta} \cos \theta + Z l_3 \dot{\rho} \cos (\theta + \rho) + Z l_3 \dot{\theta} \cos (\theta + \rho) \right\}$$

$$\frac{\partial L}{\partial x} = 0$$

$$\frac{\partial L}{\partial \dot{z}} = \frac{1}{Z} m_p \left\{ Z \dot{z} + Z l_1 \dot{\theta} \sin \theta + Z l_p \dot{\beta} \sin \beta \right\} + \frac{1}{Z} m_{v_1} (Z \dot{z})$$

$$+ \frac{1}{Z} m_{v_2} \left\{ Z \dot{z} - Z l_2 \dot{\theta} \sin \theta - Z l_3 \dot{\rho} \sin (\theta + \rho) - Z l_3 \dot{\theta} \sin (\theta + \rho) \right\}$$

$$\frac{\partial L}{\partial z} = m_T g$$

$$\frac{\partial L}{\partial \dot{\theta}} = \frac{1}{Z} m_p \left\{ Z l_1 (\dot{z} \sin \theta - \dot{x} \cos \theta) + Z l_1^2 \dot{\theta} + 2 l_1 l_p \dot{\beta} \cos (\beta - \theta) \right\}$$

$$+ \frac{1}{Z} m_{v_2} \left\{ Z l_2 (\dot{x} \cos \theta - \dot{z} \sin \theta) + Z l_2^2 \dot{\theta} + Z l_2 l_3 \dot{\rho} \cos \rho \right\}$$

$$+ I_1 \dot{\theta} + I_2 (\dot{\theta} + \dot{\rho}) + \frac{1}{Z} m_{v_2} \left\{ Z l_3 [\dot{x} \cos (\theta + \rho) - \dot{z} \sin (\theta + \rho)] \right.$$

$$\left. + Z^2 l_2 l_3 \cos \rho \dot{\theta} + Z l_3^2 \dot{\rho} + Z l_3^2 \dot{\theta} \right\}$$

$$\frac{\partial L}{\partial \theta} = \frac{1}{Z} m_p \left\{ Z l_1 (\dot{z} \cos \theta + \dot{x} \sin \theta) \dot{\theta} + Z l_1 l_p \dot{\theta} \dot{\beta} \sin (\beta - \theta) \right\}$$

$$+ \frac{1}{Z} m_{v_2} \left\{ Z l_2 (-\dot{x} \sin \theta - \dot{z} \cos \theta) \dot{\theta} \right.$$

$$\left. + Z l_3 [-\dot{x} \sin (\theta + \rho) - \dot{z} \cos (\theta + \rho)] \dot{\rho} \right\} + m_p g l_1 \sin \theta - m_{v_2} g l_2 \sin \theta$$

$$- m_{v_2} g l_3 \sin (\theta + \rho) + \frac{1}{Z} m_{v_2} l_3 [-\dot{x} \sin (\theta + \rho) - \dot{z} \cos (\theta + \rho)] \dot{\theta}$$

$$\frac{\partial L}{\partial \dot{\beta}} = \frac{1}{Z} m_p \left\{ Z l_p (\dot{z} \sin \beta - \dot{x} \cos \beta) + Z l_1 l_p \dot{\theta} \cos (\beta - \theta) \right. \\ \left. + Z l_p^2 \dot{\beta} \right\} + I_p \dot{\beta}$$

$$\frac{\partial L}{\partial \beta} = \frac{1}{Z} m_p \left\{ Z l_p (\dot{z} \cos \beta + \dot{x} \sin \beta) \dot{\beta} - Z l_1 l_p \dot{\theta} \dot{\beta} \sin (\beta - \theta) \right\} \\ + m_p g l_p \sin \beta$$

$$\frac{\partial L}{\partial \dot{\rho}} = \frac{1}{Z} m_{v_2} \left\{ Z l_3 [\dot{x} \cos (\theta + \rho) - \dot{z} \sin (\theta + \rho)] + Z l_3 l_2 \cos \rho \dot{\theta} \right. \\ \left. + Z l_3^2 \dot{\rho} \right\} + I_2 (\dot{\theta} + \dot{\rho}) + \frac{1}{Z} m_{v_2} \left\{ Z l_3^2 \dot{\theta} \right\}$$

$$\frac{\partial L}{\partial \rho} = \frac{1}{Z} m_{v_2} \left\{ Z l_3 [-\dot{x} \sin (\theta + \rho) - \dot{z} \cos (\theta + \rho)] \dot{\rho} - Z l_2 l_3 \sin \rho \dot{\theta} \dot{\rho} \right. \\ \left. - m_{v_2} g l_3 \sin (\theta + \rho) - K \rho + \frac{1}{Z} m_{v_2} \left\{ Z l_3 [-\dot{x} \sin (\theta + \rho) \right. \right. \\ \left. \left. - \dot{z} \cos (\theta + \rho)] \dot{\theta} - Z l_2 l_3 \sin \rho \dot{\theta}^2 \right\} \right\}$$

X Equation

$$\frac{d}{dt} \left\{ m_T \dot{x} + (m_{v_2} l_2 - m_p l_1) \dot{\theta} \cos \theta - m_p l_p \dot{\beta} \cos \beta + m_{v_2} l_3 \dot{\theta} \cos (\theta + \rho) \right. \\ \left. + m_{v_2} l_3 \dot{\rho} \cos (\theta + \rho) \right\} = -F_{T_1} \cos \theta - F_{T_2} \sin (\theta + \rho)$$



$$\begin{aligned}
 & m_T \ddot{x} + (m_{v_2} l_2 - m_p l_1) \ddot{\theta} \cos \theta - (m_{v_2} l_2 - m_p l_1) \dot{\theta}^2 \sin \theta \\
 & - m_p l_p \ddot{\beta} \cos \beta + m_p l_p \dot{\beta}^2 \sin \beta + m_{v_2} l_3 \ddot{\rho} \cos (\theta + \rho) \\
 & - m_{v_2} l_3 (\dot{\theta} + \dot{\rho}) \dot{\rho} \sin (\theta + \rho) + m_{v_2} l_3 \ddot{\theta} \cos (\theta + \rho) \\
 & - m_{v_2} l_3 \dot{\theta} (\dot{\theta} + \dot{\rho}) \sin (\theta + \rho) \\
 & = -F_{T_1} \sin \theta - F_{T_2} \sin (\theta + \rho)
 \end{aligned}$$

Z Equation

$$\begin{aligned}
 & \frac{d}{dt} \left\{ m_T \dot{z} + (m_p l_1 - m_{v_2} l_2) \dot{\theta} \sin \theta + m_p l_p \dot{\beta} \sin \beta - m_{v_2} l_3 \dot{\theta} \sin (\theta + \rho) \right. \\
 & \left. - m_{v_2} l_3 \dot{\rho} \sin (\theta + \rho) \right\} - m_T g = -F_{T_1} \cos \theta - F_{T_2} \cos (\theta + \rho)
 \end{aligned}$$

$$\begin{aligned}
 & m_T \ddot{z} + (m_p l_1 - m_{v_2} l_2) \ddot{\theta} \sin \theta + (m_p l_1 - m_{v_2} l_2) \dot{\theta}^2 \cos \theta \\
 & + m_p l_p \ddot{\beta} \sin \beta + m_p l_p \dot{\beta}^2 \cos \beta - m_{v_2} l_3 \ddot{\rho} \sin (\theta + \rho) \\
 & - m_{v_2} l_3 (\dot{\theta} + \dot{\rho}) \dot{\rho} \cos (\theta + \rho) - m_T g - m_{v_2} l_3 \ddot{\theta} \sin (\theta + \rho) \\
 & + m_{v_2} l_3 \dot{\theta} (\dot{\theta} + \dot{\rho}) \cos (\theta + \rho) \\
 & = -F_{T_1} \cos \theta - F_{T_2} \cos (\theta + \rho)
 \end{aligned}$$



$\theta$  Equation

$$\begin{aligned} \frac{d}{dt} & \left\{ \left( m_p l_1^2 + m_{v_2} l_2^2 + I_1 + I_2 \right) \dot{\theta} + \left( m_{v_2} l_2 - m_p l_1 \right) \dot{x} \cos \theta \right. \\ & + m_{v_2} l_3 \left[ \dot{x} \cos (\theta + \rho) - \dot{z} \sin (\theta + \rho) \right] + 2 m_{v_2} l_2 l_3 \cos \rho \dot{\theta} + m_{v_2} l_3^2 \dot{\rho} \\ & + m_{v_2} l_3^2 \dot{\theta} + \left( m_p l_1 - m_{v_2} l_2 \right) \dot{z} \sin \theta + m_p l_1 l_1 \dot{\beta} \cos (\beta - \theta) \\ & \left. + \left( m_{v_2} l_2 l_3 \cos \rho + I_2 \right) \dot{\rho} \right\} - m_p l_1 (\dot{z} \cos \theta + \dot{x} \sin \theta) \dot{\theta} \\ & + m_p l_1 l_p \dot{\theta} \dot{\beta} \sin (\beta - \theta) + m_{v_2} l_2 (\dot{x} \sin \theta + \dot{z} \cos \theta) \dot{\theta} \\ & + m_{v_2} l_3 \left[ \dot{x} \sin (\theta + \rho) + \dot{z} \cos (\theta + \rho) \right] \dot{\rho} - m_p g l_1 \sin \theta + m_{v_2} l_3 \\ & + m_{v_2} l_3 \left[ \dot{x} \sin (\theta + \rho) + \dot{z} \cos (\theta + \rho) \right] \dot{\theta} + m_{v_2} g l_2 \sin \theta \\ & + m_{v_2} g l_3 \sin (\theta + \rho) = \left[ l_3 F_{T1} + (l_1 - l_2) F_{T2} \right] \sin \rho \end{aligned}$$

$$\begin{aligned} & \left( m_p l_1^2 + m_{v_2} l_2^2 + I_1 + I_2 \right) \ddot{\theta} + \left( m_{v_2} l_2 - m_p l_1 \right) \ddot{x} \cos \theta \\ & - \left( m_{v_2} l_2 - m_p l_1 \right) \dot{x} \dot{\theta} \sin \theta + m_{v_2} l_3 \left[ \ddot{x} \cos (\theta + \rho) - \ddot{z} \sin (\theta + \rho) \right] \\ & - m_{v_2} l_3 \dot{x} (\dot{\theta} + \dot{\rho}) \sin (\theta + \rho) - m_{v_2} l_3 \dot{z} (\dot{\theta} + \dot{\rho}) \cos (\theta + \rho) \\ & + 2 m_{v_2} l_2 l_3 \cos \rho \ddot{\theta} - 2 m_{v_2} l_2 l_3 \sin \rho \dot{\rho} \dot{\theta} + m_{v_2} l_3^2 \ddot{\rho} + m_{v_2} l_3^2 \ddot{\theta} \\ & + \left( m_p l_1 - m_{v_2} l_2 \right) \ddot{z} \sin \theta + \left( m_p l_1 - m_{v_2} l_2 \right) \dot{z} \dot{\theta} \cos \theta \end{aligned}$$



$$\begin{aligned}
 &+ m_p l_1 l_p \ddot{\beta} \cos(\beta - \theta) - m_p l_1 l_p (\dot{\beta} - \dot{\theta}) \dot{\beta} \sin(\beta - \theta) \\
 &+ \left( m_{v_2} l_2 l_3 \cos \rho + I_2 \right) \ddot{\rho} - m_{v_2} l_2 l_3 \dot{\rho}^2 \sin \rho - m_p l_1 (\dot{z} \cos \theta + \dot{x} \sin \theta) \dot{\theta} \\
 &- \cancel{m_p l_1 l_p \dot{\theta} \dot{\beta} \sin(\beta - \theta)} + m_{v_2} l_2 (\dot{x} \sin \theta + \dot{z} \cos \theta) \dot{\theta} \\
 &+ m_{v_2} l_3 [\cancel{\dot{x} \sin(\theta + \rho)} + \cancel{\dot{z} \cos(\theta + \rho)}] \dot{\rho} - m_p g l_1 \sin \theta \\
 &+ \cancel{m_{v_2} l_3 \dot{x} \dot{\theta} \sin(\theta + \rho)} + \cancel{m_{v_2} l_3 \dot{z} \dot{\theta} \cos(\theta + \rho)} \\
 &+ m_{v_2} g l_2 \sin \theta + m_{v_2} g l_3 \sin(\theta + \rho) = \left[ l_3 F_{T1} + (l_1 - l_2) F_{T2} \right] \sin \rho \\
 &\left( m_p l_1^2 + m_{v_2} l_2^2 + I_1 + I_2 + m_{v_2} l_3^2 \right) \ddot{\theta} + \left( m_{v_2} l_2 - m_p l_1 \right) \dot{x} \cos \theta \\
 &+ \left( m_p l_1 - m_{v_2} l_2 \right) \dot{z} \sin \theta + m_{v_2} l_3 [\dot{x} \cos(\theta + \rho) - \dot{z} \sin(\theta + \rho)] \\
 &+ m_p l_1 l_p \ddot{\beta} \cos(\beta - \theta) - m_p l_1 l_p \dot{\beta}^2 \sin(\beta - \theta) \\
 &+ \left( m_{v_2} l_2 l_3 \cos \rho + m_{v_2} l_3^2 + I_2 \right) \ddot{\rho} - m_{v_2} l_2 l_3 \dot{\rho}^2 \sin \rho - m_p g l_1 \sin \theta \\
 &+ m_{v_2} g l_2 \sin \theta + 2 m_{v_2} l_2 l_3 \cos \rho \ddot{\theta} - 2 m_{v_2} l_2 l_3 \sin \rho \dot{\rho} \dot{\theta} \\
 &+ m_{v_2} g l_3 \sin(\theta + \rho) = \left[ l_3 F_{T1} + (l_1 - l_2) F_{T2} \right] \sin \rho
 \end{aligned}$$

$\beta$  Equation

$$\frac{d}{dt} \left\{ (m_p l_p^2 + I_p) \dot{\beta} + m_p l_p \dot{z} \sin \beta - m_p l_p \dot{x} \cos \beta + m_p l_1 l_p \dot{\theta} \cos (\beta - \theta) \right\}$$

$$- m_p l_p \dot{z} \dot{\beta} \cos \beta - m_p l_p \dot{x} \dot{\beta} \sin \beta + m_p l_1 l_p \dot{\theta} \dot{\beta} \sin (\beta - \theta)$$

$$- m_p g l_p \sin \beta = -F_{T_1} l_p \sin \delta - F_{T_2} l_p \sin (\delta - \rho)$$

$$(m_p l_p^2 + I_p) \ddot{\beta} + m_p l_p \ddot{z} \sin \beta + m_p l_p \dot{z} \dot{\beta} \cos \beta - m_p l_p \ddot{x} \cos \beta$$

$$+ m_p l_1 l_p \ddot{\theta} \cos (\beta - \theta)$$

$$- m_p l_1 l_p (\dot{\beta} - \dot{\theta}) \dot{\theta} \sin (\beta - \theta) - m_p l_p \dot{z} \dot{\beta} \cos \beta$$

$$- m_p l_p \dot{x} \dot{\beta} \sin \beta + m_p l_1 l_p \dot{\theta} \dot{\beta} \sin (\beta + \theta) - m_p g l_p \sin \beta$$

$$= -F_{T_1} l_p \sin \delta - F_{T_2} l_p \sin (\delta - \rho)$$

$$(m_p l_p^2 + I_p) \ddot{\beta} + m_p l_p \ddot{z} \sin \beta - m_p l_p \ddot{x} \cos \beta + m_p l_1 l_p \ddot{\theta} \cos (\beta - \theta)$$

$$+ m_p l_1 l_p \dot{\theta}^2 \sin (\beta - \theta) - m_p g l_p \sin \beta = -F_{T_1} l_p \sin \delta - F_{T_2} l_p \sin (\delta - \rho)$$

$\rho$  Equation

$$\frac{d}{dt} \left\{ (m_{v_2} l_3^2 + I_2) \dot{\rho} + m_{v_2} l_3 \dot{x} \cos (\theta + \rho) - m_{v_2} l_3 \dot{z} \sin (\theta + \rho) + m_{v_2} l_3^2 \dot{\theta} \right.$$

$$\left. + m_{v_2} l_2 l_3 \dot{\theta} \cos \rho \right\} + m_{v_2} l_3 [\dot{x} \sin (\theta + \rho) + \dot{z} \cos (\theta + \rho)] \dot{\rho}$$

$$+ m_{v_2} l_3 [\dot{x} \sin (\theta + \rho) + \dot{z} \cos (\theta + \rho)] \dot{\theta} + m_{v_2} l_2 l_3 \sin \rho \dot{\theta}^2$$

$$+ m_{v_2} l_3 [\dot{x} \sin (\theta + \rho) + \dot{z} \cos (\theta + \rho)] \dot{\theta} + m_{v_2} l_2 l_3 \sin \rho \dot{\theta}^2$$





$$\begin{aligned}
 & (m_{v_2} l_3^2 + I_2) \ddot{\rho} + m_{v_2} l_3 \ddot{x} \cos(\theta + \rho) - m_{v_2} l_3 \dot{x} (\dot{\theta} + \dot{\rho}) \sin(\theta + \rho) \\
 & - m_{v_2} l_3 \ddot{z} \sin(\theta + \rho) - m_{v_2} l_3 \dot{z} (\dot{\theta} + \dot{\rho}) \cos(\theta + \rho) + m_{v_2} l_3^2 \ddot{\theta} \\
 & + m_{v_2} l_3 \dot{z} \dot{\theta} \sin(\theta + \rho) + m_{v_2} l_3 \dot{z} \dot{\rho} \cos(\theta + \rho) + m_{v_2} l_2 l_3 \sin \rho \dot{\theta}^2 \\
 & + m_{v_2} l_2 l_3 \ddot{\theta} \cos \rho - m_{v_2} l_2 l_3 \dot{\theta} \dot{\rho} \sin \rho + m_{v_2} l_3 \dot{x} \dot{\rho} \sin(\theta + \rho) \\
 & + m_{v_2} l_3 \dot{z} \dot{\rho} \cos(\theta + \rho) + m_{v_2} l_2 l_3 \dot{\theta} \dot{\rho} \sin \rho \\
 & + m_{v_2} g l_3 \sin(\theta + \rho) - K \rho = F_{T_1} l_3 \sin \rho - B l_4^2 \dot{\rho}
 \end{aligned}$$

$$\begin{aligned}
 & (m_{v_2} l_3^2 + I_2) \ddot{\rho} + m_{v_2} l_3 \ddot{x} \cos(\theta + \rho) - \frac{m_{v_2} l_3 \dot{x} \dot{\theta} \sin(\theta + \rho)}{v_2} + m_{v_2} l_3^2 \ddot{\theta} \\
 & - m_{v_2} l_3 \ddot{z} \sin(\theta + \rho) - \frac{m_{v_2} l_3 \dot{z} \dot{\theta} \cos(\theta + \rho)}{v_2} + m_{v_2} l_2 l_3 \sin \rho \dot{\theta}^2 \\
 & + m_{v_2} l_2 l_3 \ddot{\theta} + m_{v_2} g l_3 \sin(\theta + \rho) - K \rho = F_{T_1} l_3 \sin \rho - B l_4^2 \dot{\rho}
 \end{aligned}$$

Linearization

$\beta \rightarrow \theta_0 + \beta$	$\delta \rightarrow \delta$	$\theta \rightarrow \theta_0 + \theta$	$\rho \rightarrow \rho$
$\dot{\beta} \rightarrow \dot{\beta}$	$\dot{\delta} \rightarrow \dot{\delta}$	$\dot{\theta} \rightarrow \dot{\theta}$	$\dot{\rho} \rightarrow \dot{\rho}$
$\ddot{\beta} \rightarrow \ddot{\beta}$	$\ddot{\delta} \rightarrow \ddot{\delta}$	$\ddot{\theta} \rightarrow \ddot{\theta}$	$\ddot{\rho} \rightarrow \ddot{\rho}$

$$x \rightarrow x$$

$$z \rightarrow z$$

$$\dot{x} \rightarrow \dot{x}$$

$$\dot{z} \rightarrow \dot{z}$$

$$\ddot{x} \rightarrow -\frac{F_T}{m_T} \sin \theta_o + \ddot{x}$$

$$\ddot{z} \rightarrow g - \frac{F_T}{m_T} \cos \theta_o + \ddot{z}$$

$$\sin \theta \rightarrow \sin \theta_o + \cos \theta_o \theta$$

$$\cos \theta \rightarrow \cos \theta_o - \sin \theta_o \theta$$

$$\sin \beta \rightarrow \sin \theta_o + \cos \theta_o \beta$$

$$\cos \beta \rightarrow \cos \theta_o - \sin \theta_o \beta$$

$$\sin \delta \rightarrow \delta$$

$$\sin \rho \rightarrow \rho$$

$$\sin (\theta + \rho) \rightarrow \sin \theta_o + \cos \theta_o \theta + \cos \theta_o \rho$$

$$\cos (\theta + \rho) \rightarrow \cos \theta_o - \sin \theta_o \theta - \sin \theta_o \rho$$

$$\sin (\beta - \theta) \rightarrow \beta - \theta$$

$$\cos (\beta - \theta) \rightarrow 1$$

$$\sin (\delta - \rho) \rightarrow \delta - \rho$$

$$\cos \rho = 1$$

In the linearized equations, substitute  $\beta = \theta + \delta$ , and eliminate the  $\beta$  equation, since  $\beta$  is not an independent variable.

Also:

$$\dot{\beta} = \dot{\theta} + \dot{\delta} \quad \text{and} \quad \ddot{\beta} = \ddot{\theta} + \ddot{\delta}$$

LINEARIZED PITCH PLANE EQUATIONS

x Equation

$$\begin{aligned}
 m_T \left( -\frac{F_T}{m_T} \cancel{\sin \theta_o} + \ddot{x} \right) + \left( m_{v_2} \left\{ l_2 + l_3 \right\} - m_{p_1} l_1 \right) \ddot{\theta} \cos \theta_o + m_{v_2} l_3 \ddot{\rho} \cos \theta_o \\
 = m_{p_p} l \cos \theta_o \delta - F_{T_1} (\cancel{\sin \theta_o} + \cos \theta_o) - F_{T_2} (\cancel{\sin \theta_o} + \cos \theta_o + \cos \theta_o \rho) \\
 m_T \ddot{x} + \left( m_{v_2} l_2 - m_{p_1} l - m_{p_p} l \right) \cos \theta_o \ddot{\theta} + m_{v_2} l_3 \cos \theta_o \ddot{\rho} = m_{p_p} l \cos \theta_o \ddot{\delta} - \left( F_{T_1} + F_{T_2} \right) \cos \theta_o \\
 - F_{T_2} \cos \theta_o \rho
 \end{aligned}$$

z Equation

$$\begin{aligned}
 m_T \left( \cancel{g - \frac{F_T}{m_T} \cos \theta_o} + \ddot{z} \right) + \left( m_{p_1} l_1 - m_{v_2} \left| l_2 + l_3 \right| \right) \sin \theta_o \ddot{\theta} + m_{p_p} l \ddot{\theta} \sin \theta_o - m_{v_2} l_3 \ddot{\rho} \sin \theta_o - \cancel{m_T g} \\
 = -m_{p_p} l \sin \theta_o \ddot{\delta} - F_{T_1} (-\sin \theta_o) - F_{T_2} (-\sin \theta_o - \sin \theta_o \rho) \\
 m_T \ddot{z} + \left( m_{p_1} l_1 - m_{v_2} l_2 \right) \sin \theta_o \ddot{\theta} + m_{p_p} l \sin \theta_o \ddot{\rho} - m_{v_2} l_3 \sin \theta_o \ddot{\rho} \\
 = \left( F_{T_1} + F_{T_2} \right) \sin \theta_o + F_{T_2} \sin \theta_o \rho - m_{p_p} l \sin \theta_o \ddot{\delta}
 \end{aligned}$$





Theta Equation

$$\begin{aligned}
 & \left( m_{p1} \ell_2^2 + m_{v2} |\ell_2 + \ell_3|^2 + I_1 + I_2 \right) \ddot{\theta} + \left( m_{v2} \ell_2 - m_{p1} \ell_1 \right) \left( -\frac{F_T}{m_T} \sin \theta_o + \ddot{x} \right) \left( \cos \theta_o - \sin \theta_o \theta \right) \\
 & + \left( m_{v2} \ell_2 - m_{p1} \ell_1 \right) g \cos \theta_o + m_{v2} g \cos \theta_o (\theta + \rho) + \left( m_{p1} \ell_1 - m_{v2} \ell_2 \right) \left( g - \frac{F_T}{m_T} \cos \theta_o + \ddot{z} \right) \\
 & \cdot (\sin \theta_o + \cos \theta_o \theta) + m_{p1} \ell_1 \ddot{\theta} + \left( m_{v2} \ell_2 \ell_3 + I_2 \right) \ddot{\rho} \\
 & = -m_{p1} \ell_1 \ddot{\delta} + \left[ \ell_3 F_{T1} + (\ell_1 - \ell_2) F_{T2} \right] \rho \\
 & \left( m_{p1} \ell_2^2 + m_{v2} |\ell_2 + \ell_3|^2 + I_1 + I_2 + m_{p1} \ell_1 \right) \ddot{\theta} + \left[ \left( m_{v2} \ell_2 - m_{p1} \ell_1 \right) \left( \frac{F_T}{m_T} \right) + m_{v2} \ell_3 g \cos \theta_o \right] \theta \\
 & + \left( m_{v2} |\ell_2 + \ell_3| - m_{p1} \ell_1 \right) \cos \theta_o \ddot{x} + \left( m_{p1} \ell_1 - m_{v2} |\ell_2 + \ell_3| \right) \sin \theta_o \ddot{z} + \left( m_{v2} \ell_3 |\ell_2 + \ell_3| + I_2 \right) \ddot{\rho} \\
 & + \left[ m_{v2} \ell_3 g \cos \theta_o - \ell_3 F_{T1} - (\ell_1 - \ell_2) F_{T2} \right] \rho \\
 & = -m_{p1} \ddot{\delta}
 \end{aligned}$$

Beta Equation

Not required.

Rho Equation

$$\begin{aligned}
 & \left( m_{p3} l_3^2 + I_2 \right) \ddot{\rho} + m_{v2} l_3 \left( \frac{-F_T}{m_T} \sin \theta_0 \right) (-\sin \theta_0) (\theta + \rho) + m_{v2} l_3 \ddot{x} \cos \theta_0 - m_{v2} l_3 \ddot{z} \sin \theta_0 \\
 & - m_{v2} l_3 \left( \frac{F_T}{m_T} \cos \theta_0 \right) (\cos \theta_0 \theta + \cos \theta_0 \rho) + m_{v2} l_3 \left( l_2 + l_3 \right) \ddot{\theta} + m_{v2} l_3 \cos \theta_0 (\theta + \rho) \\
 & = F_{T1} l_3 \rho - B l_4^2 \dot{\rho} \\
 & \left( m_{v2} l_3 \left( l_2 + l_3 \right) \right) \ddot{\theta} + m_{v2} l_3 \left( \frac{F_T}{m_T} \right) \theta + m_{v2} l_3 \cos \theta_0 \ddot{x} - m_{v2} l_3 \sin \theta_0 \ddot{z} + \left( m_{p3} l_3^2 + I_2 \right) \ddot{\rho} \\
 & - B l_4^2 \dot{\rho} + \left[ m_{v2} l_3 \left( \frac{F_T}{m_T} \right) - F_{T1} l_3 \right] \rho = 0
 \end{aligned}$$

**Table C-1. Matrix of Linearized Pitch Plane Equations of Motion for the Kinesthetic Control System**

$M_I S^2$	0	$\left[ \begin{aligned} & \left( m_{v_2} \ell_2 - m_p  \ell_1 + \ell_p  \right) \cdot \\ & \cos \theta_0 \Big] S^2 \\ & + \left( F_{T_1} + F_{T_2} \right) \cos \theta_0 \end{aligned} \right]$	$\begin{aligned} & m_{v_2} \ell_3 \cos \theta_0 S^2 \\ & + F_{T_2} \cos \theta_0 \end{aligned}$	X	$m_p \ell_p \cdot \cos \theta_0 S^2$
0	$M_I S^2$	$\left[ \begin{aligned} & \left( m_F  \ell_1 + \ell_p  - m_{v_2} \ell_2 \right) \cdot \\ & \sin \theta_0 \Big] S^2 \\ & - \left( F_{T_1} + F_{T_2} \right) \sin \theta_0 \end{aligned} \right]$	$\begin{aligned} & -m_{v_2} \ell_3 \sin \theta_0 S^2 \\ & - F_{T_2} \sin \theta_0 \end{aligned}$	Z	$-m_p \ell_p \cdot \cos \theta_0 S^2$
$\left( m_{v_2} \ell_2 - m_p \ell_1 \right) \cos \theta_0 S^2$	$\left( m_p \ell_1 - m_{v_2} \ell_2 \right) \sin \theta_0 S^2$	$\left[ \begin{aligned} & m p \ell_1^2 + m v \ell_2^2 + I_1 + I_2 \\ & + m p \ell_1 \ell_p \Big] S^2 \\ & + \left[ \begin{aligned} & \left( m_{v_2} \ell_2 - m p \ell_1 \right) \left( \frac{F_{T_1}}{m_I} \right) \\ & + m_{v_2} \ell_3 g \cos \theta_0 \end{aligned} \right]$	$\begin{aligned} & \left[ m_{v_2} \ell_2 \ell_3 + I_2 \right] S^2 \\ & + \left[ m_{v_2} \ell_3 g \cos \theta_0 \right. \\ & \left. - \ell_3 F_{T_1} - (\ell_1 - \ell_2) F_{T_2} \right] \end{aligned}$	$\theta$	$-m_p \ell_1 \ell_p S^2$
$m_{v_2} \ell_3 \cos \theta_0 S^2$	$-m_{v_2} \ell_3 \sin \theta_0 S^2$	$\begin{aligned} & m_{v_2} \ell_2 \ell_3 S^2 \\ & + m_{v_2} \ell_3 \left( \frac{F_{T_1}}{m_I} \right) \end{aligned}$	$\begin{aligned} & \left( m_p \ell_3^2 + I_2 \right) S^2 - B \ell_4^2 S \\ & + \left[ m_{v_2} \ell_3 \left( \frac{F_{T_1}}{m_I} \right) - F_{T_1} \ell_3 \right] \end{aligned}$	P	0

 $\delta$

APPENDIX C, PART 2

HARDWIRE EQUATIONS OF MOTION WITH PIVOT  
BELOW CENTER OF GRAVITY

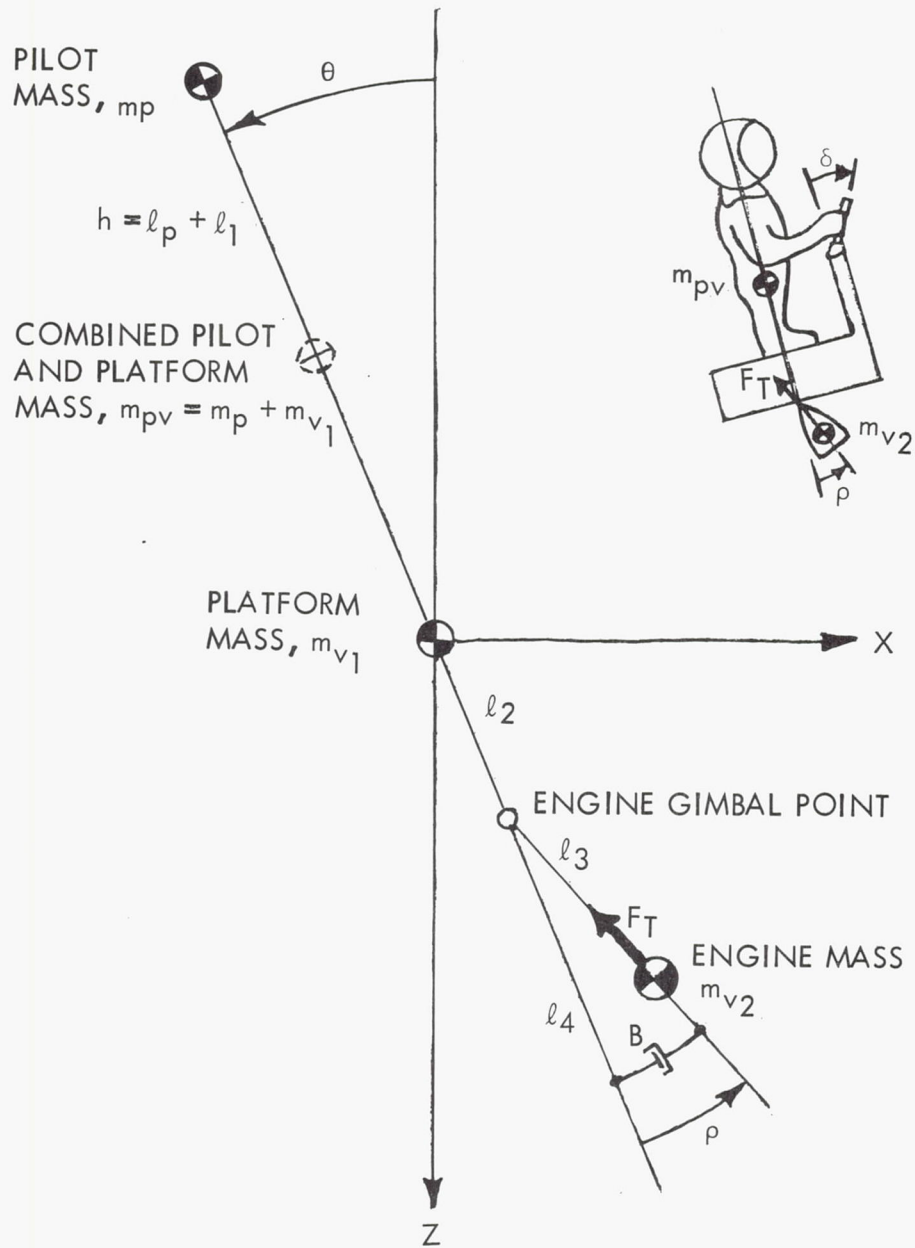


Figure C-2. Manual Control Pitch Plane General Geometry



## HARDWIRE CONTROL PITCH PLANE GENERAL EQUATIONS

### Definitions

$I_p, I_1, I_2$  are MOI about  $m_p, m_{v_1}, m_{v_2}$

$$m_T = m_p + m_{v_1} + m_{v_2}$$

$$m_{p_v} = m_p + m_{v_1}$$

$Q_T = -N\delta =$  torque supplied by pilot through stick

$$h = l_p + l_{v_1}$$

### Kinetic Energy

$$T = \frac{1}{2} m_{p_v} v_p^2 + \frac{1}{2} I_p \dot{\theta}^2 + \frac{1}{2} m_{v_1} v_1^2 + \frac{1}{2} I_1 \dot{\theta}^2$$

$$+ \frac{1}{2} m_{v_2} v_2^2 + \frac{1}{2} I_2 (\dot{\rho} + \dot{\theta})^2$$

### Potential Energy

$$V = -m_T g z + m_p g h \cos \theta - m_{v_2} g [l_2 \cos \theta + l_3 \cos (\rho + \theta)]$$

### Forces Not Derivable From a Potential

$$Q_x = -F_T \sin (\rho + \theta)$$

$$Q_z = -F_T \cos (\rho + \theta)$$

$$Q_\theta = \sum_{i=1}^n \bar{F}_i \cdot \frac{\partial \bar{r}}{\partial \theta}$$

$$\bar{F}_T = [-F_T \sin(\rho + \theta)] \bar{i} + [-F_T \cos(\rho + \theta)] \bar{k}$$

$$\bar{r} = [l_2 \sin \theta] \bar{i} + [l_2 \cos \theta] \bar{k}$$

$$\bar{F}_T \cdot \frac{\partial \bar{r}}{\partial \theta} = -F_T \sin(\rho + \theta) l_2 \cos \theta + F_T \cos(\rho + \theta) l_2 \sin \theta$$

$$\therefore Q_\theta = -F_T l_2 \sin \rho$$

$$Q_\rho = [-F_T \sin(\rho + \theta)] [l_3 \cos(\rho + \theta)] + [-F_T \cos(\rho + \theta)] [-l_3 \sin(\rho + \theta)]$$

$$= F_T l_3 [-\sin(\rho + \theta) \cos(\rho + \theta) + \cos(\rho + \theta) \sin(\rho + \theta)]$$

$$= 0 + Q_T - B l_4^2 \dot{\rho}$$

#### Velocities

$$v_p^2 = [\dot{x} - h\dot{\theta} \cos \theta]^2 + [\dot{z} + h\dot{\theta} \sin \theta]^2$$

$$= \dot{x}^2 + \dot{z}^2 - 2h\dot{x}\dot{\theta} \cos \theta + 2h\dot{z}\dot{\theta} \sin \theta + h^2 \dot{\theta}^2$$

$$v_1^2 = \dot{x}^2 + \dot{z}^2$$

$$v_2^2 = [\dot{x} + l_2 \dot{\theta} \cos \theta + l_3 (\dot{\rho} + \dot{\theta}) \cos(\rho + \theta)]^2$$

$$+ [\dot{z} - l_2 \dot{\theta} \sin \theta - l_3 (\dot{\rho} + \dot{\theta}) \sin(\rho + \theta)]^2$$

$$= \dot{x}^2 + \dot{z}^2 + 2l_2 \dot{x}\dot{\theta} \cos \theta + 2l_3 \dot{x}(\dot{\rho} + \dot{\theta}) \cos(\rho + \theta) + l_2^2 \dot{\theta}^2 \cos^2 \theta +$$

$$\begin{aligned}
& + 2 l_2 l_3 \dot{\theta} (\dot{\rho} + \dot{\theta}) \cos \theta \cos (\rho + \theta) + l_3^2 (\dot{\rho} + \dot{\theta})^2 \cos^2 (\rho + \theta) \\
& - 2 l_2 \dot{z} \dot{\theta} \sin \theta - 2 l_3 \dot{z} (\dot{\rho} + \dot{\theta}) \sin (\rho + \theta) + 2 l_2 l_3 \dot{\theta} (\dot{\rho} + \dot{\theta}) \sin \theta \sin (\rho + \theta) \\
& + l_2^2 \dot{\theta}^2 \sin^2 \theta + l_3^2 (\dot{\rho} + \dot{\theta})^2 \sin^2 (\rho + \theta) \\
= & \dot{x}^2 + \dot{z}^2 + 2 l_2 \dot{x} \dot{\theta} \cos \theta + 2 l_3 \dot{x} (\dot{\rho} + \dot{\theta}) \cos (\rho + \theta) + l_2^2 \dot{\theta}^2 \\
& + 2 l_2 l_3 \dot{\theta} (\dot{\rho} + \dot{\theta}) \cos \rho + l_3^2 (\dot{\rho} + \dot{\theta})^2 - 2 l_2 \dot{z} \dot{\theta} \sin \theta \\
& - 2 l_3 \dot{z} (\dot{\rho} + \dot{\theta}) \sin (\rho + \theta)
\end{aligned}$$

### Lagrangian

$$\begin{aligned}
L = T - V = & \frac{1}{2} m_p v_p^2 + \frac{1}{2} I_p \dot{\theta}^2 + \frac{1}{2} m_{v_1} v_1^2 + \frac{1}{2} I_1 \dot{\theta}^2 \\
& + \frac{1}{2} m_{v_2} v_2^2 + \frac{1}{2} I_2 (\dot{\rho} + \dot{\theta})^2 + m_T g z \\
& - m_p g h \cos \theta + m_{v_2} g [l_2 \cos \theta + l_3 \cos (\rho + \theta)]
\end{aligned}$$

### Lagrange Equations of Motion

$$\frac{d}{dt} \left\{ \frac{\partial L}{\partial \dot{q}_r} \right\} - \frac{\partial L}{\partial q_r} = Q_r$$

$$\frac{\partial L}{\partial \dot{x}} = \frac{1}{2} m_p [2 \dot{x} - 2 h \dot{\theta} \cos \theta] + \frac{1}{2} m_{v_1} [2 \dot{x}]$$

$$+ \frac{1}{2} m_{v_2} [2 \dot{x} + 2 l_2 \dot{\theta} \cos \theta + 2 l_3 (\dot{\rho} + \dot{\theta}) \cos (\rho + \theta)]$$

$$\frac{\partial L}{\partial x} = 0$$

$$\begin{aligned} \frac{\partial L}{\partial \dot{z}} &= \frac{1}{2} m_p [2\dot{z} + 2h\dot{\theta} \sin \theta] + \frac{1}{2} m_{v_1} [2\dot{z}] \\ &+ \frac{1}{2} m_{v_2} [2\dot{z} - 2l_2\dot{\theta} \sin \theta - 2l_3(\dot{\rho} + \dot{\theta}) \sin(\rho + \theta)] \end{aligned}$$

$$\frac{\partial L}{\partial z} = m + g$$

$$\begin{aligned} \frac{\partial L}{\partial \dot{\theta}} &= \frac{1}{2} m_p [-2h\dot{x} \cos \theta + 2h\dot{z} \sin \theta + 2h^2\dot{\theta}] + I_p \dot{\theta} \\ &+ I_1 \dot{\theta} + \frac{1}{2} m_{v_2} [2l_2\dot{x} \cos \theta + 2l_3\dot{x} \cos(\rho + \theta) + 2l_2^2\dot{\theta} \\ &+ 2l_2l_3(\dot{\rho} + \dot{\theta}) \cos \rho + 2l_2l_3\dot{\theta} \cos \rho + 2l_3^2(\dot{\rho} + \dot{\theta}) \\ &- 2l_2\dot{z} \sin \theta - 2l_3\dot{z} \sin(\rho + \theta)] + I_2(\dot{\rho} + \dot{\theta}) \end{aligned}$$

$$\begin{aligned} \frac{\partial L}{\partial \dot{\theta}} &= \frac{1}{2} m_p [2h\dot{x}\dot{\theta} \sin \theta + 2h\dot{z}\dot{\theta} \cos \theta] + \frac{1}{2} m_{v_2} [-2l_2\dot{x}\dot{\theta} \sin \theta \\ &- 2l_3\dot{x}(\dot{\rho} + \dot{\theta}) \sin(\rho + \theta) - 2l_2\dot{z}\dot{\theta} \cos \theta - 2l_3\dot{z}(\dot{\rho} + \dot{\theta}) \cos(\rho + \theta)] \\ &+ m_p g h \sin \theta - m_{v_2} g [l_2 \sin \theta + l_3 \sin(\rho + \theta)] \end{aligned}$$

$$\begin{aligned} \frac{\partial L}{\partial \dot{\rho}} &= \frac{1}{2} m_{v_2} [2l_3\dot{x} \cos(\rho + \theta) + 2l_2l_3\dot{\theta} \cos \rho + 2l_3^2(\dot{\rho} + \dot{\theta}) \\ &- 2l_3\dot{z} \sin(\rho + \theta)] + I_2(\dot{\rho} + \dot{\theta}) \end{aligned}$$



$$\frac{\partial L}{\partial \rho} = \frac{1}{2} m_{v_2} \left[ -2 l_3 \dot{x} (\dot{\rho} + \dot{\theta}) \sin(\rho + \theta) - 2 l_2 l_3 \dot{\theta} (\dot{\rho} + \dot{\theta}) \sin \rho \right. \\ \left. - 2 l_3 \dot{z} (\dot{\rho} + \dot{\theta}) \cos(\rho + \theta) \right] - m_{v_2} g l_3 \sin(\rho + \theta)$$

X Equation

$$\frac{d}{dt} \left\{ m_T \dot{x} + \left( m_{v_2} l_2 - m_p h \right) \dot{\theta} \cos \theta + m_{v_2} l_3 (\dot{\rho} + \dot{\theta}) \cos(\rho + \theta) \right\} \\ = -F_T \sin(\rho + \theta)$$

$$m_T \ddot{x} + \left( m_{v_2} l_2 - m_p h \right) \ddot{\theta} \cos \theta - \left( m_{v_2} l_2 - m_p h \right) \dot{\theta}^2 \sin \theta \\ + m_{v_2} l_3 (\ddot{\rho} + \ddot{\theta}) \cos(\rho + \theta) - m_{v_2} l_3 (\dot{\rho} + \dot{\theta})^2 \sin(\rho + \theta) \\ = -F_T \sin(\rho + \theta)$$

Z Equation

$$\frac{d}{dt} \left\{ m_p \dot{z} + m_p h \dot{\theta} \sin \theta + m_{v_1} \dot{z} + m_{v_2} \dot{z} - m_{v_2} l_2 \dot{\theta} \sin \theta \right. \\ \left. - m_{v_2} l_3 (\dot{\rho} + \dot{\theta}) \sin(\rho + \theta) \right\} - m_T g = -F_T \cos(\rho + \theta)$$

$$m_T \ddot{z} + \left( m_p h - m_{v_2} l_2 \right) \ddot{\theta} \sin \theta + \left( m_p h - m_{v_2} l_2 \right) \dot{\theta}^2 \cos \theta \\ - m_{v_2} l_3 (\ddot{\rho} + \ddot{\theta}) \sin(\rho + \theta) - m_{v_2} l_3 (\dot{\rho} + \dot{\theta})^2 \cos(\rho + \theta) \\ - m_T g = -F_T \cos(\rho + \theta)$$



Theta Equation

$$\begin{aligned} \frac{d}{dt} & \left\{ m_p (-h\dot{x} \cos \theta + h\dot{z} \sin \theta + h^2 \ddot{\theta}) + I_p \dot{\theta} + I_1 \dot{\theta} + m_{v_2} [l_2 \dot{x} \cos \theta \right. \\ & + l_3 \dot{x} \cos (\rho + \theta) + l_2^2 \ddot{\theta} + l_2 l_3 (\dot{\rho} + \dot{\theta}) \cos \rho + l_2 l_3 \dot{\theta} \cos \rho \\ & \left. + l_3^2 (\dot{\rho} + \dot{\theta}) - l_2 \dot{z} \sin \theta - l_3 \dot{z} \sin (\rho + \theta)] + I_2 (\dot{\rho} + \dot{\theta}) \right\} \\ & - m_p h \dot{x} \dot{\theta} \sin \theta - m_p h \dot{z} \dot{\theta} \cos \theta + m_{v_2} l_2 \dot{x} \dot{\theta} \sin \theta + m_{v_2} \\ & \cdot [l_3 \dot{x} (\dot{\rho} + \dot{\theta}) \sin (\rho + \theta) + l_2 \dot{z} \dot{\theta} \cos \theta + l_3 \dot{z} (\dot{\rho} + \dot{\theta}) \cos (\rho + \theta)] \\ & - m_p g h \sin \theta = m_{v_2} g [l_2 \sin \theta + l_3 \sin (\rho + \theta)] \\ & = -F_T l_2 \sin \rho \end{aligned}$$

$$\begin{aligned} -m_p h \ddot{x} \cos \theta + m_p h \dot{x} \dot{\theta} \sin \theta + m_p h \ddot{z} \sin \theta + m_p h \dot{z} \dot{\theta} \cos \theta \\ + m_p h^2 \ddot{\theta} + (I_p + I_1) \ddot{\theta} + m_{v_2} l_2 \ddot{x} \cos \theta - m_{v_2} l_2 \dot{x} \dot{\theta} \sin \theta \\ + m_{v_2} l_3 \ddot{x} \cos (\rho + \theta) - m_{v_2} l_3 \dot{x} (\dot{\rho} + \dot{\theta}) \sin (\rho + \theta) \\ + m_{v_2} l_2^2 \ddot{\theta} + m_{v_2} l_2 l_3 (\ddot{\rho} + \ddot{\theta}) \cos \rho - m_{v_2} l_2 l_3 \dot{\rho} (\dot{\rho} + \dot{\theta}) \sin \rho \\ + m_{v_2} l_2 l_3 \ddot{\theta} \cos \rho - m_{v_2} l_2 l_3 \dot{\theta} \dot{\rho} \sin \rho + m_{v_2} l_3^2 (\ddot{\rho} + \ddot{\theta}) \\ - m_{v_2} l_2 \ddot{z} \sin \theta - m_{v_2} l_2 \dot{z} \dot{\theta} \cos \theta - m_{v_2} l_3 \ddot{z} \sin (\rho + \theta) - \end{aligned}$$

$$\begin{aligned}
 & - m_{v_2} l_3 \dot{z} (\dot{\rho} + \dot{\theta}) \cos(\rho + \theta) + I_2 (\ddot{\rho} + \ddot{\theta}) - m_p h \dot{x} \dot{\theta} \sin \theta \\
 & - m_p h \dot{z} \dot{\theta} \cos \theta + m_{v_2} l_2 \dot{x} \dot{\theta} \sin \theta + m_{v_2} l_3 \dot{x} (\dot{\rho} + \dot{\theta}) \sin(\rho + \theta) \\
 & + m_{v_2} l_2 \dot{z} \dot{\theta} \cos \theta + m_{v_2} l_3 \dot{z} (\dot{\rho} + \dot{\theta}) \cos(\rho + \theta) \\
 & - m_p g h \sin \theta + m_{v_2} g l_2 \sin \theta + m_{v_2} g l_3 \sin(\rho + \theta) \\
 & = -F_T l_2 \sin \rho
 \end{aligned}$$

$$\begin{aligned}
 & [-m_p h \cos \theta + m_{v_2} l_2 \cos \theta + m_{v_2} l_3 \cos(\rho + \theta)] \ddot{x} + [m_p h \sin \theta \\
 & - m_{v_2} l_2 \sin \theta - m_{v_2} l_3 \sin(\rho + \theta)] \ddot{z} + [I_p + I_1 + m_p h^2 + m_{v_2} l_2^2 \\
 & + m_{v_2} l_2 l_3 \cos \rho + m_{v_2} l_2 l_3 \cos \rho + m_{v_2} l_3^2 + I_2] \ddot{\theta} \\
 & + [m_{v_2} l_2 l_3 \cos \rho + m_{v_2} l_3^2 + I_2] \ddot{\rho} \\
 & + [-m_{v_2} l_2 l_3 \sin \rho - m_{v_2} l_2 l_3 \sin \rho] \dot{\rho} \dot{\theta} - m_{v_2} l_2 l_3 \dot{\rho}^2 \sin \rho - m_p g h \sin \theta \\
 & + m_{v_2} g l_2 \sin \theta + m_{v_2} g l_3 \sin(\rho + \theta) \\
 & = F_T (h - l_2) \sin \rho
 \end{aligned}$$

$$\begin{aligned}
 & \left[ \left( m_{v_2} l_2 - m_p h \right) \cos \theta + m_{v_2} l_3 \cos (\rho + \theta) \right] \ddot{x} + \left[ \left( m_p h - m_{v_2} l_2 \right) \sin \theta \right. \\
 & \quad \left. - m_{v_2} l_3 \sin (\rho + \theta) \right] \ddot{z} + \left[ I_p + I_1 + I_2 + m_p h^2 + m_{v_2} l_2^2 \right. \\
 & \quad \left. + m_{v_2} l_3^2 + 2m_{v_2} l_2 l_3 \cos \rho \right] \ddot{\theta} + \left[ m_{v_2} l_3 (l_2 \cos \rho + l_3) + I_2 \right] \ddot{\rho} \\
 & \quad - 2m_{v_2} l_2 l_3 \sin \rho \dot{\rho} \dot{\theta} - m_{v_2} l_2 l_3 \dot{\rho}^2 \sin \rho \\
 & \quad + \left[ \left( m_{v_2} l_2 - m_p h \right) g \sin \theta + m_{v_2} g l_3 \sin (\rho + \theta) \right] = - F_T l_2 \sin \rho
 \end{aligned}$$

$\rho$  Equation

$$\begin{aligned}
 & \frac{d}{dt} \left\{ m_{v_2} \left[ l_3 \dot{x} \cos (\rho + \theta) + l_2 l_3 \dot{\theta} \cos \rho + l_3^2 (\dot{\rho} + \dot{\theta}) \right. \right. \\
 & \quad \left. \left. - l_3 \dot{z} \sin (\rho + \theta) \right] + I_2 (\dot{\rho} + \dot{\theta}) \right\} + m_{v_2} l_3 \dot{x} (\dot{\rho} + \dot{\theta}) \sin (\rho + \theta) \\
 & \quad + m_{v_2} l_2 l_3 \dot{\theta} (\dot{\rho} + \dot{\theta}) \sin \rho + m_{v_2} l_3 \dot{z} (\dot{\rho} + \dot{\theta}) \cos (\rho + \theta) \\
 & \quad + m_{v_2} g l_3 \sin (\rho + \theta) = Q_T - B l_4^2 \dot{\rho}
 \end{aligned}$$



$$\begin{aligned}
& m_{v_2} l_3 \ddot{x} \cos(\rho + \theta) - m_{v_2} l_3 \dot{x} (\dot{\rho} + \dot{\theta}) \sin(\rho + \theta) \\
& + m_{v_2} l_2 l_3 \ddot{\theta} \cos \rho - m_{v_2} l_2 l_3 \dot{\theta} \dot{\rho} \sin \rho + m_{v_2} l_3^2 (\ddot{\rho} + \ddot{\theta}) \\
& - m_{v_2} l_3 \ddot{z} \sin(\rho + \theta) - m_{v_2} l_3 \dot{z} (\dot{\rho} + \dot{\theta}) \cos(\rho + \theta) \\
& + I_2 (\ddot{\rho} + \ddot{\theta}) + m_{v_2} l_3 \dot{x} (\dot{\rho} + \dot{\theta}) \sin(\rho + \theta) \\
& + m_{v_2} l_2 l_3 \dot{\theta} (\dot{\rho} + \dot{\theta}) \sin \rho + m_{v_2} l_3 \dot{z} (\dot{\rho} + \dot{\theta}) \cos(\rho + \theta) \\
& + m_{v_2} g l_3 \sin(\rho + \theta) = Q_T - B l_4^2 \dot{\rho}
\end{aligned}$$

$$\begin{aligned}
& m_{v_2} l_3 \ddot{x} \cos(\rho + \theta) + \left[ m_{v_2} l_2 l_3 \cos \rho + m_{v_2} l_3^2 + I_2 \right] \ddot{\theta} \\
& + \left[ m_{v_2} l_3^2 + I_2 \right] \ddot{\rho} - m_{v_2} l_3 \ddot{z} \sin(\rho + \theta) \\
& + m_{v_2} l_2 l_3 \dot{\theta}^2 \sin \rho + m_{v_2} g l_3 \sin(\rho + \theta) = Q_T - B l_4^2 \dot{\rho}
\end{aligned}$$

### Linearization

$$x \Rightarrow \bar{x}$$

$$z \Rightarrow \bar{z}$$

$$\dot{x} \Rightarrow \dot{\bar{x}}$$

$$\dot{z} \Rightarrow \dot{\bar{z}}$$

$$\ddot{x} \Rightarrow \ddot{\bar{x}} - \frac{F_T}{m_T} \sin \theta_o$$

$$\ddot{z} \Rightarrow \ddot{\bar{z}} - \frac{F_T}{m_T} \cos \theta_o + g$$

$$\theta \Rightarrow \theta_0 + \theta \qquad \rho \Rightarrow \rho$$

$$\dot{\theta} \Rightarrow \dot{\theta} \qquad \dot{\rho} \Rightarrow \dot{\rho}$$

$$\ddot{\theta} \Rightarrow \ddot{\theta} \qquad \ddot{\rho} \Rightarrow \ddot{\rho}$$

$$\sin \theta \Rightarrow \sin \theta_0 + \cos \theta_0 \theta$$

$$\cos \theta \Rightarrow \cos \theta_0 - \sin \theta_0 \theta$$

$$\sin(\rho + \theta) \Rightarrow \sin \theta_0 + \cos \theta_0 \theta + \cos \theta_0 \rho$$

$$\cos(\rho + \theta) \Rightarrow \cos \theta_0 - \sin \theta_0 \theta - \sin \theta_0 \rho$$

$$\sin \rho \Rightarrow \rho$$

$$\cos \rho \Rightarrow 1$$

NEGLECT:

1. Constant Terms
2. Products of Variables

x Equation

$$m_T \ddot{x} - m_T \frac{F_T}{m_T} \cancel{\sin \theta_0} + (m_{v_2} \ell_2 - m_p h) \ddot{\theta} (\cos \theta_0 - \cancel{\sin \theta_0 \theta})$$

$$- (m_{v_2} \ell_2 - m_p h) \cancel{\dot{\theta}^2} (\sin \theta_0 + \cos \theta_0 \theta)$$

$$+ m_{v_2} \ell_2 (\ddot{\rho} + \ddot{\theta}) (\cos \theta_0 - \sin \theta_0 \theta - \sin \theta_0 \rho)$$

$$- m_{v_2} \ell_3 (\cancel{\dot{\rho} + \dot{\theta}})^2 (\sin \theta_0 + \cos \theta_0 \theta + \cos \theta_0 \rho)$$

$$= - F_T (\cancel{\sin \theta_0} + \cos \theta_0 \theta + \cos \theta_0 \rho)$$

$$m_T \ddot{x} + (m_{v_2} l_2 - m_p h) \cos \theta_o \ddot{\theta} + m_{v_2} l_3 (\ddot{\rho} + \ddot{\theta}) \cos \theta_o$$

$$= - F_T (\cos \theta_o \theta + \cos \theta_o \rho)$$

$$m_T x S^2 + \left[ (m_{v_2} l_2 - m_p h + m_{v_2} l_3) \cos \theta_o S^2 + F_T \cos \theta_o \right] \theta$$

$$+ \left[ + m_{v_2} l_3 \cos \theta_o S^2 + F_T \cos \theta_o \right] \rho = 0$$

z Equation

$$m_T \ddot{z} - m_T \frac{F_T}{m_T} \cos \theta_o + (m_p h - m_{v_2} l_2) \ddot{\theta} (\sin \theta_o + \cos \theta_o \theta)$$

$$+ (m_p h - m_{v_2} l_2) \dot{\theta}^2 (\cos \theta_o - \sin \theta_o \theta) + m_T g$$

$$- m_{v_2} l_3 (\ddot{\rho} + \ddot{\theta}) (\sin \theta_o + \cos \theta_o \theta + \cos \theta_o \rho)$$

$$- m_{v_2} l_3 (\dot{\rho} + \dot{\theta})^2 (\cos \theta_o - \sin \theta_o \theta - \sin \theta_o \rho)$$

$$- m_T g = - F_T (\cos \theta_o - \sin \theta_o \theta - \sin \theta_o \rho)$$

$$m_T \ddot{z} + (m_p h - m_{v_2} l_2) \sin \theta_o \ddot{\theta} - m_{v_2} l_3 \sin \theta_o (\ddot{\rho} + \ddot{\theta})$$

$$= F_T \sin \theta_o \theta + F_T \sin \theta_o \rho$$

$$m_T z S^2 + \left[ (m_p h - m_{v_2} l_2 - m_{v_2} l_3) \sin \theta_o S^2 - F_T \sin \theta_o \right] \theta$$

$$+ \left[ -m_{v_2} l_3 \sin \theta_o S^2 - F_T \sin \theta_o \right] \rho = 0$$

$\theta$  Equation

$$\cos \theta_o \ddot{x} + \frac{F_T}{m_T} \sin^2 \theta_o \theta$$

$$\underbrace{\left( m_{v_2} l_2 - m_p h \right) (\cos \theta_o - \sin \theta_o \theta) \left( \dot{x} - \frac{F_T}{m_T} \sin \theta_o \right)}_{\text{Term 1}}$$

$$+ m_{v_2} l_3 (\cos \theta_o - \sin \theta_o \theta - \sin \theta_o \rho) \left( \dot{x} - \frac{F_T}{m_T} \sin \theta_o \right)$$

$$+ \left( m_p h - m_{v_2} l_2 \right) (\sin \theta_o + \cos \theta_o \theta) \left( \dot{z} - \frac{F_T}{m_T} \cos \theta_o + g \right)$$

$$- m_{v_2} l_3 (\sin \theta_o + \cos \theta_o \theta + \cos \theta_o \rho) \left( \dot{z} - \frac{F_T}{m_T} \cos \theta_o + g \right)$$

$$+ \left[ I_p + I_1 + I_2 + m_p h^2 + m_{v_2} l_2^2 + m_{v_2} l_3^2 + 2m_{v_2} l_2 l_3 (1) \right] \ddot{\theta}$$

$$+ \left[ m_{v_2} l_3 (l_2 + l_3) + I_2 \right] \ddot{\rho} - 2m_{v_2} l_2 l_3 \dot{\rho} \dot{\theta}$$

$$- m_{v_2} l_2 l_3 \dot{\rho}^2 + \left( m_{v_2} l_2 - m_p h \right) g (\sin \theta_o + \cos \theta_o \theta)$$

$$+ m_{v_2} g l_3 (\sin \theta_o + \cos \theta_o \theta + \cos \theta_o \rho) = -F_T l_2 \rho$$

$$\begin{aligned}
& \left( m_{v_2} l_2 - m_p h \right) \left( \cos \theta_o \ddot{x} + \frac{F_T}{m_T} \sin^2 \theta_o \theta \right) + m_{v_2} l_3 \cos \theta_o \ddot{x} \\
& + m_{v_2} l_3 \frac{F_T}{m_T} \sin^2 \theta_o (\theta + \rho) + \left( m_p h - m_{v_2} l_2 \right) \left( \sin \theta_o \ddot{z} - \frac{F_T}{m_T} \cos^2 \theta_o \theta \right) \\
& - m_{v_2} l_3 \sin \theta_o \ddot{z} + m_{v_2} l_3 \frac{F_T}{m_T} \cos^2 \theta_o (\theta + \rho) \\
& + \left[ I_p + I_1 + I_2 + m_p h^2 + m_{v_2} (l_2 + l_3)^2 \right] \ddot{\theta} + \left[ I_2 + m_{v_2} l_3 (l_2 + l_3) \right] \dot{\rho} \\
& + F_T l_2 \rho = 0
\end{aligned}$$

$$\begin{aligned}
& \left\{ \left[ -m_p h + m_{v_2} (l_2 + l_3) \right] \cos \theta_o S^2 \right\} x + \left\{ \left[ m_p h - m_{v_2} (l_2 + l_3) \right] \sin \theta_o S^2 \right\} z \\
& + \left\{ \left[ I_p + I_1 + I_2 + m_p h^2 + m_{v_2} (l_2 + l_3)^2 \right] S^2 + \left[ (-m_p h \right. \right. \\
& \left. \left. + m_{v_2} (l_2 + l_3) \left( \frac{F_T}{m_T} + g \cos \theta_o \right) \right] \right\} \theta + \left\{ \left[ I_2 + m_{v_2} l_3 (l_2 + l_3) \right] S^2 \right. \\
& \left. + \left[ m_{v_2} l_3 \left( \frac{F_T}{m_T} + g \cos \theta_o \right) + F_T l_2 \right] \right\} \rho = 0
\end{aligned}$$

$\rho$  Equation

$$\begin{aligned}
& m_{v_2} l_3 \left( \ddot{x} - \frac{F_T}{m_T} \sin \theta_o \right) (\cos \theta_o - \sin \theta_o \theta - \sin \theta_o \rho) \\
& + \left[ m_{v_2} l_3 (l_2 + l_3) + I_2 \right] \ddot{\theta} + \left[ m_{v_2} l_3^2 + I_2 \right] \dot{\rho}
\end{aligned}$$

$$-m_{v_2} l_3 \left( \ddot{z} - \frac{F_T}{m_T} \cos \theta_o \right) (\sin \theta_o + \cos \theta_o \theta + \cos \theta_o \rho)$$

$$+m_{v_2} l_2 l_3 \theta^2 \rho + m_{v_2} g l_3 (\sin \theta_o + \cos \theta_o \theta + \cos \theta_o \rho)$$

$$= 0$$

$$m_{v_2} l_3 \cos \theta_o \ddot{x} + \left[ m_{v_2} l_3 \frac{F_T}{m_T} \sin^2 \theta_o + m_{v_2} l_3 \frac{F_T}{m_T} \cos^2 \theta_o \right. \\ \left. + \left[ m_{v_2} l_3 \frac{F_T}{m_T} \sin^2 \theta_o + m_{v_2} l_3 \frac{F_T}{m_T} \cos^2 \theta_o \right] \rho + \left[ m_{v_2} l_3 (l_2 + l_3) \right. \right. \\ \left. \left. + I_2 \right] \ddot{\theta} + \left[ m_{v_2} l_3^2 + I_2 \right] \ddot{\rho} - \left[ m_{v_2} l_3 \sin \theta_o \right] \ddot{z} = 0$$

$$\left[ m_{v_2} l_3 \cos \theta_o S^2 \right] x + \left[ -m_{v_2} l_3 \sin \theta_o S^2 \right] z \\ + \left\{ \left[ m_{v_2} l_3 (l_2 + l_3) + I_2 \right] S^2 + \left[ \left( m_{v_2} l_3 \frac{F_T}{m_T} \right) \right] \right\} \theta \\ + \left\{ \left[ m_{v_2} l_3^2 + I_2 \right] S^2 + \left[ B l_4^2 \right] S + \left[ m_{v_2} l_3 \left( \frac{F_T}{m_T} \right) \right] \right\} \rho = Q_T$$

**Table C-2. Matrix of Linearized, Pitch/Roll Plane Equations of Motion for Hardwire Geometry (Cont)**

$m_T S^2$	0	$\left[ \left[ m_{v_2} (\ell_2 + \ell_3) - m_p h \right] \cdot \cos \theta_o \right] S^2$ $+ F_T \cos \theta_o$	$m_{v_2} \ell_3 \cos \theta_o S^2$ $+ F_T \cos \theta_o$	X	0
0	$m_T S^2$	$\left[ \left[ m_p h - m_{v_2} (\ell_2 + \ell_3) \right] \cdot \sin \theta_o \right] S^2$ $- F_T \sin \theta_o$	$-m_{v_2} \ell_3 \sin \theta_o S^2$ $- F_T \sin \theta_o$	Z	0
$\left[ \left[ m_{v_2} (\ell_2 + \ell_3) - m_p h \right] \cdot \cos \theta_o \right] S^2$	$\left[ \left[ m_p h - m_{v_2} (\ell_2 + \ell_3) \right] \cdot \sin \theta_o \right] S^2$	$\left[ I_p + I_1 + I_2 + m_p h^2 + m_{v_2} (\ell_2 + \ell_3)^2 \right] S^2$ $+ \left[ \left[ -m_p h + m_{v_2} (\ell_2 + \ell_3) \right] \frac{F_T}{m_T} \right]$	$\left[ I_2 + m_{v_2} \ell_3 (\ell_2 + \ell_3) \right] S^2$ $+ \left[ m_{v_2} \ell_3 \left( \frac{F_T}{m_T} \right) + F_T \ell_2 \right]$	=	0
$m_{v_2} \ell_3 \cos \theta_o S^2$	$-m_{v_2} \ell_3 \sin \theta_o S^2$	$\left[ m_{v_2} \ell_3 (\ell_2 + \ell_3) + I_2 \right] S^2$ $+ \left[ m_{v_2} \ell_3 \left( \frac{F_T}{m_T} \right) \right]$	$\left[ m_{v_2} \ell_3^2 + I_2 \right] S^2$ $+ \left[ B \ell_4^2 \right] S$ $+ \left[ m_{v_2} \ell_3 \left( \frac{F_T}{m_T} \right) \right]$	p	$\theta_T$

APPENDIX C, PART 3

HARDWIRE EQUATIONS OF MOTION WITH PIVOT  
ABOVE CENTER OF GRAVITY



## EQUATIONS OF MOTION

The overhead pivot configuration of FIGURE 1a is shown schematically as a two-body problem in FIGURE C-3.  $F_A$  represents control forces applied by the pilot (or an actuator). Free body diagrams of the system are shown in FIGURE C-4. Defining unit vectors  $l_x$  and  $l_z$ , the equations of the base are now written:

$$\dot{\bar{R}}_o = \dot{R}_x l_x + \dot{R}_z l_z = u \bar{x} + w \bar{z} = \bar{V}_B \quad (C-1)$$

$$M_B \left[ \frac{\delta \bar{V}_B}{\delta t} + \bar{\omega} \times \bar{V}_B \right] = T \bar{x} - F_x \bar{x} - F_A \bar{z} + F_z \bar{z} \quad (C-2)$$

$$M_B \left[ \dot{u} \bar{x} + \dot{w} \bar{z} + \dot{\theta} w \bar{x} - \dot{\theta} u \bar{z} \right] = T \bar{x} - F_x \bar{x} - F_A \bar{z} + F_z \bar{z} \quad (C-3)$$

Rearranging to scalar form:

$$M_B (\dot{u} + \dot{\theta} w) = T - F_x \quad (C-4)$$

$$M_B (\dot{w} - \dot{\theta} u) = -F_A + F_z \quad (C-5)$$

and the moment equation is:

$$I_B \ddot{\theta} = -F_z l_B + F_A l_A \quad (C-6)$$

Proceeding now to write the equations of the pendulum:

$$\bar{r}_p = \bar{R}_o + l_B \bar{x} - l_p \bar{x} + l_p \phi \bar{z} \quad (C-7)$$

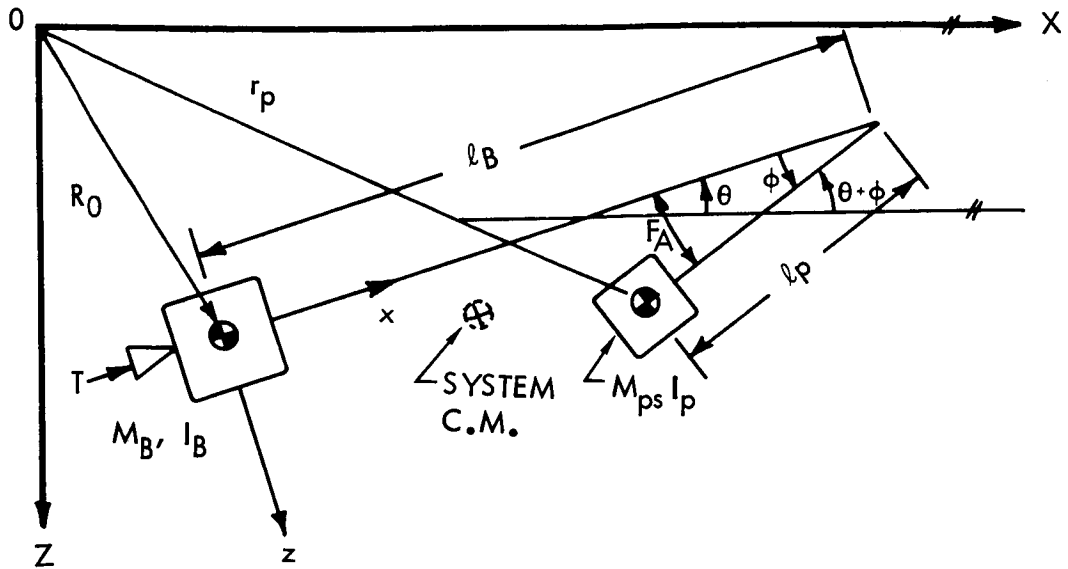


Figure C-3. Schematic Representation of the Overhead Pivot LFV

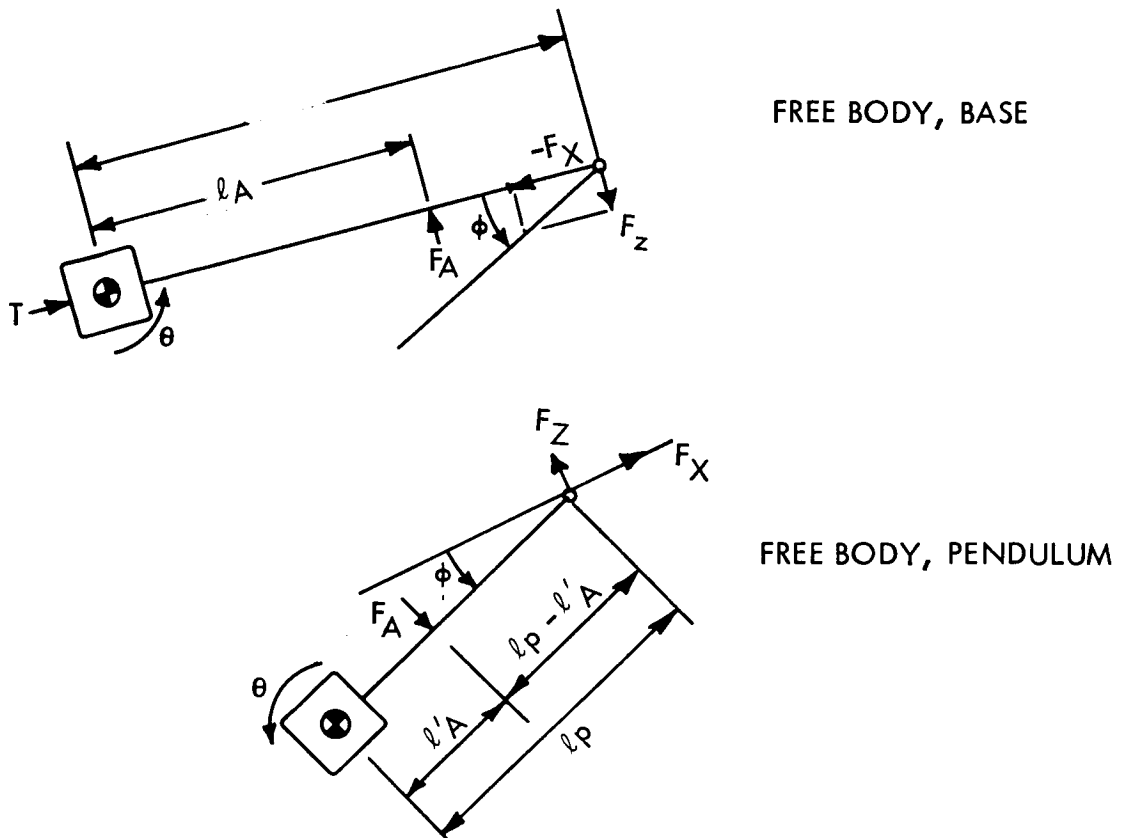


Figure C-4. System Free-Body Diagram

$$\begin{aligned}
 \dot{\bar{r}}_p &= \dot{\bar{R}}_o + \ell_p \dot{\phi} \bar{z} + \bar{\omega} \times \left[ (\ell_B - \ell_p) \bar{x} + \ell_p \phi \bar{z} \right] \\
 &= u \bar{x} + w \bar{z} + \ell_p \dot{\phi} \bar{z} - \dot{\theta} (\ell_B - \ell_p) \bar{z} + \dot{\theta} \ell_p \phi \bar{x} \\
 &= \left[ u + \ell_p \phi \dot{\theta} \right] \bar{x} + \left[ w + \ell_p \dot{\phi} - (\ell_B - \ell_p) \dot{\theta} \right] \bar{z} = \bar{V}_p \quad (C-8)
 \end{aligned}$$

$$M_p \left[ \frac{\delta \bar{V}_p}{\delta t} + \bar{\omega} \times \bar{V}_p \right] = F_x \bar{x} - F_z \bar{z} + F_A \bar{z} \quad (C-9)$$

$$\begin{aligned}
 M_p \left\{ \left[ \dot{u} + \ell_p \dot{\phi} \dot{\theta} + \ell_p \phi \ddot{\theta} \right] \bar{x} + \left[ \dot{w} + \ell_p \ddot{\phi} - (\ell_B - \ell_p) \ddot{\theta} \right] \bar{z} - \dot{\theta} \left[ u + \ell_p \phi \dot{\theta} \right] \bar{z} \right. \\
 \left. + \dot{\theta} \left[ w + \ell_p \dot{\phi} - (\ell_B - \ell_p) \dot{\theta} \right] \bar{x} \right\} = F_x \bar{x} - F_z \bar{z} + F_A \bar{z} \quad (C-10)
 \end{aligned}$$

and as before, the scalar equations are:

$$M_p \left[ \dot{u} + 2 \ell_p \dot{\phi} \dot{\theta} + \ell_p \phi \ddot{\theta} + \dot{\theta} w - (\ell_B - \ell_p) \dot{\theta}^2 \right] = F_x \quad (C-11)$$

$$M_p \left[ \dot{w} - \dot{\theta} u - \ell_p \phi \dot{\theta}^2 + \ell_p \ddot{\phi} - (\ell_B - \ell_p) \ddot{\theta} \right] = -F_z + F_A \quad (C-12)$$

and the moment equation is:

$$I_p (\ddot{\theta} + \dot{\phi}) = -F_A \ell'_A + F_z \ell_p - F_x \ell_p \phi \quad (C-13)$$

Substituting Equation C-12 into C-6 for  $F_z$ :

$$I_B \ddot{\theta} = + F_A l_A = F_A l_B + M_p l_B \left[ \dot{w} - \dot{\theta} u - l_p \phi \dot{\theta}^2 + l_p \ddot{\phi} - (l_B - l_p) \ddot{\theta} \right] =$$

$$- F_A (l_B - l_A) + M_p l_B \left[ \dot{w} - \dot{\theta} u - l_p \phi \dot{\theta}^2 - l_B \ddot{\theta} + l_p (\ddot{\phi} + \ddot{\theta}) \right] \quad (C-14)$$

and the corresponding linearized equation is:

$$I_B \ddot{\theta} = - F_A (l_B - l_A) + M_p l_B \dot{w} - M_p l_B^2 \ddot{\theta} + M_p l_B l_p (\ddot{\theta} + \ddot{\phi}) \quad (C-15)$$

Substituting again for  $F_z$  in Equation C-13

$$I_p (\ddot{\theta} + \ddot{\phi}) = - F_A l'_A + F_A l_p - M_p l_p \left[ \dot{w} - \dot{\theta} u \right.$$

$$\left. + l_p \phi \dot{\theta}^2 + l_p \ddot{\phi} - (l_B - l_p) \ddot{\theta} \right] - F_x l_p \phi \quad (C-16)$$

which linearizes to (using Equation C-4)

$$I_p (\ddot{\theta} + \ddot{\phi}) = F_A (l_p - l'_A) - M_p l_p \dot{w} + M_p l_p^2 (\ddot{\theta} + \ddot{\phi})$$

$$- M_p l_p l_B \ddot{\theta} - l_p \phi \left[ T - M_B \dot{u} \right] \quad (C-17)$$

and we have finally:

$$I_p (\ddot{\theta} + \ddot{\phi}) = F_A (l_p - l'_A) - M_p l_p \dot{w} + M_p l_p^2 (\ddot{\theta} + \ddot{\phi})$$

$$- M_p l_p l_B \ddot{\theta} - l_p \phi T \left[ 1 - \frac{M_B}{M_B + M_p} \right] \quad (C-18)$$

the linearized translation equation completes the set:

$$(M_p + M_B) \dot{w} = - M_p \ell_p \ddot{\phi} - M_p (\ell_B - \ell_p) \ddot{\theta} \quad (C-19)$$

Summarizing and regrouping the equations:

$$(I_B + M_p \ell_B^2 - M_p \ell_B \ell_p) \ddot{\theta} - M_p \ell_p \ell_p \ddot{\phi} = - F_A (\ell_B - \ell_A) + M_p \ell_B \dot{w} \quad (C-20)$$

$$(I_p - M_p \ell_p^2 + M_p \ell_p \ell_B) \ddot{\theta} + (I_p - M_p \ell_p^2) \ddot{\phi} = F_A (\ell_p - \ell_A') - M_p \ell_p \dot{w} - \ell_p \phi [T - M_B \dot{u}] \quad (C-21)$$

$$(M_p + M_B) \dot{w} = - M_p \ell_p \ddot{\phi} - M_p (\ell_B - \ell_p) \ddot{\theta} \quad (C-22)$$

$$(M_B + M_p) \dot{u} = T \quad (C-23)$$

Substituting Equation C-22 and C-23 into C-20 and C-21, laplace transforming, transforming, and casting into matrix format we have:

$$\begin{bmatrix} A^* S^2 & E^* S^2 \\ C^* S^2 & D^* S^2 + \ell_p^* T \end{bmatrix} \begin{bmatrix} \theta \\ \phi \end{bmatrix} = \begin{bmatrix} \ell_A - \ell_B \\ \ell_p - \ell_A' \end{bmatrix} F_A \quad (C-24)$$

where:

$$A^* = I_B + M_p \ell_B^2 - M_p \ell_p \ell_p + \frac{M_p^2 \ell_B (\ell_B - \ell_p)}{M_B + M_p} \quad (C-25)$$

$$D^* = I_p - M_p \ell_p^2 - \frac{M_p^2 \ell_p^2}{M_p + M_B} = I_p - M_p \ell_p^2 \left\{ 1 + \frac{M_p}{M_p + M_B} \right\} \quad (C-26)$$

$$E^* = \frac{M_p^2 \ell_p \ell_B}{M_p + M_B} - M_p \ell_B \ell_p = M_p \ell_p \ell_B \left\{ \frac{M_p}{M_p + M_B} - 1 \right\} \quad (C-27)$$

$$C^* = I_p - M_p \ell_p^2 + M_p \ell_p \ell_B - \frac{M_p^2 \ell_B (\ell_B - \ell_p)}{M_B + M_p} \quad (C-28)$$

$$\ell_p^* = \ell_p \left\{ 1 - \frac{M_B}{M_B + M_p} \right\} \quad (C-29)$$

and from the geometry of the configuration:

$$\ell_p - \ell_A' = -(\ell_A - \ell_B) \quad (C-30)$$

The transfer functions are obtained using standard methods on Equation C-24:

$$\frac{\phi}{F_A} = \frac{(\ell_p - \ell_A') A^* - (\ell_A - \ell_B) C^*}{\left[ A^* D^* - E^* C^* \right] S^2 + A^* \ell_p^* T} \quad (C-31)$$

$$\frac{\theta}{F_A} = \frac{\left[ (\ell_A - \ell_B) D^* - (\ell_p - \ell_A') E^* \right] S^2 + (\ell_A - \ell_B) \ell_p^* T}{S^2 \left[ (A^* D^* - E^* C^*) S^2 + A^* \ell_p^* T \right]} \quad (C-32)$$

APPENDIX D  
HARDOVER ACTUATOR FAILURE ANALYSIS

#### APPENDIX D. HARDOVER ACTUATOR FAILURE ANALYSIS

Figure D-1 is the generalized, three-axis attitude control system for the lunar flying vehicle. All three axes are cross-coupled through the generalized gimbal configuration, but other cross-coupling terms are neglected. In an attitude hold mode, attitude position is derived by integrating measured body rate, which is provided by a three-axis gyro package. Error signals, generated as a function of instantaneous vehicle body rate and attitude, provide corrective rotation by energizing some or all of the  $\eta$  actuators to correct the vehicle to the steady-state attitude command value. These error voltages are in body coordinates and can be represented by a vector  $V$ .

$$[V]_B = \begin{bmatrix} V_\theta \\ V_\phi \\ V_\psi \end{bmatrix}_B$$

An actuator sensitivity  $[\Gamma]$  (which is proportional to  $[\Delta]$  if cross-coupling on command is not introduced through a less than ideal transformation selection) is a body axis gain which can be represented as follows:

$$[\Gamma]_B = \begin{bmatrix} \gamma_\theta & 0 & 0 \\ 0 & \gamma_\phi & 0 \\ 0 & 0 & \gamma_\psi \end{bmatrix}_B$$

Transformation  $[A]$  defines the weighting function by which the three body-axis error voltages are combined to energize the  $\eta$  actuators.  $[A]$  transforms three body-axis signals into  $\eta$  signals which are in gimbal axis coordinates.  $[A]$  is a configuration-dependent matrix of constants,



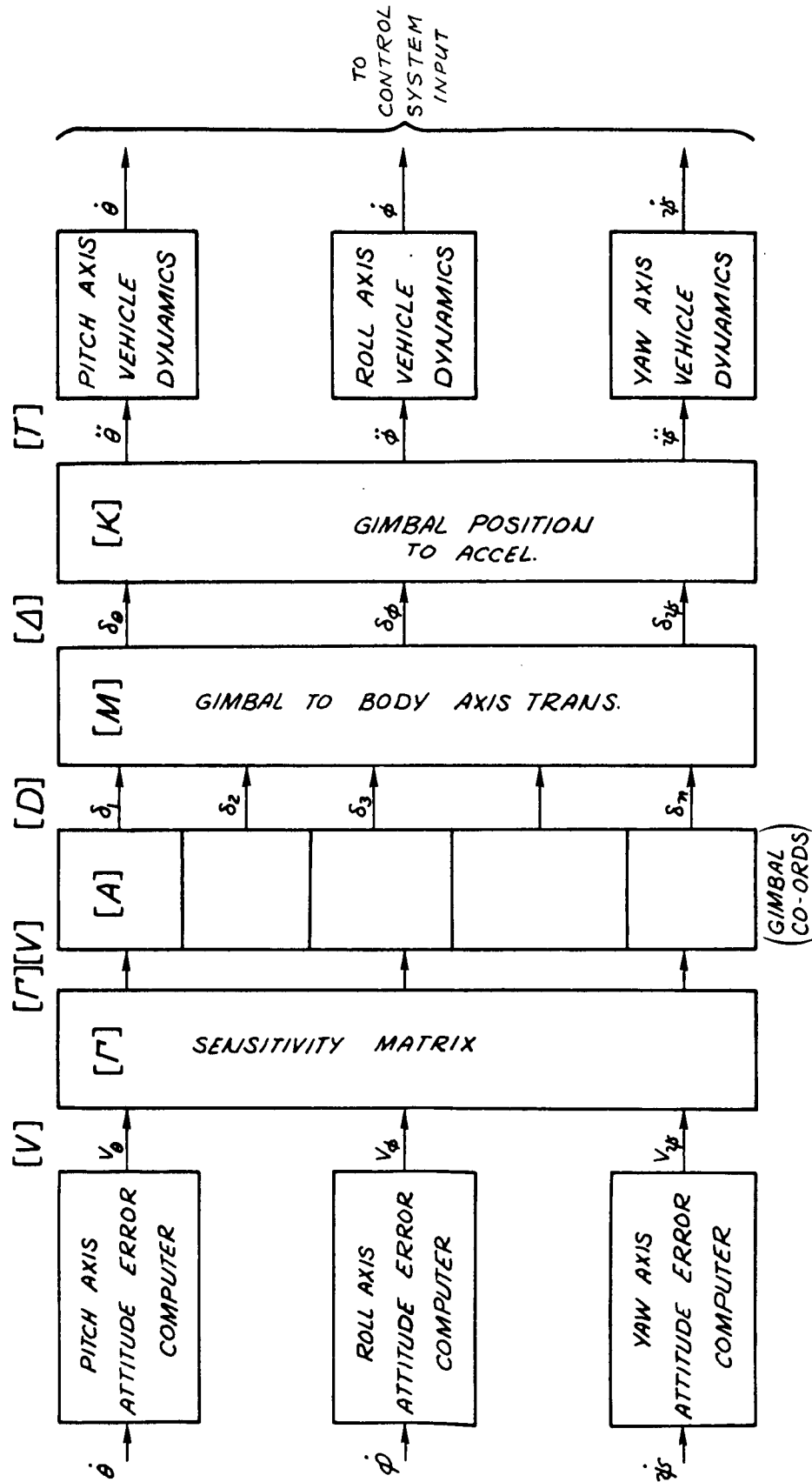


Figure D-1. Three-Axis Control System for Lunar Flying Vehicle

$$[A]_G = \begin{bmatrix} a_{11} & a_{12} & a_{13} & \vdots \\ a_{21} & \vdots & \vdots & \vdots \\ \vdots & \vdots & \vdots & \vdots \\ a_{n1} & \dots & a_{n3} \end{bmatrix}_G$$

The resultant output vector  $[D]$ , which represents true gimbal axis deflection, in gimbal coordinates, can be given as:

$$[D]_G = \begin{bmatrix} \delta_1 \\ \delta_2 \\ \delta_3 \\ \vdots \\ \delta_n \end{bmatrix}_G$$

Matrix  $[M]$  is fixed by the geometry of the actuation system selected and represents the vector transformation of actuator deflection in gimbal axis coordinates to actuator deflection in body axis coordinates. This is given as:

$$[M]_G = \begin{bmatrix} m_{11} & m_{12} & m_{13} & \dots & m_{1n} \\ m_{21} & \vdots & \vdots & \vdots & \vdots \\ m_{31} & \dots & \dots & \dots & m_{3n} \end{bmatrix}_G$$

The resultant output of M is a vector  $\Delta$  which represents a value of total actuator position in each of the body axes. The specific contribution of each of the  $\eta$  actuators to each body axis position is not discernable from this vector - it is the resultant of all gimbals as reflected into each body axis.

$$[\Delta]_B = \begin{bmatrix} \delta_\theta \\ \delta_\phi \\ \delta_\psi \end{bmatrix}_B$$

In order to determine acceleration, additional vehicle parameters must be included to indicate sensitivity of response to an acceleration command V. This is the K vector which specifies the  $Tl/I$  of the vehicle in each axis.

$$[K]_B = \begin{bmatrix} \frac{T_\theta l_\theta}{I_\theta} & 0 & 0 \\ 0 & \frac{T_\phi l_\phi}{I_\phi} & 0 \\ 0 & 0 & \frac{T_\psi l_\psi}{I_\psi} \end{bmatrix}$$

The resultant output of this weighting function is body axis acceleration.

$$[T]_B = \begin{bmatrix} \ddot{\theta} \\ \ddot{\phi} \\ \ddot{\psi} \end{bmatrix}_B$$

In order to establish whether or not the geometrical configuration chosen for thrust vector control will maintain static stability under the conditions induced by the hardover failure of one actuator, it must be determined how much acceleration capability is left after nulling out the constant disturbance acceleration presented by the failed actuator. If all or most of the other actuators saturate their maximum angle of excursion, there will be no control authority remaining to compensate for future stabilization requirements. If one or more axes can no longer be torqued by a "couple," extensive cross-coupling will result, and even though there may be some gimbal angle remaining in each body axis, a divergent limit cycle may result causing dynamic instability.

Additional analysis, then, must be made after the quiescent values of gimbal angle under hardover failure conditions are determined.

To determine the new quiescent value of each gimbal angle in response to one hardover actuator failure, the net acceleration on the vehicle must be zero.

Then

$$[T] = \begin{bmatrix} \ddot{\theta} \\ \ddot{\phi} \\ \ddot{\psi} \end{bmatrix} = [Z] = \begin{bmatrix} 0 \\ 0 \\ 0 \end{bmatrix}$$

The total expression for acceleration as a function of error signal is given by

$$[K] [M] [A] [\Gamma] [V] = [T] = [Z]$$

Now, if one actuator fails, hardover, it is generating full torque, but is unresponsive to actuation command. Therefore,  $[D]$  must be separated into responsive gimbal angles and a forcing function in the existence of the failed actuator.

Then

$$[D] = \underbrace{[D']}_{\text{Responsive Actuators}} + \underbrace{[D'']}_{\text{Forcing Function}}$$

$$[D] = \begin{bmatrix} \delta_1 \\ \delta_2 \\ 0 \\ \vdots \\ \delta_\eta \end{bmatrix} + \begin{bmatrix} 0 \\ 0 \\ \delta_k \\ 0 \\ \vdots \\ 0 \end{bmatrix}$$

Where the kth actuator is failed, hardover.

Since the kth actuator does not respond to the input voltage delivered to it, one row of the  $[A]$  matrix must be zeroed to equate the mathematical model with the hardware configuration. Zero the kth row.

$$[A'] = \begin{bmatrix} a_{11} & a_{12} & a_{13} \\ a_{21} & a_{22} & a_{23} \\ \vdots & \vdots & \vdots \\ 0 & 0 & 0 \\ \vdots & \vdots & \vdots \\ a_{n_1} & a_{n_2} & a_{n_3} \end{bmatrix}$$

Now  $[K] [M] [D] = [T] = [Z]$  for acceleration negation.

and

$$[K] [M] [D] = [K] [M] [D'] + [K] [M] [D''] = [Z]$$

$$[K] [M] [D'] = - [K] [M] [D'']$$

but

$$[D'] = [A'] [\Gamma] [V]$$

Therefore,

$$[K] [M] [A'] [\Gamma] [V] = - [K] [M] [D'']$$

pre-multiplying by  $[K]^{-1}$

$$[M] [A'] [\Gamma] [V] = - [M] [D'']$$

Define

$$[F] = [\Gamma] [V]$$

Then

$$[M] [A'] [F] = - [M] [D'']$$

The only unknown in the equation is  $[F]$  ; solve for  $[F]$  .

Then

$$[D'] = [A'] [F]$$

$[D]$  is the desired answer.

Now, a reevaluation of dynamic stability must be made as an additional step in predicting new control authority capability under dynamic conditions.

The effort required here is highly dependent upon the configuration. Many geometries can be analyzed from this point by inspection; many others require extensive analysis.

#### ANALYSIS OF A SINGLE HARDOVER ACTUATOR FAILURE ON A FOUR-ENGINE, FOUR-ACTUATOR CONFIGURATION

From the geometry (Figure D-2)

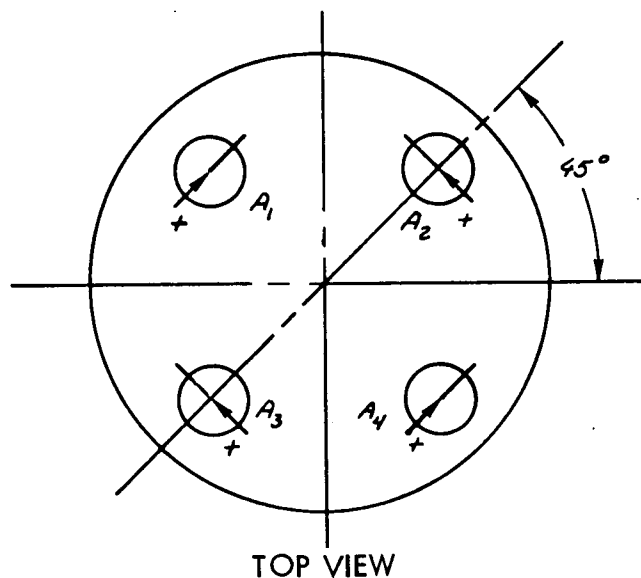


Figure D-2. Schematic Top View of a Four-Engine, Four-Actuator Configuration

$$[M] = \begin{bmatrix} 0.707 & 0.707 & 0.707 & 0.707 \\ -0.707 & 0.707 & 0.707 & -0.707 \\ 1 & -1 & 1 & -1 \end{bmatrix}$$

Select input matrix  $[A]$  to eliminate cross-coupling on command:

$$[A] = \begin{bmatrix} 1.414 & -1.414 & 1 \\ 1.414 & 1.414 & -1 \\ 1.414 & 1.414 & 1 \\ 1.414 & -1.414 & -1 \end{bmatrix}$$

Assume  $\delta_3$  failed hardover =  $-\delta_{\max}$ ;  $k = 3$

$$[D''] = \begin{bmatrix} 0 \\ 0 \\ -\delta_{\max} \\ 0 \end{bmatrix}$$

$$[A'] = \begin{bmatrix} \sqrt{2} & -\sqrt{2} & 1 \\ \sqrt{2} & \sqrt{2} & -1 \\ 0 & 0 & 0 \\ \sqrt{2} & -\sqrt{2} & -1 \end{bmatrix}$$

$$[M] [A'] [F] = - [M] [D'']$$

$$\begin{bmatrix} \frac{\sqrt{2}}{2} & \frac{\sqrt{2}}{2} & \frac{\sqrt{2}}{2} & \frac{\sqrt{2}}{2} \\ -\frac{\sqrt{2}}{2} & \frac{\sqrt{2}}{2} & \frac{\sqrt{2}}{2} & -\frac{\sqrt{2}}{2} \\ 1 & -1 & 1 & -1 \end{bmatrix} \begin{bmatrix} 2 & -2 & 1 \\ \sqrt{2} & \sqrt{2} & -1 \\ 0 & 0 & 0 \\ \sqrt{2} & -\sqrt{2} & -1 \end{bmatrix} \begin{bmatrix} F_{\theta} \\ F_{\phi} \\ F_{\psi} \end{bmatrix}$$



$$= - \begin{bmatrix} \frac{\sqrt{2}}{2} & \frac{\sqrt{2}}{2} & \frac{\sqrt{2}}{2} & \frac{\sqrt{2}}{2} \\ -\frac{\sqrt{2}}{2} & \frac{\sqrt{2}}{2} & \frac{\sqrt{2}}{2} & -\frac{\sqrt{2}}{2} \\ 1 & -1 & 1 & -1 \end{bmatrix} \begin{bmatrix} 0 \\ 0 \\ -\delta_{\max} \\ 0 \end{bmatrix}$$

$$\begin{bmatrix} 3 & -1 & -\frac{\sqrt{2}}{2} \\ -1 & 3 & -\frac{\sqrt{2}}{2} \\ -\sqrt{2} & -\sqrt{2} & 3 \end{bmatrix} \begin{bmatrix} F_{\theta} \\ F_{\phi} \\ F_{\psi} \end{bmatrix} = \begin{bmatrix} \frac{\sqrt{2}}{2} \delta_{\max} \\ \frac{\sqrt{2}}{2} \delta_{\max} \\ \delta_{\max} \end{bmatrix}$$

$$1. \quad 3F_{\theta} - F_{\phi} - \frac{\sqrt{2}}{2} F_{\psi} = \frac{\sqrt{2}}{2} \delta_{\max}$$

$$2. \quad -F_{\theta} + 3F_{\phi} - \frac{\sqrt{2}}{2} F_{\psi} = \frac{\sqrt{2}}{2} \delta_{\max}$$

$$3. \quad -\sqrt{2} F_{\theta} - \sqrt{2} F_{\phi} + 3F_{\psi} = \delta_{\max}$$

$$1. \quad F_{\phi} = 3F_{\theta} - \frac{\sqrt{2}}{2} F_{\psi} - \frac{\sqrt{2}}{2} \delta_{\max}$$

$$2. \quad -F_{\theta} + 3 \left( 3F_{\theta} - \frac{\sqrt{2}}{2} F_{\psi} - \frac{\sqrt{2}}{2} \delta_{\max} \right) - \frac{\sqrt{2}}{2} F_{\psi} = \frac{\sqrt{2}}{2} \delta_{\max}$$

$$2. \quad 8F_{\theta} - 2\sqrt{2} F_{\psi} = 2\sqrt{2} \delta_{\max}$$

$$2. \quad 4F_{\theta} - \sqrt{2} F_{\psi} = \sqrt{2} \delta_{\max}$$

$$3. \quad -\sqrt{2} F_{\theta} - \sqrt{2} \left( 3F_{\theta} - \frac{\sqrt{2}}{2} F_{\psi} - \frac{\sqrt{2}}{2} \delta_{\max} \right) + 3F_{\psi} = \delta_{\max}$$

$$3. \quad -4\sqrt{2} F_{\theta} + 4F_{\psi} = 0$$

$$F_{\theta} = \frac{4}{4\sqrt{2}} F_{\psi} = \frac{\sqrt{2}}{2} F_{\psi}$$

$$\underline{F_{\theta} = 0.707 F_{\psi}}$$

$$2. \quad 4(0.707 F_{\psi}) - \sqrt{2} F_{\psi} = \sqrt{2} \delta_{\max}$$

$$\sqrt{2} F_{\psi} = \sqrt{2} \delta_{\max}$$

$$\underline{F_{\psi} = \delta_{\max}}$$

$$3. \quad F_{\theta} = \frac{\sqrt{2}}{2} \delta_{\max} = \underline{0.707 \delta_{\max}}$$

$$1. \quad F_{\phi} = 3 \left( \frac{\sqrt{2}}{2} \delta_{\max} \right) - \frac{\sqrt{2}}{2} \delta_{\max} - \frac{\sqrt{2}}{2} \delta_{\max}$$

$$F_{\phi} = \frac{\sqrt{2}}{2} \delta_{\max} = \underline{0.707 \delta_{\max}}$$

$$[D'] = [A'] [F]$$

$$\begin{bmatrix} \delta_1 \\ \delta_2 \\ 0 \\ \delta_4 \end{bmatrix} = \begin{bmatrix} \sqrt{2} & -\sqrt{2} & 1 \\ \sqrt{2} & \sqrt{2} & -1 \\ 0 & 0 & 0 \\ \sqrt{2} & -\sqrt{2} & -1 \end{bmatrix} \begin{bmatrix} F_\theta \\ F_\phi \\ F_\psi \end{bmatrix}$$

$$\delta_1 = \sqrt{2} F_\theta - \sqrt{2} F_\phi + F_\psi = \left( \sqrt{2} \cdot \frac{1}{\sqrt{2}} - \sqrt{2} \cdot \frac{1}{\sqrt{2}} + 1 \right) \delta_{\max}$$

$$\delta_1 = \delta_{\max}$$

$$\delta_2 = \sqrt{2} F_\theta + \sqrt{2} F_\phi - F_\psi = \left( \sqrt{2} \cdot \frac{1}{\sqrt{2}} + \sqrt{2} \cdot \frac{1}{\sqrt{2}} - 1 \right) \delta_{\max} = \delta_{\max}$$

$$\delta_4 = \sqrt{2} F_\theta - \sqrt{2} F_\phi - F_\psi = \left( \sqrt{2} \cdot \frac{1}{\sqrt{2}} - \sqrt{2} \cdot \frac{1}{\sqrt{2}} - 1 \right) \delta_{\max} = -\delta_{\max}$$

Verify that the net acceleration is zero,

$$[T] = [K] [\Delta] = [Z]$$

$$[\Delta] = [M] [D]$$

and

$$[D] \equiv [D'] + [D'']$$

Then evaluate  $[K] [M] [D]$

$$[K] = \begin{bmatrix} \frac{I l_{\theta}}{I_{\theta}} & 0 & 0 \\ 0 & \frac{I l_{\phi}}{I_{\phi}} & 0 \\ 0 & 0 & \frac{I l_{\psi}}{I_{\psi}} \end{bmatrix}$$

Since  $[K]$  has no cross-product terms, it cannot cause a product of  $[K]$  and any other term to be  $[Z]$  unless  $[K] = [Z]$ . But  $[K] \neq [Z]$ , and since  $[K][\Delta] = [Z]$ ,  $[\Delta] = [Z]$

Then evaluate  $[\Delta] = [M][D]$

$$[M] = \begin{bmatrix} \frac{\sqrt{2}}{2} & \frac{\sqrt{2}}{2} & \frac{\sqrt{2}}{2} & \frac{\sqrt{2}}{2} \\ -\frac{\sqrt{2}}{2} & \frac{\sqrt{2}}{2} & \frac{\sqrt{2}}{2} & -\frac{\sqrt{2}}{2} \\ 1 & -1 & 1 & -1 \end{bmatrix}$$

$$[D] = [D'] + [D''] = \begin{bmatrix} \delta_{\max} \\ \delta_{\max} \\ 0 \\ -\delta_{\max} \end{bmatrix} + \begin{bmatrix} 0 \\ 0 \\ -\delta_{\max} \\ 0 \end{bmatrix} = \begin{bmatrix} \delta_{\max} \\ \delta_{\max} \\ -\delta_{\max} \\ -\delta_{\max} \end{bmatrix}$$

$$[M][D] = \begin{bmatrix} \frac{\sqrt{2}}{2} & \frac{\sqrt{2}}{2} & \frac{\sqrt{2}}{2} & \frac{\sqrt{2}}{2} \\ -\frac{\sqrt{2}}{2} & \frac{\sqrt{2}}{2} & \frac{\sqrt{2}}{2} & -\frac{\sqrt{2}}{2} \\ 1 & -1 & 1 & -1 \end{bmatrix} \begin{bmatrix} 1 \\ 1 \\ -1 \\ -1 \end{bmatrix} \delta_{\max}$$

$$[\Delta] = [M][D] = \begin{bmatrix} \frac{\sqrt{2}}{2} + \frac{\sqrt{2}}{2} & -\frac{\sqrt{2}}{2} & -\frac{\sqrt{2}}{2} \\ \frac{\sqrt{2}}{2} + \frac{\sqrt{2}}{2} & -\frac{\sqrt{2}}{2} & +\frac{\sqrt{2}}{2} \\ 1 & -1 & -1 & +1 \end{bmatrix} \delta_{\max} = \begin{bmatrix} 0 \\ 0 \\ 0 \end{bmatrix}$$

$$[\Delta] = [-Z]$$

This satisfies the necessary conditions for negating the acceleration in all three axes, and assures that the calculated gimbal angles are correct.

#### ANALYSIS OF A SINGLE HARDOVER ACTUATOR FAILURE ON A THREE-ENGINE, SIX-ACTUATOR SYSTEM

From the geometry (Figure D-3)

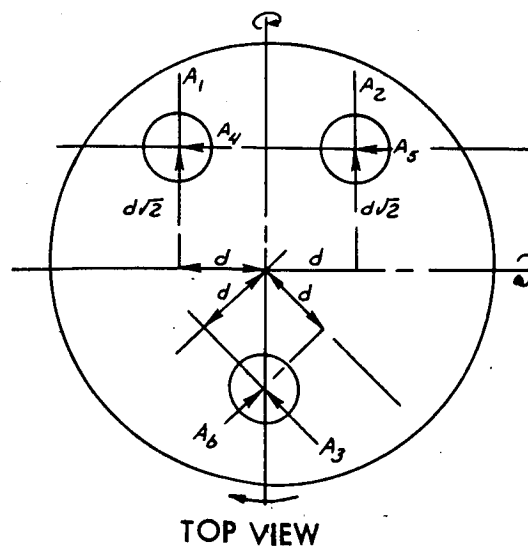


Figure D-3. Schematic Top View of a Three-Engine, Six-Actuator Configuration



$$[M] = \begin{bmatrix} 1 & 1 & 0.707 & 0 & 0 & 0.707 \\ 0 & 0 & 0.707 & 1 & 1 & -0.707 \\ 1 & -1 & 1 & -1.414 & -1.414 & -1 \end{bmatrix}$$

Select input matrix  $[A]$  to eliminate theoretical cross-coupling on command.

$$[A] = \begin{bmatrix} 1 & 0 & 1 \\ 1 & 0 & -1 \\ 1.414 & 1.414 & 1 \\ 0 & 1 & -0.707 \\ 0 & 1 & -0.707 \\ 1.414 & -1.414 & -1 \end{bmatrix}$$

Assume:  $\delta_3$  failed hardover =  $-\delta_{\max}$ ,  $k = 3$

$$[D''] = \begin{bmatrix} 0 \\ 0 \\ \delta_{\max} \\ 0 \\ 0 \\ 0 \end{bmatrix}$$

$$[A'] = \begin{bmatrix} 1 & 0 & 1 \\ 1 & 0 & -1 \\ 0 & 0 & 0 \\ 0 & 1 & -0.707 \\ 0 & 1 & -0.707 \\ 1.414 & -1.414 & -1 \end{bmatrix}$$

$$[M] [A'] [F] = - [M] [D'']$$

$$\begin{bmatrix} 1 & 1 & \frac{\sqrt{2}}{2} & 0 & 0 & \frac{\sqrt{2}}{2} \\ 0 & 0 & \frac{\sqrt{2}}{2} & 1 & 1 & -\frac{\sqrt{2}}{2} \\ 1 & -1 & 1 & -\sqrt{2} & -\sqrt{2} & -1 \end{bmatrix} \begin{bmatrix} 1 & 0 & 1 \\ 1 & 0 & -1 \\ 0 & 0 & 0 \\ 0 & 1 & -\frac{\sqrt{2}}{2} \\ 0 & 1 & \frac{\sqrt{2}}{2} \\ \sqrt{2} & -\sqrt{2} & -1 \end{bmatrix} \begin{bmatrix} F_{\theta} \\ F_{\phi} \\ F_{\psi} \end{bmatrix}$$

$$= - \begin{bmatrix} 1 & 1 & \frac{\sqrt{2}}{2} & 0 & 0 & \frac{\sqrt{2}}{2} \\ 0 & 0 & \frac{\sqrt{2}}{2} & 1 & 1 & -\frac{\sqrt{2}}{2} \\ 1 & -1 & 1 & -\sqrt{2} & -\sqrt{2} & -1 \end{bmatrix} \begin{bmatrix} 0 \\ 0 \\ -\delta_{\max} \\ 0 \\ 0 \\ 0 \end{bmatrix}$$

$$\begin{bmatrix} 3 & -1 & -\frac{\sqrt{2}}{2} \\ -1 & 3 & -\frac{\sqrt{2}}{2} \\ -\sqrt{2} & -\sqrt{2} & 5 \end{bmatrix} \begin{bmatrix} F_{\theta} \\ F_{\phi} \\ F_{\psi} \end{bmatrix} = \begin{bmatrix} \frac{\sqrt{2}}{2} \delta_{\max} \\ \frac{\sqrt{2}}{2} \delta_{\max} \\ \delta_{\max} \end{bmatrix}$$

$$1. \quad 3F\theta - F\phi - \frac{\sqrt{2}}{2} F\psi = \frac{\sqrt{2}}{2} \delta_{\max}$$

$$2. \quad -F\theta + 3F\phi - \frac{\sqrt{2}}{2} F\psi = \frac{\sqrt{2}}{2} \delta_{\max}$$

$$3. \quad -\sqrt{2} F\theta - \sqrt{2} F\phi + 5F\psi = \delta_{\max}$$

$$1. \quad F\phi = 3F\theta - \frac{\sqrt{2}}{2} F\psi - \frac{\sqrt{2}}{2} \delta_{\max}$$

$$2. \quad -F\theta + 3\left(3F\theta - \frac{\sqrt{2}}{2} F\psi - \frac{\sqrt{2}}{2} \delta_{\max}\right) - \frac{\sqrt{2}}{2} F\psi = \frac{\sqrt{2}}{2} \delta_{\max}$$

$$2. \quad 8F\theta - 2\sqrt{2} F\psi = 2\sqrt{2} \delta_{\max}$$

$$3. \quad -\sqrt{2} F\theta - \sqrt{2} \left(3F\theta - \frac{\sqrt{2}}{2} F\psi - \frac{\sqrt{2}}{2} \delta_{\max}\right) + 5F\psi = \delta_{\max}$$

$$3. \quad -4\sqrt{2} F\theta + 6F\psi = 0$$

$$\underline{F\psi = 0.94 F\theta}$$

$$2. \quad 8F\theta - 2\sqrt{2} (0.94 F\theta) = 2\sqrt{2} \delta_{\max}$$

$$5.3F\theta = 2.828 \delta_{\max} \Rightarrow F\theta = 0.530 \delta_{\max}$$

$$3. \quad 4\sqrt{2} (0.530) \delta_{\max} = 6F\psi$$

$$F\psi = 4\sqrt{2} \frac{(0.530)}{6} \delta_{\max} \Rightarrow F\psi = 0.500 \delta_{\max}$$



$$1. \quad F_{\phi} = 3(0.530) \delta_{\max} - \frac{\sqrt{2}}{2} (0.500) \delta_{\max} - \frac{\sqrt{2}}{2} \delta_{\max}$$

$$F_{\phi} = [1.59 - 0.707 (1.50)] \delta_{\max}$$

$$F_{\phi} = 0.530 \delta_{\max}$$

$$[D^T] = [A^T] [F]$$

$$\begin{bmatrix} \delta_1 \\ \delta_2 \\ 0 \\ \delta_4 \\ \delta_5 \\ \delta_6 \end{bmatrix} = \begin{bmatrix} 1 & 0 & 1 \\ 1 & 0 & -1 \\ 0 & 0 & 0 \\ 0 & 1 & -0.707 \\ & 1 & -0.707 \\ 1.414 & -1.414 & -1 \end{bmatrix} \begin{bmatrix} F_{\theta} \\ F_{\phi} \\ F_{\psi} \end{bmatrix}$$

$$\delta_1 = F_{\theta} + F_{\psi} = (0.530 + 0.500) \delta_{\max} = 1.03 \delta_{\max}$$

$$\delta_2 = F_{\theta} + F_{\psi} = (0.530 - 0.500) \delta_{\max} = 0.03 \delta_{\max}$$

$$\delta_4 = F_{\phi} - 0.707 F_{\psi} = (0.530 - 0.707 \{0.500\}) \delta_{\max} = 0.177 \delta_{\max}$$

$$\delta_5 = \delta_4 = 0.177 \delta_{\max}$$

$$\begin{aligned} \delta_6 &= 1.414 (F_{\theta} - F_{\phi}) - F_{\psi} = \delta_{\max} [1.414 (0.530 - 0.530)] - 0.500 \\ &= -0.500 \delta_{\max} \end{aligned}$$

Verify that the net acceleration is equal to zero by showing that

$$[\Delta] = [Z]$$

Evaluate

$$[\Delta] = [M] [D]$$

$$[M] = \begin{bmatrix} 1 & 1 & 0.707 & 0 & 0 & 0.707 \\ 0 & 0 & 0.707 & 1 & 1 & -0.707 \\ 1 & -1 & 1 & -1.414 & -1.414 & -1 \end{bmatrix}$$

$$[D] = [D'] + [D''] = \begin{bmatrix} 1.03 \delta_{\max} \\ 0.03 \delta_{\max} \\ 0 \\ 0.177 \delta_{\max} \\ 0.177 \delta_{\max} \\ -0.500 \delta_{\max} \end{bmatrix} + \begin{bmatrix} 0 \\ 0 \\ -\delta_{\max} \\ 0 \\ 0 \\ 0 \end{bmatrix}$$

$$[D] = \begin{bmatrix} 1.03 \\ 0.03 \\ -1.00 \\ 0.177 \\ 0.177 \\ -0.500 \end{bmatrix} \delta_{\max}$$

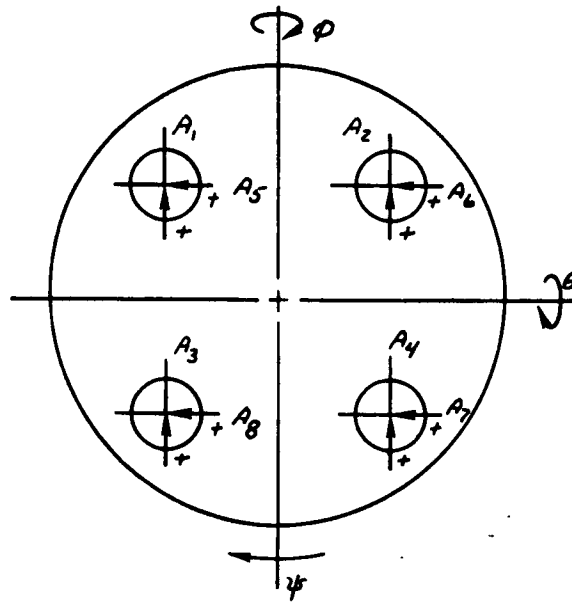
$$[M] [D] = \begin{bmatrix} 1 & 1 & 0.707 & 0 & 0 & 0.707 \\ 0 & 0 & 0.707 & 1 & 1 & -0.707 \\ 1 & -1 & 1 & -1.414 & -1.414 & -1 \end{bmatrix} \begin{bmatrix} 1.03 \\ 0.03 \\ -1.00 \\ 0.177 \\ 0.177 \\ -0.500 \end{bmatrix} \delta_{\max}$$

$$[\Delta] = [M] [D] = \begin{bmatrix} 1.03 + 0.03 - 0.707 - 0.353 \\ -0.707 + 0.177 + 0.177 + 0.353 \\ 1.03 - 0.03 - 1.00 - 0.250 - 0.250 + 0.500 \end{bmatrix} \delta_{\max}$$

$$[\Delta] = \begin{bmatrix} 0 \\ 0 \\ 0 \end{bmatrix} \delta_{\max} = [Z]$$

SINGLE HARDOVER ACTUATOR FAILURE ANALYSIS FOR A FOUR-ENGINE, EIGHT-ACTUATOR CONFIGURATION

From the geometry (Figure D-4)



TOP VIEW

Figure D-4. Schematic Top View of a Four-Engine, Eight-Actuator Configuration

$$[M] = \begin{bmatrix} 1 & 1 & 1 & 1 & 0 & 0 & 0 & 0 \\ 0 & 1 & 0 & 0 & 1 & 1 & 1 & 1 \\ 1 & -1 & 1 & -1 & -1 & -1 & 1 & 1 \end{bmatrix}$$

Select input matrix  $[A]$  so that theoretical cross-coupling on command is eliminated.

$$[A] = \begin{bmatrix} 1 & 0 & 1 \\ 1 & 0 & -1 \\ 1 & 0 & 1 \\ 1 & 0 & -1 \\ 0 & 1 & -1 \\ 0 & 1 & -1 \\ 0 & 1 & 1 \\ 0 & 1 & 1 \end{bmatrix}$$

Assume  $\delta_3$  failed hardover =  $-\delta_{MAX}$ ,  $k = 3$

$$[D''] = \begin{bmatrix} 0 \\ 0 \\ -\delta_{max} \\ 0 \\ 0 \\ 0 \\ 0 \\ 0 \end{bmatrix}; \quad [A'] = \begin{bmatrix} 1 & 0 & 1 \\ 1 & 0 & -1 \\ 0 & 0 & 0 \\ 1 & 0 & -1 \\ 0 & 1 & -1 \\ 0 & 1 & -1 \\ 0 & 1 & 1 \\ 0 & 1 & 1 \end{bmatrix}$$

$$[M][A'] [F] = -[M][D'']$$

$$\begin{bmatrix} 1 & 1 & 1 & 1 & 0 & 0 & 0 & 0 \\ 0 & 0 & 0 & 0 & 1 & 1 & 1 & 1 \\ 1 & -1 & 1 & -1 & -1 & -1 & 1 & 1 \end{bmatrix} \begin{bmatrix} 1 & 0 & 1 \\ 1 & 0 & -1 \\ 0 & 0 & 0 \\ 1 & 0 & -1 \\ 0 & 1 & -1 \\ 0 & 1 & -1 \\ 0 & 1 & 1 \\ 0 & 1 & 1 \end{bmatrix} \begin{bmatrix} F_\theta \\ F_\phi \\ F_\psi \end{bmatrix}$$

$$= - \begin{bmatrix} 1 & 1 & 1 & 1 & 0 & 0 & 0 & 0 \\ 0 & 0 & 0 & 0 & 1 & 1 & 1 & 1 \\ 1 & -1 & 1 & -1 & -1 & -1 & 1 & 1 \end{bmatrix} \begin{bmatrix} 0 \\ 0 \\ -\delta_{\max} \\ 0 \\ 0 \\ 0 \\ 0 \\ 0 \end{bmatrix}$$

$$\begin{bmatrix} 3 & 0 & -1 \\ 0 & 4 & 0 \\ -1 & 0 & 7 \end{bmatrix} \begin{bmatrix} F_{\theta} \\ F_{\phi} \\ F_{\psi} \end{bmatrix} = \begin{bmatrix} \delta_{\max} \\ 0 \\ \delta_{\max} \end{bmatrix}$$

$$1. \quad 3F_{\theta} - F_{\psi} = \delta_{\max}$$

$$2. \quad F_{\phi} = 0$$

$$3. \quad -F_{\theta} + 7F_{\psi} = \delta_{\max}$$

$$1. \quad F_{\psi} = 3F_{\theta} - \delta_{\max}$$

$$3. \quad -F_{\theta} + 7(3F_{\theta} - \delta_{\max}) = \delta_{\max}$$

$$20 F_{\theta} = 8 \delta_{\max}$$

$$F_{\theta} = 0.4 \delta_{\max}$$

$$1. \quad F_{\psi} = 3(0.4 \delta_{\max}) - \delta_{\max}$$

$$F_{\psi} = 0.2 \delta_{\max}$$

$$[D'] = [A'] [F]$$

$$\begin{bmatrix} \delta_1 \\ \delta_2 \\ 0 \\ \delta_4 \\ \delta_5 \\ \delta_6 \\ \delta_7 \\ \delta_8 \end{bmatrix} = \begin{bmatrix} 1 & 0 & 1 \\ 1 & 0 & -1 \\ 0 & 0 & 0 \\ 1 & 0 & -1 \\ 0 & 1 & -1 \\ 0 & 1 & -1 \\ 0 & 1 & 1 \\ 0 & 1 & 1 \end{bmatrix} \begin{bmatrix} F_\theta \\ F_\phi \\ F_\psi \end{bmatrix}$$

$$\delta_1 = F_\theta + F_\psi = (0.4 + 0.2) \delta_{MAX} = 0.6 \delta_{max}$$

$$\delta_2 = F_\theta - F_\psi = (0.4 - 0.2) \delta_{MAX} = 0.2 \delta_{max}$$

$$\delta_4 = F_\theta - F_\psi = (0.4 - 0.2) \delta_{MAX} = 0.2 \delta_{max}$$

$$\delta_5 = F_\phi - F_\psi = -0.2 \delta_{max}$$

$$\delta_6 = F_\phi - F_\psi = -0.2 \delta_{max}$$

$$\delta_7 = F_\phi + F_\psi = +0.2 \delta_{max}$$

$$\delta_8 = F_\phi + F_\psi = +0.2 \delta_{max}$$

Verify that the net acceleration is zero by showing that

$$[\Delta] = [M][D] = [Z]$$

$$[M] = \begin{bmatrix} 1 & 1 & 1 & 1 & 0 & 0 & 0 & 0 \\ 0 & 0 & 0 & 0 & 1 & 1 & 1 & 1 \\ 1 & -1 & 1 & -1 & -1 & -1 & 1 & 1 \end{bmatrix}$$

$$[D] = [D'] + [D''] = \begin{bmatrix} 0.6 \delta_{\max} \\ 0.2 \delta_{\max} \\ 0 \\ 0.2 \delta_{\max} \\ -0.2 \delta_{\max} \\ -0.2 \delta_{\max} \\ 0.2 \delta_{\max} \\ 0.2 \delta_{\max} \end{bmatrix} + \begin{bmatrix} 0 \\ 0 \\ -\delta_{\max} \\ 0 \\ 0 \\ 0 \\ 0 \\ 0 \end{bmatrix} = \begin{bmatrix} 0.6 \\ 0.2 \\ -1.0 \\ 0.2 \\ -0.2 \\ -0.2 \\ 0.2 \\ 0.2 \end{bmatrix} \delta_{\max}$$

$$[M][D] = \begin{bmatrix} 1 & 1 & 1 & 1 & 0 & 0 & 0 & 0 \\ 0 & 0 & 0 & 0 & 1 & 1 & 1 & 1 \\ 1 & -1 & 1 & -1 & -1 & -1 & 1 & 1 \end{bmatrix} \begin{bmatrix} 0.6 \\ 0.2 \\ -1.0 \\ 0.2 \\ -0.2 \\ -0.2 \\ 0.2 \\ 0.2 \end{bmatrix} \delta_{\max}$$

$$[\Delta] \begin{bmatrix} 0.6 + 0.2 - 1.0 + 0.2 + 0 + 0 + 0 + 0 \\ 0 + 0 + 0 + 0 - 0.2 - 0.2 + 0.2 + 0.2 \\ 0.6 - 0.2 - 1.0 - 0.2 + 0.2 + 0.2 + 0.2 + 0.2 \end{bmatrix} \delta_{\max} = \begin{bmatrix} 0 \\ 0 \\ 0 \end{bmatrix}$$

$$[\Delta] = [Z]$$



### III. THERMAL STUDIES

#### INTRODUCTION AND SUMMARY

Operation of a lunar flying vehicle on the lunar surface over extended time periods requires a detailed knowledge of the integrated natural and vehicle-induced heating environment, component temperature limits, mission time lines, and state-of-the-art of coatings, insulation, and heaters. The benefits which accrue to detailed know-how and proper use of these factors in design include minimum weight and a high level of mission flexibility. Accordingly, the thermal studies portion of this report is divided into two major technical sections. In the first section, environment and temperature criteria are detailed. In the second section, key components are analyzed with respect to their temperature histories. In some cases, detailed analyses or computer programs were available from the Apollo program. Where temperature limits were exceeded, thermal protection methods are recommended. Key components examined include the propellant tanks, engines, feed lines, structure, and attenuator. Dawn, afternoon, earthshine, and combination missions were examined.

A summary of the lunar thermal environment the LFV will experience was prepared, based on latest available astronomical and space program data. LFV component temperature limits were established, which use test data from most major U. S. lunar exploration programs such as Apollo and Surveyor.

An analysis of the lunar flying vehicle (LFV) propellant tanks to define their thermal protection system (TPS) requirements for dawn, afternoon, earthshine, and combined missions was completed. For the nominal dawn mission, a coating having a solar absorptivity to infrared emissivity ratio ( $\alpha_s/\epsilon$ ) of 0.26 is adequate. To operate in the entire envelope of possible morning missions, the use of an  $\alpha_s/\epsilon = 0.10$  external surface may be required. For late afternoon and night (earthshine) missions, an external source of heat will be needed. Lunar day storage will not be a thermal problem because of high temperature limits on the empty tanks.

Thermal protection system requirements for the LFV landing system attenuators were completed. For the nominal morning mission, a coating such as Z-93 paint having a solar absorptivity to infrared emissivity ratio ( $\alpha_s/\epsilon$ ) of 0.26 is adequate to prevent overheating of the attenuators. Radiant

heating from the engine nozzle extensions to the attenuator was calculated. Heating rates are quite low but will be incorporated into future attenuator analyses.

Base heating rates were calculated versus thrust for three engine cluster configurations over a range of gimbal angles. Maximum heating was  $0.4 \text{ Btu/ft}^2 \text{ sec}$ . These values provide input to future effort which must combine all heat transfer modes in this zone to determine thermal protection requirements.

A clustered engine analysis based on test data demonstrated that even in the most severe geometrical arrangements of four engines, clustering will not cause engine overheating.

Plume heating analyses and thermal protection requirements were calculated for a number of configurations as they evolved. The final configuration does not have plume heating problems.

## ENVIRONMENTAL CONSIDERATIONS

### THERMAL ENVIRONMENT ON THE MOON

Included herein are aspects of the lunar environment which influence the thermal design of a one-man LFV. Basic information is listed first along with the appropriate literature references and, in some instances, a discussion. A brief general review then follows of anomalous lunar surface characteristics which should be borne in mind for future detailed analytical work.

The following assumptions were made regarding the lunar surface thermal environment. The word "assumptions" is used advisedly because there are variations in the thermal models. None of these are important in preliminary design.

1. Lunar surface temperature. The surface temperature model is shown in Figure 3-1 with a maximum value of 240 F (700 R) at the subsolar point (SSP) or lunar noon and a minimum of -285 F (175 R) on the night side just before the dawn terminator. As noted on the figure, several references were consulted. Care must be taken when reading the literature - the term "brightness temperature," measured telescopically from earth, usually presumes zero lunar albedo. A number of calculated values using Lambert's cosine law are plotted. For lunar night the thermal inertia parameter, defined as  $\gamma = (k \rho c_p)^{-1/2}$ , is used often in Surveyor literature to correlate the cooldown of the lunar surface. A value of approximately 700 (in c. g. s. units) was used here. In Figure 3-1, several abscissa scales are included to agree with the varied literature systems. Henceforth, only the sun angle ( $\phi_s$ ) will be used.
2. Albedo of the lunar surface. Albedo is the ratio of reflected to total incident solar radiation. It varies considerably, both on a gross scale from the maria to the continents, inside or near various craters, and in localized areas because of the presence of rock formations. Care must be taken to avoid confusion between the albedos of total and visible radiant energy. The value of  $a = 0.084$  was chosen after study of References 3-1 through 3-3. It is consistent with environmental assumptions 1, 5, and 6.
3. The lunar surface in the vicinity of the LFV may be approximated by an infinite flat plane of uniform temperature. This is a

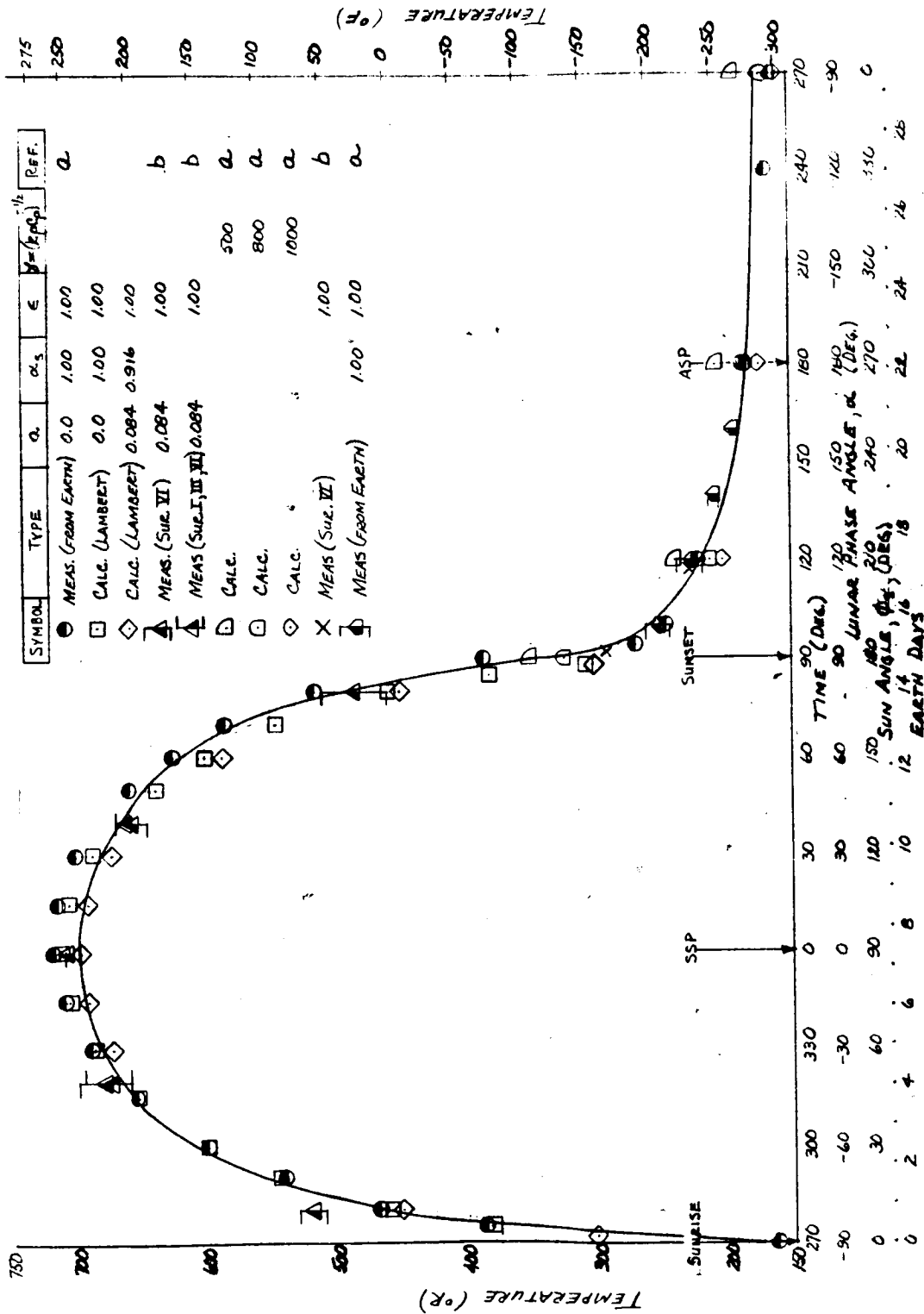
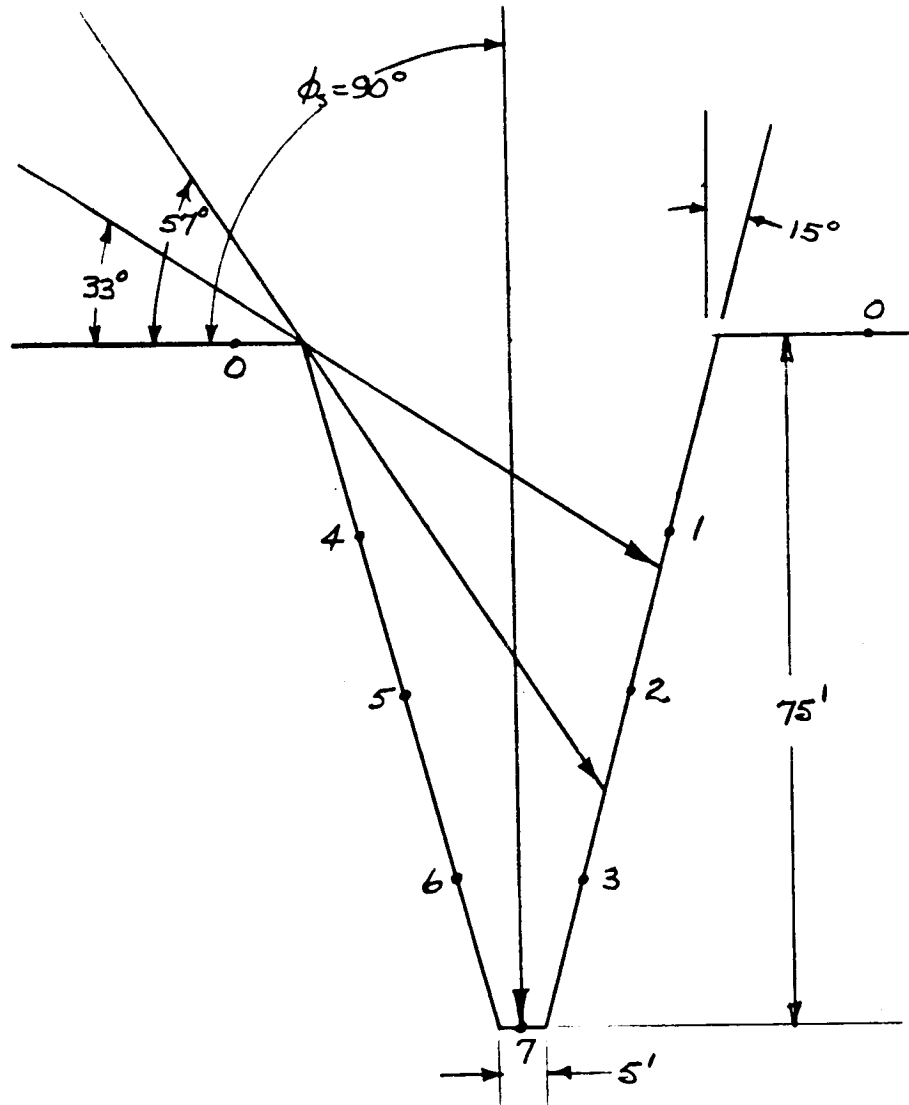


Figure 3-1. Average Lunar Surface Temperature

reasonable assumption for the areas in which early LFV's are likely to operate. Deviations are discussed later.

4. The lunar surface emits diffusely at  $\epsilon = 1.00$  (black body). Directional radiation properties are mentioned below in the general review.
5. The thermal conductivity of the lunar surface is negligible. The range, excluding rock, of thermal conductivity values given in reference (a),  $k = 0.0024$  to  $0.0068$  Btu/hr-ft- $^{\circ}$ F, compares favorably with a well-evacuated thermal insulation material.
6. The heat flux from the sun is  $442$  Btu/ft $^2$ -hr, constant during daytime, from a collimated source. Seasonal variations, reduced values of the solar constant now being reported from the Mariner 69 missions, and the possibility of a solar eclipse have been neglected.
7. The LFV operates on the lunar equator. Neglecting localized variations in surface radiative properties and physical features, this assumption leads to maximum lunar surface temperatures.
8. The ecliptic plane and the lunar equatorial plane are coplanar. The true angle between the planes is only  $1$  degree  $32'$ . As the result of the last two assumptions and consideration of the moon's rotational and orbital directions, the sun will rise directly east of the LFV, pass directly overhead, and set in the west. Since the lunation (synodic month) is  $29.53$  days, the apparent motion of the sun is only  $0.508$  degree/hr; and, as shown on Figure 3-1, the lunar day and night are each  $14.7$  earth days ( $354$  hours) long.
9. The spatial environment is considered to be a radiation sink at  $-460$  F ( $0$  R).

There are deviations from this relatively simple lunar thermal environment model. Some may become important for later detailed analysis, margin testing, or individual mission support. One of the most-up-to-date reviews and bibliographies is contained in Reference 3-1. Gross lunar features such as craters, rilles, and mountains will effect surface temperatures as well as solar insulation of the LFV. An example of this, taken from Reference 3-4, is shown in Figure 3-2. Improved models for the thermal environment in craters are contained in References 3-5 and 3-6. There are "hot spots" at various locations on the surface of the moon. This data can be estimated from Reference 3-7. Another anomaly is the deviation of the infrared radiation from a Lambert or diffuse distribution to one having



Point	Sun Angle, $\phi_s$		
	33°	57°	90°
0	160° F	217	240
1	239	236	187
2	41	267	259
3	33	157	330
4	93	152	187
5	83	204	259
6	36	171	330
7	12	143	387

Figure 3-2. Lunar Ravine Temperatures

a preferred direction. Reference 3-8 contains temperature plots which result from this phenomenon, and an empirical expression is given in Reference 3-1. Objects on or near the lunar surface will be affected by directional radiation, especially if numerous craters and rocks are in the field of view. As a first approximation, temperatures at other than equatorial locations can be estimated by  $T = T_e \cos 1/4 \beta$ , where  $T_e$  = equatorial brightness temperature and  $\beta$  = latitude. However, the aforementioned anomalies may offset expected lower temperatures. For instance, according to Reference 3-9, Surveyor VII, which landed on the ejecta blanket of the crater Tycho at 41 degrees south latitude did not operate appreciably cooler than other spacecraft near the equator.

### VEHICLE TEMPERATURE LIMITS

The previous section on lunar environment shows that during standby and flight the LFV will be exposed to direct solar heating of 442 Btu/ft<sup>2</sup>-hr and to infrared radiant energy emitted from local lunar surfaces over temperature limits between -40 to +250 F, as is brought out in Figures 3-1 and 3-4. During storage and in earthshine missions, even lower lunar surface temperatures will be seen (down to -270 F) coupled with radiation to a black sky. It is important, therefore, to use vehicle components which are capable of operating in these environments with minimum requirements for special orientation and/or thermal protection. The alternative to wide temperature limits for components is added thermal protection, which implies additional weight for insulation, coatings, and heaters. Time constraints or special orientations implies lower mission flexibility.

Many of the components and/or environments of the LFV are similar to those of the Surveyor, Apollo, command and service module, and lunar module programs. Therefore, an extensive search was made for temperature limits of components used in these programs. The results of this search are shown in Table 3-1. High and low temperature limits, both for operational and storage conditions, are given together with reasons for these limits. These limits were modified from data gathered from other programs as considerations or conditions peculiar to the LFV were identified.

The components selected to define temperature limits were selected with regard to the NR SD lunar flying vehicle proposal and analogy to previous programs. The following assumptions germane to the selection of temperature limits were made:

1. Propellants are Aerozine 50 ( $N_2H_4$  and UDMH) and  $N_2O_4$  (without NO).
2. Fuel is not allowed to boil.

3. Physical property limits chosen for propellants although their use has not necessarily been demonstrated at these temperatures.
4. Fracture mechanics limits are as high as best Apollo experience.
5. No tank bladders.
6. Duration of maximum continuous engine burn is 217 seconds.



**Table 3-1. Component Temperature Limits**

Component	Operational Limits*				Storage Limits**				Enclosure 1 Reference	Comments
	Temperature (F)		Reasons		Temperature (F)		Reasons			
	High	Low	High	Low	High	Low	High	Low		
<b>PROPULSION SUBSYSTEM</b>										
Fuel tank structure	+120 /105	-20	Fracture mechanics at 200/300 psig	Possible seal deformation	+300/ +275	None	Possible seal deformation	-	b g h m	Storage limits for empty tanks/with v. p. Assume Viton seals
Oxidizer tank structure	+105 /100	-20	Fracture mechanics at 200/300 psig	Possible seal deformation	+300	None	Possible seal deformation	-	b g h	Storage limits for empty tanks. Assume Viton seals
Fuel bulk	+140	+25	Apollo SPS experience	A -50 freezes at +19 to +21F	DNA	None	A -50 v. p. at 300F < 150 psia	Test-fired after freeze/thaw	n b j	High operating limit lower for propellant regen. engine cooling
Oxidizer bulk	+150	+15	Apollo RCS experience	Above N <sub>2</sub> O <sub>4</sub> freezing temp.	+180	None	N <sub>2</sub> O <sub>4</sub> v. p. at 195F = 250 psia	Test-fired after freeze/thaw	a b c	High storage limit to prevent venting
Propellant lines	+175	+25	Below two phase region	A -50 freezes at +19 to 21F	+300	None	Possible seal deformation	-	b j s	Prop. bulk temperature limits applies for short burn. Storage limits for empty lines
Line valves and regulators	+300	+25	Valve seat service limit	A -50 freezes at +19 to +21F	+340	None	Possible valve seat deformation	-	g h j	Assume Teflon or Kynar valve seats
Helium tank	+140	-5	Fracture mechanics	Remain above He dew point during max. burn	+140	-20	Fracture mechanics	Possible seal deformation	a b g	He dewpoint -65F. Tanks stored in ELM
Engine valves and injectors	+160	+25	Apollo SPS experience	A -50 freezes at +19 to +21F	+225	-100	Possible valve seat deformation	Possible seat deformation with repeated freeze/thaw cycle	b j n	
Engine thrust chambers	+2400	-100	Possible burn through	Vendor Experience	DNA#	None	-	Surveyor experience	c g m	High operating limit is during operation
Engine nut	+1900	-80	Vend. exper	Test minimum	DNA	None	-	-	n	
Injector flanges	+480	DNA	Possible flange burn through	-	DNA	DNA	-	-	b	
Thrust chamber flanges	+145	DNA	Surveyor experience	-	DNA	DNA	-	-	g	
<b>CONTROL SUBSYSTEM</b>										
Gyro	+185	-65	Surveyor experience	Capability of integral heater	+190	-100	Surveyor experience	Capability of integral heater	d g o	Candidate gyro assembly evidently contains heater
Engine gimbals and actuators	+200	+30	Remain below actuator clutch limit during max. h	Apollo SPS experience	+200	0	Surveyor experience	-	b g	Clutch operational limit +500F
Control unit	+200	-65	Operational range	-	+200	-65	Operational range	-	p	Heat generation unknown
Control linkage	TBD#	TBD	-	-	TBD	TBD	-	-		
Console	+150	None	Surveyor electronics limits	-	+165	-60	Surveyor electronics limits	-	g k	Glove limits for EVA suited astronaut ±250F for 3 minutes continuous
<b>STRUCTURE SUBSYSTEM</b>										
Attenuator pivots	TBD	TBD	-	-	TBD	TBD	-	-		
Foot pads	+200	-50	Surveyor experience	-	+300	None	Surveyor experience	-	c	
Legs	+160	-140	Surveyor experience	-	None	TBD	Surveyor experience	-	g c	Surveyor V and VII legs and/or shock absorbers failed during first lunar night.
Other thrust structure	+250	-140	Apollo aluminum limit	Surveyor experience	None	None	-	-	g	

**Table 3-1. Component Temperature Limits (Cont)**

Component	Operational Limits*						Storage Limits**				Enclosure 1 Reference	Comments
	Temperature (F)		Reasons		Temperature (F)		Reasons					
	High	Low	High	Low	High	Low	High	Low				
STRUCTURE SUBSYSTEM (Continued)												
Platform	+250	-250	Astronaut EVA	-	None	None	-	-	-	-	k	
Hydraulic shock absorber	+125	0	Design limits		+195	-65	Design limits					Surveyor limits per reference g: operation +125/+20 F, survival +125/-25 F
POWER SUBSYSTEM												
Battery	+130	+35	Surveyor experience	Surveyor operation	+140	-175	Surveyor experience	Tested survival limit			c e g	
Regulator/inverter	+185	None	Surveyor experience		+245	None	Apollo inverter design maximum	Surveyor experience			b f g	
* Temperature limits just before operation. Limits <u>during operation</u> , where known, are noted. ** Assumes subsequent operation after meeting operational limits. # DNA: does not apply    TBD: to be determined												
a CSM/LM Spacecraft Operational Data Book, Vol. II: LM Data Book, NASA/MSC, SNA-8-D-027 (June 1968) b CSM/LM Spacecraft Operational Data Book, Vol. I: CSM Data Book, NASA/MSC, SNA-8-D-027 (1 May 1968) c J. D. Cloud, et. al., Surveyor Spacecraft System: <u>Surveyor I Flight Performance</u> , Vol. 1: Final Report, Hughes Aircraft Co., NASA CF-93493 (October 1966) d <u>Space Programs Summary</u> , Vol. VI, Jet Propulsion Laboratory, No. 37-32 (31 March 1965) e <u>Surveyor VI Mission Report</u> , Part I: Mission Description and Performance, Jet Propulsion Laboratory, TR 32-1262 (15 September 1968) f J. D. Cloud, et. al. <u>Surveyor Spacecraft Systems: Surveyor III Flight Performance</u> , Final Report, Hughes Aircraft Co., NASA CR-93492 (July 1967) g <u>Space Programs Summary</u> , Vol. I: Flight Projects, Jet Propulsion Laboratory, No. 37-50, NASA CF-95711, (31 March 1968) h Personal Communication with R. H. Otos, NR-SD Materials & Processes, D/099-300. i <u>Proposal for a One-Man Lunar Flying Vehicle Study</u> , Space Division, North American Rockwell Corp. SD 68-646 (28 August 1968) j Personal Communication with M. W. Fisher, NR-SD Apollo, Propulsion, D/190-400 k Personal Communication with J. A. Roebuck, NR-SD, RE&T, Human Factors, D/190-500 l J. D. Cloud, et. al., <u>Surveyor Spacecraft Systems: Surveyor V Flight Performance</u> , Final Report. Hughes Aircraft Co., NASA CR-93488 (November 1967) m Personal communication with D. C. Sund, The Marquardt Corp., February 1969. n <u>LM Frozen Propellant Test</u> , The Marquardt Corporation, L-1050 (29 July 1968) o <u>Subminiature Three Axis Rate Gyroscope Assembly</u> , U.S. Time Corp. (Sept. 1967) p Personal Communication with G. C. McGee, NR-SD, RE&T Controls, D/190-320.												

## COMPONENT TEMPERATURE ANALYSIS AND THERMAL PROTECTION

### THERMAL ANALYSIS OF PROPELLANT TANKS

The spherical LFV propellant tanks for the fuel, aerazine 50 (A-50), and for the oxidizer, nitrogen tetroxide ( $N_2O_4$ ), were thermally analyzed for lunar day and night environments. The thermal model for a tank is shown in Figure 3-3. Unless specifically stated, the following assumptions were made:

1. Thermal environment is contained in the previous section on the lunar environment.
2. Steady state temperatures. With the apparent sun movement of only 0.508 degree/hr. and with specific logistic details lacking at this time (e.g. delivered propellant temperatures, filling and usage rates, shadowing, etc) this seemed to be the most fruitful approach to the analysis. Transient effects from solar heating do not appear to be important. However, other specific transients such as heat from the engine will affect the analysis.
3. No shadowing of the tanks or of the lunar surface has been considered. The actual shadowing to be encountered during LFV use will lower daytime temperatures.
4. Heat transferred by conduction has been neglected although this factor can be very important. Proper design of the tank supports can minimize conduction losses or gains. The specific design of tank supports will depend on whether it is required to gain or lose heat from the propellant.
5. Open structure of the LFV allows the use of an average emissivity,

$$\epsilon_{ij} = \epsilon_i \epsilon_j$$

6. Tank surfaces are diffuse emitters and absorbers.
7. For analytical simplicity, the tank insulation and storage blanket shown in Figure 3-3 are considered to be one continuous covering of multilayered insulation.

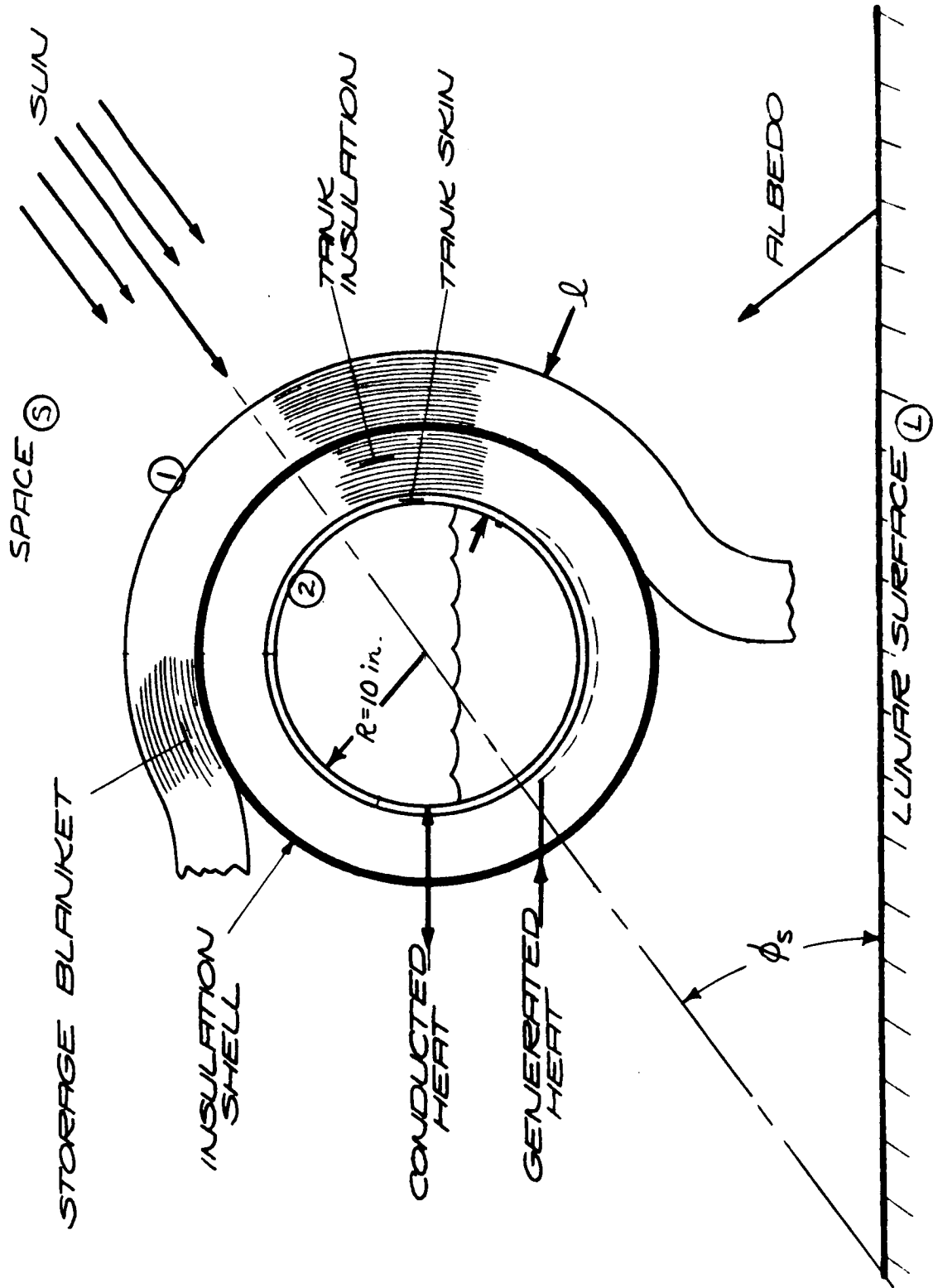


Figure 3-3. Propellant Tank Thermal Model

8. Operational (fueled and pressurized) and storage (empty and vented) temperature limits for the tanks are as shown in the section on component temperature limits.

Referring to Figure 3-3, a heat balance on surface 1 gives,

$$\alpha_{s_1} \dot{q}_s A_{p_1} + \alpha_{s_1} a \dot{q}_s A_{t_1} F_{1-L} - \sigma \epsilon_1 A_{t_1} F_{1-s} T_1^4 - \sigma \epsilon_1 \epsilon_L A_{t_1} F_{1-L} (T_1^4 - T_L^4) - \sigma \epsilon_{\text{eff}} A_a (T_1^4 - T_2^4) = 0 \quad (1)$$

where

- $a$  = lunar surface total albedo = 0.084
- $A_a$  = average insulation area =  $2\pi [R^2 + (R + l)^2]$
- $A_p$  = projected area of sphere =  $\pi (R + l)^2$
- $A_t$  = total surface area =  $4\pi (R + l)^2$
- $F$  = black body view factor based on total area
- $l$  = thickness of multilayer insulation
- $n$  = number of insulation layers  $\approx 80$  per inch
- $\dot{q}_s$  = solar heat flux = 442 Btu/ft<sup>2</sup>-hr.
- $R$  = tank radius = 10 in.
- $T$  = absolute temperature
- $\alpha_s$  = solar absorptivity
- $\epsilon$  = total hemispherical emissivity
- $\epsilon_{\text{eff}}$  = effective insulation emissivity. As used for preliminary design to permit a closed form solution  $\epsilon_{\text{eff}} \approx 0.5/n$  per Reference 3-3
- $\sigma$  = Stefan-Boltzmann constant =  $0.1713 \times 10^{-8}$  Btu/ft<sup>2</sup>-hr-°R<sup>4</sup>

A heat balance on surface 2 yields,

$$\sigma \epsilon_{\text{eff}} A_a (T_1^4 - T_2^4) + Q_g = 0 \quad (2)$$

Where  $Q_g$  = heat generated from heaters. When  $Q_g = 0$  (i. e., heaters turned off at near lunar night), equation 2 shows that  $T_2 = T_1$ . Using aforementioned assumption (5) plus  $\epsilon_L = 1.00$  and, for a sphere,  $F_{1-L} = F_{1-s} = 0.50$  and constant  $A_p/A_t = 0.25$ ; equation 1 can be reduced to

$$X_2 = 129.1 (\alpha_s/\epsilon)_1 + X_L/2 \quad (3)$$

where

$$X_2 = \text{tank temperature function} = \sigma T_2^4 = \sigma T_1^4$$

$$X_L = \text{lunar surface temperature function}$$

$$= \sigma T_L^4. \quad T_L \text{ is a function of the sun angle } (\phi_s) \text{ as shown in Figure 3-1}$$

Equation 3 was solved for a variety of  $\alpha_s/\epsilon$  ratios, representing possible thermal protection system (TPS) surfaces, at  $\phi_s$  throughout the lunar day. Steady-state tank temperatures,  $t_2 = T_2 - 460 = 10^3 (X_2/1713)^{0.25} - 460$ , are plotted versus  $\phi_s$  in Figure 3-4 for the entire lunar day. The surface optical properties were taken from References 3-12 and 3-13.

Before evaluating these analytical results, one must examine the LRV operational time lines. Figure 3-5 contains information which affects the TPS taken from Reference 3-14 for the nominal dawn mission. It should be noted that touchdown for the extended lunar module (ELM) is at  $\phi_s = 10^\circ$ , and that the propellant tanks need to stay within their operational limits only while fueled and pressurized,  $\phi_s = 19.5$  to  $36.5$  degrees.

Steady-state temperature histories for the propellant tanks during the nominal dawn mission, taken from Figure 3-4, are plotted in Figure 3-6 for two promising TPS coatings: ultraviolet degraded Z-93 white paint,  $\alpha_s/\epsilon = 0.26$ , and optical surface reflector (OSR),  $\alpha_s/\epsilon = 0.08$ . The latter is silvered quartz glass acting as a second-surface mirror. Other information shown in Figure 3-6 includes tank temperature limits, timeline considerations, and results from a transient cool-down calculation. It may be observed that the Z-93 paint will retain the temperatures within limits for the nominal dawn mission, and its use is recommended as the TPS external tank coating for this mission.

SYMBOL	$\alpha_s/\epsilon$	$\epsilon$	MATERIAL
---	0.68	0.75	ALUM. KAPTON
---	0.26	0.90	E-93 WHITE PAINT
---	0.08	0.76	OSR, 2 ND. SURF. MIBBOC
○	0.52	0.38	ANODIC
□	2.5	0.04	VDA
△	7.0	0.03	MRC-2, FOIL OUT

- NO HEAT GENERATION
- STEADY STATE
- EXPOSED SPHERICAL TANKS
- NO CONDUCTION LOSSES

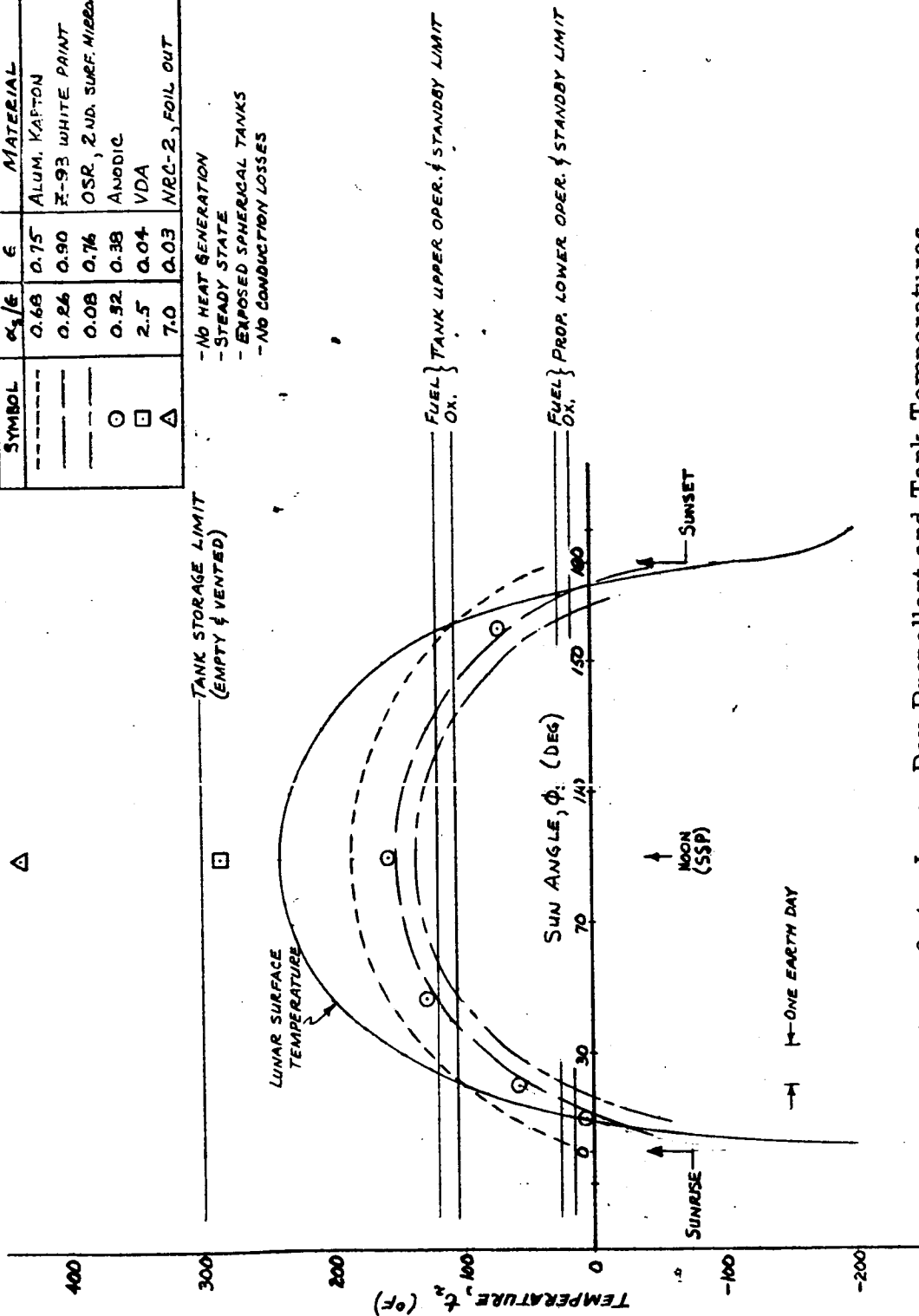


Figure 3-4. Lunar Day Propellant and Tank Temperatures

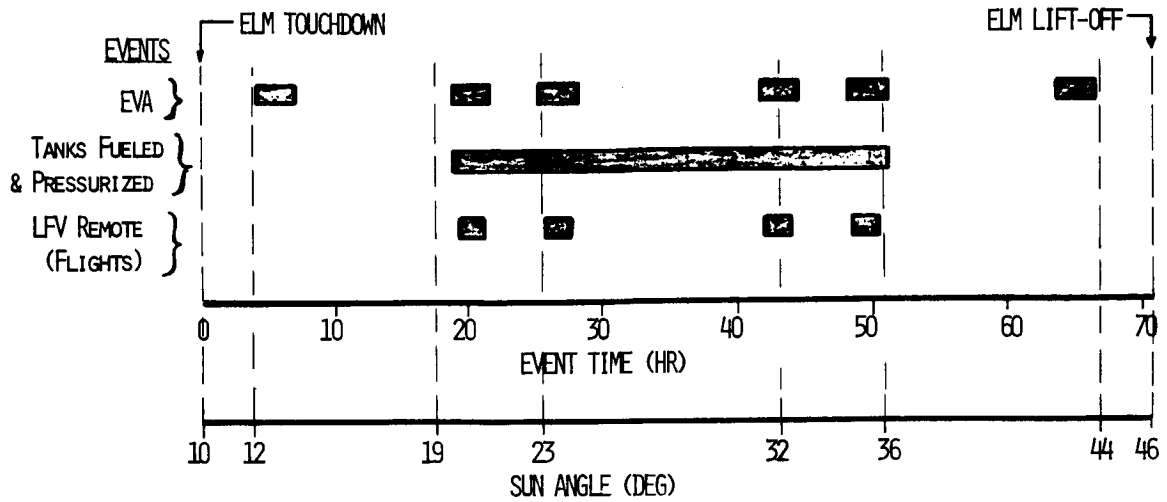


Figure 3-5. Normal Dawn Mission Timeline Considerations

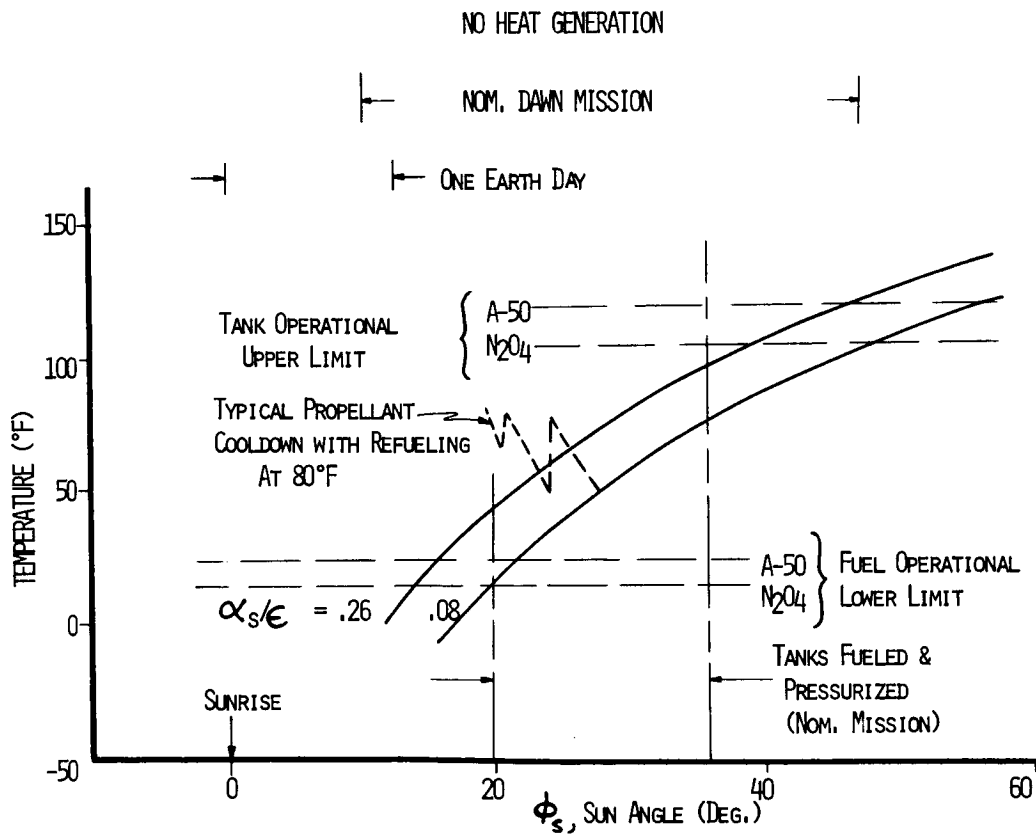


Figure 3-6. Lunar Morning Propellant and Tank Temperatures



The total three-day dawn mission envelope spans the interval between ELM touchdown at  $\phi_s = 7^\circ$  to ELM lift-off at  $\phi_s = 56^\circ$  as depicted in Figure 3-7. Even if the LFV active phase (tanks fueled and pressurized) remains at relatively the same position within the total three-day mission, the Z-93 paint will be inadequate to prevent overheating of the  $N_2O_4$  tanks at the maximum  $\phi_s = 46^\circ$ . It appears that a TPS surface with an even lower  $\alpha_s/\epsilon$  would be required, and the use of OSR with  $\alpha_s/\epsilon = 0.08$  is indicated. The most obvious drawback to its use - in addition to those associated with fabrication, handling, optical reflections, increased weight, and specular radiation analysis - is steady-state temperatures below the limit at the minimum  $\phi_s = 16.5^\circ$ . The aforementioned cool-down analysis was conducted to obviate the inclusion of tank heaters for any dawn mission.

Conduction through the insulation was not considered because it was desired to determine the minimum cooldown time for dawn missions. This results in a conservative estimate.

A basic transient equation,

$$C \frac{dT}{d\theta} = Q_{ab} - \sigma \epsilon A_t F T^4 \quad (4)$$

is solved for a time difference:

$$\Delta\theta = \frac{C}{\sigma \epsilon A_t F} \int_{T_1}^{T_2} \frac{dT}{a^4 - T^4} = \frac{b}{4a^3} \left[ \ln \left| \frac{a+T}{a-T} \right| + 2 \tan^{-1} \left( \frac{T}{a} \right) \right]_{T_1}^{T_2} \quad (5)$$

where

$$a = (Q_{ab} / \sigma \epsilon A_t F)^{0.25}$$

$$b = C / \sigma \epsilon A_t F$$

$$C = \text{thermal capacity} = \rho V c_p$$

$$c_p = \text{specific heat}$$

$$V = \text{volume}$$

$$\Delta\theta = \text{time difference}$$

$$\rho = \text{density}$$

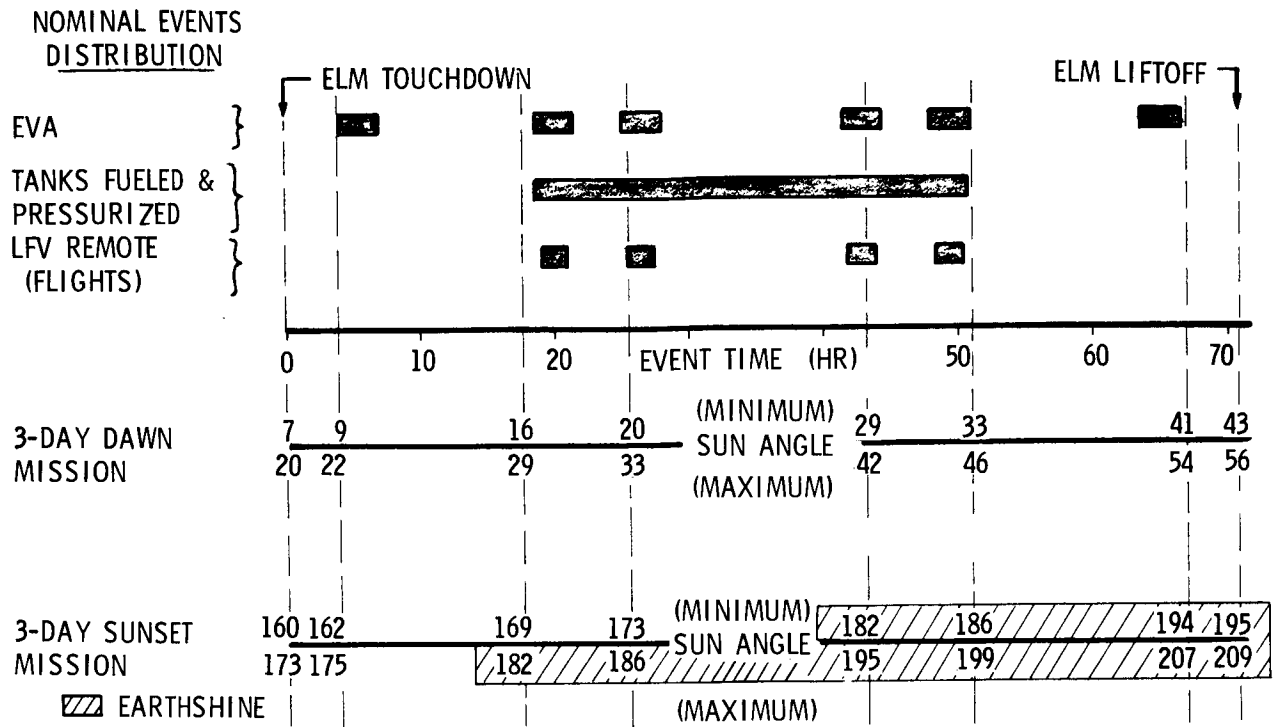


Figure 3-7. Timeline Thermal Considerations

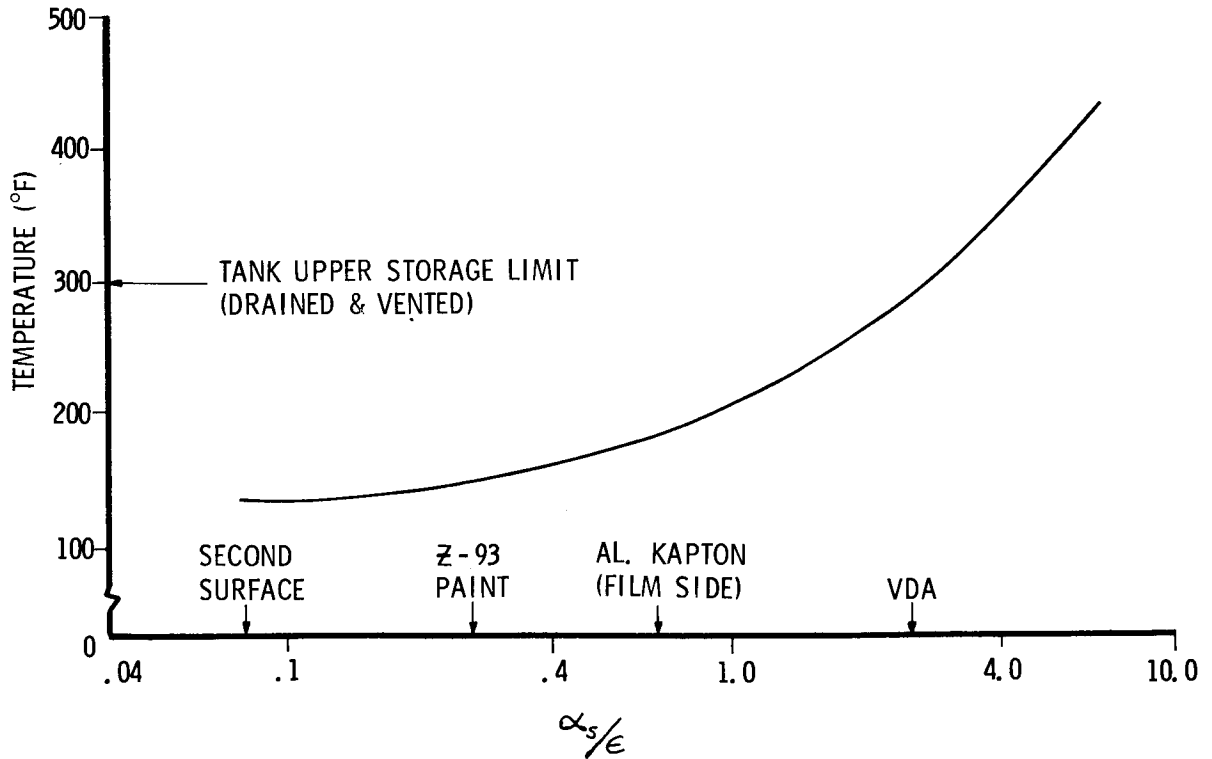


Figure 3-8. Maximum Propellant and Tank Temperatures at Subsolar Point



Equation 5 was solved in a step-wise fashion with the following conditions and assumptions: (1) full solar direct and albedo heating, (2) radiant interchange with lunar surface neglected, (3) propellant delivered from ELM at 80 F, (4) uninsulated tanks with OSR surfaces, (5) thermal capacity for 115 lb A-50,  $C = 79.7 \text{ Btu/}^\circ\text{R}$ , and for 185 lb  $\text{N}_2\text{O}_4$ ,  $C = 69.0 \text{ Btu/}^\circ\text{R}$ , and (6) thermal capacity of tank,  $C = 0.9 \text{ Btu/}^\circ\text{R}$ , neglected. The results are included on Figure 3-6 where the abrupt temperature increases are caused by refueling after each LFV flight. Therefore, the OSR covered tank surfaces would be recommended at this time for the total three-day dawn mission envelope. In view of the problems associated with the use of OSR on the LFV tanks, future detailed designs should seek to avoid it. This may be accomplished by more comprehensive analyses with more specific hardware definition and by increasing the upper temperature limits, set by fracture mechanics, through improved pressure testing plans.

Lunar day storage of the tanks is no problem as shown in Figure 3-8. The maximum tank temperature at lunar noon (subsolar point) will not exceed the upper limit for the drained and vented vessels with any of the TPS surfaces considered.

An LFV designed to operate in the lunar night (earthshine) environment will require an additional TPS. The operational time line envelope for the earthshine mission is shown at the bottom of Figure 3-7. The information contained in References 3-14 and 3-15 was used to determine the nominal distribution of events. Note in Figure 3-7 that the earthshine mission envelope is determined by a 70.8 hr staytime ( $\Delta\phi_s = 36^\circ$ ) added to ELM touchdowns which range from  $\phi_s = 160^\circ$  ( $20^\circ$  before the evening terminator) to  $\phi_s = 173^\circ$  ( $7^\circ$  before the evening terminator).

These calculations were performed early in the LFV Phase B effort while changes in the timelines and configurations were being made, before the assumption was made that sufficient power could be drawn from the ELM when the LFV was alongside. It was largely fortuitous that such a general approach was taken to the design of the TPS for the propellant tanks in the total earthshine and near-terminator environments. To understand the analyses several time intervals need to be defined:

1. The "night standby period," which is equivalent to "total earthshine mission" used on some illustrations, is the total interval from sunset (evening terminator) to the maximum ELM lift-off time,  $\phi_s = 180$  to  $210^\circ$ .
2. The "night storage period" is the total interval from maximum ELM lift-off,  $\phi_s = 210^\circ$ ; through the remainder of one lunar night; to sunrise (morning terminator),  $\phi_s = 0^\circ$ .

3. The "day standby periods" are intervals, morning and afternoon, between the terminator and the time at which the steady-state temperature of a tank passes through a specified temperature.

These latter periods are intervals of low  $\phi_s$  during lunar day when the application of energy via heaters is indicated. During LFV use these energy requirements will be negated by refueling from the ELM as shown in Figure 3-6. However, the maximum three-month lunar surface dormant storage capability required by Reference 3-16 will subject the LFV to three night storage periods plus three night "standby" and six day "standby" periods. It is assumed that the LFV will be in use (ELM present) only during 1 to 3 of these "standby" periods. During the remainder of the three months the LFV must be self-sufficient.

For the night standby and night storage periods when there is neither direct solar nor albedo radiation Equations 1 and 2 for a sphere may be combined and solved for the generated heat ( $Q_g$ ) required to maintain any tank temperature ( $T_2$ ):

$$Q_g = \epsilon_{\text{eff}}^A A \left[ X_2 - \frac{(\epsilon_{1/2} A_t X_L + \epsilon_{\text{eff}}^A X_2)}{\epsilon_1 A_t + \epsilon_{\text{eff}}^A} \right] \quad (6)$$

Selected numerical results from this equation are plotted in Figure 3-9 through 3-11 for the night standby period. The tank temperatures of 25 and 15 F are the lower operating limits for the A-50 and  $N_2O_4$ , respectively. Of the other temperatures shown, -20 and -150 F were lower limits for other items in the propellant system. The temperature of a tank in equilibrium with the lunar environment just prior to sunrise is -313 F as shown in Figure 3-11. All of the calculated data points are contained in Figure 3-15.

So that emissivities shown on the previous figures may be correlated with actual TPS surfaces, a table of optical properties taken from References 3-12 and 3-13 is attached as Table 3-2.

In view of the negligible slope of the curves in Figures 3-9 through 3-11 at  $\phi_s = 210$  degrees, values of  $Q_g$  for the night storage period were calculated with Equation 6 at  $\phi_s = 210$  and 359 degrees and then averaged.

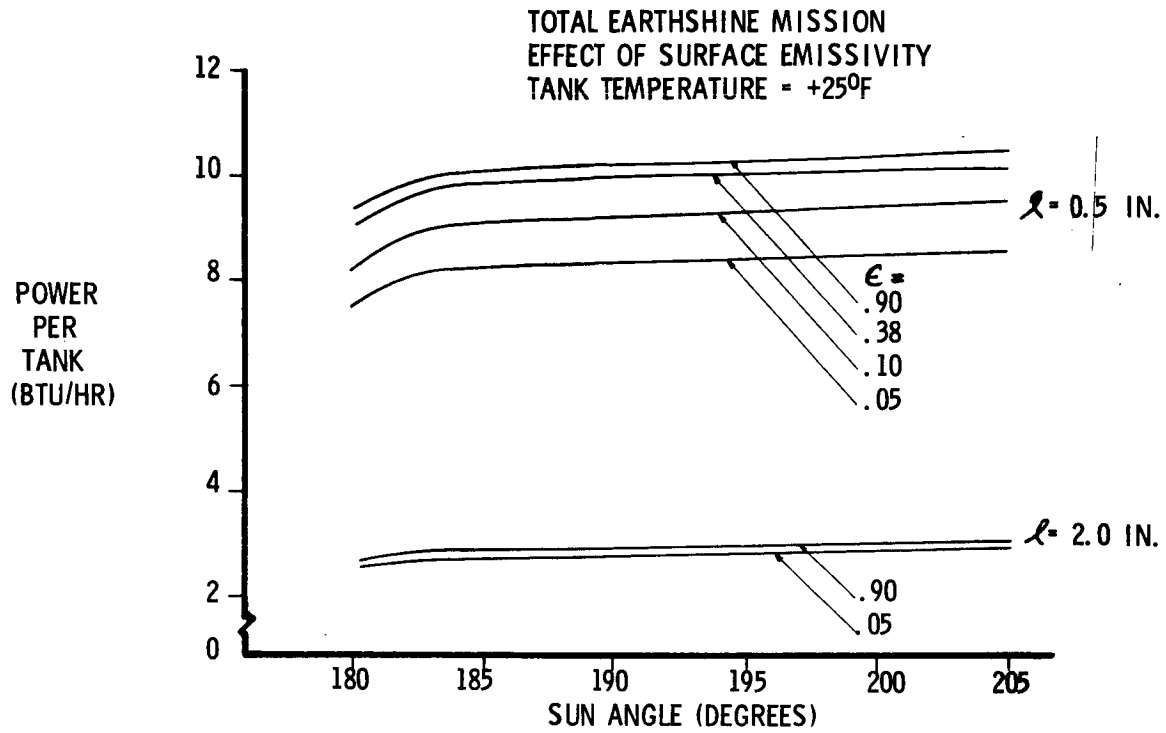


Figure 3-9. Propellant Tank Power Requirements for Various Parameters (Sheet 1 of 3)

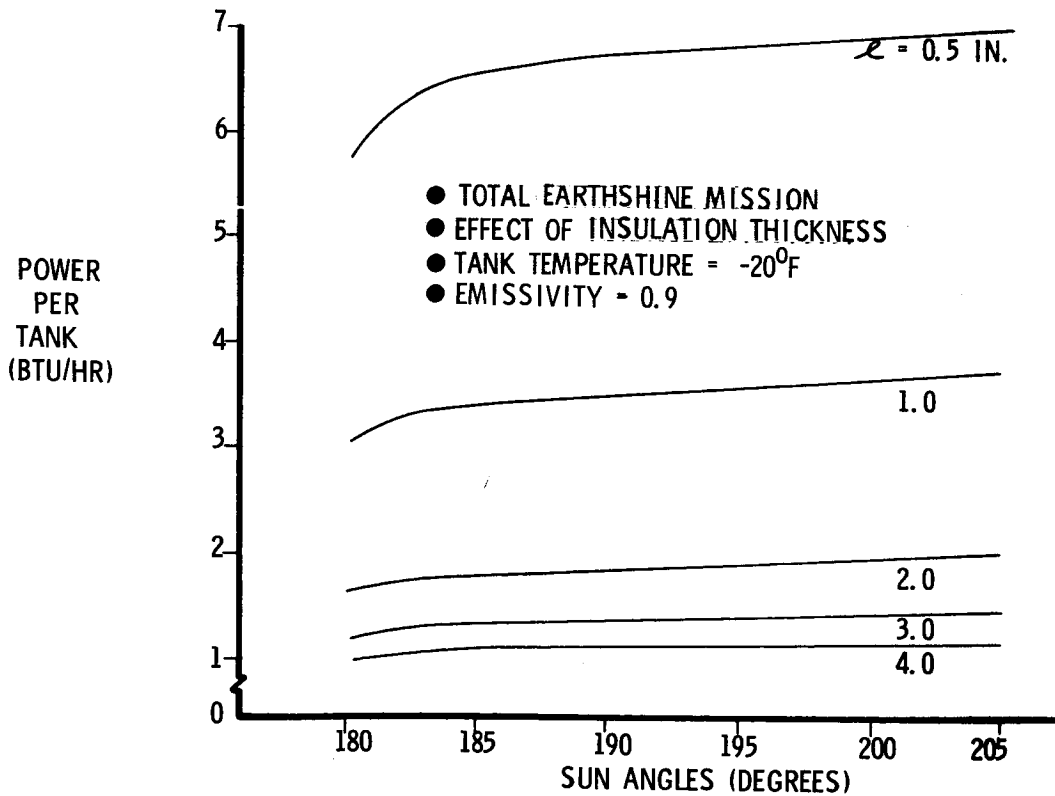


Figure 3-10. Propellant Tank Power Requirements for Various Parameters (Sheet 2 of 3)

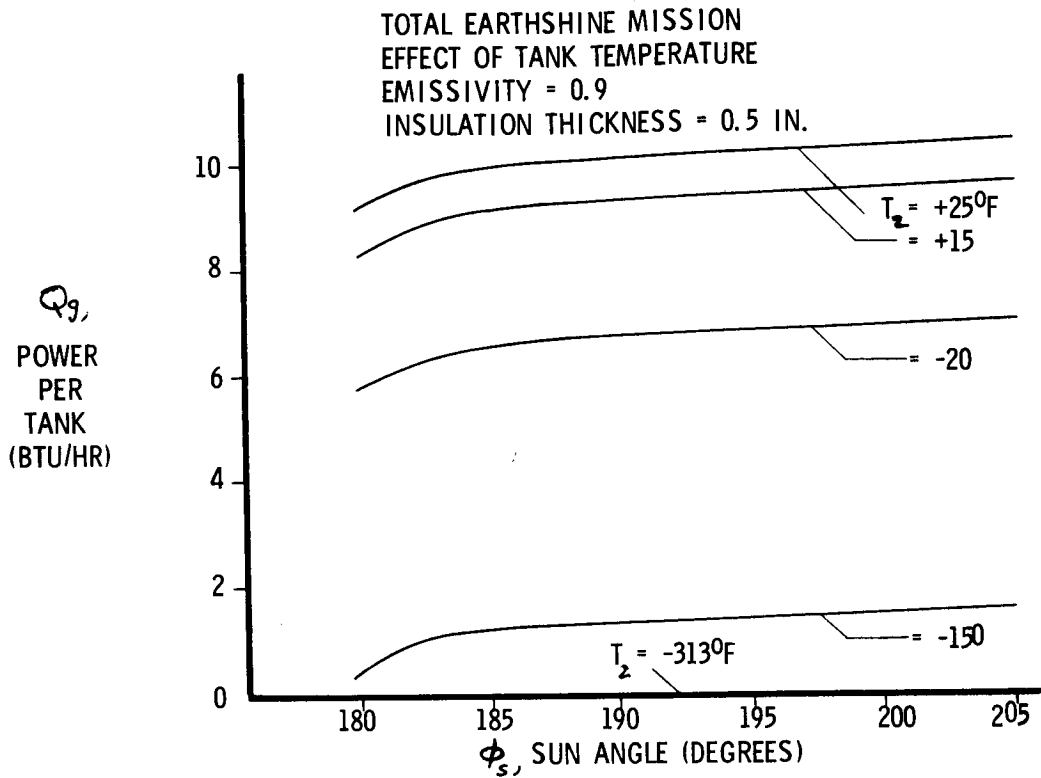


Figure 3-11. Propellant Tank Power Requirements for Various Parameters (Sheet 3 of 3)

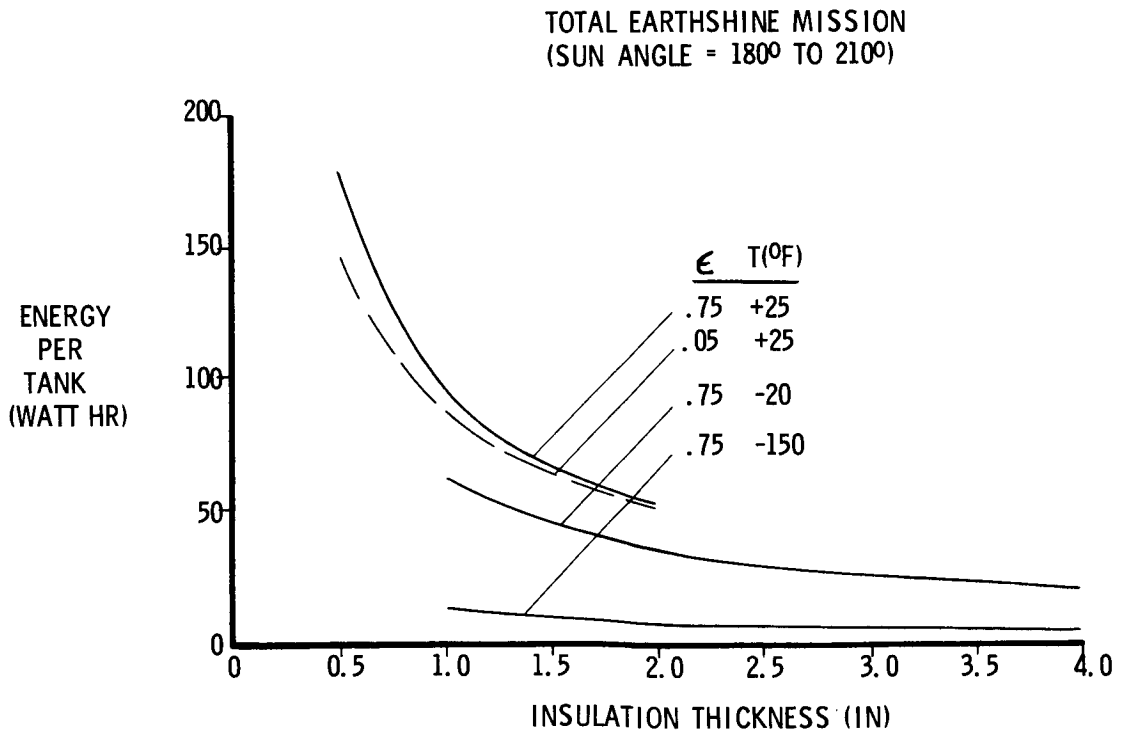


Figure 3-12. Propellant Tank Energy Requirements for Various Parameters (Sheet 1 of 3)

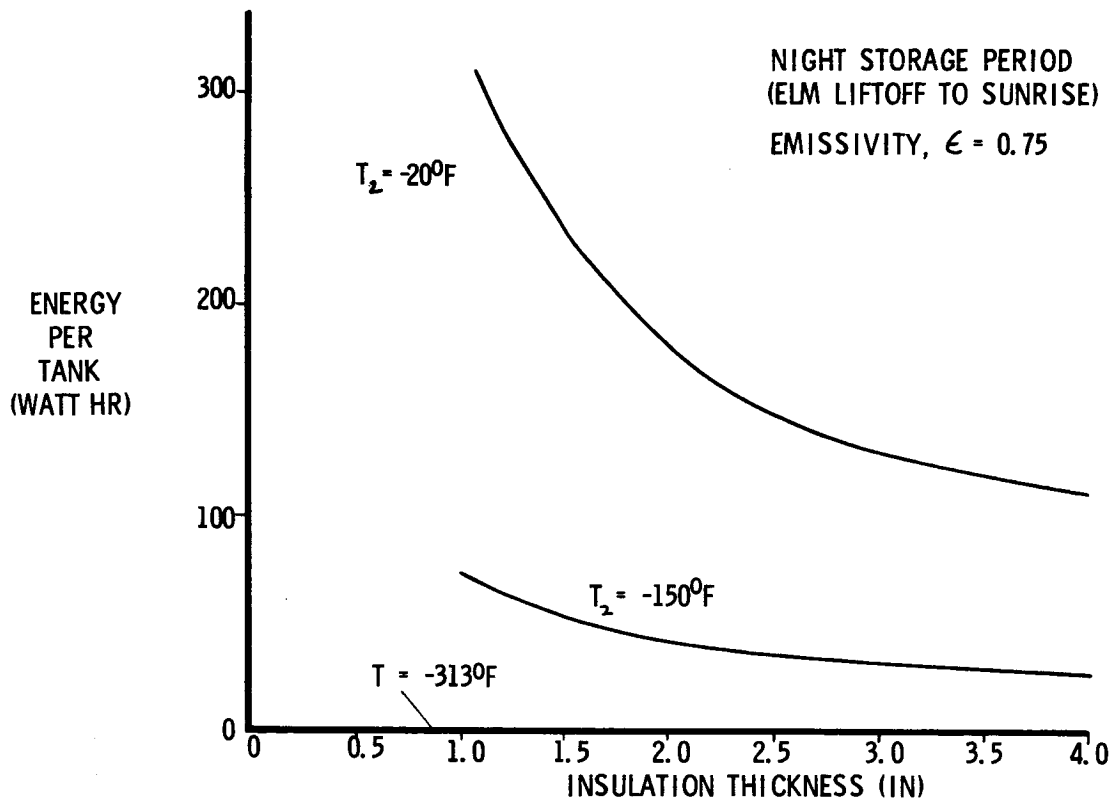


Figure 3-13. Propellant Tank Energy Requirements for Various Parameters (Sheet 2 of 3)

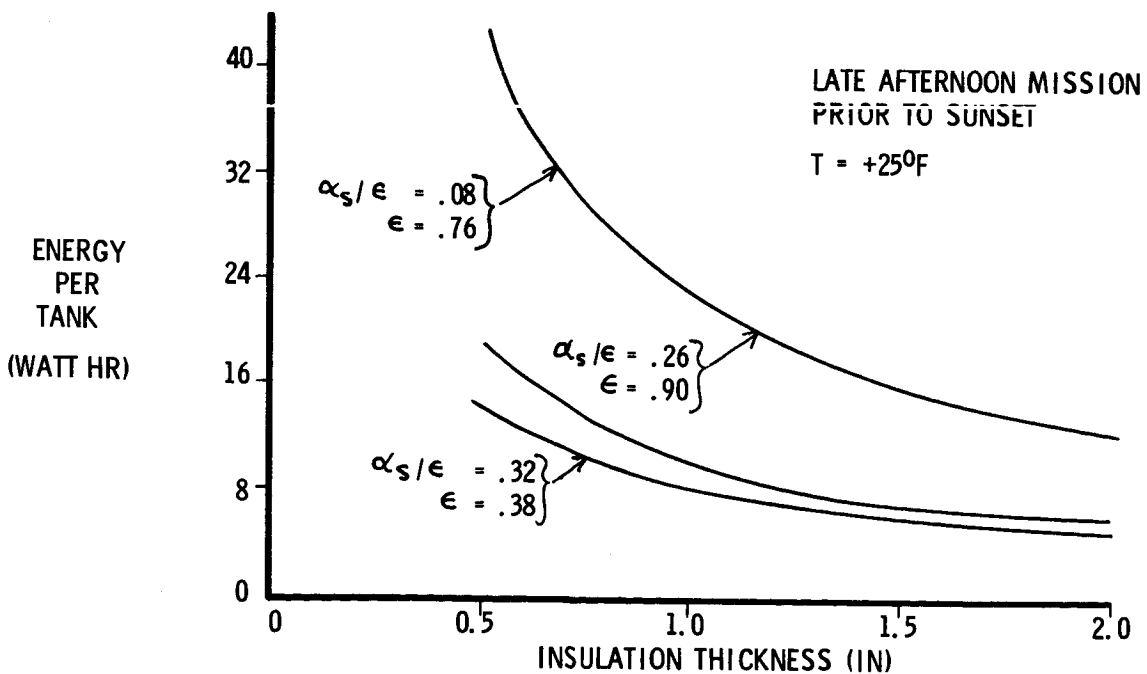


Figure 3-14. Propellant Tank Energy Requirements for Various Parameters (Sheet 3 of 3)

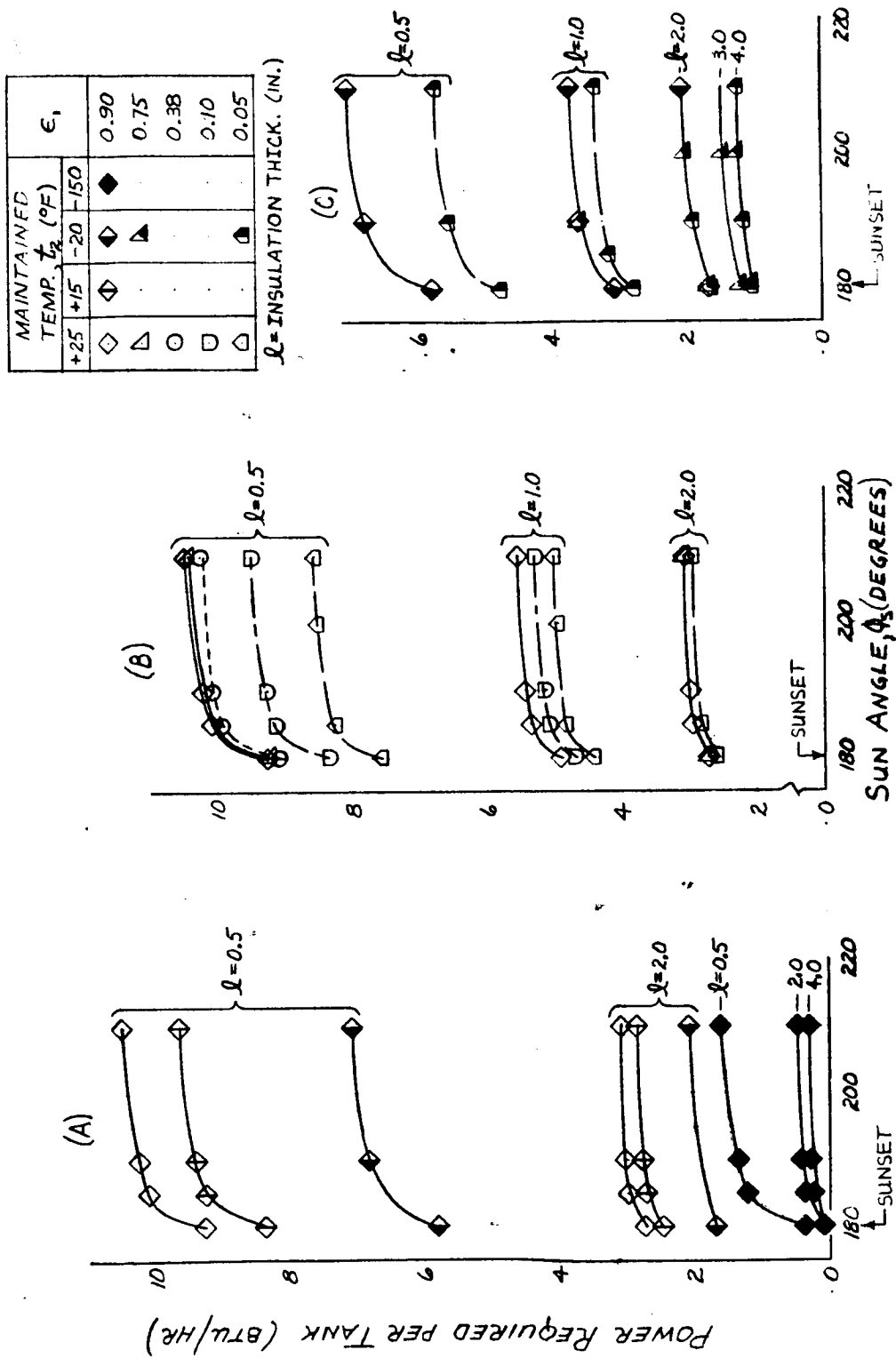


Figure 3-15. Propellant Tank Power, Night Standby Period



Table 3-2. Surface Optical Properties

Material	New		Degraded*		Comments
	$\epsilon$	$\alpha_s/\epsilon$	$\alpha_s/\epsilon$	$\alpha_s/\epsilon$	
Silver on Corning 7940 (OSR)	0.76	0.08	0.08	0.08	Second-surface mirror
IITRI Z-93 white paint	0.90	0.19	0.26	0.26	
Boeing barrier-layer anodic	0.38	0.32	0.32	0.32	Variable $\epsilon = 0.04$ to $0.5$
Aluminum on Teflon	0.82	0.31	0.39	0.39	Film side
IITRI S-13G white paint	0.88	0.26	0.40	0.40	
Schjieldal 1015	0.60	0.22	0.42	0.42	Variable $\alpha_s = 0.11$ to $0.13$ , $\epsilon = 0.1$ to $0.6$
Gold on Kapton	0.81	0.55	0.53	0.53	Film side
Aluminum on Kapton	0.67	0.73	0.68	0.68	Film side
Vapor deposited aluminum (VDA)	0.04	2.0	2.0	2.0	Stainless steel substrate
Aluminum on Mylar	0.03	7.0	8.0	8.0	NRC-2, foil side
Cobalt oxide	0.07	10.3	9.6	9.6	Aluminum substrate

\*High vacuum, 1000 ESH ultraviolet, proton flux

Reference: GE MSD Report DIN: 68SD4266 and AIAA Paper 68-794

Since solar direct and albedo heating to the tanks is present during day standby periods, the basic heat balance equations 1 and 2 are here substituted to yield:

$$Q_g = \epsilon_{\text{eff}} A_a \left\{ X_2 - \frac{\epsilon_1 A_t \left[ 129.1 (\alpha_s / \epsilon)_1 + X_L / 2 \right] + \epsilon_{\text{eff}} A_a X_2}{\epsilon_1 A_t + \epsilon_{\text{eff}} A_a} \right\} \quad (7)$$

Graphically by Weddle's rule or by simple geometry, the areas under the power versus sun-angle curves were obtained over the total time periods involved. With the proper conversion factors, these integrated areas represent the propellant tank energy requirements in watt-hours. Representative results are shown in Figures 3-12 through 3-14. The "working" plots containing all of the energy requirements information which was generated will be found in Figures 3-16 through 3-18.

Based on the energy requirements shown in Figure 3-12, a tradeoff between weight of insulation and equivalent weight of LFV battery was computed. As seen in Figure 3-19 the longest LFV sortie represents only 3.5 percent of the total earthshine mission (i. e. the night standby period). Therefore, it has been assumed that only this percentage of the total energy requirement needs to be provided by a possible battery installed on the LFV. The remainder of the energy must be furnished by the ELM while the LFV is alongside - either in directly heating the tanks or in recharging the LFV battery. Figure 3-20 depicts the tradeoff curve. In addition to the battery considerations discussed above, it was assumed (1) that 70 percent of the tank surface is covered with a heater blanket at 0.4 lb/ft<sup>2</sup> to prevent hot spots in the poorly conducting titanium wall; (2) that an OSR surface at 0.1 lb/ft<sup>2</sup> would be required by the total dawn mission envelope and is permanently installed on a fiberglass shell weighing 0.2 lb/ft<sup>2</sup> over the heaters; and (3) that this is covered for the earthshine mission with multilayer aluminized Kapton insulation having a density of 2.4 lb/ft<sup>3</sup>. According to Reference 17 the equivalent weight of the LFV battery is about 0.0675 lb/watt-hour. Under the aforementioned conditions Figure 3-20 shows a required insulation thickness of from 0.25 to 0.50 in and a total TPS weight of 6.1 lb per tank. If most of the energy required cannot be drawn from the ELM, it can be seen that the TPS weight will increase. On the other hand, reduction of the constant weights (e. g. reducing heater coverage, replacing OSR with Z-93 white paint, etc.) or delivery of relatively warm propellant from the ELM to the LFV will decrease the total TPS weight.

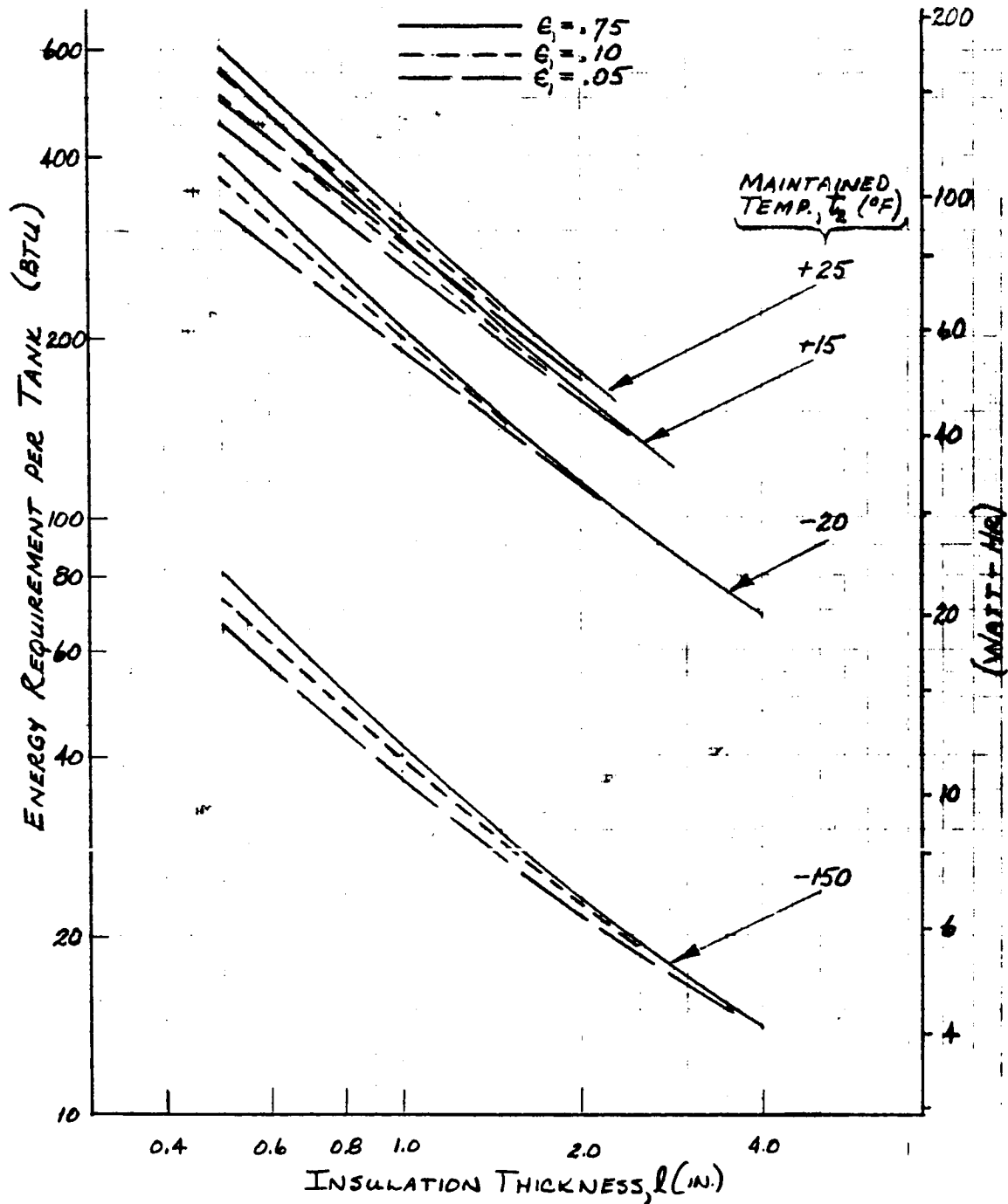


Figure 3-16. Propellant Tank Energy Requirements, Night Standby Period

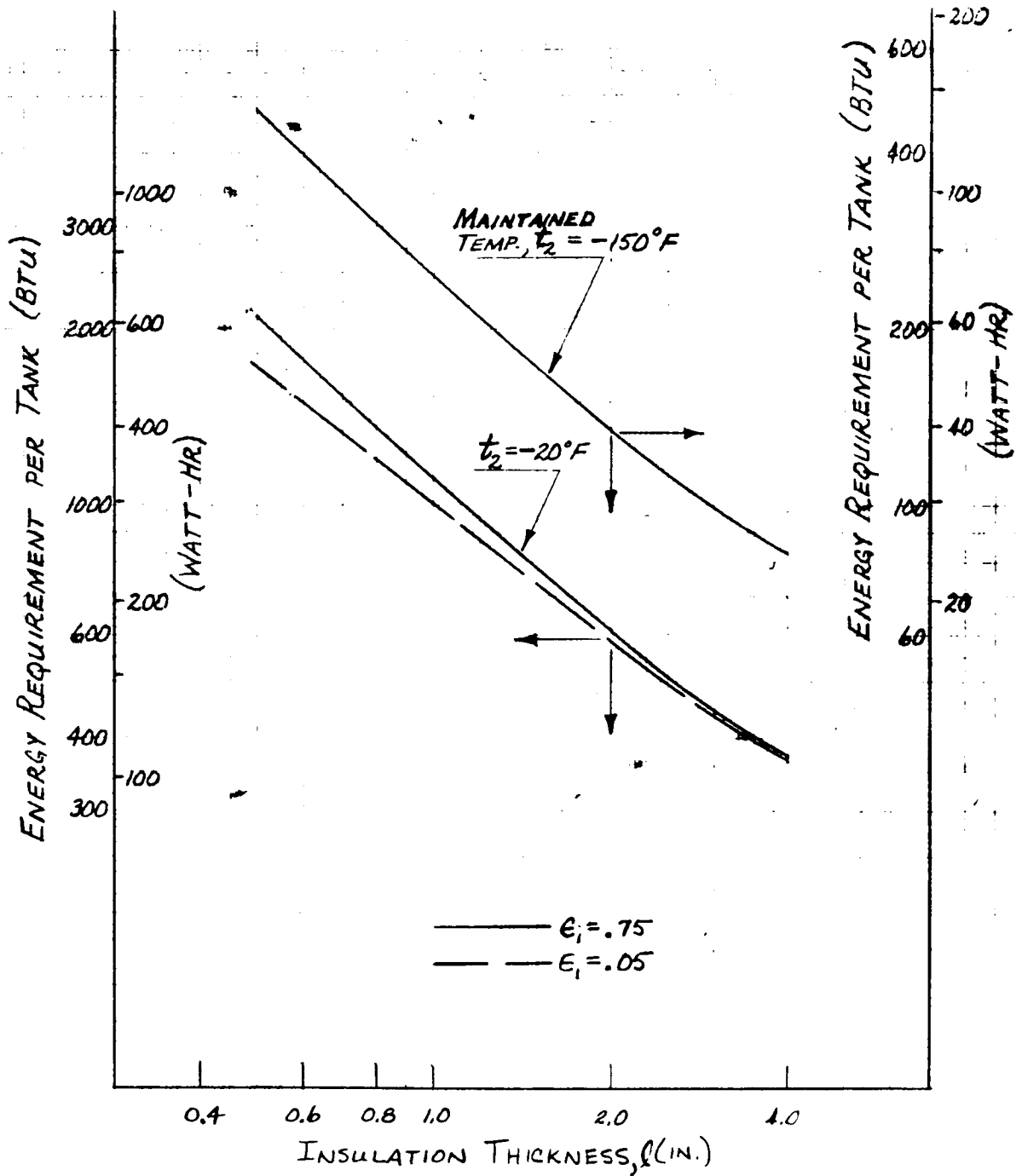


Figure 3-17. Propellant Tank Energy Requirements, Night Storage Period

	$\alpha_s/\epsilon_s$	$\epsilon_s$
—	.08	.76
—	.26	.90
- - -	.32	.38

MAINTAINED TEMP.,  $t_2 = +25^\circ\text{F}$

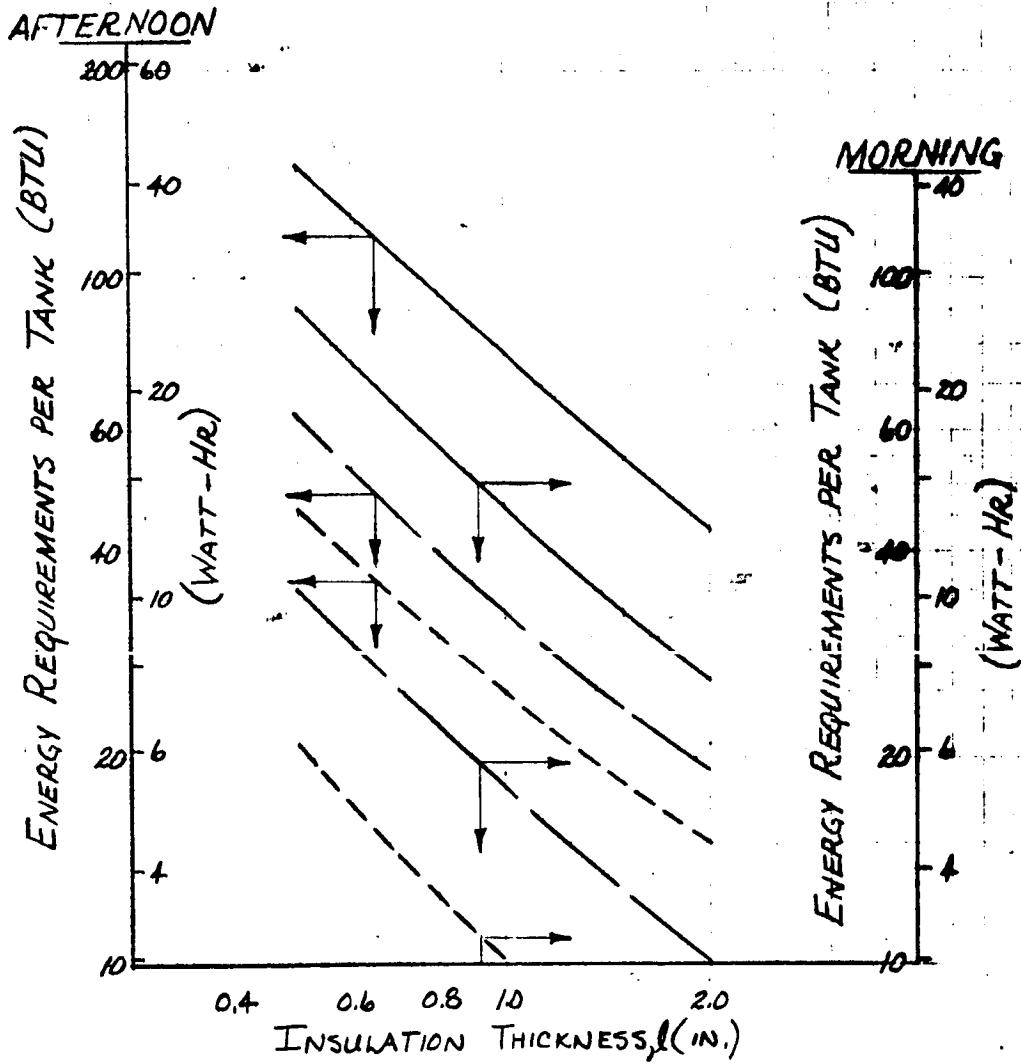


Figure 3-18. Propellant Tank Energy Requirements, Day Standby Periods

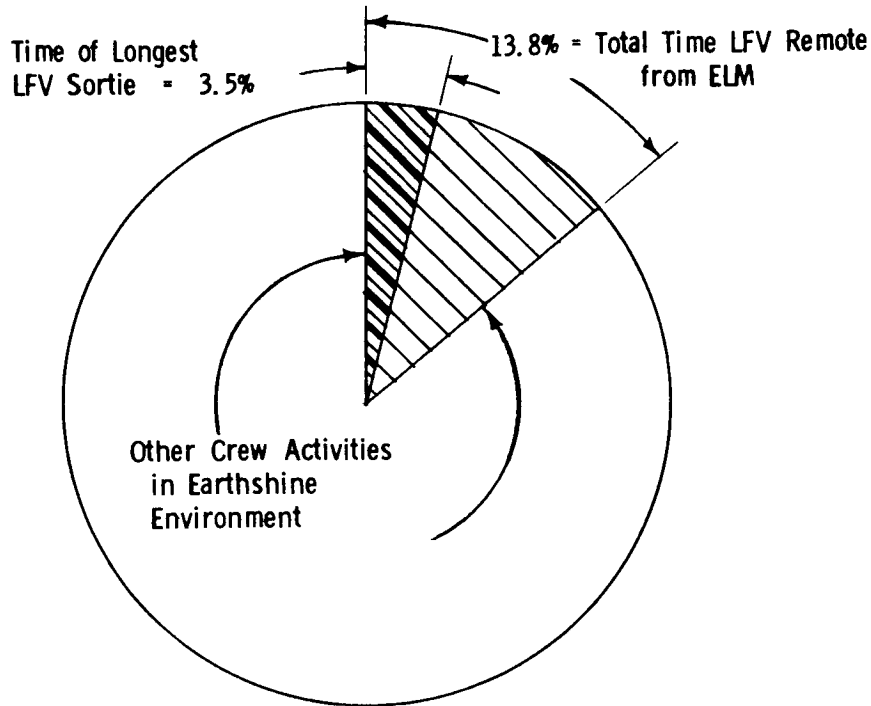


Figure 3-19. LFV Earthshine Operations, Thermal Considerations

Earthshine Mission  
70% Heater Coverage  
3.5% Equivalent Secondary Battery Weight on LFV

$R = 10$  in.  
 $T = +25^{\circ}F$   
 $\epsilon = .67$

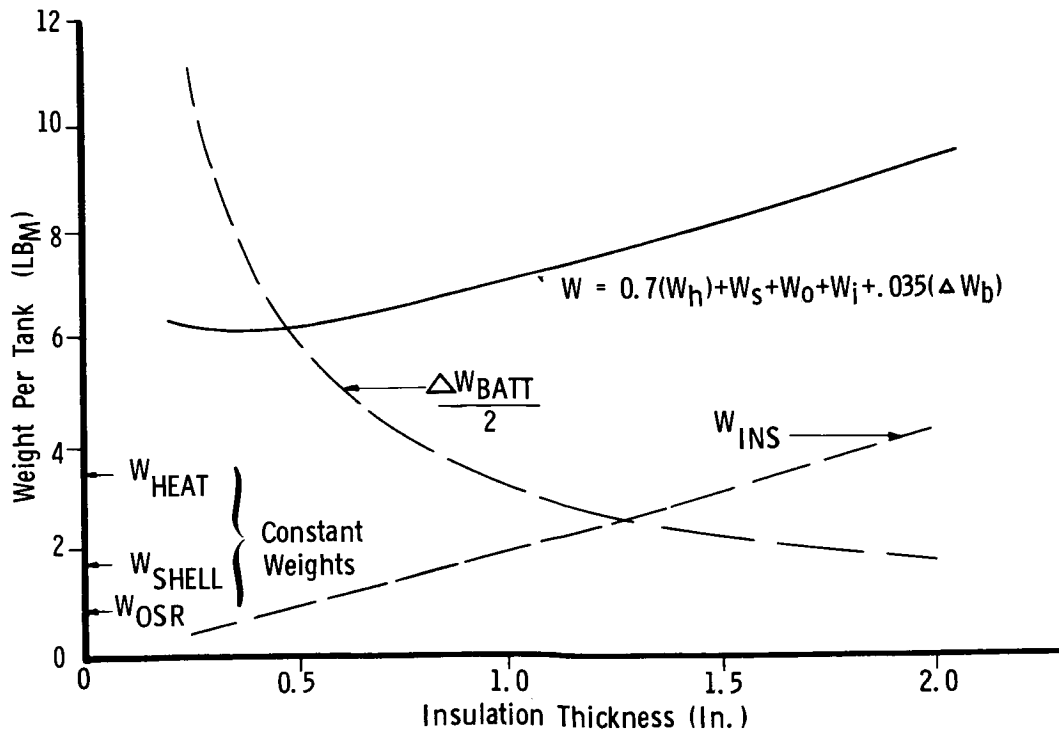


Figure 3-20. Typical Propellant Tank TPS Weights

Even though the TPS for the propellant tanks does not require heaters or insulation for any envisioned morning mission, they will be needed to satisfy the three-month storage requirement. Thus, the lunar night environment remains germane to the design of an LFV restricted to daylight operation. The thermal shroud is part of the answer, but a low level of heating will also be needed. This is one area requiring additional effort.

## ENGINE AND FEEDLINE THERMAL PROTECTION

It was felt that for lunar night conditions, the differences in geometry between Apollo SM RCS and LFV could reasonably be neglected for thermal analysis purposes. Thus advantage could be taken of extensive thermal computations from NR SD Apollo data.

As shown in Figure 3-21, the time required to cool the engines to a point where the propellant freezes at the injector is on the order of two to three hours. The maximum duration that the LFV is away from the ELM site is 2.1 hours. Since these two time periods are so close, heaters and connections from the on-board LFV battery to the heaters should be installed for contingency only. It is expected that the battery would be used only in case the mission time is extended beyond 2.1 hours. ELM power may also be required for preflight warmup of the valves. An engine temperature sensing system will be required. The LFV engines are compared with the Apollo SM and LV in Table 3-3 and a power requirement of 10 watts per engine for steady-state operation has been estimated.

## STRUCTURAL AND ATTENUATOR THERMAL PROTECTION

### Structure

View factors to space and the lunar surface for most LFV structural tubing are similar to those of the spherical propellant tanks. The established maximum and minimum temperatures for aluminum tubing are 250 F and -420 F, respectively. Therefore, a coating of Z-93 paint ( $\alpha_s/\epsilon = 0.26$ ) was chosen as adequate to limit structural temperatures in the natural lunar environment. Surfaces pointing directly at the moon, such as the bottoms of the astronaut foot and payload support plates, should be coated with vapor-deposited aluminum (VDA,  $\epsilon = 0.04$ ) to limit infrared radiation heating.

### Attenuators

In the final LFV configuration shown in earlier sections, there are two landing attenuators on each of four legs, the earlier central attenuator system having been rejected. A schematic diagram of the attenuators is

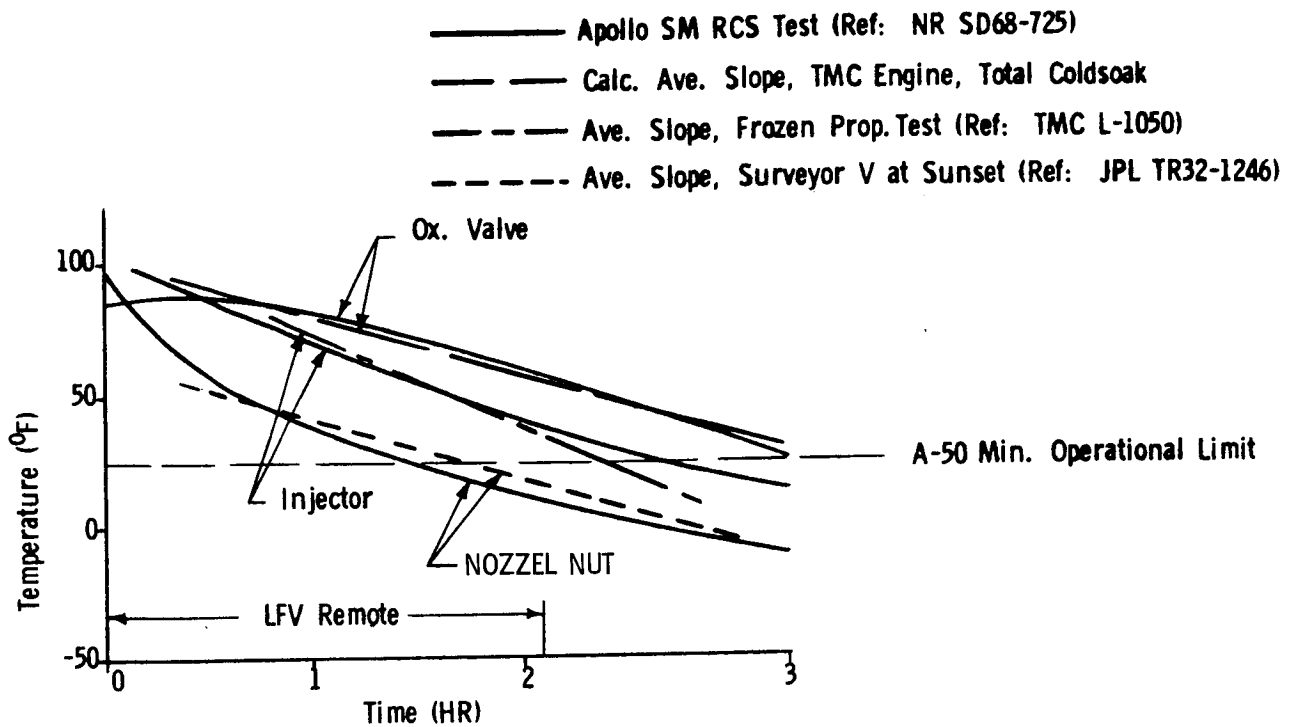


Figure 3-21. Estimated Engine Cooldown, Lunar Night

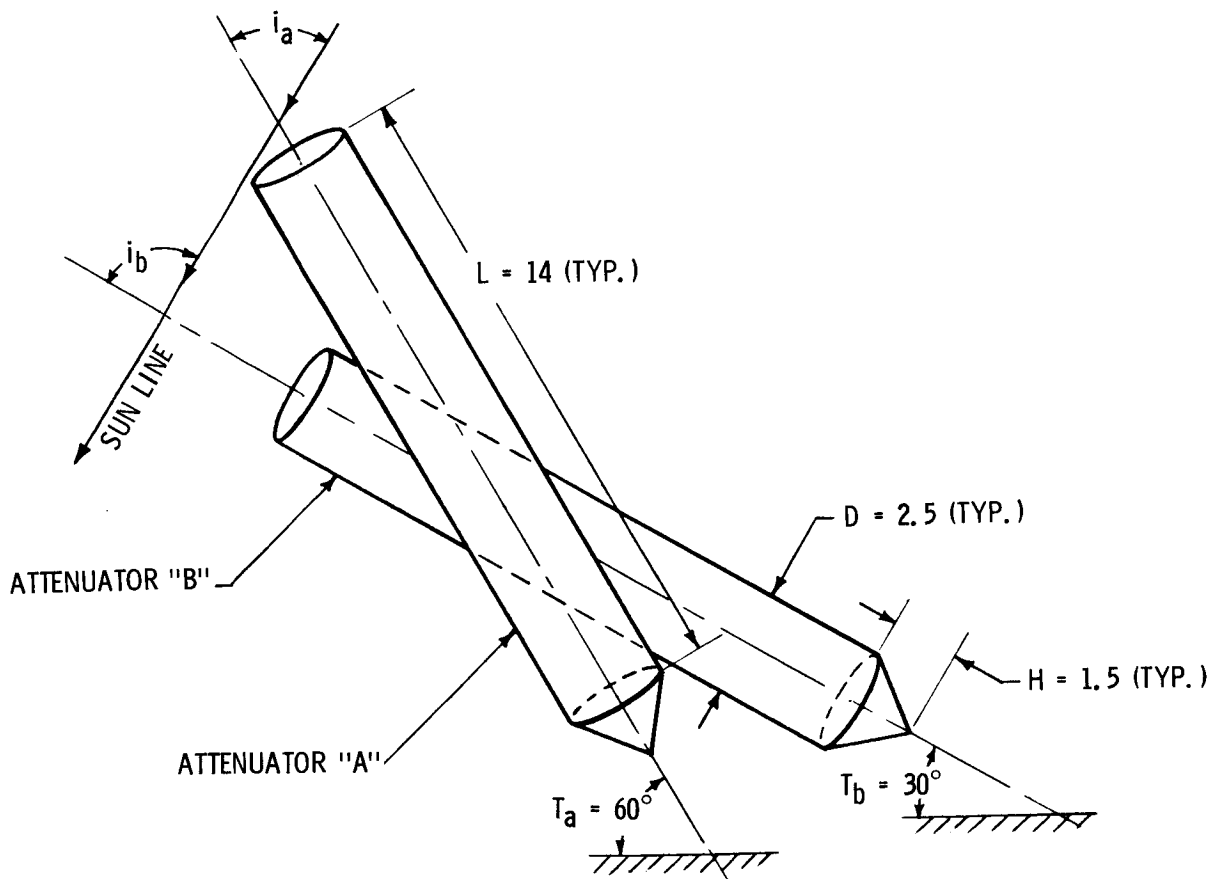


Figure 3-22. Landing Attenuators, Schematic Diagram



Table 3-3. Engine Heaters

Characteristics	SM RCS	LM RCS	LFV
Manufacturer	TMC	TMC	?
Nominal thrust (each), lb	100	100	100 or 300
Fuel	MMH	A-50	A-50
Oxidizer	N <sub>2</sub> O <sub>4</sub>	N <sub>2</sub> O <sub>4</sub>	N <sub>2</sub> O <sub>4</sub>
Thermal environment	Space	Space and lunar	Lunar
Heater watts per engine			
- Steady state	9	10	10
- Pulsed	18	36	N. A.

shown in Figure 3-22. The assumptions previously used for the thermal analysis of the propellant tanks were also used for the attenuators.

Taking these assumptions into consideration, an expression is derived in Appendix A for the steady-state temperature of any single object near the moon (assumed to be an infinite plane). It can be seen from the final equation of this appendix that the ratio of projected area to total surface area ( $A_p/A_t$ ) is significant. This ratio is plotted versus the solar incidence angle ( $i$ ) for a number of simple geometric shapes in Reference 3-18. In this reference it was noted that the equation for the ratio of projected area to convex surface area ( $A_p/A_s$ ) for a right cone was, at best, ambiguous and appeared to contain errors. Therefore, the  $A_p/A_s$  ratio for a cone is derived in Appendix A. As used in determining required area ratios for the attenuators, the relationship for the cylindrical body plus flat plate and conical ends is as follows:

$$\left(\frac{A_p}{A_t}\right)_{\text{atten}} = \left(\frac{A_p}{A_s}\right)_{\text{cyl}} \frac{A_{s, \text{cyl}}}{\Sigma A_s} + \left(\frac{A_p}{A_s}\right)_{\text{fp}} \frac{A_{\text{fp}}}{\Sigma A_s} + \left(\frac{A_p}{A_s}\right)_{\text{cone}} \frac{A_{s, \text{cone}}}{\Sigma A_s}$$

where

$$\begin{aligned}
 A_{s, \text{ cyl}} &= \pi DL \\
 A_{\text{ fp}} &= (\pi/4) D^2 \\
 A_{s, \text{ cone}} &= \left( \pi D^2 / 4 \right) \left[ 1 + 4 (H/D)^2 \right]^{0.5} \\
 \left( A_p / A_s \right)_{\text{ cyl}} &= (1/\pi) \sin i \\
 \left( A_p / A_s \right)_{\text{ fp}} &= \cos i \\
 \left( A_p / A_s \right)_{\text{ cone}} &= \text{ see Appendix B, Condition 1.} \\
 \Sigma A_s &= A_{s, \text{ cyl}} + A_{\text{ fp}} + A_{s, \text{ cone}}
 \end{aligned}$$

The results of these calculations are plotted in Figure 3-23.

An equation for determining the solar incidence angle on the attenuators is derived in Appendix B, Condition 5. This equation was utilized to calculate the incidence angles on the exposed "A" and "B" attenuators during lunar morning. Attenuators mounted on LFV legs pointing toward the cardinal and principal intermediate directions were considered. The results are shown in Figure 3-24 plotted versus sun angle ( $\phi_s$ ).

The LFV operational timeline should be considered next; and one derived from Reference 3-14 for the nominal dawn mission is charted on Figure 3-25. Note that the extended lunar module (ELM) touchdown is at  $\phi_s = 10$  degrees, that limits are from 7 to 20 degrees into daylight from either the sunrise or sunset terminator and that the attenuators need stay within their operational temperature limits (0 to 125 F) only during the LFV active phase.

With the final equation derived in Appendix A,

$$T_1 = 155.4 \left\{ 442 (\alpha_s / e) \left[ (A_p / A_t) + a F_1 - L \right] + F_1 - L X_L \right\}^{0.25}$$

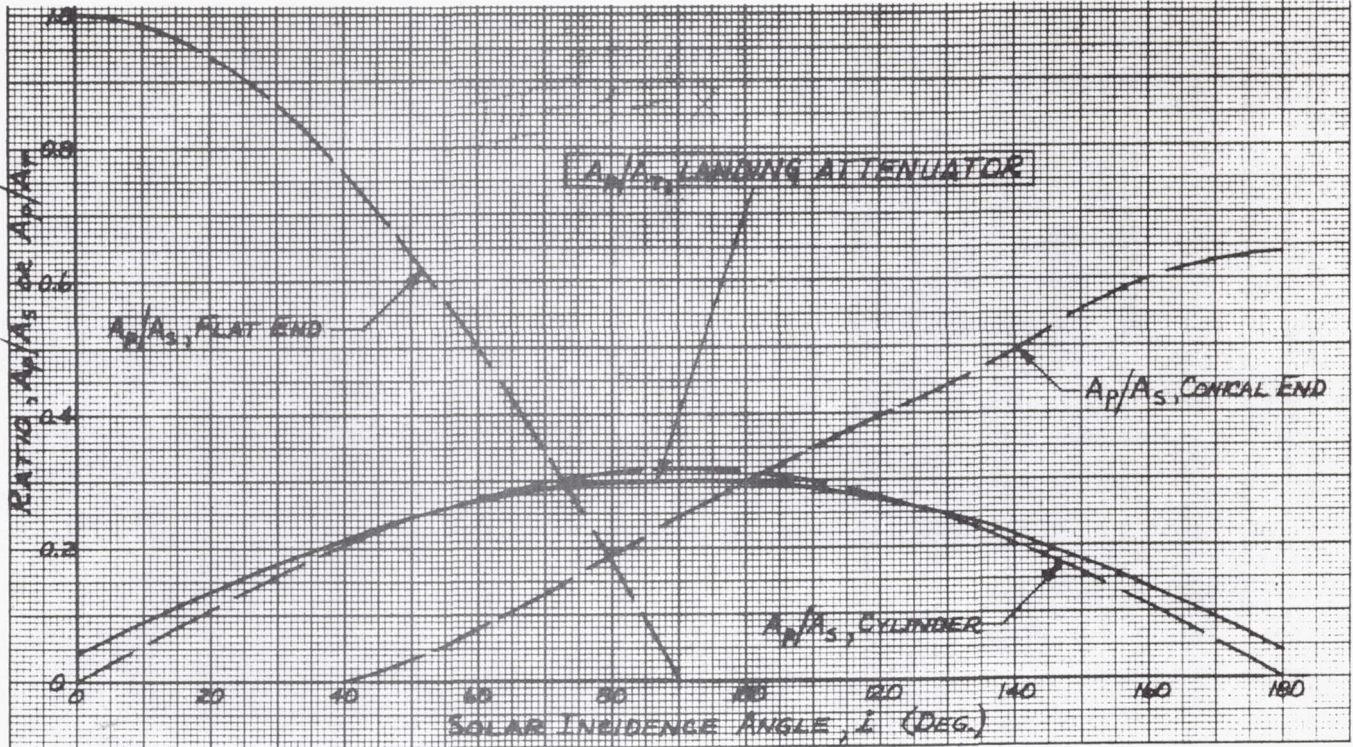


Figure 3-23. Projected Area to Surface Area Ratios for Landing Attenuators

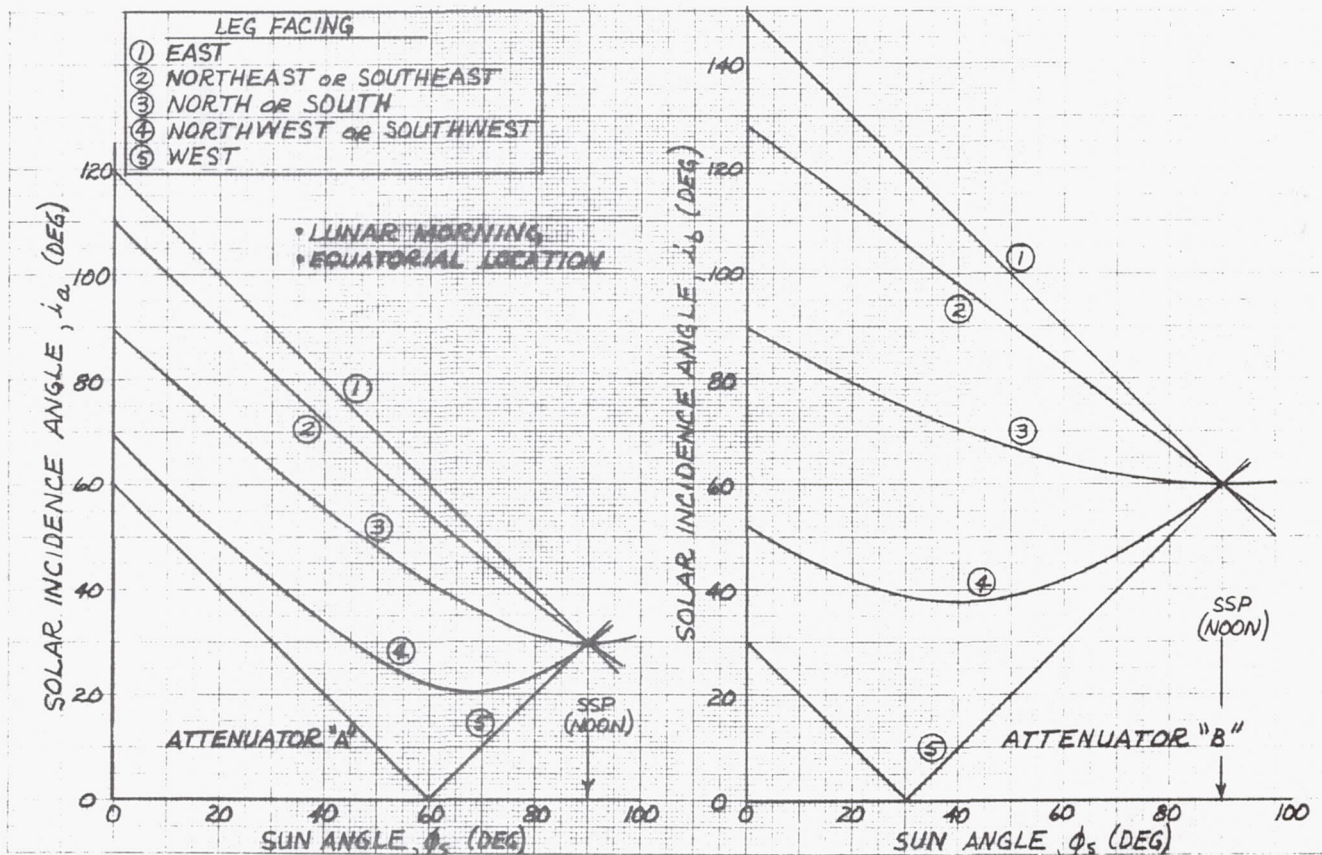


Figure 3-24. Solar Incidence on Landing Attenuators

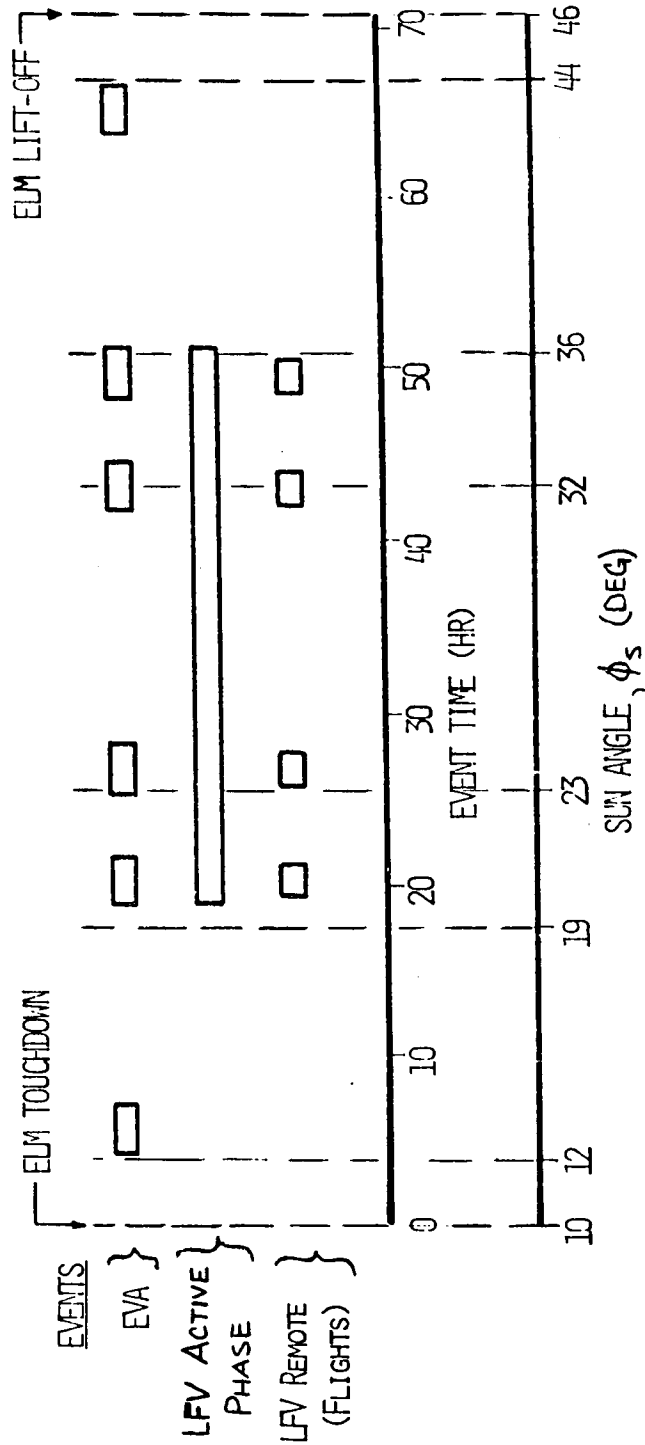


Figure 3-25. Timeline Considerations for Nominal Dawn Mission

the lunar thermal environment described earlier, and using Figures 3-23 and 3-24, steady-state attenuator temperatures were calculated. As shown in Figure 3-26, a TPS coating having an  $\alpha_s/\epsilon = 0.26$  is adequate to maintain all attenuator temperatures within operational limits during the active phase of the nominal dawn mission. These coating properties are representative of Z-93 white paint, even following ultraviolet degradation (Reference 3-19). The three-day dawn mission envelope shown on Figure 3-26 spans the interval from the minimum ELM touchdown at  $\phi_s = 7$  degrees to a maximum ELM liftoff at  $\phi_s = 56$  degrees (maximum ELM touchdown at  $\phi_s = 20$  degrees plus  $\phi_s = 36$  degrees or 70.8 hours stay time). If the LFV active phase remains at relatively the same position within the total three-day mission, the attenuator temperatures will not exceed their limits. This is because the maximum envelope of the LFV active phase could then extend only from  $\phi_s \approx 16.5$  to 46.5 degrees.

At the subsolar point (SSP) or lunar noon the calculated maximum temperatures for the "A" and "B" attenuators is 147 F and 153 F, respectively. These are well below the maximum storage limit of 195 F. Therefore, the use of Z-93 white paint or the equivalent is recommended for the attenuators.

Another thermal analysis of the landing attenuators was conducted to estimate the radiation heating to them from the hot engine nozzle bell. Figure 3-27 is a schematic diagram of the engine-to-actuator relationship. The configuration shown is actually for an earlier central attenuator concept having only a single actuator per leg. However, the spatial relationships are very similar to the present arrangement. First, the radiation view factor from a single engine bell to an attenuator, skewed relative to the bell, was calculated using the CONFAC II computer program (Reference 3-20). Although the view factor is low, the exchange coefficient ( $A_i F_{ij}$ ) is relatively high when the surface areas of the engine bell and attenuator are considered. Each attenuator is irradiated by two engines. The calculated radiation heating rate is plotted in Figure 3-28 versus engine bell temperature with emissivities as a parameter. Numerically, the heating appears to be low; however, they should be placed in proper perspective with other environmental heating. For instance, engine radiation heating of 0.034 Btu/sec applied to 0.69 ft<sup>2</sup> (the attenuator surface area considered in the model) is a flux of 0.049 Btu/ft<sup>2</sup>-sec, and the latter value is 40 percent as great as the full solar constant ( $q_s$ ) of 442 Btu/ft<sup>2</sup>-hr = 0.123 Btu/ft<sup>2</sup>-sec. On Figure 3-28, it can be seen that, with best-estimate emissivities of 0.3 and 0.9 for the bell and attenuator, respectively, the 0.034 Btu/sec heating results for a bell temperature of 1750 F—quite reasonable for a radiation-cooled engine. In addition, steady-state temperatures shown in Figure 3-26 are all lower than those of the lunar

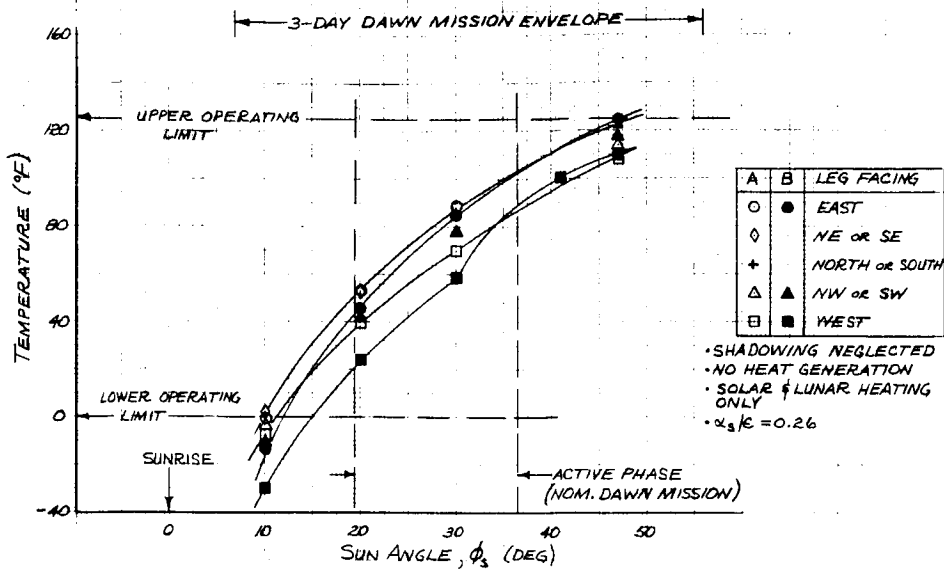


Figure 3-26. Lunar Morning Landing Attenuator Temperatures

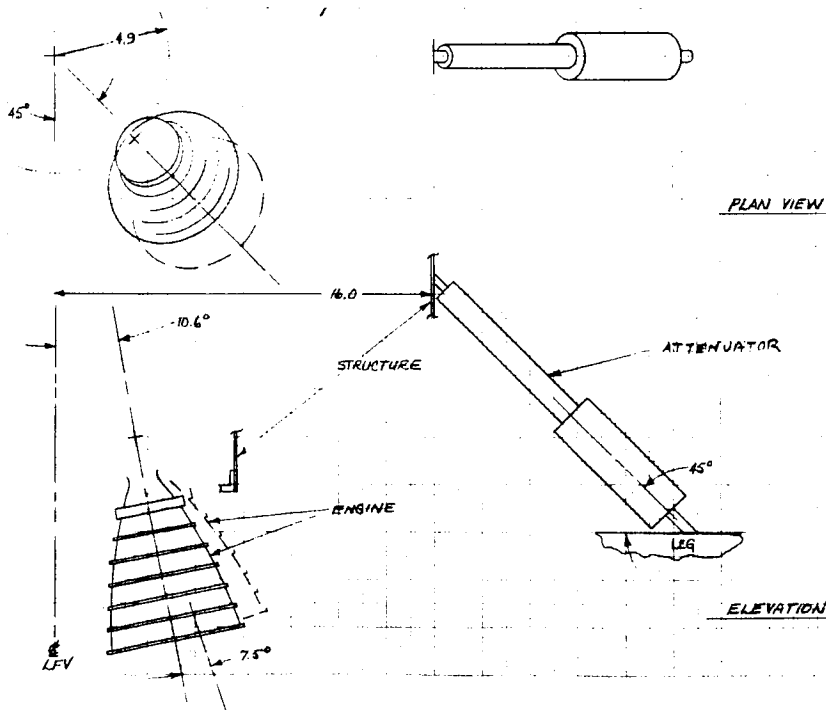


Figure 3-27. Engine to Actuator Relationships

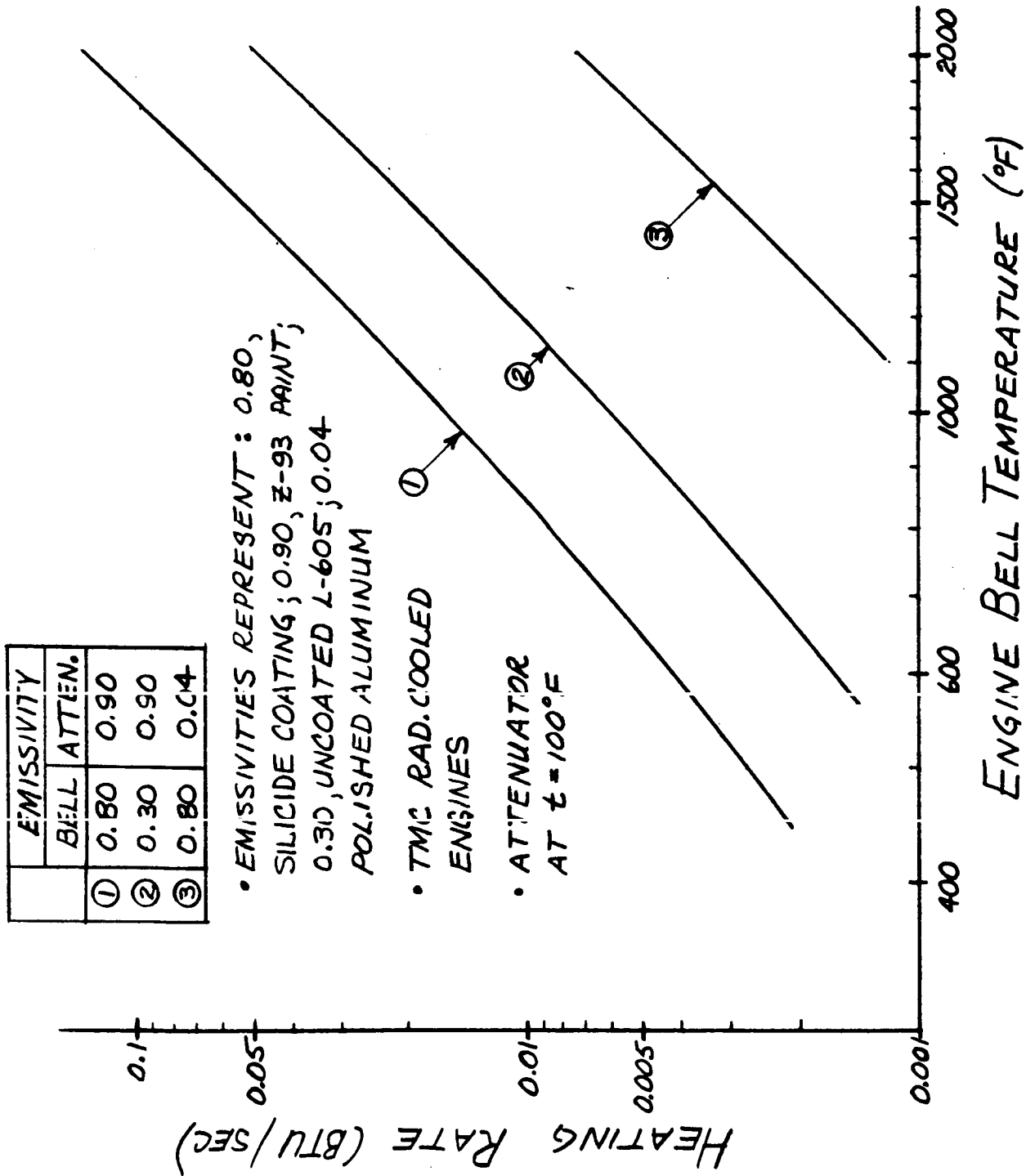


Figure 3-28. Radiative Heating to Landing Attenuators

surface at the same  $\phi_s$ , thereby indicating a net heat flow away from the attenuators. The net radiation exchange between operating engines and the attenuators will always be into the latter, and it must be considered in subsequent integrated analyses.

A polished aluminum surface on the attenuators would drastically lower heating from the engines, as shown in Figure 3-28. However, its use cannot be recommended at this time because the high  $\alpha_s/\epsilon$  of polished aluminum could lead to overheating from solar heating. A carefully tailored TPS coating scheme involving both Z-93 paint and polished aluminum might be prescribed in a more detailed design.

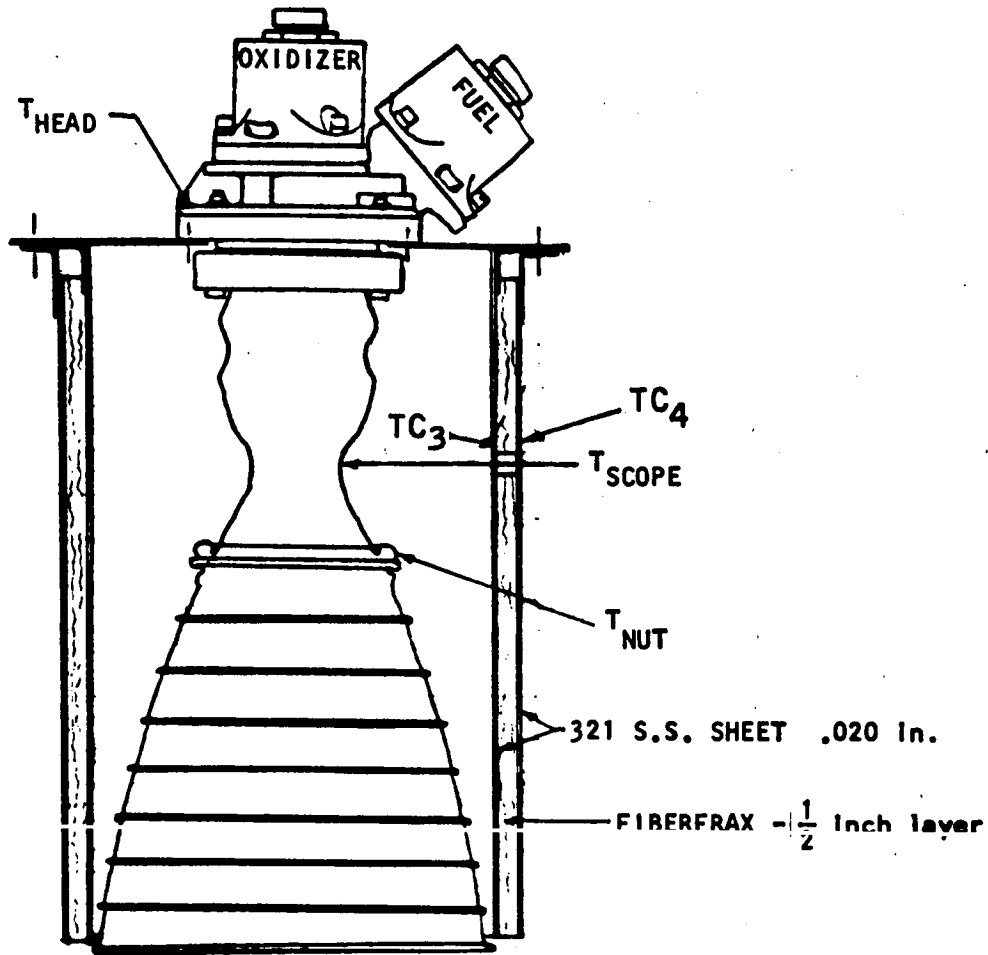
A close inspection of the LFV arrangement reveals that the greatest obstacle to an adequate TPS design for the attenuators may well be excessively low temperatures, not overheating. The design tucks the attenuators under and/or quite close to other structure, and shadowing will be a problem. The attenuators on the +X axis leg will be in total shadow from the astronaut leg support most of the time. This situation suggests the undesirable possibility of requiring strip heaters even during day missions. In any event, a rigorous thermal analysis of the attenuators will be complex and time consuming, but it may well be required considering the Surveyor analytical and operational experiences.

#### CLUSTERED ENGINES HEAT TRANSFER

As a result of the choice of four 100-pound engines in a cluster form, the possibility of exceeding the engine wall temperature limits due to reduced view factors was investigated. A review of the literature was conducted to determine if data were available on wall temperatures of radiation cooled engines with reduced view factors. Data were available (Reference 3-21) on the Marquardt R4D engine for both totally exposed and totally submerged installations. A schematic of the totally submerged installation is shown in Figure 3-29.

The approach used in this study was (1) to review the critical temperature limits and (2) to interpolate between the fully exposed and fully submerged cases using the view factors of the clustered configuration. Since the configuration is subject to change and since the gimbal and cant angles may vary, a worse-case analysis was performed in order to bound the problem. The conditions of this analysis are (1) all four engines are vertical with exit lips touching (this condition implies zero cant and zero gimbal angles), (2) full thrust, and (3) no circumferential conduction.





**TEMPERATURE MEASUREMENT LOCATIONS AS SHOWN**

$T_{HEAD}$	INJECTOR HEAD TEMPERATURE (T/C)
$T_{NUT}$	CHAMBER-TO-BELL ATTACH NUT TEMPERATURE (T/C)
$T_{SCOPE}$	CHAMBER THROAT TEMPERATURE (THERMOSCOPE RECORDING PYROMETER)
$TC_3$	INNER SHIELD TEMPERATURE (T/C)
$TC_4$	OUTER SHIELD TEMPERATURE (T/C)

Figure 3-29. SM RCS Engine Submerged Installation, Schematic Drawing

Table 3-4 shows the test results (taken from Reference 3-21) of fully submerged and free radiation conditions for a single Marquardt R4D 100-pound thrust engine. It can be seen that the critical temperature is the nut temperature. The nut is that point at about an area ratio of six where the thrust chamber and the skirt are mated.

The basic equation used for the analysis was

$$\dot{q} = h_g (T_g - T_w) = \sigma (\epsilon_1 F_1 + \epsilon_0 F_0) T_w^4$$

where

$\dot{q}$  = Heat transfer rate from combustion gas to wall

$h_g$  = Gas side heat transfer coefficient

$T_g$  = Combustion gas temperature

$T_w$  = Thrust chamber wall temperature

$\sigma$  = Stefan-Boltzman constant

$\epsilon_1$  = Emissivity of thrust chamber internal surface

$\epsilon_0$  = Emissivity of thrust chamber external surface

$F_0$  = View-factor of thrust chamber external surface

$F_1$  = View-factor of thrust chamber internal surface

The radiation from the insulating wall to the environment was considered to be negligible. In addition, the wall temperature was not measured in Reference 3-21, so that a reasonable assumption of this type is necessary to complete the analysis.

Table 3-5 shows the results of clustered engine analysis. Using the basic heat transfer equation, the emissivities and view factors shown in the table, the calculated nut temperature was 1900 F. The conclusion reached was that any clustering arrangement is acceptable since the actual nut temperature will be lower than 1900 due to relaxed geometric and/or thrust conditions. Meetings with technical personnel of Marquardt and Rocketdyne confirmed the fact that they were in agreement with this conclusion based on independent analysis.

Table 3-4. Comparison of Submerged and Free Radiation Thermal Characteristics (O/F = 1.6, N<sub>2</sub>O<sub>4</sub>/A-50, 100-Lb Thrust)

	Test Temperature		
	T <sub>HEAD</sub> (°F)	T <sub>THROAT</sub> (°F)	T <sub>NUT</sub> (°F)
Free Radiation	180	2400	1700
Shielded	180	2550	2050
Temperature limits	300 - 350	~2800	1900
Temperature rise	0	+150	+350

Table 3-5. Clustered Engine Thermal Results

● Basic Data			
Emissivities			
ε <sub>0</sub> = 0.2 (outside)			
ε <sub>1</sub> = 0.7 (inside)			
View factors at nut			
	<u>Inside</u>	<u>Outside</u>	<u>ΣεF</u>
Fully exposed	0.1	1.0	0.27
Fully shrouded	0.1	0	0.07
Clustered	0.1	0.3	0.13
● Results			
Calculated nut temperature = 1900 F (same as max allowed)			
● Conclusion			
Any clustering arrangement is acceptable because actual nut temperature will be below 1900 F due to relaxed conditions			

## BASE HEATING STUDIES

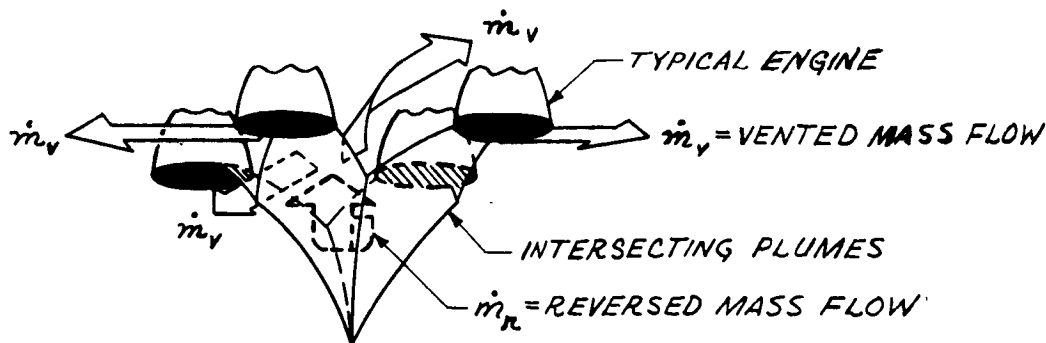
To partially define the thermal environment of the LFV, a parametric study was made of the base flow heating between its clustered engines. Heating was calculated at several gimballed angles for each of three configurations as a function of total engine thrust.

A number of the configurations considered for the LFV were powered with multiple engines. In these cases, one facet of the in-flight thermal environment is the heating to structure between the engines due to the flow of reversed plume gases. The basic analytical model for this base flow attributes the reversal of the plume gases to the compression resulting from impingement of adjacent plumes. The low velocity gases in the shear layers bounding the plumes are assumed to have insufficient momentum to penetrate into this high-pressure impingement zone and are thus forced to return toward the base region. Steady-state base flow at very low ambient pressures is considered to be established when the net mass flow being reversed is just equal to the mass flow vented through the available passages between engines. A diagram of the plume is shown at the top of Figure 3-30. The engine and plume data taken from References 3-22 and from Reference 3-23 scaled for 100 psi rated combustion chamber pressure by Reference 3-24, are presented in Figure 3-30.

Base heating to LFV structure was calculated at several gimballed angles for each of three configurations as a function of total engine thrust. The gimballed angles chosen are not, for the most part, values expected during normal operation. Rather, they represent a failure mode situation and serve to bound the problem. Geometrical considerations related to the gimbaling are depicted in Figure 3-31. Shown in Figure 3-32 are schematics of the configurations considered. Configuration I (open) was never part of the LFV design but is included as a reference point. Configuration II (skirted) is representative of LFV configurations in which the gimballed engines are enclosed within a box-like structure, thus reducing the area available for venting the flow. Here the skirt is considered flush with the exit plane of the engines. Configuration III (cruciform) is one of the latest LFV concepts with each engine positioned between a pair of legs. The surface at which base heating is calculated is relatively close to the exit plane, but the arrangement provides extra flow vent area.

The computer program discussed in Reference 3-25 was utilized to compute base flow heat fluxes. It is written for clustered layouts with all engines fixed normal to the base plane. This program was modified to account for canted engines and for handling variations in normal vent area.

PLUME FLOW



ENGINE AND PLUME DATA

EXIT RADIUS ( $r_e$ ) = 2.73 in.  
 BASE RADIUS ( $r_b$ ) = 1.5 in.  
 BASE TO EXIT HEIGHT ( $h$ ) = 9.0 in.  
 AREA RATIO ( $\epsilon$ ) = 40  
 EXIT HALF-ANGLE ( $\theta_e$ ) = 8.3 deg.

EXIT SPECIFIC HEAT RATIO ( $\gamma_e$ ) = 1.30  
 PRANDTL NUMBER ( $P_r$ ) = 0.779  
 MOLECULAR WEIGHT ( $M_e$ ) = 20.65 lb/mole  
 DYNAMIC VISCOSITY ( $\mu$ ) = 0.0374 cp  
 EXIT MACH NUMBER ( $M_e$ ) = 4.60  
 SINGLE ENGINE THRUST ( $F$ ) = 30 to 100 lb<sub>f</sub>

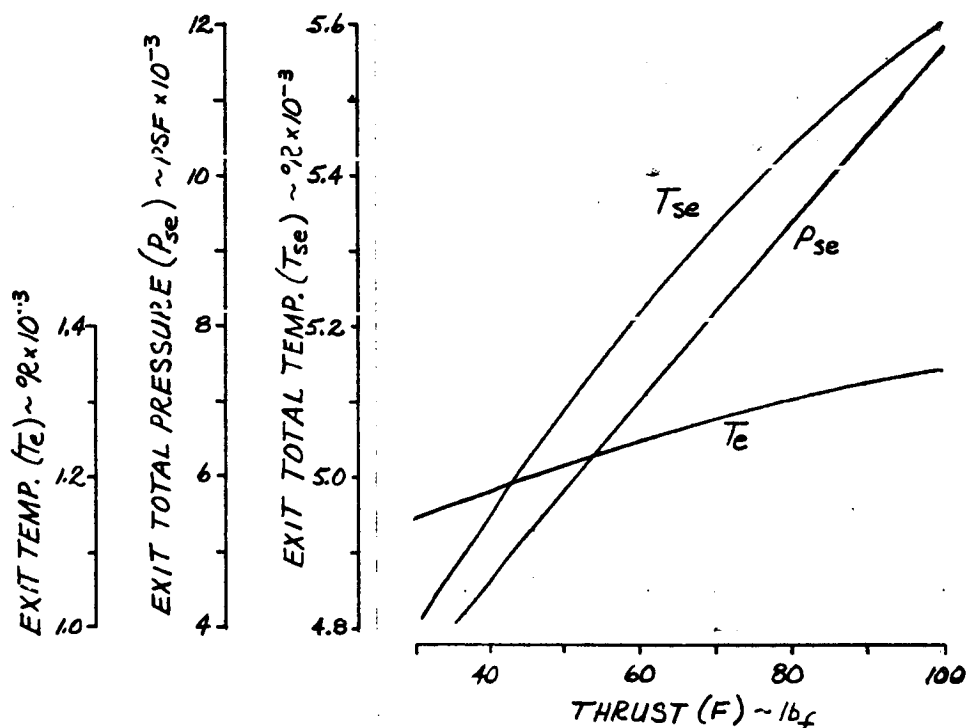


Figure 3-30. Flow Model and Physical Data

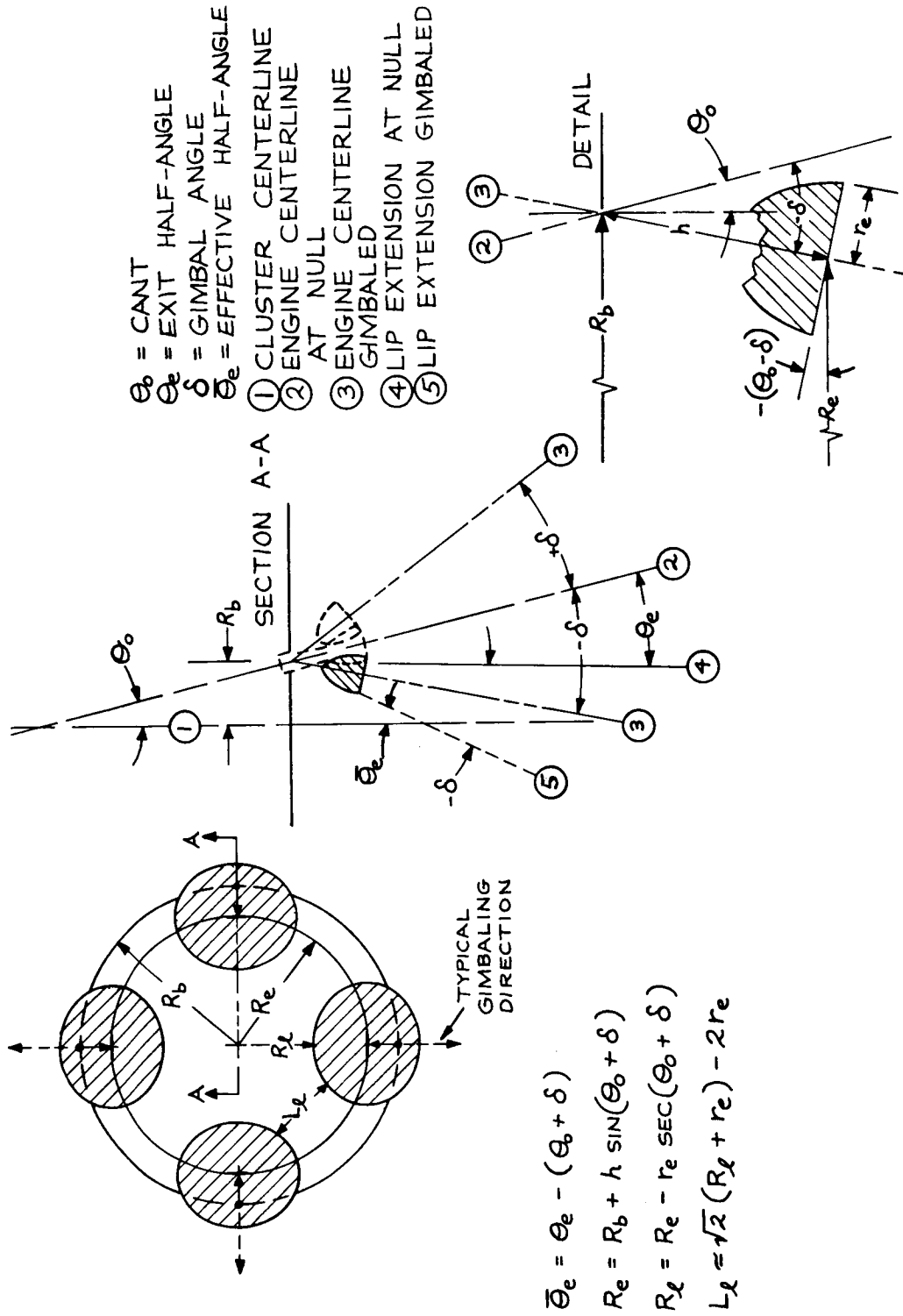


Figure 3-31. Base Heating Geometry

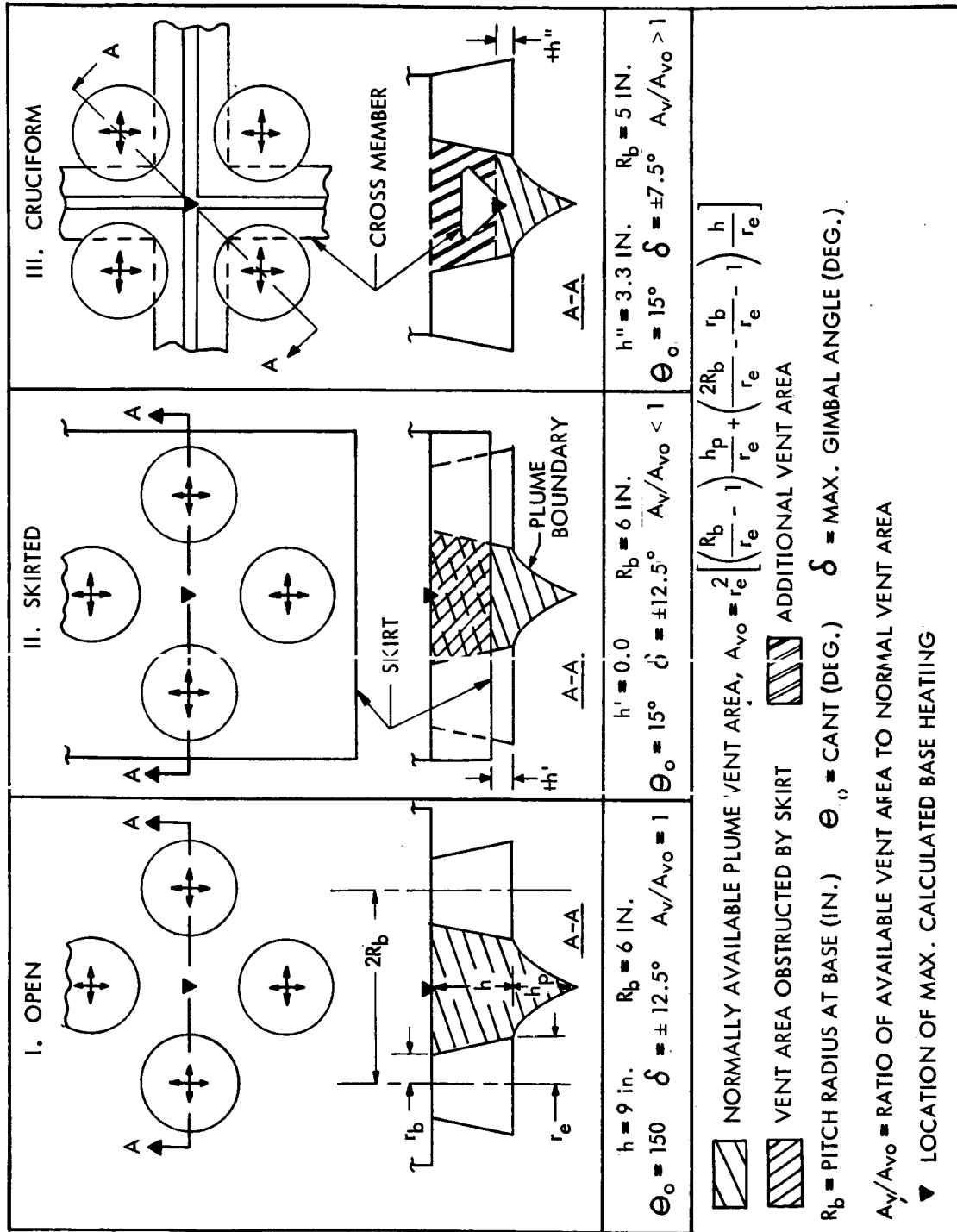


Figure 3-32. Base Bleeding Schematic Drawings

As shown in Figure 3-33, base heating is predicted to be less than  $0.4 \text{ Btu/ft}^2\text{-sec}$ . These rates are relatively low because of the engine area ratio and their outboard cant angle. However, they are not insignificant compared with other fluxes in the total thermal environment.

The translating thrust vector control (i. e., sliding plate) configuration was not considered in this study. However, it can be surmised from the Figure 3-33 data that, with four engines on a 5-inch radius pitch circle, this configuration would have higher base heating rates. This is because the engines are fixed, normal to the base area; and the effective half-angle ( $\bar{\theta}_e$ ) is equivalent to the engine exit half-angle ( $\bar{\theta}_e = 8.3$  degrees). Thus, plume impingement angles would be higher in the sliding plate configuration than any for which heating was calculated.

Thermal protection system requirements in the vicinity of the engines can be compared using total in-flight heating environment composed of (1) base flow heating, (2) radiation heating from the engine nozzles — expected to be on the order of  $2.0 \text{ Btu/ft}^2\text{-sec}$  based on Apollo SM RCS engine analyses, (3) plume convective heating — appreciable only in configurations where the engine exit plane is above nearby structure, and (4) solar and lunar surface heating. Of those configurations considered during the LFV study, the cruciform configuration seems to be best from the thermal viewpoint concerning engine placement: reradiation relief is improved, direct plume impingement is eliminated, and inter-engine thermal problems are minimized.

## PLUME HEATING

Plume heating thermal protection analyses were carried out on a number of configurations prior to the final choice of the cruciform configuration III of Figure 3-32. The use of the cruciform essentially eliminates the plume impingement problem. The analyses shown here are given (1) to show the distinct advantages of the cruciform from the plume protection point of view and (2) to display the work carried out as required by the LFV work statement. The choice of corkboard as an ablator material was not upgraded further because the choice of the cruciform became obvious and further analysis was not required.

Results shown on Figure 3-34 are for a 0.050-inch thick aluminum plate protected with 0.1, 0.2, and 0.3 inch of corkboard ablator against a plume heating of  $1.5 \text{ Btu/ft}^2\text{-sec}$  for 217 seconds. This heating rate was extrapolated from Reference 3-26 data and represented an earlier (and rejected) configuration as shown in Configuration II of Figure 3-32. Interpolating from this plot, 0.22 inch of corkboard is required to prevent the plate from exceeding a 100 F temperature rise (150 F initial to 250 F aluminum limit) during the inboard leg of one LFV sortie. To this thickness



SYMBOL	CONFIGURATION	GIMBAL ANGLE (DEG.)		EFFECTIVE HALF-ANGLE, $\theta_e$ (DEG.)
		$\delta$	$\delta'$	
□	OPEN	-7.7 <sup>(1)</sup>	-	1.0
▽		-12.5	-	5.8
○	SKIRTED	-12.5	-	5.8
◇		-7.7	-	1.0
◇	CRUCIFORM	-7.5	-10.6 <sup>(2)</sup>	3.9
◇		-5.4	-7.7	1.0
◆		0	0	-6.7 <sup>(3)</sup>

NEGATIVE VALUES INDICATE: (1) GIMBAL ANGLE TOWARD LFV CENTERLINE IN ONE PLANE PER ENGINE, (2) GIMBAL ANGLE TOWARD LFV CENTERLINE RESULTING FROM  $\delta$  MOVEMENT IN EACH OF TWO PERPENDICULAR PLANES PER ENGINE, (3) DIVERGENCE OF LIP EXTENSION LINE FROM LFV CENTERLINE.

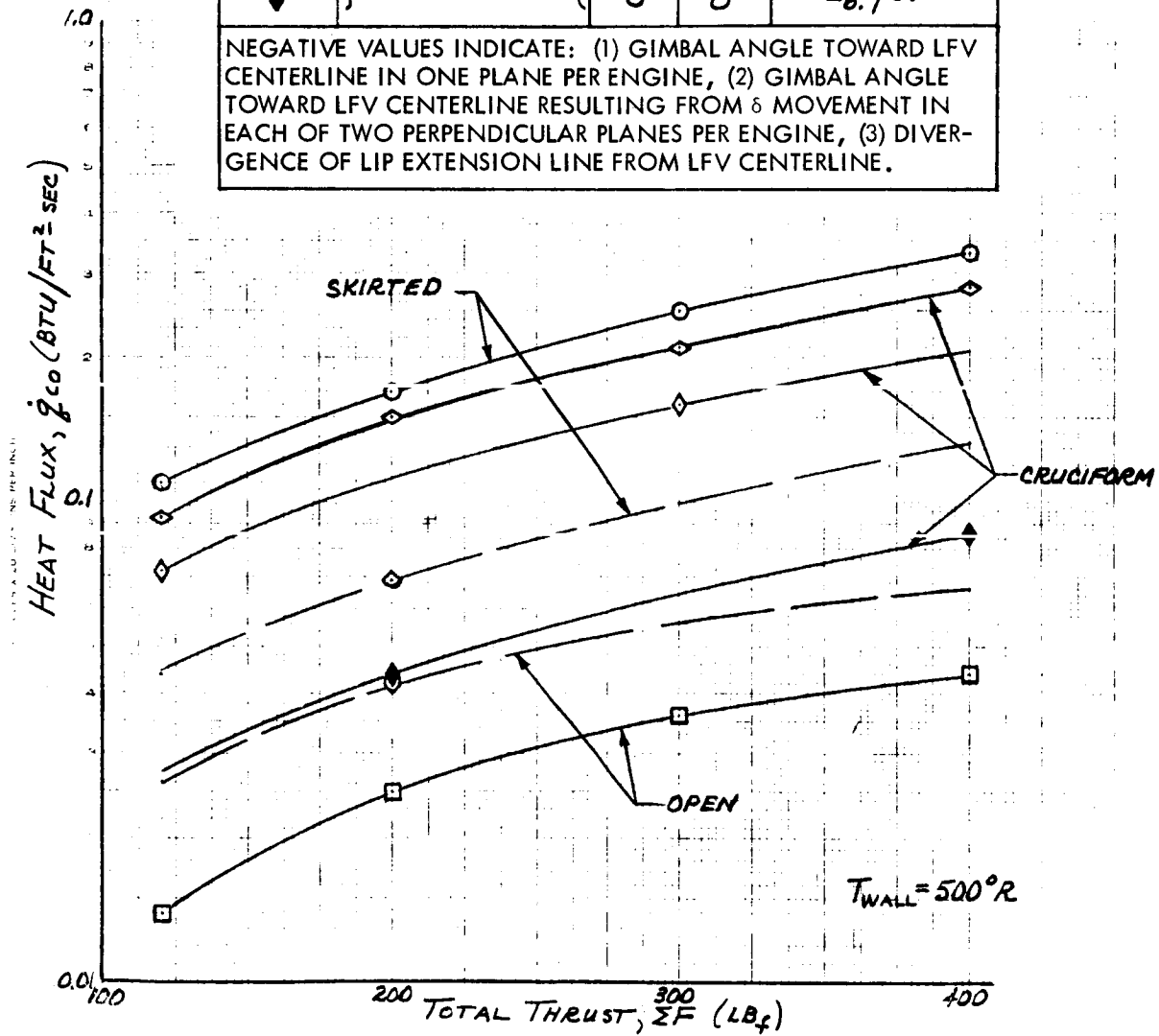
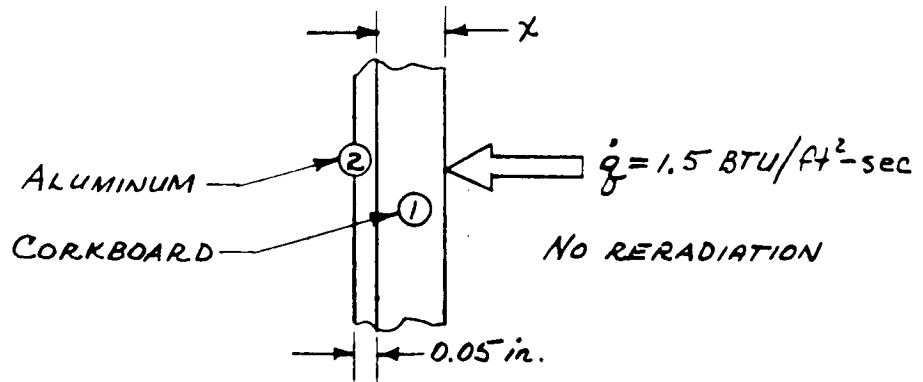


Figure 3-33. Base Heating Results



DENSITY ( $\rho$ ),  $lb_m/ft^3$

$\rho_1 = 30.5$   $\rho_2 = 172.$

SPECIFIC HEAT ( $C_p$ ),  $BTU/lb_m-^{\circ}F$

$C_{p1} = 0.47$   $C_{p2} = 0.22$

THERMAL CONDUCTIVITY ( $k$ ),  $BTU/hr-ft-^{\circ}F$

$k_1 = 0.047$   $k_2 = 109.$

$$\text{STEADY STATE RECESSION RATE } (\dot{s}_1) = \frac{\dot{q}}{\rho_1 q_i^*}$$

$$= 4.54 \times 10^{-4} \text{ in./sec.}$$

WHERE EFFECTIVE HEAT OF ABLATION ( $q_i^*$ ) = 1300  $BTU/lb_m$

STEADY STATE ABLATION TEMPERATURE ( $T_{a1}$ ) = 1000 $^{\circ}R$

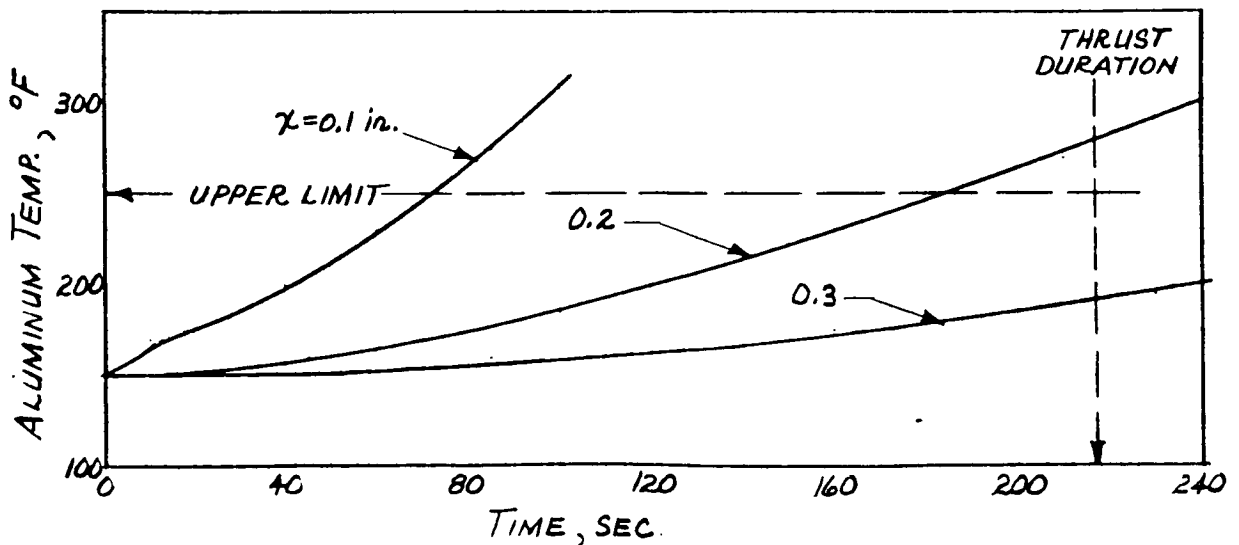


Figure 3-34. Structural Ablator Protection

must be added 0.10 inch of corkboard to offset the design surface recession rate(s) of  $4.54 \times 10^{-4}$  in./sec during the outboard leg. The sum, 0.32 inch of ablator, is required for one sortie. The RFP calls for an LFV capable of 30 sorties. Hence, the options appear to be (1) change aluminum to a material having a higher temperature limit, (2) add thermal capacitance (i. e., weight) to the plate, (3) use a reradiation type heat shield (e. g., polished nickel shield backed with insulation), (4) investigate reusable heat shields having very low recession rates, (5) use cork ablator because of its desirable qualities of low cost, ease of application, low density, etc., but replace after several sorties, (6) use interregenerative engines with lower nozzle temperatures, or (7) open up the structure around the engines to lower radiative and plume heating and increase reradiation relief. Alternative 7 was chosen as a result of selecting the cruciform configuration.

## DESIGN IMPLICATIONS

Program experience in previous successful spacecraft systems shows that a working set of component temperature limits based on current state of the art is required as a design tool. This set of temperature limits was prepared as shown in Table 3-1.

Perhaps the main thermal protection item will be the propellant tanks. The key design points are summarized as follows:

1. Nominal dawn mission - a coating with an  $\alpha_s/\epsilon$  of about 0.30 will be adequate.
2. All possible morning missions - an external surface with  $\alpha_s/\epsilon = 0.10$  may be required.
3. Earthshine missions (including late afternoon) - heaters will be required. The choices of heater (battery) and insulation thickness are summarized in Figure 3-20.
4. Lunar day storage - no thermal problems because of the high temperature limits on the empty tanks.

Engine and propellant feedlines will require that heaters and connections to the on-board LFV battery be installed for contingency only. A power requirement of 10 watts per engine for steady-state operation has been calculated.

For the landing system attenuators, a coating with an  $\alpha_s/\epsilon \cong 0.30$  is adequate to maintain temperatures within operating limits during the nominal dawn mission (Figure 3-26).

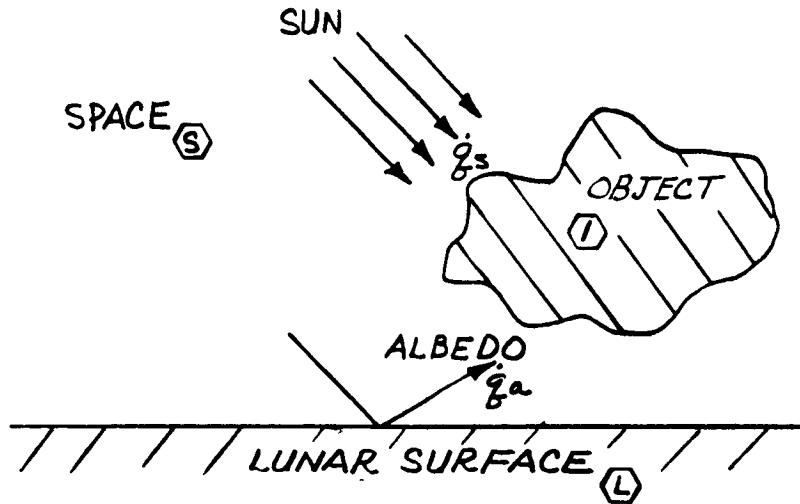
The attenuators remain below their maximum storage temperature of 195 F at lunar noon. Radiation of heat from the engines to the attenuators is not expected to put the attenuators over their upper temperature limit. The low-temperature problems of the attenuator may be important but will require design details beyond the scope of this study.

Analysis of clustering of engines has shown that this will not be a problem. Even with the worst-case configurations, the upper limit temperature of 1900 F is not exceeded.

Base heating studies were completed for open and skirted configurations and for a cruciform structure, the final design choice. The calculated heating rates were quite low, less than 0.4 Btu/ft<sup>2</sup>-sec for any case. Information is presented in Figure 3-33 which can be combined with more specific design and mission details and engine radiation to the cruciform, solar and lunar surface heating, and base flow heating to yield thermal protection requirements.

Although plume heating thermal protection requirements were calculated for a number of design candidates, the final choice of a cruciform structure essentially bypassed this problem.

APPENDIX E. STEADY-STATE TEMPERATURES OF SINGLE OBJECTS ON THE MOON



Heat balance on (1) :

$$\alpha_{s1} \dot{q}_s A_{p1} + \alpha_{s1} \dot{q}_a A_{t1} F_{1-L} - \sigma \epsilon_{1t1} A_{t1} F_{1-s} T_1^4 - \sigma \bar{\epsilon} A_{t1} F_{1-L} (T_1^4 - T_L^4) = 0$$

with  $\dot{q}_a = a \dot{q}_s$  and assuming  $\epsilon = \epsilon_1 \epsilon_L$ ,

$$\alpha_{s1} \dot{q}_s (A_{p1} + a F_{1-L} A_{t1}) - \sigma \epsilon_{1t1} A_{t1} F_{1-s} T_1^4 - \sigma \epsilon_1 \epsilon_L A_{t1} F_{1-L} (T_1^4 - T_L^4) = 0$$

Letting

$$X_i = \sigma T_i^4 = 0.1713 \times 10^{-8} (T_i^4) = 1713 (T_i/1000)^4 \text{ and}$$

$$\dot{q}_s = 442 \text{ Btu/ft}^2 \text{ - hr,}$$



$$X_1 = \frac{442 (\alpha_s / \epsilon)_1 \left[ \left( \frac{A_p}{A_t} \right)_1 + aF_{1-L} \right] + \frac{\epsilon_L F_{1-L} X_L}{F_{1-s} + \epsilon_L F_{1-L}}}{F_{1-s} + \epsilon_L F_{1-L}}$$

assuming  $\epsilon_L = 1.00$  and remembering  $F_{1-s} + F_{1-L} = 1.00$ ,

$$T_1 = 155.4 \left\{ 442 (\alpha_s / \epsilon)_1 \left[ \left( \frac{A_p}{A_t} \right)_1 + aF_{1-L} \right] + F_{1-L} X_L \right\}^{0.25}$$

Nomenclature:

$a$  = Lunar surface total albedo

$A_p$  = Projected area

$A_t$  = Total surface area

$F$  = Black body view factor based on total area

$T$  = Absolute temperature

$X_L$  = Lunar surface temperature function

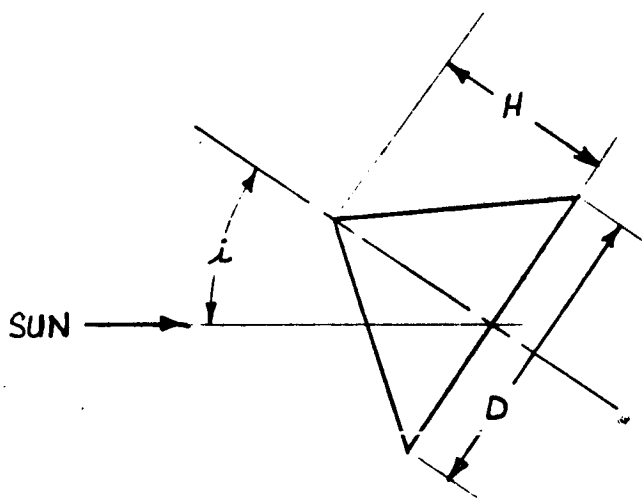
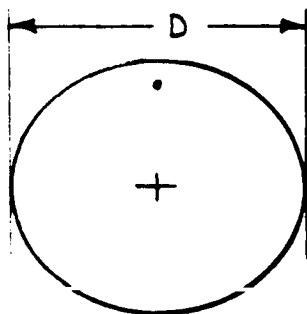
$\alpha_s$  = Solar absorptivity

$\epsilon$  = Total hemispherical emissivity

APPENDIX F.  $A_p/A_s$  FOR LATERAL SURFACE OF A RIGHT CONE

CONDITION 1

When  $i \leq \tan^{-1} \left[ \frac{1}{2 (H/D)} \right]$ ,



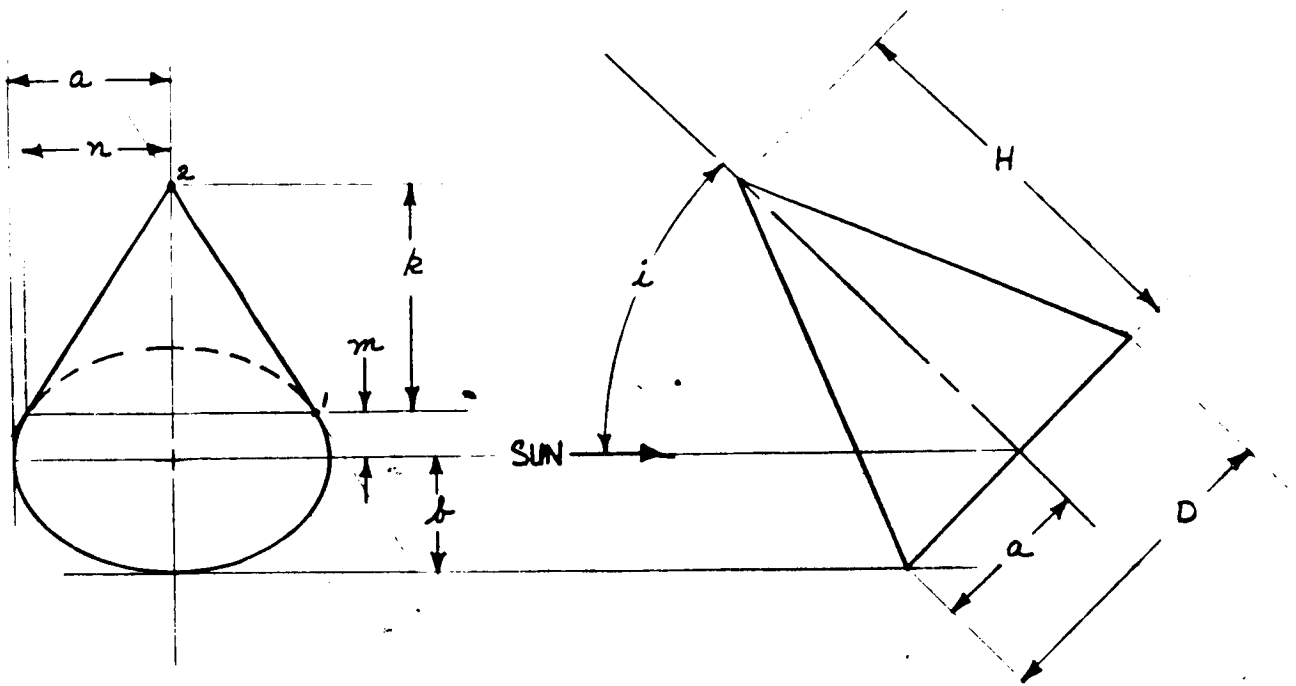
$$A_p = A_{\text{ellipse}} = \pi \left( \frac{D}{2} \right) \left( \frac{D}{2} \cos i \right) = \pi (D/2)^2 \cos i$$

$$A_s = A_{\text{cone}} = \frac{\pi D}{2} \left[ \left( \frac{D}{2} \right)^2 + H^2 \right]^{1/2} = \pi (D/2)^2 \left[ 1 + 4(H/D)^2 \right]^{1/2}$$

$$\therefore \left( \frac{A_p}{A_s} \right) = \frac{\cos i}{\left[ 1 + 4(H/D)^2 \right]^{1/2}}$$

CONDITION 2

When  $\tan^{-1} \left[ \frac{1}{2 (H/D)} \right] < i < 90$  degrees,



$$a = D/2$$

$$b = (D/2) \cos i$$

$$ab = (D/2)^2 \cos i$$

$$\frac{a}{b} = \frac{(D/2)}{(D/2) \cos i}$$

From the equation of a line tangent to the ellipse,

$$\frac{x_2 x_1}{a^2} + \frac{y_2 y_1}{b^2} = 1$$

$$y_1 = \frac{a^2 b^2 - b^2 x_2 x_1}{a y_2}$$

But  $x_a = 0$  and  $y_2 = k + m = H \sin i$



$$y_1 = m = \frac{b^2}{y_2} = \frac{(D/2)^2 \cos^2 i}{H \sin i} = \frac{(D/2)^2 \cos i}{H \tan i} = \frac{(D/4) \cos i}{(H/D) \tan i}$$

From the equation of the ellipse

$$\frac{x_1^2}{a^2} + \frac{y_1^2}{b^2} = 1$$

$$\begin{aligned} x_1^2 &= a^2 - \left(\frac{a}{b}\right)^2 y_1^2 = \left(\frac{D}{2}\right)^2 - \frac{1}{\cos^2 i} \frac{(D/4)^3 \cos^2 i}{(H/D)^2 \tan^2 i} \\ &= \left(\frac{D}{2}\right)^2 \left[ 1 - \frac{1}{4 (H/D)^2 \tan^2 i} \right] \end{aligned}$$

$$\begin{aligned} x_1 = n &= \left(\frac{D}{2}\right) \frac{1}{2 (H/D) \tan i} \left[ 4 (H/D)^2 \tan^2 i - 1 \right]^{1/2} \\ &= \frac{(D/4)}{(H/D) \tan i} \left[ 4 (H/D)^2 \tan^2 i - 1 \right]^{1/2} \end{aligned}$$

$$k = (k + m) - m = H \sin i - \frac{(D/4) \cos i}{(H/D) \tan i}$$

$$\frac{m}{b} = \frac{1}{(D/2) \cos i} \frac{(D/4) \cos i}{(H/D) \tan i} = \frac{1}{2 (H/D) \tan i}$$

$$A_p = \frac{1}{2} A_{\text{ellipse}} + A_{\text{ellipse segment}} + A_{\text{triangle}}$$

$$= \frac{\pi}{a} ab + \left[ mn + ab \sin^{-1} \left( \frac{m}{b} \right) \right] + \frac{1}{2} (2n) (k)$$

$$= ab \left[ \frac{\pi}{2} + \sin^{-1} \left( \frac{m}{b} \right) \right] + n (k + m)$$

$$= \left(\frac{D}{2}\right)^2 \cos i \left[ \frac{\pi}{2} + \sin^{-1} \left( \frac{1}{2 (H/D) \tan i} \right) \right] \\ + \frac{(D/4)}{(H/D) \tan i} \left[ 4 (H/D)^2 \tan^2 i - 1 \right]^{1/2} (H \sin i)$$

$$A_p = \left(\frac{D}{2}\right)^2 \cos i \left\{ \frac{\pi}{2} + \sin^{-1} \left[ \frac{1}{2 (H/D) \tan i} \right] \right. \\ \left. + \left[ 4 (H/D)^2 \tan^2 i - 1 \right]^{1/2} \right\}$$

$$\left(\frac{A_p}{A_s}\right) = \frac{\cos i \left\{ \frac{\pi}{2} + \sin^{-1} \left[ \frac{1}{2 (H/D) \tan i} \right] + \left[ 4 (H/D)^2 \tan^2 i - 1 \right]^{1/2} \right\}}{\pi \left[ 1 + 4 (H/D)^2 \right]^{1/2}}$$

### CONDITION 3

When  $i = 90$  degrees, since

$$\sin^{-1} x = \tan^{-1} \left[ \frac{x}{\sqrt{1-x^2}} \right],$$

the aforementioned equation for  $A_p/A_s$  becomes

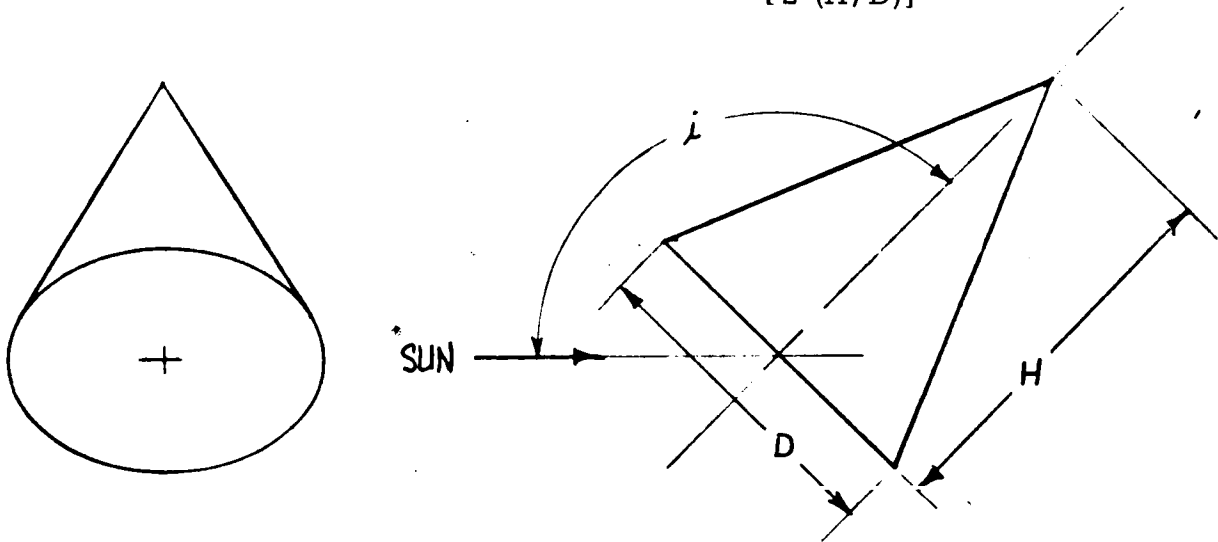
$$\left(\frac{A_p}{A_s}\right) = \frac{\left[ \frac{\pi + 2 \tan^{-1} \left\{ \frac{1}{\left[ 4(H/D)^2 - \frac{1}{\tan^2 i} \right]^{1/2} \tan i} \right\}}{2\pi} \right] \cos i + \frac{1}{\pi} \left[ 4(H/D)^2 - \frac{1}{\tan^2 i} \right]^{1/2} \sin i}{\left[ 1 + 4 (H/D)^2 \right]^{1/2}}$$

which, when  $i = 90$  degrees, reduces to

$$\left(\frac{A_p}{A_s}\right) = \frac{2 (H/D)}{\pi \left[1 + 4 (H/D)^2\right]^{1/2}} = \frac{A_{\text{triangle}}}{A_s}$$

CONDITION 4

When  $90 \text{ degrees} < i < 180 \text{ degrees} - \tan^{-1} \left[ \frac{1}{2 (H/D)} \right]$



In the same manner as used in Condition 2,

$$A_p = A_{\text{ellipse segment}} + A_{\text{triangle}} - \frac{1}{2} A_{\text{ellipse}}$$

$$\left(\frac{A_p}{A_s}\right) = \frac{\cos i \left\{ \frac{\pi}{2} - \sin^{-1} \left[ -\frac{1}{2 (H/D) \tan i} \right] - \left[ 4 (H/D)^2 \tan^2 i - 1 \right]^{1/2} \right\}}{\pi \left[ 1 + 4 (H/D)^2 \right]^{1/2}}$$

In terms of arc tan instead of arc sin,

$$\left(\frac{A_p}{A_s}\right) = \frac{- \left[ \frac{\pi - 2 \tan^{-1} \left\{ \frac{1}{\left[ 4(H/D)^2 - \frac{1}{\tan^2 i} \right]^{1/2}} \right\} \tan i}{2\pi} \right] \cos i + \frac{1}{\pi} \left[ 4(H/D)^2 - \frac{1}{\tan^2 i} \right]^{1/2} \sin i}{\left[ 1 + 4(H/D)^2 \right]^{1/2}}$$

CONDITION 5

When  $i \geq 180$  degrees -  $\tan^{-1} \left[ \frac{1}{2(H/D)} \right]$ ,

$$\left(\frac{A_p}{A_s}\right) = 0$$

## REFERENCES

- 1-1. Hydrodynamic Stability of Capillary Barriers for Spacecraft Propellant Position Control. North American Rockwell Space Division Report SID 66-1087 (August 1966).
- 1-2. Mears, R. B. Evaluation of Positive Expulsion Devices for Upper Stage Vehicles. CPIA No. 176, Vol. I, USAF-RPL (October 1968).
- 1-3. AAP Study - Utilization of LM for Advanced Applications, Final Report on Tasks Terminated During November 1967. Contract NAS9-6608, Supplement No. 1. Grumman Aircraft Engineering Corporation Report ARP 325-3 (December 15, 1967).
- 1-4. Jacquer, I. Comparative Reliability Analysis of Propellant Module Interconnect Concepts. North American Rockwell Space Division Apollo Applications Program Design Data Sheet DDS-D/A-03/9-003 (March 6, 1969).
- 1-5. Space Engine Design Handbook. North American Rockwell Rocketdyne Division Report R-8000P-1.
- 2-1. McRuer, D. T. and E. S. Krendel. Dynamic Response of Human Operators, WADC TR 56-524, Wright Patterson AFB, Ohio (October 1957).
- 2-2. McRuer, D. T., Ashekas, I. L., and C. L. Guerre. A Systems Analysis View of Longitudinal Flying Qualities, WADD TR 60-43, Wright-Patterson AFB, Ohio (January 1960).
- 2-3. Cooper, G. E. Understanding and Interpreting Pilot Opinion, Aeronautical Engineering Review, Vol. 16, No. 3, pp 47-52 (March 1957).
- 2-4. AIAA Professional Study Series. Pilot Dynamics and Aircraft Handling Qualities (August 1968).
- 2-5. Bergeron, H. et al. Human Transfer Functions in Multi-Axis and Multi-Loop Control Systems, NASA, TN D 3305 (April 1966).

- 2-6. Bergeron, H., J. Adams. Measured Transfer Functions of Pilots During Two-Axis Tasks With Motion, NASA, TN D-2177 (March 1964).
- 2-7. Hands Free Precision Control for Small Hovering Vehicles - A Flying Qualities Study, Grumman Report RE-276, Bethpage, New York (January 1967).
- 2-8. Proposal For A One-Man Lunar Flying Vehicle Study, North American Rockwell Corporation, Space Division, SD 68-646 (23 August 1968).
- 3-1. R. E. Smith and D. K. Weidner, Space Environment Criteria Guidelines for Use in Space Vehicle Development (1968 Revision), NASA/MSFC, TM X-53798 (31 October 1968).
- 3-2. J. W. Lucas, et al. "Lunar Surface Temperatures and Thermal Characteristics," in Surveyor VI, A Preliminary Report, NASA, SP-166 (March 1968).
- 3-3. E. H. Christensen, Temperature Characteristics of the Lunar Surface - A Literature Survey and Analysis, Convair Div., General Dynamics Corp., A-PD-92 (22 May 1961).
- 3-4. J. C. Grafton and H. L. Nordwall, Radiation Heat Transfer Analysis for Space Vehicles, Aeronautical Systems Division, USAF, ASD TR 61-119 (Part II), 1 April 1962.
- 3-5. A. S. Adorjen, "Temperature Distribution in Shadowed Lunar Craters," pre-print 69-595, presented AIAA 4th Thermophysics Conference, San Francisco, Calif., 16 June 1969.
- 3-6. R. U. Sexl, et al., "A Crater Model for Lunar Thermal Radiation," pre-print 69-598, presented AIAA 4th Thermophysics Conference, San Francisco, Calif., 16 June 1969.
- 3-7. J. M. Szari and R. W. Shorthill, Isothermal and Isophotic Atlas of the Moon, NASA, CR-855, September 1967.
- 3-8. C. G. Montgomery, et al. Directional Characteristics of Lunar Thermal Emission, Research Laboratories, Brown Engineering Company, Huntsville, Alabama, TN R-213, August 1966.
- 3-9. Personal Communication with R. R. Garipay, Hughes Aircraft Company, April 1969.

- 3-10. Proposal for a One-Man Lunar Flying Vehicle Study, North American Rockwell Corporation, Space Division, SD 68-646 (28 August 1968).
- 3-11. Personal Communications with R. R. Watanabe, NR/SD, D/190-204 and R. R. Garipay, Hughes Aircraft Company.
- 3-12. J. P. Millard, "Results from the Thermal Control Coatings Experiment on OSO-III," paper 68-794, presented AIAA 3rd Thermophysics Conference, Los Angeles, California, June 1968.
- 3-13. S. J. Babjak, et al., Planetary Vehicle Thermal Insulation Systems, Missile and Space Div., General Electric Corp., DIN: 68SD4266 (3 June 1968).
- 3-14. A. D. Kazanowski, NR/SD, D/093-500, "Timeline of a 3-day Dawn Mission with Only One LFV," 10 March 1969.
- 3-15. A. D. Kazanowski, NR/SD, D/093-500, "3-Day Lunar Sunset Mission Timeline," 10 February 1969.
- 3-16. "One Man Lunar Flying Vehicle," Exhibit A (Work Statement), NASA/MSC, 18 June 1969.
- 3-17. Personal Communication with R. E. Domshy, NR/SD, D/190-400, March 1969.
- 3-18. J. C. Ballinger and E. H. Christensen, Environmental Control Study of Space Vehicles, Part III: "Thermal Control Techniques and Systems" Convair Division, General Dynamics Corp., ERR-AN-051 (31 December 1960).
- 3-19. J. P. Millard, "Results from the Thermal Control Coatings Experiment on OSO-III," paper 68-794, presented AIAA 3rd Thermophysics Conference, Los Angeles, Calif. (June 1968).
- 3-20. CONFAC II computer program.
- 3-21. Roote, J. F., "Design Study for Precision Control Rocket Engines of 400-2200 Pounds Thrust," the Marquardt Corp., Report S-926, March 1969.
- 3-22. F. G. Etheridge, Attitude Control Rocket Exhaust Plume Study, Space Division, North American Rockwell Corporation, SD 68-1054 (December 1968).



- 3-23. IL from A. Africano to A. D. Kazanowski, dated February 14, 1969, subject "Soil Erosion Studies (Task 1.2.2)," reference 190-400-APT69-021.
- 3-24. Personal Communications with D. L. Jones, D/190-400, May 1969.
- 3-25. E. P. French and K. D. Korkan, Quantitative Models of Base Flow for Multiple Engine Vehicles, Space Division, North American Rockwell Corporation, SD 68-759 (December 1968).
- 3-26. E. T. Piesik, R. R. Koppang, D. J. Simkin, "Rocket Exhaust Impingement on a Flat Plate at High Vacuum," J. Spacecraft and Rockets 3, No. 11, page 1650 (November 1966).